Crustal structure, gravity anomalies and subsidence history of the Parnaíba cratonic basin, Northeast Brazil

A thesis submitted for the degree of Doctor of Philosophy

Brook J Tozer
Wolfson College



Supervised by:
Prof. A.B. Watts, FRS
Dr. M.C. Daly
Department of Earth Sciences
University of Oxford

Trinity 2017

This thesis is dedicated to my Mum and Dad —
Thank you for everything.

Crustal structure, gravity anomalies and subsidence history of the Parnaíba cratonic basin, Northeast Brazil

A thesis submitted for the degree of Doctor of Philosophy

Brook J Tozer
Wolfson College

Trinity 2017

Abstract

Cratonic basins cover more than 10% of Earth's continental surface area, yet their origin remains enigmatic. In this thesis a suite of new and legacy geophysical and geological data are integrated to constrain the origin of the Parnaíba basin, a cratonic basin in Northeast Brazil. These data include a 1400 km long, deep (20 s two-way travel time) seismic reflection profile, five $\pm$ 110 km offset wide-angle split-spread receiver gathers, gravity anomaly, and well data.

In the centre of the basin, the depth to pre-Paleozoic basement is $\sim$ 3.3 km, a zone of midcrustal reflectivity (MCR) can be traced laterally for $\sim$ 250 km at depths between 17–25 km and Moho depth is $\sim$ 42 $\pm$ 2 km. Gravity and P-wave modelling suggests that the MCR represents the upper surface of a high density (2985 $kg\ m^3$) and V_p (6.75–7.0 $km\ s^{-1}$) lower crustal body, likely of magmatic origin. Backstripping of well data shows a concave up decreasing tectonic subsidence, similar in form to that commonly observed in rift-type basins. It is shown, however, that the seismic and gravity data are inconsistent with an extensional origin. It is shown that an intrusive body in the lower crust that has loaded and flexed the surface of the crust, combined with sediment loading, provides a satisfactory fit to the observed gravity anomaly, sediment thickness and basin shape. A buried load model is also consistent with seismic data, which suggest that the Moho is as deep or deeper beneath the basin centre than its flanks and accounts for at least part of the tectonic subsidence through a viscoelastic stress relaxation that occurs in the lithosphere following load emplacement.

Comparative analysis of the Michigan and Congo basins shows gravity data from these basins is also consistent with a lower crustal mass excess, while subsidence analysis shows viscoelastic stress relaxation may also contribute to their early subsidence histories. However,

unlike Parnaíba, both of these basins appear to have been subjected to secondary tectonic processes that obscure the primary 'cratonic basin' subsidence signals. Parnaíba basin, therefore, offers an excellent record for the investigation of cratonic basin formation.

Crustal structure, gravity anomalies and subsidence history of the Parnaíba cratonic basin, Northeast Brazil

A thesis submitted for the degree of Doctor of Philosophy

Brook J Tozer
Wolfson College

Trinity 2017

Extended Abstract

Cratonic sedimentary basins occupy greater than 10 % of the Earth's continental surface area, yet despite over fifty years of investigation, their tectonic origin remains enigmatic. In this thesis, a suite of new geophysical and geological data is analysed and integrated to elucidate the origin of the Parnaíba cratonic basin of Northeast Brazil. This analysis is then extended to two further cratonic basins, the Congo basin of Central Africa and the Michigan basin of North America, to compare and contrast results and assess whether generic conclusions regarding the formation of cratonic basins can be drawn.

Numbering > 20 worldwide, cratonic basins have typical areal extents on the order of a few hundred thousand to a few million square kilometres. They are usually infilled by 3–6 km of mostly subaerial, estuarine and lacustrine, marginal and shallow-marine sediments that young towards their centre and display simple bowl-shaped geometries with minimal internal deformation. Sediment accumulation rates are slow in comparison to rift, foreland and strike-slip type basins (of the order of meters to tens of meters per million years) and their tectonic subsidence spans extended periods of geological time, often on the order of several hundreds of million years.

Many previous studies investigating the origins of cratonic basins have focused on developing theoretical models that are capable of explaining their characteristic slow and long-lived subsidence. From these studies, a wide-range of geodynamic scenarios have been postulated and the main processes invoked can be categorised as follows: (1) Thermal subsidence following lithosphere extension, thinning and cooling; lithospheric accretion and cooling above a

subduction mantle wedge; or erosion, thinning and cooling following lithospheric thickening. (2) Lithospheric folding caused by far-field in-plane stresses. (3) The isostatic response to dense loads produced by metamorphic phase changes or cooling of igneous intrusions within the lower crust and/or mantle lithosphere. (4) Dynamic topography driven by large scale mantle convection or isolated convective instabilities. Some authors have proposed models in which a combination of two or more of these processes act together, or at different times during basin evolution. For example, extension coupled with buried loading, buried loading and in-plane stress variations, extension and dynamic topography.

Most of these models would be expected to produce identifiable geological structures as well as distinct crustal structure and gravity anomalies. For example, recent studies have proposed that low strain rate lithospheric extension, is the primary mechanism responsible for cratonic basin formation. In this case, beta factors (i.e., the ratio of pre- to post-stretched lithospheric thickness) are small (e.g., 1.2). Nonetheless, a crustal thinning of $\sim 6\ km$ beneath the basin would be expected; a thinning that should be detectable using geophysical methods. However, a lack of relevant data pertaining to the crustal and lithospheric structure beneath cratonic basins has limited our ability to constrain, compare and contrast model predictions with observations.

In light of this data gap, an observational approach is adopted in this study. The initial analysis is focused on constraining present day sedimentary and crustal structure of Parnaíba basin and its subsidence history in both space and time. These observations are then used to constrain and test models of basin formation.

Sedimentary basin and crustal structure are firstly investigated using active source seismic data. Analysis is principally focused on an approximately east–west $\sim 1400\ km$ two-dimensional regional profile. This spans the full width of the basin, from the Amazonian craton in the west to the Neoproterozoic Borborema Province in the east. The profile is constrained using a crustal scale, vertical-incident seismic reflection profile and an auxiliary wide-angle reflection/refraction dataset, consisting of five receiver gathers located in the centre of the profile, which recorded arrivals at offsets of up to $\pm 110\ km$. Both datasets were acquired using a four-truck, low frequency vibroseis source (6–60 Hz and 4–32 Hz respectively)

and were recorded to 20 seconds two-way-travel-time (TWTT).

Depth migrated seismic reflection data suggest the maximum depth to pre-Paleozoic basement is $\sim 3.3\ km$ near the centre of the basin. There is little evidence for extensional strain within the sedimentary basin or basement, with no appreciable normal faults observed and no central rift graben imaged in the basement. A zone of Mid-Crustal Reflectivity (MCR) can be traced laterally for $\sim 250\ km$ at depths between 17–25 km beneath the basin's centre. Moho is well imaged below the basins eastern and western margins but is unresolved beneath much of the central basin. In the east, the crust is characterised by crustal scale reflection events that dip eastward at $\sim$ 20–30°, interpreted as crustal scale shear zones. The Moho deepens from $\sim 35\ km$ at the edge of the profile to $\sim 44\ km$ depth, 150 km basinward of the basins edge. Here, an abrupt termination of reflections marks a steep terrane boundary related to the continental scale Trans-Brasiliano Shear Zone, which separates the Borborema Province and Parnaíba Block crustal terranes. In the west, the Moho is resolved at $\sim$ 40–42 km depth beneath the Amazonian craton. This deepens to $\sim 44\ km$ beneath the basin margin, where again, reflectively abruptly terminates, likely across a terrane boundary between the allochthonous Araguaia Group (overthrust upon the Amazionian craton) and Parnaíba Block to the east.

Forward modelling of P-wave (V_p) phase arrivals recorded on a suite of five receiver gathers in the basin centre, suggests V_p in the upper crust is relatively low (6–6.15 $km\ s^{-1}$) with respect to values for cratons globally. A prominent wide-angle reflection phase at $\sim$ 8 s TWTT (zero offset), is consistent with the MCR observed on normal incident reflection data. At far offsets ($> 70\ km$) a linear arrival occurs above this reflection and is interpreted as a refraction from the MCR region. Below the MCR, at offsets $< \pm\ 40\ km$, a zone of anastomosing reflectively occurs down to $\sim$ 15 s TWTT (zero offset). The base of this reflectively is interpreted as the reflection Moho. Monte Carlo modelling of these data suggest lower crustal Vp is high $\sim$ 6.75–7.0 $km\ s^{-1}$ and the depth to Moho is $\sim 42 \pm 2\ km$. These results are corroborated by a low-fold wide-angle stack of these receiver gathers.

These results from seismic analysis are used to constrain a two-dimensional crustal scale density model. This is based on terrestrial gravity measurements, acquired at a spacing of

$\sim$ 1–2 km, coincident to the regional reflection profile. This model was constructed using a Graphical User Interface (GUI) software package developed as part of this thesis. It is shown that, once the gravity effects of the sedimentary basin and Moho topography are accounted for, an additional mass excess is required to fit observations. A model in which the MCR represents the upper surface of a relatively high-density lower crust is capable of explaining this discrepancy. The required density contrast of +175 kg m^{-3} is suggestive of an intrusive magmatic origin, as the likely metamorphic phase change at these depths (gabbro to eclogite) would be expected to produce a much larger density contrast of $\sim$ 400 $kg\ m^{-3}$.

Gravity analysis is extended to three dimensions using the EGM2008 composite global gravity field model. These data were reduced to residual Bouguer anomalies, which reflect lithospheric anomalies, using a novel reduction procedure: firstly, standard Bouguer and terrain corrections were applied, followed by corrections for the gravitational contributions from the regional long wavelength field and basin sediment fill, as these are deemed unrelated to lithospheric density structure. Ensemble-averaged sampling of the residual Bouguer anomaly reveals the basin is characterised by a residual $\sim$ 30–40 mGal central high. We interpret this anomaly as originating from the dense lower crust inferred from two-dimensional modelling. Three-dimensional gravity and flexural modelling results reveal that a simple Gaussian-shaped body, with a density contrast of +175 $kg\ m^{-3}$ and maximum thickness of $\sim$ 15 km, emplaced on a plate with an effective elastic thickness (T_e) equal to 25 km, can explain the amplitude and first order shape of the residual gravity anomaly, as well as the thickness and shape of the sedimentary basin and Moho depth.

The temporal subsidence and uplift history of the basin is then investigated using data from forty-two exploration and fifty-four hydrology well records. These data include formation top depth records and a suite of petrophysical logs. Wells that reach basement were 'backstripped' using a one-dimensional Airy approach to remove the amplifying effects of sediment and water loading, revealing the temporal 'tectonic' subsidence signal. This reveals a concave up tectonic subsidence, similar in form to that observed in rift-type basins, with a maximum tectonic subsidence of $\sim$ 1.2 km near the basin centre. The subsidence predicted by a finite rifting model provides an excellent fit to these data, provided the rift duration is long ($\sim$ 65 Ma) and the beta factor is low (β=1.15). It is shown, however, that the three-dimensional morphology

of the basin depocenter through time, as well as our seismic and gravity data, are inconsistent with an extensional origin.

Three-dimensional flexural backstripping of sediment isopachs show the basin was characterised by a sub-circular shaped depocenter early in its evolution (i.e., the Silurian). This morphology appears to persist through to the Triassic, with the overall areal extent of the basin decreasing through time. This is significant as in rift basins, syn-rift sequences are normally deposited in localised narrow linear half-grabens, while only the later stage post-rift sequences form broad regional sags. Furthermore, assuming an initial crustal thickness of 35 km, the best-fit rifting model implies a Moho depth $\sim$ 30.5 km. This is far shallower than that derived from seismic data (42 $\pm$ 2 km). Moreover, Process Oriented Gravity Modelling (POGM) shows an extensional scenario produces a near zero gravity anomaly across the basin, irrespective of the assumed starting crustal thickness and T_e. Whereas, a model in which a +175 $kg\ m^{-3}$ load is emplaced within the lower crust, produces a regional long wavelength negative anomaly of $\sim$ -30 to -50 $mGal$ across the basin, similar (to first order) to the observed anomaly.

The tectonic subsidence predicted for a buried load model is tested using a viscoelastic plate model, defined using a simple three-layered continental viscosity structure. It is found that for a realistic viscosity structure, consisting of an upper 0–50 km, essentially elastic 10^{30} $Pa\ s$ layer; a middle 50–75 km 10^{27} $Pa\ s$ layer; and a lower 75–300 km 10^{24} $Pa\ s$ layer, that the response to the emplacement of an axially symmetric load (estimated from geophysical modelling results), can account for the long-lived, concave up tectonic subsidence signal. This occurs due to a viscoelastic stress relaxation in the lithosphere following load emplacement. However, the initial (elastic) subsidence occurs more rapidly than is observed. This may reflect the instantaneous nature of loading used in the model and suggests that temporal changes in load size (i.e., a finite load growth) during the first few million years of loading, may play an important role in modulating the early subsidence response.

Finally, analysis is extended to the Michigan and Congo basins to test the generality of results deduced from the Parnaíba investigation. It is found from gravity analysis, that both Michigan and Congo are also characterised by residual Bouguer anomaly highs in their centre

of up to 40–60 *mGal*. Airy and flexural backstripping reveal, however, that the subsidence records of these basins are more greatly affected by secondary processes, such as dynamic topography, than Parnaíba. Nevertheless, flexural backstripping shows Michigan basin is also characterised by sub-circular morphology during its early subsidence, while seismic reflection profiles do not show any evidence of extensional tectonics. Furthermore, their initial backstripped subsidence profiles appear consistent with subsidence predicted by a viscoelastic response to load emplacement.

Contents

Abstract i

Extended Abstract iii

Table of Contents ix

List of Figures xv

List of Tables xix

Acknowledgements xxi

1 Introduction 1
- 1.1 Isostasy . . . 3
  - 1.1.1 "Local" isostatic compensation models . . . 4
  - 1.1.2 Airy isostasy . . . 5
  - 1.1.3 Pratt isostasy . . . 5
  - 1.1.4 "Regional" isosatic compensation models . . . 6
    - 1.1.4.1 The elastic plate model, flexure and T_e . . . 7
    - 1.1.4.2 Viscoelastic plate model . . . 8
- 1.2 The lithosphere . . . 10
- 1.3 Sedimentary basin formation . . . 11
  - 1.3.1 Extensional basins . . . 12
  - 1.3.2 Foreland basins . . . 13
- 1.4 Cratonic basins . . . 14
  - 1.4.1 Basin geometry . . . 14
  - 1.4.2 Stratigraphy . . . 14
  - 1.4.3 Subsidence style . . . 15
  - 1.4.4 Plate setting and initiation timing . . . 16
  - 1.4.5 Cratonic basin crustal structure . . . 16
  - 1.4.6 Summary of cratonic basin characteristics . . . 17
- 1.5 Proposed mechanisms for cratonic basin formation . . . 19
  - 1.5.1 Early models of cratonic basin formation . . . 23
  - 1.5.2 Buried loading . . . 24
    - 1.5.2.1 Buried loading: lower crust . . . 24
    - 1.5.2.2 Buried loading: mantle lithosphere . . . 25
  - 1.5.3 In-plane compression and lithospheric folding . . . 25
  - 1.5.4 Dynamic topography . . . 26
  - 1.5.5 Low strain rate extension . . . 27
  - 1.5.6 Lithospheric accretion and thermal cooling . . . 28

1.5.7 Lithospheric thickening, radiogenic heating and instantaneous erosion 29
1.6 Thesis objectives, scope and research approach . . . 32
1.7 Thesis outline . . . 33
1.8 Relationship to published work . . . 35

2 Parnaíba basin geological setting 37
2.1 Introduction . . . 37
2.2 Neoproterozoic/Cambrian tectonic evolution of Northeast Brazil . . . 39
2.2.1 The Parnaíba Block . . . 40
2.2.2 800-500 Ma: The Brasiliano/Pan-African Orogeny and amalgamation of West Gondwana . . . 42
2.2.3 The Northern Brasilia belt, Amazonian and São Francisco cratons . . . 46
2.2.4 Borborema Province . . . 48
2.2.4.1 Borborema Province collision I . . . 49
2.2.4.2 Borborema Province collision II . . . 49
2.2.5 The Gurupi Belt and São Luiz Craton . . . 50
2.2.5.1 Araguaia Belt Amazonian Craton . . . 50
2.3 Parnaíba basin stratigraphy . . . 51
2.3.1 TS-1: Riachão basin . . . 51
2.3.2 TS-2: Jaibaras basin . . . 52
2.3.3 Triassic Volcanism . . . 52
2.3.4 TS-4: Mearim basin . . . 55
2.3.5 Cretaceous Volcanism . . . 56
2.3.6 TS-5: Grajaú basin . . . 57
2.4 TS-3: The Parnaíba cratonic basin . . . 58
2.4.0.1 Serra Grande Megasequence . . . 58
2.4.0.2 Canindé Megasequence . . . 61
2.4.0.3 Balsas Megasequence . . . 63
2.5 Summary of previous work in Parnaíba basin . . . 64
2.6 Summary . . . 65

3 Seismic imaging of Parnaíba sedimentary basin and crustal structure 67
3.1 Introduction . . . 67
3.2 Seismic reflection analysis . . . 68
3.2.1 Seismic reflection data . . . 68
3.2.2 Seismic Attributes . . . 69
3.2.2.1 Instantaneous amplitude (reflectivity strength) . . . 70
3.2.2.2 Amplitude Volume . . . 70
3.2.3 Parnaíba sedimentary basin seismic reflection structure . . . 71
3.2.3.1 Seismic basement . . . 73
3.2.3.2 Basin structure . . . 74
3.2.3.3 Basin edges and stratigraphic younging . . . 76
3.2.4 Pre-Silurian sediments . . . 80
3.2.4.1 Jaibaras basin: Rift or pull-apart? . . . 80
3.2.4.2 Riachão basin . . . 81
3.2.5 Regional crustal structure . . . 83
3.3 Wide-angle reflection/refraction “box wave” receiver gathers . . . 90
3.3.1 Wide-angle reflection/refraction acquisition testing . . . 90
3.3.2 "Box wave" methodology: Array theory and application . . . 91
3.3.3 Noise attenuation method . . . 93

3.3.4 PBASS Chebyshev array . . . 95
3.4 Box wave array receiver gathers . . . 96
3.5 Box wave two-dimensional P-wave velocity model . . . 103
3.5.1 Adopted modelling technique . . . 103
3.5.1.1 Model geometry . . . 104
3.5.2 Modelling strategy and assumptions . . . 104
3.5.3 Modelling results . . . 105
3.5.4 Model assessment . . . 109
3.5.5 V_p perturbation tests . . . 109
3.5.6 Inversion recovery tests . . . 110
3.5.7 Monte Carlo simulation . . . 115
3.6 Low-fold wide-angle reflection stack . . . 116
3.6.1 Survey Geometry . . . 116
3.6.2 Pre-stack processing . . . 117
3.6.2.1 Data resampling and anti-aliasing filter . . . 118
3.6.2.2 Trace quality-control and spacing . . . 118
3.6.2.3 Spherical divergence amplitude recovery . . . 118
3.6.2.4 Static corrections . . . 119
3.6.2.5 Surgical refraction mute . . . 119
3.6.2.6 FX Deconvolution . . . 120
3.6.2.7 f—k filter . . . 121
3.6.2.8 Semblance coherency filter . . . 123
3.6.2.9 Predictive Deconvolution . . . 125
3.6.3 Velocity analysis . . . 126
3.6.4 CDP sort and Stack . . . 127
3.6.5 Post-stack processing . . . 127
3.6.5.1 Post-stack f—k filter . . . 128
3.6.5.2 Post-stack FX deconvolution . . . 128
3.6.5.3 Trace running mix . . . 128
3.6.5.4 Frequency filter . . . 128
3.6.6 Final stack . . . 129
3.7 Summary . . . 134

4 Parnaíba basin gravity anomalies and crustal structure 137
4.1 Introduction . . . 137
4.2 Earth's gravity and gravity anomalies . . . 138
4.2.1 Reference datums . . . 139
4.3 Gravity data . . . 141
4.4 Terrestrial gravity data reduction . . . 141
4.4.1 Conversion from relative to absolute gravity . . . 141
4.4.2 Drift correction . . . 143
4.4.3 Latitude correction . . . 144
4.4.4 Elevation correction . . . 145
4.4.5 Bouguer correction . . . 146
4.4.6 Terrain correction . . . 147
4.4.7 Gravity anomalies . . . 149
4.4.8 Regional correction . . . 150
4.5 PBAP regional transect gravity anomalies . . . 153
4.6 Two-dimensional forward model . . . 155

4.6.1 Two-dimensional gravity modelling technique . . . 155
4.6.2 Lithospheric reference model . . . 157
4.6.3 Model constraints . . . 159
4.6.3.1 Sedimentary formation densities . . . 160
4.6.3.2 Seismic reflection structure . . . 163
4.6.3.3 Boxwave P-wave velocity model . . . 163
4.6.4 Model results . . . 163
4.7 Process oriented gravity modelling . . . 167
4.7.1 Gravity anomaly calculation method . . . 168
4.7.2 POGM: Rifting model . . . 169
4.7.3 POGM: Buried load model . . . 170
4.8 Three dimensional modelling . . . 175
4.8.1 Sediment corrected "residual" anomaly reduction . . . 175
4.8.2 Residual anomaly interpretation . . . 178
4.8.3 Three dimensional buried load model . . . 180
4.9 Summary . . . 182

5 Subsidence analysis and geodynamics of Parnaíba basin 185
5.1 Introduction . . . 185
5.2 Vertical motions of Earth's surface . . . 186
5.2.1 Basin exhumation and missing section . . . 186
5.2.2 Quantifying tectonic subsidence . . . 187
5.3 One-dimensional Airy backstripping . . . 189
5.3.1 Airy backstripping assumptions . . . 191
5.3.2 Airy backstripping parameters . . . 192
5.3.2.1 Decompaction approach . . . 192
5.3.2.2 Petrophysical porosity estimates: sonic porosity . . . 196
5.3.2.3 Grain density estimates . . . 196
5.3.2.4 Eustatic sea level change . . . 197
5.3.2.5 Paleobathmetry . . . 200
5.3.3 Airy backstripping: Volcanic intrusions . . . 201
5.3.4 Airy backstripping results . . . 201
5.4 Three-dimensional flexural backstripping . . . 206
5.4.1 Flexural backstripping methodology . . . 206
5.4.2 Three dimensional Flexural backstripping input data . . . 207
5.4.3 Flexural backstripping results . . . 208
5.5 Testing an extensional origin for Parnaíba basin subsidence . . . 211
5.5.1 Finite rifting: Adopted modelling technique . . . 211
5.5.2 Finite rifting: model parameters . . . 214
5.5.3 Extensional modelling results . . . 215
5.6 Time dependent flexure: Buried loading and viscoelastic stress relaxation . . . 217
5.6.1 Viscosity structure . . . 218
5.6.2 Viscoelastic modelling results . . . 221
5.6.3 Sensitivity tests . . . 225
5.6.3.1 Layer two viscosity . . . 225
5.6.3.2 Layer three viscosity . . . 225
5.6.3.3 Load width . . . 226
5.6.3.4 Load Height . . . 227
5.6.3.5 Load density . . . 227

5.6.3.6 Viscosity structure: two-parameter grid search 227
5.7 Summary 229

6 A comparative study of the Parnaíba, Michigan and Congo cratonic basins 231
6.1 Introduction 231
6.2 Morphology and stratigraphy 232
6.2.1 Michigan basin 233
6.2.2 Congo Basin 235
6.3 Isopachs and Sedimentary thickness maps 238
6.3.1 Michigan basin isopachs and flexural backstrips 239
6.3.2 Congo basin isopachs 241
6.3.3 Cratonic basin sedimentary thickness maps 241
6.4 Gravity anomalies 248
6.4.1 Sediment corrected residual gravity anomalies 249
6.5 Airy backstripping 255
6.6 Viscoelastic subsidence 257
6.7 Summary 259

7 Discussion, conclusions and future work 261
7.1 Introduction 261
7.2 Discussion 261
7.2.1 Parnaíba basin summary 261
7.2.2 Assessment of proposed mechanisms for cratonic basin formation and there applicability to Parnaíba basin 262
7.2.3 Reconciling long-lived subsidence with a mechanical loading mechanism 266
7.2.4 Geological origin of the proposed lower crustal buried load 267
7.2.5 Surface magmatism? 267
7.2.6 Additional and alternative subsidence mechanisms 268
7.3 Conclusions 270
7.4 Future work 272
7.4.1 Reconciling lower crustal composition 273
7.4.2 Numerical modelling of basin evolution 274
7.4.3 Metamorphic petrology 274
7.4.4 Wide-angle reflection and refraction surveying 275

A Software development: geophysical modelling GUI (gmg) 277
A.1 Introduction 277
A.2 Software summary 278
A.3 Coding language, adopted GUI development toolkit and software dependencies 278
A.4 Software architecture 279
A.5 Potential field algorithms 280
A.5.1 Two-dimensional gravity anomalies: Bott (1965) algorithm 280
A.5.1.1 Bott (1965) algorithm testing 281
A.5.2 Two-dimensional magnetic anomalies: Talwani and Heirtzler (1964) algorithm 286
A.5.2.1 Talwani and Heirtzler (1964) method testing 289
A.6 Software layout 291
A.7 Software features 293
A.7.1 Loading data 293
A.7.2 Layer attributes 293

A.7.3 Seismic reflection data 294
A.7.4 Well horizon top data 294
A.7.5 Layer pinching/snapping 295
A.7.6 Data filters 295
A.7.7 Exporting data 296
A.7.7.1 Figure export 296
A.7.7.2 Modelled anomalies and layers 296
A.7.7.3 RayInvr c.in model export 296
A.7.8 Future modules 296

B Seismic processing supplementary figures **299**

References **307**

List of Figures

1.1 Global distibution of Cratonic basins 3
1.2 Isostatic compenstation models 7
1.3 Isostatic response for different load durations 9
1.4 Typical sedimentary basin tectonic subsidence curves 12
1.5 Cratonic basin tectonic subsidence curves 18
1.6 Cratonic basin formation models 30

2.1 Geological setting of the Parnaíba cratonic basin, Northeast Brazil 38
2.2 Basement terranes in South America 41
2.3 Basement terranes of Northeast Brazil 42
2.4 Western Gondwana reconstruction at 410 Ma 43
2.5 Gross tectonic history of basement terrains in the vicinity of Parnaíba basin during the amalgamation of Western Gondwana 46
2.6 Summary stratigraphic column for the Parnaíba cratonic basin 53
2.7 Parnaíba basin sedimentary formation isopach maps 54
2.8 440–220 Ma paleogeography reconstructions of Parnaíba basin 59

3.1 Parnaíba basin seismic data distribtuion map. Red line shows regional transect. 69
3.2 Sedimentary basin regional post-stack depth migrated reflection profile 72
3.3 Three-dimensional perspective of Parnaíba basin 73
3.4 Example of sills with the Parnaíba basin sedimentary section 75
3.5 Sketch cross sections showing the structural evolution through time of the two half graben on the western margin of the Parnaíba basin (after, Daly et al., 2014) 77
3.6 Sesimic reflection profiles of the western and eastern margins of Parnaíba basin 79
3.7 Jaibaras basin seismic reflection profile 82
3.8 Riachão basin seismic reflection profile 84
3.9 Regional Post-Stack Depth Migrated reflection profile 86
3.10 Regional Post-Stack Time Migrated reflection profile 89
3.11 Parnaíba Box Array Seismic Survey (PBASS) geometry 92
3.12 Schematic illustrations showing the dependence of apparent wavelength on emergence angle (after Pap, 1983) 92
3.13 Array response diagram 94
3.14 Box wave areal receiver array geometry 96
3.15 Box wave receiver gather processing example 97

3.16 Box-2 receiver gather interpretation 98
3.17 Box-3 receiver gather interpretation 99
3.18 Box-4 receiver gather interpretation 100
3.19 Box-5 receiver gather interpretation 101
3.20 Box-6 receiver gather interpretation 102
3.21 Schematic diagram demonstrating the projection of shot and receivers onto a two-dimensional model profile (modified after Scherwath, 2002) 104
3.22 Grid search result for variations in upper crustal V_p structure and MCR reflection interface dpeth 107
3.23 Box wave V_p model assessment 108
3.24 V_p perturbation test results for the upper crust 111
3.25 V_p perturbation test results for the lower crust 112
3.26 V_p inversion recovery test for the upper crustal laye 113
3.27 V_p inversion recovery test for the lower crustal layer 114
3.28 Box wave V_p Monte Carlo uncertainty analysis 116
3.29 PBASS low-fold reflection survey geometry 117
3.30 Box wave surgical refraction mute example 120
3.31 Box wave amplitude decay plot example 121
3.32 FX-deconvolution filter example 122
3.33 F–k filter example 124
3.34 Semblance coherency filter example 130
3.35 Predictive deconvolution example 131
3.36 onstant Velocity Stack (CVS) analysis example 132
3.37 Box wave low-fold seismic reflection stack 133

4.1 Gravity reference datums 140
4.2 Parnaíba basin gravity survey map 142
4.3 Schematic illustration of the latitudinal variation in Earth's gravity 144
4.4 Gravity correction examples 148
4.5 Global free-air anomaly power spectra 151
4.6 Parnaíba basin long wavelength regional gravity anomlies 152
4.7 PBAP regional transect gravity anomolies 154
4.8 Two-dimensional gravity modelling technique 156
4.9 Global crustal thickness estimates for elevations within $\pm$ 150 m of mean sea level 159
4.10 Isostatic balance of a mid-ocean ridge creat and "reference" continental lithopsheric section 160
4.11 Parnaíba basin sedimentary formation bulk density estimates 161
4.11 162
4.12 Parnaíba basin two-dimensional gravity model 166
4.13 Two-dimensional gravity modelling method comparison 169
4.14 Process-Oriented Gravity Modelling example 170

4.15 Process-Oriented Gravity Modelling for a lithospheric rifting process 171
4.16 Process-Oriented Gravity Modelling for a buried loading process 173
4.17 Comparison of the observed Bouguer gravity anomalies with predictions from Process-Oriented Gravity Modelling 174
4.18 Parnaíba basin gravity anomalies and gravity components 177
4.19 Sedimentary basin gravity effect 178
4.20 Ensemble averaged gravity profile 179
4.21 Three dimensional gravity model of Parnaíba basin 181

5.1 Porosity depth curves from the Parnaíba and Congo basins 188
5.2 Airy backstripping methodology 190
5.3 Parnaíba basin well distribution map 193
5.4 Schematic diagram of sediment decompaction 195
5.5 Sonic porosity curves from Parnaíba basin exploration wells 198
5.6 Parnaíba basin sedimentary formation grain densities 199
5.6 200
5.7 Parnaíba basin Airy backstripped tectonic subsidence curves 203
5.7 204
5.7 205
5.8 Three dimensional flexural backstripping of Parnaíba basin 210
5.9 Mckenzie lithospheric extension model 212
5.10 Subsidence history at well 2-BAC 215
5.11 Parnaíba basin tectonic subisence map 217
5.12 Temperature depth slices beneath Parnaíba basin (after, Priestley and McKenzie, 2013) 220
5.13 Present-day geothermal gradient for Parnaíba basin and predicted viscosity structure 222
5.14 Subsience modelling using a multilayered viscoelastic plate loading model . . 224
5.15 Single parameter sensitivity tests for viscoelastic modelling 226
5.16 viscosity structure sensitivity tests for viscoelastic modelling 228

6.1 Present-day topography within the Parnaíba, Michigan and Congo basins . . 232
6.2 Michgan basin geological map 234
6.3 Stratigraphic elements of the Parnaíba, Michigan and Congo cratonic basins . 236
6.4 Congo basin geological map 237
6.5 Comparison of seismic reflection profile data from the Parnaíba, Michigan and Congo basins 241
6.6 Three dimensional flexural backstripping of Michigan basin 243
6.7 Congo basin isopach maps 246
6.8 Parnaíba, Michigan and Congo basin sedimentary thickness maps 247
6.10 Michigan basin gravity anomalies 251
6.11 Congo basin gravity anomalies 252

6.12 Residual Bouguer gravity anomalies 253
6.13 Ensemble averaged residual gravity profiles 253
6.14 Michigan basin flexural backstrip 254
6.15 Tectonic subseince curves from the Parnaíba, Michigan and Congo basins . . 257
6.16 Multilayered viscoelastic model for the flexure due to a lower curstal load . . 258

A.1 Simplified software architecture map for gmg 280
A.2 Two-dimensional gravity anomaly modelling method 282
A.3 Two-dimensional geometric parameters required for calculating the gravity anomaly produced by a buried cylinder 283
A.4 A comparison of two-dimensional gravity modelling algorithms with an exact analytical solution 284
A.4 284
A.4 285
A.4 285
A.4 286
A.5 Geometric parameters used for solving for the magnetic anomaly produced by an infinite body with one sloping interface 288
A.6 Perspective three-dimensional view of the total magnetisation vector $\vec{J}$ 289
A.7 Comparison between the magnetic anomaly calculated using the Talwani and Heirtzler (1964) algorithm and an exact analytic solution 291
A.8 gmg software layout 292
A.9 gmg seismic display 294
A.10 gmg well log example 295

B.1 FX deconvolution filter design test panels: number of tace 300
B.2 FX deconvolution filter design test panels: time window length 301
B.3 f—k filter design test panels: k-axis cut-off 302
B.4 Sembsmooth filter design test panels: number of traces 303
B.5 Sembsmooth filter design test panels: percentage add-back 304
B.6 Predictive deconvolution filter design test panels: operator length 305
B.7 Predictive deconvolution filter design test panels: gap length 306

List of Tables

1.1 Summary of proposed models for cratonic basin formation 22

3.1 Seismic acquisition parameters 68

4.1 Summary of parameters used in isostatic balancing and POGM. 157
4.2 Summary of parameters used in three-dimensional flexural and gravity modelling.177

5.1 Standard values used in the Wyllie equation for converting sonic velocity to porosity 197
5.2 Summary of parameters used in the thermal and mechanical modelling. . . . 214
5.3 Summary of parameters used to calculate a geothermal gradient for Parnaíba basin. 221

7.1 Assessment of proposed models for cratonic basin formation with respect to key interpretations and observations made in Parnaíba basin 265

Acknowledgements

Firstly, I extend a sincere amount of gratitude to my advisor Tony Watts for providing me with the opportunity to undertake this project and the freedom to develop and explore the aspects I found personally most interesting. As a young scientist from the other side of the world, this experience has been invaluable. I thank both Tony and Mike Daly, my secondary advisor, for all the great advice, ideas and insightful discussions over the past few years both regarding this body of work and in general. You have been fantastic mentors and I have enjoyed working with you both immensely, not least for the rugby and football banter. A further thank you to Tony and Mary for rescuing us from the horrors of the Oxford housing market and providing us with top notch accommodation over the past year!

During this thesis, I have received financial support from BP for which I am incredibly grateful. I also acknowledge the contribution of the collaborating institutions and groups that made the Parnaíba Basin Analysis Project (PBAP) possible — BP, Global Geophysical, Agéncia Nacional do Petróleo, Observatório Nacional, the University of Aberdeen, the University of Brasilia, the University of Cambridge, Federal University of Rio Grande do Norte and the Federal University of Bahia. A further thank you to those involved with PBAP that I have personally worked with — Amanda Porto and Lucy Andrew.

Thanks to Steve Usher for providing IT support throughout. Seismic analysis was conducted using GLOBE Claritas seismic processing software and most figures were generated using the Generic Mapping Tools (Wessel et al., 2013). Seismic reflection analysis conducted use of OpendTect.

Thanks to my thesis examiners Richard England and Conall MacNiocaill for their time, useful suggestions and for an interesting and thought provoking discussion during my viva

voce which helped improve the final version of this thesis.

To my great office mates, past and present — Brook Keats, Rebecca Morgan, Dan Bassett, Dirk Metz, Jacob Smith, Johnny Hunter, Lily Muller, Maria Tsekhmistrenko and Michele Paulatto — thanks for all the insightful (as well as the aimless!) conversations throughout. I've learnt a lot from each of you, both scientific and otherwise and I've really enjoyed our time together in the "marine lab".

To the "kiwi crew" — particularly Matt, Laura, Kate, Tim, Eric, Alice and Sam — it has been a pleasure spending time in Europe with you all, the Christmas getaways and London outings will be memories for life.

A big thanks to everyone involved with OUAFC, my team mates and particularly Micky Lewis, for all the great times away from the office.

Thanks to all the friendly staff down at the OWC for all the great coffees which got me going during the tiresome mornings of the write up phase!

To my parents, Kevin and Jacaleen, Nana Patrica, as well as Kelly and Adam and the Kennedy's, Gemma and Mark, Holly and Andrew — your continued love and encouragement have been much appreciated and I look forward to seeing you all!

Lastly, to Clare, I extend an extreme amount of gratitude for all your patience, help, love and support. I am so glad we shared this time in Oxford together. It's impossible to put down in words how large a part you have played – you have been more than wonderful. Thanks so much for proofreading so diligently – I'll do more of the cooking next year, I promise!

Chapter 1

Introduction

Over the past two centuries, two concepts have come to define the framework within which variations of the Earth's morphology—such as the presence of mountain belts and deep ocean basins—are understood. The first of these is the recognition that the Earth's outer-most layers, in the absence of external forces, will tend towards a state of hydrostatic equilibrium; a process that has come to be known as isostasy (e.g., Airy, 1855; Pratt, 1855; Dutton, 1889; Bowie, 1927). The second is the theory of plate tectonics, in which the outer layer of the Earth (the lithosphere) is made up of distinct rigid "plates" that overly a convecting mantle (the asthenosphere) and are capable of moving relative to one another and transmitting stresses over thousands of kilometres (e.g., Dietz, 1961; Hess, 1962; Wilson, 1965; McKenzie and Parker, 1967: Morgan, 1968).

Together, these concepts have proved extremely successful in explaining almost all of the Earth's morphological features. Perhaps the most famous example is that of the "ocean conveyor belt" (Hess, 1962), consisting of the global mid-ocean ridge system, deep-sea trenches, and the symmetric and ubiquitous deepening of the seafloor away from the ridges towards the trenches (Fig. 1.1). Within the framework of plate tectonics, it was quickly realised that mid-ocean ridges are sites where thermally buoyant mantle material upwells from beneath the plates, creating new seafloor and crustal "plate" material, while dating of the crust perpendicular to the ridges confirmed that the ocean floor is youngest at the ridge axes and ages systematically trenchward, and is in motion (Vine and Matthews, 1963; Maxwell, 1971). It

followed that, to maintain an approximately constant surface area, there must be means by which the plates are destroyed or "recycled" back into the underlying mantle – the deep-sea trenches (Hess, 1962). Between these sites of creation and destruction it was later shown that the evolution of oceanic lithosphere can be remarkably well explained as a plate that is losing heat conductively, coupled with the associated isostatic consequences (Parsons and Sclater, 1977). As the seafloor moves away from the ridge it cools, contracts, thickens, increases in density, and, to maintain isostatic equilibrium, subsides. Hence, together plate tectonics and isostasy provide an elegant explanation for the increase in ocean depth away from the ridges.

Many other geological processes—particularly those in regions of obvious deformation near plate boundaries—are also simply explained within the unifying context of plate tectonics. However, plate tectonics is mainly concerned with horizontal motions, and the origins of some localised and relatively smaller amplitude vertical tectonic motions are more difficult to interpret. This is especially true for regions of surface subsidence, manifest as large sedimentary basins (i.e., thick sequences of sediments that infill such depressions), within the interior of continents, away from the deformational plate boundaries. This discrepancy was highlighted by Hallam (1973) in his review of the plate tectonic revolution, where he wrote on the questions that remained unanswered by plate tectonics at the time:

"...More obscure still, what controls epeirogenic movements in so-called stable shields or cratons, which are supposed in plate theory to be tectonically inert?"

Over the proceeding decades, the nature of deformation within continental interiors, including the origin of sedimentary basins that form in this environment, have been the subject of much research and speculation. This thesis is concerned with the geological origin of such basins, often referred to as cratonic basins (Fig. 1.1). In particular, this study focuses on understanding the origin of the Parnaíba cratonic basin, located in Northeast Brazil.

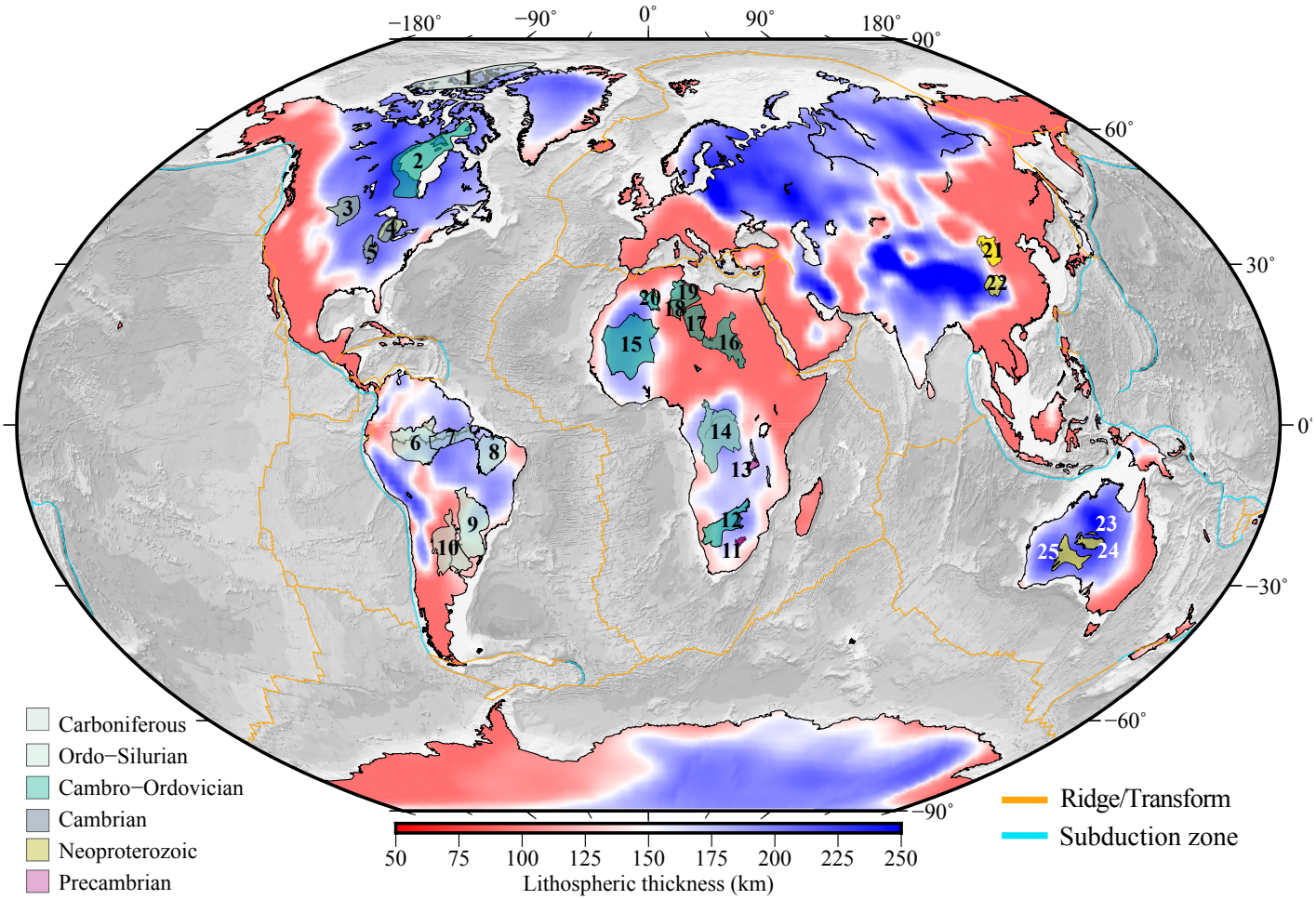


Figure 1.1: Global distribution of selected cratonic basin locations (basin outlines after T. Torsvik, personal communication, June 30^{th} 2016) and their relationship with present day thermal lithospheric thickness (after, Priestley and McKenzie, 2013). The basins are coloured in line with the approximate age of their initiation. Note the proliferation of basins forming soon after the Cambrian stabilisation of Gondwana and Laurentia. (1) (South) West Siberian basin (2) Hudson Bay; (3) Williston; (4) Michigan; (5) Illinois; (6) Solimoes; (7) Amazonian; (8) Parnaiba; (9) Parana; (10) Chaco-Parana; (11) Witwatersrand; (12) Nama-kalahari; (13) Mporokoso; (14) Congo; (15) Taoudeni; (16) Al Kufrah; (17) Murzuq; (18) Illizi; (19) Ghadames; (20) Tindouf; (21) Ordos; (22) Sichuan; (23) Ngalia; (24) Amadeus; (25) Officer. Ocean bathymetry (after GEBCO, 2003); plate boundaries (after Bird, 2003).

1.1 Isostasy

The analysis of biostratigraphic data from deep boreholes reveals that sedimentary basins are dominated during their evolution by two main processes: sediment and water loading and subsidence and uplift driven by an unknown tectonic 'driving' mechanism (e.g., Watts

and Ryan, 1976; Steckler and Watts, 1978). The way by which the Earth responds to these loading processes is modulated by the physical state of the outer solid layer of the Earth (the Lithosphere) and applies a first order control over the spatial and temporal evolution of sedimentary basins and, hence, their gross structure.

Central to the Earth's load response is the concept of Isostasy. Isostasy refers to the tendency of the Earth's outer layers to approach a state of hydrostatic equilibrium. Hence, isostasy is a restoring action, in which isostatic equilibrium is achieved once the pressure at a particular depth in all adjoining regions is equal. This depth is termed the "depth of compensation".

The first quantitative evidence that the Earth tends towards a state of isostatic equilibrium was recorded by Bouguer (1749) while making measurements of the local plumb line for navigational purposes in the vicinity of large mountains in Ecuador. Bouguer (1749) noted that the local plumb line was deflected far less than expected given the perceived large mass excess of the mountains. Boscovich (1755) later suggested this could be due to a mass deficit at depth, which "compensates" for the mass excess of the mountain range. Such mass deficiencies were confirmed much later, following the advent of modern gravimeters and the discovery of an association of mountain ranges with large amplitude Bouguer gravity anomaly 'lows' that could be reconciled by applying a correction for their isostatic compensation.

1.1.1 "Local" isostatic compensation models

Although Bouguer's (1749) observation strongly supported the existence of isostasy, the way in which isostatic compensation is achieved remained unknown at this time. The first two formal models of isostasy were proposed by Airy (1855) and Pratt (1855). These models offer end-member modes of isostatic compensation, in which loads are supported "locally", independent from adjoining regions. These models are therefore idealised cases with respect to their applicability to the actual Earth. Nevertheless, they remain very useful and widely applied in modern studies, including within this thesis.

1.1.2 Airy isostasy

In Airy-type isostasy (Airy, 1855) the density of the crust is assumed to be constant, such that, in order to maintain equal pressure at the depth of compensation, elevated and depressed regions of the crust are underlain by either "roots" or "anti-roots" of greater or lesser thickness than in adjacent regions (Fig. 1.2a). The depth of compensation (D_c), is then defined as the depth that the deepest of the surrounding columns reaches. By equating the pressures at D_c for adjacent columns, the thickness of a root which compensates for a given load is given by:

$$r = \frac{h\rho_c}{\rho_m - \rho_c} \tag{1.1}$$

Where r is the thickness of the root in km; h is the load height in km and ρ_c and ρ_m are the densities of load and displaced material in $kg\ m^{-3}$ respectively.

This style of isostasy can be considered as a "shallow" compensation scheme, whereby the compensation occurs via local variations in crustal thickness.

1.1.3 Pratt isostasy

In contrast to the Airy model, Pratt (1855) proposed that lateral variations in the density of adjacent lithospheric columns provide the means of compensation (Fig. 1.2b). Again, by equating the pressures at depth D_c of adjacent columns, the elevation change for a given lateral change in density can be calculated using Equation 1.2. In this case, the depth of compensation coincides with the base of the columns, such that there are no changes in basal depth (Fig. 1.2b).

$$h = \frac{D_c(\rho_0 - \rho_1)}{\rho_1} \tag{1.2}$$

Where h is the height difference with respect to the reference column in m; $\rho_0 - \rho_1$ is the difference in density between the reference column and the varied column in $kg\ m^{-3}$ and ρ_1

is the density of the varied column in $kg\ m^{-3}$.

In modern applications of Pratt-type isostasy the depth of compensation is often considered the base of the lithosphere. In contrast to the Airy model, this mode of compensation can be considered as a "deep" compensation scheme, as the compensating mass is distributed throughout the entire lithosphere.

Both the Airy and Pratt models are referred to as "local" models of compensation as the compensating masses occur directly below (or above) the feature that disturbs the state of isostatic equilibrium. Intrinsic to these models is the notion that the lithosphere exhibits zero internal strength and, hence, does not play any role in supporting any loads.

1.1.4 "Regional" isosatic compensation models

In the late 1800's and early 1900's attempts were made to reconcile various geological features and processes using the local isostatic models of Pratt and Airy. Some studies, however, found these models were incapable of explaining many observations. For example, Gilbert (1890) found that the surface uplift that had occurred following the removal of Lake Bonneville in the western United States was less than expected from Airy isostasy. Such departures are, however, expected if the lithosphere retains a finite strength when loaded or unloaded, and is thus capable of supporting or partly supporting loads.

Given such discrepancies, alternative views from that of the local compensation models began to emerge. For example, Putnam (1912) showed that differences in Pratt-type isostatic gravity anomalies, calculated at station pairs at Mauna Kea and Honolulu in Hawaii (which are in close proximity, but varying elevations), could be minimised by extending the area of compensation, such that, the excess mass is compensated "regionally". Subsequently, models invoking regional isostatic compensation became well established and better defined (see Jeffreys, 1926; Meinesz, 1941; Gunn, 1943; Walcott, 1970). It was found that a model in which the lithosphere is treated as a purely elastic beam overlying an inviscid (zero strength) substrate is capable of reconciling the regional isostatic compensation of many geological features, as constrained by their associated gravity anomalies (e.g., Walcott, 1970).

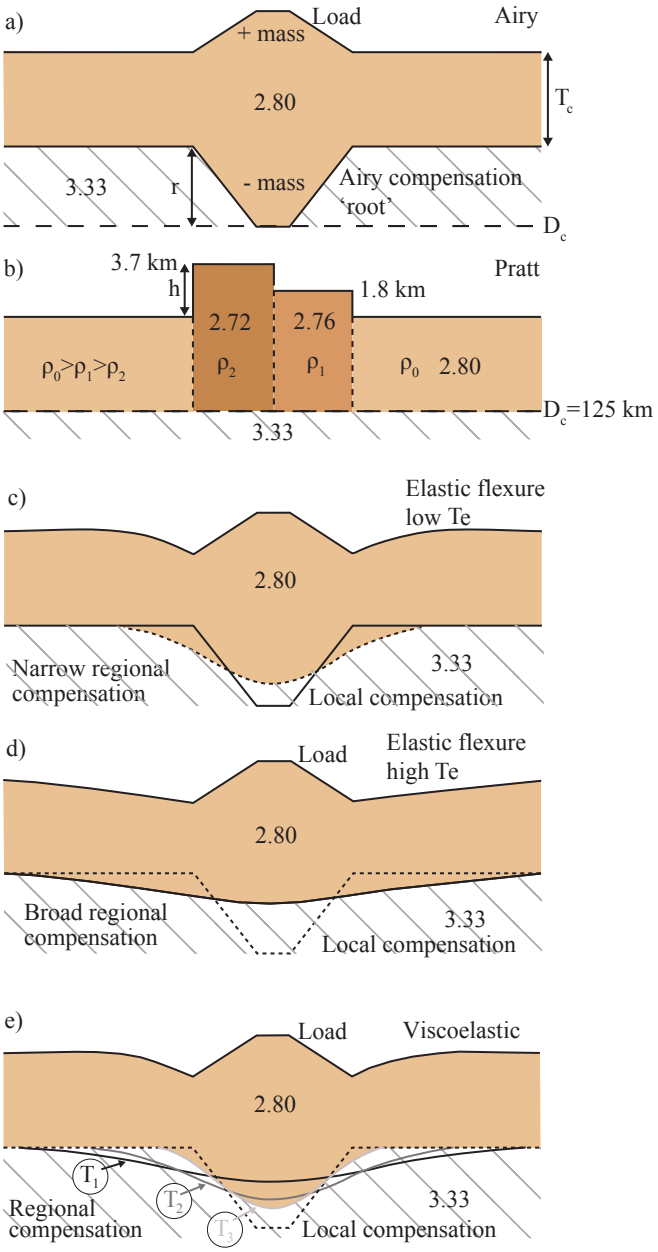


Figure 1.2: Schematic illustrations of different models of isostatic compensation. a) Airy model. b) Pratt model. c) Regional compensation model (elastic flexure) on a weak plate. d) Regional compensation model (elastic flexure) on a strong plate. e) Regional compensation model with a time dependent viscoelastic response.

1.1.4.1 The elastic plate model, flexure and T_e

In elastic flexural isostasy, it is assumed that the lithosphere is capable of supporting stresses over geological time-scales by bending via elastic flexure. In such a case, the lithosphere is considered as a thin elastic beam, and the wavelength and amplitude of the flexure are

modulated by the beams flexural rigidity—the resistance offered to bending—which is, in turn, largely dependent on the thickness of the beam. When applied to the case of a load emplaced on the lithosphere, the thickness of the beam represents the effective elastic thickness of the lithosphere (T_e). It should be noted that T_e does not reflect a physical thickness, but the depth-integrated thickness of those portions of the lithosphere that are capable of supporting elastic stresses, regardless of their physical depth. T_e is, therefore, a proxy for lithospheric strength and can be considered as an "equivalence" quantity.

It follows that the strength of the lithospheric plate (and variations in its strength in both space and time) upon which a sedimentary basin develops imposes a first order control on the gross basin morphology, as this dictates the degree to which the sediment load is supported by the lithosphere. A basin that forms on a weak plate (low T_e) will be deep and narrow, nearer the Airy isostatic case (Fig. 1.2c); while a basin that forms on a strong plate (high T_e) will be broad and shallow, as the lithosphere will partially support the load by regional distribution of stresses (Fig. 1.2d).

1.1.4.2 Viscoelastic plate model

All of the isostatic models discussed above may be considered as long-term "steady-state" loading responses, achieved once isostatic equilibrium occurs. Accordingly, none of these models incorporate a temporal aspect over which isostatic adjustment occurs; neither do they offer an explanation for the observation that the portion of the lithosphere that responds elastically to a given load decreases with increased temporal load duration (e.g., Watts et al., 2013) (Fig. 1.3). Moreover, several authors have noted the elastic plate model is unable to satisfactorily explain stratigraphic patterns (which are modulated by the mode of isostatic compensation) in a wide range of tectonic settings (e.g., Sleep and Snell, 1976; Beaumont, 1981; Quinlan and Beaumont, 1984; Watts and Zhong, 2000).

This led to the use of a viscoelastic plate model. Most early viscoelastic models invoked a single-layered "Maxwell" (uniform viscosity) plate (e.g., Walcott, 1970; Sleep and Snell, 1976; Beaumont, 1981; Quinlan and Beaumont, 1984). These latter models provide a means of modelling time-dependent isostatic adjustment (e.g., Fig. 1.2e). However, one problem with

the single layer case is that all stresses eventually relax (achieving an Airy-type compensation) and hence the long-term elastic response, as evident from geological observations, is not achieved. More recently, multilayered models, in which each layer can be prescribed a different viscosity have been developed (e.g., Watts and Zhong, 2000; Zhong and Watts, 2013; Watts et al., 2013). In this case, the inclusion of a very high viscosity, effectively elastic, upper layer can be included and therefore also account for the long-term elastic response (e.g., Watts et al., 2013).

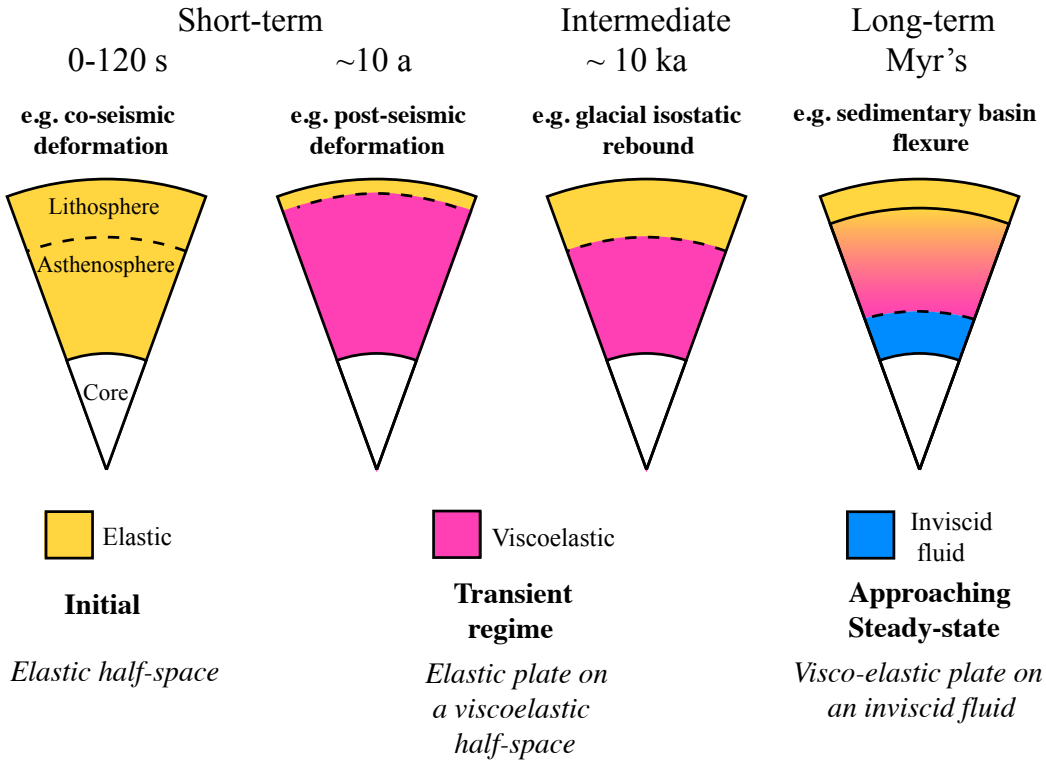


Figure 1.3: Schematic diagram illustrating how the outermost layers of the Earth respond to loads of different duration for continental lithosphere (modified after, Watts et al., 2013). At very short durations (seconds to minutes) the entire upper mantle appears elastic and capable of transmitting seismic waves. On short geological time-scales (Kyr's) the asthenosphere appears to flow in a viscous manner, while the lithosphere remains essentially elastic. On long-term geological time-scales the lithosphere responds as an elastic plate of thickness equal to its effective elastic thickness (T_e), which is less than the thickness of the lithospheric plate.

1.2 The lithosphere

The lithosphere is thought of as the outer rheologically strong layer of the Earth, consisting of the crust and upper most mantle (e.g., Artemieva, 2011). Mechanically, this is equivalent to the rigid "plate" in the context of plate tectonics (e.g., McKenzie, 1967). The lithosphere can, however, be defined in various other ways, depending on the physical process of interest. Definitions include the elastic lithosphere, as outlined in Section 1.1.4.1, as well as the thermal, seismic, electrical and petrological lithospheres. The thermal lithosphere, for example, is often relevant in sedimentary basin modelling, when basin subsidence is thought to occur, in part, due to the decay of a lithospheric thermal perturbation (e.g., McKenzie, 1978). The thermal lithosphere is considered the mechanical boundary layer of the mantle convection system and is defined as the upper section of the Earth in which heat is transferred primarily via conduction, above the vigorously convecting mantle (e.g., Artemieva and Mooney, 2001).

The lithosphere also comprises two fundamentally different entities. These are the geologically "juvenile" oceanic lithosphere and older continental lithosphere. The oceanic lithosphere is capped by a thin, typically $\sim$ 7 km thick mafic crust. This is constantly created at mid-ocean ridges and destroyed at subduction zones, such that, there is presently no oceanic lithosphere older than $\sim$ 180 Myr (e.g., Müller et al., 2008). Furthermore, the oceanic lithosphere increases in thickness with age as it cools, predicted to reach a final thermal thickness of $\sim$ 125 km based on a cooling plate model (Parsons and Sclater, 1977). In contrast, the continental lithosphere is capped by a thicker, felsic crust of variable thickness, with an average of $\sim$ 35 km (e.g., Allen and Allen, 2013). It is thought much of the continental crust likely formed via differentiation of a predominately mafic crust early in Earth's evolution (2–3 Ga ago; Hawkesworth et al., 2010). Like the crust, the underlying lithospheric-mantle is also considerably older than its oceanic counterpart. This does not exhibit a simple thickness/age relationship, although generally increases in thickness with age (Artemieva and Mooney, 2001). Recent studies have shown that many of the old Archaean/Proterozoic cratons are generally associated with thicker lithosphere than Phanerozoic mobile belts (e.g., Priestley and McKenzie, 2006; Priestley and McKenzie, 2013). However, beneath some cratons, the lithospheric-mantle appears to have undergone tectonic rejuvenation during the

Phanerozoic, such that, the chemical age of the lithosphere is far younger than the overlying Achaean crust (e.g., Artemieva, 2011) and the thickness of the lithosphere is reduced (Priestley and McKenzie, 2006). In terms of isostatic stability, the bulk density of thickened cratonic lithospheric-mantle must be reduced relative to standard oceanic and Phanerozoic sections, likely achieved via chemical depletion (e.g., Jordan, 1975; Artemieva and Mooney, 2001).

The physical nature of the lithosphere (i.e., its thickness, thermal and composition structure) plays a fundamental role in modulating sedimentary basin formation, as differences in these key parameters lead to variations in the lithosphere's isostatic response to tectonic forces (e.g., McKenzie, 1978; McKenzie and Priestley, 2016). Two key physical constants of the lithosphere, which modulate its flexural response to loading, are Young's modulus, E, and Poisson's ratio, σ. Although laboratory measurements of these quantities have been made for oceanic and upper mantle rocks (collected from ophiolites) at a range of pressures up to 1000 MPa (e.g., Christensen, 1978), as well as continental crustal rocks (e.g., Christensen, 1996), how these quantities scale to geological time scales is unknown. Hence, similarly to many geophysical studies, values of $E = 100\ GPa$ and $\sigma = 0.25$ are adopted in this thesis (e.g., Watts et al., 2013). This value for σ is slightly lower than the average value of 0.265 determined for continental crustal rocks from laboratory measurements (Christensen, 1996).

1.3 Sedimentary basin formation

Sedimentary basins represent sites of localised subsidence of the Earth's surface, formed in response to tectonic processes and amplified by sediment loading as the basin is infilled. As such, distinctive basin types are formed in different plate tectonic settings and are usually intimately related to the prevailing in-plane (horizontal) stress regime. They can, however, also be affected by processes operating within the underlying convecting mantle, such as dynamic topography (e.g. Coakley and Gurnis, 1995). Nevertheless, basin types can generally be divided into those formed in extensional tectonic settings (e.g., passive margins, active and failed rifts), those related to compressive tectonic settings (e.g., foreland and fore-arc basins), and those that form in predominantly strike-slip settings. The general tectonic regime within which cratonic basins form is still a matter of debate and various proposed models are discussed

in Section 1.5.

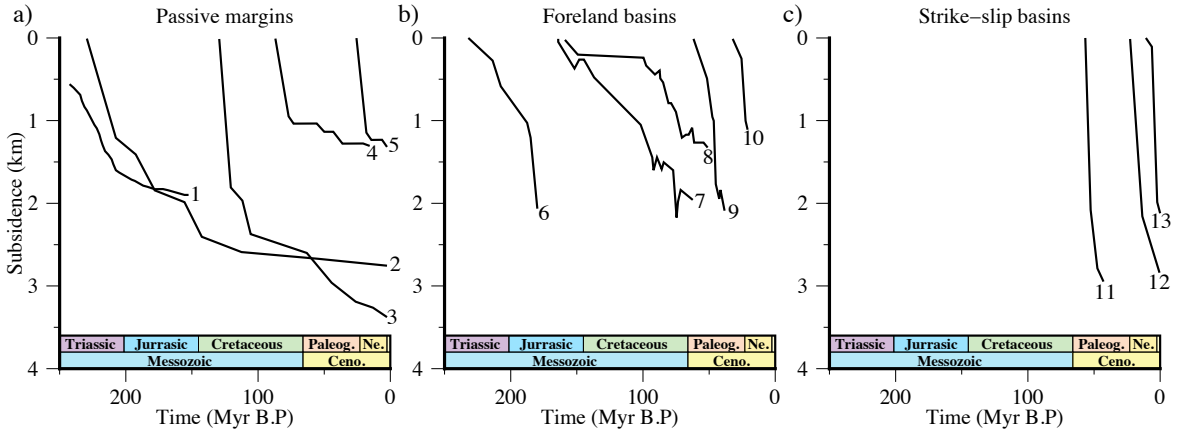


Figure 1.4: Typical sedimentary basin tectonic subsidence curves. a) Passive margins. 1=Paleozoic Miogeocline, southern Canadian Rocky Mountains; 2=Moroccan Basin; 3=Campos Basin; 4=Gippsland Basin; 5=Gulf of Lion. b) Foreland basins. 1=Eastern Avalonia, Anglo-Brabant fold belts; 2=Southern Alberta Basin; 3=San Rafael Swell, Utah; 4=Pyrenean foreland basin, Gombrèn; 5=Swiss Molasse basin. c) Strike-slip basins. 1=Chuckanut Basin; 2=Ridge Basin; 3=Death Valley (modified after Xie and Heller, 2009).

1.3.1 Extensional basins

Extensional basins are probably the most well understood type of basin. These form principally as a consequence of the mechanical and thermal effects of thinning the crust and mantle-lithosphere (rifting) (e.g., McKenzie, 1978). The stresses that promote rifting are thought to originate from either (or a combination of) "active" far-field plate tectonic processes, such as subduction slab pull, or the response to excess gravitational potential energy, generated when the lithosphere is buoyed up by a thermal upwelling in the underlying mantle, known as "passive" rifting. Extensional basins form a continuum of basin types in response to the degree of lithospheric stretching that is achieved, known as the "rift-drift" suite. These basins include active continental rifts, failed rifts and passive continental margins that form in response to the various stages of continental rifting, breakup, and the eventual formation of an ocean basin.

Extensional basins are characterised by a two-phase subsidence history (Fig. 1.4a). An initial "syn-rift" stage during which mechanical extension is accommodated in the upper crust

by normal faulting, usually developing a central rift-graben in the basin centre and a series of tilted basement fault blocks. This is followed by a longer-lived, “post-rift”, thermal subsidence phase in which the heat flow anomaly produced by thinning of the lithosphere decays. This results in cooling, contraction, an increase in bulk density and subsidence.

In the context of the stratigraphic "architecture" produced by extensional basins, the post-rift stage of subsidence is characterised by a draping of sediments over a wider region than that of the initial syn-rift depocentre, with an onlapping pattern of sediments onto the surrounding basement. Watts (1982) suggested such onlap may form as a consequence of increasing lithospheric rigidity during the post-rift cooling phase (as T_e is strongly dependent on temperature), resulting in a broader flexural response to sediment loading. Alternatively, White and McKenzie (1988) proposed the onlap of post-rift sediments may be the direct result of depth-dependent extension, showing that if extension is distributed over a wider region in the mantle-lithosphere than in the crust, a stratigraphic onlap pattern can be generated. Regardless of the mechanism that generates onlap, it is undoubtedly a characteristic of lithospheric extension. This is interesting in the context of cratonic basin formation, as these basins usually exhibit the opposite, with a well developed (apparent) stratigraphic offlap pattern observed.

1.3.2 Foreland basins

In contrast to extensional basins, the development of foreland basins is chiefly mechanical in nature. These basins develop as the flexural response to the emplacement of fold and thrust belt loads and/or buried loads upon the lithosphere during compressive tectonics (e.g., Price, 1973; Beaumont, 1981 Karner and Watts, 1983; Ali and Watts, 2009). Foreland basins are characterised by an initially slow subsidence rate, that increases with time (Fig. 1.4b), in step with the growth of the developing fold and thrust mountain belt. They form as asymmetric basins, with the maximum amplitude of subsidence adjacent to the thrust belt diminishing with distance away from the load.

The asymmetric morphologies and convex subsidence trajectories of foreland basins are inconsistent with cratonic basins. However, the long-lived nature of cratonic basins renders

them susceptible to varying tectonic processes through time. For example, the Williston basin is one cratonic basin where late-stage foreland style subsidence has overprinted the earlier cratonic basin (e.g., Ahern and Mrkvicka, 1984; Hamdani et al., 1994). This subsidence occurred during the Cretaceous in response to the growth of the Corilleran thrust belt and can be seen as the kink down in tectonic subsidence record from Saskatchewan (e.g., curve 6 in Fig. 1.5). The Parnaíba basin on the other hand is underlain by an earlier Neoproterozoic foreland basin (e.g., Porto et al., in press).

1.4 Cratonic basins

More than twenty Cratonic sedimentary basins exist worldwide, occupying at least 10 % of the Earth's continental surface area (Fig. 1.1). These basins generally exhibit a suite of characteristics that distinguish these from other basin types, such as rift basins, as outlined below.

1.4.1 Basin geometry

Cratonic basins typically exhibit large areal extents on the order of a few hundred thousand to a few million square kilometres and are often sub-circular in shape. This is in contrast to most other basin types, such as passive margins, rifts, strike-slip and foreland basins which usually form with a distinct linearity, inherited from the in-plane tectonic stresses responsible for their development (e.g., Roberts and Bally, 2012).

1.4.2 Stratigraphy

Cratonic basins are usually in-filled by about 3–6 km of mostly estuarine and lacustrine, marginal and shallow marine, shales, limestones, and aeolian sandstones that exhibit stratigraphic younging toward their centre and simple bowl-shaped geometries with minimal internal deformation (e.g., Sloss, 1963; Sleep, 1971; Sloss, 1988; Sleep et al., 1980; Xie and Heller, 2009). Moreover, it appears these sediments are usually, and potentially always, deposited

above a basin-wide regional unconformity surface (Daly et al., accepted). Sediment accumulation rates are slow in comparison to rift-, foreland-, and strike-slip basins (of the order of metres to tens of metres per million years) and their tectonic subsidence spans extended periods of geological time, often on the order of several hundreds of million years (e.g., Sloss, 1963; Sleep, 1971; Sloss, 1988; Sleep et al., 1980; Armitage and Allen, 2010; Allen and Armitage, 2012) (Fig. 1.5).

1.4.3 Subsidence style

The temporal evolution of cratonic basin subsidence, as revealed, for example, by Airy-style backstripping (see Chapter five) exhibits a variety of subsidence styles for these basins (Fig. 1.5a). Collectively they all exhibit slow long-lived subsidence histories and often to exhibit relatively faster subsidence rates early in their evolution that slow with time. This pattern is often in the form of a distinct two-phase subsidence, similar to extensional basins. However, their subsidence histories are often interrupted by one or more periods of non-deposition or inversion, reflected in a stratigraphic hiatus, and may also be punctuated by relatively short periods of rapid subsidence. It is likely that such short-lived periods of rapid subsidence reflect secondary tectonic processes, such as dynamic topography, superimposed on the primary long-lived cratonic basin subsidence signal (e.g., Coakley and Gurnis, 1995; Armitage and Allen, 2010). Furthermore, the long-lived nature of sedimentation at the sites where cratonic basins are found means they often record polyphase sedimentary histories consisting of distinct "tectonostratigraphic units" of unrelated tectonic genesis (Allen and Armitage, 2012). For example, the Phanerozoic Parnaíba cratonic of Northeast Brazil is underlain in its southwest section by a Neoproterozoic foreland basin (e.g., Porto et al., In press) and is overlain by a Mesozoic passive margin along its north-western edge. It is therefore important when analysing cratonic basin subsidence histories to identify and isolate the cratonic basin tectonostratigraphic unit as well as identify and account for secondary processes (Armitage and Allen, 2010).

1.4.4 Plate setting and initiation timing

Recent heat flow and seismic tomographic studies (e.g., Koptev and Ershov, 2011; Priestley and McKenzie, 2013) reveal that most cratonic basins are located above regions of thick (thermally defined) lithosphere (Fig. 1.1). Although a few basins, such as Murzuq and Ghadames in North Africa, appear to have formed above young thin lithosphere (Holt et al., 2014), plate reconstructions (Scotese, 2016) show that most are located on old, thick lithosphere far from present day plate boundaries, although may overlie preceding orogenic regions.

Another intriguing aspect of these basins is the apparent grouping of subsidence initiation times (Fig. 1.5). Previous authors have linked cratonic basin initiation to episodes of supercontinental breakup and dispersal, leading some authors to invoke a genetic link between extensional settings and cratonic basin initiation (e.g., Klein and Hsui, 1987; Allen and Armitage, 2012). However, as can be seen in Figures 1.1 and 1.5, basin initiation in Gondwana (South America and Africa) occurred in the Cambrian and Ordo-Silurian. This is after the stabilisation of Gondwana during the Brasiliano/Pan African orogenic amalgamation period (650–500 Ma) and well before extensive break-up began in the Mesozoic. Similarly, the basins formed in Laurentia (North America) mostly initiated in the Cambrian. Again, at a time when Laurentia was stable. Thus, Daly et al., (Accepted) have suggested that, within the context of the Wilson cycle, cratonic basins occur in the post-collision and pre-break-up phase. Interestingly, Daly et al., (Accepted) also noted this period is very long-lived in Gondwana and Laurentia ($\sim$ 200 Ma), but was much shorter for Pangaea, with final collision followed by break-up within < 50 Ma. These authors, therefore, speculated that the short-lived nature of Pangaea may have prevented the conditions required for cratonic basin formation of Pangean age.

1.4.5 Cratonic basin crustal structure

There is limited data on the deep structure of cratonic basins with which to constrain, compare, and contrast predictions from basin formation models. Two basins that have previously been investigated using active source seismic techniques are the Williston and Michigan basins

of North America. Beneath the Williston basin centre, Baird et al. (1995) imaged several westward dipping reflections within the crust, which in places reach depths of $\sim 60\ km$ and therefore appear to extend into the mantle. However, they noted a distinctive absence of a reflection Moho, at odds with the well-imaged Moho in the central Saskatchewan region at the northern edge of the basin (Morel-A-L Huissier et al., 1987). The dipping reflectors were interpreted as a Hudsonian Orogeny structural fabric developed in the Paleoproterozoic ($\sim 1.8\ Ga$). The missing Moho was then attributed to the absence of any appreciable impedance contrast due to gradational eclogitization of a remnant Hudsonian crustal root beneath the basin (see Section 1.5). Beneath the Michigan basin centre, Zhu and Brown (1986) imaged an $\sim 12\ km$ thick reflective succession in a narrow $\sim 70\ km$ wide rift basin, the Mi-Continent Rift, interpreted as a volcanoclastic sequence of upper and Middle Keweenawan age $\sim 1.1\ Ga$ (Van Der Voo and Watts, 1978) emplaced $\sim 600\ Ma$ prior to the formation of the overlying cratonic basin. They also imaged a potential Moho reflection at $\sim 43\ km$ depth, a result that has recently been corroborated by EarthScope receiver function studies (Shen et al., 2013). In both Williston and Michigan, the crust has clearly been profoundly modified by pre-basin formation events making it difficult to distinguish between these structures and those potentially related to the formation of the overlying cratonic basins. However, an important observation is that neither basin shows evidence of appreciable crustal thinning nor rift related structures, as one may expect for an extensional origin.

1.4.6 Summary of cratonic basin characteristics

Although cratonic basins appear to generally exhibit a set of unique classifying characteristics, it should be noted that the classification of some basins is not straightforward and subject to debate. For example, there are many other continental sedimentary basins that are not included in Figure 1.1 but are of similar size and intraplate locations, that have been referred to as cratonic basins in the past (e.g., Xie and Heller, 2009; Allen and Armitage, 2012). These include basins such as the Paris, Western Siberian and Canning basins. These are not included here as investigation has shown that they have likely to have formed, at least in part, as failed rift basins (e.g., Prijac et al., 2000; Saunders et al., 2005; Czarnota and White, 2016).

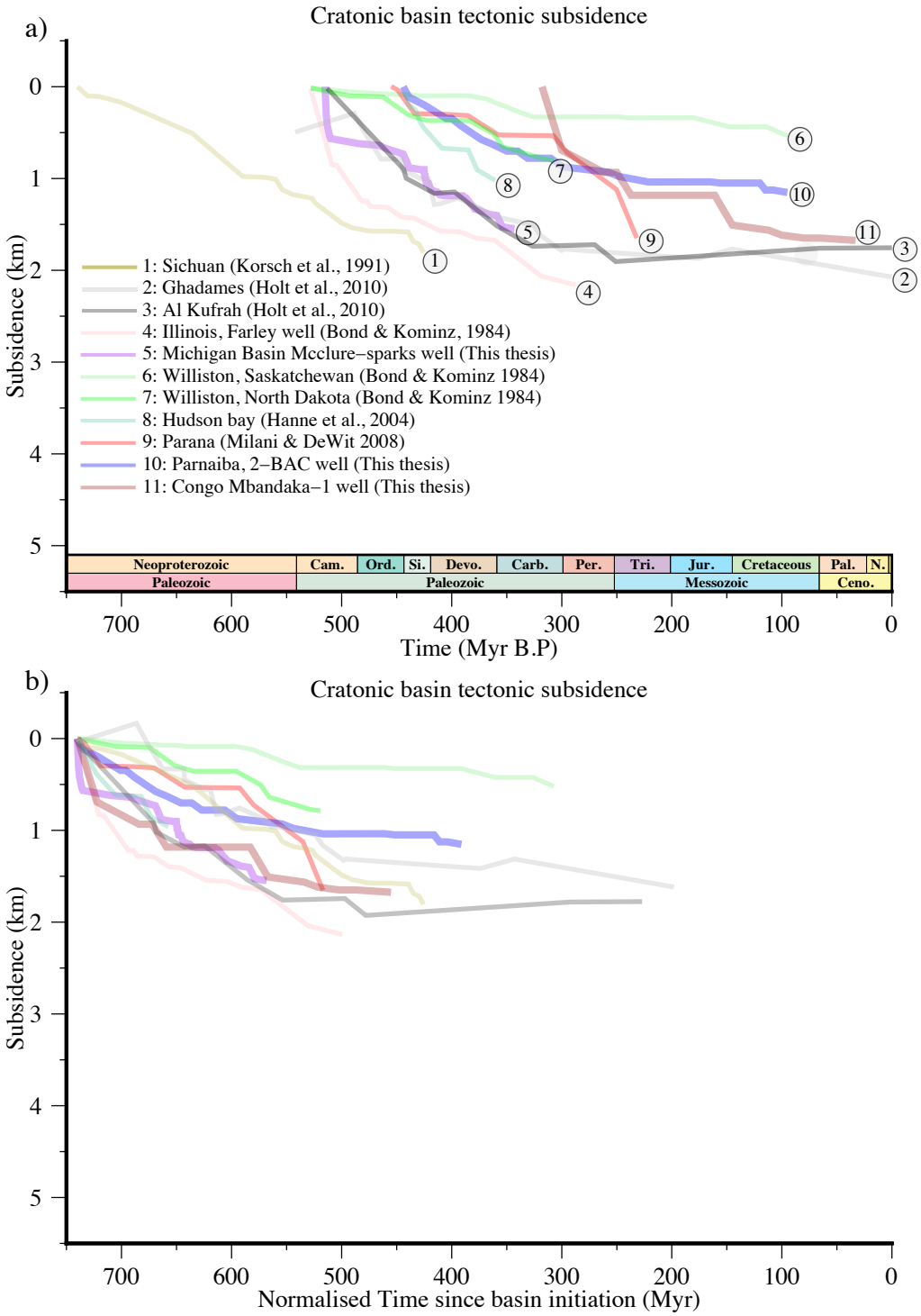


Figure 1.5: A compilation of water loaded backstripped tectonic subsidence curves from a selection of cratonic basins as labelled. Note, some backstrips have sea-level corrections applied while others do not. Thicker lines indicate backstrips calculated in this study (modified after, Xie and Heller, 2009).

1.5 Proposed mechanisms for cratonic basin formation

Many geodynamic models have been proposed to explain the origin of cratonic basins, yet no consensus has been reached. Both Hartley and Allen (1994) and Klein (1995) provided reviews of the various processes, and with the addition of more recent contributions, most can be categorised by subsidence resulting from:

1. Thermal subsidence following some form of lithospheric heating event. Proposed processes include lithosphere extension, thinning, and cooling; emplacement of a mantle plume within the mantle lithosphere; lithospheric accretion and cooling above a subduction mantle wedge; or erosion, thinning and cooling following crust and lithosphere thickening (e.g., Sleep and Snell, 1976; Sleep et al., 1980; Ahern and Mrkvicka, 1984; Nunn and Sleep, 1984; Kaminski and Jaupart, 2000; Sleep, 2009; Kadima et al., 2011; Holt et al., 2010, Holt et al., 2014; Lucazeau et al., 2015; McKenzie and Priestley, 2016).

2. Lithospheric folding caused by far-field in-plane stresses (e.g., Lambeck, 1983a; Lambeck, 1983b; Cloetingh, 1988).

3. Lithospheric flexure resulting from dense loads produced by metamorphic phase changes or cooling of igneous intrusions within the lower crust and/or mantle lithosphere (e.g., Haxby et al., 1976; Nunn and Aires, 1988; Fowler and Nisbet, 1985; Klein, 1991; Baird et al., 1995; Naimark and Ismail-Zadeh, 1995)

4. Dynamic topography driven by large scale mantle convection or isolated convective instabilities (e.g., Middleton, 1989; Hartley and Allen, 1994; Downey and Gurnis, 2009).

Some authors propose that a combination of two or more of these processes act together, or at different times, during a given basin's evolution. For example, extension coupled with buried loading (e.g., Hamdani et al., 1991; Hamdani et al., 1994; Stel et al., 1993), buried loading and in-plane stress variations (e.g., Howell and van der Pluijm, 1999), extension and dynamic topography (e.g., Armitage and Allen, 2010; Crosby et al., 2010).

Each of these models is expected to produce a range of distinct geological and geophysical characteristics in response to the tectonic processes that are invoked. Testing such predictions using appropriate observational techniques is critical for distinguishing whether a given model is suitable for explaining the formation of Parnaíba basin, and cratonic basins in general. In Table 1.1, a selection of prominent previously proposed models are listed along with key predictions from each of these. The techniques most useful for testing each prediction are also listed and accompanied by an indication as to whether the relevant data have been acquired for Parnaíba basin and whether these data are available for analysis in this study. These models are also conceptualised in Figure 1.6 and discussed below.

Model type & selected references	Model predictions	Observational technique	Data availability in Parnaíba
Buried loading: lower crust			
[1]Haxby et al., (1976)	Thermally driven domal uplift[1,2,3,4]	—	—
[2]Nunn & Aries (1988)	Regional unconformity below cratonic basin [1,2,3,4]	Shallow SR/surface outcrop	Yes/No
[3]Stel et al., (1993)	Flexed crust (Moho deepening basinward)[1,2,3,4]	Deep SR/WARR/RF	Yes/Yes/No*
[4]Baird et al., (1995)	Dense lower crust (Eclogite: $\Delta\rho \sim 400\ kg\ m^{-3}$)[1,4]	WAR/Gravity	Yes/Yes
	Dense lower crust (Basaltic: $\Delta\rho \sim 150$–$250\ kg\ m^{-3}$)[2,3]	WAR/Gravity	Yes/Yes
	Mafic dyke swarms in basement[2]	Basement samples/exposures	Yes/No
	Strong mid-crustal reflection[1,2,3,4]	Deep SR/WARR/RF	Yes/No*/No**
	Absent or weak Moho reflection[2,4]	Deep SR/WARR/RF	Yes/No*/No**
	Circular basin geometry	Geological mapping	Yes
Buired loading: mantle lithosphere			
Kaminski & Jaupart (2000)	Thermally driven domal uplift (lower amplitude than predicted for a lower crust intrusion)	—	—
	Regional unconformity below cratonic basin	Shallow SR/surface outcrop	Yes/No
	Flexed crust (Moho deepening basinward)	Deep SR/WARR/RF	Yes/No*/No**
	Mantle lithosphere mass excess ($\Delta\rho \sim 85\ kg\ m^{-3}$)	Gravity***/tomography***	Yes/No
	Thick cratonic lithosphere	ST/RF	Yes/No**
	Circular basin geometry	Geological mapping	Yes
In-plane compression			
Lambeck (1983a&b)	Crustal folding (basement/Moho topography in-phase)	Deep SR/WARR	Yes/Yes
Cloetingh (1988)	Late-stage thrust faulting	Shallow SR	Yes
	Increase in subsidence and uplift rates with time	Backstrips	Yes
	Negative Bouguer gravity anomaly over basin	Gravity	Yes
	Continuous sedimentation record (no unconformities)	Borehole records/Outcrops	Yes
	Linear basin geometry	Geological mapping	Yes
Dynamic topography			

Hartley and Allen (1994)	Flexed crust (Moho deepening basinward)	Deep SR/WARR/RF	Yes/No*/No*
Burgess et al., (1997)	Gravitational admittance $\sim 40\ mGal\ km^{-1}$	Gravity/Tectonic subsidence	Yes/Yes
	Consistent with Mantle flow models	Geodynamic modelling	No
	Potentially a conformable basin/basement contact	Shallow SR	Yes
	Non-exponential subsidence profile (linear?)	Backstrip	Yes
Low strain rate extension			
Armitage and Allen (2010)	Stratigraphic onlap (basin widening with time)	Shallow SR/Outcrops	Yes/Yes
Allen and Armitage (2012)	Central "syn-rift" graben & "post-rift" widening	Shallow SR/Borehole logs	Yes/Yes
	Syn-rift normal faulting in upper section	Shallow SR	Yes
	Linear basin geometry	Geological Map	Yes
	Thinned crust beneath the basin	Deep SR/WARR/RF	Yes/No*/No*
	Thick cratonic lithosphere	ST/RF	Yes/No**
	Negative exponential or kinked-linear subsidence profile	Backstrip	Yes
Lithospheric accretion			
Holt et al., (2010;2014)	"Intra" cratonic basin setting	Shallow SR/Deep SR/Basement samples	Yes/Yes/Yes
	Accretion immediately prior to basin initiation	Geological record	Yes
	"Regular" lithospheric thickness ($\sim 125\ km$)	ST	Yes
	Linear basin geometry	Geological map	Yes
	Exponential subsidence profile	Backstrip	Yes
Lithospheric thickening–heating–erosion			
McKenzie & Priestley (2016)	Presence of high grade granulites at basement level	Basement outcrops/Boreholes	No/Yes
	High V_p values in upper crust	WARR	Yes
	Exponential subsidence profile	Backstrips	Yes
	Predictable P-T-t path for basement rocks	Basement outcrop/Borehole samples	No/No

Table 1.1: Summary of proposed models for cratonic basin formation with selected references. Column two lists predicted consequences of each model. Column three lists observational techniques that could be used to test for the presence/absence of each prediction. Column four indicates whether data required for applying the methods listed in Column three are available in Parnaíba basin. SR=Seismic reflection; WARR=Wide-angle reflection/refraction; RF=Receiver function; ST=Seismic tomography. *Limited offset Vibroseis WARR data is analysed in this study (see Section 3.3). Basin wide explosive source WARR data has been acquired as part of PBAP but was not available for interpretation in this study (see Soures et al., (In review)). **A Receiver function study has been carried out as part of PBAP separately from the current study (see Julia et al., (In review)). ***Beyond the current resolution limit of the given technique.

1.5.1 Early models of cratonic basin formation

Two early models proposed to explain cratonic basin formation were those from the classic studies of Haxby et al. (1976) and Sleep and Snell (1976), both of which focused on the Michigan basin. Haxby et al. (1976) postulated a model invoking the impingement of a narrow mantle diapir on the base of the crust (Fig. 1.6a). This was envisioned to prompt heating, metamorphism and eventual ecologisation of the lower crust. The large density increase associated with this phase change then promotes a flexural isostatic response, resulting in a surface depression, infilled by sediments. Such a model was shown to also be in accord with the Bouguer gravity anomaly over the basin, as well as the basins circular shape. Many of the features predicted by this model are testable using the data available in Parnaíba basin. A deepening of the Moho towards the basin centre and the density/V_p structure of the lower crust are particularly important, testable, features of this model. Alternatively, Sleep and Snell (1976) proposed that the tectonic subsidence resulted from a thermal contraction load emplaced on a Maxwell viscoelastic plate, in a style similar to passive margin post-rift subsidence. Although the source of the thermal perturbation remained unknown. Such a model is more difficult to test, as although an exponential tectonic subsidence profile is predicted for a thermally driven subsidence, other processes which produce similar subsidence profiles can not be ruled out (e.g., viscoelastic plate flexure).

Subsequent to these studies, Nunn and Aires (1988) modelled the large Bouguer gravity anomaly evident through the Amazon basin and proposed a model similar to that of Haxby et al. (1976) for the origin of this basin, with the emplacement of a dense lower crustal body responsible for driving surface flexure, while also reconciling the observed gravity anomaly. However, these authors suggest igneous material intruded into the lower crust forms the buried load. Again, this model predicts a present-day crustal structure that is testable for the Parnaíba basin case (Table 1.1).

1.5.2 Buried loading

1.5.2.1 Buried loading: lower crust

Several authors have proposed models similar to that of Haxby et al. (1976), in which, surface flexure is driven by the compensation of a buried load formed via ecologisation of a lower crustal "root". However, various processes for instigating metamorphism have been postulated (e.g., Baird et al., 1995; Hamdani et al., 1994; Naimark and Ismail-Zadeh, 1995; Eaton and Darbyshire, 2010). For example, Baird et al. (1995) speculated that beneath Williston basin ecologisation could have been triggered by a transient heating event or by the injection of mantle-derived metasomatic fluids (Fig. 1.6c). One criticism of this model as a general model for cratonic basin formation is that the gabbro–garnet granulite–eclogite phase transition requires the presence of interstitial water (Ahrens and Schubert, 1975), and as discussed by Armitage and Allen (2010) this is an unlikely condition in dry cratonic regions, which are isolated from processes that may produce large-scale hydration such as subduction.

Stel et al. (1993) also developed a model which evokes a lower crustal buried load, however, similarly to Nunn and Aires (1988), without the necessity of ecologisation (Fig. 1.6d). These authors inferred that deeply eroded Proterozoic sediments found in southern Finland are remnants of a former cratonic basin. Based on observations of the surrounding exposed basement geology, namely mafic dyke swarms, silicic dykes and A-type granite batholiths, they suggested a model in which passive upwelling of asthenospheric material leads to melting of the lower lithosphere and emplacement of basaltic melt at lower crustal levels. Upon crystallisation, this melt becomes a mass excess (buried load), thereby driving plate flexure and basin formation. They also speculated that the basaltic lower crust could potentially enter the ecologite stability field at a later stage and result in a second phase of subsidence, similar to observed at some Phanerozoic basins.

The presence of surface volcanism predicted by this model is difficult to test for well preserved Phanerozoic basins, owing to the lack of exposure due to the blanketing of the sediment cover. However, some conclusions to be drawn from careful consideration of borehole records, flanking basement exposures and integrated interpretation of geophysical data, particularly

magnetotellurics and shallow focused seismic reflection, refraction and gravity.

1.5.2.2 Buried loading: mantle lithosphere

As an alternative model to those discussed above, Kaminski and Jaupart (2000) proposed a buried loading model in which the load is not located in the lower crust, but is instead confined within the mantle lithosphere (Fig. 1.6e). These authors suggested that when sub-lithospheric plume material is injected into thick cratonic lithosphere (which is compositionally depleted with respect to "regular" lithosphere) that this material will reach a neutral buoyancy level within the lithospheric mantle and therefore not penetrate to lower crustal levels. Then, upon solidification, the denser "juvenile" material will represent a mass excess (buried load) driving plate flexure. They also predict a thermal contribution to subsidence as the thermal anomaly created due to the addition of ponded plume material dissipates. This style of buried loading has many similar predictions to that of lower crustal buried loading (Table 1.1), however, the expected pre-subsidence thermal uplift would be subdued due to the smaller positive density contrast during intrusion (e.g. $\sim 15\ kg\ m^{-3}$). Furthermore, the present-day density contrast of the load is also expected to be much smaller compared to that of a lower crustal load (e.g. $\sim 85\ kg\ m^{-3}$), moreover, as this is located in the deep mantle-lithosphere, such a contrast becomes more difficult to detect using current geophysical techniques. The most useful test is the calculation of the expected gravity anomaly and comparison of this to a "residual" Bouguer anomaly over the basin.

1.5.3 In-plane compression and lithospheric folding

Some authors have postulated that in-plane plate tectonic compressional forces may be responsible for cratonic basin formation (e.g., Lambeck, 1983a; Lambeck, 1983b; Cloetingh, 1988). For example, Lambeck (1983a), while investigating the origins of the cratonic basins of central Australia, suggested that the fold-like "basin and basement arch" structure could be explained by folding of the lithosphere due to in-plane compressional stresses (Fig. 1.6b), provided the lithosphere behaves in a viscoelastic manner such that the bending stresses were not unrealistically high. However, Watts (2001) noted two problems with this model: First,

there is a trade-off between the compressive stress and viscosity structure, which can be tailored to fit the subsidence without constraint. The second, and more important, is that it is difficult to explain the five major unconformities that punctuate the evolution of these basins in the context of this process.

Similarly to the buried loading models, this model has predictable features that can be tested simply by analysing the relevant data. The most obvious features are the linearity of the basin, although this may be modified by subsequence processes, the existence of a folded Moho which deepens basinward and is raised either side of the basin, along with an associated Bouguer gravity high–low–high across the basin. Another test, as alluded to above, is the presence of unconformities throughout the sedimentary record as well as tectonic reconstruction evidence for prevailing compression stresses through time. Further features are listed in Table 1.1.

1.5.4 Dynamic topography

Given the large size of cratonic basins and their apparent isolation from plate boundaries, some authors have suggested that they develop in response to underlying mantle processes, as a manifestation of dynamic topography. As recently highlighted by Molnar et al. (2015), this term has been used with various meanings and definitions by different studies. This can make it difficult to distinguish whether a study is postulating some form of lithospheric density perturbation, which would strictly be considered an isostatic process, or a solely non-isostatic process, involving surface deflections driven by the transfer of stresses to the overlying lithosphere from flow in the underlying mantle (i.e., flow-induced normal tractions applied to the base of the lithosphere (Molnar et al., 2015)). For example, Downey and Gurnis (2009) have argued on the basis of its bowl-shape and its close association with a region of high S-wave speeds in the subcrustal lithosphere, that the Congo cratonic basin may have formed in response to a localised downwelling in the lithospheric-mantle, driven by a compositional mass excess. As the mass is constrained within the lithosphere, such a process could be considered as a traditional isostatic response. Alternatively, some authors have argued for a dynamic topography origin in the non-isostatic sense of basal tractions applied to the base of

the lithosphere (e.g., Middleton, 1989; Hartley and Allen, 1994; Fig. 1.6f). Hartley and Allen (1994) argued for a mantle downwelling origin for the Congo basin on the basis of the close correlation of negative Bouguer and isostatic gravity anomalies. Although such a process may modify cratonic basins during their evolution (e.g., Coakley and Gurnis, 1995), it is difficult, however, to reconcile the long-lived (100 Myr's) subsidence of cratonic basins as resulting solely from such a "draw-down" process. The rate of dynamic surface subsidence/uplift caused by mantle flow appears to occur at faster rates than is observed in cratonic basins (e.g., Zhang et al., 2012) and over geological time scales, plate reconstructions show the lithosphere moves thousands of kilometres relative to the underlying asthenosphere, such that the asthenospheric downwelling would be required track with the overlying lithospheric plate in order to maintain the normal stresses holding down the basin. That is to say, dynamic topography is a transient, reversible process.

The best means for testing the validity of dynamic topography as the primary means for cratonic basin formation is

1.5.5 Low strain rate extension

More recently, following the observation that cratonic basins appear to correlate with regions of relatively thick ($> 150\ km$) lithosphere (Priestley and McKenzie, 2006), several authors have modelled cratonic basin subsidence as a consequence of mild extension of the lithosphere at low-strain rates ($< 10^{-16}\ s^{-1}$), with small beta factors, β, (< 1.2) (e.g., Xie and Heller, 2009; Armitage and Allen, 2010; Crosby et al., 2010; Fig. 1.6i). This model is similar to the stretching model of McKenzie (1978) that has proved successful in explaining passive margin and failed rift type basin subsidence. In this sense, cratonic basins are viewed as the end-member case of the "rift-drift" suite of extensional basins (Allen and Allen, 2013). Such a mechanism is attractive for thickened lithosphere as the thermal diffusion time constant of the lithosphere is proportional to the square of its thickness, such that, the cooling of thick lithosphere may explain the long-lived nature of cratonic basin subsidence while also providing a well understood thermal heat source. However, this mechanism would be expected to produce brittle faulting, the development of extensional graben structures and crustal

thinning, features which can be easily scrutinized using seismic reflection data (Table 1.1). To date, such features appear largely absent beneath cratonic basins in seismic images (e.g., Brown et al., 1982; Baird et al., 1995; Daly et al., 2014). Furthermore, from limited crustal structure data beneath cratonic basins (see Section 1.4.5), no obvious thinning of the crust is observed.

1.5.6 Lithospheric accretion and thermal cooling

Holt et al., (2010; 2014) proposed a model in which cratonic basins form as the isostatic response of cooling and thickening of originally thin lithosphere following the amalgamation/accretion of juvenile terranes such as island arcs, accretionary prisms and melanges. These authors highlighted that such crustal assemblages are consistent with those found beneath the North African Ghadames and Al Kufrah basins (e.g., Fig. 1.1), which began forming soon ($\sim 10\ Ma$) after accretion occurred. This model predicts that basin subsidence will continue until isostatic equilibrium of the lithosphere is achieved, as the mantle lithosphere cools and thickens from its thin starting thickness to that which is in isostatic balance, presumably with a mid-ocean ridge column. The resulting subsidence curve is a smooth negative exponential, similar in form to that of the "post-rift" phase of extensional basins.

Fundamentally, for this model to be applicable to any given cratonic basin, the basin must be located above an amalgamation of accretionary terranes in an "intra" cratonic setting. Moreover, the subsidence must initiate immediately after the culmination of the accretionary episode. These features are testable by investigation basement lithologies and geophysical delineation of crustal terranes and dating of syn-tectonic (amalgamation) volcanics along with the earliest sediments of the overlying cratonic basin (Table 1.1). Another important aspect to this model, which cannot be determined, is the starting thickness of the accretionary mantle-lithosphere, which must be thin enough as to promote sustained subsidence for > 150 Ma once final accretion occurs and cooling commences. Holt et al. (2010) suggest that the mantle-lithosphere is likely to be as thin as 20 km at this stage, however, if the initial value is appreciably thicker, subsidence will not be maintained for a sufficient duration.

1.5.7 Lithospheric thickening, radiogenic heating and instantaneous erosion

As an alternative source of heating from that of lithospheric extension, McKenzie and Priestley (2016) have recently suggested that appreciable crustal thickening during orogeny could produce the required thermal perturbation necessary to cause long-lived thermal subsidence of thickened lithosphere (Fig. 1.6h). In this model, the crust is assumed to thicken by a factor of two (from 40 to 80 km) via either a period of orgenesis or gravitational crustal flow. If this thickened crust is maintained for at least 200 Myr, the resulting internal radiogenic heating—which increases by a factor close to four when the crustal thickness is doubled—can result in appreciable heating of the entire lithosphere. A period of rapid (geologically instantaneous) erosion of ~ 40 km of crustal material is then required, leaving a heated block of lithosphere that then cools, contracts and subsides until isostatic equilibrium is achieved, forming a surface depression within which sediments accumulate to form a cratonic basin.

Several observations can be made to test this model (Table 1.1) with McKenzie and Priestley (2016) suggesting the best means is a detailed analyse of the pressure-temperature-time (P-T-t) paths recorded by metamorphic rocks beneath the basin or within the flanking region. This is because the model follows a predictable path which can be compared directly to observations. Direct observations of the basement lithologies are also relevant as these must be consistent with rocks exhumed from ~ 40 km depth. Another test for this model comes from measurement of seismic wave velocities and model of the density of the upper most crust, as the emplacement of high grade granulates at this level would be expected to be reflected in high V_p and densities relative to global averages.

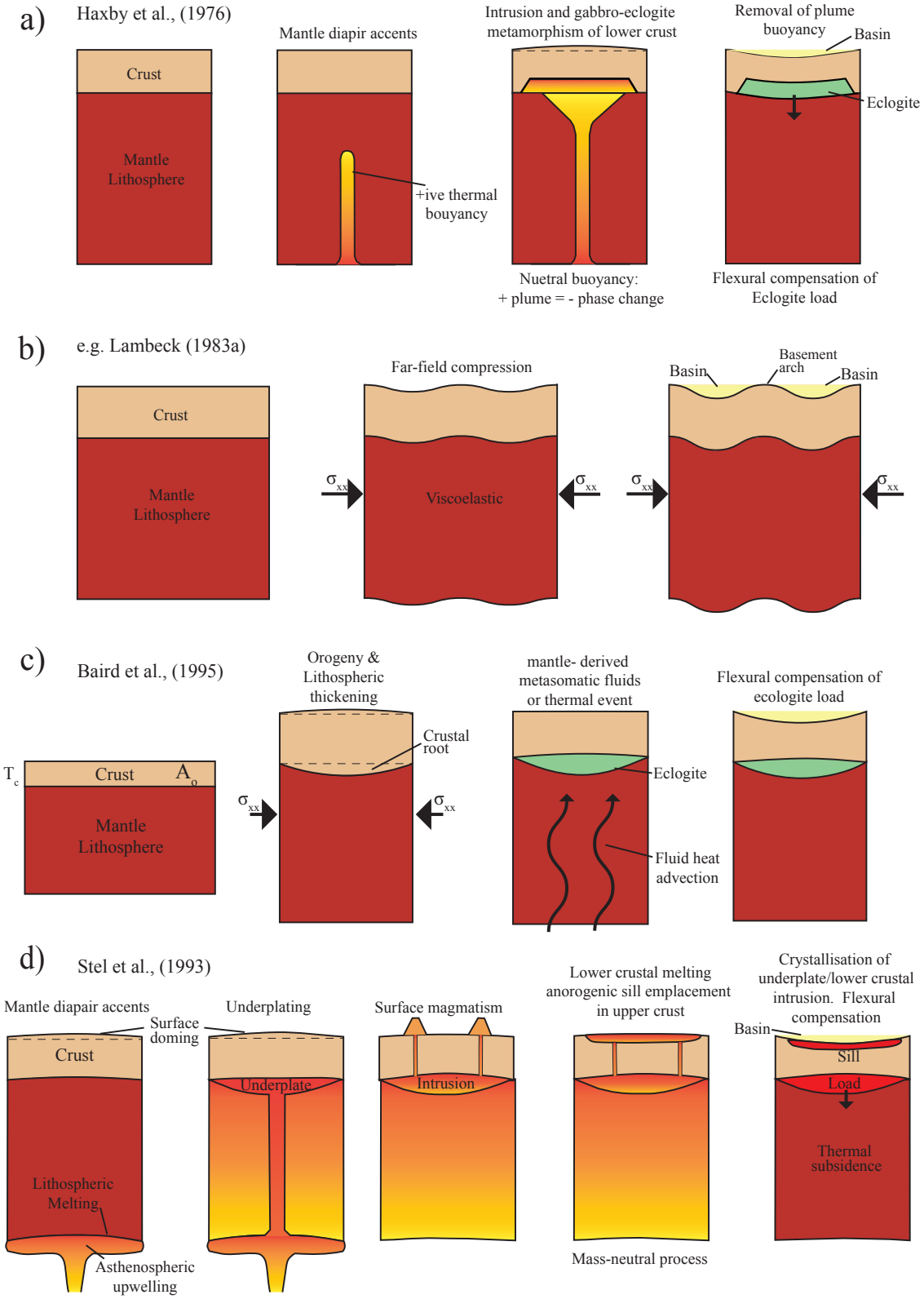


Figure 1.6: Cartoons summarising the main features of some proposed models for cratonic basin formation. See figure text, Table 1.1 and main text for references and model details.

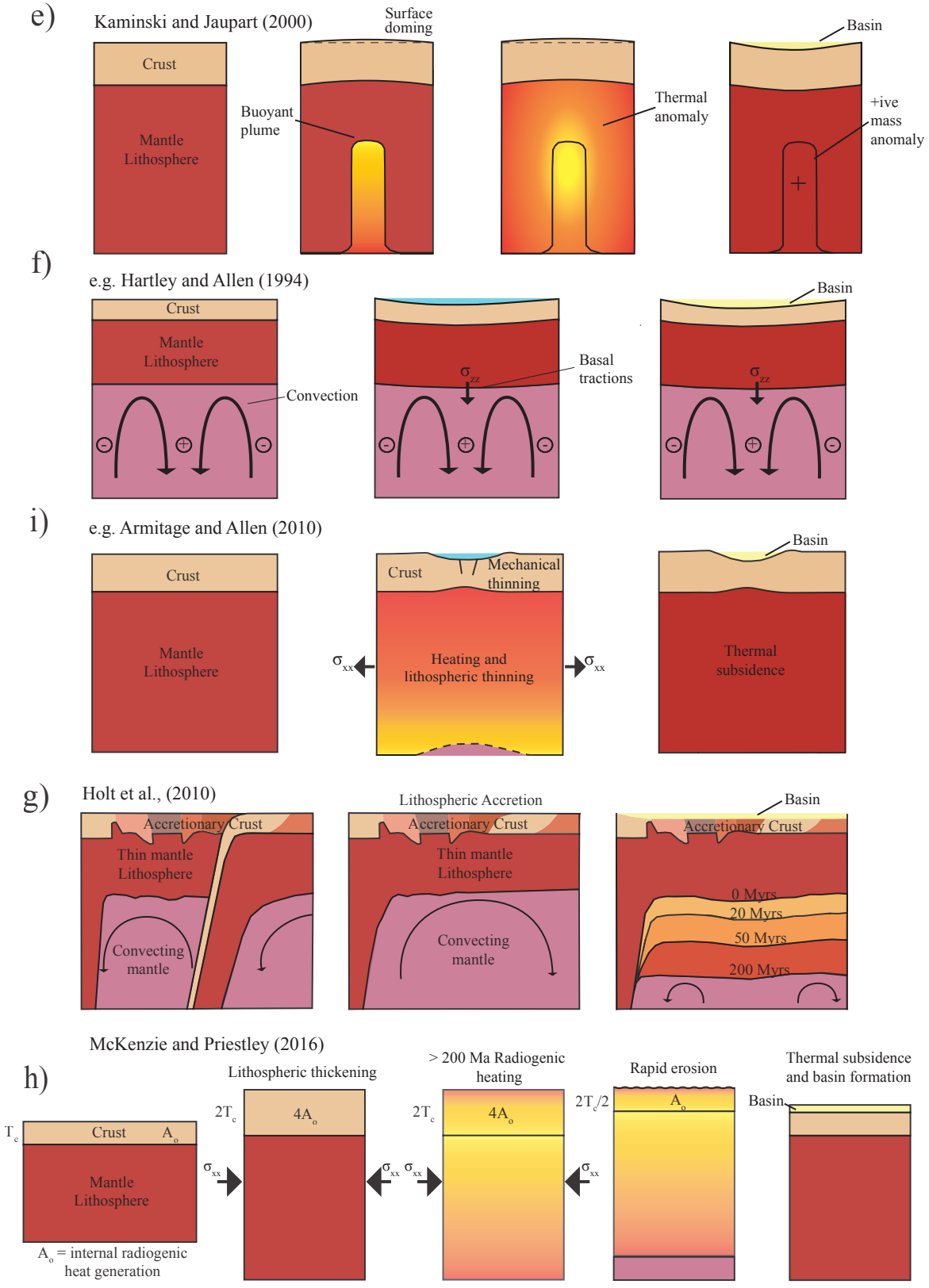


Figure 1.6 continued

1.6 Thesis objectives, scope and research approach

Although many processes have been postulated to explain cratonic basin formation, the origins of these basins remain enigmatic. Many of the mechanisms discussed in the previous section would be expected to produce identifiable geological structures as well as distinct crustal structure and gravity anomalies which could be constrained using geophysical techniques. One limiting factor in improving our understanding of cratonic basins has been a paucity of observational data, particularly on the deep crustal structure with which to constrain, compare, and contrast model predictions.

In order to address this problem, the Parnaíba Basin Analysis Project (PBAP) was instigated by BP and the Agéncia Nacional do Petróleo in collaboration with several British and Brazilian universities, to examine the tectonic origin of a particular cratonic basin in detail—the Parnaíba cratonic basin located in Northeast Brazil—using an observational approach. This basin was selected because it exhibits many of the general characteristics of cratonic basins, including a sub-circular shape, younging of sediments toward the basin centre, a long history of sediment accumulation, and an association with thick lithosphere ($> 150\ km$) far from present-day plate boundaries. Moreover, the Parnaíba basin is one cratonic basin that is easily accessible for fieldwork. As part of PBAP, the fundamental objective of this thesis is to elucidate the crustal structure, subsidence history and tectonic evolution of Parnaíba basin, in order to constrain the formation mechanism of this basin and potentially cratonic basins in general. This is achieved using a suite of newly acquired (as part of PBAP) and legacy geophysical and geological data.

Central to this analysis is a regional $\sim 1400\ km$, 20 s two-way travel time (TWTT) seismic reflection profile acquired by Global Geophysical (Global Geophysical Services, 2012). These data, in conjunction with five wide-angle split-spread receiver gathers collected near the centre of the basin (maximum offsets of $\pm\ 110\ km$) and coincident terrestrial gravity data are used to constrain the sedimentary and crustal structure of Parnaíba basin. Next, gravity data are analysed using a process-oriented approach in order to test basin formation processes. Gravity analysis is also extended to three-dimensions using satellite derived data. The temporal

subsidence history of the basin is then investigated by performing one dimensional Airy-type backstripping of well log data and three-dimensional flexural backstripping of sediment isopachs. Constraints on basin and crustal structure, as well as subsidence history, are then used to test two potential modes of basin formation. Namely, an extensional model or one involving buried-load induced surface flexure.

Finally, similar subsidence and gravity analysis is extended to two additional basins, the Michigan (North America) and Congo (Central Africa) (Fig. 1.1) in order to compare and contrast results from the analysis of Parnaíba basin. These two additional basins were chosen as, collectively, these three basins provide a range of spatial and temporal evolution histories which may help distinguish whether a fundamental basin forming process is (at least partly) responsible for subsidence initiation of all cratonic basins, or whether a variety of processes operate, to ultimately form basins with similar overall character.

1.7 Thesis outline

This thesis is structured as follows:

Chapter one – Introduction

Chapter one provides an overview of the motivation for this study, an introduction to key concepts used throughout, and a summary of the characteristics and previously proposed formation mechanisms for cratonic basins.

Chapter two – Parnaíba basin geological setting

Chapter two provides an overview of the tectonic and sedimentation history of the Parnaíba basin and places basement terranes within the context of the Western Gondwana Orogeny. This is intended to provide context for the interpretation of Parnaíba crustal data presented in the following chapters. A brief review of previous work regarding Parnaíba basin crustal structure and basin formation is also included.

Chapter three – Seismic imaging of the Parnaíba sedimentary basin and crustal structure

Chapter three details the analysis of active source seismic reflection and wide-angle reflection/refraction data along a regional two-dimensional basin-wide transect. The purpose of this analysis is to illuminate the sedimentary basin and crustal structure of Parnaíba basin.

Chapter four – Gravity anomalies and crustal structure

Chapter four builds on the work of Chapter three by utilising terrestrial gravity data to further constrain crustal and lithospheric structure within Parnaíba basin. These data are also used to test models of basin formation via a process oriented approach. Gravity modelling is also expanded to three dimensions using satellite derived data.

Chapter five – Subsidence analysis and geodynamics of the Parnaíba basin

Chapter five is concerned with the temporal evolution of the Parnaíba basin. This is investigated by analysing the subsidence/uplift history preserved within the sedimentary record by performing both one-dimensional and three-dimensional backstripping of sedimentary well logs. These records are then used to test geodynamic models for basin subsidence.

Chapter six – A Comparative study of the Parnaíba, Michigan and Congo cratonic basins

In Chapter six, analysis is extended to the Michigan and Congo basins, in order to compare and contrast the gravity anomalies and subsidence histories of these basins with results obtained from Parnaíba. This analysis is conducted in order to test whether generic conclusions regarding the formation of cratonic basins can be drawn.

Chapter seven – Discussion, conclusions and future work

Chapter seven provides a concise discussion regarding the main findings of this thesis and lists the key conclusions. Recommended future avenues of research are also discussed.

Appendix 1 – Software Development: Geophysical Modelling GUI (gmg)

This appendix provides details regarding the development and usage of a Graphical User Interface (GUI) software package designed for the integrated interpretation and analysis of two-dimensional potential field and seismic reflection data.

Appendix 2 – Seismic processing supplementary figures

This appendix contains supplementary figures from seismic processing presented in Chapter 3.

1.8 Relationship to published work

All of the research presented in this thesis has been published or is intended for publication in peer reviewed journals. This section describes the relationship between published works and theses chapters.

A condensed version of the work presented in Chapters three, four and five has been peer reviewed and published in the Journal of Geophysical Research: Solid Earth under the title:

Tozer, B., A. B. Watts, and M. C. Daly (2017), Crustal structure, gravity anomalies, and subsidence history of the Parnaíba cratonic basin, Northeast Brazil, J. Geophys. Res. Solid Earth, 122, doi:10.1002/2017JB014348

All work presented in Chapter Six is included as part of an article, which has been peer reviewed and accepted for publication in the Journal of the Geological Society under the title:

Watts, A. B., B. Tozer, and M. C. Daly (Accepted), A comparative study of the Parnaíba, Michigan and Congo cratonic basins

Aspects from all chapters have contributed towards an article that has been peer reviewed and is under revision for publication as part of a Special Publication of the Geological Society. This article discusses cratonic basins within the context of the Wilson cycle, under the title:

Daly M. C., B. Tozer, and A. B. Watts (In revision). Cratonic basins and the Wilson Cycle: a perspective from the Parnaíba Basin Brazil. In: Wilson, Houseman, MaCaffrey, Dore & Royden (eds.), 2017, Tectonic evolution: 50 years of the Wilson Cycle concept. Special Publication of the Geological Society

Chapter two is intended to be included as part of a paper focused on the interpretation of

the regional basement tectonic history of Northeast Brazil within the context of the PBAP seismic reflection profile interpretation, intended for submission under the following title:

Tozer, B., M. C. Daly, and A. B. Watts (in prep), Brasiliano tectonic history of Northeast Brazil: insights from crustal scale seismic reflection profiling across Parnaíba basin

The geophysical modelling software developed during this thesis (see Appendix 1) is intended for publication in the Journal of Open Source Software under the following title:

Tozer, B., (in prep), Geophysical modelling GUI (gmg): An open source, python driven, graphical user interface for geophysical modelling, Journal of open source software

Chapter 2

Parnaíba basin geological setting

2.1 Introduction

The Parnaíba basin of Northeast Brazil is one of five cratonic basins located within the South American plate (Fig. 1.1). The others being the Solimões, Amazon, Paraná and Chaco-Paraná basins. Each these basins are infilled with $\sim$ 3–6 km of sediment, contain similar stratigraphic records and share an approximately coincident initiation time in the late Ordovician/Early Silurian (e.g., Milani and Zalan, 1999). They also all exhibit a typical sub-circular geometry, with the exception of the Amazon basin, which has a distinct linear east-west trend. Furthermore, all of these basins, with the exception of the Paraná, are known to be underlain by localised, pre-cratonic basin sedimentary sequences, of Ordovician/Cambrian age (e.g., Milani and Zalan, 1999).

The Parnaíba basin may be considered an "intra"-cratonic basin in that it is located between and above a complex basement comprising several Archaean and Proterozoic terranes that stabilised at the culmination of Brasiliano orogeny (800–500 Ma) with the formation of West Gondwana (e.g., de Brito Neves et al., 1984; Cordani, 1984; Fetter et al., 2000; Cordani et al., 2009). The Phanerozoic basin largely conceals the boundaries between underlying terranes and their precise distribution (Fig. 2.1). However, recent crustal scale seismic facies interpretation from Daly et al. (2014) and potential field work of de Castro et al. (2014)

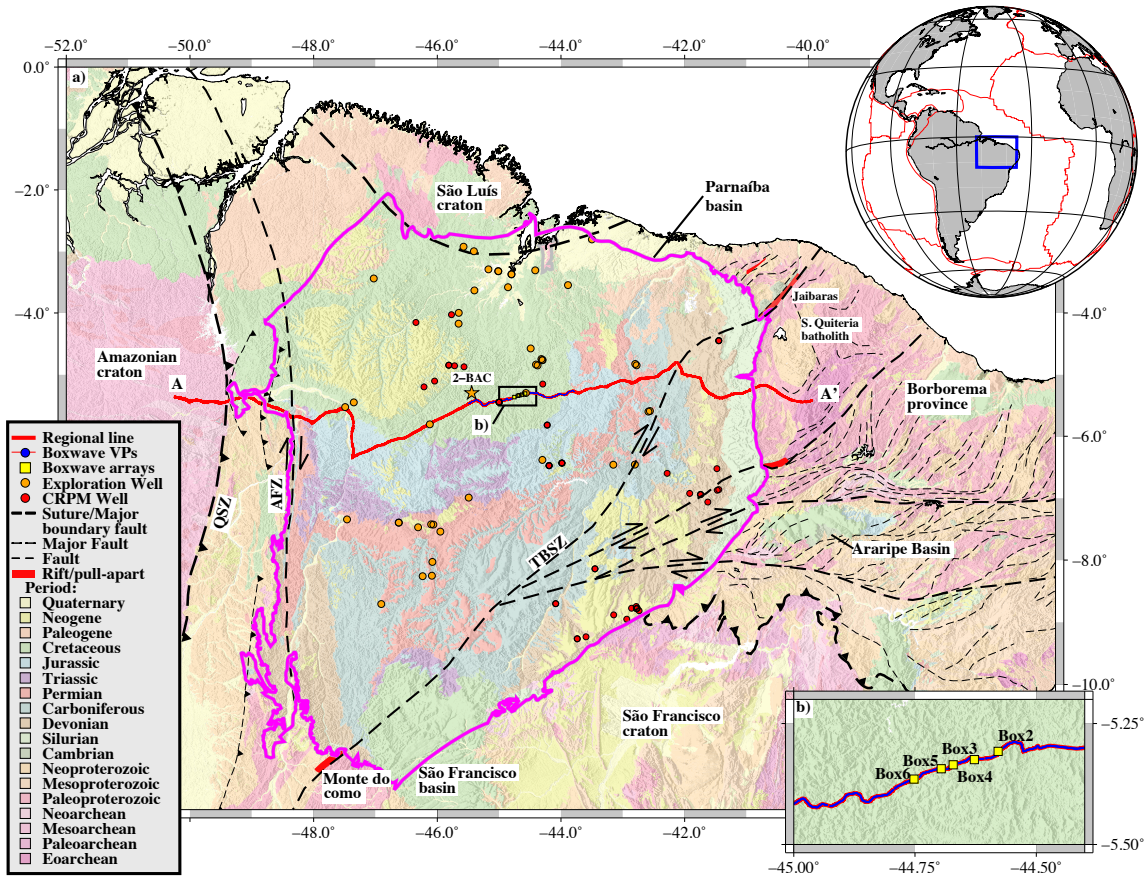


Figure 2.1: Geological setting of the Parnaíba cratonic basin, Northeast Brazil. Solid pink line shows the areal extent of the basin. Red line shows the PBAP seismic reflection profile. Orange filled circles show the locations of exploration well data. Red filled circles show the location of relatively shallow hydrology wells from the Companhia de Pesquisa de Recursos Minerais (CPRM) database. Inset top right shows bounding box of Figure 1a. Inset lower right shows the box wave survey geometry. Yellow stars show the location of the box wave receiver gathers. Dashed lines show principal tectonic features. AFZ = Araguaina Fault Zone, TBSZ = Transbrasiliano Shear Zone (Daly et al., 2014), and QSZ = Quatipuru Suture Zone. Fault locations in the Borborema Province are based on Ganade de Araújo et al. (2014b). Geological map modified from Bizzi et al. (2003).

has demonstrated the three dimensional form of these boundaries, enabling the definition of distinct crustal terranes with abrupt and apparently steep boundaries. There is no evidence for reactivation of these structures during early stages of basin initiation, although, there is strong evidence for episodic reactivation later, throughout the Phanerozoic. The Parnaíba basin has a sub-circular area of $\sim$ 670,000 km^2, however, its stratigraphic boundaries are erosional, suggesting it may have once extended over a wider region, as evidenced by the presence of small outlier basins both to the west (Daly et al., 2014) and east (Matos, 1992) of the basin. Furthermore, the Palaeozoic Saltpond basin, located along the Ghana coast (e.g.,

Atta-Peters et al., 2015), appears to be a stratigraphic equivalent of Parnaíba and may once have been contiguous with Parnaíba prior to break-up of South America and Africa in the Upper Albian at ca. 105 Ma (e.g., Moulin et al., 2010). The stratigraphic record spans from late Neoproterozoic through to the Cretaceous and documents a polyphase subsidence history with five distinct tectono-stratigraphic units separated by regional unconformities.

This chapter reviews the Neoproterozoic/Cambrian tectonic evolution of Northeast Brazil and provides brief descriptions of relevant basement terrains. New constraints from crustal scale seismic data, presented in detail later in this thesis (see Chapter 3), are integrated within this review. This is followed by a description of the Parnaíba basin's stratigraphy and sedimentation history. Finally, results from previous studies regarding the tectonic processes responsible for the formation of Parnaíba basin are summarised. The primary purpose of this review is to provide a tectonic context for the proceeding geophysical work regarding the crustal structure and subsidence history of Parnaíba basin.

2.2 Neoproterozoic/Cambrian tectonic evolution of Northeast Brazil

Our understanding of the gross tectonic evolution of continental lithosphere, that has formed via the amalgamation of several independent terranes, is primarily derived from the recognition, interpretation and radiometric dating of key geological features — diagnostic of particular tectonic environments and processes. These are principally (1) Ophiolites – slices of oceanic crust and upper mantle that have been emplaced upon continental lithosphere during oceanic-continent collision; (2) Island arc terranes - igneous terranes formed as a volcanic island chain during oceanic-oceanic subduction; (3) Magmatic arc terranes - igneous terranes formed during oceanic-continent or continent-continent subduction; (4) Fold and thrust belts, formed during continent-continent collision; and (5) Geophysically imaged crustal scale boundaries, which may or may not be associated with an ophiolite and/or magmatic arc (i.e., a suture or "cryptic" suture). All of these features are found in Northeast Brazil in the vicinity of the Parnaíba basin and help constrain this regions complex amalgamation history. When

available, paleomagnetic data provide key constraints on plate kinematics and paleo-locations. However, in Western Gondwana, there is a paucity of such data for the key time period of 620–520 Ma, particularly for the Amazonian craton (Rapalini et al., 2016).

2.2.1 The Parnaíba Block

A key component in understanding the tectonic history and structural configuration of the basement terrains in the vicinity of the Parnaíba basin, and Northeast Brazil in general, is the recognition of a distinctive terrain, concealed beneath the basin sediments, thought to be a relatively small cratonic fragment (Cordani et al., 2016). This is known as the Parnaíba block and has long been suspected based on plate reconstructions, the ages and lithologies of basement samples recovered from exploration wells, and orogenic polarities surrounding Parnaíba basin (e.g., de Brito Neves et al., 1984; Cordani, 1984; Fuck et al., 2008). de Castro et al. (2014) recently corroborated the existence of a distinctive Parnaíba block based on variations in the character of basin-wide aero gravity and magnetic data. Moreover, Daly et al. (2014) described a newly acquired E-W orientated, crustal scale seismic reflection profile that spans the width of the basin (A–A'; Fig. 2.1), and based on mapping of the crustal seismic facies, these authors identified a distinct Parnaíba block and three other adjacent terranes and their boundaries (See Chapter 3; Fig. 3.9). From these studies it appears that the Parnaíba basin is developed primarily upon the Parnaíba block and the boundaries and sutures between this and the adjacent terrains (Fig. 2.1). The amalgamation process and geologic nature of these terrains as they are presently understood, are summarised in the following sections

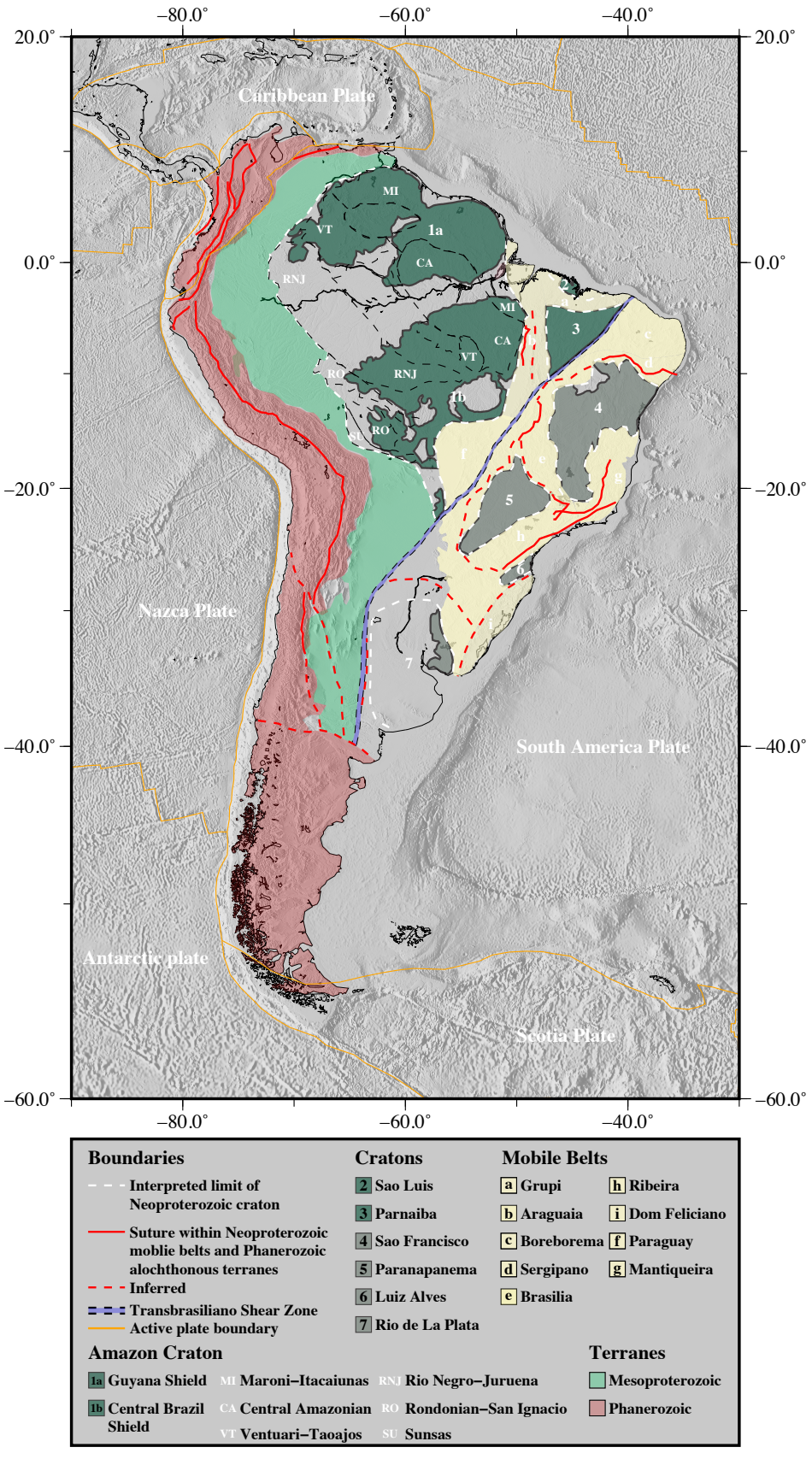


Figure 2.2: Simplified map of the present day basement terrane distribution in South America. Dark green and grey shades differentiate cratons that were part of the Western and Central domains of Gondwana respectively. Light green and pink shade show regions which stabilised in the Mesoproterozoic and Phanerozoic respectively (modified after, Cordani et al., 2016).

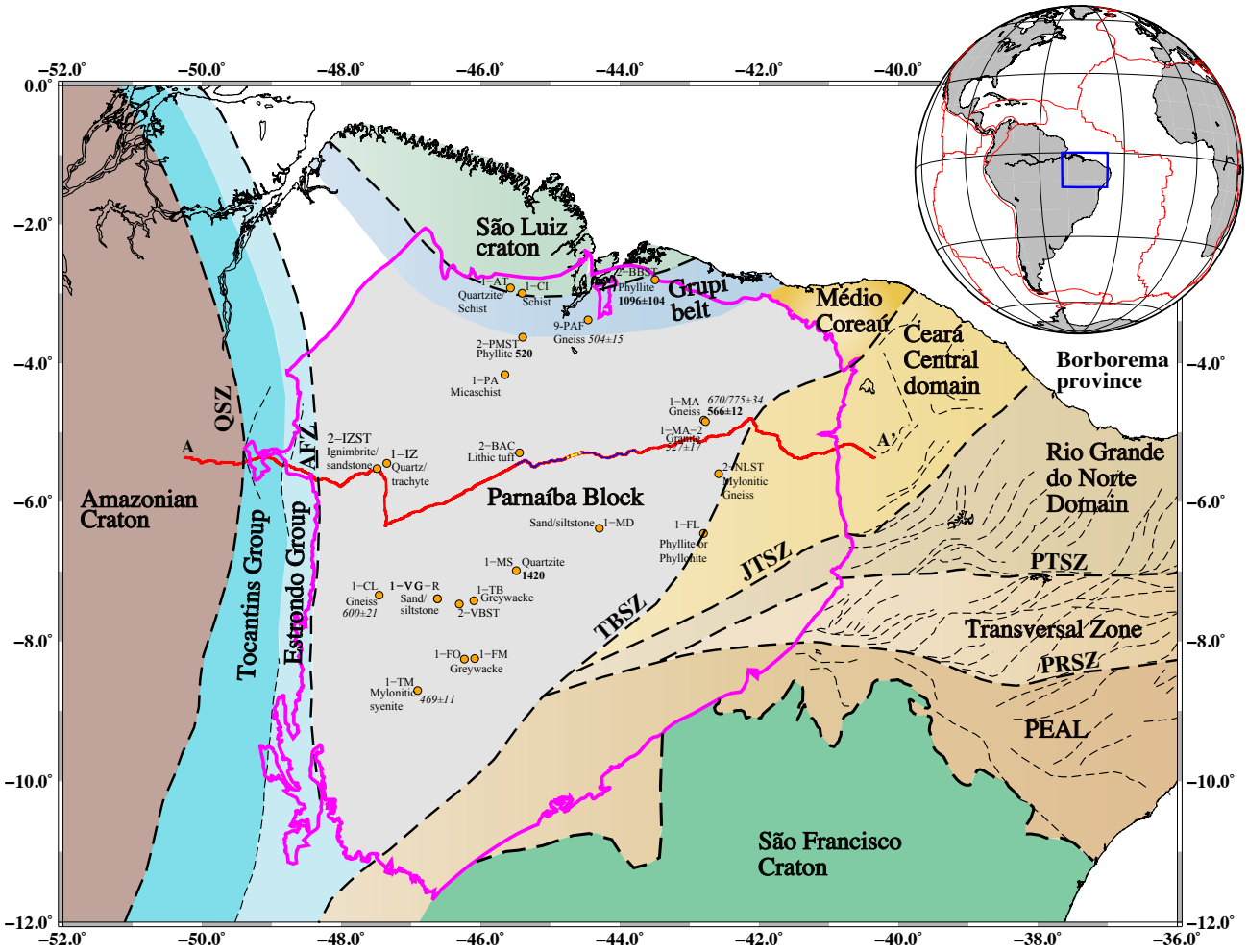


Figure 2.3: Basement terranes of Northeast Brazil. Note boundaries beneath Parnaíba basin (pink line) are inferred. Orange circles show exploration wells from which lithologic samples from below the basal (Silurian) Ipu Formation were recovered; bold numbers are Rb/Sr ages; italic numbers are K/Ar ages (after, Góes et al., 1993 and Sousa, 1996). AFZ = Araguaina Fault Zone, TBSZ = Transbrasiliano Shear Zone; QSZ = Quatipuru Suture Zone; PTSZ = Patos Shear Zone; PRSZ = Pernambuco Shear Zone; JTSZ = Jaguaribe-Tatajuba Shear Zone; PEAL = Pernambuco-Alagoas Massif.

2.2.2 800-500 Ma: The Brasiliano/Pan-African Orogeny and amalgamation of West Gondwana

The present configuration of basement terranes in Northeast Brazil (Figs. 2.2 and 2.3) is primarily the result of Neoproterozoic to Early Cambrian (ca. 800–500 Ma) collisional events, which culminated in the amalgamation of Western Gondwana (Figs. 2.4 and 2.5; e.g., de Brito Neves and Cordani, 1991; Hoffman, 1991; Trouw et al., 2000; Cordani et al., 2013a; Stampfli

et al., 2013; de Brito Neves and Fuck, 2014; Ganade de Araújo et al., 2014a; Ganade de Araújo et al., 2014b; Pimentel, 2016).

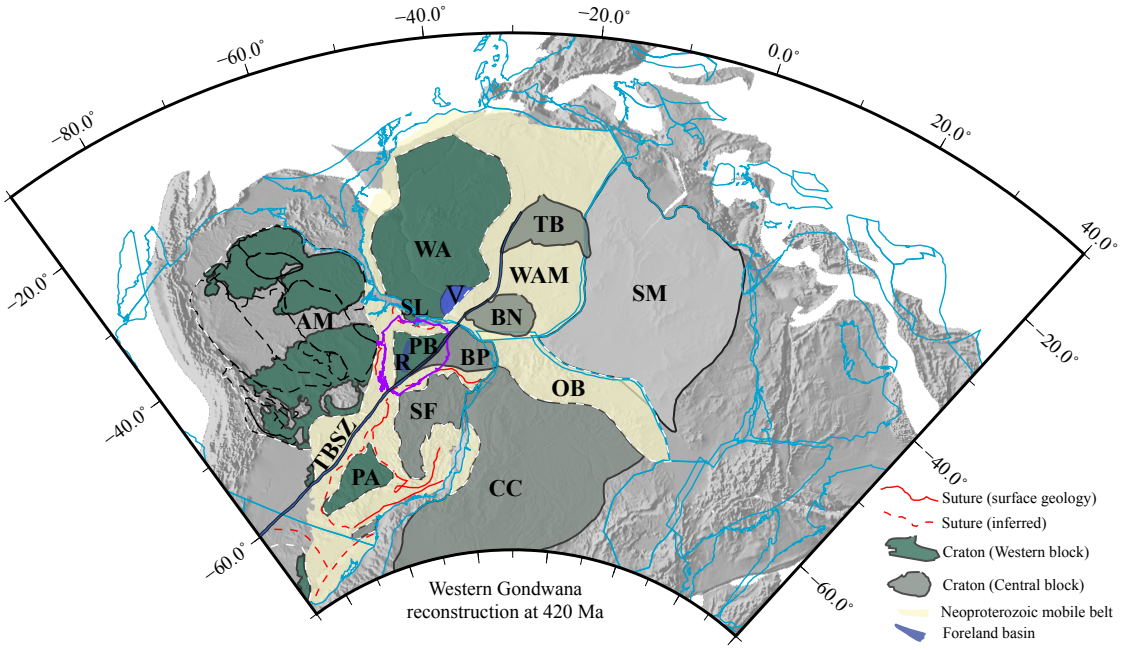


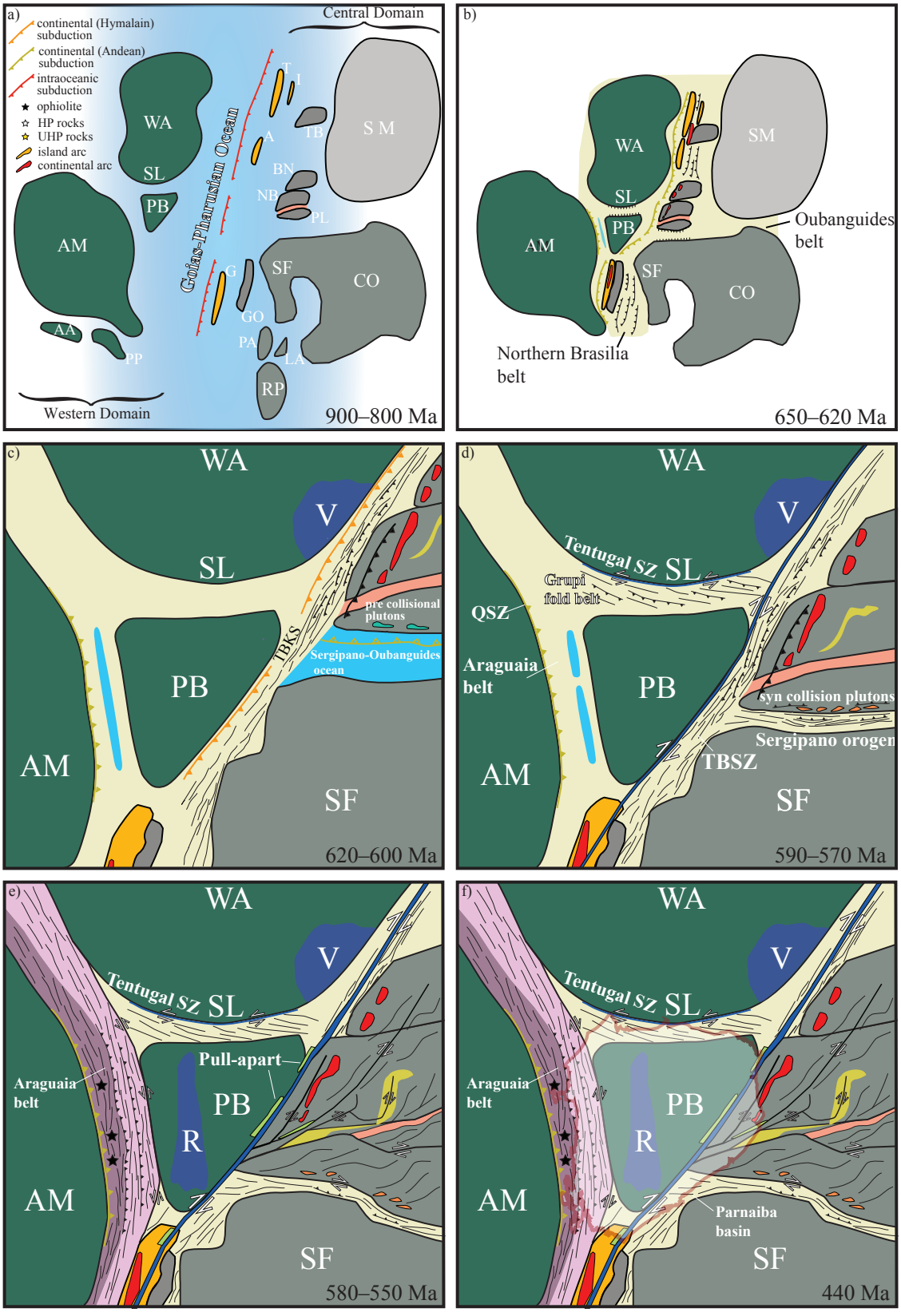
Figure 2.4: Western Gondwana reconstruction at 410 Ma. Grey shade is present day topographic relief. Reconstructed using the finite Euler rotations of Matthews et al. (2016). African plate motion is relative to the true polar wonder-corrected reference frame of (Torsvik et al., 2012). Blue lines are continental outlines of reconstruction polygons. South American and African basement terranes and suture locations are from Cordani et al. (2016) and Begg et al. (2015) respectively. WA = West African Craton; SL = São Luiz Craton; PB = Parnaíba Block; AM = Amazonian Craton; TB = Tuareg Block; WAM = West African Mobile Zone; BN = Benin-Nigerian Block; SM = Sahara Metacraton; SF = São Francisco Craton; CC = Congo Craton; PA = Paranapanema; V = Volta basin; R = Riachão basin; TBSZ = Transbrasiliano Shear Zone.

These events are often collectively referred to as part of the widespread Brasiliano/Pan-African Orogeny, hereafter referred to as the Brasiliano Orogeny. Although subject to extensive and continued debate in the literature (e.g., Meert and Van Der Voo, 1997; Trompette, 1997; Valeriano et al., 2008; Stampfli et al., 2013; Cordani et al., 2013a; Ganade de Araújo et al., 2016; Rapalini et al., 2016), on the basis of U-Pb dating of collisional arcs and the lack of evidence for the existence of any oceanic lithosphere post ca. 600 Ma, the view of Cordani et al. (2013a) is favoured, in that the major event leading to the amalgamation of Western Gondwana was the closure of Goiás-Pharusian Ocean, completed by ca. 600 Ma (Fig. 2.5).

At ca. 800 Ma, when the breakup of Rodinia had commenced, the cratonic blocks and accretionary terranes that now comprise the South American continent were fragmented or formed parts of oceanic domains (Fig. 2.5a; e.g., Cordani et al., 2013a; Oriolo et al., 2017). The Goiás-Pharusian Ocean separated the Amazonian/West-African cratons (Western domain) to the west from the Saharan Metacraton and São Francisco-Congo cratons to the east (Central domain). Subsequent subduction and closure of this ocean basin resulted in the formation of orogenic belts between these cratons and smaller cratonic fragments such as the Goiás Massif and Parnaiba Block; with associated accretion to their margins and eventual continent-continent collision (Fig. 2.5b and 2.5c). In the vicinity of the Parnaíba basin, suturing occurred along the Quatipuru Suture Zone (QSZ; Daly et al., 2014) and Transbrasilano-Kandi tectonic corridor (TBTC; Cordani et al., 2013b) (Figs. 2.4; 2.5c and 2.5d). Based on analysis of ultrahigh-pressure metamorphic rocks from the Dahomey belt in West Africa and Borborema Province in Northeast Brazil, Ganade de Araújo et al. (2014a) suggested this orogenesis produced a mountain belt comparable to that of the Himalaya along the axis of the TBTC. The Volta basin (Figs. 2.4; 2.5c) formed in response to orogenic loading and flexure, and is presumably the remnant of a much larger foreland. The Riachão basin (Porto et al., In press), concealed beneath the Phanerozoic sediments of the Parnaíba basin, is a foreland that is potentially one equivalent of the Volta (Fig. 2.4).

The final stage of deformation involved the activation of the TBTC as a continental scale strike-slip plate boundary, the Transbrasilano-Kandi Shear Zone (TBSZ). Although poorly constrained, Ganade de Araújo et al. (2016) argue that between 400-1400 km of dextral displacement was accommodated along this shear zone between ca. 610–550 Ma. Concurrently, a subsidiary network of crustal scale shear zones, developed within Borborema Province, splaying from the TBSZ (Fig. 2.5e; e.g., Neves et al., 2012; Archanjo et al., 2013; Ganade de Araújo et al., 2014b). This shearing extensively reworked this domain and facilitated the development of several narrow (10–20 km) pull-apart grabens adjacent to the major faults (e.g., Guimarães et al., 2005).

On the eastern edge of the Parnaíba block, the metasedimentary rocks of the Araguaia belt were overthrust upon the Amazonian craton with a westward vergence along the Quatipuru suture zone (QSZ; Moura et al., 2008; Daly et al., 2014). This was followed by dextral shear


a)
continental (Hymalain) subduction
continental (Andean) subduction
intraoceanic subduction
ophiolite
HP rocks
UHP rocks
island arc
continental arc
Central Domain
Western Domain
WA
SL
PB
AM
AA
PP
Goias-Pharusian Ocean
T
I
A
TB
BN
NB
PL
G
GO
PA
LA
RP
SF
CO
S M
900–800 Ma
b)
WA
SL
PB
AM
SM
SF
CO
Oubanguides belt
Northern Brasilia belt
650–620 Ma
c)
WA
V
SL
PB
AM
SF
IBKS
pre collisional plutons
Sergipano-Oubanguides ocean
620–600 Ma
d)
WA
V
Tentugal SZ
SL
Grupi fold belt
QSZ
Araguaia belt
PB
AM
SF
syn collision plutons
Sergipano orogen
TBSZ
590–570 Ma
e)
WA
V
Tentugal SZ
SL
Araguaia belt
Pull-apart
PB
R
AM
SF
580–550 Ma
f)
WA
V
Tentugal SZ
SL
Araguaia belt
PB
R
AM
Parnaiba basin
SF
440 Ma

motion, accommodated along the Araguaia Fault Zone (AFZ; Fonseca et al., 2004). Ganade de Araújo et al. (2014b) and Fonseca et al. (2004) postulate that these shear motions facilitated north-eastward extrusion of Borborema Province and Parnaíba block, caught between the Amazonian, West African and São Francisco cratons.

Although the São Francisco and São Luiz cratons were rifted from the Congo and West African cratons during opening of the equatorial Atlantic in the Albian ca. 105 Ma (e.g., Moulin et al., 2010) the basement terrane configuration achieved by end of the Brasiliano/Pan-African Orogeny at ca. 500 Ma, has remained stable throughout the Phanerozoic (Almeida et al., 1981). Deposition of the oldest preserved sediments of the Parnaíba cratonic basin —the Ipu formation—occurred $\sim$ 60 Myr after the culmination of these events in the early Silurian (Grahn et al., 2005) (Fig. 2.5f).

2.2.3 The Northern Brasilia belt, Amazonian and São Francisco cratons

The first orogenic event to occur in the Northeast Brazilian region involved convergence between the Amazonian Craton, the adjacent Goiás massif and the São Francisco Craton,

Figure 2.5 ***(preceding page)*:** Cartoon illustrating the gross tectonic history of basement terrains in the vicinity of Parnaíba basin during the amalgamation of Western Gondwana. a) Schematic positions of cratons, cratonic fragments and island arcs prior to convergence. b) Initiation of the Brasiliano/Pan African Orogeny in the Western Gondwana region. Formation of the Northern Brasilia fold and thrust belt between the Amazonian and São Francisco cratons. c) Magnified view of the Parnaíba basin region. Note subduction of the Amazonian craton beneath the Araguaia passive margin. Opening of the Sergipano-Oubanguides Ocean and continental-continental collision between the "Western" and "Central" domains leading to the development of the Volta (V) and Riachão (R) foreland basins. d) Overthrusting of the Araguaia group upon the Amazonian Craton with associated ophiolite emplacement and suturing along the Quatipuru Suture Zone (QSZ). Convergence between the São Luiz Craton and Parnaíba Block forming the Gurupi fold and thrust belt. Suturing of the Western and Central Domains along the Transbrasiliano-Kandi Shear Zone (TBKS) and reactivation as a dextral shear zone (TBSZ). e) Dextral shearing along the TBSZ and development of an associated complex shear zone network within Borborema Province promoting NW extrusion. Dextral shear along the Araguaia Fault Zone (AFZ). f) Stabilisation of basement terrains and initiation of Parnaíba basin subsidence. Abbreviations as defined in Figure 2.4. Based on interpretations of Klein et al. (2005); Begg et al. (2015) and Ganade de Araújo et al. (2014a). (Modified after Cordani et al., 2013a; Ganade de Araújo et al., 2014b; Ganade de Araújo et al., 2016).

resulting in the formation of the northern section of the Brasilia fold belt (Fig. 2.5b; Alkmim et al., 2001; Valeriano et al., 2008; Cordani et al., 2013a; Coelho et al., 2017). Dating of syn-tectonic granites suggest this occurred at ca. 650–630 Ma (e.g., Ebert et al., 1996; Campos Neto and Caby, 1999; Valeriano et al., 2004).

From west-to-east the Brasilia belt consists of the Goiás magmatic arc, Goiás Massif and a suite of Meso-Neoproterozoic metasedimentary units that overthrust Paleoproterozoic basement forming east-verging nappes and thrust sheets on the western margin of the São Francisco craton (e.g., Alkmim et al., 2001; Laux et al., 2005; Valeriano et al., 2008; 2012; Pimentel, 2016).

The Goiás Massif contains Achaean and Paleoproterozoic terrains of unknown provenance (Fuck et al., 2008) and is possibly a cratonic fragment Valeriano et al. (2008). The Goiás magmatic arc is thought to represent a composite terrain of intraoceanic island arcs, formed within the Goiás Ocean at ca. 900–800 Ma and two younger (790–786 Ma and 669–630 Ma), more evolved and possibly continental arcs (Pimentel and Fuck, 1992; Pimentel et al., 2000; Pimentel, 2016). The older 900 Ma ages indicate that subduction within the Goiás Ocean was active at this time, coeval with the breakup of Rodinia (Pimentel and Fuck, 1992; Laux et al., 2005). A recent geochemical study also suggests that arc terrains found in West Africa adjacent to the TBSZ (Tilemsi and Amalaoulaou) are Goiás equivalents, implying the arc system may have spanned some 4000 km (2.5a; e.g., Cordani et al., 2013b; Ganade de Araújo et al., 2014a; Pimentel, 2016).

The Amazonian craton consists of five tectonic provinces with distinct structure and geochronological ages (Cordani et al., 2009). The Maroni-Itacaiunas Province bounds Parnaíba basin to the Northwest, while the Central Amazonian Province is found further southward (Fig. 2.2). Internally, the Amazonian craton has been stable since the Paleoproterozoic with no evidence of younger (e.g., Transbrasiliano) tectonic signatures identified (e.g., de Brito Neves and Cordani, 1991). The Maroni-Itacaiunas Province contains predominantly Paleoproterozoic gneiss, migmatites and granitoids both reworked and juvenile, granite-greenstone terrains and local high-grade polymetamorphic Archean nuclei (Teixeira et al., 1989). The Central Amazonian Province comprises Archaean/Paleoproterozoic high-grade metamorphic

rocks such as orthogneiss, migmatites and tonalites, granite-greenstone terranes and minor metasediments and igneous rocks that are unconformably overlain by local supracrustal sequences consisting of greenschist metavolcanics, a banded iron formation and platform sediments (e.g., Herz et al., 1989; Teixeira et al., 1989).

The São Francisco craton, which was contiguous with the Congo craton prior to the opening of the Atlantic Ocean (e.g., Teixeira and Figueiredo, 1991), consists of high-grade and highly migmatised Archean gneissic basement, intruded by granitoid and mafic/ultramafic volcanics (e.g., Almeida et al., 1981; Brueckner et al., 2000). Supracrustal Paleoproterozoic medium-grade metasedimentary and metavolcanic rocks, locally overlie the basement complexes (Almeida et al., 1981; Brueckner et al., 2000) and Neoproterozoic platform sediments cover much of the craton's interior (e.g., Alkmim et al., 2001).

Further south, in the southern Brasilia belt, some authors argue that collision occurred following west-directed subduction of the São Francisco passive margin beneath the Paranapanema Craton (e.g., Coelho et al., 2017). Further northward, Valeriano et al. (2008) also favour west-directed subduction of São Francisco passive margin beneath the Goiás Massif. However, subduction polarity is poorly constrained in this region and the alternative interpretation of Ganade de Araújo et al. (2014a), in which east-directed subduction of the Western domain cratons beneath the Central Domain cratons occurred, is preferred (Fig. 2.5). This interpretation follows magnetotelluric imaging of an east dipping structure within the mantle beneath the Borborema province to the north, which could possibly represent a fossil slab (Padilha et al., 2014; 2017) and evidence of coeval east dipping subduction in West Africa (Caby, 2003; Duclaux et al., 2006).

2.2.4 Borborema Province

The Borborema Province flanks the eastern side of the Parnaíba basin and is generally considered to comprise of five major domains (Fig. 2.3; e.g., Almeida et al., 1981; dos Santos et al., 2010). These domains are separated by a complex pattern of continental scale E-W, ENE-WSW trending dextral shear zones that developed in the Late Neoproterozoic/Cambrian near the culmination of the Brasiliano orogeny and splay from the TBSZ (Fig. 2.3; e.g., Almeida

et al., 1981; Neves, 2003; Ganade de Araújo et al., 2014b; Neves et al., 2015). The basement terrains comprise predominantly Paleoproterozoic gneiss and migmatitic rocks, some of which are juvenile, while others have been reworked from older Archean nuclei (e.g., Fetter et al., 2000; Neves, 2003; Neves et al., 2006).

These basement terrains were extensively reworked during the Brasilano Orogeny, with associated deposition of supracrustal sequences, metamorphism, granite batholith emplacement and pluton intrusion. Development of the shear zones occurred subsequent to these events, as revealed by the deformation of the pre-existing regional foliation fabric (e.g., Neves, 2003; Neves et al., 2006; Neves et al., 2012; Neves et al., 2015).

2.2.4.1 Borborema Province collision I

Based on magmatic and metamorphic ages Ganade de Araújo (2014a; 2016) suggest Borborema Province was involved in two major collisional events during the Brasilano Orogeny. The first occurred between ca. 615–630 Ma, and involved collision between Northern Borborema Province and a Western domain craton—most likely the southern part of the West African craton (Ganade de Araújo et al., 2016)—resulting in suturing along the TBKS (Fig. 2.5c). The Santa Quiteria magmatic arc of Northern Borborema Province (Fig. 2.1) returns dates of 644–630 Ma and records the subduction phase prior to continental collision (e.g., Ganade de Araújo et al., 2012).

2.2.4.2 Borborema Province collision II

A second collisional event occurred at ca. 590–570 Ma involving the closure of a restricted ocean between the Pernambuco-Alagoas Massif (PERL) of southern Borborema Province and the São Francisco craton, forming the Sergipano fold belt (Fig. 2.5d and 2.5e; Bueno et al., 2009; Oliveira et al., 2010; Ganade de Araújo et al., 2014b; Oliveira et al., 2015). This is a south verging thrust zone which emplaced supracrustal rocks onto the northern margin of São Francisco Craton (Ganade de Araújo et al., 2014b). Syn-orogenic leucogranites return ages of 584 ± 10 Ma and 571 ± 9 Ma (Bueno et al., 2009).

2.2.5 The Gurupi Belt and São Luiz Craton

The São Luiz Craton and Gurupi Fold Belt bound Parnaíba basin to the north. The São Luiz craton is thought to be a dissected piece of the Paleoproterozoic West African Craton, left behind in South America during Atlantic rifting (e.g., Bullard et al., 1965). It consists of a range of meta-sedimentary, meta-igneous and mostly granitoid igneous assemblages that are predominantly derived from island-arc and collisional settings (e.g., Klein et al., 2005 and references therein). The Tentugal shear zone separates the southern edge of the São Luiz Craton from the NNW/SSE trending Gurupi mobile belt (Klein et al., 2005). The history of this fold belt is poorly understood due to a lack of exposure. Its basement consists primarily of Paleoproterozoic rocks with some subordinate metatonalite Achaean rocks that are likely related to the original formation of the São Luiz craton (Klein and Moura, 2008). Klein et al. (2005) synthesised lithological and geochronology data from both the São Luiz craton and Gurupi fold belt and concluded that a Neoproterozoic rifting phase at ca. 730 Ma (potentially forming an ocean basin), preceded late Neoproterozoic closure which lead to convergence between the Parnaiba Block and São Luiz craton. Thus, forming the NNE verging Gurupi fold and thrust belt (Fig. 2.5d). The timing of this collisional episode lacks geochronological constraints, however, a post-orogenic granite returns a U-Pb age of 549 $\pm$ 4 Ma (de Moraes Palheta et al., 2009) suggesting deformation/metamorphism is likely to have occurred at ca. 580–550 Ma (Klein et al., 2005).

2.2.5.1 Araguaia Belt Amazonian Craton

The Araguaia belt marks the western boundary of Parnaíba basin, separating the basin from the Amazonian Craton (de Almeida et al., 1967). This consists of Neoproterozoic metasediments that were overthrust upon the Amazonian craton, with a WNW vergence, along the Quatipuru Suture zone (e.g., Ussami and Molina, 1999; Fonseca et al., 2004; Paixao et al., 2008; Daly et al., 2014). Syntectonic granites date this event at ca. 550 Ma (Moura et al., 2008). The belt consists of two main Groups: the basal Estrondo and the upper Tocantins Groups (Herz et al., 1989). The Estrondo Group, on the eastern side of the belt, contains Archean Gneissic/migmatitic basement domes surrounded by supracrustal Neoproterozoic

metasediments up to amphibolite facies. While to the west, the Tocantins Group consists of lower grade psammites, pelites and schists (e.g., Herz et al., 1989; Fonseca et al., 2004; Paixao et al., 2008) with interleaved Neoproterozoic ophiolitic mafic-ultramafic assemblages, such as the Quatipuru and Serra do Tapa ophiolites (e.g., Paixao et al., 2008). The thrusting fabric is overprinted by a later phase of dextral shear motion (Fig. 2.5e), which was accommodated along the north-south oriented Araguaia Fault Zone (Fonseca et al., 2004).

2.3 Parnaíba basin stratigraphy

Like many cratonic basins, the sedimentary record of Parnaíba basin documents a polyphase history. Five distinct tectono-stratigraphic Units (TS-U) are recognisable and are separated by regional unconformities (e.g., de Castro et al., 2014; 2016). In this study we term these the Riachão (TS-1); Jaibaras (TS-2); Parnaíba (TS-3); Mearim (TS-4); and Grajaú (TS-5) Units (Fig. 2.6). The Parnaíba cratonic basin sequence (TS-3) is the focus of this study. This spans the Lower Silurian–Middle Triassic and is characterised by relatively slow subsidence and stratigraphic thickening towards the basin depocenter, indicative of local subsidence relative to the basin surroundings. This phase of basin subsidence and the corresponding stratigraphy are discussed in detail below in Section 2.4. An understanding of the other TS-Units is, however, important in order to place TS-3 within the context of the geological evolution of this region. These units are therefore briefly described below.

2.3.1 TS-1: Riachão basin

The Riachão unit (TS-1) includes the oldest preserved sediment in the basin. These sediments are believed to be Late Neoproterozoic to Cambrian in age (Mesner and Wooldridge, 1964; Porto et al., In press) and are recorded from seismic and well data in the southwestern area of Parnaíba. de Castro et al., (2014; 2016) interpreted the Riachão package as a Neoproterozoic rift. However, this view has recently been challenged by Porto et al., (In press), who, on the basis of industry two-dimensional seismic data and two well records, interpreted the Riachão as a remnant foreland basin, bounded by thick skinned thrust faults of Cambro-Ordovician

age.

2.3.2 TS-2: Jaibaras basin

Unit TS-2 comprises the volcanic dominated Jaibaras Group (Sousa, 1996; Milani and Zalan, 1999). This sequence outcrops within the graben-like Jaibaras and Monte do Carmo troughs, adjacent to the TBSZ at the northeast and southwest edges of Parnaíba basin respectively (Figure 2.1). The equivalent sequence is also seismically imaged and drilled adjacent to the TBSZ beneath the basin (e.g., Figure 3.7; de Castro et al., 2016). The Jaibaras formation has been interpreted as a rift infill resulting from a pervasive Cambro-Ordovician rifting event (e.g., de Oliveira and Mohriak, 2003). However, the long and narrow (50km by 15 km) form, NE/SW alignment and spatial association of these rifts with the TBSZ, appears to suggest a a pull-apart origin is more likely, with formation occurring during dextral strike-slip motion along the TBSZ during the Cambrian/Early-Ordovician (e.g., Guimarães et al., 2005). TS-3, the Parnaíba cratonic basin sequence, follows TS-2 and is discussed in detail later in section 2.4.

2.3.3 Triassic Volcanism

A Middle Triassic unconformity marks the termination of the Parnaíba cratonic basin sequence sedimentation record. Midway through this time-gap, the western side of the basin experienced a phase of predominantly extrusive volcanism, with the deposition of basaltic lava flows known as the Mosquito Formation (Góes et al., 1993; Merle et al., 2011). These are individually up to ~ 200 m thick and $40^{Ar}/39^{Ar}$ dating returns ages of $199.4 \pm 2.7\ Ma$ (Merle et al., 2011). Furthermore, Merle et al. (2011) showed that although returning identical ages, these magmas contain three distinct chemical compositions, suggesting a primary asthenospheric source (high-Ti); lithospheric contamination (or melting of the most fusible part of a metasomatized lithospheric mantle) (low-Ti); and crustal contamination (modified high-Ti). Their origin is attributed to the Central Atlantic Magmatic Province (CAMP) which is related to the formation of the East Coast, USA and West Africa rifted margins and the opening of the Central Atlantic Ocean (e.g., Baksi and Archibald, 1997; Merle et al., 2011).

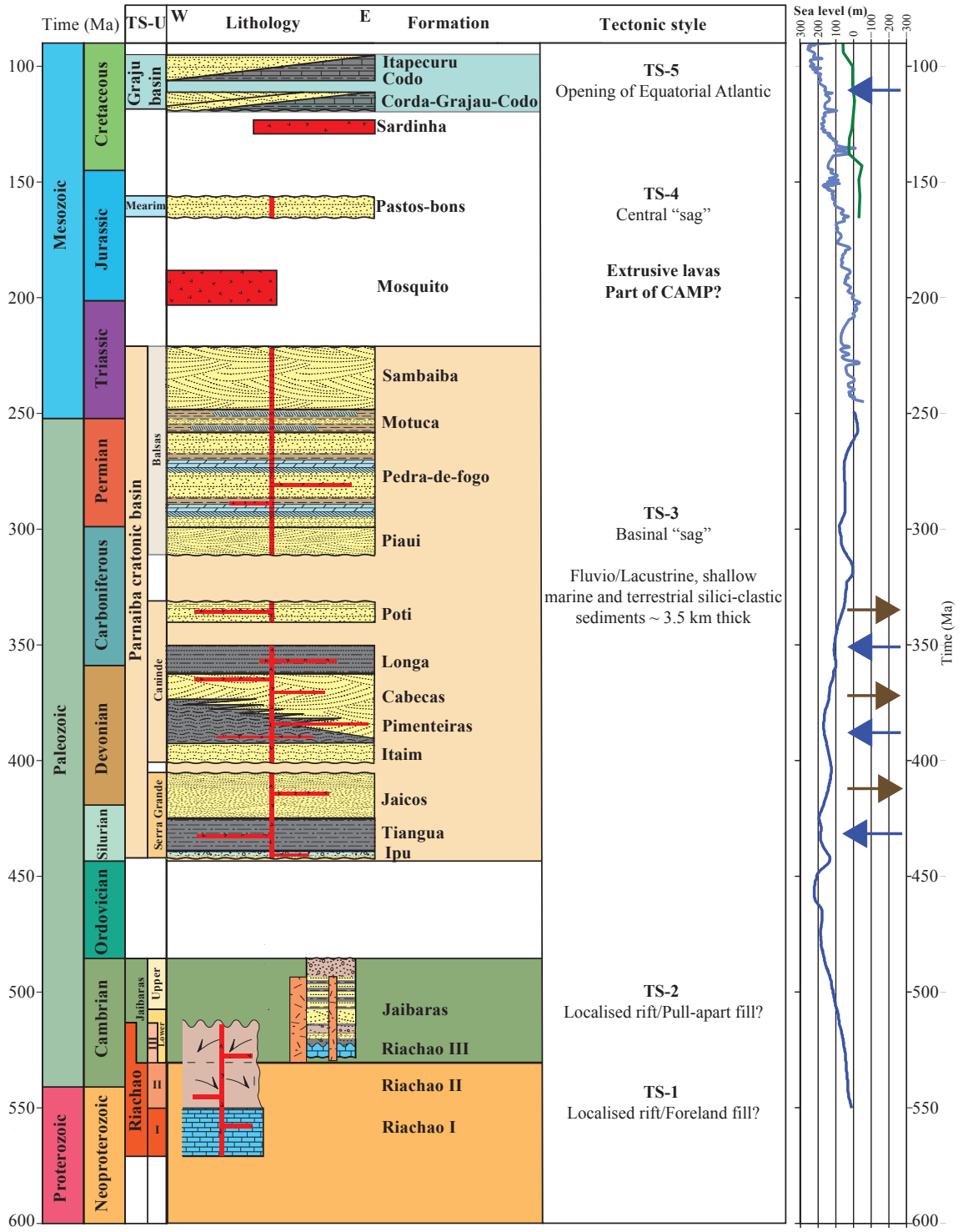


Figure 2.6: Summary stratigraphic column for the Parnaíba cratonic basin illustrating the main tectonostratigraphic (TS) units, lithologies, major unconformities, and regional tectonic events and eustatic sea level. TS-1–TS-3 all reside above crystalline basement. Stratigraphic column is based on Vaz et al. (2007) and de Oliveira and Mohriak (2003). Paleozoic eustatic sea level curve is the "long-term" curve from Haq and Schutter (2008); Blue and green Mesozoic eustatic sea level curves from Haq et al. (1987) and Steckler and Watts (1978) respectively. Blue arrows indicate marine transgressions and brown arrows indicate marine regressions.

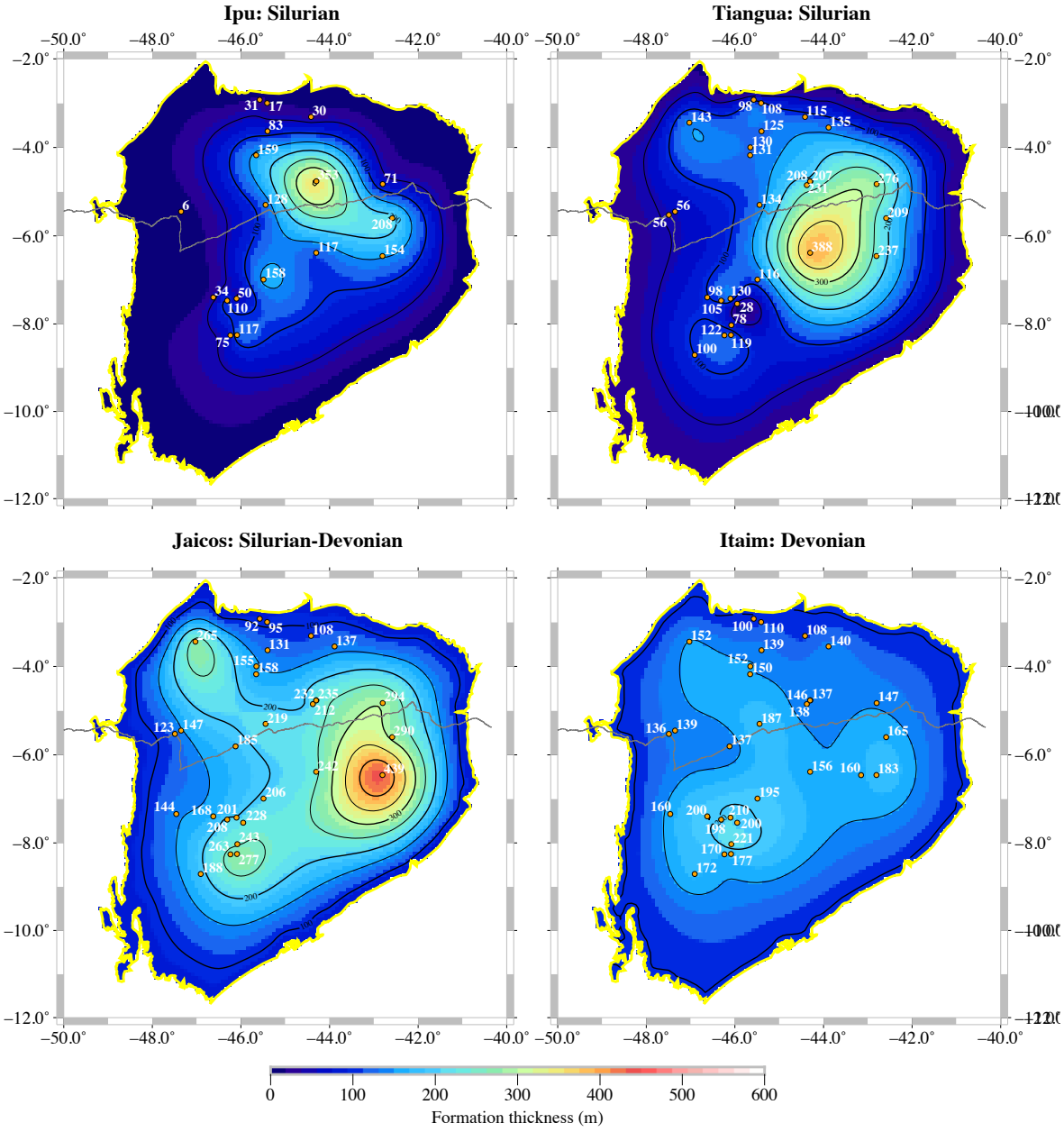


Figure 2.7: Isopach maps for sedimentary formations of the Ipu through Itapecuru formations of Tectono-Stratigraphic Units 3–5 (i.e., the cratonic basin sequence and younger) (Fig. 2.6). Yellow line shows the present-day basin outline. Green dashed line is the outcrop extent for the given formation. Grey line is a regional seismic reflection profile (see Chapter 3). Orange and red circles are exploration and CPRM wells used in isopach construction; numbers are thickness of unit in meters. Note thicknesses in these maps have not been corrected for post-deposition igneous intrusion volumes. Furthermore, data from the offshore shelf and slope deposits are not included in the Cretaceous isopachs and hence these are not representative beyond the basin limit (yellow line).

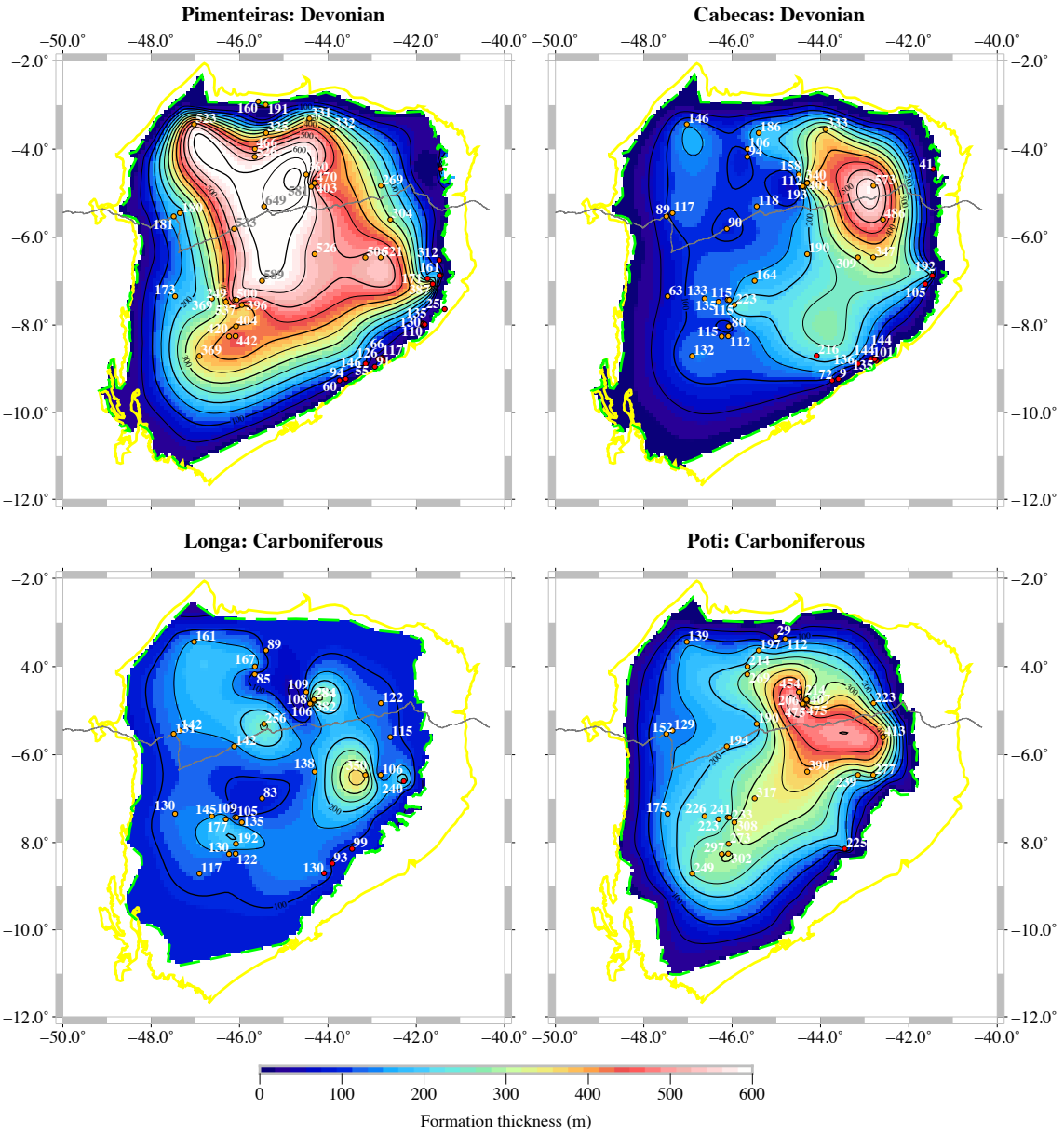


Figure 2.7 continued

2.3.4 TS-4: Mearim basin

Following Mosquito magmatism, the Mearim megasequence (TS-4) was deposited during the late Jurassic. This contains sediments of the Pastos-Bons and Corda Formations, deposited in aeolian/fluviolacustrine environments (Góes et al., 1993). Isopach contours show these are restricted to the centre of the basin (Fig. 2.7), and appear to broadly correlate with the distribution of Mosquito volcanics. Given this correlation, it has been suggested that accommodation space was created by isostatic compensation of the dense volcanic material

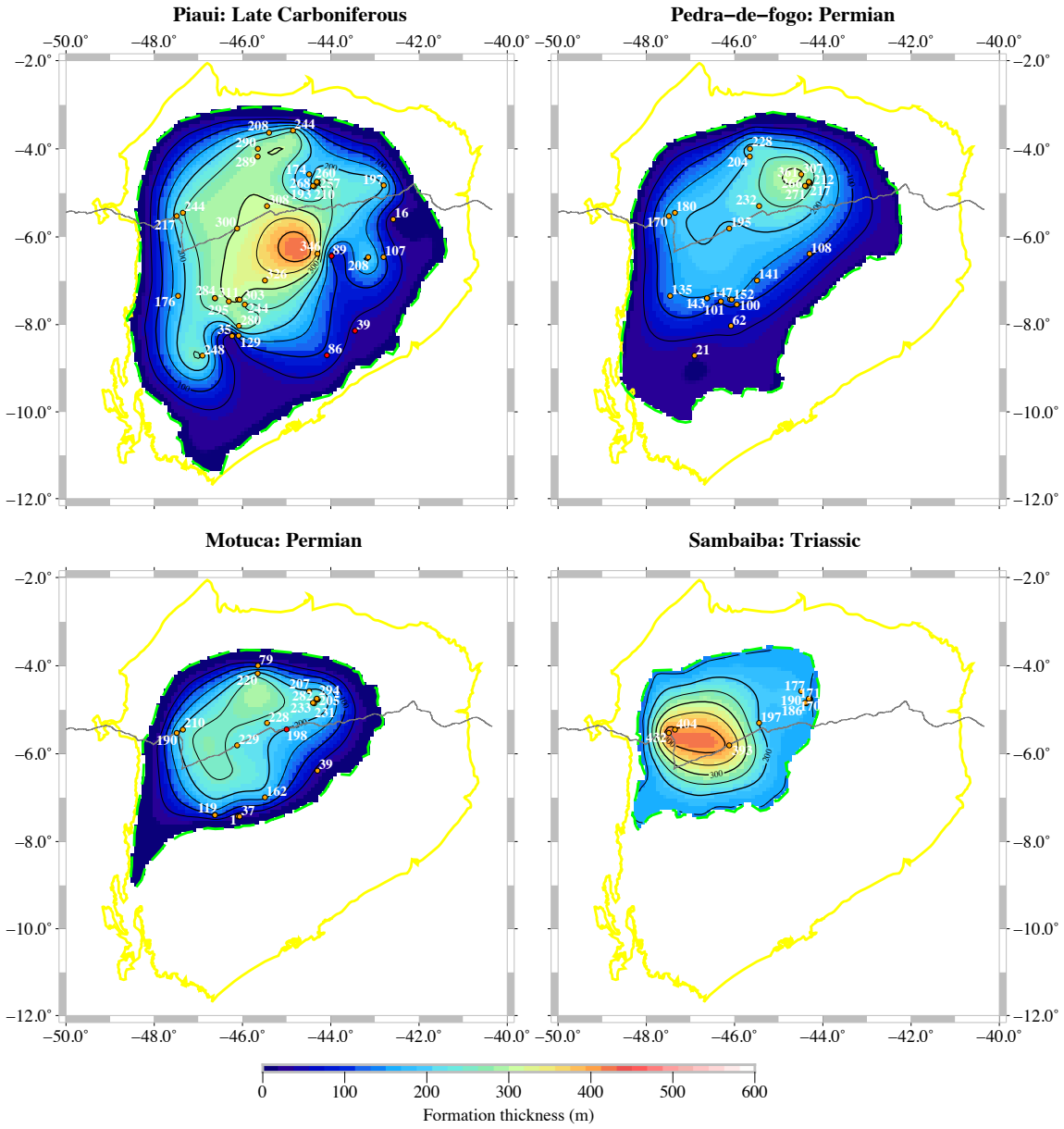


Figure 2.7 continued

(e.g., Góes and Feijó, 1994).

2.3.5 Cretaceous Volcanism

Subsequent to Mearim sedimentation, a second phase of basaltic magmatism took place during the mid-Cretaceous. These volcanics have a high-Ti composition and are known as the Sardinha Formation. They are found mostly in the NE section of the basin, with individual sills up to 400 m thick. Merle et al. (2011) determined $40^{Ar}/39^{Ar}$ and K/Ar whole-rock ages

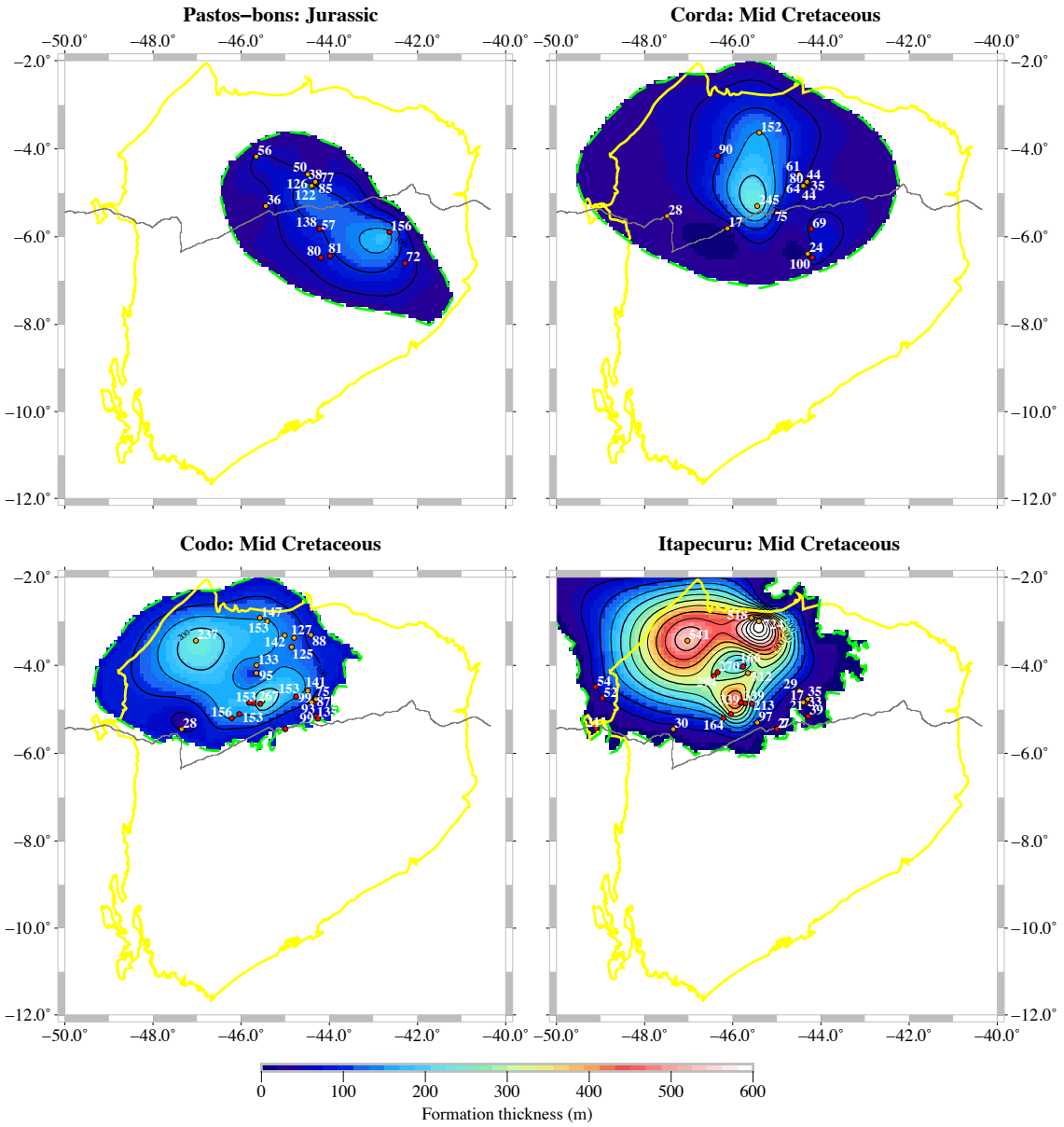


Figure 2.7 continued

of $\sim$ 129–124 Ma. Their origin has been attributed to the opening of the South Atlantic (e.g., Góes et al., 1993; Baksi and Archibald, 1997; Merle et al., 2011).

2.3.6 TS-5: Grajaú basin

The youngest Unit (TS-5) is the Cretaceous Grajaú sub-basin. This unit is restricted to the north-western part of the basin and unconformably blankets the underlying sequences (Fig. 2.1). It comprises of the Grajaú, Codó and Itapecuru Formations (Figs. 2.6; 2.7), which

consist of near shore, shallow marine and fluviolacustrine clastic sediments respectively. This phase of deposition has been attributed to early opening of the south Atlantic (e.g., Rossetti et al., 2004). Tertiary and recent fluvial deposits also outcrop locally within the basin.

2.4 TS-3: The Parnaíba cratonic basin

The sedimentary record of the Parnaíba cratonic basin (TS-3) spans from Early Silurian to Middle Triassic and consists of three megasequences separated by regional unconformities. These are comprised of predominantly shallow marine, fluvio-lacustrine and terrestrial siliciclastic sediments that record three transgressive/regressive sea level cycles (Fig. 2.6) and reach a maximum thickness of $\sim 3.5\ km$.

Individual formation isopach maps from units TS-3 to TS-5 are shown in Figure 2.7. These were derived from well horizon top depths and a regional seismic reflection profile (see Chapter 3). The three-dimensional depositional history of the basin is, however, better revealed by flexural backstripping of these isopachs, as performed in chapter 5. Nevertheless, these maps show the gross regional pattern of deposition and the regional extent (as presently preserved) for each formation. Paleoreconstructions from Scotese (2016), from 440–220 Ma at 20 Ma intervals, are shown in Figure 2.8 and show predicted paleogeography surrounding Parnaíba basin during the deposition of the cratonic basin sediments (TS-3). Note the intraplate location of the basin through time.

2.4.0.1 Serra Grande Megasequence

The oldest megasequence is the Serra Grande, spanning the Early Silurian to Lower Devonian. This rests unconformably above the crystalline basement and locally above the Riachão, and Jaibaras basins. This is dominated by escarpment forming white quartz and sub arkosic arenites deposited in fluvioglacial, glacial marine and shallow marine environments and accounts for a complete transgressive/regressive cycle (e.g., Milani and Zalan, 1999; de Oliveira and Mohriak, 2003).

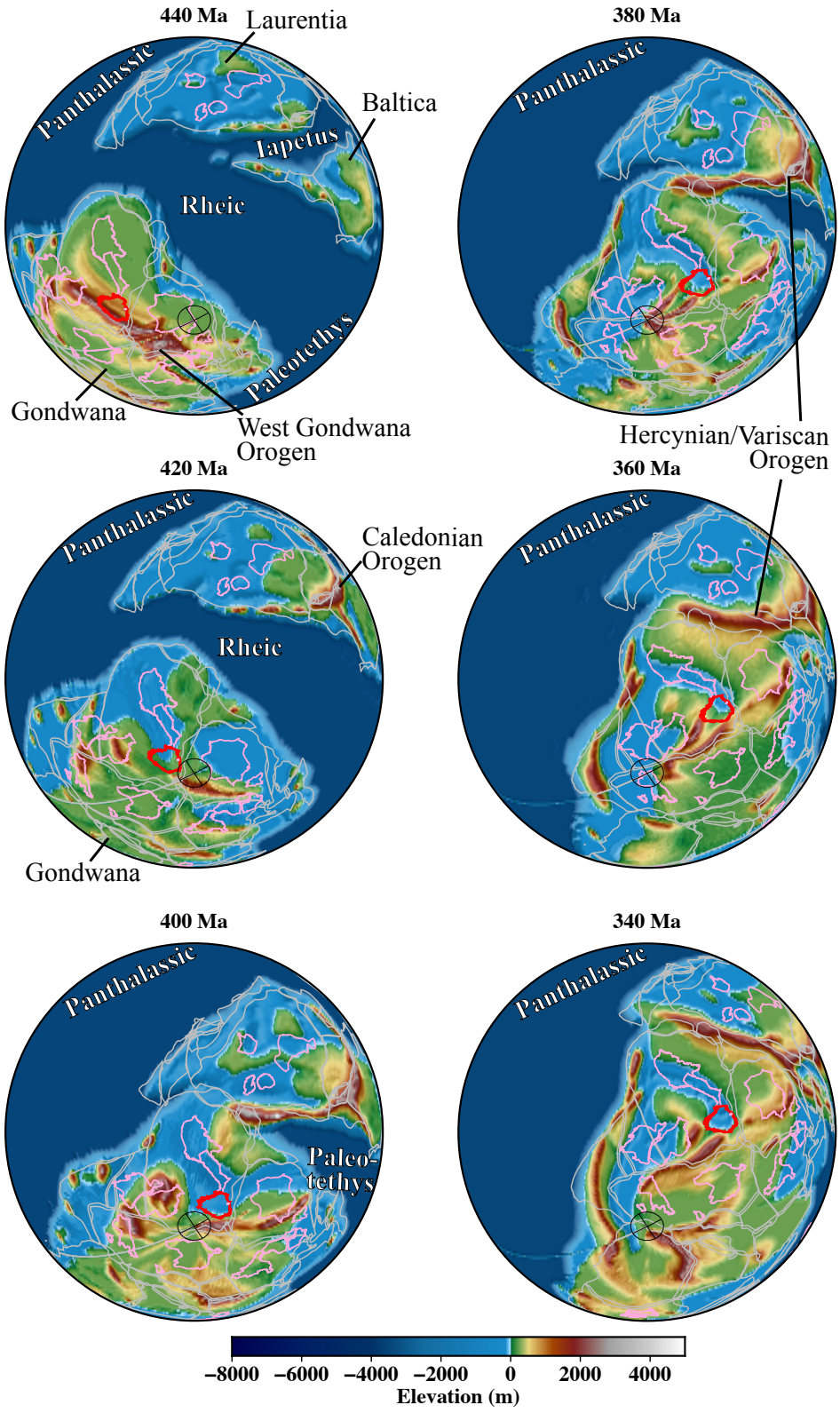


Figure 2.8: Paleogeographic reconstructions at 20 Ma intervals during the deposition of the Parnaíba cratonic basin (modified after Scotese, 2016 and references therein). Parnaíba basin outline shown as thick red line. Other cratonic basins shown as thin pink lines. Grey lines are reconstruction polygons (approximate continental crust limits). Note pole shown is the south pole. The map projection centre from 440–320 Ma is -60° longitude -60° latitude and is -20° longitude -30° latitude from 300–220 Ma.

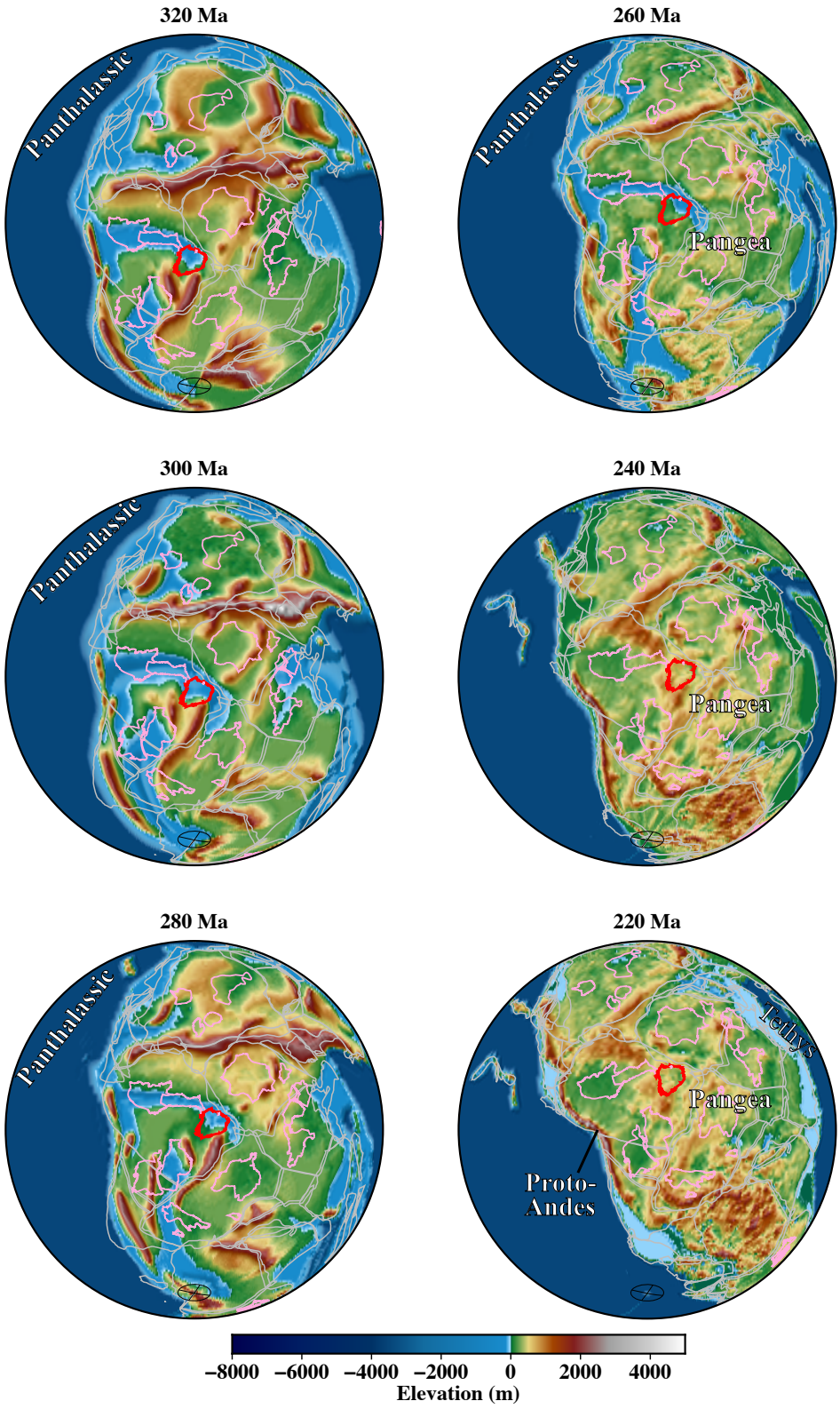


Figure 2.8 continued

The basal Ipu Formation was deposited during the Llandovery (Early Silurian) and reaches a thickness of $>$ 350 m in the northeastern part of the basin. This contains sandstones, conglomerates and shales, with glaciogenic beds in the upper section (Grahn et al., 2005), indicating a glacial fluviatile to deltaic environment (Grahn, 1992). The overlying Tianguá Formation is also Llandovery in age (Grahn et al., 2005) and its maximum drilled thickness is $\sim$ 390 m. It is comprised predominantly of mudstones, sandstones and shale with siltstone intercalations, indicative of a marine transgression and shoreface/shallow marine environments (Grahn, 1992). The Serra Grande is capped by the Jaicós Formation, which spans the Early Silurian to Early Devonian (Emsian Stage) (Grahn et al., 2005). This formation is at least 450 m thick and consists of coarse-grained, massive or cross-bedded sandstones, often with basal cross-bedded conglomerates (Caputo, 1984), that have been interpreted as a braided alluvial-fluvial system, representing a marine regression (e.g., Milani and Zalan, 1999).

A regional unconformity marks the termination of the Serra Grande megasequence, and given its timing, has tentatively be related to far-field inversion driven by the Caledonian orogeny (Góes et al., 1993). There is, however, little evidence for inversion structures associated with this event, suggesting inversion was minor or of an epirorogenic origin (e.g., Góes et al., 1990).

2.4.0.2 Canindé Megasequence

The Canindé megasequence unconformably overlies the Serra Grande. This spans the Lower Devonian-Carboniferous and exhibits a predominantly shallow marine/deltaic depositional environment with little change in depocenter location with respect to the Serra Grande (e.g., Góes et al., 1990; Trindade et al., 2015).

The basal Itaim Formation spans the Early-Mid Devonian (latest Emsian to early Eifelian) (Grahn et al., 2005), reaches a thickness of at least 220 m and contains fine-to-medium grained well-sorted sandstones and shales, deposited in deltaic/coastal environment with storm and tide related influences (e.g., Mabesoone, 1977; Góes and Feijó, 1994; Milani and Zalan, 1999; Trindade et al., 2015).

The Pimenteiras Formation spans the Eifelian to Frasnian (Barbosa et al., 2015) and reaches a

thickness of at least 650 m. This formation contains interbedded organic-rich mudstones and fine-grained sandstones (Góes and Feijó, 1994), characteristic of a storm-dominated epeiric sea and deltaic environments (Ponciano and Della Fávera, 2009; de Miranda, 2014).

The Cabeças Formation spans the Eifelian to Famennian (Barbosa et al., 2015), reaches a thickness of at least 570 m and was deposited primarily in the east of the basin. This formation consists primarily of fine-to-coarse grained, cross-bedded sandstones and subordinate interbedded siltstones characteristic of a fluvio-deltaic system with a strong storm and tide influence (Ponciano and Della Fávera, 2009; Trindade et al., 2015), while tillites and glaciotectonic structures indicate a Famennian glacial influence in the upper section of the formation (Barbosa et al., 2015).

The Longá Formation is Early Carboniferous (Tournaisian) in age (Barbosa et al., 2015). The thickness of the Longá formation is variable throughout the basin, reaching up to at least 350 m. It contains interbedded black shales, siltstones and fine-grained sandstones suggestive of a neritic environment and onset of a post-glacial transgression (e.g., Soares et al., 1978; Milani and Zalan, 1999; Barbosa et al., 2015).

The Poti Formation is late Visean in age (di Pasquo and Iannuzzi, 2015) and reaches at least 470 m in thickness. This formation contains well-sorted basal sandstones, with intercalations of finer grained siltstones in the upper section, typical of regression from a beach environment into an alluvial plain (Mabesoone, 1977; Soares et al., 1978).

A Late Carboniferous regional unconformity accounting for ~ 40 Myr marks the termination of the Canindé megasequence. This has been attributed to far-field inversion driven by the Hercynian orogeny (Góes et al., 1990), which was active along the northwestern coast of Gondwana at this time. Appreciable deformation caused by this event is documented in the intermediary basins and shields of northwest Africa between Parnaíba and the deformation front (e.g., Haddoum et al., 2001), but inversion in Parnaíba basin appears minor.

2.4.0.3 Balsas Megasequence

The Balsas megasequence unconformably overlies the Canindé megasequence. This spans the Late Carboniferous to Middle Triassic and consists predominantly of clastic sandstones and evaporites deposited in subaerial environments (e.g., Góes and Feijó, 1994; Milani and Zalan, 1999). During this time, the sedimentation pattern became more concentric, and the depocenter migrated to slightly west of the present-day basin centre.

The basal Piauí Formation is late Carboniferous in age (Dino and Playford, 2002) and reaches a thickness of at least 350 m. This consists of fine-grained sandstones that exhibit sigmoidal, trough and tangential stratification, deposited in a fluvial environment (e.g., Araújo et al., 2016).

The Pedra-de-Fogo Formation is considered to span the Early-Mid Permian (Cisuralian–Guadalupian) (Kauffmann et al., 2016) and reaches a thickness of at least 310 m. This formation is composed of fine-to-coarse grained sandstones and mudstones, with subordinate intercalations of silicified carbonates and evaporites (anhydrite and dolomite) (e.g., Mabesoone, 1977; Soares et al., 1978 Araújo et al., 2016), characteristic of a shallow lacustrine environment (e.g., Araújo et al., 2016).

The Motuca Formation is Lopingian (Late Permian) in age (Kauffmann et al., 2016) and reaches a thickness of at least 300 m. This formation conformably overlays the Pedra-de-Fogo Formation and consists of red-beds interbedded with fine-grained sandstones and evaporites, characteristic of a lacustrine environment (Góes and Feijó, 1994; Araujo et al., 2016).

The Sambaìba Formation is Lower Triassic in age (Kauffmann et al., 2016) and reaches a thickness of at least 430 m. The Sambaìba formation has a gradational contact with the underlying Motuca Formation, and its upper surface is either erosional or truncated by basaltic flows of the Mosquito formation (Mabesoone, 1977). It comprises well-sorted fine-to-medium grained sandstones, with large cross-bedding that represent aeolian deposition in a desert environment (Góes and Feijó, 1994).

The Parnaíba basin cratonic basin sequence is terminated by a Middle Triassic unconfor-

mity at the top of the Motuca formation, followed by subsequent TS-4 and TS-5 deposition and Mosquito and Sardinha volcanism (Fig. 2.6).

2.5 Summary of previous work in Parnaíba basin

Prior to the current decade, Parnaíba basin had been subjected to relatively little geophysical investigation related to crustal structure and basin origin. In 2014, however, de Castro et al. (2014) used basin-wide aero-gravity and magnetic data to interpret the basement structure concealed beneath Parnaíba basin in detail. They applied a variety of filtering and transform techniques to these data and were able to map terrain boundaries based on trends in the derived potential field maps. Residual gravity and magnetic anomalies revealed several linear, up to 60 km wide, negative anomalies. These were interpreted as an extensive pattern of Neoproterozoic and Cambrian rift grabens orientated approximately North–South and Northwest–Southeast, and exclusively developed beneath the Parnaíba cratonic basin sequence. Hence, they suggested that the Phanerozoic sedimentary sequence represents the post-rift thermal subsidence response to a postulated Cambrian rifting event.

de Castro et al. (2016) continued this work by analysing industry two-dimensional seismic profiles and well data. These authors imaged the Jaibaras basin adjacent to the TBSZ beneath the centre of Parnaíba basin and plotted the sedimentary accumulation history of the basin as recorded in four deep exploration wells, but did not backstrip these records. These authors concluded that the Jaibaras basin was a Cambrian "syn-rift" section and that these data were consistent with their previous interpretation, that the basin formed via extensional processes.

Previously, Sousa (1996) used a compilation of terrestrial gravity data and well core records to model the crustal structure and subsidence history of the Parnaíba basin. This author concluded that the basin's free-air and Bouguer gravity anomalies are best explained by an additional mass excess of $+100\ kg\ m^{-3}$ within the lower crust/upper mantle and interpreted this anomaly to represent the partial replacement and/or intrusion of the lower crust by mafic material. He also performed Airy-style backstripping of well logs and modelled basin subsidence using a two-layer Royden-Keen extensional model (Royden and Keen, 1980), suggesting

that basin subsidence occurred due to thermal contraction following extension, accommodated on the TBSZ and related structures. Best-fit crustal and mantle-lithosphere beta factors of 1.14 and 1.28 within the basins centre were suggested.

Daly et al. (2014) recently interpreted a crustal scale seismic reflection profile that spans east-west across Parnaíba basin. This profile is discussed in detail in the following chapter.

2.6 Summary

In this chapter, the Neoproterozoic/Cambrian tectonic evolution of Northeast Brazil has been reviewed from the perspective of basement terranes in the vicinity of the Parnaíba basin. The Parnaíba basin stratigraphy and sedimentation history has also been outlined and results from previous studies regarding the tectonic processes responsible for the formation of Parnaíba basin discussed. The key points are as follows:

- The Parnaíba basin is one of five Paleozoic cratonic basins within South America. Each of these basins records a similar stratigraphic record, initiating in the Late Ordovician/Early Silurian.
- The Parnaíba basin is located between and above a complex basement comprising several Archaean and Proterozoic terranes, separated by apparent steep crustal boundaries, stabilised at the culmination of Brasiliano orogeny (800–500 Ma) with the formation of West Gondwana. These include, from west to east, the Amazon craton, Araguaia Group, Parnaíba Block and Borborema Province. Parnaíba basin may, therefore, be considered an "intra"-cratonic basin.
- The Parnaíba basin presently occupies a sub-circular area of $\sim$ 670,000 km^2. However, its stratigraphic boundaries are erosional, suggesting it may have once extended over a wider region. Small outlier basins and the Palaeozoic Saltpond basin, located along the Ghanaian coast appear to be a stratigraphic equivalents and may once have been contiguous with Parnaíba.
- The stratigraphic record spans from late Neoproterozoic through to the Cretaceous and

documents a polyphase subsidence history with five distinct tectono-stratigraphic units separated by regional unconformities.

- In the west, the cratonic basin is underlain by a Neoproterozoic/Cambrian foreland — the Riachão basin. In the east, adjacent to the Transbrasiliano Shear Zone and its subsidiaries, the cratonic basin is underlain by narrow and linear "graben-like" structures, Cambrian in age and of probable pull-apart origin. In the north-western part of the basin, the cratonic basin section is unconformably overlain by a Cretaceous marine transgression, thought to be related to the early opening of the south Atlantic.

- The Parnaíba cratonic basin stratigraphic record spans the Early Silurian–Middle Triassic and is characterised by relatively slow subsidence and stratigraphic thickening towards the basin depocenter, indicative of local subsidence relative to the basin surroundings. The basin consists of three megasequences separated by regional unconformities. These are comprised of predominantly shallow marine, fluvio-lacustrine and terrestrial siliciclastic sediments that record three transgressive/regressive sea level cycles and reach a maximum thickness of $\sim 3.5\ km$.

Chapter 3

Seismic imaging of Parnaíba sedimentary basin and crustal structure

3.1 Introduction

In this chapter, active source seismic reflection and wide-angle reflection/refraction data are analysed in order to illuminate the sedimentary and crustal structure of the Parnaíba basin. This analysis is principally focused on an approximately east-west $\sim 1400\ km$ profile, spanning the full width of the basin from the bounding Amazonian craton in the west to the Borborema Province in the east (Fig. 3.1). This profile is constrained using a crustal scale normal-incident seismic reflection profile and an auxiliary wide-angle reflection/refraction dataset, consisting of five receiver gathers acquired in the centre of the profile, with offsets up to $\pm$ 110 km. These data were acquired as part of the ***P***arnaíba ***B***asin ***A***nalysis ***P***roject (PBAP) using a four-truck vibroseis source and recorded to 20 seconds two-way-travel-time (TWTT). Previously acquired industry seismic data provide additional constraints on the sedimentary basin structure.

Seismic processing and receiver gather interpretation was conducted using *GLOBE Clar-*

itas™, and reflection interpretation was conducted using the open source software *OpenDtect*.

3.2 Seismic reflection analysis

3.2.1 Seismic reflection data

Seismic reflection data analysed in this section were acquired by Global Geophysical Services, as contracted by BP, between June-November 2012. The seismic source consisted of a four-tuck vibroseis fleet with a total force of 108,800 kg. Further acquisition parameters are listed in Table 3.1. The reflection profiles were processed by BP Houston and supplied as post-stack-time migrated (PSTM) and post-stack-depth-migrated (PSDM) sections for use in this study (Allen Poole, Pers. Comms. 2014). Further post-stack processing, including coherency filtering and attribute analysis was applied during this study in order to further illuminate deep structure.

Parameter	MCS reflection	Box wave	Units
Receiver interval	50, 25*	$\sim$ 5000	m
Source interval	50	50	m
Maximum offset	$\pm$ 12	$\pm$ 110	km
Record length	20	40	s
Number of sweeps	2	2, 4, 8, 16	-
Sweep length	24	40	s
Sweep frequencies	6–60	4–32	Hz
Peak force/vibrator	27,200	27,200	kg
Total force/sweep	108,800	108,800	kg
Fold	240, 480*	low ($\leqslant$ 8)	-
Number of vibrators/fleet	4	4	-

Table 3.1: Seismic acquisition parameters used during the acquisition of the regional multi-channel-seismic reflection profile and Box wave wide-angle reflection/refraction survey (after, Daly et al., 2014). *The receiver interval was reduced to 25 m and fold increased to 480 during the acquisition of the third (eastern) section of the profile (between vibration points 34439.5–58183.5).

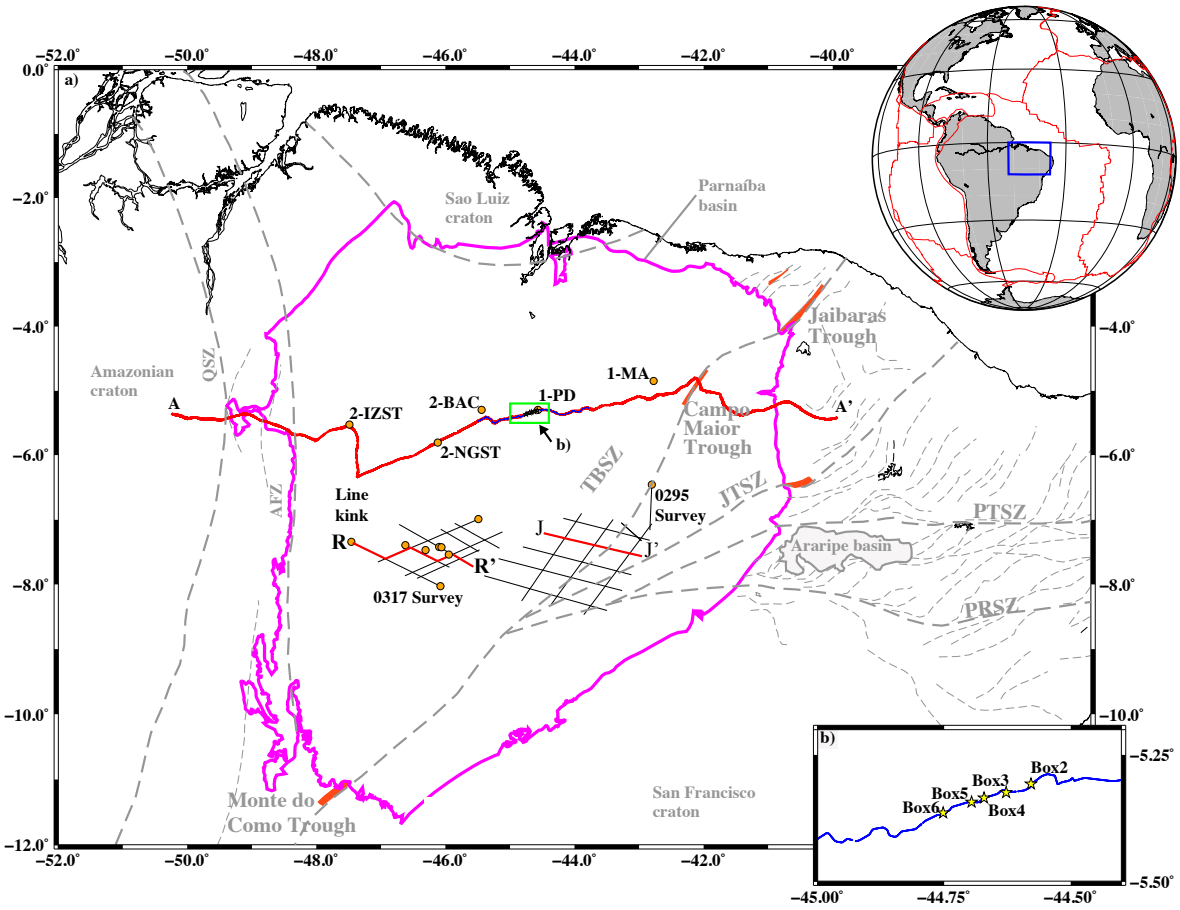


Figure 3.1: a) Parnaíba basin seismic data distribution map. Red line (A–A') shows regional seismic transect. Black solid lines show seismic profiles from local industry surveys. Red line (J–J') shows the seismic profile displayed in Figure 3.7. Red line (R–R') shows the composite seismic profile displayed in Figure 3.8. Orange circles show well locations in the vicinity of seismic profiles. Dashed grey lines show major faults. b) Inset showing the location of box wave receiver arrays used in wide-angle reflection and refraction imaging (Section 3.3).

3.2.2 Seismic Attributes

Seismic attributes are used to aid in the interpretation of seismic data by extracting and displaying auxiliary information that is not provided by a traditional seismic trace. Attributes are derived by performing a mathematical operation on trace sample values. Depending on the attribute being calculated, operations are performed either trace-by-trace on each individual sample value or over a finite window of samples/traces. In this study, two seismic attributes were used as visual aids during reflection interpretation, namely, instantaneous amplitude and amplitude volume. For clarity, the nature of these attributes are described below.

3.2.2.1 Instantaneous amplitude (reflectivity strength)

Taner and Sheriff (1977) and Taner et al. (1979) introduced the concept of the complex seismic trace, showing that a traditional seismic trace can be considered the real part of a complex signal and that the imaginary part can be determined by applying a Hilbert transform to this. This allows the separation of the amplitude and phase information. Instantaneous amplitude can then be determined as the envelope of the real and imaginary parts, which mathematically, is calculated as the square root of the sum of the squares of the two components, at each instance in time (Taner et al., 1979; Chopra and Marfurt, 2005).

Thus, instantaneous amplitude is proportional to the total energy of a seismic signal at an instance in time and represents the maximum amplitude obtainable given a constant phase rotation (Taner et al., 1979; Yilmaz, 2001; Barnes, 2007). It, therefore, represents reflectivity strength and is useful for accentuating changes in acoustic impedance, especially on deep crustal data, when the signal-to-noise ratio is low and simply identifying a reflection takes priority over vertical resolution and preservation of the wavelet.

3.2.2.2 Amplitude Volume

As described by Vernengo and Trinchero (2015), the amplitude volume attribute is a useful visualisation aid for highlighting incoherence in reflection events and illuminating unconformities and truncations caused by, for example, faults or dykes. This is calculated using a sliding window down each trace to extract sample amplitudes within a specific time window. The root-mean-squared amplitude within the given window (centred on the current input sample) is calculated, providing an output of only positive values. These values are then rotated -90° via the inverse Hilbert transform, producing an output with both positive and negative values. Visually, this results in a "*pseudo relief*" image of the seismic data (e.g., Fig. 3.2d).

3.2.3 Parnaíba sedimentary basin seismic reflection structure

Figure 3.2 shows the upper 5 km of the Post-Stack Depth Migrated (PSDM) regional seismic reflection profile, which provides a cross section through the entire Parnaíba basin sedimentary section. However, in comparison with shallow industry reflection profiles acquired within the basin (e.g., Figs 3.7–3.8 and de Castro et al., 2014), data quality is relatively poor. This is principally due to the acquisition parameters. Parameters were tuned for crustal structure imaging during the acquisition of this profile, such that, the fold (240–480) and frequency range (6–60 Hz) were too low to adequately resolve fine structure within the upper sedimentary basin section. Nonetheless, the holistic nature of the profile provides insight into the tectonic history of the basin that is not obtainable when analysing standard, localised industry profiles.

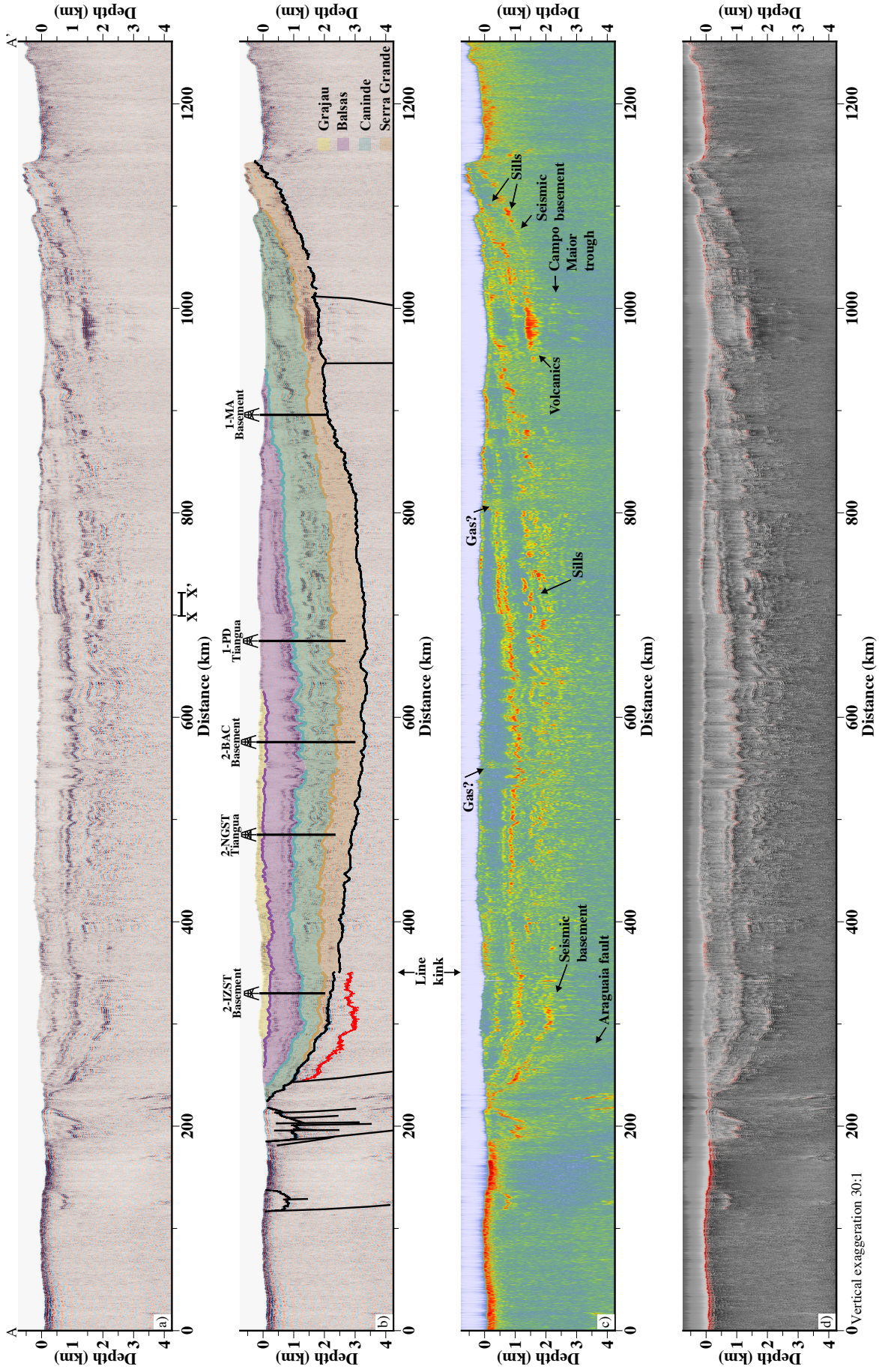


Figure 3.2: a) Sedimentary section of the regional post-stack depth migrated reflection profile. A–A' as shown on figure 3.1. Note the line kink at ~ 47.5°W (Fig. 3.1) has been removed. b) Showing interpreted mega-sequence boundaries. c) Displayed using instantaneous amplitude. d) Displayed using amplitude volume.

3.2.3.1 Seismic basement

On the regional reflection profile seismic basement is identifiable as a prominent reflection on both the eastern and western sides of the basin (Fig. 3.6). This horizon is traceable from surface outcrops at the western and eastern basin edges, $\sim$ 130 km and 200 km basinward respectively (Fig. 3.2). Within the central section of the basin, however, data quality is poor at inferred basement depths, and the seismic basement can not be confidently identified. Hence, the basement horizon was picked with the aid of interpolated well control (Fig. 3.3). This reveals the striking bowl-shaped geometry of the basin, characteristic of cratonic basins in general. Basement depth reaches a maximum of $\sim$ 3.3 km on the regional profile, while the maximum depth of $\sim$ 3.5 km occurs slightly north of this profile.

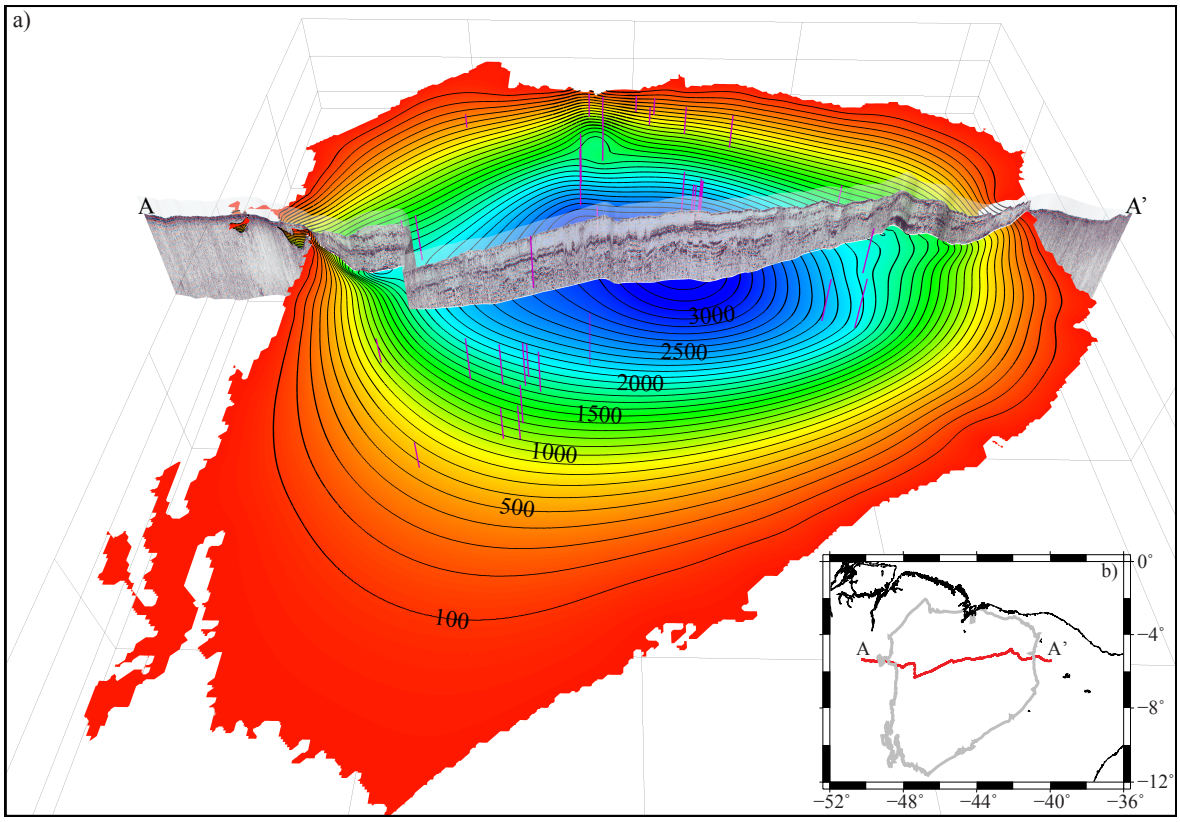


Figure 3.3: a) Three-dimensional perspective viewed from the south of the basin, showing the Pre-Silurian/Basement isosurface contoured at 100 meter intervals, created by minimum curvature interpolation of well control points (pink lines) and seismic picks from the edges of the regional reflection profile. b) Inset map showing the location of the basin outline and regional seismic profile (A–A') as in (a).

3.2.3.2 Basin structure

As discussed in Chapter 1, some authors postulate that cratonic basins form due to lithospheric extension and therefore represent the low-strain rate end-member of rift-type basins (e.g., Armitage and Allen, 2010; Allen and Armitage, 2012; Cacace and Scheck-Wenderoth, 2016). It is, therefore, significant that there is little evidence for extensional strain on the regional reflection profile within the sedimentary basin or underlying basement (Fig. 3.2). This implies that, if extension of the lithosphere is responsible for basin formation, then extension must be accommodated in a manner that differs from the brittle normal faulting commonly observed in rift basins. For example, Armitage and Allen (2010) speculated, assuming a rift origin and low strain rates implied by the longevity of cratonic basin subsidence (10^{-16} s^{-1}), extension may be accommodated in some diffusive manner, such that it is not resolved in seismic imaging. However, as discussed by Holt et al. (2014), analogue models (Bellahsen et al., 2003) and field observations (Mazzarini et al., 2004) suggest that at low strain rates, extension is more likely to become localised on fewer, large faults. It therefore appears an extensional origin is inconsistent with Parnaíba basin sedimentary and basement structure and an alternative mechanism must be responsible for basin subsidence (e.g., Stel et al., 1993; Hamdani et al., 1991; Hamdani et al., 1994; Sleep, 2009; Holt et al., 2010; Holt et al., 2014; McKenzie and Priestley, 2016).

Although extensional deformation appears absent within the regional seismic profile, several areas of localised deformation are evident. These appear to be predominantly associated with the emplacement volcanic sills and potentially regions of gas escape. Dolerite sills have been drilled in numerous wells throughout the basin and shown to correlate with high amplitude reflections on seismic reflection profiles (e.g., de Castro et al., 2014; Porto and Pereira, 2014). On the regional profile, sills are identified as strong reflections that are very prominent when displayed using instantaneous amplitude or amplitude volume (Fig. 3.4). These often exhibit a "top hat" structure that resembles a fault offset. These structures appear to parallel bedding, however, the reason why these sills "jump" is currently poorly understood. Presumably, this occurs as the injecting magma preferentially follows bedding planes and "jumps" when the facies of the host rock changes, such that, the pressure required to jump is less than

that required to continue intruding along the current bedding plane. Interestingly, it has been found that local metamorphism in the vicinity of sill emplacement is the only proven method of hydrocarbon maturation in the basin (Porto and Pereira, 2014). Furthermore, the "top hat" structures may produce three-dimensional closures, and act as structural traps (Porto and Pereira, 2014).

There are also some areas of localised reflection coherency destruction which may represent regions of gas escape (Fig. 3.2)

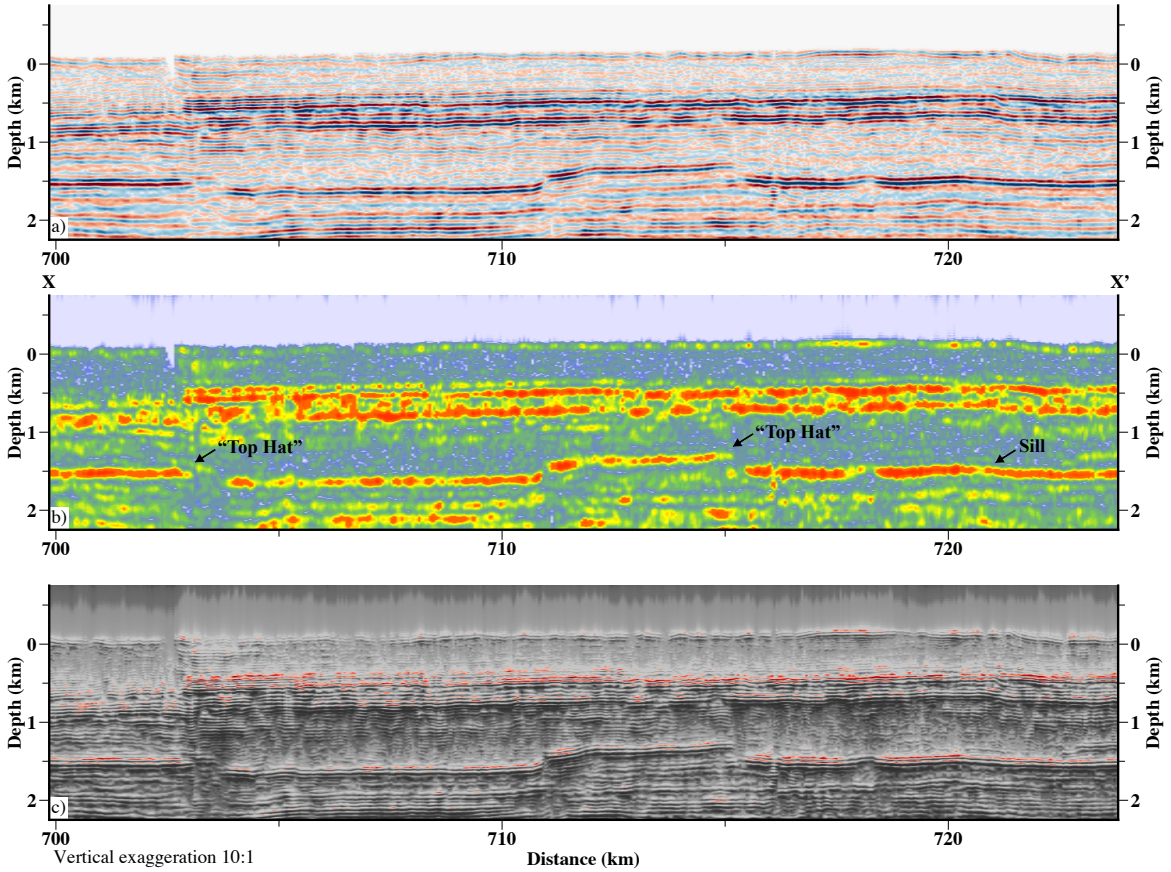


Figure 3.4: Example of a dolerite sill imaged on the regional reflection profile exhibiting a characteristic *top hat* structure (X–X' as shown on Fig. 3.2a). a) Seismic reflection display. b) displayed using instantaneous amplitude. c) displayed using amplitude volume.

3.2.3.3 Basin edges and stratigraphic younging

Figure 3.2 shows that the basin is characterised by an overall simple "layer-cake" geometry. Formation contacts can be traced from their surface outcrops, east-to-west, throughout the basin, with little internal deformation evident. Sedimentary formations young towards the basin centre, with a well-developed basinward younging pattern evident in both the east and west. However, on both margins, the basin edges appear erosional and have been subject to exhumation. Furthermore, the mechanism of uplift appears to differ in the east compared to the west, such that the nature of the stratigraphic younging and the morphology of the basin edges are asymmetric (Fig. 3.2).

Towards the eastern edge of the basin, elevation increases gradually over a lateral distance of $\sim 130\ km$, from $\sim 200\ m$ within the basin to a height of $\sim 750\ m$ at the basin edge (Fig. 3.6d). Sediments display a gentle dip of 1° or less towards the basin centre, approximately parallel to that of the basement reflection, and exhibit a well developed basinward younging at the surface. These characteristics are consistent with a broad post-deposition long-wavelength uplift of the Borborema Province which underlays the eastern side of the basin. This is evidenced by the presence of Albian limestones at present-day elevations of up to 800 m in the Araripe Basin (Fig. 3.1). Indeed, Morais Neto et al. (2009) identified two major uplift events in this region via apatite fission track analysis. The first occurred in the late Cretaceous, followed by a second during the Miocene. The geodynamic processes responsible for the Borborema Province plateau uplift have been subject to debate (e.g., Morais Neto et al., 2009; de Oliveira and de Medeiros, 2012; Luz et al., 2015a; Luz et al., 2015b), though recent studies favour an uplift related to crustal thickening, resulting from outflow of material from the adjacent rifting region during central Atlantic breakup and potentially a small contribution from magmatic underplating for the late Cretaceous event (e.g., Morais Neto et al., 2009; Luz et al., 2015a).

In contrast, at the western edge of the basin, there is no change in surface elevation, and both the basement and overlying sediments dip more steeply, albeit still at modest angles of $\sim 1.5°$. The oldest sediments of the Serra Grande megasequence do not out crop at the surface, and seismic data show these onlap onto basement slightly west of a basement 'hinge

point' (Fig. 3.6b). Similarly to the eastern margin, Phanerozoic sediments exposed at the surface exhibit an offlap pattern, however, this occurs over a relatively narrower distance. Furthermore, two half-graben are imaged to the west of the present day basin extent, which at the surface contain Cretaceous sediments of the Itapercuru formation (Fig. 3.6b). Beneath the flat lying Cretaceous sediments, internal reflections display an easterly dip. Daly et al. (2014) interpreted these observations as the result of compressional reactivation of the underlying Araguaia Fault Zone (see Section 3.2.5), post-Permian and pre-Albian, with structural collapse facilitating the development of the observed grabens (Fig. 3.5).

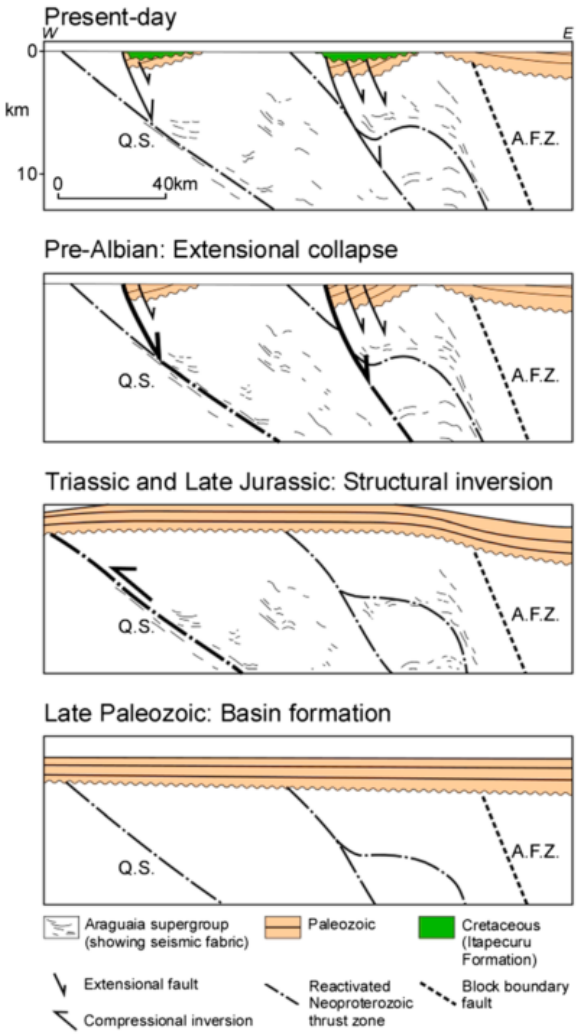


Figure 3.5: Sketch cross sections showing the structural evolution through time of the two half graben on the western margin of the Parnaíba basin. The graben are interpreted as collapse features triggered by the Triassic and/or Late Jurassic/Early Cretaceous inversions. Key: QS = Quatipuru suture; AFZ = Araguaina fault zone; the bold lines indicate the fault zones active during a particular time period (after, Daly et al., 2014).

The basinward younging of sediments is a characteristic common to many cratonic basins (e.g., Sloss and Scherer, 1975; Sleep and Snell, 1976; Sweeney, 1977; Beaumont, 1978). However, the process(es) responsible for generating this pattern have been subject to debate. Some authors have suggested a geodynamic origin during sedimentation, while others favour a post-deposition geological explanation. In the geodynamic case, it has been shown that if the lithosphere is modelled using a viscoelastic rheology, its response to loading results in progressive localisation of subsidence and a basin that narrows and deepens with time (e.g., Sleep and Snell, 1976; Beaumont, 1978; Watts et al., 2013). This in turn results in uplift at the basin edges as a flexural bulge, which migrates basinward with time, resulting in an outcrop pattern with the oldest sediments at the basin margins and the youngest sediments restricted to the basin centre. Alternatively, Sloss and Scherer (1975) showed, based on stratigraphic evidence, that in the case of the Michigan basin of North America, it is likely that the basin formed in a similar manner to the post rift phase of a typical rift basin (i.e., it *widened with time*, with stratigraphic onlap onto the basement at its edges) but has subsequently been modified by basin wide erosion, that has cut down into the stratigraphy, resulting in the *apparent* basinward younging pattern.

In the case of Parnaíba basin, both the east and western edges of the basin appear to have been subject to tectonic uplift and erosion, and it may be inferred that this pattern is structurally controlled, similarly to as has been suggested in Michigan by Sloss and Scherer (1975). However, as will be discussed in Chapter 5, the temporal subsidence history of Parnaíba basin appears consistent with that of a viscoelastic response to loading, and hence a geodynamic contribution from bulge migration cannot be ruled out.

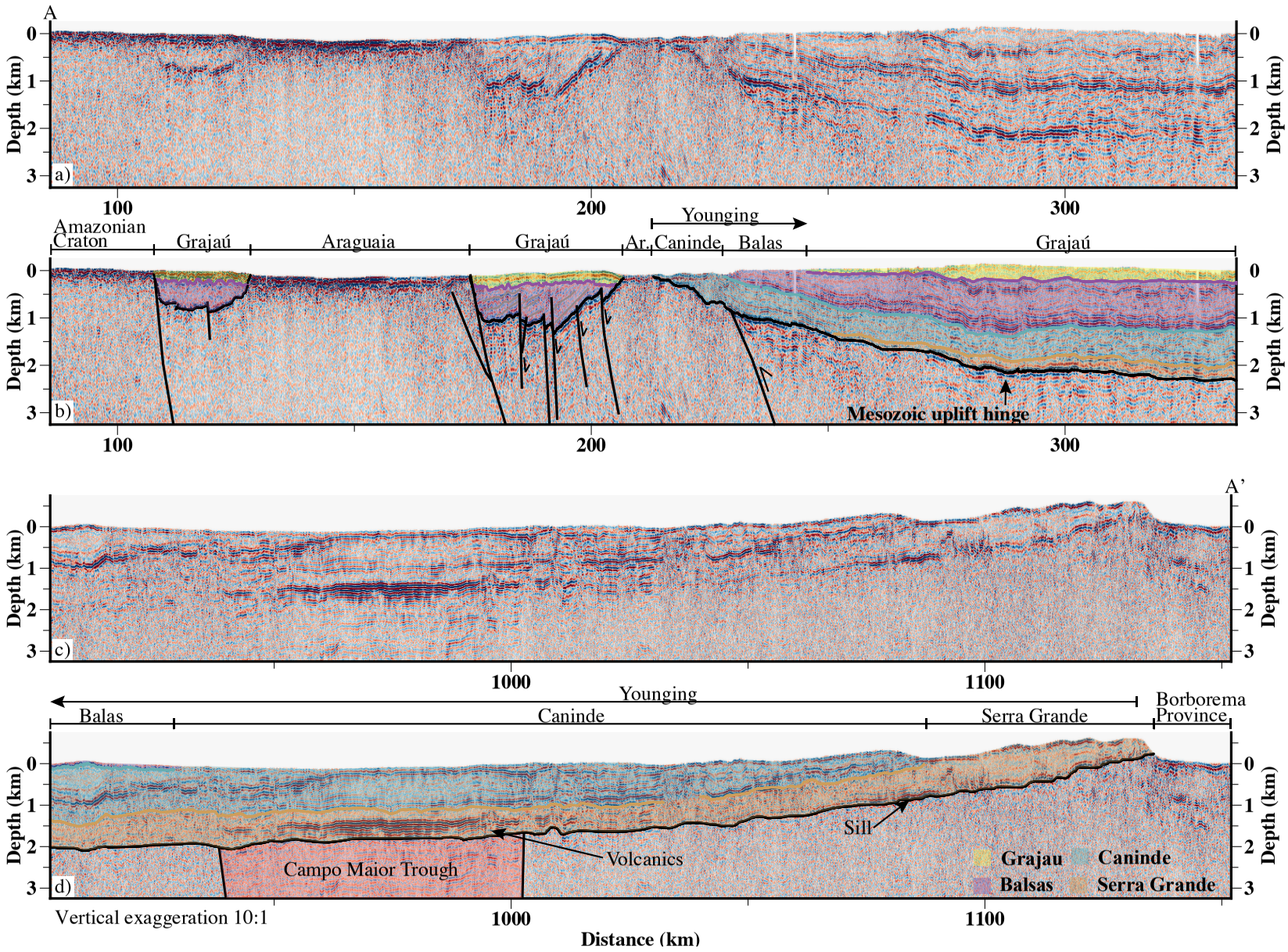


Figure 3.6: a) Western margin of Parnaíba basin as imaged on the PSDM regional reflection profile. b) Same as in (a) with interpretation. Note the faulting associated with the Argauaia Fault Zone (AFZ) and Quatipuru Suture Zone and relatively short lateral distance over which baswinward younging of stratigraphy occurs. c) Eastern margin. d) same as in (c) with interpretation. Note the broad uplift of the basin towards its present day edge and the relatively large lateral distance over which baswinward younging of stratigraphy occurs. A–A' as shown on figure 3.1.

3.2.4 Pre-Silurian sediments

As discussed in Section 2.3 the Parnaíba basin preserves a polyphase sedimentation history. Two pre-Silurian tectonstratigraphic units underlie the cratonic basin sequence, namely, the Jaibaras and Riachão units. These units are imaged on seismic reflection profiles from the 0295 and 0317 surveys respectively (Fig. 3.1). These surveys focused on shallow structure with narrower CDP spacing of 12.5 m, while the 0317 also has a higher peak frequency of 75 Hz, with respect to the regional reflection profile presented in Figure 3.2.

3.2.4.1 Jaibaras basin: Rift or pull-apart?

Figure 3.7 shows the seismically imaged Jaibaras basin on survey line 0295-0007. This sequence resides beneath the pre-Silurian unconformity of the Parnaíba basin cratonic basin sequence, as confirmed by the 2-PI well, which was drilled to basement through this structure (de Castro et al., 2016). Equivalents of the Jaibaras sequence outcrop within the Jaibaras and Monte do Carmo troughs, adjacent to the TBSZ at the Northeast and Southwest edges of Parnaíba basin respectively (Fig. 3.1). de Oliveira and Mohriak (2003) described the Jaibaras trough stratigraphy and showed it is comprised predominantly of the volcaniclastic deposits named the Jaibaras Group (Fig. 2.6).

Previously, the Jaibaras formation has been interpreted as a rift infill resulting from a pervasive Cambro-Ordovician rifting event (e.g., de Oliveira and Mohriak, 2003; de Castro et al., 2016). These authors also suggest that the overlying cratonic basin sequence represents a post-rift sag phase to this Cambrian/Early Ordovician event. However, U-Pb dating of the Meruoca pluton, which cross-cuts all of the Jaibaras trough stratigraphy, except the youngest Aprazivel Formation, returned an age of 523 $\pm$ 10 Ma (Archanjo et al., 2009). This suggests that if the Jaibaras basin did form via rifting, then most of the "syn-rift" deposition occurred $\sim$ 80 Ma prior to the deposition of the earliest cratonic basin sediments. This time gap makes it difficult to reconcile the Parnaíba cratonic basin sedimentation as a "post-rift" phase of subsidence following a Jaibaras rifting event. For example, the thermal time constant of diffusion for the lithosphere, may be given by Equation 3.1:

$$\tau = \frac{L^2}{\pi^2 \kappa} \tag{3.1}$$

Where L is lithospheric thickness (m); and κ is thermal diffusivity (assumed as 10^{-6} m^2 s^{-1}).

In this form, Equation 3.1 returns an estimate for the time taken for heat flow to reach a value of $1/e$ of the initial value or $\sim 2/3$ of the thermal anomaly to decay. For a standard lithospheric thickness of 125 km (Cochran, 1981) this implies a thermal time constant of $\sim$ 62 Myr. While for a lithospheric thickness of 170 km, as is predicted beneath Parnaíba basin by surface wave tomographic modelling (Priestley and McKenzie, 2013), a time constant of 116 Myr is obtained. In either case, it is difficult to reconcile the $\sim$ 200 Myr of cratonic basin subsidence, which begins at ca. 443 Ma ($\sim$ 80 Myr later) as "post-rift", as most of the thermal diffusion, and hence thermal subsidence, would have occurred prior to this.

It is more likely, given their long ($<$100 km) and narrow ($\sim$ 20 km) form and their NE/SW alignment and spatial association with the TBSZ, that these graben-like structures are of a pull-apart origin, formed during dextral strike-slip motion along the TBSZ during the Cambrian (e.g., Curto et al., 2014). This interpretation is shown in figure 3.7b, where the fault offsets define a well developed negative flower structure, typical of strike-slip style basins. Analogues for these basins are found adjacent to major strike-slip systems worldwide, for example, along the North Anatolian fault of northern Turkey (e.g., Carton, 2007) and San Andreas Fault of California (e.g., Brothers et al., 2009).

3.2.4.2 Riachão basin

Figure 3.8 shows the seismically imaged Riachão basin. This sequence occurs beneath the western side of the basin and is well imaged by the 0317 reflection survey (e.g., Fig. 3.8; Porto et al., In press). This includes the oldest preserved sediment in the basin, believed to be Late Neoproterozoic to Cambrian in age (Mesner and Wooldridge, 1964; Porto et al., In press). de Castro et al., (2014; 2016) interpreted the Riachão basin as a Neoproterozoic rift. However, this view has recently been challenged by Porto et al., (In press), who interpreted

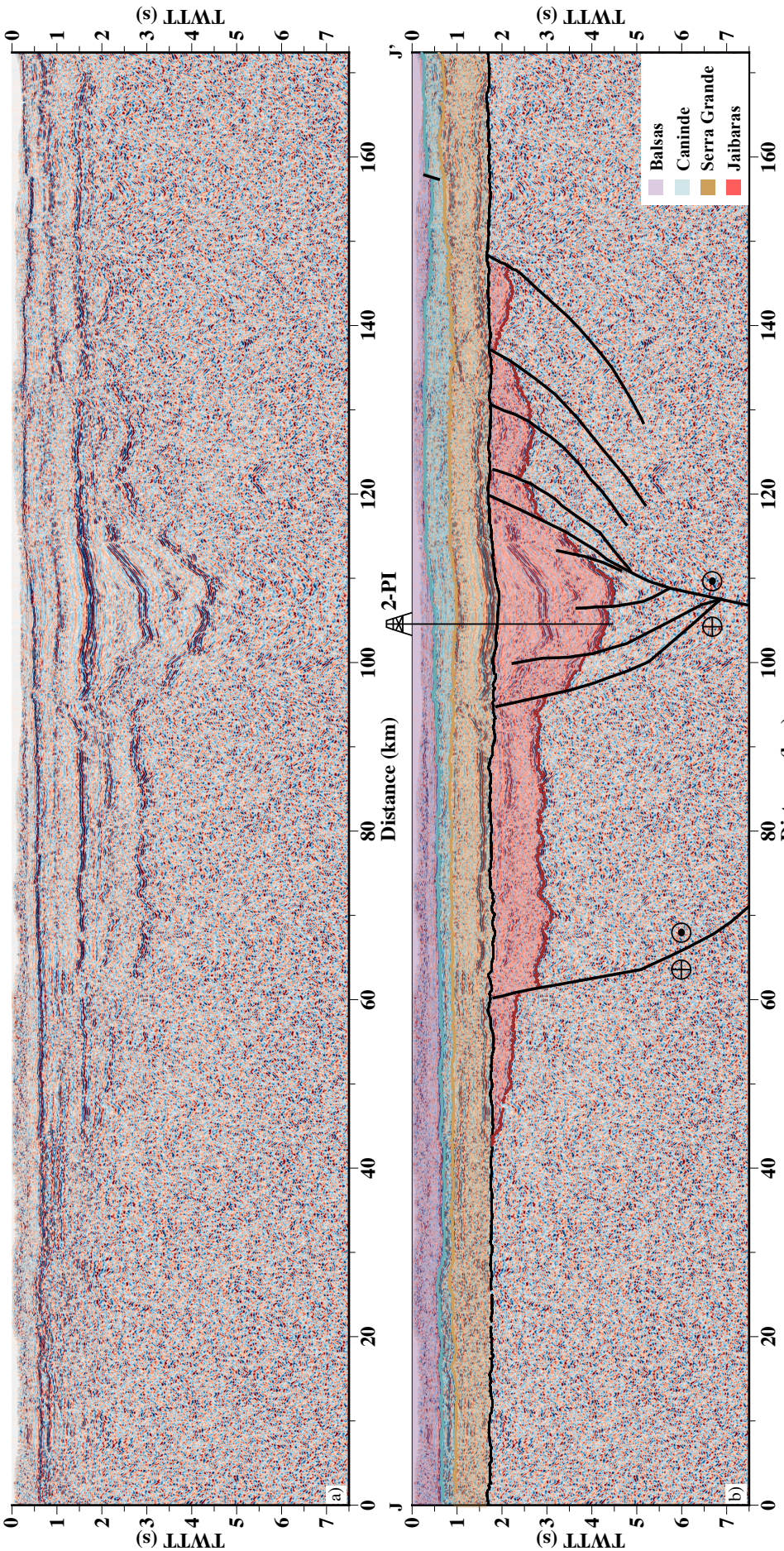


Figure 3.7: a) Uninterpreted aeismic reflection profile 0295-0007 from the south-east section of Parnaíba basin showing the underlying Jaibaras basin. b) same as in (a) with interpretation section overlain. J–J' as shown in Figure 3.1.

industry two-dimensional seismic data and two wells in detail. These authors proposed that the Riachão basin is a remnant foreland basin, bounded by thick skinned thrust faults of Cambro-Ordovician age. In this case, the Riachão basin may be an equivalent of the Volta basin of west Africa, which is a foreland basin of the West Gondwana Orogen (see Section 2.2.2; Ganade de Araújo et al., 2014a).

3.2.5 Regional crustal structure

The PSDM regional seismic reflection profile is shown in Figure 3.9 and as a PSTM section in Figure 3.10. The profile is based on the same data as discussed in Daly et al. (2014), however, an additional post-stack semblance smoothing coherency filter (Milkereit and Spencer, 1989) has been applied to the stack in order to enhance the deep crustal reflectivity. A further difference is that the section of the profile that trends north-south, located $\sim 47.5°$ has been removed, such that the profile is a more reasonable representation of the basin in cross-section. Additionally, in figure 3.9c the data are displayed using amplitude volume attribute, which further aids in the identification of deep reflections and the sedimentary/basement contact.

Daly et al. (2014) interpreted the seismic structure of the regional reflection profile on the basis of variations in reflection facies. They concluded that the crust is characterised by three distinct basement blocks, with clear evidence for the presence of a concealed Parnaíba block beneath the basin, in agreement with plate reconstructions and potential field data (e.g., de Brito Neves et al., 1984; Cordani, 1984; Fuck et al., 2008; de Castro et al., 2014; de Castro et al., 2016). The interpretation of Daly et al. (2014) is adopted in this study, however, the interpretation is extended by also modelling the density structure along this profile (see Chapter 4). From west-to-east, the crust is comprised of the (1) the Amazonian craton and Araguaia Supergroup; (2) the potential continuation of the Goiás magmatic arc; (3) the Parnaíba block and (4) the Borborema Province. It should be noted that the velocity model used in this depth migration is only constrained in the upper $\sim 5\ km$, where semblance analysis was viable. Below these depths, a simple one-dimensional velocity gradient was imposed. Hence, in the absence of coincident crustal scale refraction data, interface depths obtained via wide-angle reflection/refraction modelling in the centre of the basin and gravity

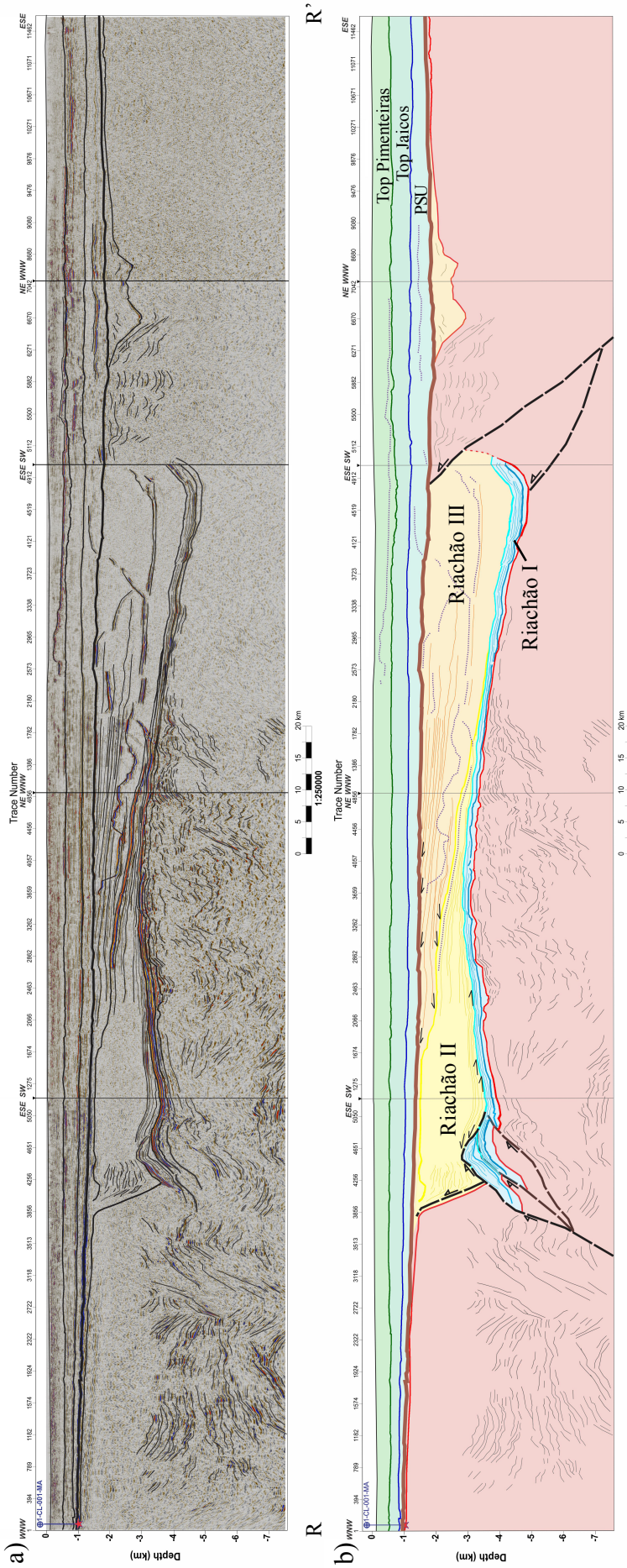


Figure 3.8: a) Uninterpreted composite seismic reflection profile imaging the Riachão basin from the beneath the western section of Parnaíba basin(R–R' as shown in Figure 3.1). b) same as in (a) with interpretation section overlain. Blue dashed lines are igneous sills. Upward open arrows show thrust faults. Upward filled arrows show onlap; downward arrows show truncations. PUS = Pre-Silurian unconformity (after, Porto et al., In press).

modelling results were used to test the validity of the depth conversion (See Section 3.5 and Chapter 4). It was found that these depths are broadly consistent with depths derived from wide-angle reflections and gravity modelling, with maximum deviations of $\sim 2\ km$.

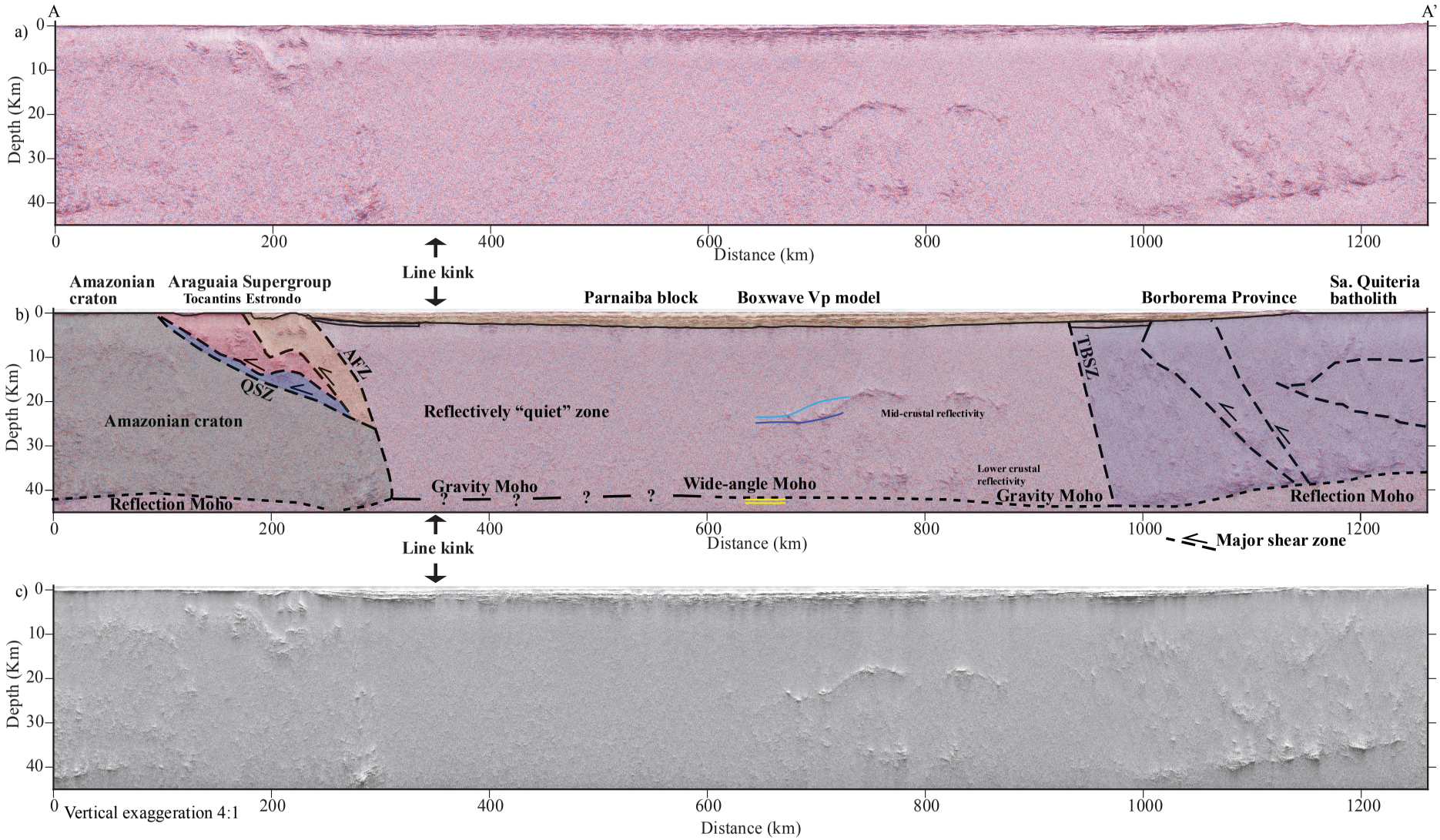


Figure 3.9: a) Post-stack depth migrated seismic reflection profile with coherency filter applied. Note the link kink $\sim$ 47.5°W has been removed (Figure 3.1). b) Same as in (a) with interpretation overlain (modified from Daly et al. 2014). AFZ=Araguaia Fault Zone, QSZ=Quatipuru Suture Zone and TBSZ=Trans Brasiliano Shear Zone. Light blue, dark blue and yellow lines are interfaces derived from forward P-wave velocity modelling (see Section 3.5). c) same as in (a) but displayed using amplitude volume.

The Amazonian craton in the west is characterised by flat-lying reflections within the upper crust and a Moho depth of $\sim$ 40–42 km. Basinward, a highly complex pattern of reflections in the upper part of the crust is observed with a general eastward dip, defining the Araguaia belt metasediments of the Tocantins and Estrondo groups, which were emplaced northwestward along the Quatipuru Suture Zone (QSZ; Fig. 3.9) during Brasiliano orogenesis (Cordani et al., 2000; Moura et al., 2008). Beneath this package, the Moho dips basinward, deepening locally to $\sim$ 44.5 km (Daly et al., 2014). This is indicative of a crustal flexure driven by the emplacement of Araguaia fold and thrust belt load as proposed by Ussami and Molina (1999).

Further eastward, reflectivity terminates abruptly. This contrast marks the crustal expression of the Araguaia Fault Zone, where at the surface, late stage Brasiliano North-South dextral strike-slip displacement was accommodated (Fonseca et al., 2004). The AFZ marks the boundary between the Araguaia Supergroup and the western section of the Parnaíba block, which appears acoustically featureless on this profile. The eastern section, however, is characterised by a prominent zone of Mid-Crustal Reflectivity (MCR) at depths between $\sim$ 17–25 km and a $\sim$ 12–18 km thick reflective lower crust. Interestingly, preliminary results from long offset ($\gg$ 100 km) explosive source wide-angle reflection/refraction P-wave velocity modelling has shown this boundary continues to the west, where no reflectively is present on the reflection profile (Soures et al., In review).

The Moho is not easily identified in the basin centre in Figure 3.9. Originally, the base of the high-amplitude reflections near model km 780 were suspected as Moho (e.g., Daly et al., 2014). However, between model km 680 and 750, these reflections exhibit an eastwardly dip, shallowing to $\sim$ 28 km depth. This is much shallower than the Moho depth of $\sim$ 42 $\pm$2 km determined by gravity (Chapter 4) and P-wave velocity modelling (as discussed in the following sections), and hence, these reflections appear to occur within the lower crust.

Further east, another abrupt change in the seismic facies occurs. This is interpreted as the crustal expression of the Trans-Brasiliano Shear Zone (TBSZ), separating the Parnaíba block from the Borborema Province. The Borborema Province is characterised by extensive crustal-scale shear zones, with apparent easterly dips of $\sim$ 20–30°. These appear to sole into a

well-resolved reflection Moho, which steadily deepens basinward from $\sim 35\ km$ at the profile edge to $\sim 44\ km$ at its intersection with the TBSZ.

Most significantly, the depth converted Moho reflections beneath the basin, appear as deep or deeper than the Moho in the flanking regions, with no appreciable change in crustal thickness. This is at odds with an extensional origin, in which case, the crust would be expected to thin by $> 5\ km$, for a stretching factor, β, on the order of 1.2. In the following section and in Chapter 4, investigation of crustal structure is expanded by analysing wide-angle reflection/refraction and gravity data that were also acquired along the PBAP regional profile. Specifically we explore outlining questions including: What is the geological nature of the MCR and what are its tectonic implications? Are the Moho depths robust and consistent with the gravity data? What is the nature of the crust beneath the seismically opaque western section of the basin?

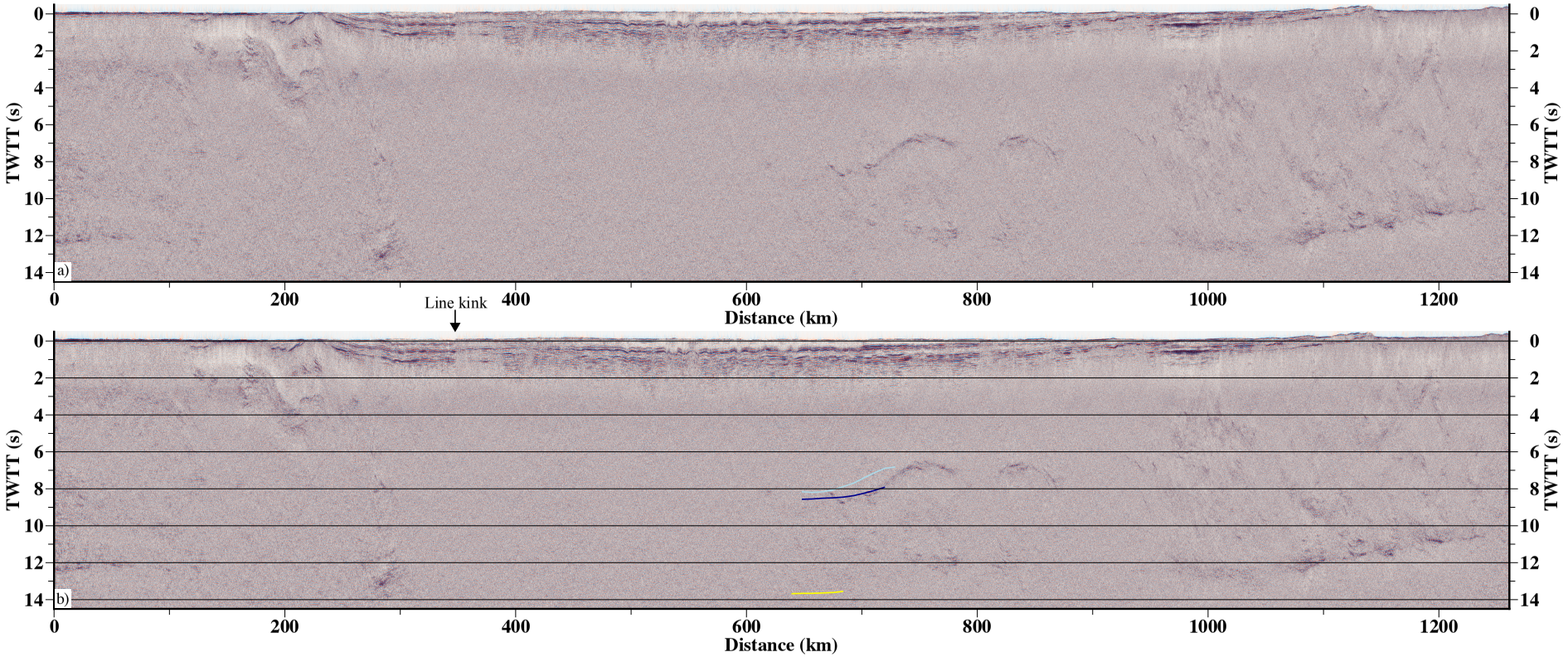


Figure 3.10: a) Post-stack time migrated seismic reflection profile with coherency filter applied. Note the line kink at model km 340 ($\sim$ 47.5°W) has been removed (Figure 3.1). b) Same as in (a) but with interfaces derived via forward P-wave velocity modelling and converted to TWTT overlain (Section 3.5).

3.3 Wide-angle reflection/refraction "box wave" receiver gathers

3.3.1 Wide-angle reflection/refraction acquisition testing

During the acquisition of the regional reflection profile, several test surveys were conducted to evaluate the viability of acquiring wide-angle reflection/refraction data (offsets up to ± 110 km) within Parnaíba basin using a vibroseis source. The variation in data quality produced by the various modifications of the source and receiver parameters were visually assessed to determine whether any of the configurations were able to recover crustal phase arrivals.

Initially, testing focused on increasing the energy input at the source, in an attempt to overpower noise, by increasing the number of sweeps performed by each vibroseis truck. The number of sweeps tested were 2, 4, 8 and 16. These provided little improvement in data quality, with the offset range of first arrivals increasing by only a few kilometres and no deep reflection events identifiable.

Given the poor source performance, the focus shifted to the receiver configuration. Firstly, a reduction in the receiver group interval was tested during the acquisition of three MCS regional tie lines (Fig. 3.11b). By decreasing the group interval from 50 m to 25 m the data quality did improve within the first $\sim$ 6 s $TWTT$, however, there was no noticeable improvement within the deeper section.

As it appeared that high amplitude surface wave noise was particularly problematic during the first two tests, the final test aimed to attenuate these arrivals at the receiver. This involved using a receiver array in an attempt to attenuate arrivals based on their apparent spatial wavelengths. The particular array style used was an areal array of 225 receivers deployed in a 280 m x 280 m square known as a "box wave" array (Regone, 1997). The data were then acquired in the common receiver domain as "receiver gathers" (i.e., by recording a profile of vibration shot points at each receiver array).

As discussed by Regone (1997), an areal array of this kind can be used to identify coherent

scattered noise events from both in-line and cross-line directions and determine the horizontal velocities of these events. Additionally, by constructing a series of progressively larger nested arrays (corresponding to greater levels of attenuation) the signal-to-noise ratio (SNR) can be quantitatively estimated, based on the attenuation level at which the desired signal appears. Details regarding this methodology are discussed in section 3.3.2.

During testing, Vibration Points (VPs) were recorded at offsets up to 85 km, and analysis of the gather was performed by BP Houston. This revealed that surface wave noise, generated by both the source and traffic from the nearby highway, was primarily responsible for masking the desired signal. By attenuating this noise, clear first arrivals and deep reflection events between 7–15 s $TWTT$ at the maximum offsets of 85 km were revealed.

Given the vast improvement in data quality achieved using this method, a survey was designed to further test the method's applicability and act as a complimentary/comparative dataset for the regional reflection profile. This survey—named here the "Parnaíba Box Array Seismic Survey" (PBASS)—involved recording VPs at offsets of up to $\pm$ 110 km at five box wave arrays, deployed $\sim$ 5 km apart near the centre of the regional reflection profile (Fig. 3.11).

3.3.2 "Box wave" methodology: Array theory and application

It has long been known that noise recorded during active source seismic surveys—both coherent (e.g., surface waves and vehicle traffic) and incoherent (e.g., wind)—can be attenuated by using receiver and/or shooting arrays, thereby improving the SNR (e.g., Taylor, 1931; McKay, 1954; Parr and Mayne, 1955; Holzman, 1963; Sheriff and Geldart, 1995; Regone, 1997). Array techniques are particularly attractive when the frequency band of noise overlaps that of the desired signal, such that frequency filters are rendered impractical. This is because arrays form a spatial wavenumber filter, attenuating arrivals based on their apparent wavelengths. For example, Rayleigh waves (ground roll) generated by a seismic source, with a typical peak frequency of 20 Hz, may overlap the frequency band of desired reflection signals. As shown in figure 3.12, such arrivals exhibit a relatively higher wavenumber (as a function of their much slower apparent velocities and larger angle of incidence) than desired reflection signals and

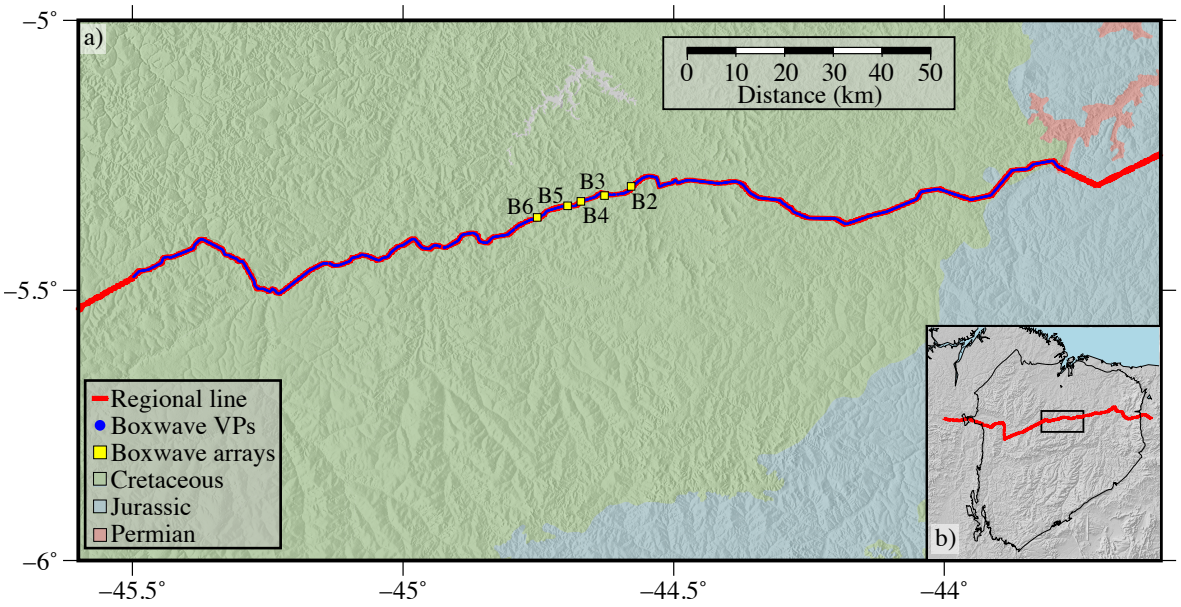


Figure 3.11: a) PBASS survey geometry. Yellow squares are box array receiver locations. Blue line shows the vibration points (VPs) recorded during the PBASS survey. Red line is the regional seismic reflection profile. b) Map showing the location of (a) (black box) with respect to the Parnaíba basin outline (black line).

hence can be filtered on this basis (e.g., Pap, 1983; Glangeaud et al., 1999).

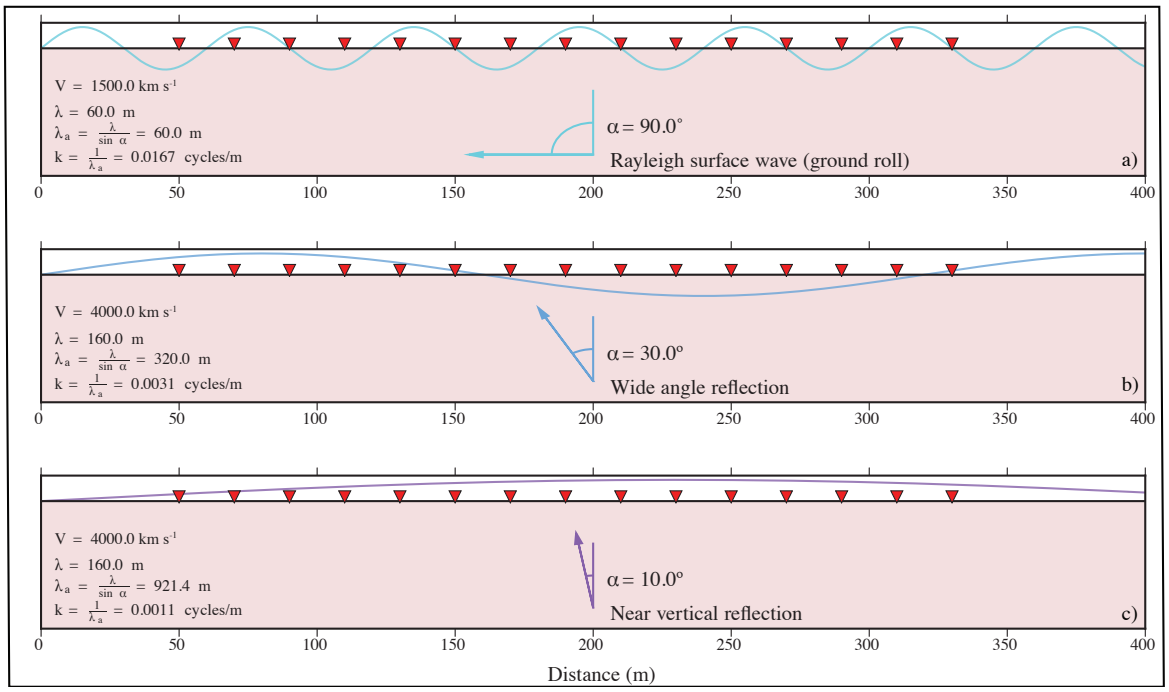


Figure 3.12: Schematic illustrations showing the dependence of apparent wavelength on emergence angle (after Pap, 1983). Note that as emergence angle decreases the apparent wavelength approaches infinity.

3.3.3 Noise attenuation method

Arrays are primarily designed to attenuate coherent noise by forming a spatial wavenumber filter. These filters operate by adding together the signal recorded at each element of the array to form a single output signal. In this way, in-phase arrivals tend to add constructively and are passed, while out of phase arrivals tend to add destructively and are attenuated. For a given wave, the phase angle recorded at each station is determined by the apparent wavelength of the wave, which is a function of the wave's frequency, velocity and angle of incidence with respect to the array. For example, figure 3.12 shows three harmonic waves recorded by a fifteen geophone linear array with an element spacing of 20 m.

These waves all have a temporal frequency of 20 Hz but vary in incidence angle and velocity, resulting in different apparent wavelengths. The attenuation level achieved by an array may be represented by an "array response" diagram, as shown in figure 3.13a. This shows the level of attenuation achieved for each wave number, with respect to the signal that would be recorded by an equal number of geophones placed at a single location (e.g., Sheriff and Geldart, 1995). The pass and reject bands show the wavenumbers that are added constructively and passed, and those that are added destructively and are attenuated. The "notches" between the lobes occur when the apparent wavelength is such that the phase difference across the array is equal to 180°, and theoretically, complete attenuation occurs. The side lobes occur where the apparent wavelength is such that the signal summed across the array results in a poor attenuation level. The alias lobe occurs when the wavelength is equal to the geophone spacing, such that the signal is in phase at all geophones and the output adds constructively when summed. Beyond the alias lobe, the array response repeats for the aliased wavelengths.

For two-dimensional surveys, linear arrays are usually placed in-line with the direction of shooting and used to attenuate coherent noise within the plane of the survey. However, arrays may also be deployed with some form of areal geometry and can be used to attenuate coherent noise arriving from all azimuths. Furthermore, the level of attenuation achieved can be increased by assigning a weighting value to each receiver element.

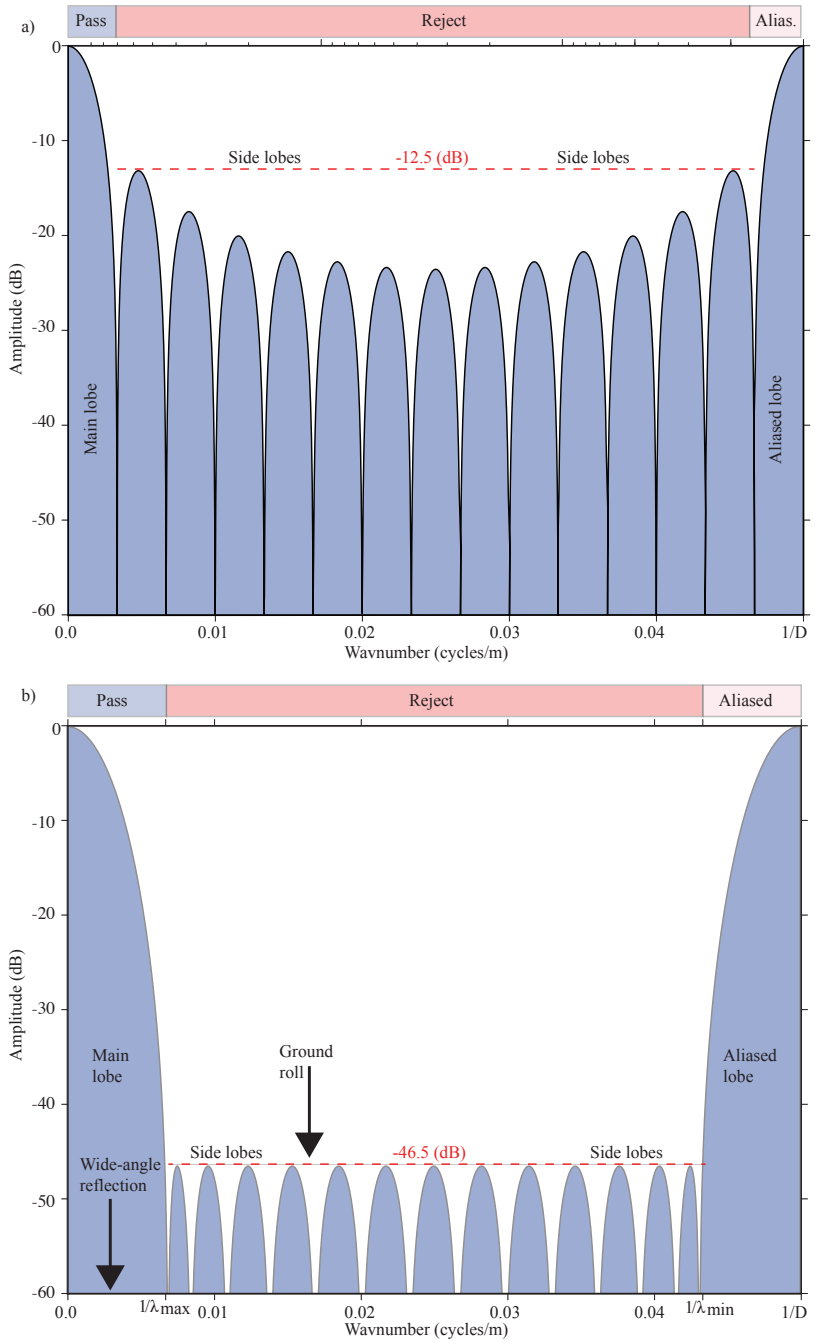


Figure 3.13: a)Array response diagram showing the theoretical attenuation achieved using a linear 15 geophone array with respect to the signal that would be recorded by an equal number of geophones placed at a single location (e.g., Sheriff and Geldart, 1995). b) Array response diagram showing the theoretical attenuation achieved using the areal array shown in (a) and a Chebychev weighting scheme (Holzman, 1963) with respect to the signal that would be recorded by an equal number of geophones placed at a single location (Sheriff and Geldart, 1995). Arrows show the wavenumbers for the wide-angle reflection and ground roll as shown in figure 3.12

Arrays also attenuate random noise. Similarly to a traditional central-depth-point stack, the SNR improvement for an array is theoretically equal to $\sqrt{N}$, where N is the number of geophones within the array. However, in practice the attenuation level achieved will be less than $\sqrt{N}$, as geophones spacing is not usually sufficient to ensure noise is completely incoherent across an array (Cooper and Cook, 1984) and other factors such as variations in topography can affect the stacking procedure.

3.3.4 PBASS Chebyshev array

The specific array type used during this study was that of a Chebyshev optimised array (Holzman, 1963). The arrays were designed and deployed following the method outlined by Regone (1997). This style of array consists of an areal geometry of equalled spaced elements deployed as a square (Fig. 3.14), with each element weighted by means of Chebyshev optimisation (e.g., Holzman, 1963; Regone, 1997). Chebyshev weighting is advantageous as this: (1) ensures the level of attenuation is equal for all lobes within the reject zone; (2) allows the width of the reject zone to be modified by simply adjusting the weighting values; and (3) ensures the minimum attenuation achieved is a function of the number of array elements and the effective width of the reject zone (Regone, 1997).

During the PBASS survey, a total of five box wave arrays, each consisting of 225 receiver elements, were acquired. These were deployed as 280 m × 280 m squares with 20 m spacings between each element (Fig. 3.14). Given the narrow spacing and large number of geophones within each sub-array, variations of the signal recorded at each geophone are averaged during summation. Furthermore, variations in instrument response, due for example, to variations in ground coupling, can be eliminated during processing (Regone, 1997). The theoretical array response for these arrays is shown in figure 3.13b.

Table 3.1 shows the box wave acquisition parameters and compares these to those used during the acquisition of the regional reflection profile.

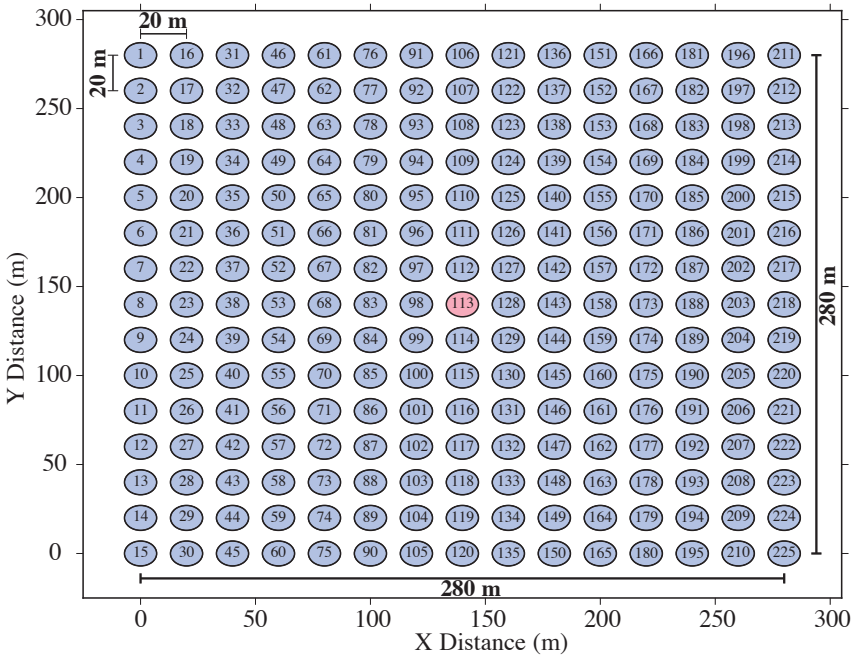


Figure 3.14: Schematic layout of the box wave areal receiver array used to acquire the five receiver gathers analysed in this study. Blue circles represent receiver nodes. Note the location of the central receiver node (113) is the geographic location of the receiver gather, with trace offsets measured relative to this.

3.4 Box wave array receiver gathers

The box wave receiver gathers exhibit a far superior data quality in comparison with the standard shot gathers acquired for the seismic reflection profile. However, dispersive surface waves are still prevalent on the near offset traces ($< 35\ km$) and degrade deep reflections at wider offsets (Figs. 3.15–3.20). Figure 3.15 shows the gather collected at Box-2 pre and post signal processing, as described in the figure caption.

Nevertheless, clear P-wave refraction and reflection phase arrivals are observable on all five gathers. Refracted first arrivals (Pg) are visible at offsets up to $\sim \pm\ 30\ km$ (Figs. 3.16–3.20). Most prominent is a $\sim 5.3\ s$ thick package of continuous to semi-continuous reflections from $\sim$ 8.5–13.8 s. The reflection from the top of this package (P_cP) extends to offsets of $\sim$ 35–45 km both east and west and reappears as a strong reflection to the east at offsets of $\sim$ 50–100 km. The poor data quality at offsets between $\sim$ 35–50 km is likely the result of destructive interference with the dispersive surface wave energy that intersects the P_cP phase at these

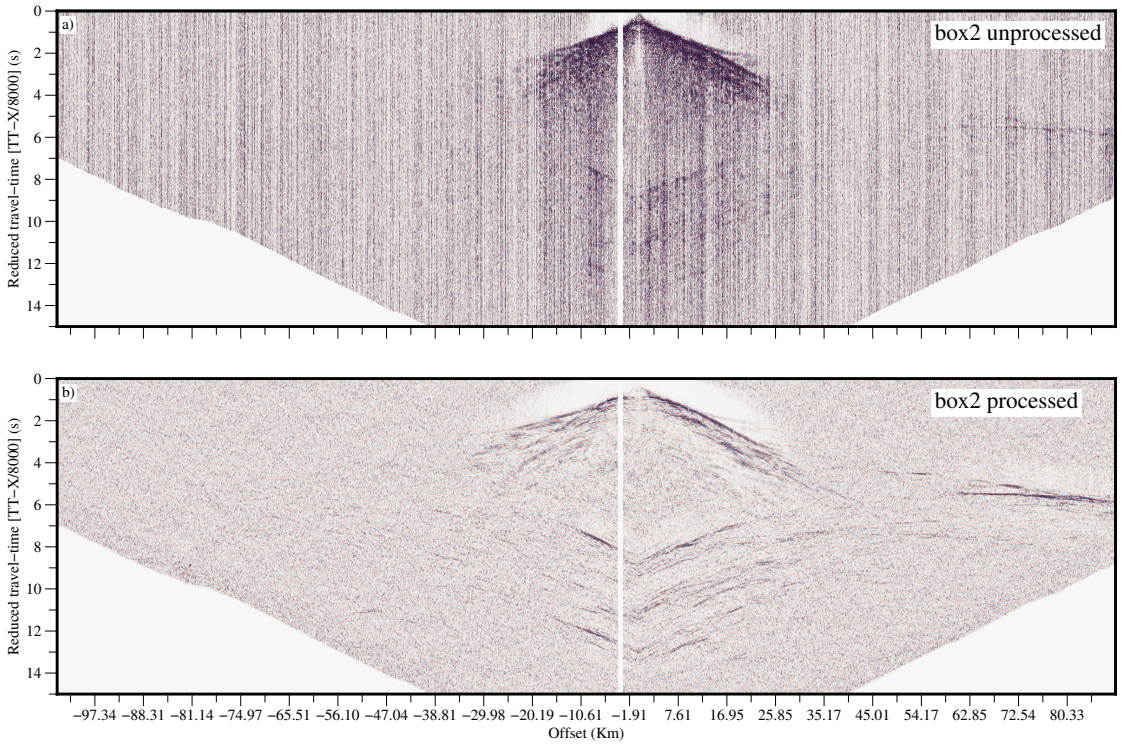


Figure 3.15: a) Box-2 Raw receiver gather displayed using reduced travel time using a reduction velocity of 8 $km\ s^{-1}$. b) Same as in (a) with signal processing applied. Processing included an FK filter, FX-deconvolution and sembsmooth coherency filters, predictive deconvolution; a [2-4-12-15] Hz bandpass filter; full trace balance and 3000 ms AGC.

offsets.

On the eastern side of the gathers, a prominent linear arrival is evident above the P_cP reflection at offsets $> 55\ km$ (P_i). This is interpreted as a refracted head wave from an interface related to that which produces the P_cP reflection.

At the base of the reflectivity package, the latest arriving, laterally coherent reflection phase (P_mP) is picked and interpreted as the reflection Moho (e.g., Cook, 2002). This reflection is identifiable to offsets of $\sim \pm\ 45\ km$.

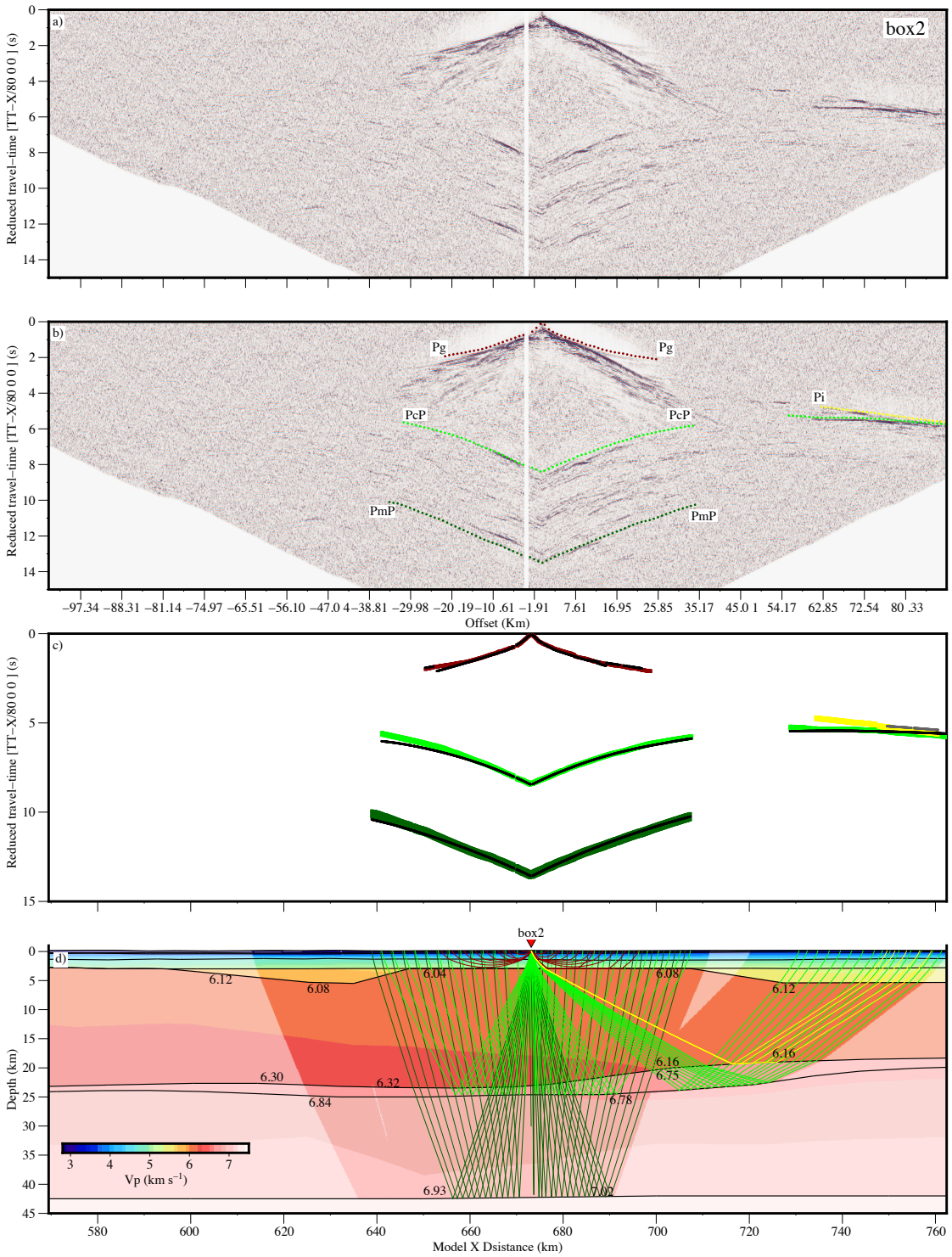


Figure 3.16: (a) Box-2 receiver gather with signal processing applied to aid in phase identification. Processing includes an FK filter, FX-deconvolution and sembsmooth coherency filters, predictive deconvolution; a [2-4-12-15] Hz bandpass filter; full trace balance and 3000 ms AGC. (b) Same as above but with picked phase interpretations shown. (c) Picked (coloured) and modelled (black and grey (P_i)) travel-time arrivals. (d) Modelled crustal V_p structure with a subset of ray paths from each phase. Numbers are V_p in v. Transparent mask indicates regions unsampled by rays.

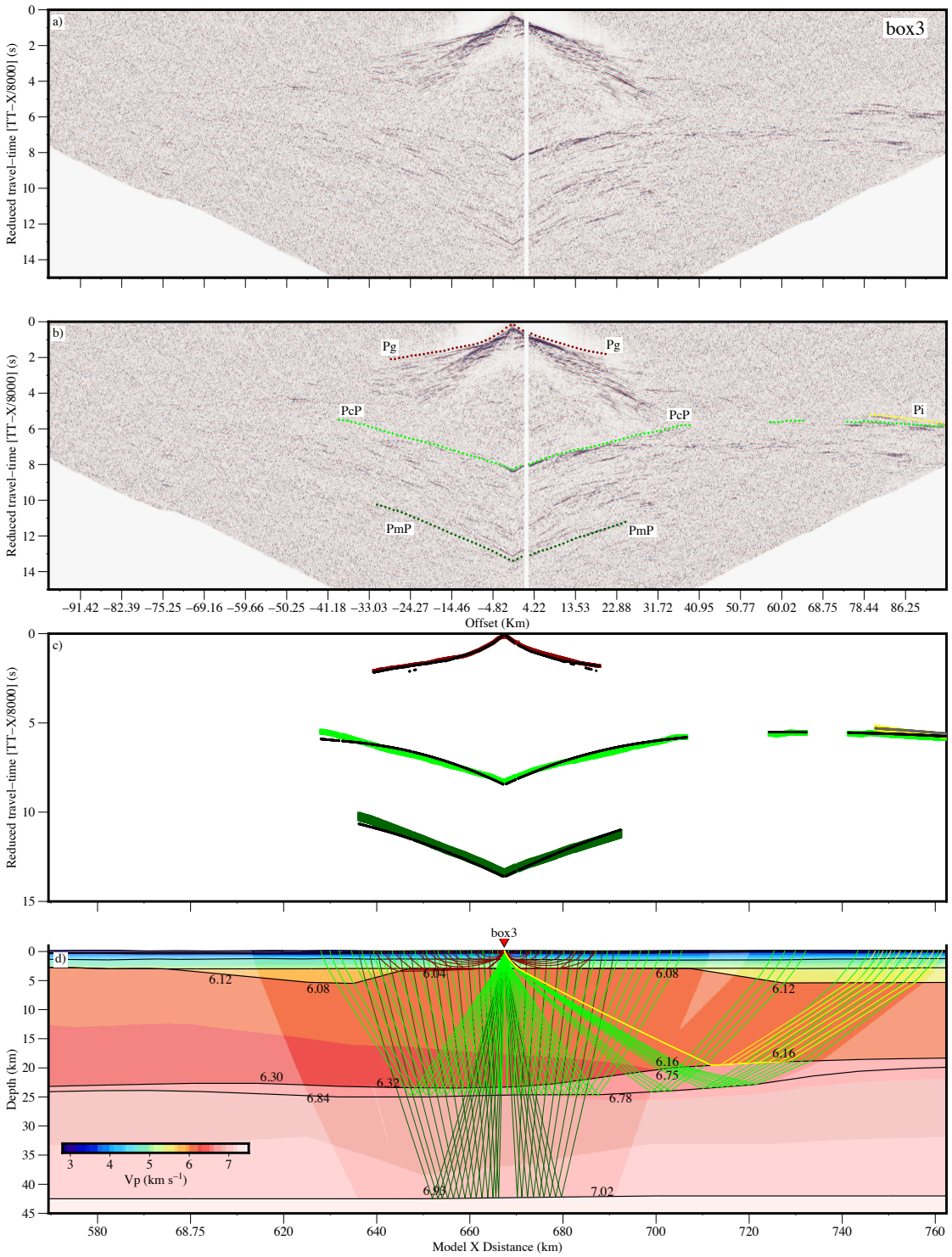


Figure 3.17: (a) Box-3 receiver gather with signal processing applied to aid in phase identification. Processing includes an FK filter, FX-deconvolution and sembsmooth coherency filters, predictive deconvolution; a [2-4-12-15] Hz bandpass filter; full trace balance and 3000 ms AGC. (b) Same as above but with picked phase interpretations shown. (c) Picked (coloured) and modelled (black and grey (P_i)) travel-time arrivals. (d) Modelled crustal V_p structure with a subset of ray paths from each phase. Numbers are V_p in $km\ s^{-1}$. Transparent mask indicates regions unsampled by rays.

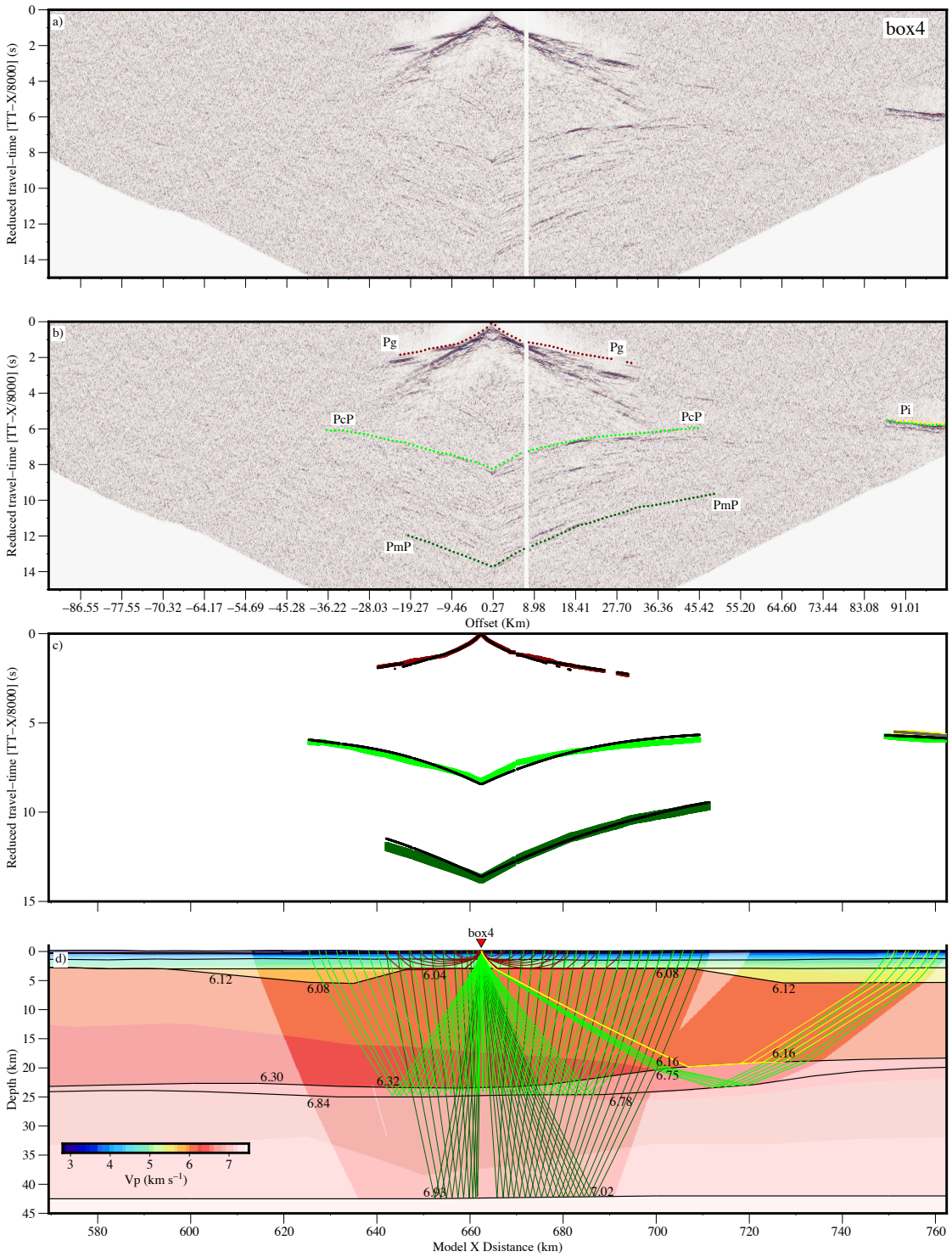


Figure 3.18: (a) Box-4 receiver gather with signal processing applied to aid in phase identification. Processing includes an FK filter, FX-deconvolution and sembsmooth coherency filters, predictive deconvolution; a [2-4-12-15] Hz bandpass filter; full trace balance and 3000 ms AGC. (b) Same as above but with picked phase interpretations shown. (c) Picked (coloured) and modelled (black and grey (P_i)) travel-time arrivals. (d) Modelled crustal V_p structure with a subset of ray paths from each phase. Numbers are V_p in $km\ s^{-1}$. Transparent mask indicates regions unsampled by rays.

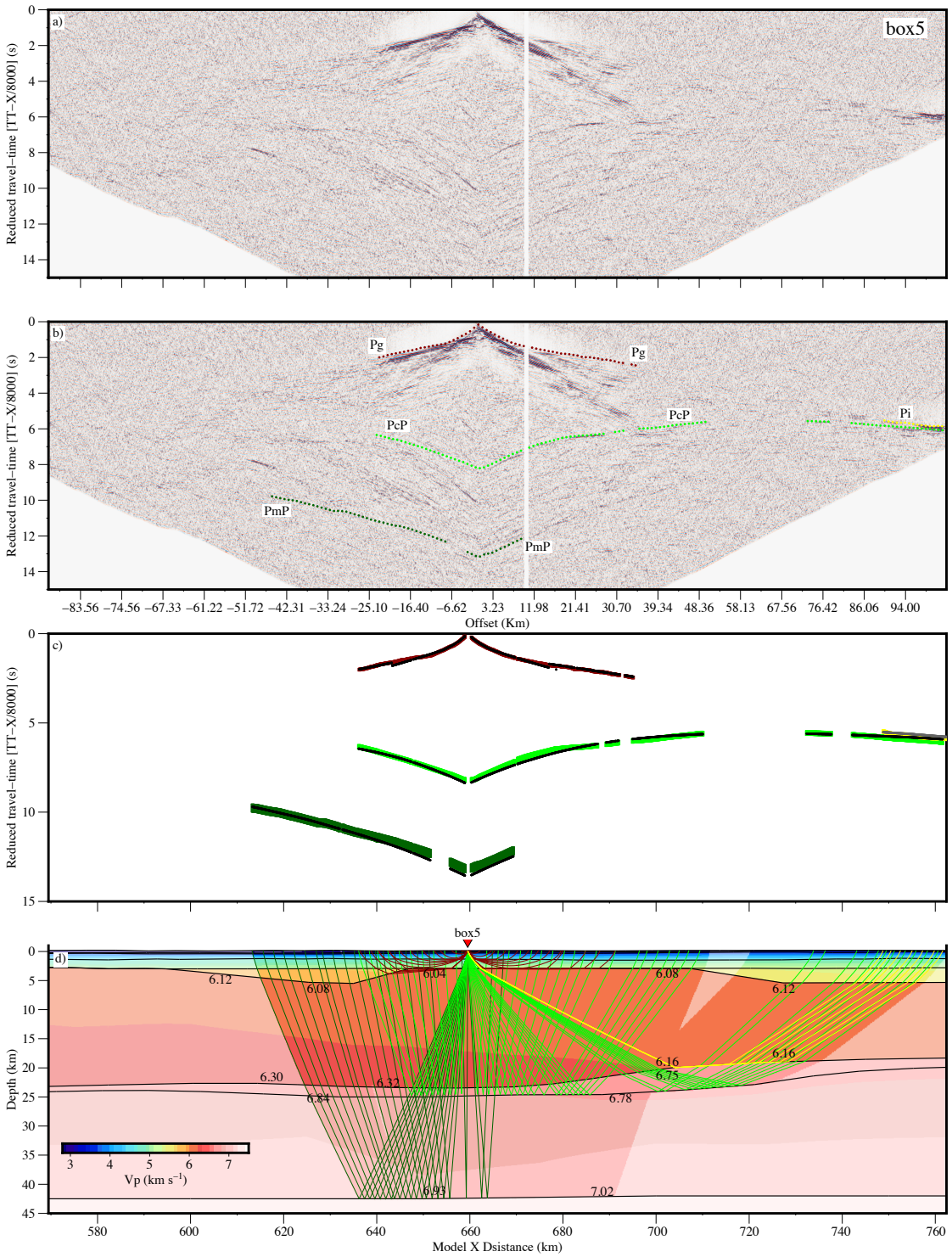


Figure 3.19: (a) Box-5 receiver gather with signal processing applied to aid in phase identification. Processing includes an FK filter, FX-deconvolution and sembsmooth coherency filters, predictive deconvolution; a [2-4-12-15] Hz bandpass filter; full trace balance and 3000 ms AGC. (b) Same as above but with picked phase interpretations shown. (c) Picked (coloured) and modelled (black and grey (P_i)) travel-time arrivals. (d) Modelled crustal V_p structure with a subset of ray paths from each phase. Numbers are V_p in $km\ s^{-1}$. Transparent mask indicates regions unsampled by rays.

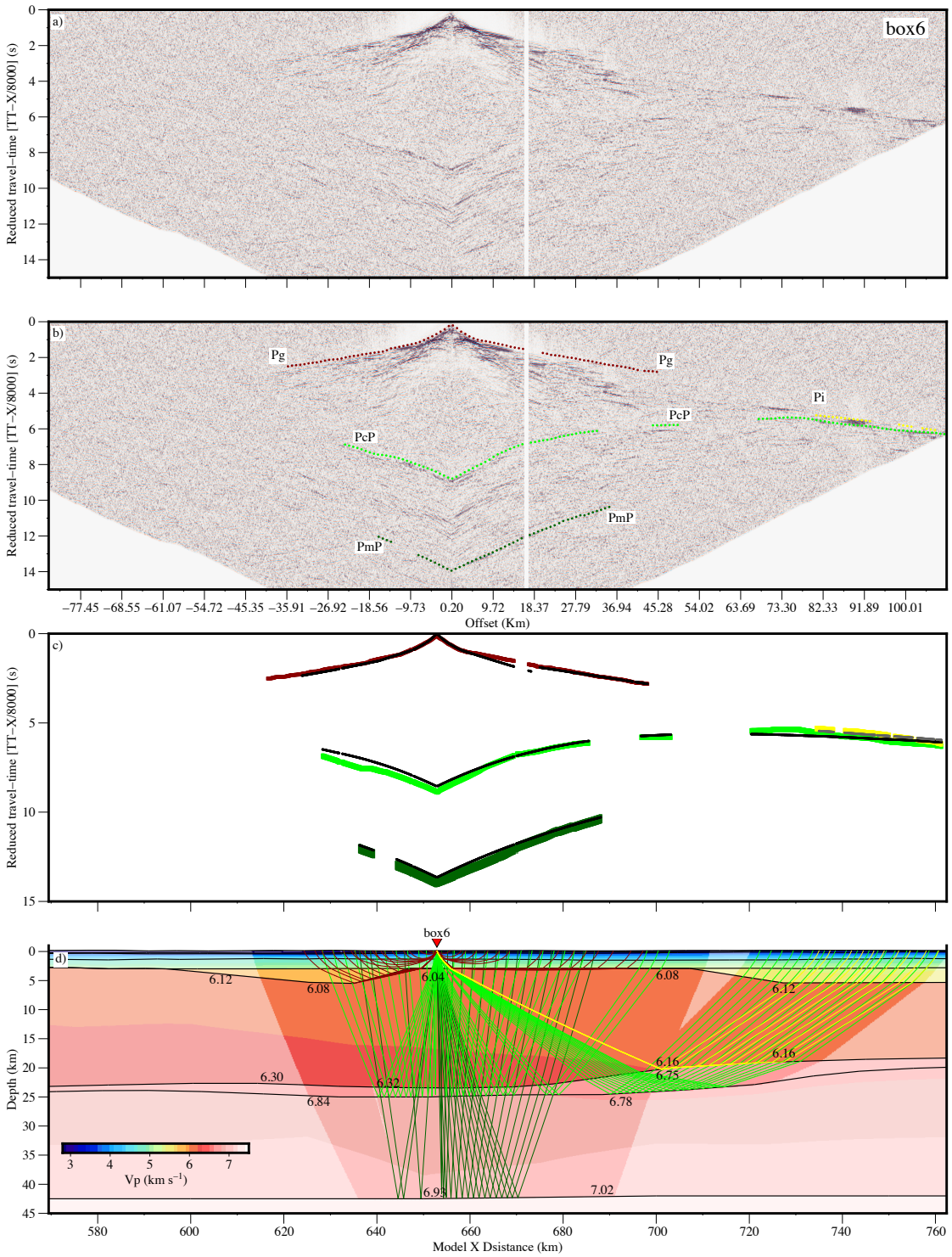


Figure 3.20: (a) Box-6 receiver gather with signal processing applied to aid in phase identification. Processing includes an FK filter, FX-deconvolution and sembsmooth coherency filters, predictive deconvolution; a [2-4-12-15] Hz bandpass filter; full trace balance and 3000 ms AGC. (b) Same as above but with picked phase interpretations shown. (c) Picked (coloured) and modelled (black and grey (P_i)) travel-time arrivals. (d) Modelled crustal V_p structure with a subset of ray paths from each phase. Numbers are V_p in $km\ s^{-1}$. Transparent mask indicates regions unsampled by rays.

3.5 Box wave two-dimensional P-wave velocity model

Modelling of active source seismic wave travel-time data (and more recently, full waveforms) is the primary means by which the internal structure of Earth's crust and upper most mantle is deduced. In this section the method used to constrain a crustal scale P-wave velocity (V_p) model within the centre of Parnaíba basin, using the PBASS dataset, is described.

3.5.1 Adopted modelling technique

A variety of techniques can be used to constrain V_p structure using wide-angle reflection and refraction data and can be broadly divided into forward (trial-and-error) and inverse (inversion or tomographic) methods (e.g., Hole, 1992; Zelt and Smith, 1992; Korenaga et al., 2000; Hobro et al., 2003). The choice of which method is most appropriate for modelling a given dataset is primarily dictated by the survey geometry and spatial ray coverage. Inverse methods are advantageous as they are less time consuming, are less likely to result in unnecessary structure being introduced into the model and can recover heterogeneous structure, that may be difficult to resolve using a forward modelling approach. However, previous studies have shown that to derive geologically meaningful results, a dense ray coverage is required when using an inverse approach (e.g., Scherwath, 2002). Given the modest data volume offered by the PBASS dataset, a predominantly forward modelling approach was adopted for this study using the ray tracing method of Zelt and Smith (1992). This approach allows greater control over model parameters and incorporation of constraints from complimentary datasets (i.e., the regional seismic reflection profile and gravity modelling results (see Chapter 4). Inversion of specific model parameters was also performed when appropriate. This method also allows for the incorporation of topography, preventing the requirement of arduous static corrections. Within the model, each layer is defined by an arbitrary number of boundary and velocity nodes connected by linear interpolation and modelled arrival times are derived by tracing rays through the model by solving 2-D ray tracing equations numerically (Zelt and Smith, 1992; Červený et al., 1977).

3.5.1.1 Model geometry

Given the box wave survey was acquired as a two-dimensional (2D) profile the data are modelled using a strictly 2D approach. However, as is the case for most onshore surveys, the distribution of the shot points and receivers were dictated by the physiography and land access of the survey region. Hence, the instruments violate the 2D assumption and form a "crooked-line" geometry (Fig. 3.11). The source and receiver positions were therefore projected onto a 2D model profile as shown in figure 3.21. Shots are projected perpendicularly, while receivers are projected radially, in order to preserve offset distances. Elevations at shot and receiver locations are also projected in order to preserve ray-path lengths.

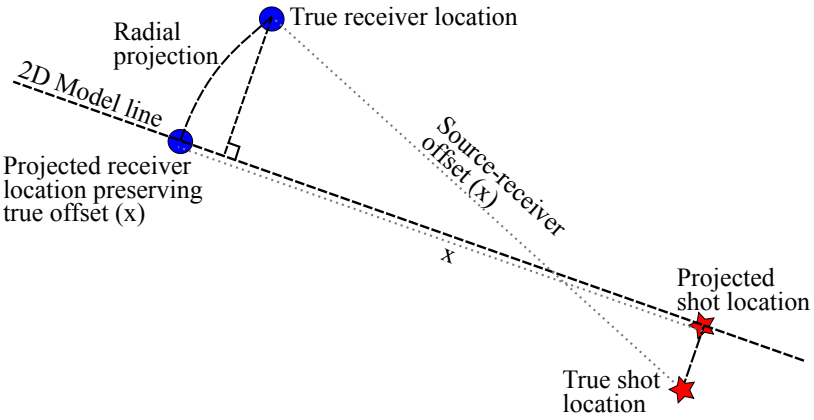


Figure 3.21: Schematic diagram demonstrating the projection of shot and receivers onto a two-dimensional model profile. Note that shots are projected perpendicularly, while receivers are projected radially to preserve offset distance (x) (modified after Scherwath, 2002).

3.5.2 Modelling strategy and assumptions

Various strategies can be adopted when forward modelling V_p structure, depending on survey geometry and data availability (e.g., Zelt and Smith, 1992; Zelt, 1999). The model developed in this study was constructed using a 'top-down' and 'prior-structure' approach (Zelt, 1999). Given the 2D modelling approach used, picked phase arrivals are assumed to originate from within the model plane, i.e., out-of-plane three dimensional structure is neglected. Ray-tracing is conducted using Cartesian coordinates as it has been shown that travel time variations

caused by the spherical nature of the Earth only become non-negligible at offsets greater than $\sim 500\ km$ (Zelt, 1999).

The sedimentary basin geometry and V_p structure were constrained using reflection depths and interval velocities from the depth migrated regional reflection profile (Daly et al., 2014) and held fixed during modelling of the deeper structure. This is important, as errors in the relatively low velocities of the sediment fill can result in large travel-time errors propagating into deeper sections of the model, producing large errors in interface depths (see Stern et al., 2010). The depth of the MCR (Fig. 3.9) was also incorporated in the starting model, defining the boundary between the upper and lower crust.

Misfits between the calculated and observed travel-times were then reduced by manual adjustment of model parameters or when appropriate, by using damped-least-squares inversion of specific parameters, while holding all others fixed.

Once the model was constrained within an acceptable misfit, the final model was obtained by inverting for best fits to the upper and lower crustal layers using damped least squares and applying a three node median smoothing between inversion iterations, to prevent the development of large V_p gradients. Inversions were run until the updated model failed a statistical F-test for significant difference at the 5% confidence level (e.g., Zelt and Smith, 1992).

Assessment of the goodness of model fit was performed by statistical analysis of a travel-time misfit using root-mean-squared (RMS) and normalised Chi-squared (χ^2) values as well as ray density analysis and residual travel time verses offset visualisation (Fig. 3.23). Model non-uniqueness and uncertainties are estimated by performing V_p perturbation tests, V_p inversion recovery tests and parameter grid search tests on selected parameters (Figs. 3.24–3.27) and by using a bounded Monte Carlo method to explore a larger parameter space (Fig. 3.28).

3.5.3 Modelling results

Pg refraction arrivals constrain upper crustal V_p to values between 6.04–6.12 $km\ s^{-1}$. Given these only sample the top of the upper crust, a 1D velocity gradient was assumed and a pa-

rameter search method to determine which combinations of V_p gradient and interface depth provide an adequate fit to the PcP reflections, while holding the geometry of the MCR determined from the regional reflection profile fixed (Fig. 3.22a and b).

The resulting model provided an excellent fit to the PcP arrivals; however, an acceptable fit of the observed P_i refraction arrivals was not possible with this geometry. It was found that the P_i arrivals require a shallower interface than the P_cP reflections, which reflect from an interface approximately $\sim$ 2–3 km deeper and parallel to the refraction interface. These two layers then define a mid-crustal zone, consistent with approximately the top and base of the $\sim$ 3 km thick band of reflectively that defines the MCR on the regional reflection profile (Figure 3). V_p in the upper crustal section appears slightly lower than the global average for shields and platforms (Christensen and Mooney, 1995) and reaches a maximum of 6.30 $km\ s^{-1}$ at a depth of $\sim$ 23 km.

In order to fit the gradient of the P_i refraction phase the lower layer requires a large increase in V_p to 6.75 $km\ s^{-1}$, consistent with a large acoustic impedance contrast evident by the high amplitude of the MCR on the regional reflection profile.

In the absence of any lower crustal refraction arrivals, a 1D V_p gradient was assumed for the lower crust, and the P_mP arrives were modelled as originating from the Moho. Again, a grid search approach is used to test which combinations of V_p gradient/interface depth provide an adequate fit to the travel times (Fig. 3.22c and d). This shows an inherent trade-off between interface depth and V_p gradient. However, the travel time misfit only resides within the pick error (200 ms) along a narrow band, constraining the depth to Moho of 42 $\pm$ 1 km (Fig. 3.22).

Due to the reverberant nature of the box wave gathers, travel-time picks were assigned relatively large uncertainties of 100, 150, 150 and 200 ms for the P_g, P_cP, P_i and P_mP phases respectively. Given these uncertainties, the majority of travel-times are modelled within reasonable χ^2 bounds. The overall RMS misfit for the model is 0.162 s and a χ^2 value of 1.079, with individual χ^2 values range between 0.081–6.306 and the vast majority between 0.5 and 1.5.

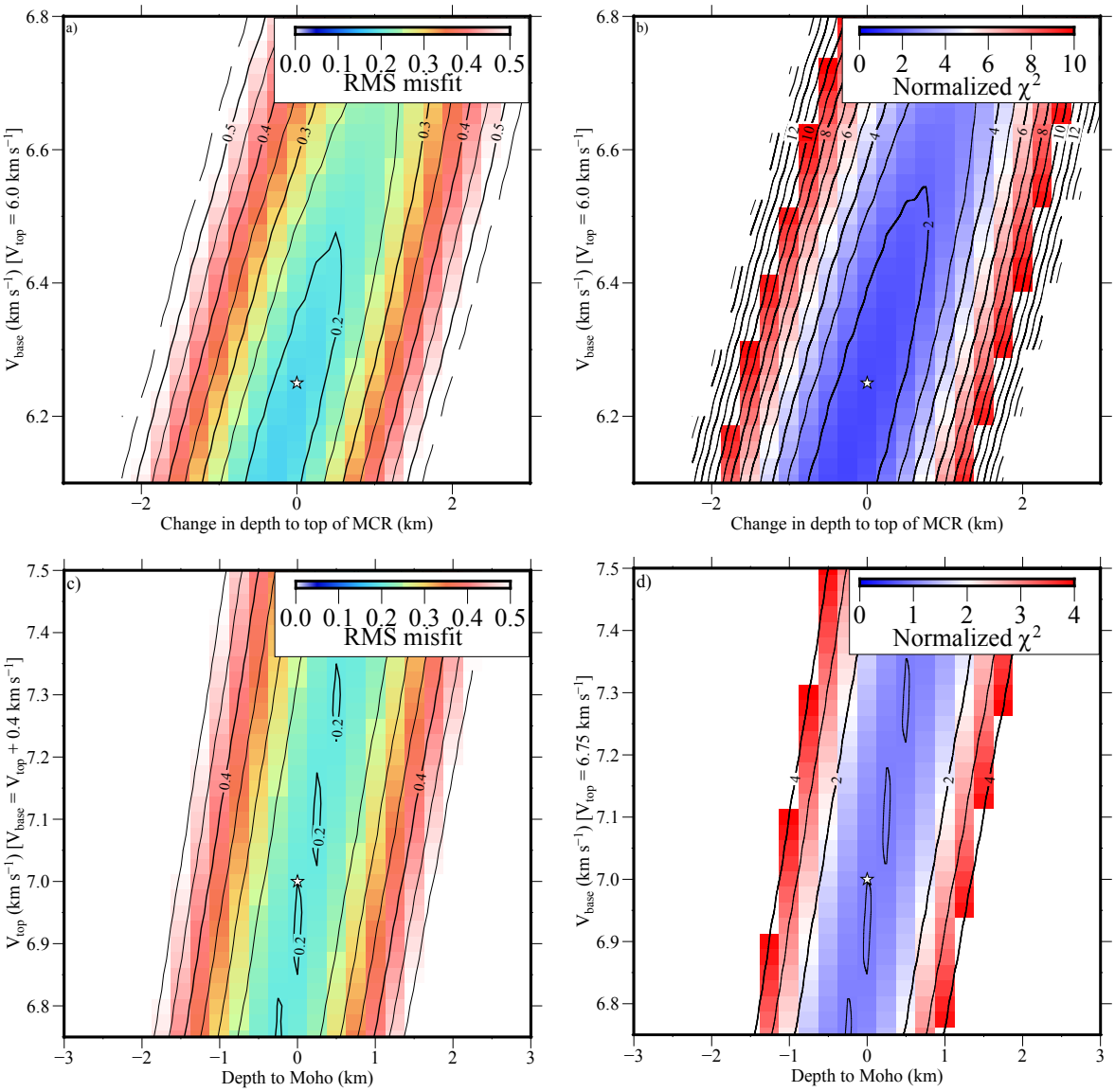
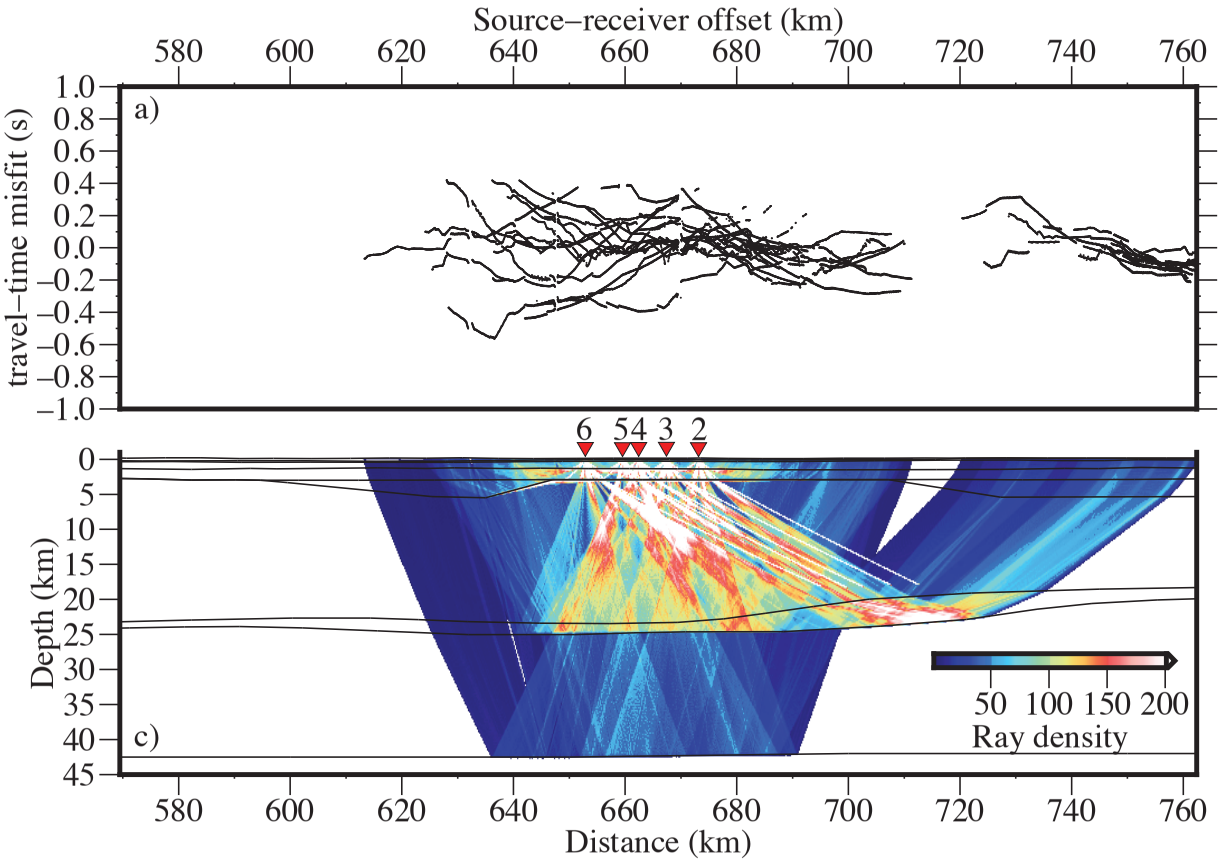
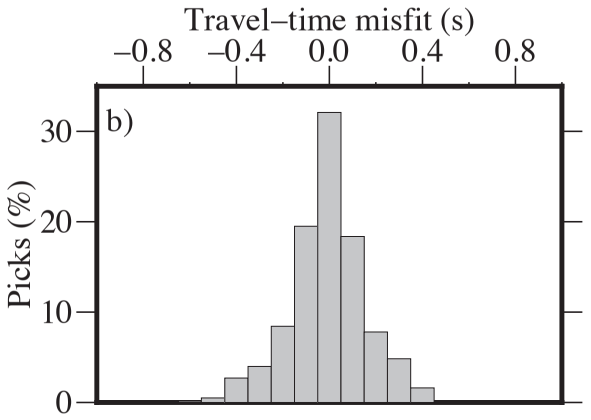


Figure 3.22: a and b) Grid search result for variations in upper crustal V_p structure and depth to the MCR reflection interface. The depth to the refraction interface above the MCR is also varied while the width of this zone kept constant. c and d) Grid search result for variations in lower crustal V_p structure and depth the Moho reflection interface. (a, c) RMS values and (b, d) normalised χ^2 values. White star indicates the values closest to the final model.





d)

Phase Data

Phase	N*	Av. U.	RMS	χ^2
Pg	5500	0.100	0.081	0.661
Pi	1638	0.100	0.097	0.899
PcP	10956	0.150	0.152	1.031
PmP	6240	0.200	0.199	0.918

N*=Number of picks.
Av. U.=Average pick uncertainty.

Figure 3.23: a) Travel-time residuals for all modelled rays plotted against true receiver locations. b) Same data as in (a) but plotted as a percentage histogram, binned in 50 ms intervals. c) Ray hit count computed using 200 × 200 m grid cells. Dashed black lines are model layers and inverted red triangles are box wave receiver locations 2–6. d) Model statistics for each picked phase group.

Figure 3.23a shows most travel-time residuals are within ± 200 ms and no large outliers exist. There is also no strong correlation between high residuals and a particular region of the model. Furthermore, Figure 3.23b shows there is no strong bias towards positive or negative residuals. Individual phase statistics are listed in Figure 3.23d.

A limitation of the model is the inability to trace arrivals to observations of the nearest offset P_i head waves observed on the Box-2 gather (Figure 3.16). These arrivals can be well fit if they are modelled as a reflection phase from an interface located ~ 2 km above the P_i interface and dipping steeply to the east, however, given no structure of this nature is imaged on the seismic reflection profile (Fig. 3.9), a head wave interpretation is preferred.

Although the box wave survey consists of a relatively small data volume, the narrow station spacing of ~ 6 km produces ray sampling overlap, providing data redundancy for the estimates of interface depths (Fig. 3.23). The model is best sampled between model coordinate 640–690 km where P_g, P_cP, P_i and P_mP rays from multiple gathers sample the upper most, middle crust and lower crust respectively. The MCR is also well sampled by wide-angle reflections between model coordinates 700–725 km.

3.5.4 Model assessment

3.5.5 V_p perturbation tests

Perturbation tests were used to estimate V_p uncertainty in the box wave model (Figure 3.24) by creating a series of models within which V_p nodes were perturbed by specified values relative to the final model. Perturbation values up to ± 0.25 $km\ s^{-1}$ at 0.025 $km\ s^{-1}$ increments were tested. Two types of tests were performed. For test type-1, a constant perturbation was applied to all V_p nodes. For test type-2, perturbations were limited to every second node. A normalised χ^2 cut-off of 1.5 was chosen as the limit for an acceptable fit as at this value, misfits are 50 % greater than pick uncertainties. Perturbation test results for the upper and lower crustal layers of our final model are shown in Figures 3.24 and 3.25 respectively. Figure 3.24 shows that for the upper crust, there is a monotonic increase in travel-time misfit for perturbations greater than 0.05 $km\ s^{-1}$ in both the constant (type-1) and alternating (type-

2) tests. Normalised χ^2 misfits become greater than 1.5 for V_p perturbations greater than $\pm$ 0.1 $km\ s^{-1}$ in both tests, suggesting a $\pm$ 0.1 $km\ s^{-1}$ uncertainty in V_p for the upper crust. Furthermore, for V_p accuracy of $\pm$ 0.1 $km\ s^{-1}$, the results of test type-2 suggest the lateral spatial resolution is equal to or potentially greater than the lateral node spacing of 25 km, which, given our small data volume, is adequate for our estimates of the bulk V_p structure. For the lower crust, Figure 3.25 shows that V_p is poorly constrained. For test type-1 the increase in misfit is monotonic with increasing perturbation size, and normalised χ^2 becomes greater than 1.5 for values greater than $\pm$ 0.2 km (Fig. 3.25a and b). However, for test type-2 (Fig. 3.25c and d) it can be seen that there is only a small ($\sim$ 25 ms) increase in RMS misfit for perturbations as great as $\pm$ 0.25 $km\ s^{-1}$. The alternating V_p "strips" imposed by only perturbing every second node in test type-2 are geologically unreasonable, but the fact that they result in only a small increase in misfits suggests poor lateral spatial resolution in V_p for the lower crust.

3.5.6 Inversion recovery tests

To further investigate crustal V_p uncertainty, inversion recovery tests were run for the upper and lower crustal layers. These tests were performed by perturbing the layer of interest with alternating V_p perturbations of $\pm$ 0.4 $km\ s^{-1}$ with a lateral spacing of 25 km. Damped-least-squares inversions were then run until the updated V_p model failed a statistical f-test for significance difference at the 5 % level. Between each inversion, the V_p nodes were smoothed with a three point median filter to force the updated values towards the original unperturbed values. V_p values within the ray coverage mask, that are not recovered to within $\pm$ 0.1 $km\ s^{-1}$ at the conclusion of the inversion remain coloured in the final recovered models and highlight areas where V_p is poorly constrained.

Figure 3.26 shows the recovery test for the upper crustal layer. Figure 3.26b shows all the upper V_p nodes are recovered to within $\pm$ 0.1 $km\ s^{-1}$. However, V_p nodes at the base of this layer are poorly constrained between model coordinates 620-660 km with the V_p node at model coordinate 625 km, exhibiting an error of $> 0.2\ km\ s^{-1}$. The V_p node at model coordinate 750 km is also not fully recovered, exhibiting an error of $> 0.1\ km\ s^{-1}$, however, this region falls

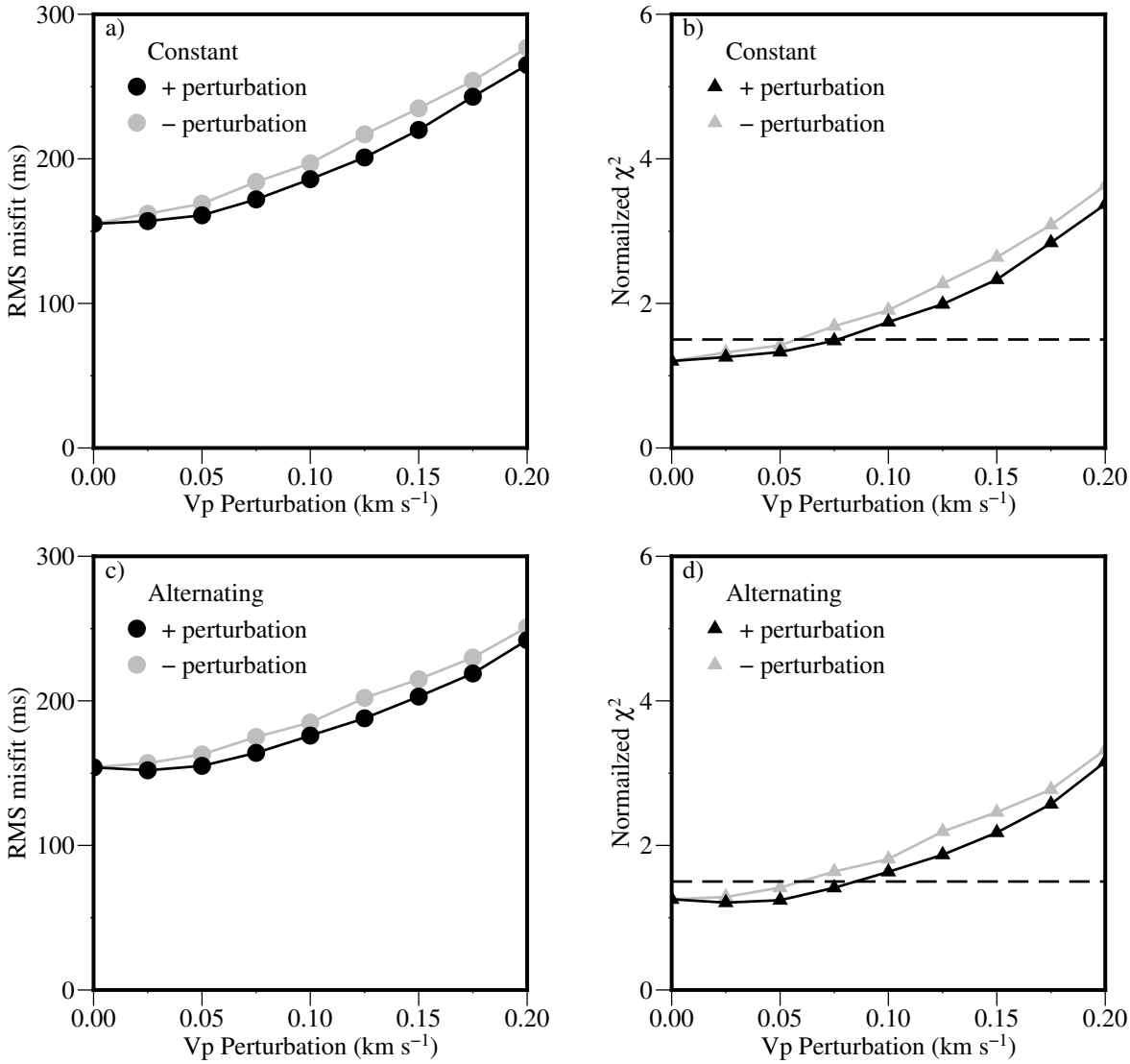


Figure 3.24: V_p perturbation test results for the upper crust. a) and b) RMS and normalised χ^2 values for test type-1 (constant perturbation values to all nodes). c) and d) RMS and normalised χ^2 values for test type-2 (perturbations applied to only every second node).

outside of the ray coverage. Overall, the bulk velocity structure is well recovered suggesting our derived velocities and estimated error of $\pm$ 0.1 $km\ s^{-1}$ are robust for this layer. Figure 3.27 shows the recovery test for the lower crustal layer. Similarly to the upper crustal layer, most of the V_p field is recovered to within $\pm$ 0.1 $km\ s^{-1}$. Given the perturbation results shown in Figure 3.25b, which shows the lateral spatial resolution for this layer is poor, this test corroborates the results of Figure 3.25a and suggests that for a horizontally uniform (geologically reasonable) velocity field, then V_p uncertainty for the lower layer is $\sim \pm$ 0.2 $km\ s^{-1}$. However, as discussed below, this uncertainty only holds true if the selected Moho

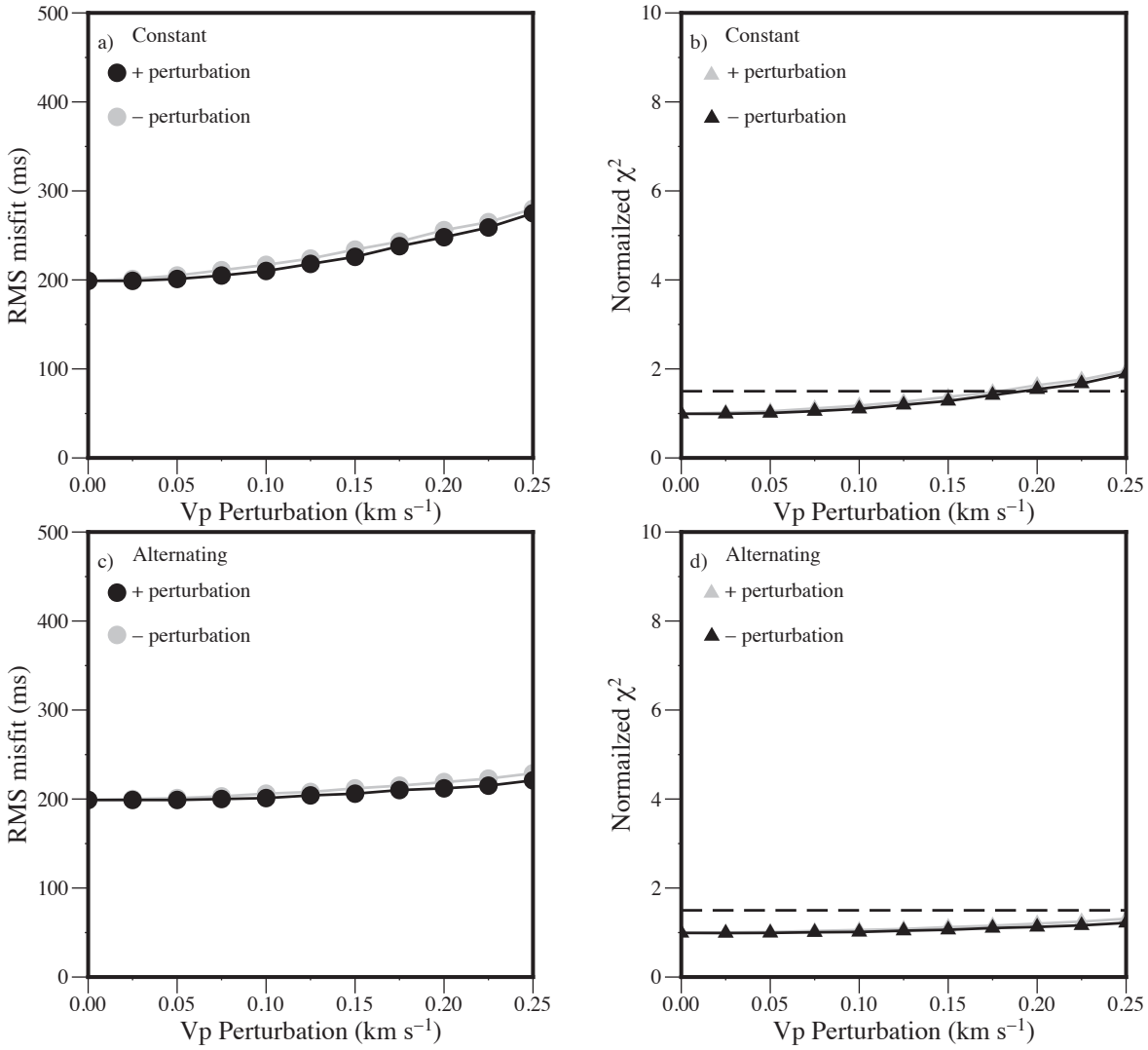


Figure 3.25: V_p perturbation test results for the lower crust. a) and b) RMS and normalised χ^2 values for test type-1 (constant perturbation values to all nodes). c) and d) RMS and normalised χ^2 values for test type-2 (perturbations applied to only every second node).

interface depth is accurate.

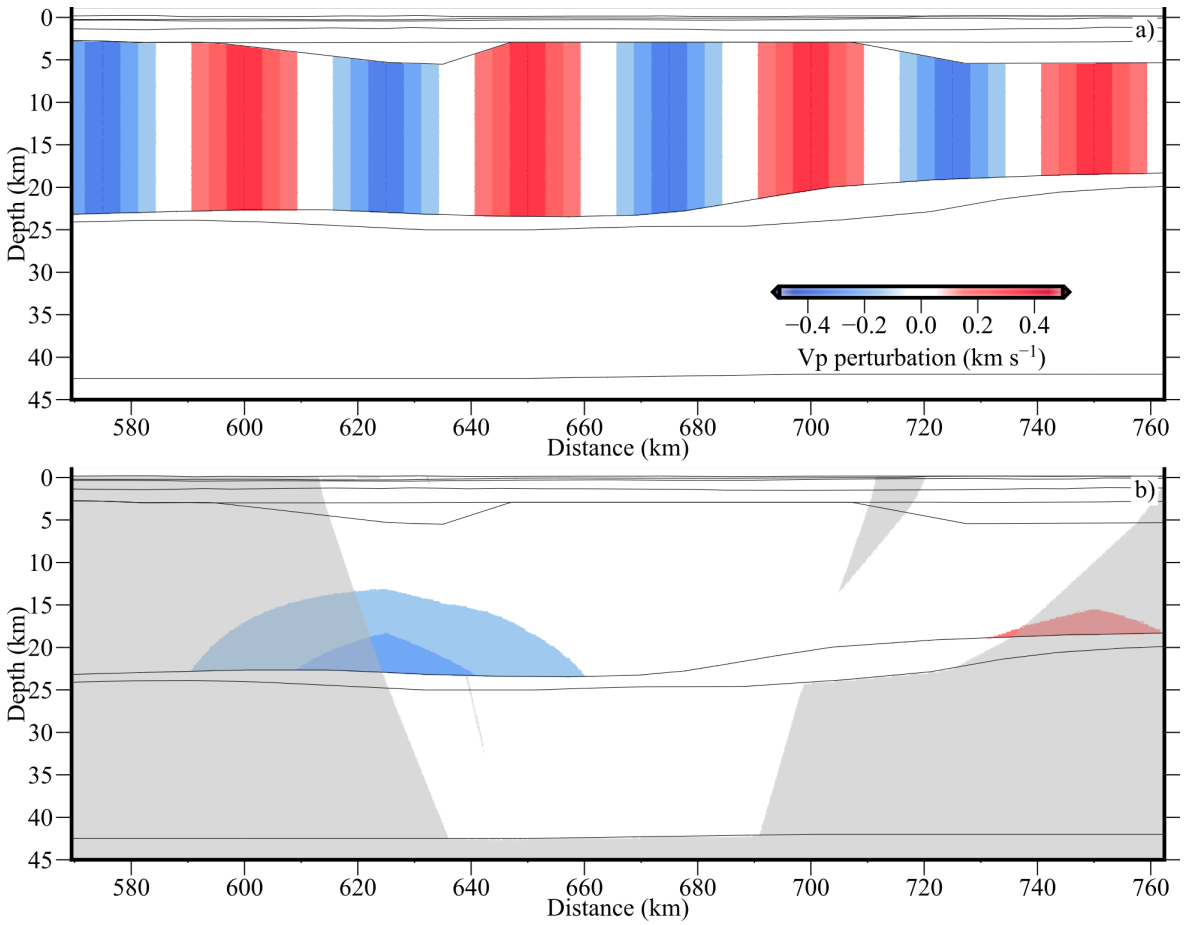


Figure 3.26: V_p inversion recovery test for the upper crustal layer. a) Starting perturbed model (V_p values are relative to the final forward model e.g., Figure 3.16d). b) Recovered V_p field after running damped-least-squares inversions (with intermediate median smoothing) until f-test failure at the 5% level.

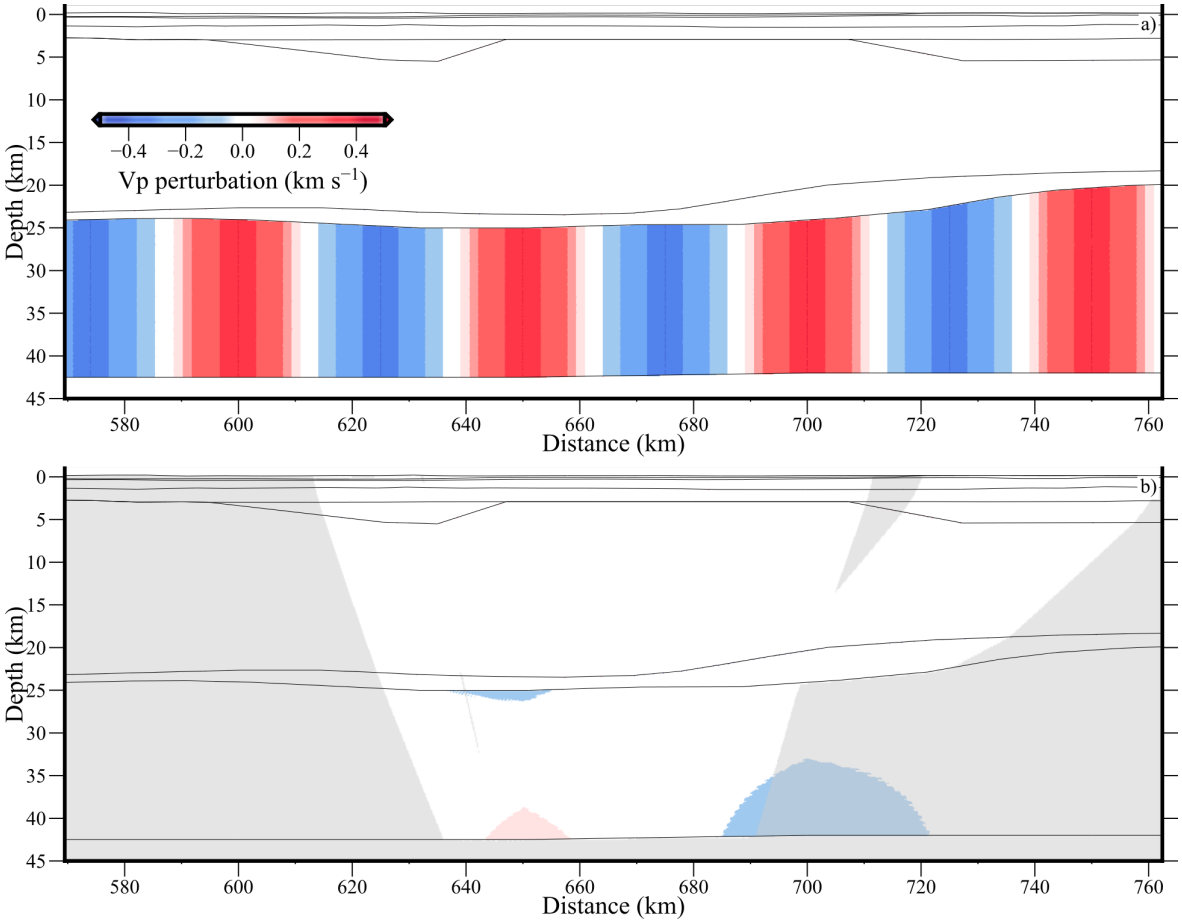


Figure 3.27: V_p inversion recovery test for the lower crustal layer. a) Starting perturbed model (V_p values are relative to the final forward model e.g., Figure 3.16d). b) Recovered V_p field after running damped-least-squares inversions (with intermediate median smoothing) until f-test failure at the 5% level.

3.5.7 Monte Carlo simulation

Following the perturbation tests carried out in sections 3.5.5 and 3.5.6, to assign final uncertainties to model parameters a bounded Monte Carlo approach was used to generate 60,000 random models using the method of Loureiro et al. (2016). This method explores a greater parameter space than those used in sections 3.5.5 and 3.5.6 and therefore provides more robust uncertainty estimates. For this simulation, the sedimentary basin layers (constrained by the regional reflection profile) and V_p nodes at the top of the upper crust (constrained by P_g refractions) were held fixed. The remaining model parameters (i.e., upper and lower crustal V_p and layer boundary nodes) where allowed to vary within specified bounds. Velocity nodes were allowed to vary by $\pm$ 0.30 $km\ s^{-1}$ and depth nodes by $\pm$ 3.0 km with respect to the values of the final forward model. These values were chosen, as it was found that simulations with larger limits failed to find models capable of adequately fitting the data. From the generated models, those which were capable of tracing $\geq$ 95 % of rays and with an overall RMS misfit leq 115 % of the final forward model value (0.179) were used to assign uncertainties. Figure 3.28 shows the maximum acceptable positive and negative V_p deviations from the final model and indicate bulk V_p values are constrained to within $\pm$ 0.25 $km\ s{-}1$ or less. Layer interfaces are associated with large V_p uncertainties. However, these are artefacts due to large V_p discrepancies that arise when comparing models that place different layers (with large V_p differences) at the same depths (Loureiro et al., 2016). Dashed yellow lines show the best fit layer interfaces. The P_i and MCR interfaces have large uncertainties due to the velocity-depth trade-off. The Moho interface is constrained to a depth between 41–44 km.

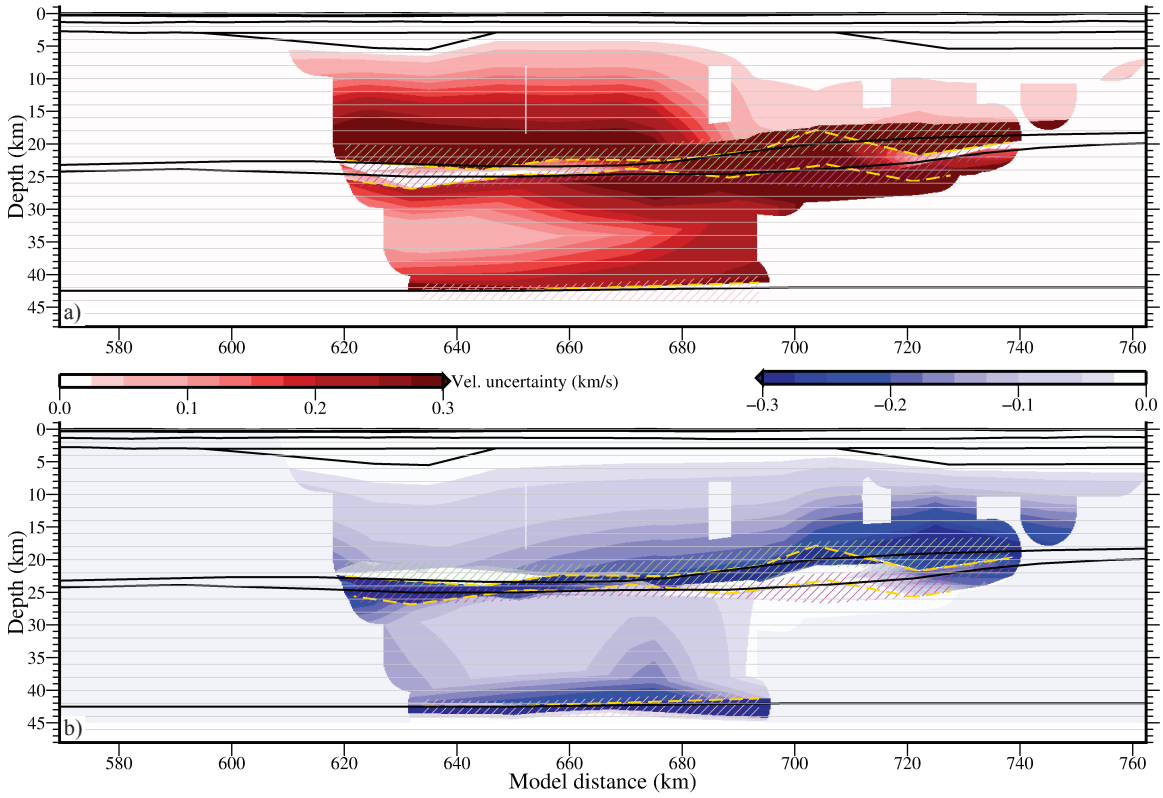


Figure 3.28: a) and b) Maximum allowable V_p variations from the final model values derived from Monte Carlo uncertainty analysis. Black lines are layer interfaces from the final forward model. Dashed yellow lines are interface depths that provide the best fit within Monte Carlo limits. Coloured dashes show maximum depth variation for each model interface.

3.6 Low-fold wide-angle reflection stack

3.6.1 Survey Geometry

Figure 3.29 shows the survey geometry used for constructing a low-fold reflection stack from the box wave receiver gathers. Note that the maximum offsets incorporated in the gathers was limited to $\pm$ 50 km (green VPs) in order to avoid stacking post-critical reflections. Rectangular CDP bins with large widths (4 km) were used. In the presence of cross-dip, this will result in *smearing* of reflections (Ravens, 1999), however, it was important to incorporate as many traces as possible given the low fold, hence the large geometry variation was deemed necessary. The fold coverage shown in figure 3.29 shows the variable fold produced by the unconventional geometry, reaching a maximum value of 8 in the centre of the profile.

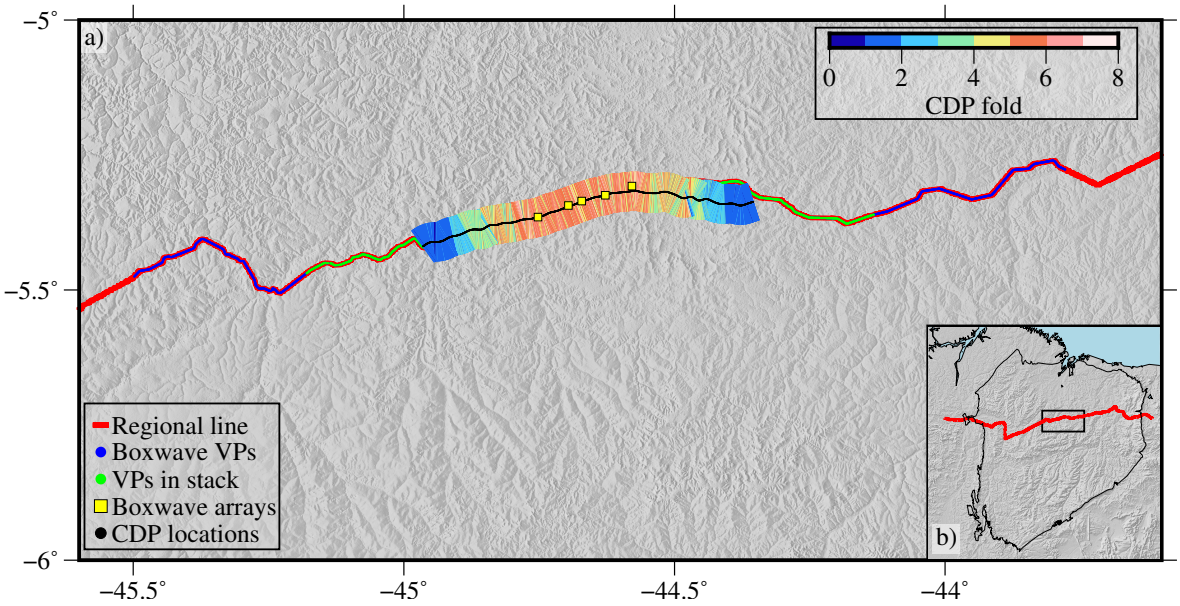


Figure 3.29: a) PBASS survey geometry. Yellow squares are box array receiver locations. Green line shows the vibration points (VPs) used in construction of stacked section. Blue line shows the VPs recorded during the PBASS survey. Red line is the regional seismic reflection profile. b) location of (a) with respect to the outline of Parnaíba basin.

3.6.2 Pre-stack processing

Pre-stacking processing focused on enhancing the coherency and strength of deep reflection events evident between $\sim$ 8–15 s $TWTT$. Standard reflection processing techniques were tested and applied. However, given that this processing scheme was focused on imaging deep, lower crustal events, values used for some filters were unconventional with respect to those used in typical shallow structure imaging. Each filter was created using test panels to assess the effects of the various filter parameters, and examples of these are presented in Appendix B. Figures in the following sections provide comparisons of the Box-2 gather, pre and post the application of the chosen filters.

3.6.2.1 Data resampling and anti-aliasing filter

The box wave data were acquired using a frequency sweep from 4–32 Hz and were recorded at a sampling rate of 4 ms. Given the maximum signal frequency of 32 Hz, the data were resampled to 8 ms with a new Nyquist frequency of 62.5 Hz. An anti-alias filter was applied prior to resampling to remove frequencies above the new Nyquist frequency.

3.6.2.2 Trace quality-control and spacing

All of the traces from the five gathers were inspected manually, and obviously noisy traces were removed. Root-mean-squared full trace amplitude plots were also used to identify any additional noisy traces. Furthermore, because of the crooked line geometry, trace spacing is not consistent. As some processing sequences, such as f—k filtering, require a constant trace spacing, redundant traces were removed in order to approximate, as best as possible, a trace spacing of 50 m.

3.6.2.3 Spherical divergence amplitude recovery

The amplitude of a given seismic wave is attenuated during propagation due to several factors. Notably these include: (1) geometrical expansion of the wavefront, which effectively spreads the input source energy over an increasingly larger surface area; (2) partitioning of the wavefront into transmitted and reflected primaries and mode conversions at acoustic impedance boundaries; (3) scattering of energy by inhomogeneities and (4) absorption via heat conversion due to anelastic rock deformation (Hatton and Worthington, 1986). In reflection seismology, recovery of wave amplitudes is routinely attempted via two methods. Firstly, a spherical divergence correction is applied by multiplying each trace by a series of scalars designed to compensate for the attenuation effects. This process is implemented using equation 3.2:

$$G(t) = V(t)^{Vpower} t^{Tpower} e^{V(t)t\alpha} X^{Xpower} \tag{3.2}$$

Where $V(t)$ is wave velocity as a function of travel-time and V_{power}, T_{power} and X_{power} are the power values for the average velocity at t, the two-way time and offset, X, respectively.

Secondly a linear gain function (in decibels) is applied. Amplitude recovery was applied to the box wave gathers during gather preparation by BP Houston as can be observed in figure 3.31, which shows the well balanced amplitude decay curve for western side of the Box-2 receiver gather.

3.6.2.4 Static corrections

On an idealised seismic gather, the observed move-out of reflection events is solely a function of the subsurface velocity structure and interface geometries. However, onshore seismic surveys require corrections that compensate for variations in elevation and the thickness/velocity of the very near surface weathering layer, known as static corrections. Static corrections are applied to each trace in order to correct travel-times for the variation in receiver elevations (*elevation static*) and the thickness and V_p of the sub-weathering layer (*weathering static*). Elevation corrections were applied by shifting each trace to a fixed reference datum using each receivers elevation and a constant replacement velocity of 2.5 $km\ s^{-1}$. Given the large trace spacing (50 m) and limited near offset first arrival ray coverage provided by this dataset, a weathering layer velocity model could not be constrained, and hence these statics were neglected.

3.6.2.5 Surgical refraction mute

First arrival refractions and surface wave noise, which did not overlap with desired reflection events, were removed by manually picking a surgical mute, which was applied using a cosine taper to avoid edge effects (Fig. 3.30).

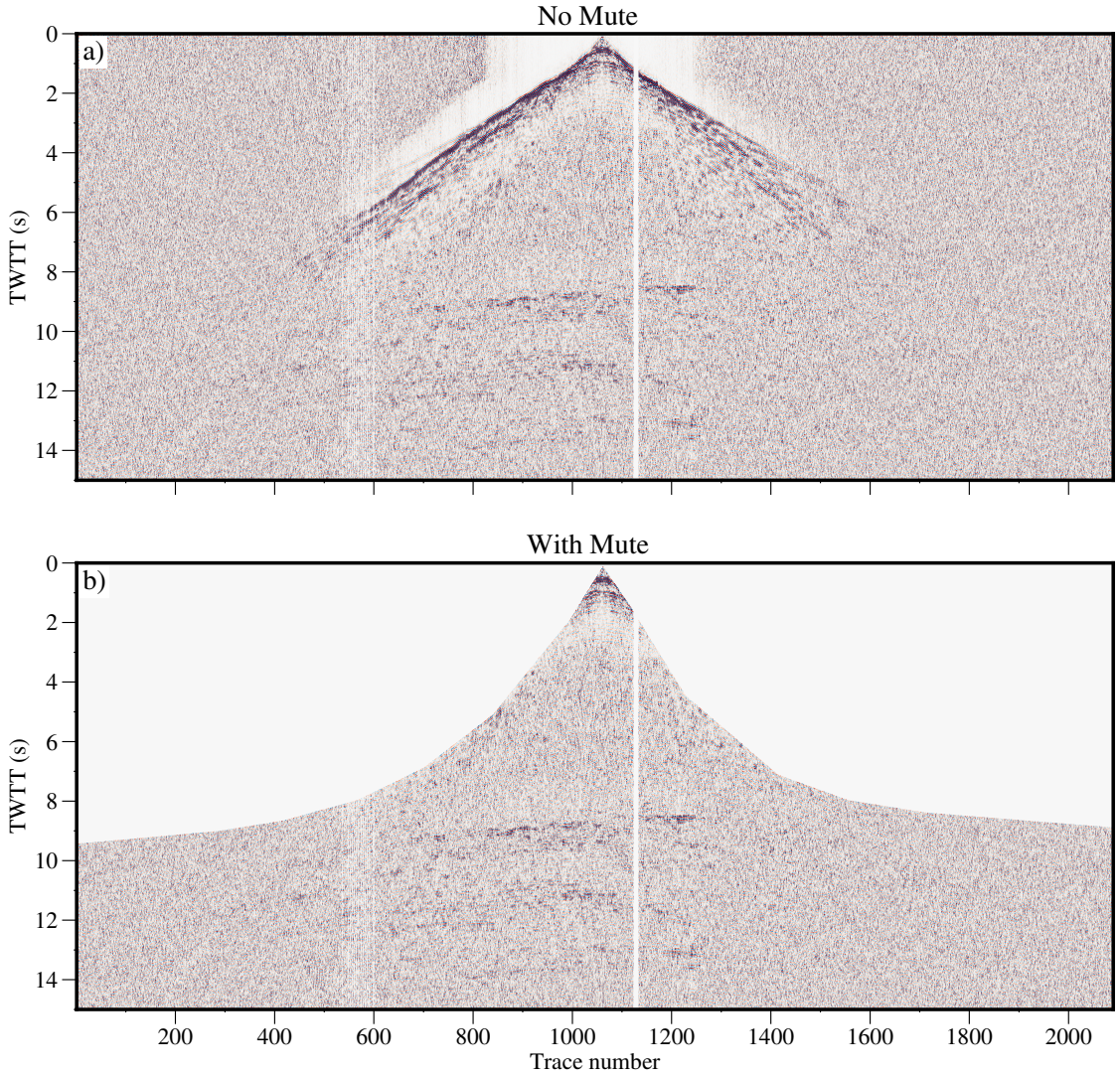


Figure 3.30: Example of surgical refraction mute applied to Box-2. a) Box-2 gather pre-mute application. b) Box-2 gather post-mute application.

3.6.2.6 FX Deconvolution

FX-deconvolution is a filtering method designed to suppress random noise. The process is implemented in the F-X (spatial-frequency) domain and operates by taking advantage of the predicable nature of the frequency content of reflection arrivals on adjacent traces in the X-direction (Harrison, 1990). Within a given time and trace window, a prediction operator is designed for each frequency using complex Weiner deconvolution as described by Treitel (1974). The predicted frequency content on adjacent traces can then be compared to the input and the difference between the predicted and observed data classified as noise and discarded

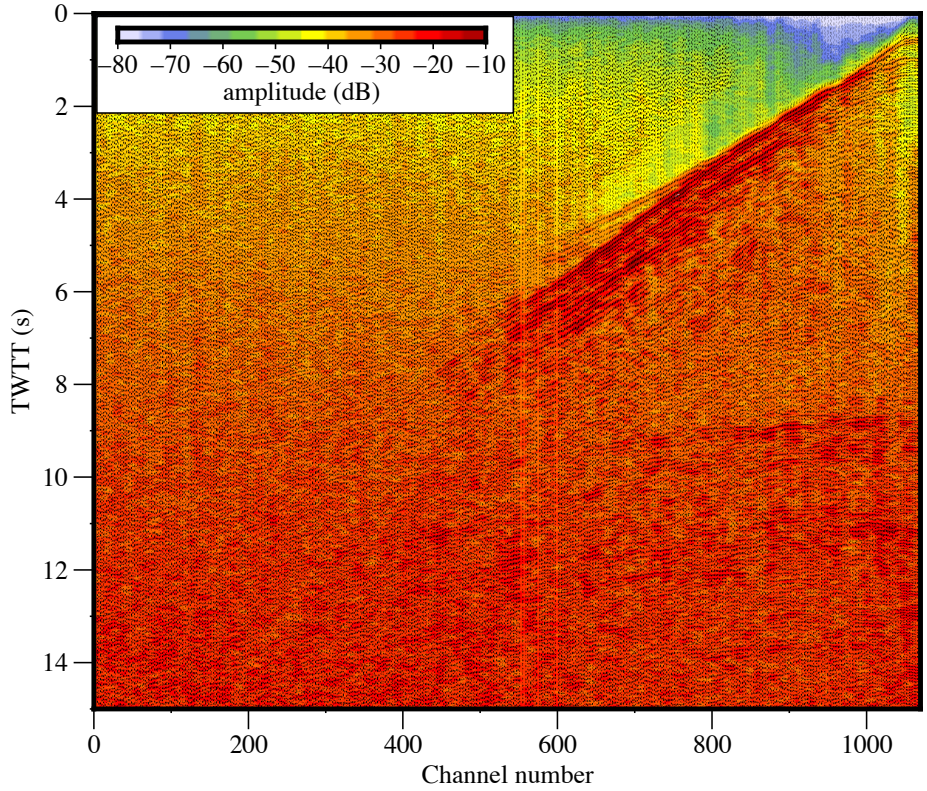


Figure 3.31: Amplitude decay plot for the western side of the Box-2 receiver gather. Note the amplitudes are well balanced both in time and increasing offset.

(Ravens, 1999). Because the FX-deconvolution process can only work on a single dip at any one time, the gather is divided into small time-distance panels to approximate linear dips. Furthermore, the process is run in the forward and reversed x-direction and the final output is given as the average of the two results. This prevents an apparent half-trace width shifting of the input gather (Ravens, 1999). Figure 3.32 shows the result of applying the chosen FX-deconvolution filter on Box-2.

3.6.2.7 *f*—*k* filter

The areal receiver array used to record these gathers was designed as a spatial wavenumber filter to prevent the recording of undesired events during acquisition (see section 3.3.4). However, in practice, the ability of arrays to achieve the theoretical level of noise suppression is limited by natural variables such as imperfect geophone spacing and elevation changes across the array, so some coherent noise events are inevitability recorded. Hence, f—k filters were

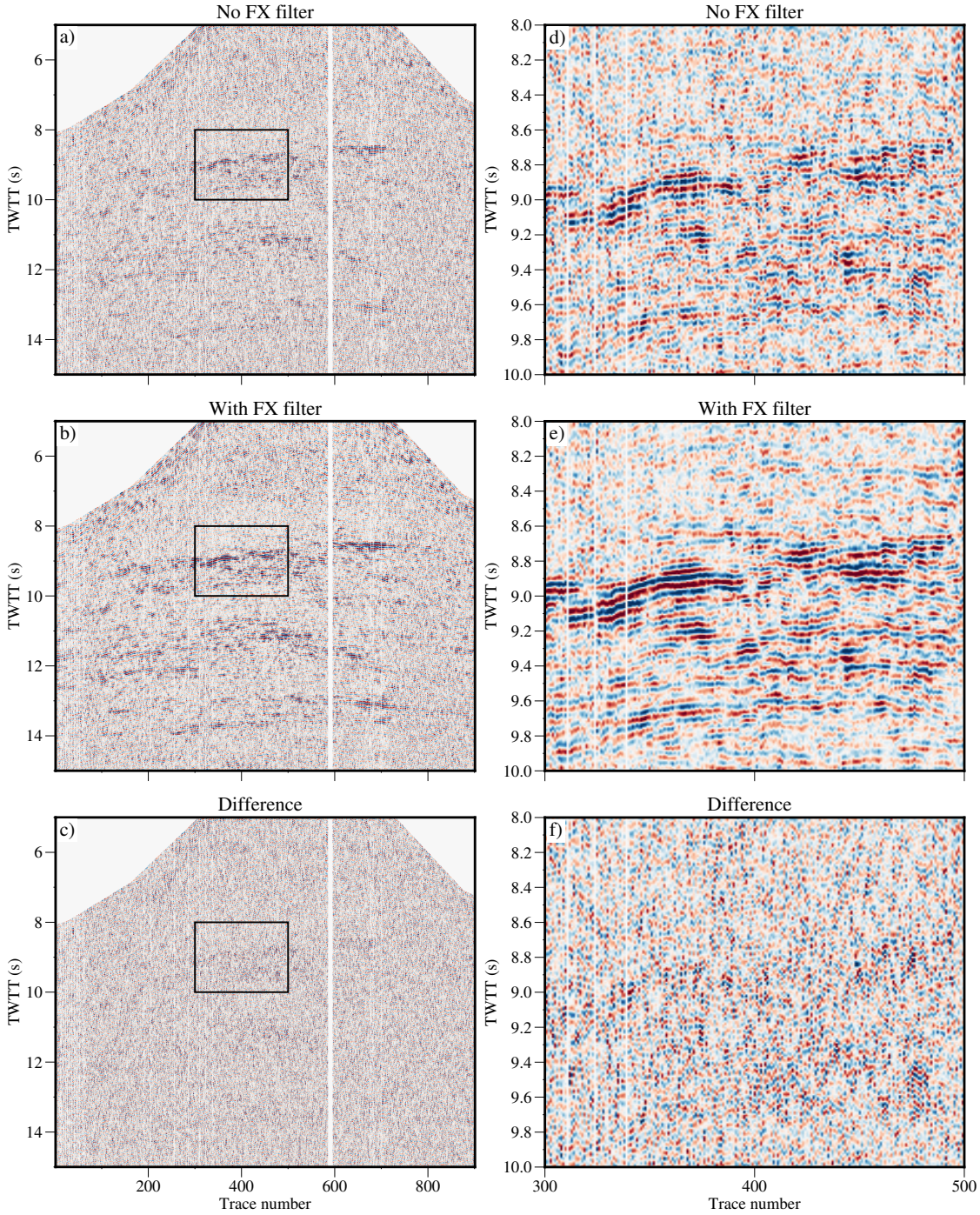


Figure 3.32: Pre and post and difference comparison plots for the application of an FX-deconvolution filter on a selection of the Box-2 receiver gather between 5–15 s $TWTT$ (a, b, c) and an enlarged section of the strong events at $\sim$ 9.0 s as shown by the black box (d, e, f). a) Prior to filter application. b) Post filter application. c) Difference between (a) and (b). d) Prior to filter application. e) Post filter application. f) Difference between (d) and (e). Note the improvement in reflection coherency in (b) and (e) and the randomness of (c) and (e) indicating coherent signal has not been removed.

designed to further remove linear noise events.

f—k filters operate by transforming the records from the time-distance to frequency-wave number (f—k) domain, within which linear events can be isolated and filtered. Across a gather each given sinusoid of a particular wave will have an apparent wave-number k_a and frequency f, which are related to its apparent velocity, v_a:

$$v_a = \frac{f}{k_a} \tag{3.3}$$

Plotting f against k_a produces a straight line with a slope equal to v_a (Kearey et al., 2013). Linear noise and ground-roll usually display lower apparent velocities than reflection events, and can therefore be filtered in the f—k domain while preserving the more steeply dipping reflection events. Because of the potential of overlap between signal and noise, the f—k filters were designed interactively to determine which dip cut-off was best suited for enhancing the lower crustal reflections of interest. Figure 3.33 shows a comparison between the Box2 gather before and after the application of the chosen f—k filter. The f—k filters were wrapped with trace interpolation from a 50 m trace spacing to a 12.5 m to avoid spatial aliasing in the f—k domain.

3.6.2.8 Semblance coherency filter

Identification of deep reflections is often inhibited by a low signal-to-noise ratio and poor vertical resolution (sharpness) due to attenuation and absorption of high frequencies during wave propagation. Local coherency is therefore often the primary characteristic for identifying such reflections. As such, spatial coherency filters are useful for accentuating these reflections and suppressing surrounding noise. The sembsmooth filter, first described by Milkereit and Spencer (1989), is one coherency filter that is useful in such circumstances.

As outlined by Ravens (1999), this filter operates by using a sliding window to select narrow sub-sections of traces. The window is centred on each sample, and then the semblance along a range of linear dip angles is calculated, with the maximum semblance value retained.

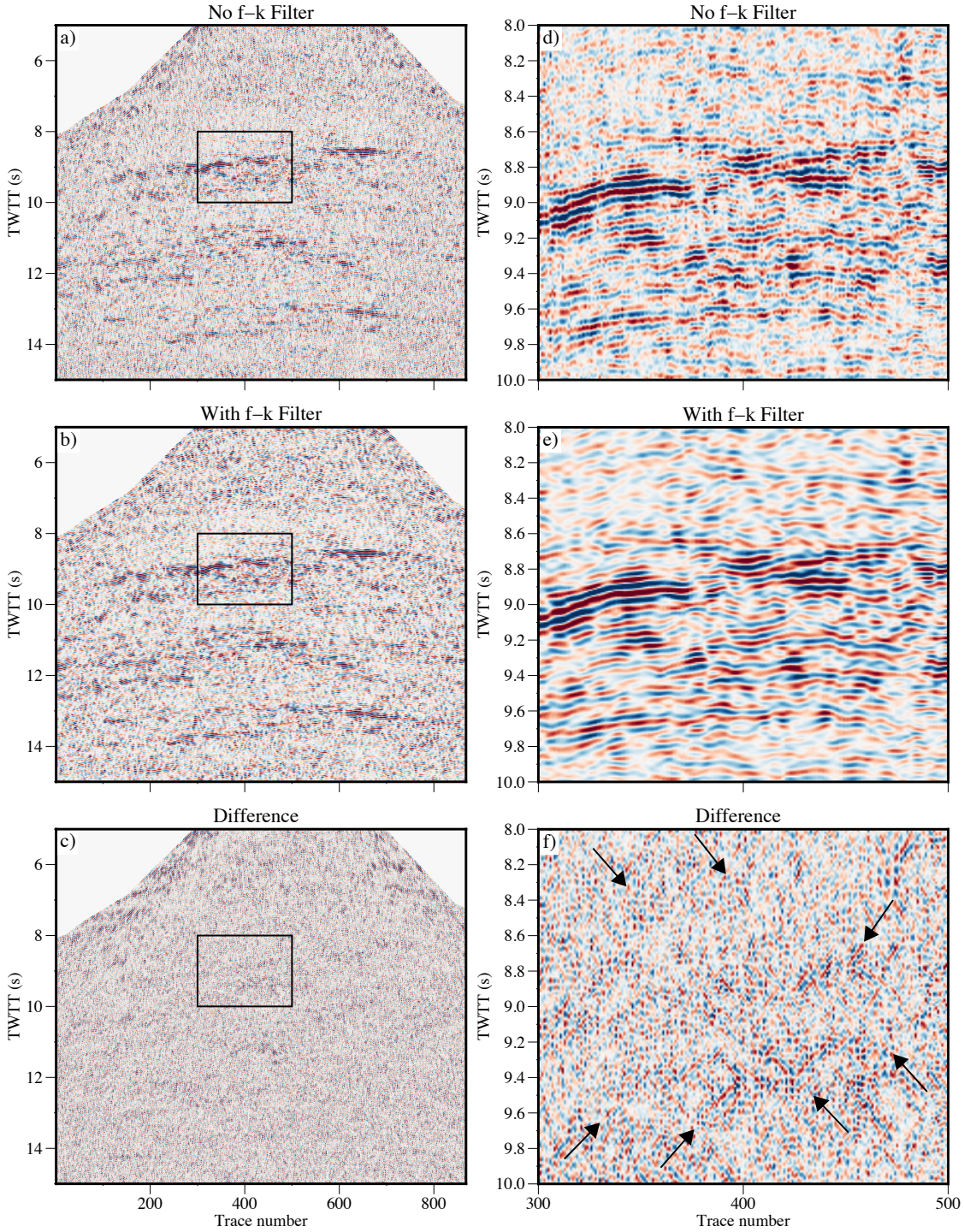


Figure 3.33: Pre and post and difference comparison plots for the application of an F–k filter on a selection of the Box-2 receiver gather between 5–15 s $TWTT$ (a, b, c) and an enlarged section of the strong events at ~ 9.0 s as shown by the black box (d, e, f). a) Prior to filter application. b) Post filter application. c) Difference between (a) and (b). d) Prior to filter application. e) Post filter application. f) Difference between (d) and (e). Note the improvement in reflection coherency in (b) and (e) and the steeply dipping coherent noise on (c) and (e) representing coherent noise trains that have been removed.

A coherency for each sample is determined by raising the semblance to a chosen exponent, which controls the extent to which incoherent noise (as well as the less coherent events) are suppressed. Finally, the data are filtered by replacing the input sample with the average value in the direction of maximum semblance multiplied by the coherency value for each sample. A percentage of the original trace may also be retained and used to control the degree to which the output is filtered. Figure 3.34 shows the result of applying the chosen semblance filter on Box-2. As can be seen when comparing Figures 3.34a and 3.34b, and Figures 3.34d and 3.34e, the semblance coherency filter accentuates the coherent reflection events and extends the offset range over which events can be traced. Of particular note is the illumination of deep events at ~ 14 s $TWTT$ on Figure 3.34b.

3.6.2.9 Predictive Deconvolution

Strong "ringing" events produced by reverberations are apparent throughout the box wave gathers (Fig. 3.35a). Hence, predictive deconvolution was applied to attenuate these events.

Following a convolution model, a recorded seismogram $\gamma(t)$, can be considered as the convolution of the Earth's impulse response $E(t)$ with the seismic wavelet, which consists of the input source signature $g(t)$, as well as other factors such as the receiver response $R(t)$, recording instrument response $I(t)$ and random ambient noise $n(t)$ as shown in equation 3.4:

$$\gamma(t) = g(t) * E(t)R(t) * I(t) + n(t) \tag{3.4}$$

Where $*$ denotes convolution.

The general purpose of deconvolution is to recover, as best as possible, Earth's reflectivity function, that is, Earth's impulse response $E(t)$ with other adverse effects, such as reverberations and multiples removed (Yilmaz, 2001). This is usually achieved by designing a Weiner filter, which when convolved with input seismogram, shapes the seismogram to the desired output in a least-squares sense. In the case of predictive deconvolution, the desired output is the input trace shaped such that its autocorrelation between the *predictive gap* and *operator length* is zeroed (e.g., Peacock and Treitel, 1969). Hence, reverberations within the *operator*

length are removed. The *predictive gap* refers to position into the future where the trace amplitude becomes predictable (also called the prediction distance, minimum autocorrelation lag or lag). Shortening these values will also result in wavelet compression and an increase in resolution. The *operator length* refers to the length over which the filter is applied (also called the operator lag).

One of the assumptions made when applying deconvolution is that the seismic wavelet of the input trace is minimum-phase (Yilmaz, 2001). In theory, a correlated vibroseis trace is created by cross correlation of a pilot (source) sweep with the recorded sweep, thereby collapsing the recorded sweep into a zero-phase Klauder wavelet (e.g., Baradello and Accaino, 2013). Therefore, this assumption will not be satisfied as the trace is zero- rather than minimum-phase. It has been shown by Dong et al. (2004), however, that real vibroseis records are often close to minimum phase. This is not well understood but is likely due to the minimum-phase earth filter having a large effect in shaping the Vibroseis wavelet. In a practical sense, this means the application of predictive deconvolution to Vibroseis data often provides adequate results (e.g., Yilmaz, 2001; Dong et al., 2004; Baradello and Accaino, 2013).

The predictive gap and operator length applied to the box wave gathers were determined by inspection of the autocorrelation functions and using panel tests. The predictive gap was tested first with a constant operator length of 300 ms. Values of 56–96 ms were tested at increments of 8 ms. Next, the predictive gap was held constant at 80 ms and the operator length was varied between 100–300 ms at 50 ms increments. The best result is achieved, using a gap of 68 ms and operator length of 300 ms. A [2-4-32-37] Hz bandpass frequency filter was applied post deconvolution, to attenuate high- and low-frequency noise that also benefits from the deconvolution process (e.g., Yilmaz, 2001). Figure 3.35 shows the result of applying the chosen deconvolution operator on Box-2.

3.6.3 Velocity analysis

Prior to producing a stacked section, velocity analysis was undertaken to produce a stacking velocity model. Standard semblance analysis was prohibited by the low fold (due to a lack of sufficient traces within each CDP gather) and poor performance of semblance at large travel

times, where the move-out of reflection events is relatively small over the offset range recorded. Thus, *Constant Velocity Stacks* (CVS) and *Constant Velocity Gathers* (CVG) were used to create a stacking velocity model. These techniques create a series of repeat windows where a range of constant velocities are used to apply a normal-move-out correction on a subset of CDPs and section of the stack respectively. For example, figure 3.36 shows a suite of CVS focused on a region where the prominent mid-crustal reflection occurs. Constant velocities between 5.6–6.7 $km\ s^{-1}$ at increments of 0.1 $km\ s^{-1}$ are plotted. Stacking velocities were then assigned based on visual inspection as to the value that produces the best phase alignment on the CVG and most coherent reflection event within the CVS. In the example shown in figure 3.36, a value of 6.2 $km\ s^{-1}$was chosen.

3.6.4 CDP sort and Stack

Receiver gathers were sorted to central-depth-point (CDP) gathers and stacked using a conventional trace normalised method (Eq. 3.5). This ensures amplitude variations due to spatial variations in fold are minimised. The square-root of N is used in the normalisation term, as experience shows this is more effective when the input data is noisy and when the upper section of some input traces have been muted earlier in the processing scheme (Hatton and Worthington, 1986).

$$A(t) = \frac{1}{\sqrt{N}} \sum_{i=1}^{N} a_i(t) \tag{3.5}$$

3.6.5 Post-stack processing

After stacking, the base of the sedimentary section, a prominent mid-crustal reflection and bands of events in the lower crust, to depths of $\sim$ 13.5 $s\ TWTT$, are identifiable. However, some obvious coherent noise was evident. Hence, post-stack processing was applied to attenuate this noise and further enhance prominent reflections.

3.6.5.1 Post-stack *f*—*k* filter

A post-stack f—k filter (e.g., Section 3.6.2.7) was applied to attenuate steeply dipping coherent noise that was not removed by the pre-stack processing. In particular, surface wave arrivals that were not removed by the pre-stack surgical mute. The filter design was implemented with a simple linear dip of 10 ms/trace and a k-axis protection of $\pm$ 0.1 to protect near horizontal events.

3.6.5.2 Post-stack FX deconvolution

A random noise FX-deconvolution filter (e.g., Section 3.6.2.6) was also applied post-stack. This is common practice in conventional seismic processing schemes and resulted in a slight improvement to the stacked image in this case.

3.6.5.3 Trace running mix

A trace mixing algorithm, *RunMix* (Ravens, 1999) was applied as an additional coherency filter. This filter replaces each input trace with a weighted stack of a specified number of adjacent traces, centred on the input trace. In this case, five traces with weightings [0.05 0.2 0.5 0.2 0.05] were used. In regions were coherent reflections are present, this aids the conventional stacking process by further enhancing the reflection events, while attenuating random noise.

3.6.5.4 Frequency filter

Finally, a bandpass [2-4-20-25] Hz frequency filter was applied to limit the frequency band and better illuminate the low frequency, deep reflections of interest.

3.6.6 Final stack

As described in section 3.2.2.1, it is advantageous to display low fold reflection images as instantaneous amplitude plots, because identifying reflection events takes priority over vertical resolution and preservation of the wavelet (e.g., Oncken et al., 2003; Henrys et al., 2013). Hence, the final stack was converted to instantaneous amplitude and is shown in figure 3.37a. Reflections are best resolved directly beneath Boxes 2–6, where the CDP fold is largest and where, on the raw gathers, deep reflections are also more easily identified (e.g., Figs. 3.16–3.20). The MCR is identifiable at $\sim$ 8.5 s $TWTT$ and closely correlates with the MCR interface from the wide-angle V_p model when converted to TWTT (dashed lines in Figure 3.37b). It can be seen the MCR exhibits a relatively high amplitude, as would be expected from the large impedance contrast implied by our V_p model (e.g., Fig. 3.16). Several high amplitude events are visible beneath the MCR down to a depth of $\sim$ 13.5 s $TWTT$. The base of this reflectivity is interpreted as the reflection Moho (e.g., Cook, 2002). Again, this correlates well with the Moho depth derived by forward V_p modelling in section 3.5 when converted to TWTT (Fig. 3.37b).

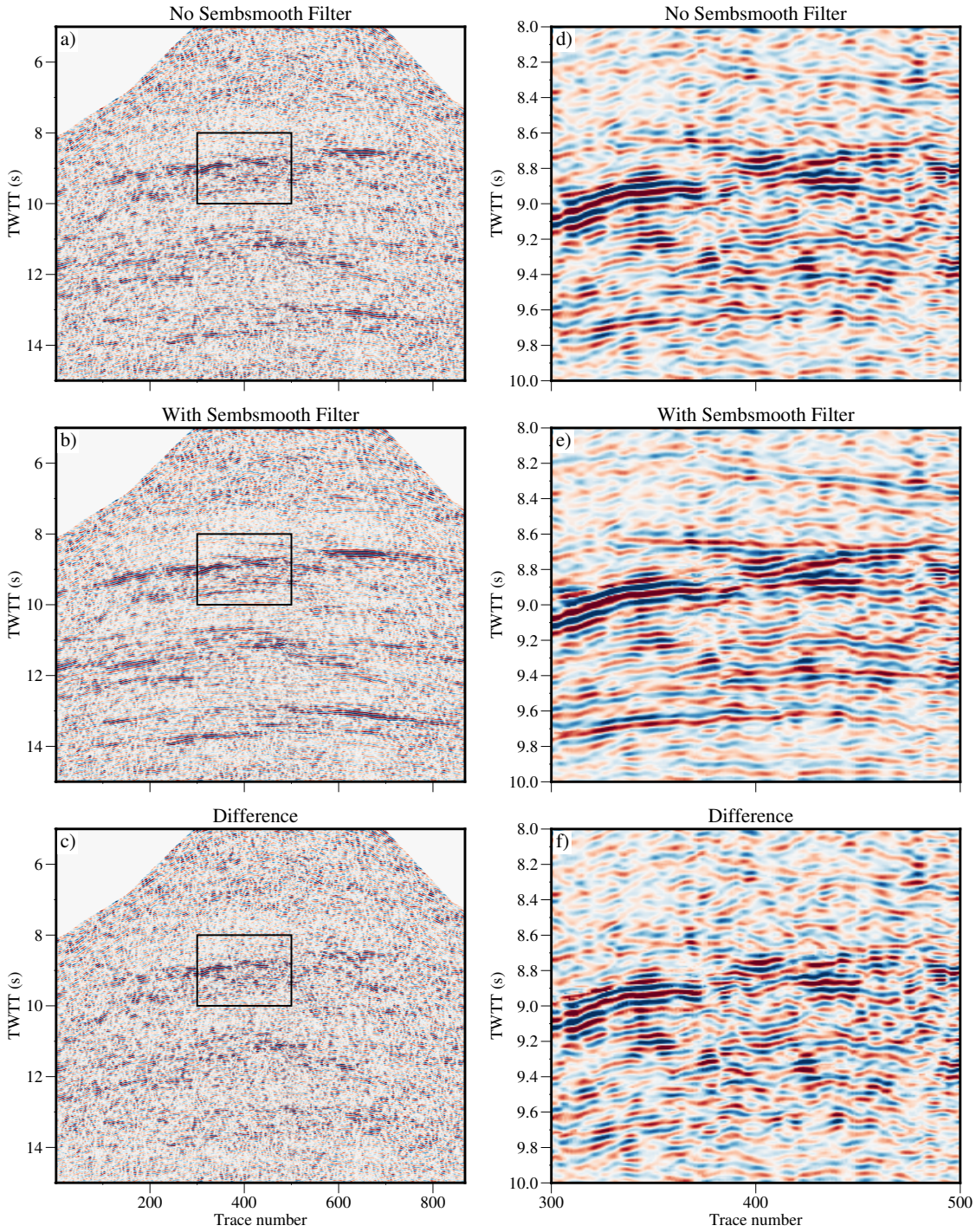


Figure 3.34: Pre and post and difference comparison plots for the application of a semblance coherency filter on a selection of the Box-2 receiver gather between 5–15 s $TWTT$ (a, b, c) and an enlarged section of the strong events at ~ 9.0 s as shown by the black box (d, e, f). a) Prior to filter application. b) Post filter application. c) Difference between (a) and (b). d) Prior to filter application. e) Post filter application. f) Difference between (d) and (e); black arrows show linear noise events removed by the filter. Note the improvement in reflection coherency in (b) and (e) and in particular the greater offset range over which reflections are visible in (b) compared to (a).

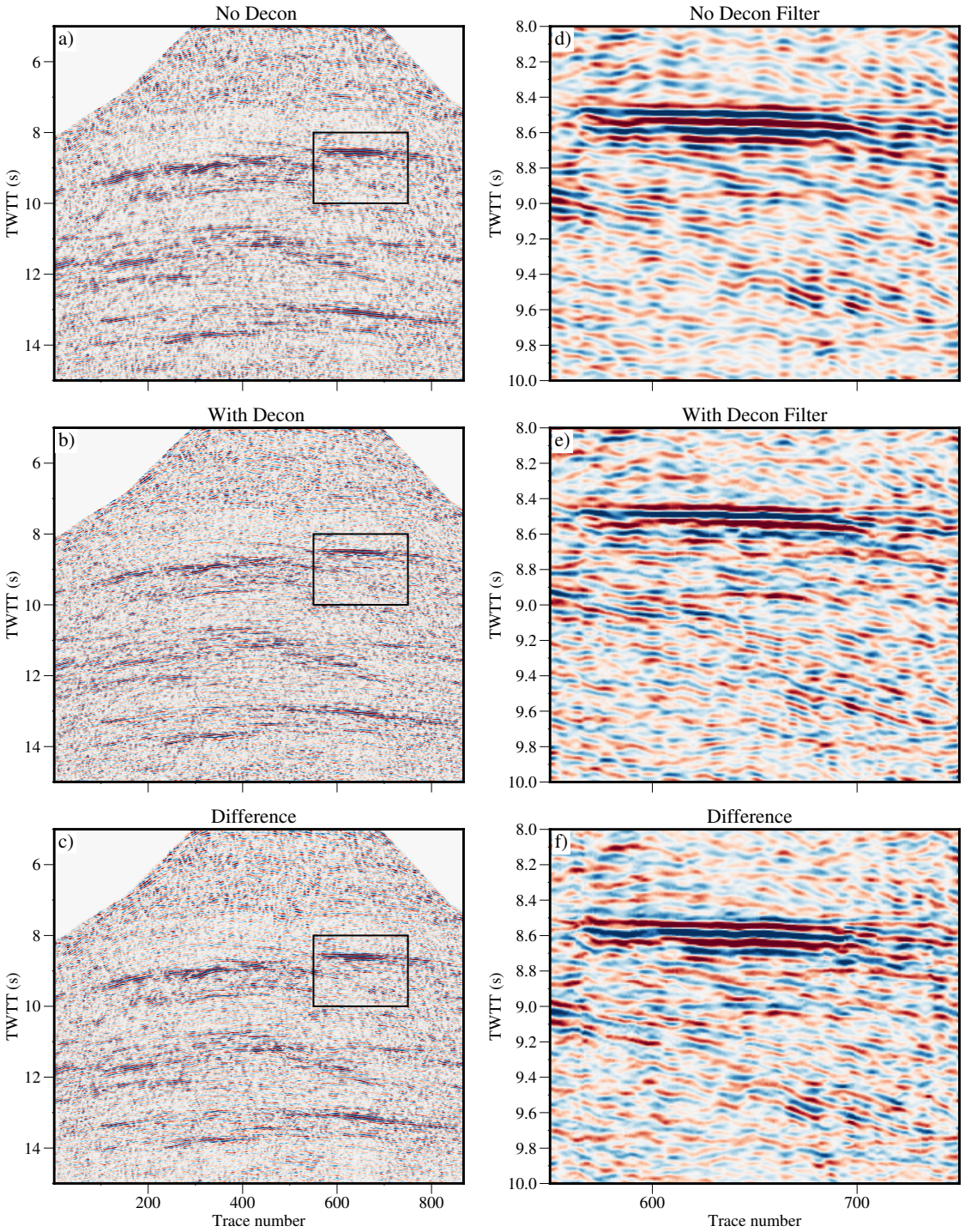


Figure 3.35: Pre and post and difference comparison plots for the application of predictive deconvolution on a selection of the Box-2 receiver gather between 5–15 s $TWTT$ (a, b, c) and an enlarged section of the strong events at $\sim$ 9.0 s as shown by the black box (d, e, f). a) Prior to filter application. b) Post filter application. c) Difference between (a) and (b). d) Prior to filter application. e) Post filter application. f) Difference between (d) and (e). Note the reduction in "ringing" in (b) and (e) and the removed ringing below the strong reflection in (e) as shown in (f).

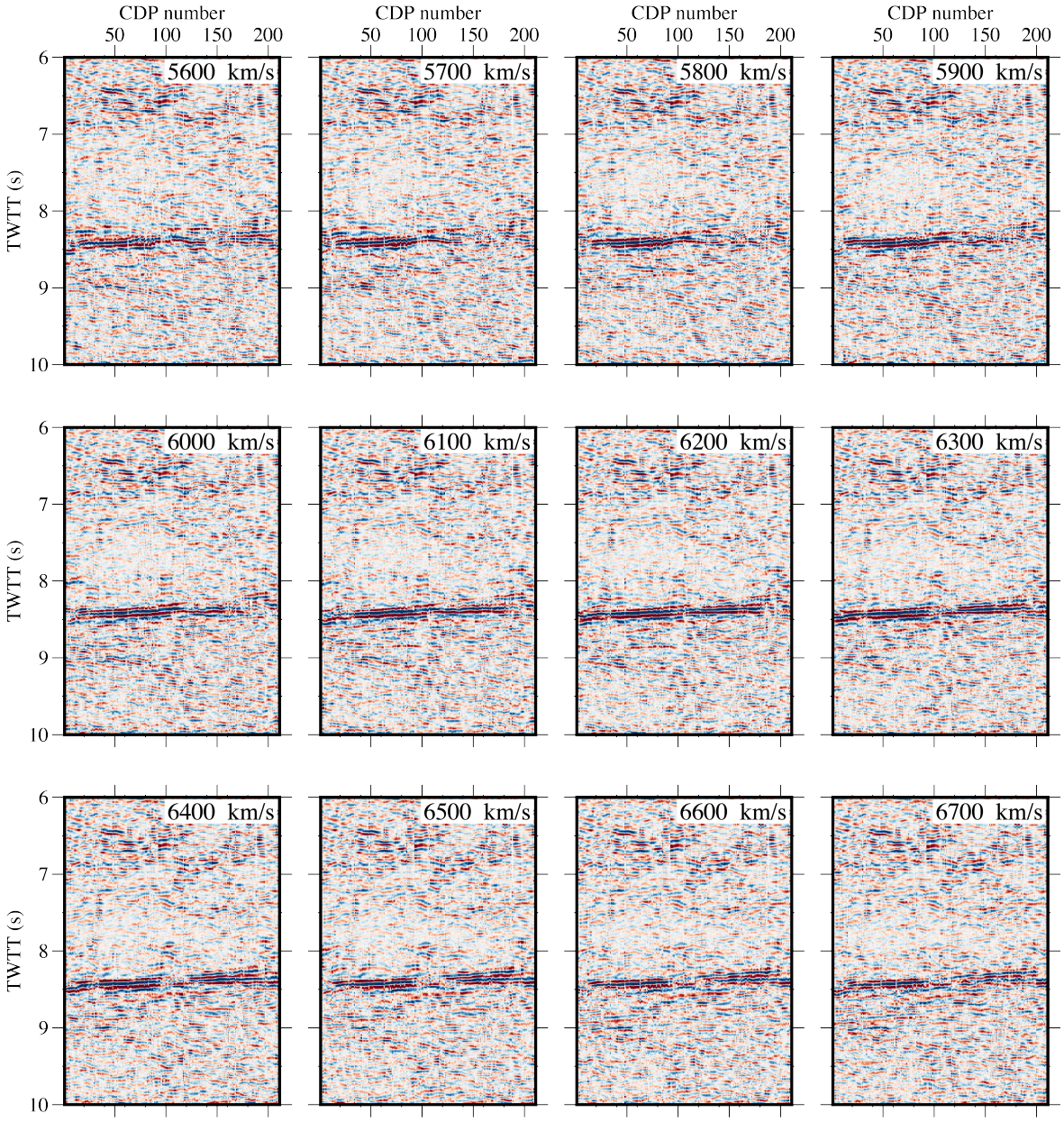


Figure 3.36: Example of Constant Velocity Stack (CVS) analysis showing the stacks produced for a subset of CDP traces centred on a portion of the prominent mid-crustal reflection at $\sim$ 8.5 s using a range of constant velocities from 5.6–6.7 $km\ s^{-1}$. Note a value of 6.2 $km\ s^{-1}$ produces the most coherent stack in this case.

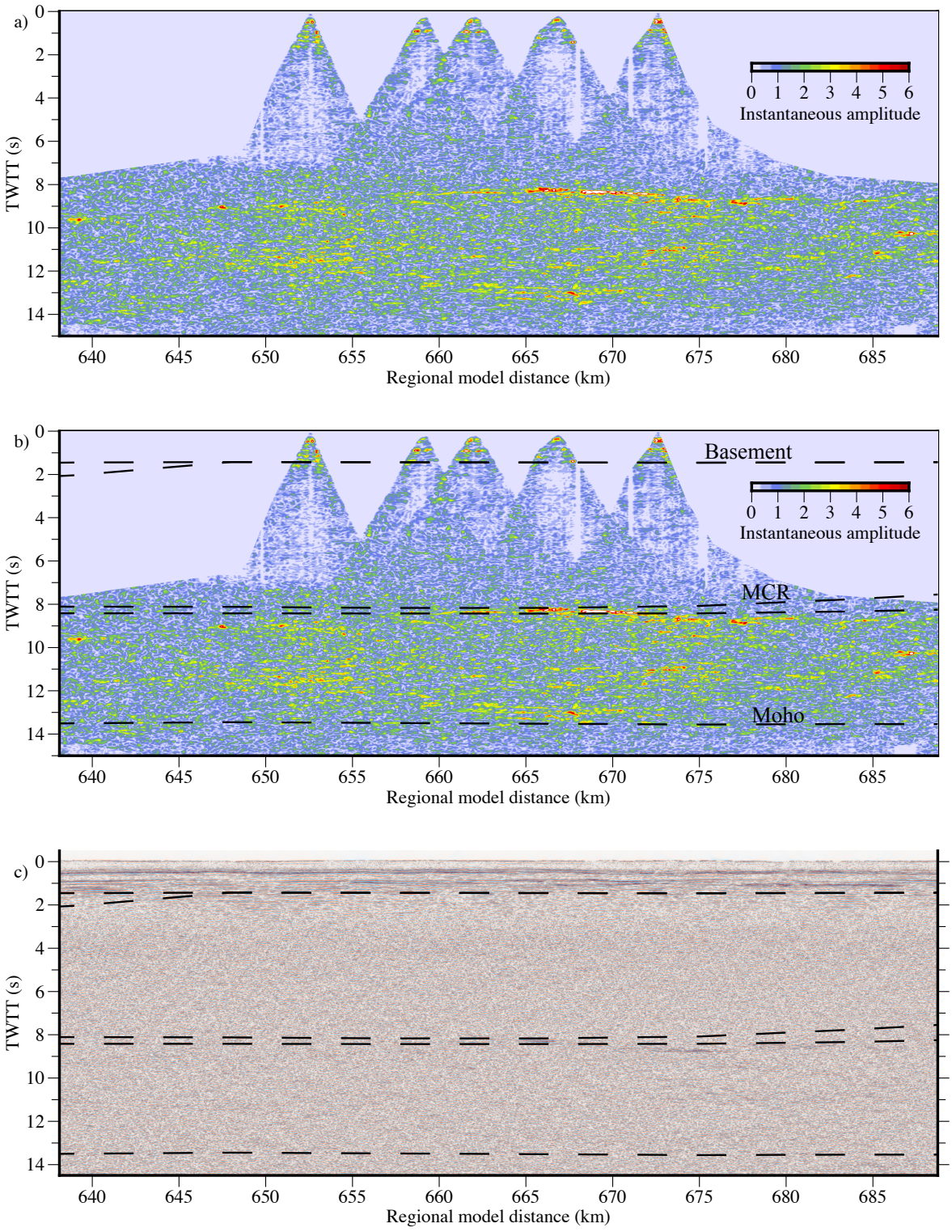


Figure 3.37: a) Unmigrated low-fold seismic reflection stack of the five box wave wide-angle receiver gathers displayed using instantaneous amplitude (e.g., Yilmaz, 2001). b) Same as in (a) but with depths of the basement, MCR and Moho interfaces from the V_p model converted to Two Way Travel Time overlain (dashed lines). Note the good agreement of the basement and MCR, while the Moho appears slightly shallower on the stack. c) Post-stack-time-migrated regional reflection profile with the same interfaces as in (b) overlain. Note in this section the MCR is less prominent and the Moho is unresolved.

3.7 Summary

A combination of vertical incident reflection and wide-angle reflection/refraction data, collected using a low frequency (4–60 Hz) vibroseis source have been used to image the sedimentary basin and crustal structure along a two-dimensional transect spanning the full $\sim$ 1200 km width of Parnaíba basin. This places the first active source seismic constraints on the crustal structure beneath Parnaíba basin. Key findings from this analysis are:

- Parnaíba basin is characterised by a simple-bowl shaped geometry, typical of cratonic basins. There is little evidence of extensional deformation within the basin or underlying basement. This suggests extension is not the primary mechanism for basin formation and played a minor role, if any.
- The Jaibaras basin is imaged seismically adjacent to the TBSZ and can be interpreted as a negative flower structure, typical of a strike-slip pull-apart origin. This structure, and its equivalents, therefore, do not represent extensional grabens formed during a Cambrian rift event.
- The Parnaíba basin resides above at least four distinctive crustal domains and conceals the precise locations and natures of the contacts/sutures between these. From west to east, these are the: Amazonian craton, Araguaia supergroup, Parnaíba Block and Borborema Province.
- A prominent zone of Mid-crustal reflectively can be traced laterally for at least 250 km at depths of $\sim$ 17–25 km beneath the centre of the basin.
- At the basin's western margin post-stack depth migrated reflection data suggest that the Moho depth varies between 40–44 km beneath the Amazonian craton and has been flexed by the load of the over-thrust Araguaia belt. At the eastern margin the Moho deepens from $\sim$ 35.5 km beneath the Borborema Province to 42 km at its intersection with the TBSZ, over a lateral distance of $\sim$ 250 km.
- Wide-angle reflection/refraction data from the centre of the basin suggest upper crustal V_p values are 6.00–6.15 $km\ s^{-1}$, typical of continental upper crust. However, below a

prominent zone of Mid Crustal Reflectivity (the MCR), these data suggest V_p increases to 6.7–7.0 $km\ s^{-1}$within the lower crust.

- Wide-angle reflection/refraction data constrain the Moho depth to $42 \pm 2\ km$ beneath the centre of the basin. The depth to Moho therefore appears as deep or deeper beneath the centre of the basin as the flanking regions, inconsistent with a rifting origin for the basin.

Chapter 4

Parnaíba basin gravity anomalies and crustal structure

4.1 Introduction

In this chapter, gravity data are analysed to further constrain Parnaíba basin crustal structure and to investigate possible basin forming processes. Firstly, a brief overview of the fundamental physics from the perspective of geophysical modelling is given. Next, terrestrial gravity measurements collected along the regional Parnaíba Basin Analysis Project (PBAP) transect, coincident with the regional seismic reflection profile analysed in the previous chapter, are reduced to free-air and Bouguer gravity anomalies. These anomalies are then modelled using an object-oriented two-dimensional forward modelling approach to predict crustal density structure. Process Oriented Gravity Modelling (POGM) is then used to investigate possible basin forming mechanisms. Finally, reductions are applied to satellite-derived Earth Gravitational Model (EGM2008) free-air anomaly data (Pavlis et al., 2012) in order to produce sediment-corrected residual anomalies, used to constrain a three-dimensional gravity and flexural model for Parnaíba basin.

4.2 Earth's gravity and gravity anomalies

In geophysical studies, the Earth's gravity field is treated using classical *Newtonian* mechanics in order to deduce information regarding the internal nature of the Earth. Newtons law of universal gravitation is the fundamental basis of such analysis. This law states that the force, F, acting on either of two masses m_1 and m_2 separated by distance r, is given by:

$$F = G\frac{m_1 m_2}{r^2} \tag{4.1}$$

Where G is a constant known as the universal gravitational constant. G has been empirically derived and is equal (to four significant figures) to:

$$G = 6.673 \times 10^{-11}\ Nm^2\, kg^{-2} \tag{4.2}$$

Newtons second law of motion states that force, F, is related to a particles mass,(m) and acceleration, (a), by:

$$F = ma \tag{4.3}$$

In the simplest case—in which the Earth is considered as a non-rotating, perfect sphere of homogeneous density—its mass can be considered as a point source located at its centre. Hence, in Equation 4.1, m_1 may be considered as Earth's mass, M_e, and for a given object located on Earth's surface of mass m_2, r is then equal to the radius of the Earth, denoted R. Equation 4.1 may then be considered in the form of Equation 4.3:

$$F = ma = mg = m\frac{GM_e}{R^2} \tag{4.4}$$

The acceleration of a given mass, m, towards Earth's centre due to the gravitational force,

g, is therefore given by:

$$g = \frac{GM_e}{R^2} \tag{4.5}$$

Gravitational acceleration, g, henceforth referred to simply as *gravity*, has the units $m\ s^{-2}$. However, gravity is often referred to using the unit Gal, which is equivalent to $cm\ s^{-2}$. In Geophysical gravity surveying, variations of interest are usually much smaller than 1 Gal and so the unit milliGal ($mGal$) is usually used. Where 1 $mGal$ is equal to $1e \times 10^{-5}\ m\ s^{-2}$.

Equation 4.5 shows that for the case outlined above (i.e., for an idealised homogeneous Earth), the value of gravity would be everywhere constant. However, due to distortions in Earth's shape, surface relief, and its rotation and internal mass distribution, the magnitude of Earth's gravity varies in both space and time. The magnitude of gravity at a given point can, therefore, be considered a function of five factors: latitude, elevation, the surrounding topography, Earth tides and variations in the internal density structure (Telford et al., 1990).

By determining the contribution of the first four factors listed above, toward the total magnitude of gravity at a particular location, the contribution due to internal mass anomalies can be isolated. This approach forms the basis of geophysical investigation of Earth's internal structure using measurements of the gravity field.

4.2.1 Reference datums

In order to accurately map changes in the gravity field, all measured values must be reduced to a common reference datum. A useful reference surface for this purpose is one on which the vector of gravity is everywhere perpendicular. This condition is met by a hypothetical surface on which gravitational potential is everywhere equal. One such "equipotential" surface, which also most closely approximates the shape of the Earth, is known as the geoid (e.g., Hinze et al., 2013). Under the influence of a gravitational field, a fluid in rotation will take the shape of an equipotential surface, hence, in the oceans, mean sea level (MSL) closely approximates the geoid (e.g., Garland, 1965). The geoid is, therefore, a convenient reference datum for defining

both gravity anomalies and surface elevation.

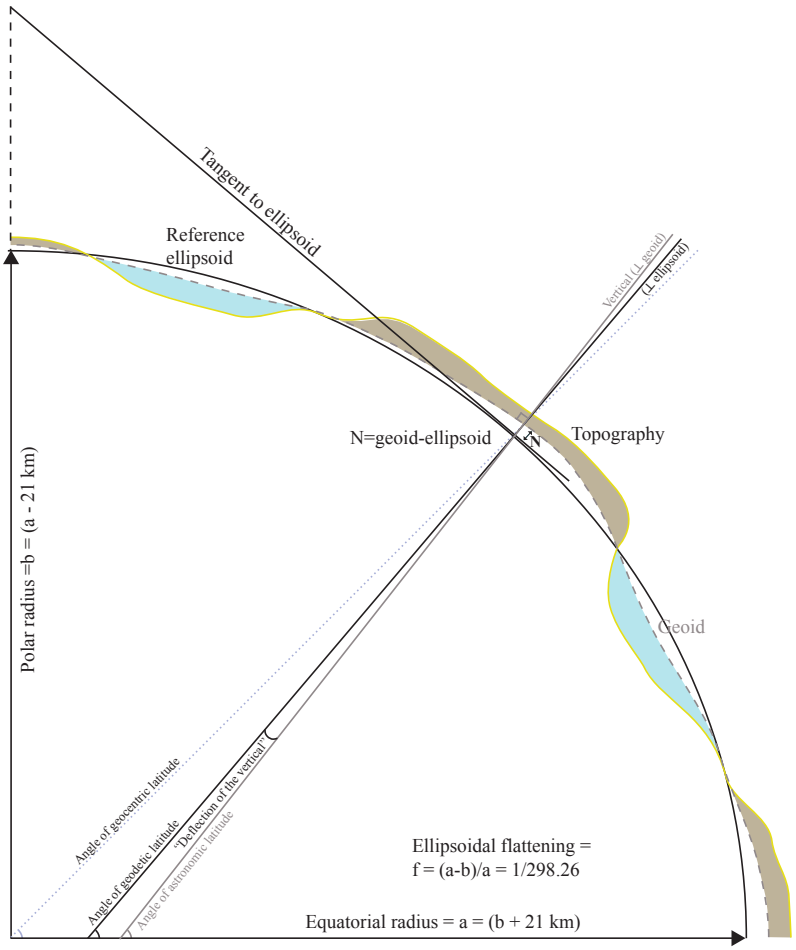


Figure 4.1: Schematic illustration of reference datums used during gravity surveying. The dashed grey line shows the geoid which is approximately equal to mean sea level in the ocean. The solid black line is the best fit mathematical representation of the Earth, the reference ellipsoid. Gravity measurements are made on the physical surface of the Earth and must be reduced to the geoid. N is the difference between the geoid and reference ellipsoid (after Hinze et al., 2013).

A more simple mathematical representation of the Earth is that of an oblate ellipsoid (reference ellipsoid) that best fits the geoid (Fig. 4.1). Assuming a homogeneous and rotating Earth, the theoretical value of gravity can be determined for all points on the surface of the reference ellipsoid. Thus, formulas such as the International Gravity Formula 1967 (IGF, 1967) (see Section 4.4.3) based on a satellite-derived value for Earth's flattening, are used to derive the expected gravity field on the reference ellipsoid, known as "normal gravity". A gravity anomaly is then defined as the difference between the magnitude of gravity measured

on, or reduced to, the geoid and that predicted for the reference ellipsoid (normal gravity). The resulting gravity anomaly may be attributed to mass anomalies within the Earth.

4.3 Gravity data

As part of PBAP, 823 terrestrial gravity measurements were acquired at a spacing of 1–2 *km* along the PBAP regional transect (Fig. 4.2). These data were acquired coincident to the regional seismic profile analysed in the Chapter 3, during two field campaigns between July/August and September/October 2013.

A Scintrex CG-5 Autograv gravimeter (Scintrex, 2006) was used to acquire these data. The CG-5 instrument has a standard measurement resolution of 1×10^{-3} *mGal* and standard deviation of $< 5 \times 10^{-3}$ *mGal*. Geographic positions and elevations were determined using a differential Trimble GPS system. A vertical precision of 30 *cm* for 90 % of the points was achieved, corresponding to errors of 9.2×10^{-4} *mGal* and 3.0×10^{-2} *mGal* for the derived free-air and Bouguer anomalies (see Section 4.4.7) respectively (Andrew, 2014).

4.4 Terrestrial gravity data reduction

This section describes the data reduction procedure used to reduce 823 *relative* terrestrial gravity measurements, acquired along the PBAP regional transect (Fig. 4.2), to both free-air and Bouguer gravity anomalies.

This section is indebted to the work of Andrew (2014) who participated in data acquisition, catalogued the raw data, converted the measurements to absolute values and calculated and applied the drift corrections.

4.4.1 Conversion from relative to absolute gravity

The CG-5 instrument used to acquire these data measures the displacement of an internal mass that occurs in response to the magnitude of local gravity. This is known as *relative* gravity

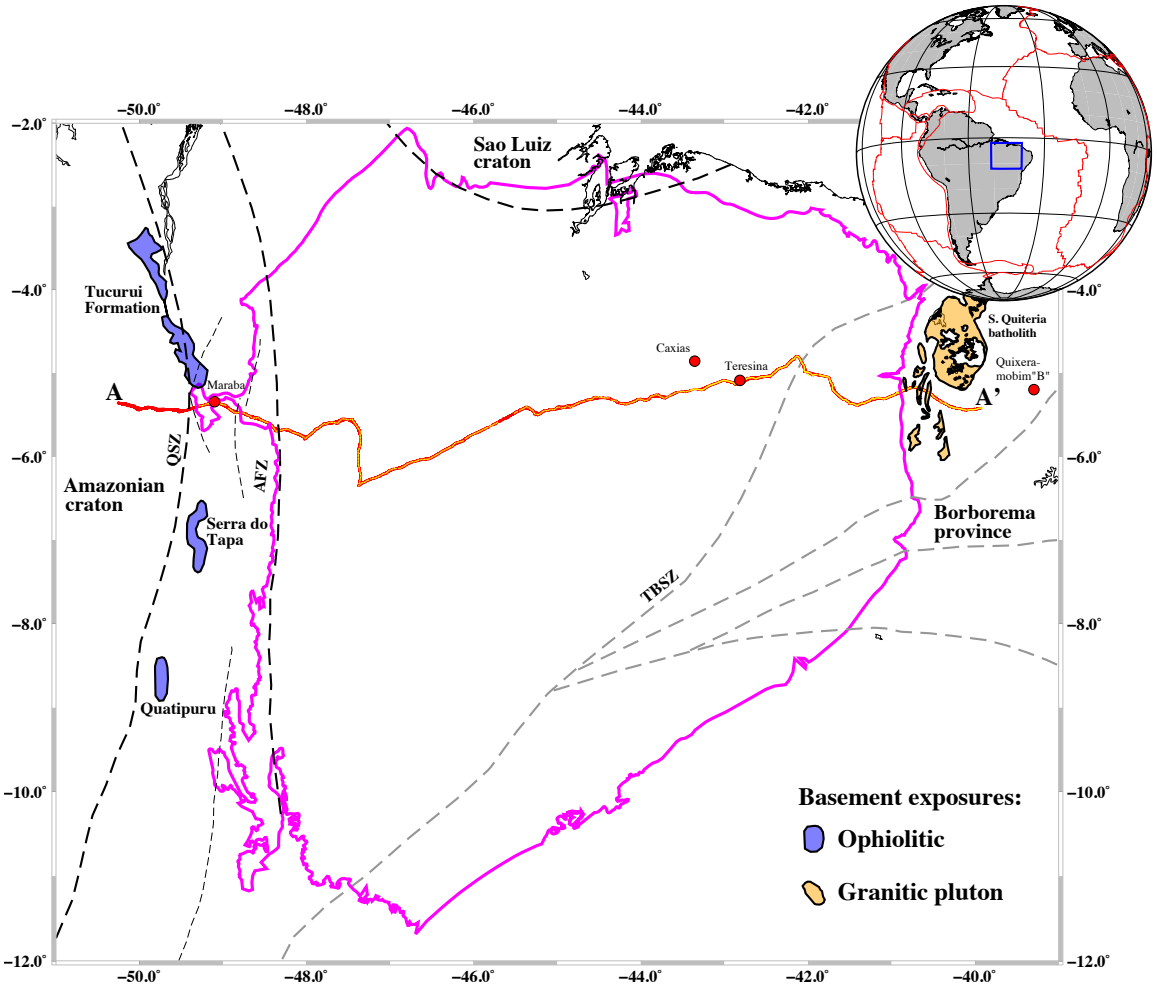


Figure 4.2: Parnaíba basin gravity survey map. Red line shows the PBAP seismic reflection profile. Yellow circles show the locations of gravity survey points. Red circles shows the location of Brazilian Geodetic System absolute base stations used for absolute gravity ties. Black dashed lines show major tectonic boundaries/faults. Blue shaded regions show ophiolitic outcrops. Orange shaded regions show granitic pluton outcrops. Inset top right shows bounding box of the main figure (blue box).

as only the relative displacement of the mass is known. Such recordings must be "tied-in" at a site at which absolute gravity is known in order to convert the relative measurements to absolute gravity values.

During the PBAP survey relative measurements were converted to absolute measurements by tying the survey to four "base stations", at which absolute gravity measurements have been made as part of the Brazilian Geodetic System. The base stations used were located in Quixeramobim, Teresina, Carolina and Marabá (Fig. 4.2). The conversion is computed using the simple equation below:

$$g_{abs} = g_{rel} - g_{ref} + g_{abs-ref} \tag{4.6}$$

Where g_{abs} is absolute gravity at the observation point of interest; g_{rel} is relative gravity value measured at the observation point; g_{ref} is the relative gravity value measured at the absolute gravity base station; and $g_{abs-ref}$ is the absolute gravity value at the base station determined using a method for measuring absolute gravity.

4.4.2 Drift correction

A *drift correction* is applied to account for any temporal variation in gravity that may have occurred during acquisition. Such "drift" occurs due to two primary reasons: 1) The redistribution of mass caused by Earth tides, which are controlled by orbital forcing from the Sun and Moon. Note, the effect of ocean tides were corrected for at the time of acquisition by an inbuilt CG-5 instrument tidal model (Andrew, 2014). 2) Instrumental drift that may result from physical changes of the internal instrument components caused by changes in, for example, the thermal state of the instrument.

Drift corrections were determined by performing a looping procedure. Repeat measurements were made at a base station at the beginning and end of each day during acquisition. Linear interpolation between measurements was assumed and this revealed an average ~ 0.3 $mGal/day$ drift (Andrew, 2014). Drift corrections were then calculated using the standard drift correction formula:

$$g_{drift} = \frac{g_1 - g_0}{t_1 - t_0} \times t_{obs} \tag{4.7}$$

Where, for the given survey measurement that is being reduced, t_0 and t_1 are the times at which base station readings were obtained before and after the survey point was measured and g_0 and g_1 are the corresponding values recorded at the base station. t_{obs} is the time of the given survey measurement relative to t_0.

4.4.3 Latitude correction

Gravitational acceleration on Earth decreases latitudinally from the poles towards the equator, with a total difference of $\sim 5200\ mGal$ (Hinze et al., 2013). This variation is the result of three phenomena:

Firstly, because the Earth is rotating, a centrifugal force is generated. The radial component of this (i.e., $f\ cos\ \phi$) opposes the Earth's attraction, and increases in magnitude from zero at the pole to its maximum at the equator, as shown in Figure 4.3. This results in a decease in the magnitude of gravity from the poles to the equator.

Secondly, in its long-term (millions of years) response to rotation, the Earth behaves similarly to a fluid, resulting in a bulge at the equator, such that, its radius is $\sim 21\ km$ greater at the equator than at the poles (Hinze et al., 2013). Hence, the shape of the Earth approximates an oblate spheroid (or ellipsoid of revolution) with a flattening ratio of $\sim 1/298$ between the polar and equatorial radii (Hinze et al., 2013). A point on Earth's surface is thus closer to the centre of mass at the poles than at the equator, which also results in a decease in the magnitude of gravity from the poles to the equator.

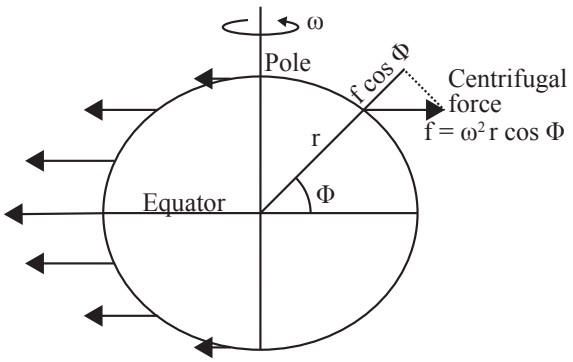


Figure 4.3: Schematic illustration of the latitudinal variation in Earth's gravity as a result of the opposing centrifugal force. w = angular velocity; ϕ = latitude; $r = radius$. Note this example is for the idealised case of a perfect sphere (modified after, Tsuboi, 1983).

Finally, the increase in radii of the Earth towards the equator results in additional mass within the subsurface causing an increase in gravity. This effect competes against and partially subdues the centrifugal force and radii effects.

Clairaut (1743) derived a formula that accounts for variation in gravity due to latitude and flattening of a rotating ellipsoid. Although this varies from the more complex shape of the geoid, it provides an approximation for the expected magnitude of gravity on the ellipsoid as a function of latitude. The constants in Clairaut (1743) formula, which are related to shape and angular velocity of the Earth, have been iteratively improved through time as they have become more well constrained. For this survey, the International Gravity Formula (1967) solution was used to produce the latitude corrections. This is given by:

$$g_\phi = 978031.85(1 + 0.005278895 \sin^2 \phi + 0.0000058 \sin^2 2\phi \tag{4.8}$$

Where ϕ is the latitude at which the observation is made.

4.4.4 Elevation correction

As shown in Section 4.2, gravitation acceleration is inversely proportional to the distance between the interacting masses. When reducing gravity measurements to the geoid, a correction must therefore be applied to compensate for the elevation between the measurement point and the geoid (Fig. 4.4a). As shown by Garland (1965), for example, this correction is given by differentiation of Equation 4.5 with respect to r:

$$\frac{dg}{dR} = \frac{GM_e}{R^2}\, dR = -2\frac{GM}{R^3} = -\frac{2g}{R} \tag{4.9}$$

For average mid-latitude values of g and R, i.e., $9.83\,\mathrm{m\,s^{-2}}$ and $6371 \times 10^3\ m$ respectively, the decrease in gravity with increasing elevation is $\sim 0.3086\ mGal\ m^{-1}$. This is known as the free-air effect.

For a measurement made at height, h (m), the free-air correction (FAC) that accounts for the free-air effect in $mGal\ m^{-1}$ is then given by:

$$FAC = 0.3086h \tag{4.10}$$

4.4.5 Bouguer correction

Although the free-air anomaly accounts for the elevation above the geoid at which a measurement was made, it does not consider the gravitational effect of the mass between the observation point and the geoid. Hence, at short wavelengths, free-air anomalies often reflect the surrounding topography, as this mass dominates the gravity signal due to proximity to the observation point. This phenomenon was noted by Bouguer (1749) and later a method was derived to account for the mass between the observation point elevation and the geoid, which is now known as the Bouguer correction. Using the Bouguer correction, the gravity effect of the intervening mass is removed from the observed value by subtracting the effect of a horizontal sheet, infinite in all directions and of thickness equal to that of the observation point height above the geoid, with a density equal to the intervening material. The Bouguer correction is given by:

$$BC = 2\pi G\rho h \tag{4.11}$$

Where G is the universal gravitational constant (Eq. 4.2), ρ is the density of the intervening material in $kg\ m^{-3}$, set here as 2650 $kg\ m^{-3}$ as an intermediary between the average sediment and basement densities, h is the elevation of the observation in m.

Bullard (1936) recognised that the infinite slab approximation over-corrects gravity due to two reasons: 1) the curvature of the Earth and 2) the mistreatment of intervening topography variations. Two further corrections were therefore devised to modify the simple Bouguer correction.

The correction that accounts for Earth curvature is known as the Bullard B correction, which can be calculated using methods such as those given by Takin and Talwani (1966) or Nowell (1999). A correction that accounts for intervening topographic variations (Bullard C) is commonly referred to as the terrain correction and is discussed in the next section.

4.4.6 Terrain correction

To correct the Bouguer slab for topographic variations a terrain correction is applied. For example, Figure 4.4a illustrates the relationship between a gravity measurement made on Earth's surface at point P with the associated Bouguer slab and surrounding terrain. The application of a Bouguer slab erroneously over-corrects the observed data for the areas labelled A, which consists of air rather than rock. Conversely, the area labelled B, which occurs above the measurement point, applies an upward attraction that opposes gravity. Hence, the terrain correction involves calculating the gravity effect of "A" sections and adding these to the Bouguer correction to "complete" the Bouguer slab; additionally, the effect of "B" sections is calculated and also added to the Bouguer slab, in order to compensate for their upward attraction. Hence, the terrain correction is always *positive* in sign.

Terrain corrections are usually divided into *inner* and *outer* corrections, defined by circular sectors of increasing radius relative to the measurement point.

Traditionally, these sectors are then divided into zones of equal area with the average elevation within each zone used to calculate that portion of the terrain correction, the sum of all zones then defines the correction for the given sector (e.g., Hammer, 1939). The areal extent of zones is usually smallest near the observation point and set so as to become progressively more coarse away from the measurement point as inner terrain corrections may contribute a large portion of the total terrain correction due to the proximity to the measurement point.

In this study, inner terrain corrections were recorded infield by estimating topographic undulations out to a radius of 170 m (equivalent to Hammer zone D), and recorded within the CG-5 gravimeter (Andrew, 2014). Unfortunately, these records were lost internally. Inner terrain corrections have therefore not been applied in the study. This problem is being worked on at Observatório Nacional, Rio de Janeiro, using a high resolution local digital elevation model (DEM). Nevertheless, terrain corrections are expected to be small, given the flat topography and the avoidance of topographic undulations during acquisition. For example, as a conservative estimate, using the Hammer (1939) method and assigning a elevation difference of 20 m within all inner zones (much larger than those anticipated for this survey), a

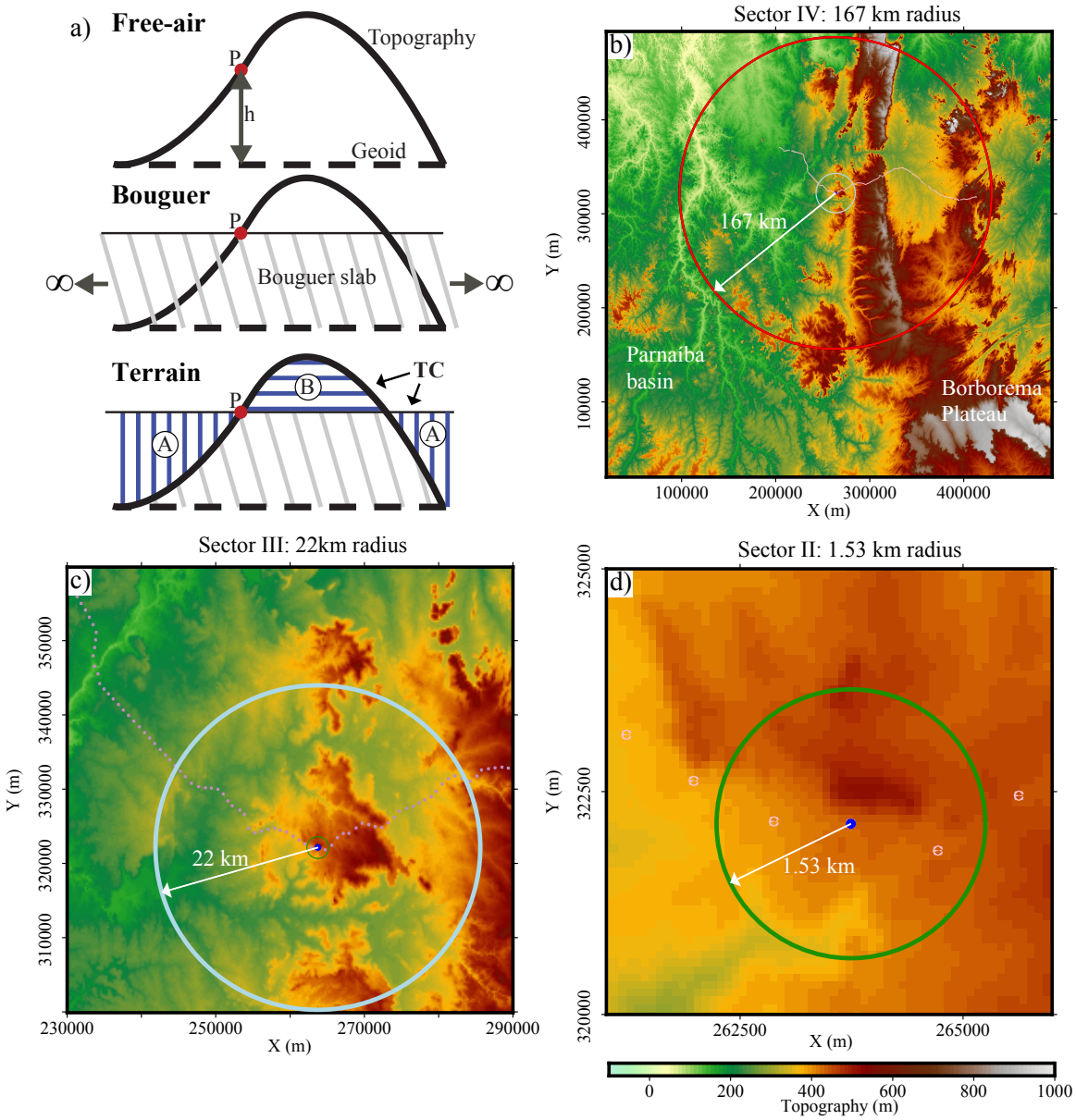


Figure 4.4: a) Schematic illustration showing the principles of free-air, Bouguer and terrain corrections. The Free-air correction (FAC) accounts for the elevation of the observation point (P) above the reduction datum (i.e., the geoid). The Bouguer slab corrects for the mass between the observation point (P) and the geoid. The terrain correction corrects the infinite Bouguer slab that overestimates the gravitational attraction of material between the measurement point, P, and the geoid (after, Kearey et al., 2013). b–d) Maps showing examples of digital elevation models (DEMs) used to calculate the outer terrain corrections for an example survey point near the eastern edge of Parnaíba basin (blue circle). The resolution of the DEMs used for the three sectors were 510, 255 and 85 *m* for sectors IV (red), III (light blue) and II (green) respectively. Pink circles PBAP survey gravity points.

terrain correction of 1.54 *mGal* would be required. However, near the eastern edge of the basin inner terrain corrections may be appreciable, given the highway along which data were

acquired crosses the Borborema plateau ridge, here, $\sim$ 10 points may have average elevation differences of $\sim$ 50 m, with equivalent terrain values of 3.90 $mGal$.

Outer terrain corrections were calculated using the computational method of Cella (2015). This involves using a Digital Elevation Model (DEM) and the analytical solution for the gravitational effect of flat top prisms, given by, for example, Blakely (1996), to calculate the gravitational effect of topography out to a maximum distance of 167 km. The Shuttle Radar Topography Mission 3-arc second ($\sim$ 90 m spatial resolution) digital elevation model (Farr et al., 2007) was used for this purpose. The Cella (2015) method divides the terrain into four sectors defined by inner and outer radii relative to each measurement point. Similarly to the traditional chart method of Hammer (1939), the sectors are assigned DEMs of decreasing spatial resolution in order to increase computational efficiency. In this study, the radius of the inner most sector (Sector I) was set as 170 m, which equivalent to the maximum radius of the traditional inner terrain correction Zone D of Hammer (1939). Sector I is not included in the terrain correction calculations as a higher spatial resolution DEM than the SRTM data is required. Sectors II–IV were defined as shown in the example given in Figure 4.4b–d. These calculations revealed that most outer terrain corrections were < 0.5 $mGal$ within the basin, with a maximum value of 2.26 $mGal$ near the eastern edge of the basin, where the only large topographic undulations occur (e.g., Fig. 4.4b and c).

4.4.7 Gravity anomalies

Once all relevant corrections have been applied to reduce a gravity measurement made on the physical surface to the geoid, the gravity anomaly, which may be attributed to the anomalous mass distribution within the subsurface, is defined as the difference between the value of gravity measured on the geoid, g_{obs}, and that predicted for the same location on the reference ellipsoid, $g_{ellipsoid}$, (i.e., as predicted by Equation 4.8).

The free-air gravity anomaly, which does not consider the Bouguer or Terrain corrections is given by:

$$g_{FA} = g_{obs} - g_{ellipsoid} \pm FAC \tag{4.12}$$

While the complete Bouguer anomaly is given by:

$$g_{BA} = g_{FA} - BC + TC \tag{4.13}$$

In this reduction procedure, corrections for atmospheric effects (the atmospheric correction) and the departure between the geoid and reference ellipsoid (the indirect effect) have been neglected.

4.4.8 Regional correction

As the modelling conducted in this section is concerned with gravity anomalies generated by the density structure within the crust and mantle-lithosphere, long wavelength gravity anomalies, which are unrelated to relatively shallow structure, were removed. These are dominated by, for example, the gravity highs associated with subducted slabs and the lows associated with late glacial rebound. This was achieved by synthesising the EGM2008 Earth Model (Pavlis et al., 2012) spherical harmonic coefficients up to and including degree and order 12. Degree and order 12 includes all anomalies with wavelengths greater than or equal to $\sim$ 3330 km. This cut-off was chosen as a global assessment of Earth's free-air power spectra (Watts and Moore, 2017) shows that for n $>$ 12 lithospheric flexure processes can explain most, if not all, of the of the observed spectra. Below n=12, departure between the observed spectra and that predicted from flexure compensation highlights the relatively high contribution of sub-lithospheric processes, such as dynamic mantle processes, to the gravity anomaly at these wavelengths.

Figure 4.6 shows the long wavelength component of the gravity field surrounding Parnaíba basin from synthesis of spherical harmonics degree and order 8–18. The gravity anomaly at these wavelengths is dominated by a long wavelength low that spans much of the east coast of North America and Brazil.

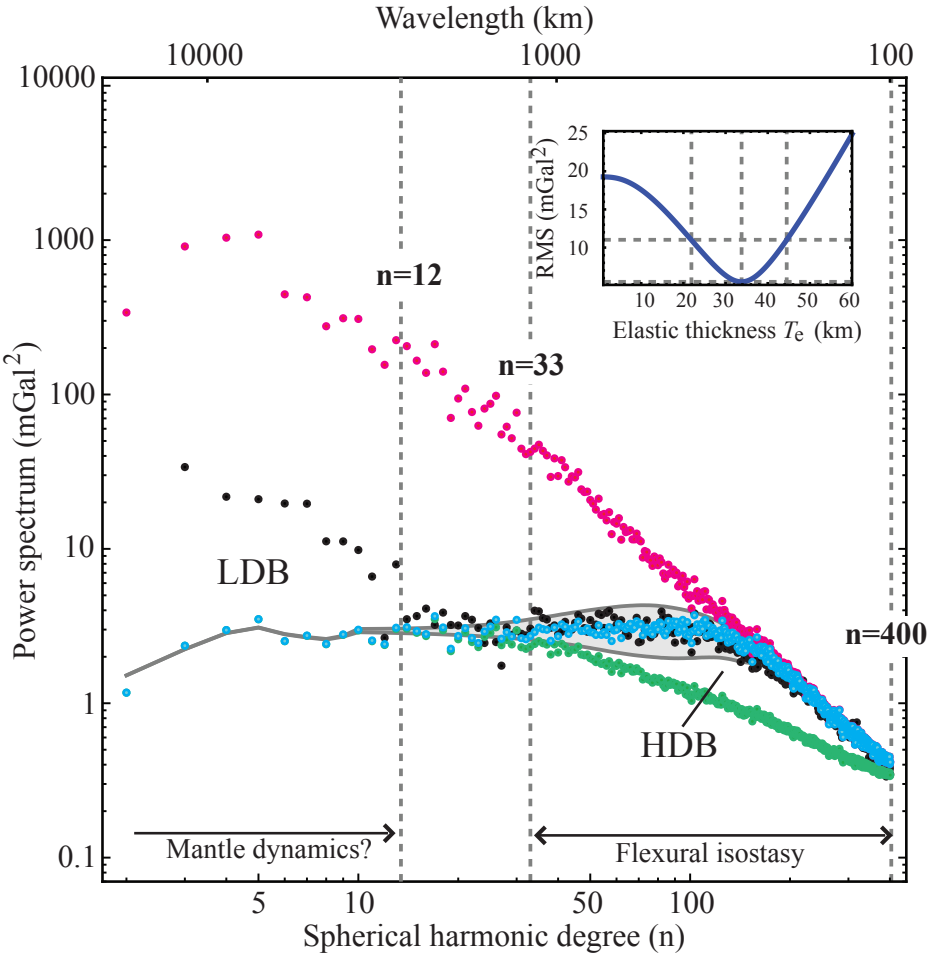


Figure 4.5: Comparison of the power spectrum of Earth's free-air gravity anomaly field (filled black circles) to calculated spectra based on the gravity effect of uncompensated topography (Red filled circles) and the gravity effect of the topography and its Airy compensation (Green filled circles) and flexural compensation (Light blue filled circles). The observed spectra have been calculated from the spherical harmonic coefficients that describe the EGM2008 gravity field model (Pavlis et al., 2012) and the uncompensated and isostatic spectra have been calculated from the Earth2014 topography model (Hirt and Rexer, 2015). HDB = High Degree Band. LDB = Low Degree Band. Inset shows the Root Mean Square (RMS) error between the observed spectra and the calculated spectra of the gravity effect of the topography and its flexural compensation as a function of the effective elastic thickness, T_e. Grid lines indicate best fit elastic thickness and band of twice the minimum RMS, used to define a region of permissibility for illustrative purposes (after, Watts and Moore, 2017).

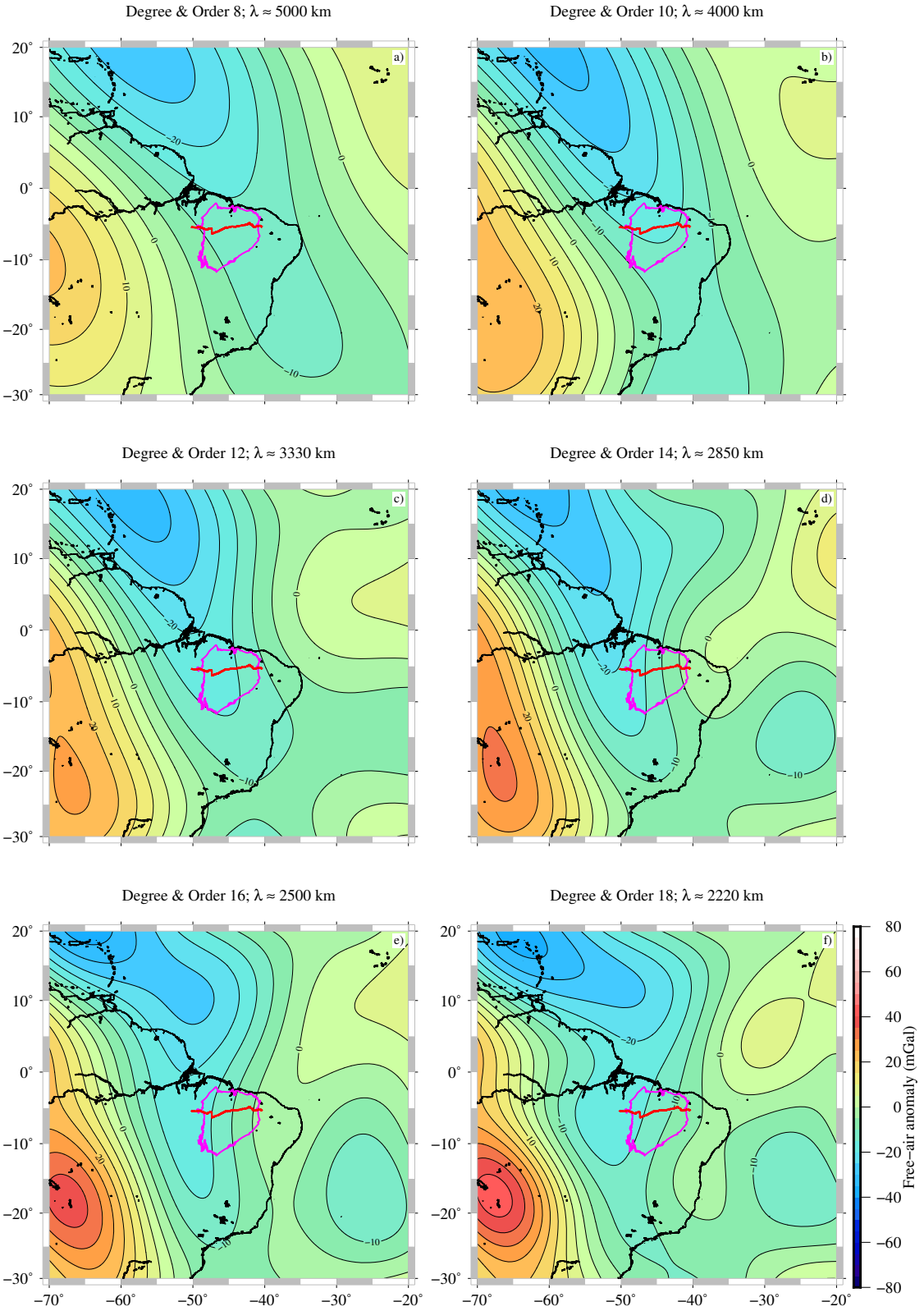


Figure 4.6: Regional gravity anomalies in the vicinity of Parnaíba basin synthesised from EGM2008 spherical harmonic coefficients. The pink solid line shows the outline of Parnaíba basin and the red solid line shows the regional PBAP transect. Note the anomaly shown in (c) was removed from the observed Bouguer anomaly during data reduction.

4.5 PBAP regional transect gravity anomalies

Figure 4.7 shows the free-air and Bouguer (with a reduction density of 2650 $kg\ m^{-3}$) gravity anomalies determined along the PBAP regional transect, as well as the topographic profile and regional seismic reflection data. It can be seen that Parnaíba basin is characterised by both free-air and Bouguer gravity lows. Short wavelength free-air anomaly highs that correlate with topography, such as those at the eastern edge of the basin, are removed in the Bouguer anomaly.

In detail, the Bouguer gravity anomaly data show that Parnaíba basin is associated with a broad "low" of $\sim 40\ mGal$ (purple dashed line in Fig. 4.7d). Superimposed on the low is a long wavelength ($\lambda \sim 1200\ km$) central gravity anomaly "high" of $\sim +25\ mGal$ (green dashed line in Fig. 4.7d), with shorter wavelength ($\lambda < 50\ km$) localised lows of $\sim 20\ mGal$. The western edge of the basin, which is approximately coincident with the QFZ, is characterised by a local high with flanking lows to either side. West of the basin exit, two small local lows, a few $mGal$ in amplitude, correlation with small sub-basins that are evident in the seismic reflection profile (Fig. 4.7e). The eastern edge of the basin and the Transbrasiliano shear zone (TBSZ) do not correlate with any significant Bouguer anomalies. The $\sim 15\ mGal$ low at the eastern end of the profile is attributed to the Santa Quiteria batholith, a Neoproterozoic granitic pluton.

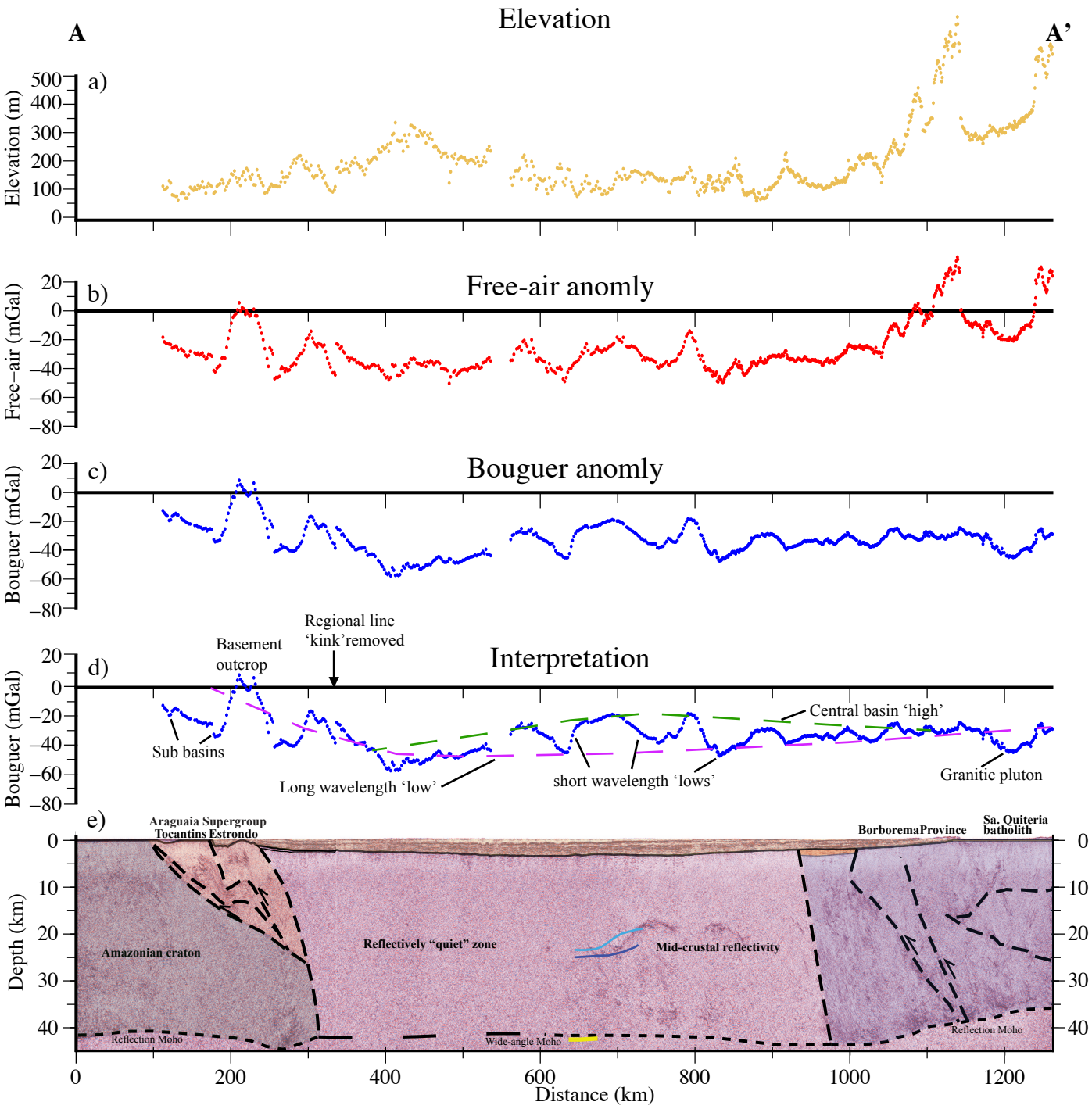


Figure 4.7: PBAP regional transect gravity data. a) Topography point measurements at the PBAP gravity survey locations. b) Free-air gravity anomaly. c) Bouguer gravity anomaly with long wavelength component removed. d) General interpretation of first order Bouguer anomaly features. The purple dash line highlights the regional long wavelength Bouguer "Low" across the basin. The dashed green line highlights the shorter wavelength central "high" across the basin centre. e) Regional seismic reflection profile with interpretations overlain. Note the position where the regional line "kink" located at $\sim 47.5°W$ has been removed (Fig. 4.2).

4.6 Two-dimensional forward model

4.6.1 Two-dimensional gravity modelling technique

Two-dimensional gravity anomalies are calculated using the line-integral technique of Bott (1969). The calculation of gravity anomalies produced by the two-dimensional anomalies was first discussed by Hubbert (1948) who showed that an areal integral solution for the vertical component of gravitational attraction produced by a two-dimensional body of constant density contrast, can also be obtained by performing a line integral around the body's periphery. This is advantageous as the areal method is inapplicable when bodies are required to extend to infinity or occur very close to the origin (Hubbert, 1948). Subsequently, Talwani et al. (1959) formulated an algorithm for solving this line integral by setting the observation point as the origin of a Cartesian coordinate system and treating the periphery of the body as an n-sided polygon, defined by a discrete set of nodal points. The total gravity anomaly is then calculated by evaluating the integral between each set of nodal point pairs and summing the results. Bott (1969) formulated a similar algorithm but used a slightly different trigonometric parametrisation. In this case, the integral solved is that for a semi infinite horizontal slab with one sloping interface. The analytic solution for this case is given, for example, by (Heiland, 1940 p. 153) as:

$$\Delta g = 2G\Delta\rho \left[-\{x_1 \sin\theta + z_1 \cos\theta\} \times \left\{ \sin\theta \log_e \frac{r_2}{r_1} + \cos\theta(\phi_2 - \phi_1) \right\} + z_2\phi_2 - z_1\phi_1 \right] \tag{4.14}$$

Where G is the Universal Gravitational Constant (Eq. 4.2); $\Delta\rho$ is the density contrast ($kg\ m^{-3}$) between the polygon and the surrounding material; x_i, z_i and r_i are the horizontal and vertical components and absolute distance (m) between each node and observation point, P, respectively; θ_i is the angle between the sloping edge and the horizontal; and ϕ_i is the angle between the x-axis and r_i respectively as shown in Figure 4.8. The geometry of this parametrisation is shown in Figure 4.8a.

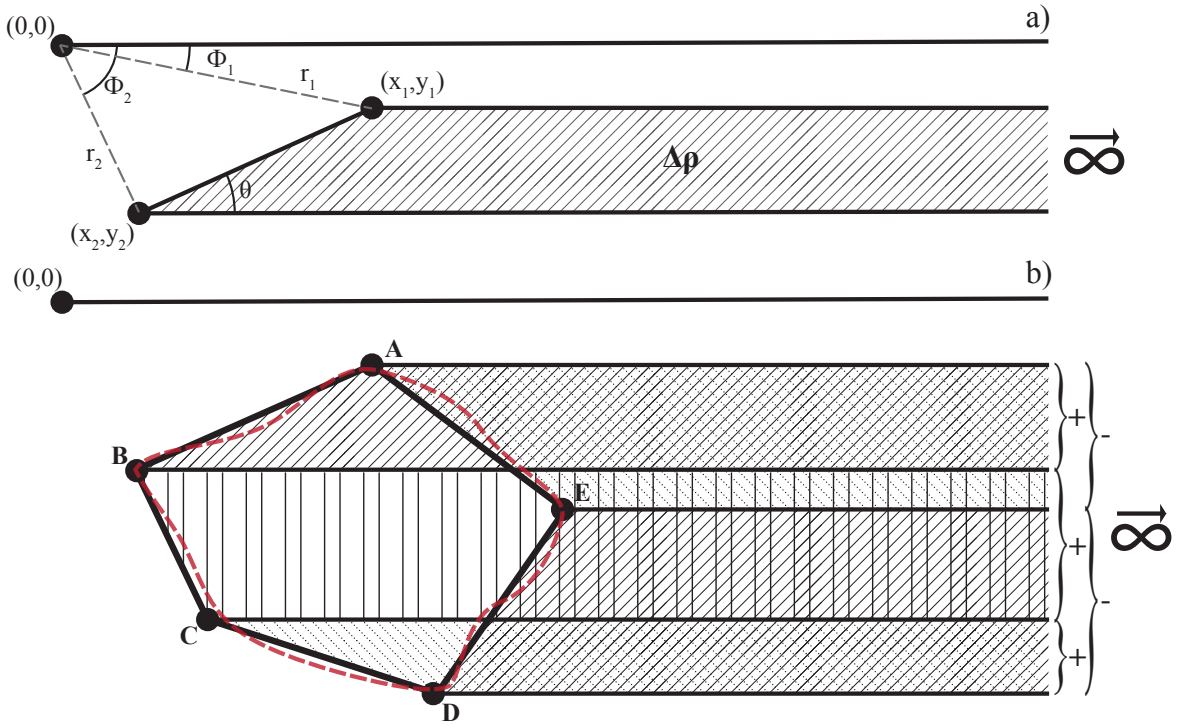


Figure 4.8: a) An example of an infinite slab with one sloping horizontal side, showing the geometric values relative to the observation point (0,0) used when solving Equation 4.14. b) Example of methodology for calculating the gravity anomaly due to a two-dimensional body (red dashed line) estimated using five nodal points (A-E) by summing the effects of the five infinite slabs with sloping sides (modified after, Kearey et al., 2013).

The total gravity anomaly produced by a given polygon is then determined by moving progressively counter-clockwise around the polygon and summing the contribution of each side (Equation 4.15).

$$\Delta g = \sum_{i=1}^{N} \Delta g_i \tag{4.15}$$

When $z_2 > z_1$ the contribution is positive and when $z_2 < z_1$ the contribution is negative, such that, in the summation, the contributions outside of the polygon cancel, leaving only the gravity anomaly produced by the polygon itself (Fig. 4.8b).

This algorithm has been integrated into a Graphical User Interface (GUI) software which was developed as part of the thesis (see Appendix 1). This software was designed to facilitate potential field forward modelling and integration with complementary data sets such as

topography, seismic and well data.

4.6.2 Lithospheric reference model

Parameter	Symbol	Value	Units
Thermal thickness	T_L	170	km
Zero elevation crustal thickness	T_c	35	km
Crustal density at 0 $^\circ C$	ρ_c^*	2810	$kg\ m^{-3}$
Mantle density at 0 $^\circ C$	ρ_m^*	3310	$kg\ m^{-3}$
Water density	ρ_w	1030	$kg\ m^{-3}$
Coefficient of thermal expansion	α	3.28×10^{-5}	$^\circ C^{-1}$
Mantle potential temperature	T_p	1333	$^\circ C$
Thermal diffusivity	κ	0.008	$cm^2\ s^{-1}$
Crustal thermal conductivity	K_c	3.138	W $m^{-1}\ K^{-1}$
Lithospheric mantle thermal conductivity	K_m	3.138	$W\ m^{-1}\ K^{-1}$
Acceleration due to gravity	g	9.81	$m\ s^{-2}$
Internal heat generation	HFC	0	HFU
Young's modulus	E	100	GPa
Poisson's ratio	v	0.25	–
Infill density	ρ_{infill}	1030	$kg\ m^{-3}$
Sediment density (POGM)	ρ_s	2460	$kg\ m^{-3}$
Buried load density (POGM)	ρ_l	2985	$kg\ m^{-3}$

Table 4.1: Summary of parameters used in isostatic balancing and POGM.

Gravity anomalies are calculated by determining the effects of mass anomalies, as defined by density contrasts with respect to a reference section. For the case of crustal scale gravity modelling, a useful approach is to define a lithospheric reference section against which density anomalies are modelled. Of particular importance is the thickness of the reference section crust, as the contribution of Moho topography to the calculated gravity anomaly will vary in both wavelength and amplitude depending on the depth of the reference interface. Crucially, the reference section is assumed to be in a state of local isostatic equilibrium and produces no gravity anomaly.

Worzel and Shurbet (1955) were the first to attempt to define reference sections for both continental and oceanic lithosphere. Their approach involved determining which values for the relevant parameters (densities and thicknesses) could be used to achieve local isostatic equilibrium between idealised continental and oceanic reference sections, while also producing

the best agreement with observed gravity, elevation and crustal thickness data from a suite of locations worldwide, where these parameters were thought to be well constrained.

An alternative approach is to ascertain what parameters are required to isostatically balance a reference continental section at zero elevation, against a standard mid-ocean ridge crest, which is known to be in local isostatic equilibrium (i.e., the integration of the free-air gravity anomaly with respect to distance along a ridge-normal profile approximately sums to zero) (e.g., Cochran, 1981; Cochran, 1983).

In this study, the latter approach is adopted. A lithosphere thickness of 170 km is assumed for Parnaíba basin, following the results of surface wave tomography modelling (Priestley and McKenzie, 2013) and a continental crustal thickness at zero elevation of 35 km is assumed. There is some uncertainty as to what value is most reasonable to assume as the reference crustal thickness in this setting; however, an initial crustal thickness of 35 km is assumed given (1) seismically derived present-day crustal thickness in the flanking regions of the basin is typically ∼32–38 km (e.g., Assumpção et al., 2013; Luz et al., 2015b) and (2) most of the early sediments of Serra Grande megasequence were deposited at or near sea level. This is significant as global compilations of crustal thickness (Bassin, 2000) and elevation (Amante and Eakins, 2009) show a peak at 30–32 km for elevations of ± 150 m, while thicknesses of > 40 km are usually associated with high topography due to isostasy (Fig. 4.9).

This lithospheric section is balanced against a mid-ocean ridge crest consisting of a 5 km thick crust at 2.5 km water depth (e.g., Fig. 4.10; Cochran, 1982), assuming the parameters in Table 4.1 and a simple linear geotherm from 0 $°C$ at the surface to 1333$°C$ at the base of the lithosphere (e.g., Cochran, 1981). The mantle potential temperature was set as 1333$°C$ following results from Parsons and Sclater (1977) and the 0°C lithospheric-mantle density was solved for, so as to produce an internally consistent isostatic balance of the two columns (e.g., Fig. 4.10; Cochran, 1982). This returns a lithospheric mantle density of 3310 $kg\ m^{-3}$ and suggests a -20 $kg\ m^{-3}$ reduction in density is required with respect to the density obtained (i.e., 3330 $kg\ m^{-3}$) for balancing a standard 125 km thick lithosphere (e.g., Cochran, 1982). This is consistent with chemical depletion predicted for thickened continental cratonic lithosphere in order to maintain buoyancy and prevent the development of a gravitational instability (e.g.,

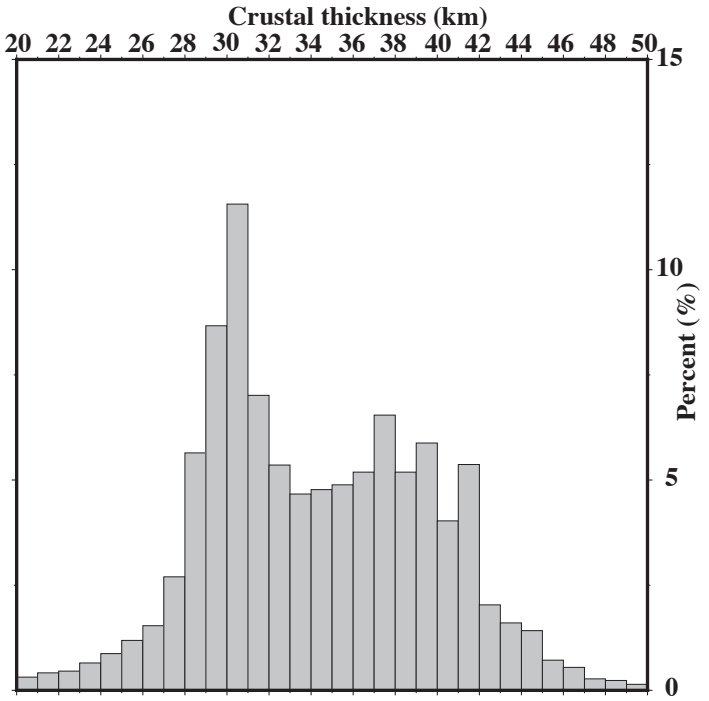


Figure 4.9: Histogram of global crustal thickness estimates for elevations within ± 150 m of mean sea level. Elevation data are from ETOPO1 (Amante and Eakins, 2009) and crustal thickness estimates are from CRUST1.0 (Bassin, 2000).

Jordan, 1975; Artemieva and Mooney, 2001; Crosby et al., 2010).

4.6.3 Model constraints

Non-uniqueness is a well known problem in gravity modelling. Theoretically, an infinite number of models exist that can explain a given anomaly (Hjelt, 2006). Therefore, all available independent data were used to constrain the model in order to reduce ambiguity. Specifically, bulk densities of sedimentary formations recorded in well logs, the depth converted regional PBAP seismic reflection profile (Fig. 3.9), the box wave wide-angle reflection model (Fig. 3.16) and surface geology outcrops were used to constrain the gravity models presented in this chapter.

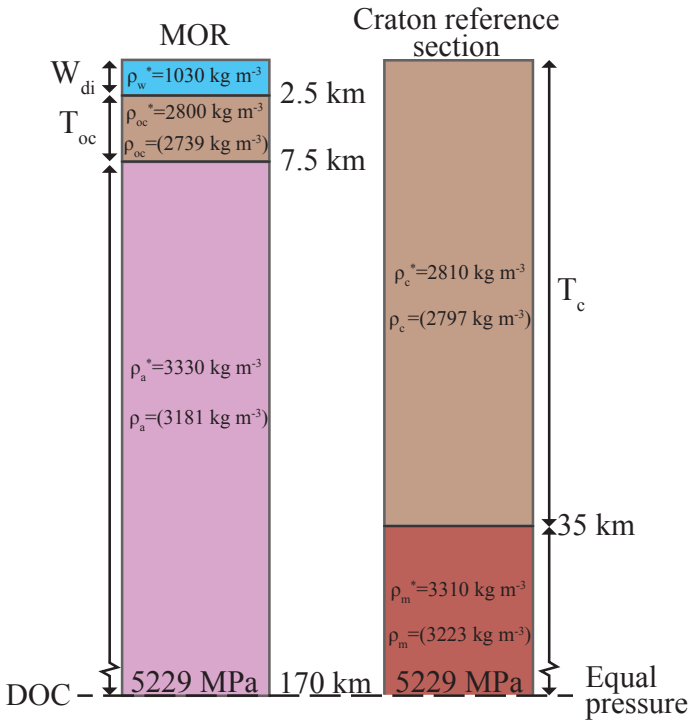


Figure 4.10: Isostatic balance of a standard mid-ocean ridge crest assumed to be in isostatic equilibrium, balanced against a "reference" continental lithospheric section, 170 km thick. Assuming standard parameters for the mid-ocean ridge section and continental crust (as depicted) and a constant coefficient of thermal expansion, α, of $3.28e^{-5}$ $^{\circ}C^{-1}$. *Densities are those at $0^{\circ}C$ and those in brackets are average densities once thermal expansion is accounted for.

4.6.3.1 Sedimentary formation densities

Average bulk densities for each stratigraphic formation were obtained from bulk density measurements made within six boreholes throughout Parnaíba basin. These data are shown in Figure 4.11. In construction of the forward model presented below, the density of each sedimentary formation was assigned as the mean value obtained from these measurements and held fixed during the forward modelling procedure.

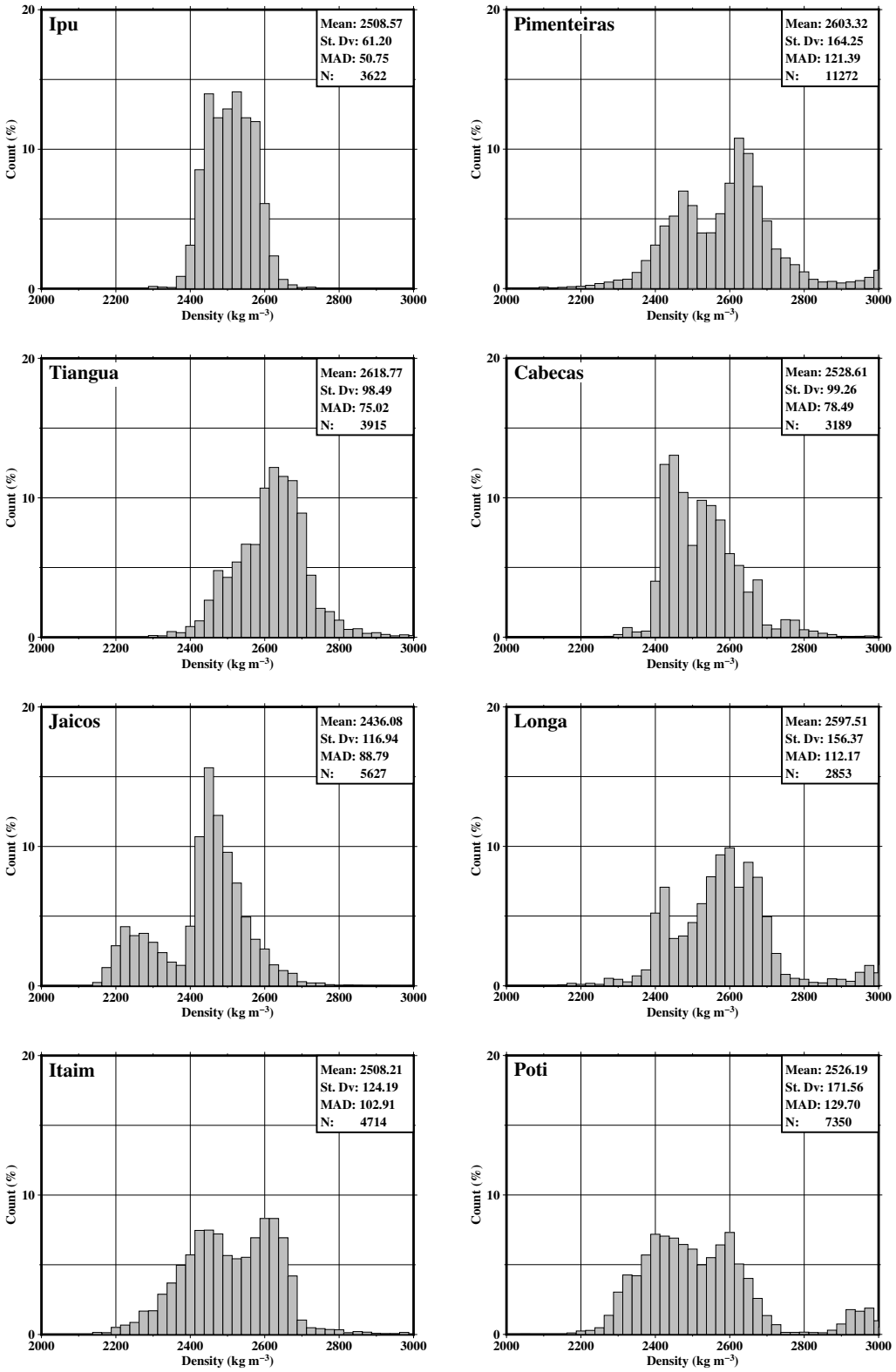


Figure 4.11: Formation bulk density estimates from compilations of petrophysical log records for all formations with Parnaíba basin. The mean values are used for gravity modelling obtained from bulk density measurements obtained from a variety of boreholes throughout the basin at various depths. St. Dv = Standard deviation; MAD = Mean absolute deviation; N = Number of data points.

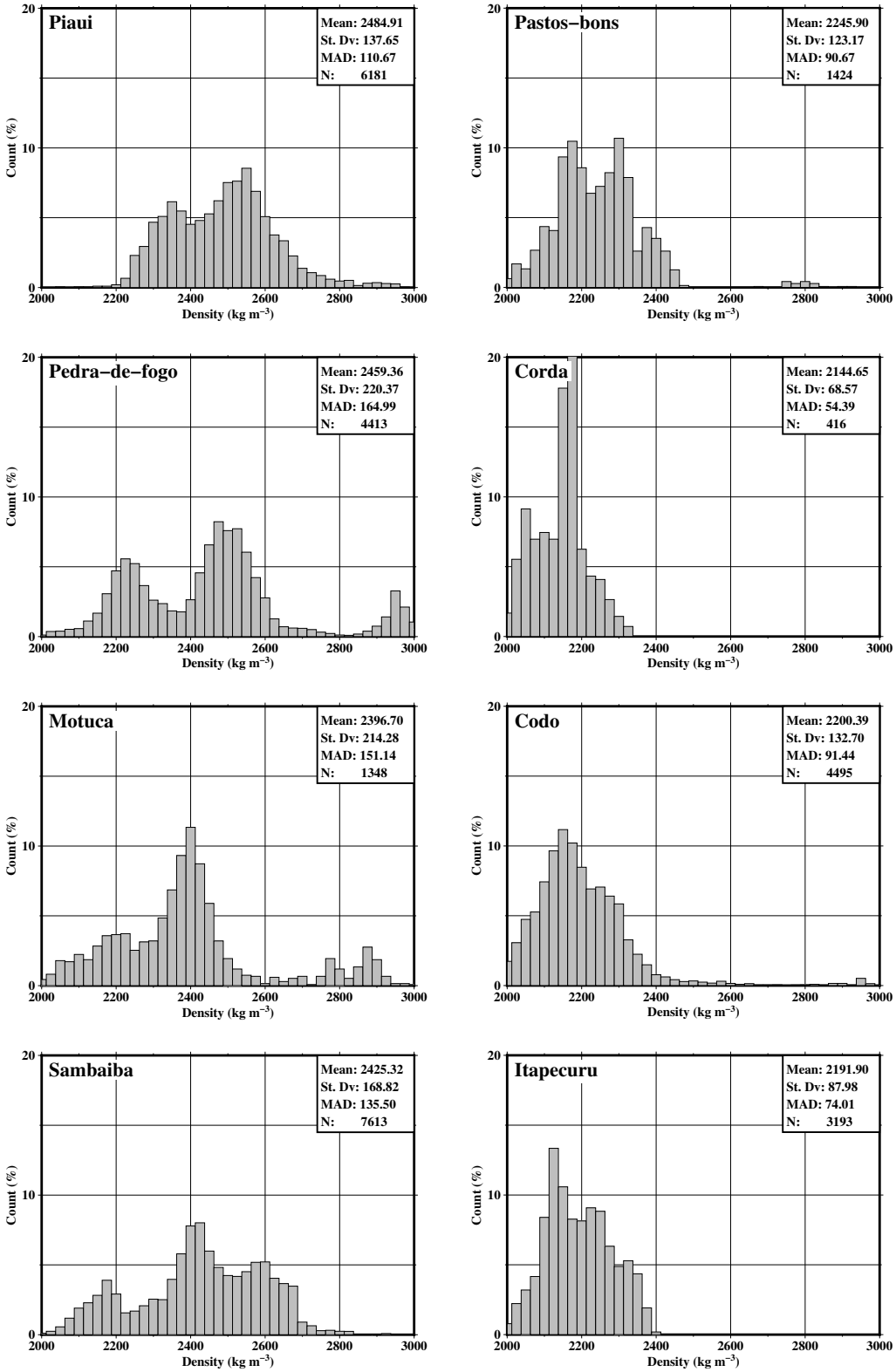


Figure 4.11 continued

4.6.3.2 Seismic reflection structure

The geometries of sedimentary formations were determined from interpretation of the regional seismic reflection profile and surface outcrops (see Section 3.2.3). Similarly, surface boundaries between crustal terrains (e.g., the Amazonian craton and Araguaia belt) were defined from their geological outcrops constrained at depth using the post-stack depth migrated regional reflection profile. However, the velocity model used to perform the post-stack depth migration of the regional reflection profile is not constrained below a depth of ~ 5 km, and hence, the deep interfaces, such as the Moho and MCR, were not held fixed at their exact reflection depths during modelling; instead, the reflections were used as starting estimates and modified as required to satisfy the gravity data.

4.6.3.3 Boxwave P-wave velocity model

Interface depths derived via forward P-wave velocity (V_p) modelling (Chapter 3) were used as constraints in the starting forward gravity model for the Moho and middle crust. However, given that the relationship between V_p and density is dependent on rock composition (which is unknown) the density model was constructed independently from the V_p structure derived in Section 3.5). Consistency between the final density and V_p values was tested by converting the final V_p values to densities using the empirically derived curves of Ludwig et al. (1970) and Brocher (2005) and comparing them to the final density values. The Ludwig et al. (1970) curve was constructed mainly using sedimentary and some igneous rocks (i.e., oceanic crust samples), while the Brocher (2005) curve used a wide range of rock types including mafic and ultramafics. This showed that the densities are within $\pm$ 3 % of the average relationship given by the Nafe-Drafe curve and are also consistent with the values presented in the global data compilations of Christensen and Mooney (1995) and Vacher and Souriau (2001).

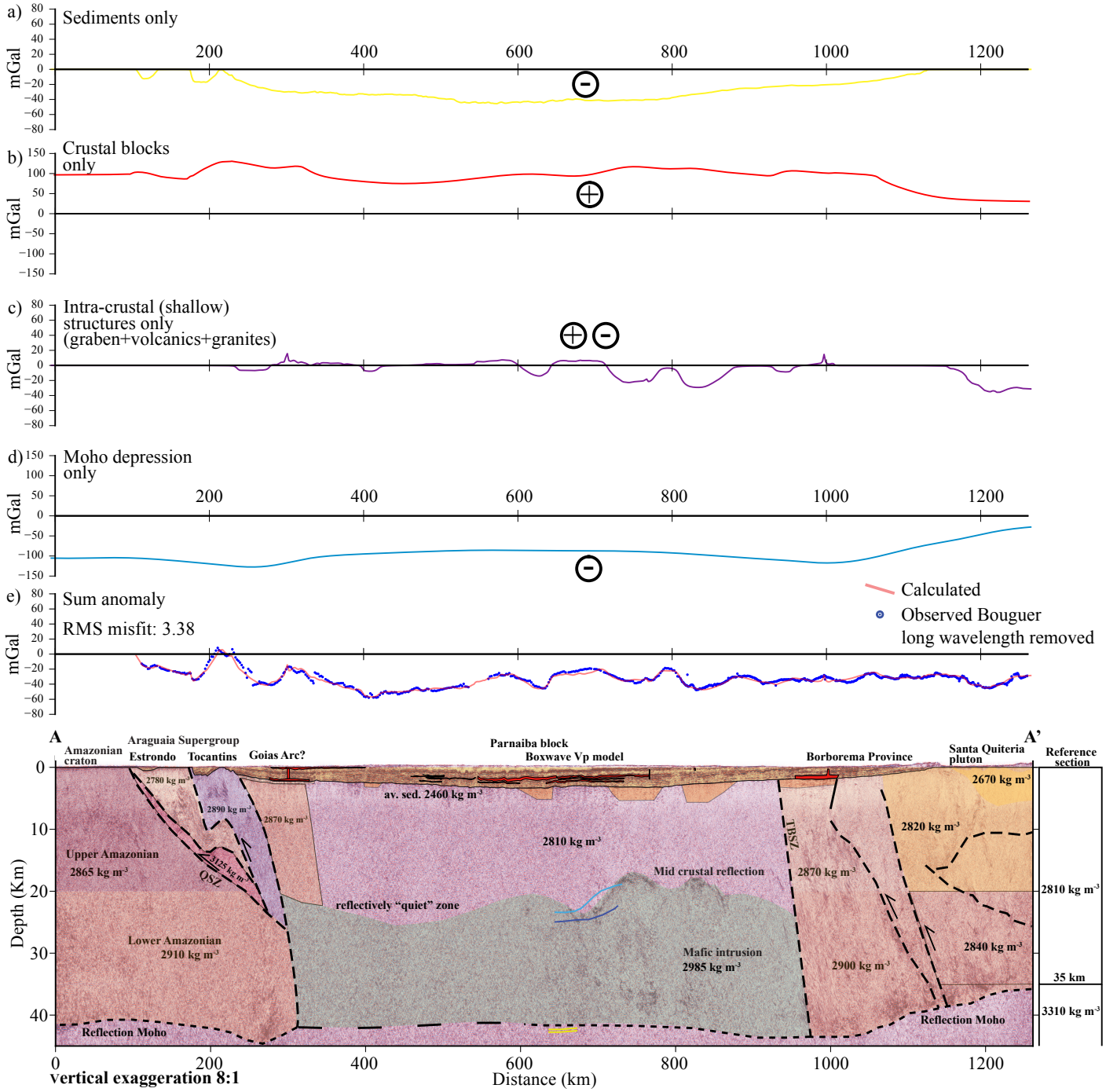
4.6.4 Model results

Figure 4.12 shows the final two-dimensional Bouguer anomaly forward model derived for the regional PBAP transect. The contribution towards the total calculated anomaly of particular

aspects of the model are shown as panels in (Fig. 4.12a–d). The final sum anomaly is shown in Figure 4.12e. The sum anomaly comprises two main negative contributions: one from the relatively low density sediments ($\sim$ 45 $mGal$) and the other from the displacement of low-density crust into denser mantle ($\sim$ 90 $mGal$). The combined negative contribution amounts to some $\sim$ -135 $mGal$. The main positive contribution arises from the relatively high density lower crust (the upper surface of which is defined by the MCR) compared to surrounding regions and results in a positive anomaly of up to $\sim$ + 100 $mGal$. The existence of an anomalously dense body within the lower crust of the Parnaíba basin has also been suggested by Sousa (1996). When the gravity effect of this mass excess is combined with the mass deficiency due to the sediments and crustal thickening, it yields a net gravity anomaly of -135 + 100 = $\sim$ -35 $mGal$, which is of similar amplitude to the observed Bouguer gravity anomaly. It is noteworthy that the dense lower crust in Figure 4.12 has been modelled as a single body with a uniform bulk density contrast with its surroundings. This is not the only explanation of the gravity anomaly. For example, the anomaly could have been modelled equally well with a number of smaller bodies, as has been recently suggested by inversion of magnetotellurics data acquired along the PBAP regional profile (Solon et al., 2016). These smaller bodies would, however, require higher-density contrasts than is used for the single body.

The relatively large Moho depression of the Amazonian craton beneath the Araguaia belt produces a large negative gravity anomaly at the western edge of the basin (Model km 250–300). The inclusion of relatively high-density crustal densities for the amphibolites and schists of the Estrondo and Tocantins groups respectively are unable to fully compensate for this anomaly. It was found, through forward modelling, that the amplitude and wavelength of this anomaly could be reconciled by including a high-density (3125 $kg\ m^{-3}$) body at the base of this sequence, representing the subsurface extension of the ophiolitic Quatipuru and Serra do Tapa ophiolites (e.g., Paixao et al., 2008) that outcrop adjacent to the Araguaia belt near the western edge of Parnaíba basin (Fig. 4.2).

The other main features of the observed Bouguer gravity anomaly are local lows of $\sim$ 20 $mGal$ which are attributed to (1) pre-Silurian narrow graben-like structures, containing sediments of the Jaibaras or Riachão formations; and/or (2) anorogenic granites equivalent to those that outcrop near the Northeast edge of the basin, adjacent to the Jaibaras trough.


a) Sediments only
b) Crustal blocks only
c) Intra-crustal (shallow) structures only (graben+volcanics+granites)
d) Moho depression only
e) Sum anomaly
RMS misfit: 3.38
mGal
Calculated
Observed Bouguer
long wavelength removed
A
A'
Amazonian craton
Araguaia Supergroup
Estrondo
Tocantins
Goias Arc?
Parnaiba block
Boxwave Vp model
Borborema Province
Santa Quiteria pluton
Reference section
2780 kg m-3
2890 kg m-3
2870 kg m-3
av. sed. 2460 kg m-3
2810 kg m-3
2670 kg m-3
2820 kg m-3
Upper Amazonian
2865 kg m-3
QSZ
3125 kg m-3
Mid crustal reflection
TBSZ
2870 kg m-3
reflectively "quiet" zone
Lower Amazonian
2910 kg m-3
Mafic intrusion
2985 kg m-3
2900 kg m-3
2840 kg m-3
35 km
3310 kg m-3
Reflection Moho
Reflection Moho
Depth (Km)
Distance (km)
Vertical exaggeration 8:1

Unfortunately, the image quality at basement depths along the PBAP reflection profile is poor and no structure is resolved. The best fit geometry of these structures have inwardly directed edges, characteristic of grabens. However, the anomalies are similar in form to others identified elsewhere in the basin on shallow focused industry reflection data (e.g., de Castro et al., 2016) which were found to be sourced within the basement, adjacent to pre-Silurian graben-like structures. Hence, de Castro et al. (2016) suggested these anomalies could be caused by the presence of relatively low density of granite.

Irrespective of these uncertainties in the origin of the short wavelength gravity anomalies, Figure 4.12 shows that it is possible to account for the observed Bouguer anomalies in a way that is compatible with the seismic reflection and refraction data presented in Chapter 3. The fact that our best fit model has a relatively dense lower crust is clearly significant for our understanding of the origin of the basin and key to this is the tectonic subsidence and uplift history of the basin as revealed, for example, by backstripping well and sediment isopach data, as presented in the next Chapter.

Figure 4.12 ***(preceding page)*:** Comparison of observed and calculated Bouguer gravity anomalies along the PBAP seismic reflection profile. (a) Gravity effect of the sediments only. (b) Gravity effects of intracrustal structures only. (c) Gravity effect of the main crustal blocks. (d) Gravity effect of the Moho depression. (e) Comparison of observed and calculated Bouguer gravity anomalies. The observed anomaly (blue circles) has had the regional gravity field (to degree and order 12) removed. The calculated anomaly (red line) is based on the sum of the anomalies shown in a–d. (f) Crustal structure showing the depth converted seismic data and the body geometries and densities used in the gravity calculations. Red shaded areas within the sedimentary basin are volcanics interpreted from wells and reflectivity. The reference section for the calculation of the density contrasts is shown to the right of the seismic profile. Coloured lines are interfaces from the box wave V_p model shown in Figure 3.16. av. Sed. = sediment density averaged over all formations.

4.7 Process oriented gravity modelling

An alternative approach for modelling gravity anomalies from the "object oriented" approach taken in the previous section is one in which geological processes such as those involved in sedimentation, crustal thinning and magmatism are explicitly included in the modelling process. A useful first order approach is to consider the lithosphere as a simple elastic beam overlying an inviscid fluid, such that, the response to loading is modelled using the well-understood phenomena of elastic plate flexure. Using such an approach, the gravity anomaly predicted for a given load, such as basin sediment infill, as well as the gravity anomaly due to the flexural compensation of the load are computed. In this way, the first order geological history of a given locality can be recovered if a particular set of processes is shown to reproduce the observed gravity anomaly. Moreover, the long-term equivalent elastic thickness T_e of the lithosphere can also be constrained. Watts et al. (1988) used this approach to develop a technique termed Process Oriented Gravity Modelling (POGM). POGM has been successfully applied to a number of rift-type basins in the East Coast USA, Mozambique, Antarctica and India margins where it has been used with some success to constrain T_e of extended continental lithosphere and the location of the Ocean-Continent Boundary (e.g., Watts, 1988; Watts and Fairhead, 2013; Close et al., 2009; Krishna et al., 2000).

As a comparative example between the differing approaches, i.e., process and object oriented modelling, consider the formation and gravity anomaly produced by a simple sedimentary basin. Using a process oriented approach this may be considered as a two step process: first, a depression forms and is infilled by water. If a 3 km deep depression is formed and water and crust densities of 1000 and 2800 $kg\ m^{-3}$ are assumed, this would produce a negative gravity anomaly of $\sim -230\ mGal$. Next, if the depression is then filled with sediment and there is no additional "tectonic processes" (i.e., isostatic load response or Moho involvement) and a sediment infill density of 2400 $kg\ m^{-3}$ is assumed, a resulting positive anomaly of $\sim +176\ mGal$ would be produced. Hence, the net anomaly is a negative of $\sim -54\ mGal$. In "object-oriented" modelling, this anomaly would be modelled using a traditional forward modelling approach, using the basins observed geometry and a density contrast of $2400 - 2800\ kg\ m^{-3}$ (i.e., sediment relative to the surrounding crust) and the resulting anomaly is the same.

However, from a geological "process-oriented" perspective, it is expected that basin formation involves some form of isostatic compensation, such as crustal thinning, which also needs to be included in the model. By taking this approach, the gravity anomaly can then be modelled in such a way as to deduce information regarding the tectonic history of a region.

4.7.1 Gravity anomaly calculation method

In POGM, gravity anomalies are calculated using a Fourier domain method (e.g., Karner, 1982; Watts, 2001). This method is used in place of the analytical solution used for forward modelling as the Fourier transform of layer interfaces are also required for the flexure calculations and this method is more computationally efficient than the space domain method. Using this method, the gravity anomaly is given by:

$$\Im[\Delta g(x)] = 2\pi G \Delta\rho \, \Im[h(x)] e^{-kd} \tag{4.16}$$

Where $\Im$ is the Fourier domain equivalent of the given parameter; Δg is the gravity anomaly at position x; G is the universal gravitational constant; $\Delta\rho$ is the density contrast across the interface; $h(x)$ is the vertical deviation of the interface relative to its mean depth, d, and k is the wavenumber related to wavelength, λ, by $2\pi/\lambda$.

It should be noted that this is a first order approximation to the Frequency domain expression. The full expansion is given by Parker (1973) as:

$$\Im[\Delta g(x)] = 2\pi G \Delta\rho \, e^{-kd} \sum_{n=1}^{\infty} \frac{k^{n-1}}{n\,!} \, \Im[h^n(x)] \tag{4.17}$$

However, this solution converges rapidly due to the $n\,!$ term. If extra accuracy is required for undulating interfaces, summing up to and including the forth term is usually sufficient.

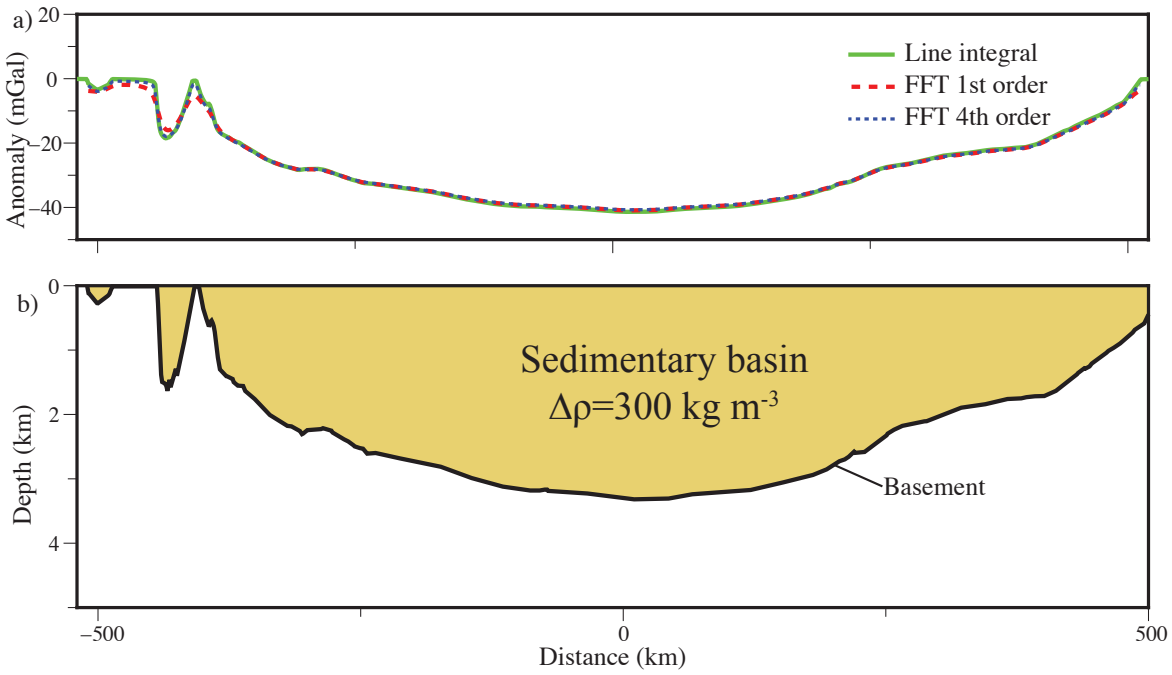


Figure 4.13: Comparison of gravity anomalies computed using an exact line-integral method (green line) and both first (dashed red line) and fourth-order (dashed blue line) Fourier methods for a simple sedimentary basin, similar in shape to Parnaíba basin, with a bulk density contrast of -300 $kg\ m^{-3}$. Note the first-order method fails to compute the anomaly accurately near the steep gradients on the western side of the basin.

4.7.2 POGM: Rifting model

In the case of extensional sedimentary basins and rifted continental margins, POGM, as described by Watts and Fairhead (1999), is a three-step process: First, the known sediment distribution is flexurally backstripped for a particular T_e and the backstrip used to restore the crustal structure at the time of rifting assuming isostasy (see Section 5.4.1 for a detailed discussion regarding flexural backstripping). Second, the 'rifting anomaly' is calculated from the sum of the negative gravity effect of the backstripped, water (or air) filled basin subsidence, and the positive gravity effect of the thinned, rifted crust and the 'sedimentation anomaly' is given by the sum of the gravity effect of the sediment load and its flexural compensation. Finally, the rifting anomaly and sedimentation anomaly are summed to produce the predicted anomaly (Fig. 4.14).

In order to quantify the role that rifting may have played in the development of the Parnaíba basin, POGM was applied to the regional PBAP transect. Figure 4.15 shows the

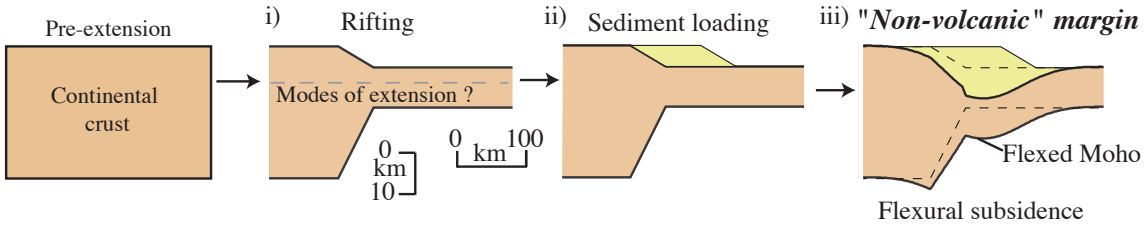


Figure 4.14: A simple example of geological processes that may be considered when applying Process-Oriented Gravity Modelling. i) Continental rifting, which involves thinning of the crust and basin formation. ii) Sedimentation. iii) Flexural compensation of the sediment load at the basement and Moho. Dashed grey lines are pre-flexed interfaces.

'rifting', 'sedimentation' and 'sum anomaly' for a zero elevation, 1000 km wide and 3.5 km deep symmetric basin, of similar geometry to Parnaíba basin with a basin-wide mean sediment density of 2460 $kg\ m^{-1}$. The assumed values of the unstretched, zero elevation crustal thickness and density of water, sediments, crust and mantle are listed in Table 4.1. The rifting anomaly shows an edge effect 'high-low' couple, typical of rifted margins. The sedimentation anomaly shows a broad high and two flanking lows due to the mass excess of the sediments and the mass deficiency of their flexural compensation. As would be expected for an isostatic process, the sum anomaly averages to zero and comprises a small amplitude 'high' over the basin centre, which is flanked by a broad 'low'.

Comparison of the predicted depths to Moho and gravity anomalies to observations show significant discrepancies. First, the predicted depth to Moho in the centre of the basin is less than the seismic depth to Moho (by $\sim 8\ km$) as determined by wide-angle seismic data. Second, the predicted anomalies are near zero or positive over the basin, in contrast to the observed Bouguer anomaly which exhibits a regional negative anomaly of $\sim$ -30 $mGal$. Hence, a basin evolution which consists solely of lithospheric rifting appears inconsistent with the basins gravity anomaly.

4.7.3 POGM: Buried load model

Given it was shown in the previous section that a rifting model appears incapable of reproducing the observed gravity anomaly, a buried loading model was also investigated using POGM. The physical parameters of the buried load (i.e., width, thickness, and density contrast) were

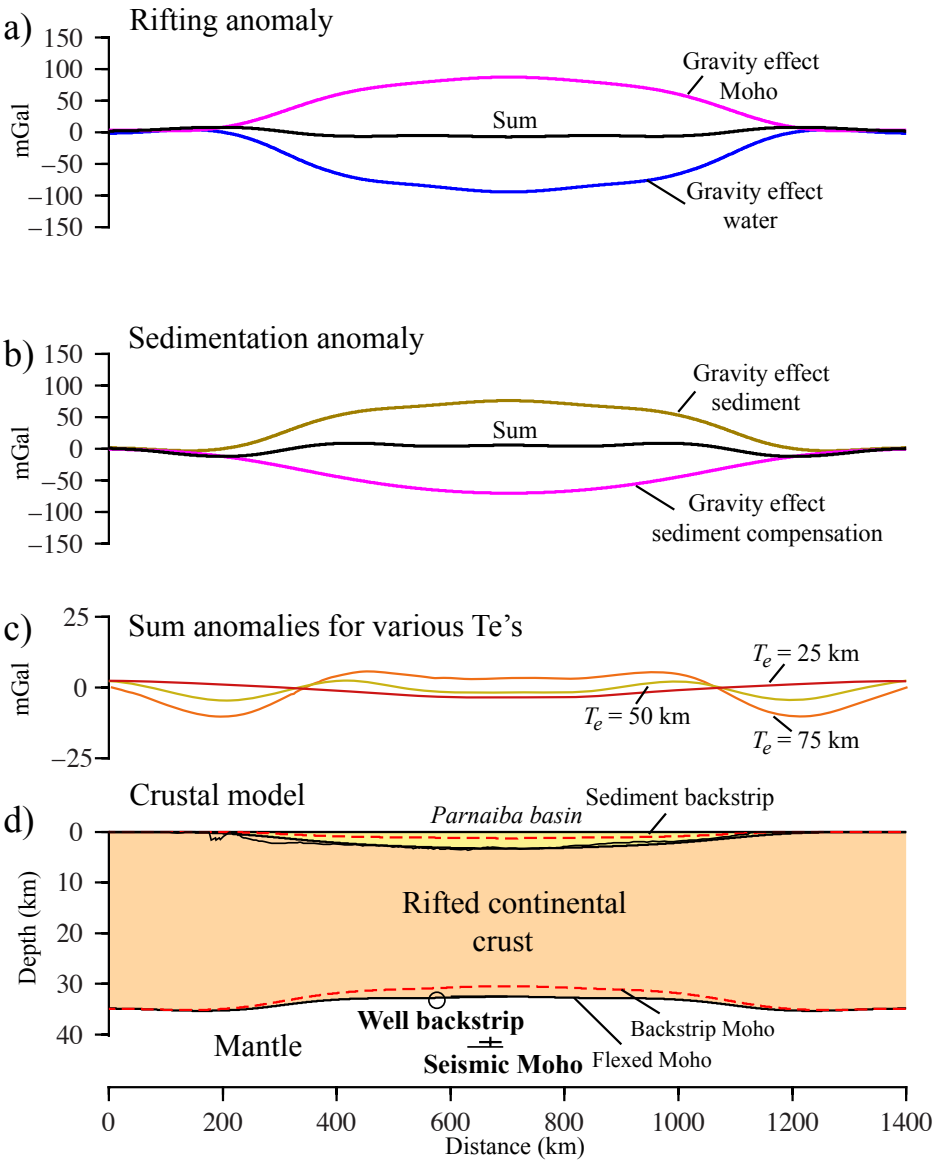


Figure 4.15: Process-Oriented Gravity Modelling (POGM) of a symmetric basin with a similar geometry (i.e., width and depth) to the Parnaíba basin assuming that the only processes that are operative are rifting, which thins the crust, and sediment loading. The thickness of zero elevation crust and the densities assumed for the water, sediment, crust, and mantle are summarised in Table 4.1. (a) Gravity effect of rifting showing the individual contributions from the water-filled depression and the elevation of the Moho. (b) Gravity effect of the sediment load and its compensation at the sediment/basement and crust/mantle interfaces. (c) Sum anomalies obtained by summing the rifting and sedimentation anomalies. (d) Crustal model. The modelling shows that irrespective of the elastic thickness, a rifting model predicts near zero gravity anomalies and a shallower Moho beneath the basin than its flanks. Seismic Moho and MCR (Mid Crustal Refection interfaces) from seismic analysis (see Chapter 3). Backstrip Moho = predicted Moho from Air-backstripping (see Section 5.5.)

prescribed using constraints from the seismic and gravity modelling presented in Chapter 3 and Section 4.6. The gravity anomalies produced by the buried load, along with the surface

and Moho flexure it causes, assuming that the surface flexure is infilled by water, were calculated. This is the so-called "buried loading" anomaly. Second, sediments are assumed to infill the surface flexure by displacing water, and constituting an additional load on the crust, causing additional flexure of the basement and Moho. This is the sedimentation anomaly. Finally, the sum is calculated by combining the buried loading and sedimentation anomalies (Fig. 4.16).

Figure 4.17 compares the sum anomalies from POGM for the rifting and buried loading cases to the observed Bouguer gravity anomaly. For the purposes of the comparison, the measured gravity anomalies are extended along the PBAP transect by $\sim 150\ km$ using data sampled from the $2.5' \times 2.5'$ EGM2008 gravity model (Pavlis et al., 2012).

The buried loading model, in which a dense body in the lower crust causes a surface flexure into which sediments can accumulate does appear capable of explaining the broad negative anomaly over the basin and is also in closer agreement to the observed crustal structure. Although for a case where $Te = 50\ km$ (as shown in Figure 4.17) the Moho is slightly shallower in the basin centre ($\sim 40\ km$) than predicted from wide-angle seismic data ($\sim 42\ km$) but is within the predicted error of of $\pm\ 2\ km$. The Moho is, however, deeper in the centre of the basin than in the flanking regions (e.g., Assumpção et al., 2013; Luz et al., 2015a), as is evident beneath Parnaíba basin on the regional region profile (e.g., Daly et al., 2014; Fig. 3.9).

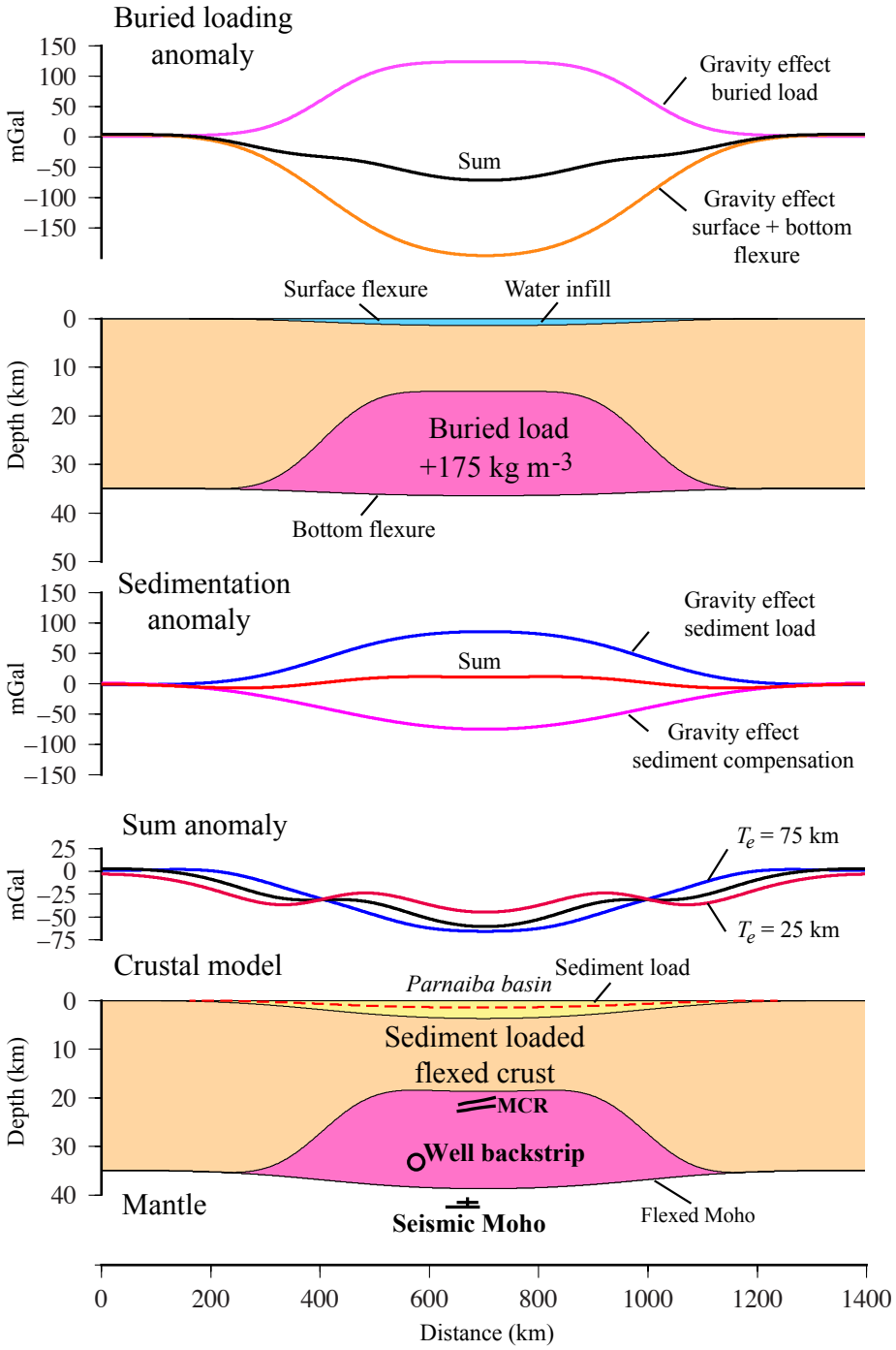


Figure 4.16: Process-Oriented Gravity Modelling (POGM) of a sedimentary basin with a similar geometry (i.e., width and depth) to the Parnaíba basin that formed by buried loading. The gravity effect of buried loading and its resulting water-filled surface flexure was calculated using the same method densities and T_e as assumed in Figure 4.15. (a) Gravity effect of buried loading showing the individual contributions from the buried load and its resulting water-filled surface flexure. (b) Crustal model. (c) Gravity effect of the sediment load and its compensation at the sediment/basement and crust/mantle interfaces. (d) Sum anomalies obtaining by adding the buried and sediment gravity anomalies. (e) Crustal model. The modelling shows that irrespective of the assumed elastic thickness, negative gravity anomalies are predicted. In addition, Moho occurs at a deeper depth beneath the basin than its flanks. Seismic Moho and MCR (Mid Crustal Refection interfaces) from seismic analysis (see Chapter 3). Backstrip Moho = predicted Moho from Air-backstripping (see Section 5.5.)

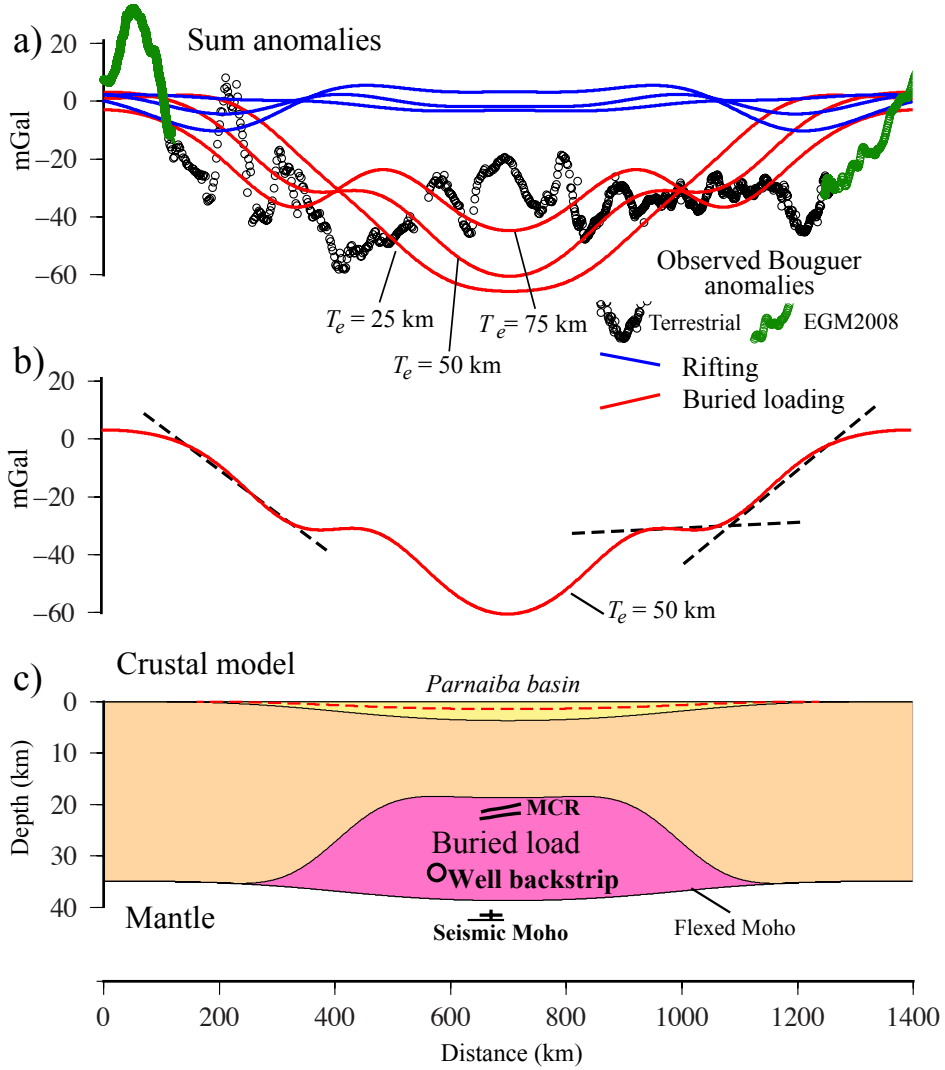


Figure 4.17: Summary diagram showing the results of Process-Oriented Gravity Modelling (POGM). (a) Comparison of the observed Bouguer gravity anomalies (black + green open circles) to the calculated sum anomalies derived from POGM of rifting (blue curves) and buried loading (red curves). (b) Calculated gravity anomaly for buried loading with Te = 50 *km*. Dashed black lines show those segments of the calculated gravity anomalies that explain the observed anomalies particularly well. (c) Crustal structure implied by the buried loading model. Seismic Moho and MCR (Mid Crustal Refection interfaces) from seismic analysis (see Chapter 3). Backstrip Moho = predicted Moho from Air-backstripping (see Section 5.5.)

4.8 Three dimensional modelling

Gravity analysis was extended to three-dimensions using the composite satellite and terrestrial derived EGM2008 $2.5' \times 2.5'$ free-air gravity anomaly data (Fig. 4.18b) (Pavlis et al., 2012).

4.8.1 Sediment corrected "residual" anomaly reduction

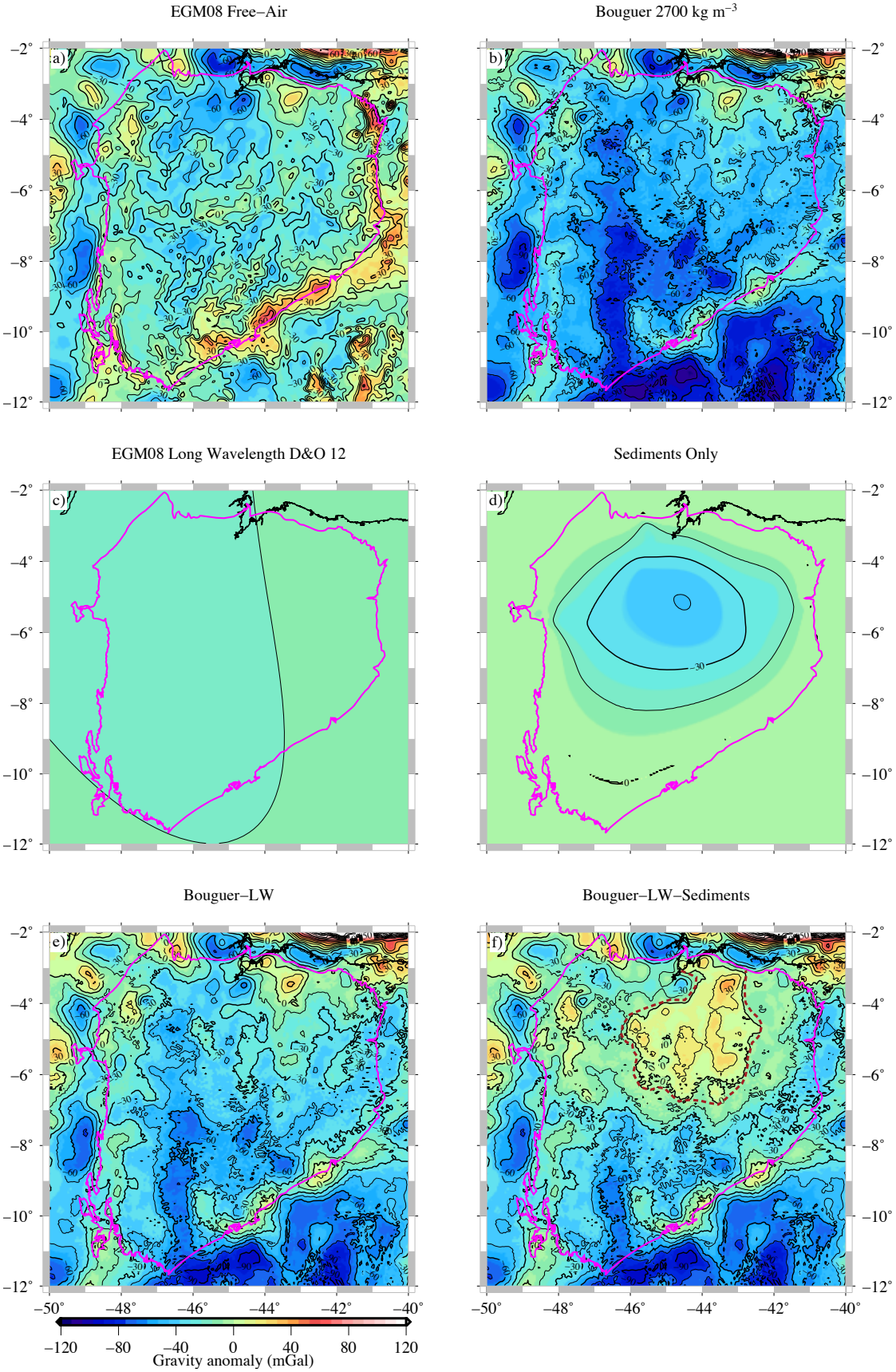
In order to better understand the crustal and lithospheric structure beneath Parnaíba basin, EGM2008 data were corrected for the effect of the sedimentary basin, in order to isolate the anomaly associated with the sub-sediment deeper structure, such as a dense lower crust.

To derive these "residual" Bouguer anomalies, three reduction steps were applied:

Firstly, standard Bouguer and terrain corrections were applied, as described in Section 4.4 but using a Bouguer slab density of 2700 $kg\ m^{-3}$ (an average of the basin sediments and surrounding basement). This reduction density is similar to that used by Mooney and Kaban (2010) for continental North America and is used for consistency with equivalent analysis that is applied to the Michigan and Congo cratonic basins in Chapter 6. The resulting Bouguer gravity anomaly is shown in Figure 4.18b. It can be seen that the regional basin-wide Bouguer anomaly beneath Parnaíba basin is similar to that observed along the two-dimensional PBAP regional transect, characterised by a ~ -30 to -60 $mGal$ low.

Secondly, the very long wavelength portion of the gravity anomaly, as defined by EGM2008 spherical harmonic coefficients up to and including degree and order 12 (minimum wavelength ~ 3330 km), were removed from the Bouguer anomalies. Similarly to as described in Section 4.4.8.

Finally, the static gravity effect of the cratonic basin sedimentary fill was calculated based on the regional sediment thickness map derived from well and seismic data (Figs. 3.3 and 4.19) using the three-dimensional analytic solution of Talwani and Ewing (1960). Using this method, the three-dimensional structure is treated as a series of n-sided horizontal laminae of constant density and thickness (defined by structural depth contours), the gravity anomaly


EGM08 Free–Air
Bouguer 2700 kg m^{-3}
EGM08 Long Wavelength D&O 12
Sediments Only
Bouguer–LW
Bouguer–LW–Sediments
a)
b)
c)
d)
e)
f)
−2°
−4°
−6°
−8°
−10°
−12°
−50°
−48°
−46°
−44°
−42°
−40°
−120
−80
−40
0
40
80
120
Gravity anomaly (mGal)

of each laminae is then determined and summed to produce the total anomaly. A contour interval of 100 m and basin-wide average sedimentary basin bulk density of 2460 $kg\ m^{-3}$ were used for this calculation.

The residual anomaly is shown in Figure 4.18f. This reveals the basin is characterised by a sub-circular residual anomaly "high" in the central/northern section of the basin. The position of this high becomes more basin-central if one considers the likely northern extension of the basin prior to the opening of the Atlantic ocean, i.e., what is now the Saltpond basin, located off the Ghanaian coast of West Africa (Atta-Peters et al., 2015). In the South, the basin is characterised by a residual low. Much of this anomaly correlates with the Riachão basin, which underlays Parnaíba basin in this region and reaches a maximum thickness of $>$ 3 km (Porto et al., In press).

Parameter	Symbol	Value	Units
Density of load	ρ_l	2985	$kg\ m^{-3}$
Base radius of load	Lr	400	km
Maximum height of load	Lh	20	km
Density of crust	ρ_c	2810	$kg\ m^{-3}$
Density of surface infill	ρ_w	1030	$kg\ m^{-3}$
Density of sediment infill	ρ_s	2460	$kg\ m^{-3}$
Density of mantle	ρ_m	3310	$kg\ m^{-3}$
Initial crustal thickness	Tc	35	km
Elastic thickness	Te	25, 50 and 75	km
Young's modulus	E	100	GPa
Poisson's ratio	σ	0.25	-
Gravitational acceleration	g	9.81	$m\ s^{-2}$

Table 4.2: Summary of parameters used in three-dimensional flexural and gravity modelling.

One source that has not been considered in the derivation of the residual anomaly is the intrusive volcanics of the Sardinha and Mosquito formations. These are thought to have a bulk

Figure 4.18 ***(preceding page)*****:** Parnaíba basin gravity anomalies and gravity components as labelled. Note all anomalies are plotted using the same colour scale. Note the long wavelength anomaly shown in (c) is the same as that shown in figure 4.6c and the sedimentary basin anomaly (d) is the same as that shown in 4.19b. The pink solid line shows the Parnaíba basin outline. The dashed red line in (f) outlines the general extent of the central gravity "high".

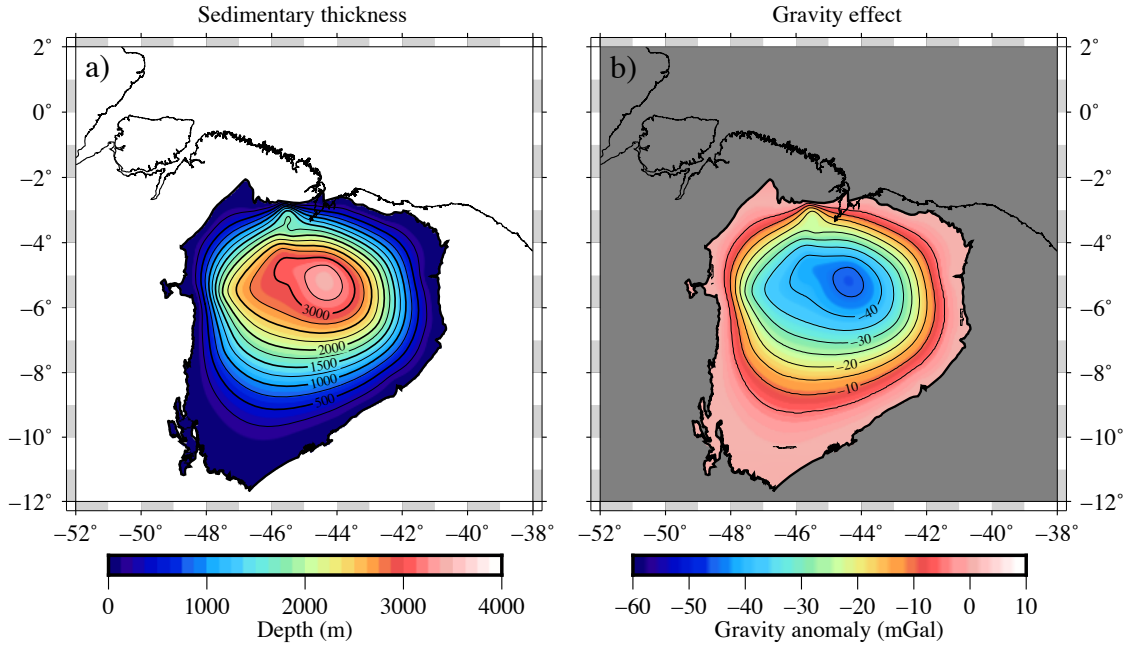


Figure 4.19: a) Regional sediment thickness contour map of the Parnaíba cratonic basin section of the Parnaíba basin as derived in Figure 3.3. b) Gravity effect of the basin shown in (a) calculated using the method of Talwani and Ewing (1960) and a sedimentary bulk density of 2460 $kg\ m^{-3}$.

density of $\sim$ 2900 $kg\ m^{-3}$ (e.g., de Castro et al., 2014) and may, in places, have a cumulative thickness great enough to contribute to the central gravity high. Daly et al. (2014) showed, based on well data, that at their thickest the cumulative thickness of intrusive volcanics reaches $\sim$ 600 m. Given a density contrast of $\sim$ +200 $kg\ m^{-3}$ a maximum contribution of $\sim$ 7 $mGal$ is expected. This is much less than the $\sim$ 40 $mGal$ central gravity high, which therefore must originate from beneath the sedimentary basin.

4.8.2 Residual anomaly interpretation

One possible source of the residual gravity anomaly 'high' shown in Figure 4.18f is the thinning of the crust and shallowing of the Moho beneath this section of the basin. For example, a first order Bouguer slab approximation suggests a relatively subtle Moho shallowing of $\sim$ 2.7 km could account for the high, assuming crust and mantle densities of 2800 and 3310 $kg\ m^{-3}$ respectively. However, as discussed in previous Sections (3.2.3.2 and 4.7), an extensional model appears inconsistent with the position of the moho as defined by seismic reflection

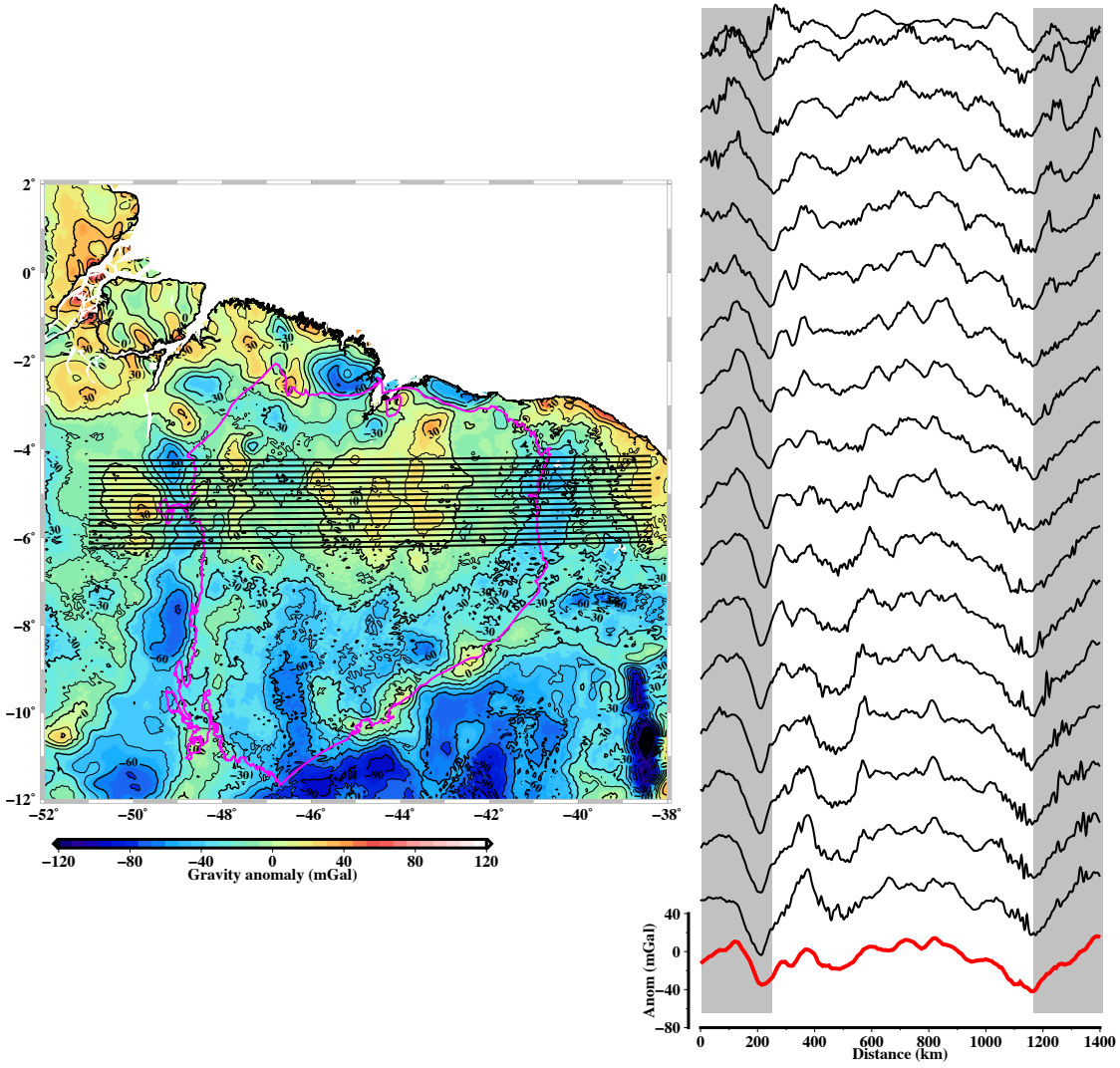


Figure 4.20: Ensemble average of sediment corrected Bouguer gravity anomaly. a) Location map showing the 'swath' of ensemble profiles. b) Sediment corrected Bouguer gravity anomaly profiles (Black lines) and the ensemble average or 'typical' profile (Red line). Grey shaded regions delineate the basin edges.

profiling (Daly et al., 2014), wide-angle reflection data (Section 3.5) and POGM modelling results (Fig. 4.17).

Another possible source of the residual anomaly "high" is a density anomaly within the mantle lithosphere, as has been suggested beneath cratonic basins of North America by Kaminski and Jaupart (2000). These authors proposed that material from mantle plumes has been emplaced within the mantle lithosphere, creating mass anomalies on the order of 200 km in height and 50 km in radius beneath these basins. The isostatic compensation of these loads then results in basin formation. Such large masses would require a density contrast

of $\sim 25\ kg\ m^{-3}$ to produce an anomaly on the order of 40–60 $mGal$. However, the wavelength of such an anomaly would be expected to be larger than for a body within the lower crust, and as yet, there is no seismic data of sufficient resolution to test this hypothesis.

Alternatively, an interpretation that is more in-line with the seismic data analysed in Chapter 3 and 2D gravity modelling presented above, is that the residual high is sourced from a density anomaly within the crust. Again, a first order Bouguer slab approximation suggests a 10 km thick anomalous body with a density contrast of 200 $kg\ m^{-3}$ would produce an anomaly similar to that observed. If the flexure and the associated Moho depression caused by such a load is taken into account, then the thickness and/or density contrast of the body would be required to increase. A critical test for this model is whether it could also produce a basin of similar shape and thickness of Parnaíba basin. This scenario is modelled in detail in the following section.

4.8.3 Three dimensional buried load model

In order to test the validity of a buried load model in three-dimensions, the gravity anomaly predicted for simple three-dimensional shapes, in addition to their flexural effects (i.e., Moho depression and basin sediment infill) were calculated (Fig. 4.21). Furthermore, in order for comparison between the observed residual gravity anomaly and that predicted by the buried load, an ensemble averaging technique was used to derive a two-dimensional profile through the residual gravity anomaly, such to reduce short-wavelength features and enhance the central gravity high (Fig. 4.20). Figure 4.21d shows the observed ensembled gravity profile and those predicted by various simple shaped bodies.

It was found that a Gaussian-shaped load emplaced on a plate with a T_e of 20–30 km is capable of explaining the residual gravity "high" while also creating a basin of similar depth and shape of Parnaíba basin. Higher values of T_e predict too large a gravity 'high' and too shallow a basin, while lower values of T_e predict too small a gravity 'high' and too deep a basin. However, one problem is that the lateral extent of the predicted basin is less than that of Parnaíba basin. This could potentially be reconciled by using a more sophisticated model than that of simple elastic plate flexure. Indeed, basin formation models that invoke a

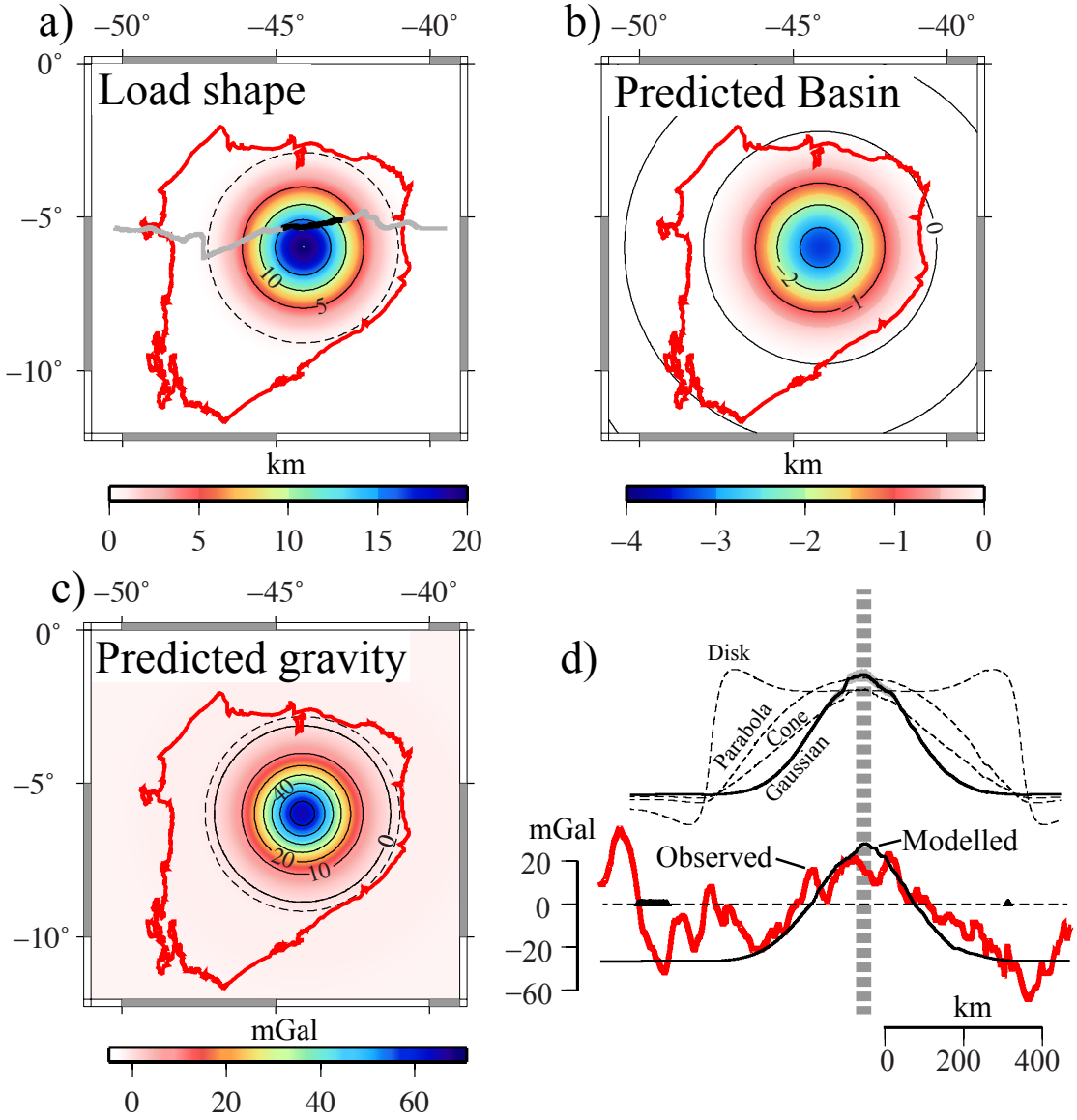


Figure 4.21: Three dimensional gravity model based on the emplacement of a Gaussian-shaped load within the lower crust centred at longitude 44.1°W and latitude 6.0°S. a) Contour of load shape and height in *km*. b) The predicted sediment-filled basin due to flexure from the load shown in (a), assuming the parameters shown in Table 4.2 and for a $T_e = 25$ *km*. c) The predicted sum gravity anomaly due to the emplaced load, Moho flexure and sedimentary basin infill. d) Predicted gravity anomalies for various simple-shaped bodies (as labelled) and the comparison between the observed gravity anomaly along the regional transect and that given by the cone shown in (a).

viscoelastic rheology predict that basins are widest early in their evolution and narrow with time as the lithosphere relaxes from its short-term (seismic?) thickness towards its long-term elastic thickness (e.g., Watts et al., 2013).

Although this model does not predict the precise spatial extent of the basin, that it is able

to explain the residual gravity anomaly, basin thickness and first order basin shape, and is also consistent with the seismic and POGM results presented earlier, is compelling evidence in favour of this model. A further test is whether this model is able to explain the temporal subsidence history of the basin, as documented within the sedimentary record. This question is explored in the following chapter.

4.9 Summary

In this chapter terrestrial gravity data acquired along the regional PBAP transect have been reduced to gravity anomalies and modelled using both forward "object" oriented and "process" oriented techniques. Additionally, composite satellite and terrestrial derived data from the EGM2008 model have been used to extend analysis to three dimensions and derive sediment corrected "residual" Bouguer gravity anomalies. The key findings are as follows:

- Parnaíba basin is characterised by broad, basin-wide, free-air and Bouguer anomaly lows, both with maximum amplitudes of $\sim -30\ mGal$.
- Forward two-dimensional modelling shows that gravity anomaly implied by the sedimentary basin and depth to Moho along th PBAP transect, as constrained by seismic reflection and refraction data, predicts a very large negative anomaly, far in excess to that observed. One way of reconciling this dependency, which is also consistent with the seismically constrained crustal structure, is the inclusion of a high-density ($+175\ kg\ m^{-3}$) lower crust.
- A density contrast of $+175\ kg\ m^{-3}$ is less than would be expected for eclogisation but may be consistent with the magmatic intrusion of basaltic material and/or garnet granulite metamorphism.
- Process-oriented gravity modelling suggests that a model which invokes solely lithospheric rifting can not explain the basin formation as such a model fails to reproduce the observed Bouguer gravity anomaly low across the basin, regardless of the assumed elastic thickness and starting crustal thickness.

- Process oriented gravity modelling of a buried load, with parameters consistent with those from seismic and forward gravity modelling can, however, reproduce a broad, basin wide gravity low, similar, to first order, of that observed.

- EGM2008 basin wide Bouguer gravity anomalies were corrected for the gravitational effect of the sedimentary basin. This reveals that Parnaíba basin is characterised by a central residual gravity anomaly "high" of maximum amplitude +40 $mGal$ and wavelength up to 1200–2000 km. This may reflect the three-dimensional form of the lower crustal mass excess predicted from forward and POGM modelling of the regional PBAP transect.

- Three-dimensional gravity and elastic flexural modelling shows that a Gaussian-shaped load with characteristics similar to those independently derived from seismic and forward two-dimensional gravity modelling, emplaced within a lithosphere of $T_e = 25\ km$, is capable of explaining, to first order, the residual gravity anomaly high, basement depth and sub-circular basin shape.

Chapter 5

Subsidence analysis and geodynamics of Parnaíba basin

5.1 Introduction

In this chapter the temporal evolution of the Parnaíba basin is investigated by analysing its regional subsidence and uplift history, as preserved within the sedimentary record. Central to this analysis is the separation of the portion of basin subsidence that is caused by tectonic processes, from that of the amplifying water and sediment loading effects. This is achieved using one-dimensional (Airy-type) and three-dimensional (flexural-type) "backstripping" techniques. These observations are then used, in addition to the observations made in Chapters 3 and 4, to test geodynamic models of basin forming processes. Specifically, models of pure shear lithospheric extension or the emplacement of a buried load within the lower crust are tested to address whether either of these models are able to reproduce the observations. The extensional model is predominantly a thermal model, while the buried load model is purely mechanical. In the latter case, the lithosphere requires a viscoelastic rheology in order to produce a time dependent flexural response to loading.

5.2 Vertical motions of Earth's surface

Constraining the timing and magnitude of subsidence and uplift events is central to understanding the temporal evolution of a sedimentary basin and the tectonic processes that formed it. For basins where an appreciable thickness of sediment is preserved, it follows that subsidence must have been the dominant vertical motion of the region through time. Periods of basin inversion can, however, play important roles in modifying and punctuating a basins overall subsidence history and present-day morphology. In the case of cratonic basins, their long-lived nature renders them susceptible to changes from, for example, relatively short-lived processes such as uplift related to mantle dynamics and/or changes in the regional stress regime resulting in periods of basin inversion and exhumation (e.g., Coakley and Gurnis, 1995; Howell and van der Pluijm, 1999). Therefore, it is important to assess whether inversion events have affected the sedimentary record before proceeding to model a basin's subsidence history.

5.2.1 Basin exhumation and missing section

Uplift events are more difficult to identify and quantify than subsidence. Unconformities within the sedimentary succession may be formed by periods of non-deposition and/or exhumation (i.e., the removal of overburden that exposes previously buried material (Doré et al., 2002)), and hence, represent missing section from the sedimentary record. If an appreciable amount of section is missing relative to the total sediment thickness, it is important that this is considered when modelling a basins subsidence history. There are several techniques that can be used to quantify exhumation events in sedimentary basins (see Corcoran and Doré, 2005), these include: (1) thermal indicators such as vitrinite reflectance and fission track analysis; (2) stratigraphic considerations of unit thickness variations, as measured in wells and on seismic reflection profiles; and (3) compaction analysis using porosity records from well log measurements. In the case of Parnaíba basin, the use of thermal indicators was inhibited due to a lack of data, while sediment thickness variations are subtle and more suited to analysing localised uplifts, rather than basin-wide inversions. Thus, porosity well logs derived from sonic velocity measurements, where used to assess whether any of the regional unconformities

recognised un the Parnaíba basin sedimentary record (Fig. 2.6) are likely to represent an appreciable amount of missing section.

Porosity-depth curves in sedimentary basins are often, to first order, exponential in form. This reflects the mechanical compaction of the sediments that occurs with increased lithostatic stress with depth. If it is assumed that this porosity loss is non-recoverable, then in the upper section, where the gradient of porosity loss with depth is greatest, any "step" in porosity that occurs across an unconformity likely reflects missing section. The thickness of missing section can be estimated by fitting an exponential function to the porosity-depth curve, and determining what thickness is required to provide a best-fit to such a function (e.g., Figure 5.1).

As shown in Figure 5.1a the sonic porosity log from well 2-BAC, near the centre of Parnaíba basin (Fig. 5.3), does not exhibit any appreciable "steps" across the upper two unconformities (Balsas and Caninde megasequence boundaries), and hence it is unlikely an appreciable amount of overburden was removed at these times. For comparison, a porosity-depth curve from well Mbandaka-1 of the Congo basin is shown in Figure 5.1b. Note the large step that occurs across the unconformity at the top of the Stanleyville Formation (Fig. 5.1b). As shown in figure 5.1c, the porosity data suggest $\sim 400\ m$ of section has been exhumed. Another proxy for the maximum burial depth of sediments is the thermal maturity of source rocks. In Parnaíba basin, source rocks are thermally immature, indicating these have not entered the oil generation window (Milani and Zalan, 1999). This suggests these rocks are unlikely to have been buried to appreciably greater depths than present day, thus corroborating the porosity curves and suggesting that there has not been appreciable exhumation of the cratonic basin sediments. Hence, in the following sections, no modifications are applied to the recorded sediment thickness records to account for missing section when backstripping and modelling Parnaíba basin subsidence history.

5.2.2 Quantifying tectonic subsidence

The total subsidence of the original basement surface beneath a sedimentary basin can be considered as the sum of three main processes:

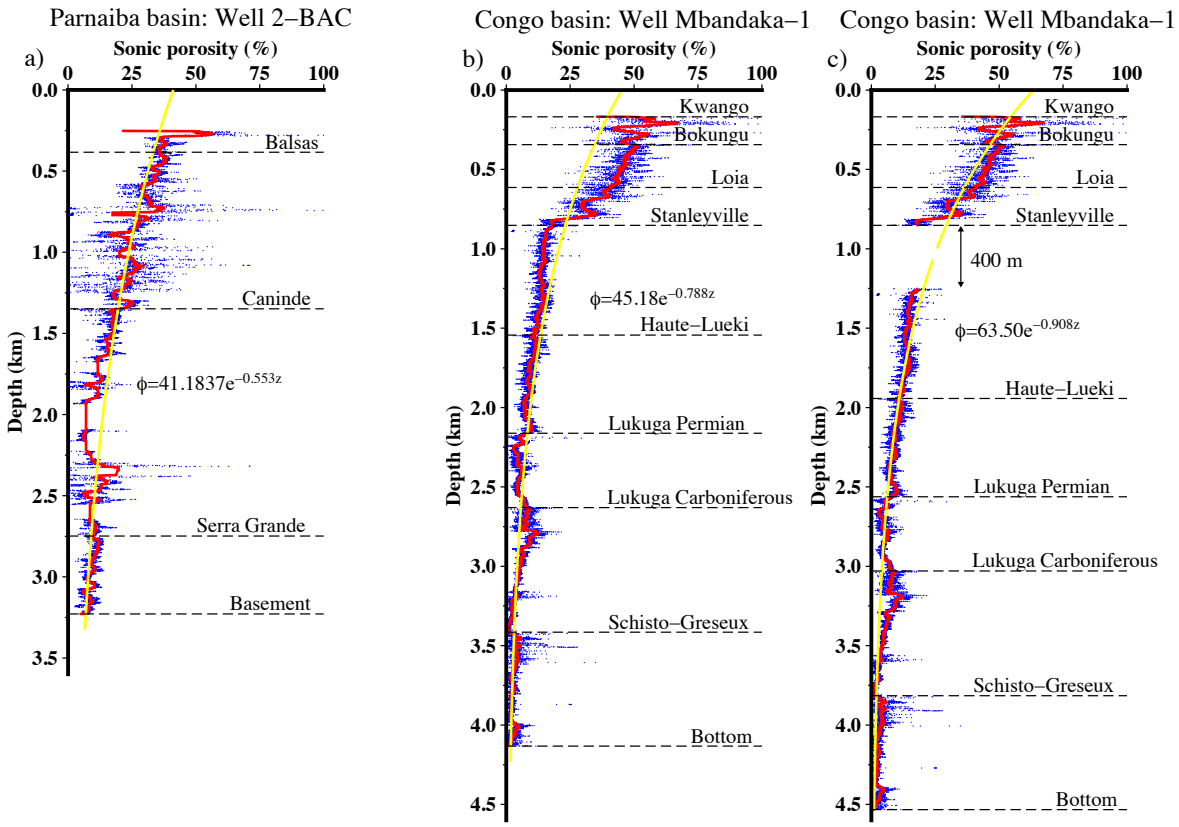


Figure 5.1: Porosity depth curves from wells 2-BAC located in Parnaíba basin and Mbandaka-1 from the Congo basin, Central Africa. Blue points are raw sonic porosity estimates, red curves are 181 point median filters and yellow curves are best fit exponential functions. a) sonic porosity curve from well 2-BAC near the centre of Parnaíba basin. b) Sonic porosity curve for well Mbandaka-1 from the Congo basin. Note the "step" in the porosity curve across the unconformity marked by the the top of the Stanleyville formation. c) Same is in (b) but with an estimated 400 m of missing section restored to produce a best-fit for the exponential function.

1. Tectonic subsidence — caused by the tectonic process(es) operating to drive surface uplift or subsidence.

2. Water loading subsidence — caused by the loading/unloading effect of eustatic sea level changes.

3. Sediment loading subsidence — caused by the loading effect of sediments that replace the water or air within the tectonically derived basin accommodation space.

In order to interpret what tectonic mechanism(s) may be responsible for creating a basin, it is useful to isolate the tectonic subsidence (i.e., the portion of subsidence caused by tectonic driving forces) from the modifying effects of sediment and water loading, which obscure the

tectonic signal. One method to achieve this involves "stripping" the sediment and water loading subsidence from the total subsidence signal. This "backstripped" signal can then be compared directly to the subsidence predicted by a given tectonic model.

Backstripping is achieved using the techniques devised by Watts and Ryan (1976). Firstly, Airy-style one-dimensional backstripping is performed on vertical sedimentary records derived from exploration well logs. This technique utilises a series of simplifying assumptions, most importantly, the notion of Airy isostatic compensation, to achieve this purpose. Next, a flexural backstripping approach is used. During flexural backstripping the lithosphere retains an inherit finite strength when loaded, such that, it is capable of partially supporting loads by regional elastic flexure rather than responding in a local Airy isostatic manner. Using the flexural method, the sediments can also be backstripped in three-dimensions, thus revealing the gross basin configuration through space and time.

5.3 One-dimensional Airy backstripping

Airy backstripping is used to determine tectonic subsidence through time, as recorded through one-dimensional vertical sections (e.g., well log records) of the sedimentary sequence, assuming Airy-style isostatic compensation. In this case, the pressures at the "depth of compensation" (Fig. **??**) of a sediment/water loaded column and that which is "backstrip" unloaded can be equated (Eq. 5.1):

$$\rho_w g W_d + \rho_s^* S^* g + T\rho_c g = Y_i \rho_w g + T\rho_c g + x\rho_m g \tag{5.1}$$

Where the values are as shown in Figure **??**b. It follows from Figure **??**b that x is equal to:

$$x = W_d + S^* + T - (Y_i + \Delta_{sli} + T) \tag{5.2}$$

By substituting the above term for x into Equation 5.1, it can be rearranged to solve for

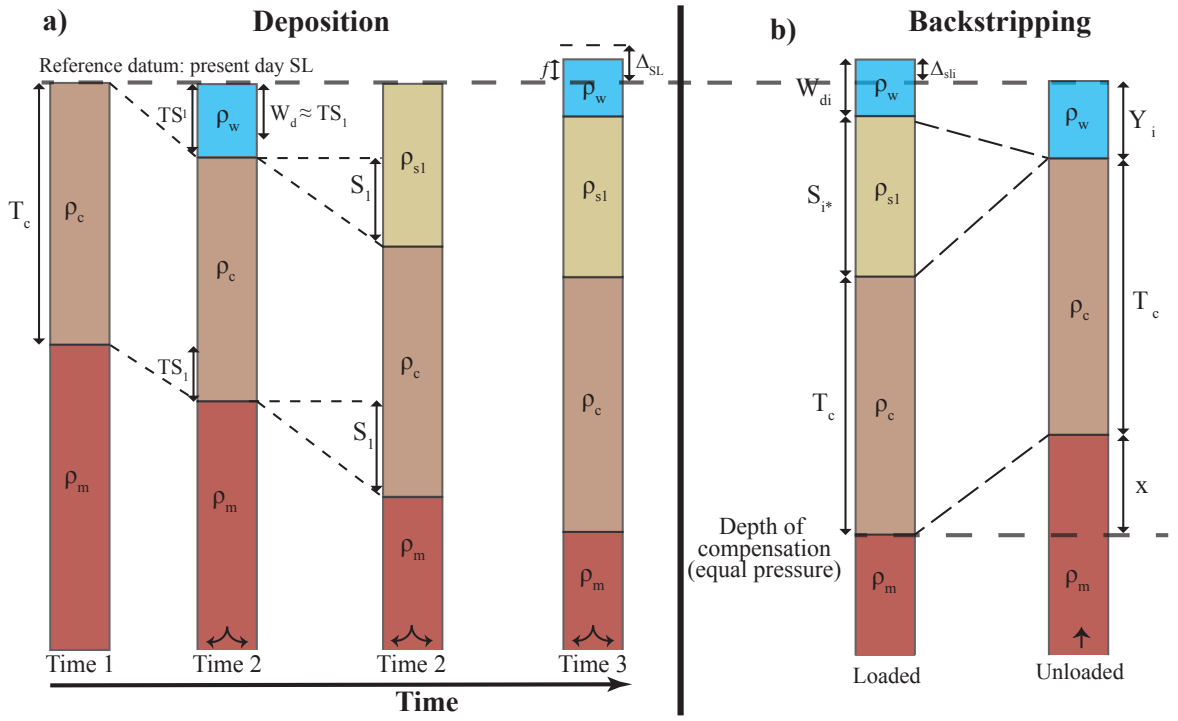


Figure 5.2: Airy backstripping methodology. a) Depositional history of a hypothetical single layered sedimentary basin compensated in an Airy isostatic manner. An initial water filled basin is created by a tectonic subsidence equal to TS_1. Sediments then infill the basin until Airy compensation is achieved, with a resulting sediment thickness of $S_1 + TS_1$. A change in sea level of Δ_{SL} occurs and after isostatic compensation occurs, the remaining sea level rise, f, remains. This is known as the "free board" and is labelled Δ_{sli} in (b). b) Principle of backstripping. The basin created in (a) is "backstripped" to recover Y_i, the tectonic subsidence in the absence of sediment and water loading. ρ_w, ρ_{si}, ρ_c, ρ_m are the densities of water, sediment grains, crust and mantle respectively. W_d is water depth; Δ_{sli} is the observed eustatic sea level change after isostatic compensation; S_i^* is the total thickness of the sediments; ρ_w, ρ_s*, ρ_c and ρ_m are the bulk densities of the water fill, sediments, crust and mantle respectively and Y_i is the total tectonic subsidence.

Y_i, the depth the basement would be in the absence of sediment and water loading. This gives the general Airy backstripping equation (Watts and Ryan, 1976):

$$Y_i = W_d + S^* \left[\frac{(\rho_m - \rho_s^*)}{(\rho_m - \rho_w)} \right] - \triangle_{sli} \frac{\rho_m}{(\rho_m - \rho_w)} \tag{5.3}$$

Where the variables are as previously described, and the three terms are known as the water depth, sediment decompaction and sea level terms respectively.

To determine tectonic subsidence through time, Equation 5.3 is solved at each time step

(i.e., at the time of deposition of each lithostratigraphic unit that is being backstripped). It follows that the values of S^* and ρ_s^* (i.e. the total sediment thickness and the bulk density of the sedimentary column) change at each time step. S^* is simply the sum of the unit thicknesses at each time step, while ρ_s^* is given by Equation 5.4:

$$\rho_s^* = \frac{\sum_{i=1}^{n} \left[\rho_w \phi_{si^*} + \rho_{gi}(1 - \phi_{si^*})\right] S_i^*}{S^*} \tag{5.4}$$

Where ϕ_{si^*}, ρ_{gi} and S_i^* are the porosity, sediment grain density and thickness of the i^{th} layer respectively. These parameters are discussed below in Section 5.3.2.

5.3.1 Airy backstripping assumptions

The Airy backstripping technique relies on a several simplifying assumptions, these include: (1) the lithosphere compensates loads in a local Airy-type manner; (2) The bulk properties of the crust and lithospheric mantle and crustal thickness are constant through time (i.e., there are no phase changes); and (3) The process by which sediments compact during burial is simply a function of depth and occurs in a quantifiable manner.

Assumption 2 is clearly not valid in the case of extensional tectonics, where the crust is thinned during the syn-rift phase. Moreover, a constant lithospheric mantle density is also invalid when thermal processes such as rifting are invoked, as the mantle is heated at the time of rifting, thermally expands (bulk density decreases) and then cools with time.

Assumption 3 is required in order to facilitate the decompaction of sediments. It is assumed that sediment compaction can be described by a continuous exponential loss with increased depth (e.g., Athy, 1930), is a non-reversible process and is purely mechanical in form (i.e., other compaction processes such as chemical compaction and diagenesis are neglected). In this case, two parameters can describe this process, namely the surface porosity, ϕ_o, and an exponential depth coefficient, c, (e.g., Sclater and Christie, 1980) as discussed in Section 5.3.2.1.

Despite these assumptions, the Airy-backstripping technique provides a useful method for quantifying tectonic subsidence as well as the timing, duration and magnitude of various tectonic events that affect a given region though time (e.g., Steckler and Watts, 1978; Coakley and Gurnis, 1995; Madon and Watts, 1998; Ali and Watts, 2009).

5.3.2 Airy backstripping parameters

In this study, formation top picks and petrophysical logs from forty-six exploration wells were analysed, from which, fifteen wells that penetrate through the Phanerozoic section to basement or pre-Silurian sediments were backstripped. In order to conduct an Airy backstrip, values must be assigned for various parameters, some of which can be well constrained by data, while others are less well known. These parameters include:

(1) Bulk densities for the relevant entities. These include the sedimentary grains for each formation (ρ_s) and the pore fluid that fills any pore space (ρ_f) as well as the material displaced by the sediments (usually ocean water, ρ_w) and the underlying mantle (ρ_m).

(2) The present day "compacted" porosity of the various sedimentary formations, and to facilitate decompaction during the backstripping process, parameters that describe their porosity loss with depth. These are described in Section 5.3.2.1.

(3) The water depth (W_{di}) and value of global sea level at the time of deposition of each sedimentary unit relative to present day ($\triangle_{sli}$).

5.3.2.1 Decompaction approach

Since it's introduction by Watts and Ryan (1976) the Airy backstripping technique has become a standard tool for investigating the subsidence and uplift histories of sedimentary basins. Although the technique was first introduced some forty years ago, the only major modification was introduced by Sclater and Christie (1980) who modified the way in which decompaction is performed, by integrating over an exponential porosity-depth function for each sedimentary unit, rather than using an average value for each unit. This depth-integrated decompaction

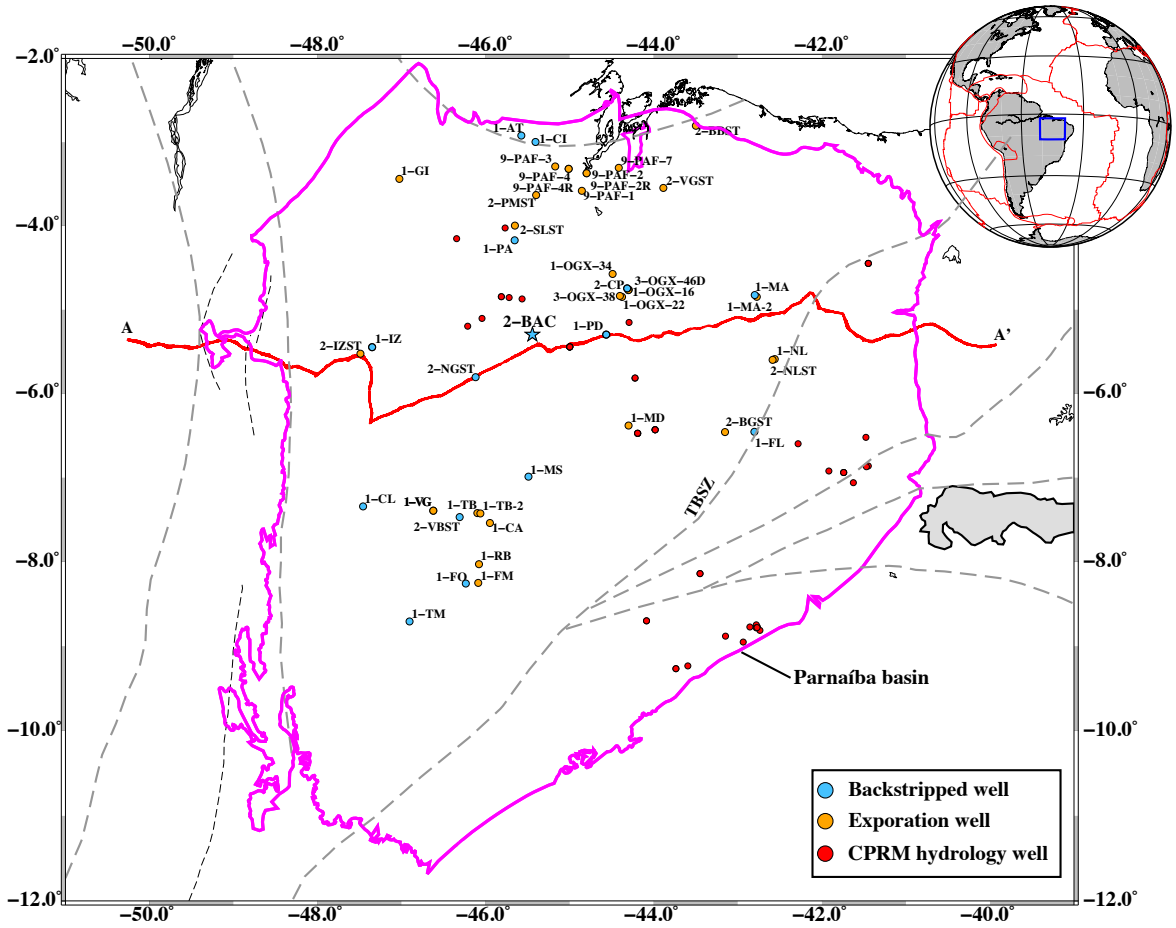


Figure 5.3: Parnaíba basin well distribution map. Red line shows the PBAP seismic reflection profile. Blue, orange and red filled circles show the locations of backstripped wells, exploration wells that don't penetrate to basement and relatively shallow hydrology wells from the Companhia de Pesquisa de Recursos Minerais(CPRM) database, respectively. Star shows the location of exploration well 2-BAC (Fig. 5.10). Inset in top right shows bounding box of the main figure (blue box).

method is adopted in this study, as outlined below.

The depositional history is modelled as discrete steps through time, in which each time step is represented by a given lithostratigraphic unit. To calculate the decompacted unit thickness, the formation is 'slid up' the relevant porosity/depth curve and the porosity of the unit is increased from its present day recorded value to that which it would have had at the time of deposition at the surface (Fig. 5.4). The oldest (deepest) layer (unit 1) is brought to the surface and allowed to decompact. Next, the second oldest formation (unit 2) is brought to the surface and decompacted, while the underlying unit 1, is partially compacted due to the overburden of unit 2. The depth to the base of unit 1 (i.e., basement) is then determined as

the sum of the unit thicknesses. The mathematical treatment is given by Sclater and Christie (1980) and repeated for clarity below.

Following Figure 5.4, the volume of pore space, V_w, within a given unit cross-sectional area between z_1 and z_2 is given by:

$$V_w = \int_{z1}^{z2} \phi_o e^{-cz} dz \tag{5.5}$$

Where ϕ_o is the surface porosity; z is depth and c is the coefficient which governs the decrease in porosity with depth. On integration this gives:

$$V_w = \frac{\phi_o}{c}\left(e^{-cz_1} - e^{-cz_2}\right) \tag{5.6}$$

The volume of given unit occupied by sediment grains V_s, is given by:

$$V_s = V_t - V_w \tag{5.7}$$

Where V_t is the total volume of the unit.

Hence, prior to decompaction, z_s, the unit cross-sectional area occupied by sediment grains, is given by the subtraction of the total pore-space from the total unit thickness:

$$z_s = (z_2 - z_1) - \left[\frac{\phi_o}{c}\left(e^{-cz_1} - e^{-cz_2}\right)\right] \tag{5.8}$$

It follows from Equation 5.8 that when decompacted, the unit cross-sectional area occupied by pore space is given by:

$$z'_w = \frac{\phi_o}{c}\left(e^{-cz'_1} - e^{-cz'_2}\right) \tag{5.9}$$

This can be thought of as sliding the given formation up the relevant porosity/depth curve.

As the volume of sediment grains remains the same when decompacted (i.e., only the volume of porosity increases) the decompacted cross-sectional unit thickness is given by the sum of the thickness of sediment grains and the total decompacted porosity thickness:

$$z'_2 - z'_1 = z_{sg} + z'_w \tag{5.10}$$

This is given by adding Equation 5.8 and Equation 5.9:

$$z'_2 - z'_1 = \left[z_2 - z_1 - \frac{\phi_o}{c}\left(e^{-cz_1} - e^{-cz_2}\right)\right] + \left[\frac{\phi_o}{c}\left(e^{-cz'_1} - e^{-cz'_2}\right)\right] \tag{5.11}$$

To determine the decompacted unit thickness (z'_2 - z'_1), z'_2 must be known and since this appears on both sides of the equation, it is found using an iteration scheme (e.g., Allen and Allen, 2013).

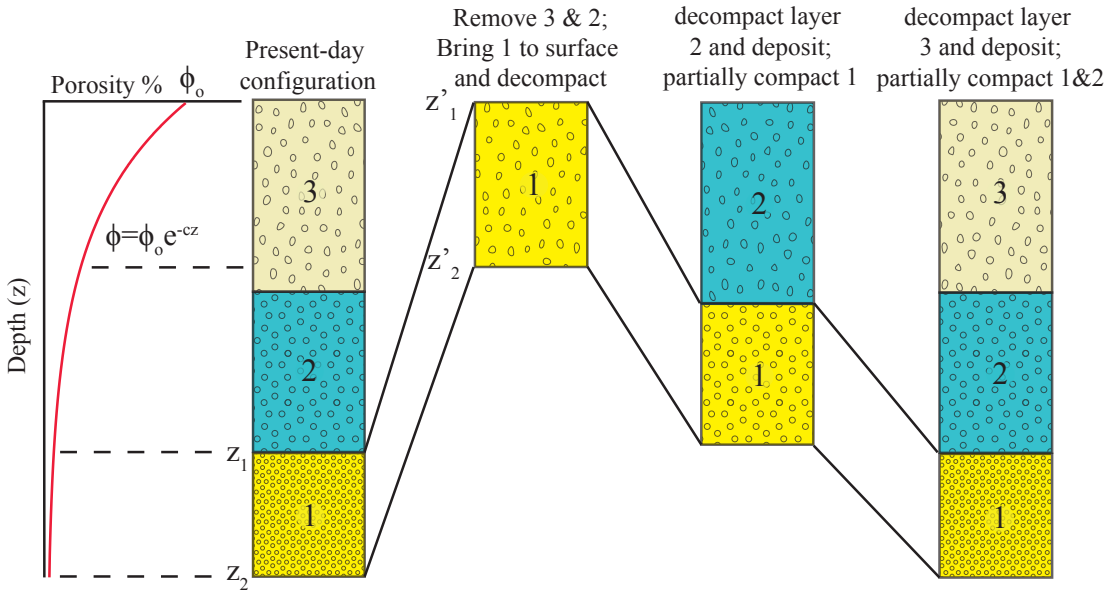


Figure 5.4: Schematic diagram illustrating the decompaction and partial compaction of sedimentary formations through time using an exponential porosity/depth function (modified after, Allen and Allen, 2013).

5.3.2.2 Petrophysical porosity estimates: sonic porosity

In the absence of in situ porosity measurements, petrophysical logs are used to estimate porosity. Sonic log measurements are the most common porosity proxy within the Parnaíba well log dataset, and so, for self consistency, this log is used for assigning porosity values. When porosity data was unavailable for a given well, values from a well in close proximity or values obtained from global compilations were used.

Several empirical formulas exist for converting sonic measurements into porosity values (e.g., Wyllie et al., 1956; Raymer et al., 1980; Raiga-Clemenceau et al., 1986; Issler, 1992; Kamel et al., 2002). All of these techniques require knowledge of the sonic travel time for the given lithologies sediment grains and drilling fluid, and in some cases the travel time in shale and specific constants that are a function of lithology. Some methods have been shown to be unreliable away from the region at which they were derived. However, the Wyllie time-average equation (Wyllie et al., 1956) has been proved to be universally robust and is hence used in this study. This is defined as:

$$\phi_{sonic} = \left(\frac{\Delta t_{log} - \Delta t_{ma}}{\Delta t_f - \Delta t_{ma}} \right) \tag{5.12}$$

Where Δt_{log} Δt_{ma} Δt_f are the measured acoustic travel time, acoustic transit time of the rock matrix and the acoustic travel time of the interstitial fluid respectively. Table 5.1 lists values for common lithologies used in this study.

5.3.2.3 Grain density estimates

Another important variable in the backstripping equation is the bulk density of the sedimentary overburden at each time step. This is a function of the average grain density, porosity and pore fluid density (Equation 5.13).

Lithology	Δt_f ($\mu s/ft$)	Δt_{ma} ($\mu s/ft$)
Sst	189	53.20
Shl	189	104.5
Lst	189	47.60
Dol	189	43.50
Anhy	189	54.00
Gypm	189	53.00
Salt	189	67.00

Table 5.1: Standard values used in the Wyllie equation for converting sonic velocity to porosity from Carmichael (1982). Δt_f is that of standard drilling fluid (water with 20% NaCl).

$$\rho_b = \phi\rho_f + (1-\phi)\rho_g \tag{5.13}$$

Where ρ_b is bulk density; ϕ is porosity; ρ_g is grain density.

Through time, the average grain and pore fluid densities are considered constants, while the porosity value changes due to compaction. Pore fluid density is assumed as a constant 1000 $kg\ m^{-3}$ for fresh water. Grain densities were assigned based on values obtained from petrophysical log measurements when available (Fig. 5.6), or from global lithologic compilation averages (e.g., Allen and Allen, 2013).

5.3.2.4 Eustatic sea level change

The second term in Equation 5.3 is the *water loading* term, which accounts for changes in global sea level relative to the reference — present day mean sea level. At each given time step, a relative sea level rise or fall acts as additional load or unload in the Airy isostatic balance. However, one problem when backstripping Phanerozoic sedimentary basins, is the uncertainty in Paleozoic eustatic sea level, particularly with regards to the amplitudes of changes (Watts, 2001). Haq and Schutter (2008) calculated a Paleozoic sea level curve on the basis of stratigraphic relationships recorded in cratonic and pericratonic sections, revealing 172 "short-term" changes superimposed on overall "long-term" trends. These authors suggest a maximum amplitude of $\sim$ 125 m relative to present day sea level. The long-term trend suggests sea level was higher than present day, throughout the Paleozoic, with the exception

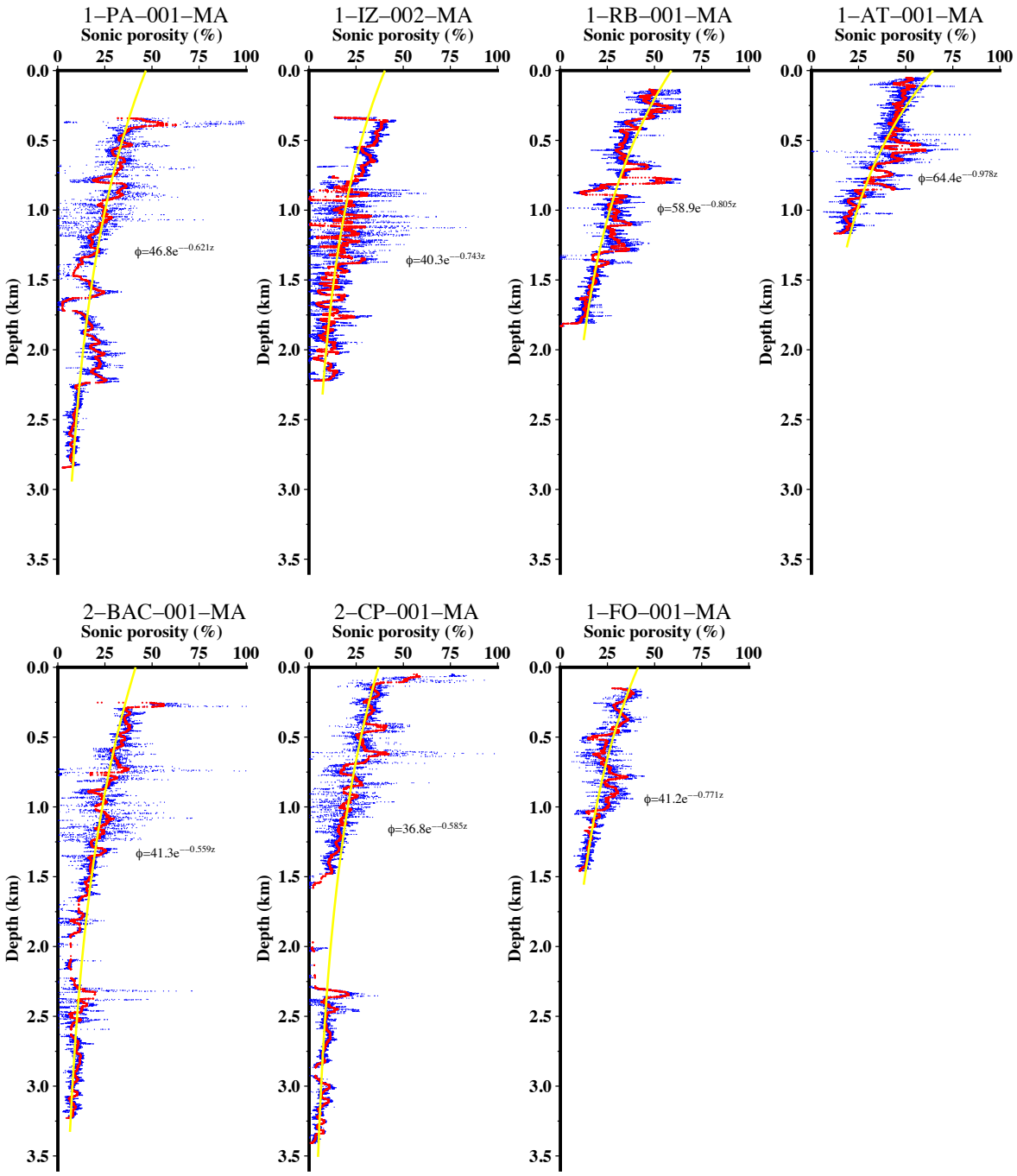


Figure 5.5: Sonic porosity/depth curves derived from wells that are backstripped within Parnaíba basin. Blue points are raw sonic porosity estimates, red curves are 181 point median filters and yellow curves are best fit exponential functions.

of a Late Permian lowstand (Fig. 2.6). The effects of sea level changes on the Parnaíba basin backstrips are examined by including the changes predicted by Haq and Schutter's (2008) "long-term" Phanerozoic sea level curve. However, it is not obvious, given its mix of terrestrial and shallow marine lithologies, when, if at all, the Parnaíba basin was fully connected to the

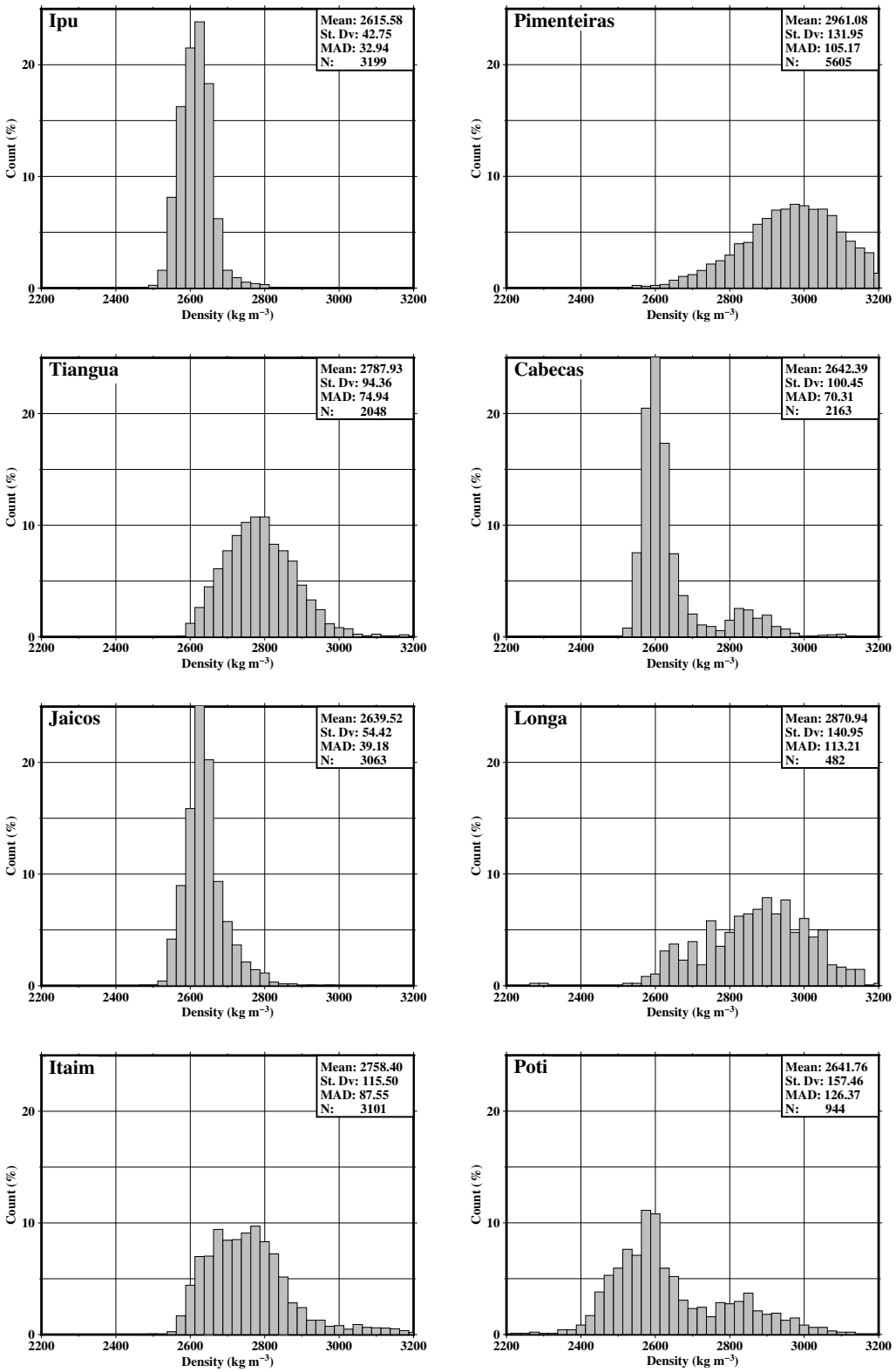


Figure 5.6: Formation grain density estimates from compilations of petrophysical log records for formations Ipu to Pedra-de-fogo. The mean values are used for backstripping. St. Dv = Standard deviation; MAD = Mean absolute deviation; N = Number of data points.

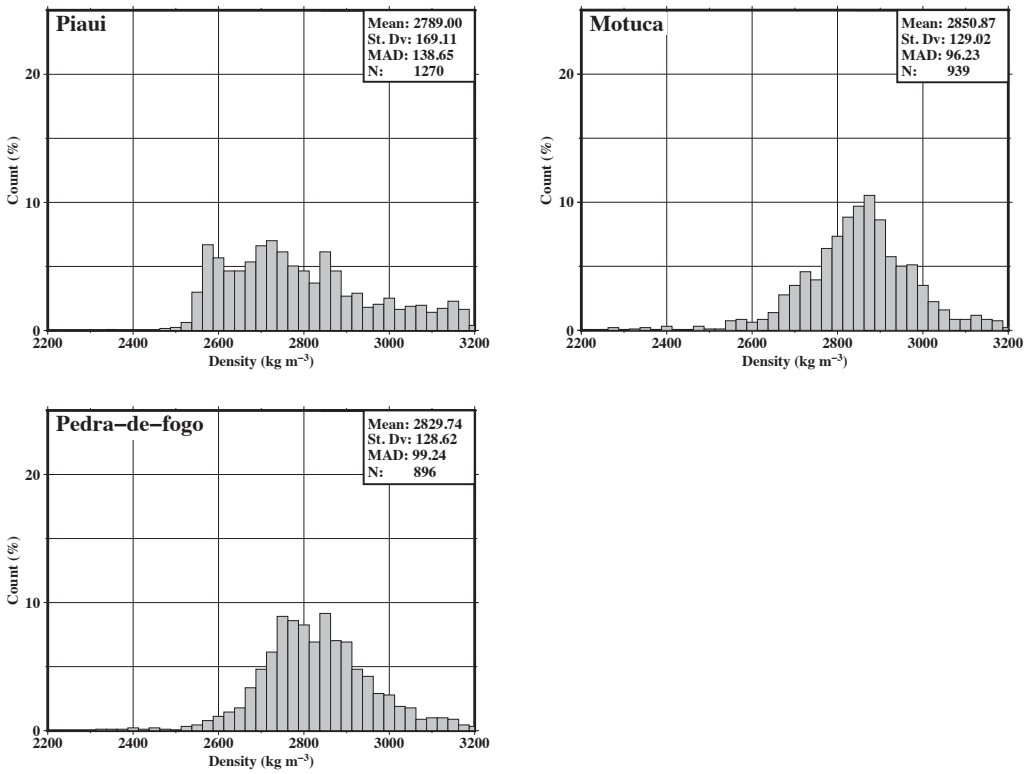


Figure 5.6 continued

global ocean. Some paleo-reconstructions, such as those from Scotese (2016), shown in Figure 2.8, suggest Parnaíba basin was connected to the global ocean by an epeiric seaway, extending through the Amazon basin to the west. It is possible, however, that this seaway may have been analogous to that of the Mediterranean during the Neogene, and, at least at times, been isolated from the global ocean. Due to this uncertainty, backstripped curves without eustatic sea level corrections applied are used for comparison with model predictions (Figs. 5.10 and 5.11). Moreover, curves with sea level corrections applied have the same overall shape as those in (Figs. 5.10 and 5.11).

5.3.2.5 Paleobathmetry

The final term in Equation 5.3 refers to the paleo-water depth at the time of deposition. The most reliable estimates of paleobathmetry are usually obtained from biostratigraphic proxies, such as benthic micro-fossils, as certain species are known to occupy specific water depths. Unfortunately, such data are unavailable for Parnaíba. However, given that the inferred de-

positional environments within the basin are predominantly lacustrine and estuarine, shallow marine, and terrestrial (aeolian), paleobathmetric values are likely to have been relatively small (i.e., $<$ 100 m) and therefore, paleobathymetric corrections are not applied. Instead, informal errors of $\pm$ 100 m are assign to individual estimates of the tectonic subsidence.

5.3.3 Airy backstripping: Volcanic intrusions

In the Parnaíba basin, intrusive volcanics add volume to the sedimentary column at the time they are emplaced. At their greatest thickness, these volcanics account for $\sim 1/5$ of the sedimentary section and must be accounted for in the backstripping process. The intrusive Mosquito Formation and extrusive Sardinha Formation were emplaced during the Middle Jurassic and Early Cretaceous respectively. Hence, during the cratonic basin phase of subsidence (Silurian–Triassic) this volcanic material did not exist. To account for this, the cumulative volume of volcanic material within each formation is removed prior to backstripping, with the remaining unit thicknesses assigned as the true thicknesses at the time of deposition. The cumulative thickness of the volcanics are then emplaced at the time of intrusion, such that, the underlying units are buried to and decompacted from, their present day depths. In this way, the load of the volcanics are still accounted for while backstripping, without over estimating the thicknesses of formations that have been intruded by volcanic material. Furthermore, as no tectonic subsidence is predicted to be associated with emplacement of the volcanic material, the relevant physical properties required for backstripping analysis are tuned so as to produce no tectonic subsidence at the time of emplacement. It was found that an emplacement density of 2780 $kg\ m^{-3}$ and porosity of 10% allows for this and are hence the values predicted at the time of injection.

5.3.4 Airy backstripping results

Figure 5.7 shows the backstrip curves derived from wells which penetrate to basement or pre-Silurian sediments. In the centre of Parnaíba basin (e.g., wells 2-BAC and 2-CP), tectonic subsidence accounts for $\sim$ 1200 m over $\sim$ 260 Myr. Over 70 % of the total tectonic subsidence occurs within the first $\sim$ 100 Myr after basin initiation, at which time the curve kinks slightly

with the remaining portion of the subsidence occurring at a much slower rate over the next $\sim$ 100 Myr. The form of the subsidence profiles are consistent with an initial $\sim$ 100 Myr linear subsidence trajectory followed by a shift to a shallower gradient for the remaining subsidence. Equally, a concave up gentle decreasing exponential subsidence can also provide an excellent fit to the cratonic basin phase of subsidence (green curves).

Wells in the northern part of the basin (e.g., 1-AT and 1-CI) record the Cretaceous subsidence associated with the deposition of the Grajaú Unit (TS-5 in Figure 2.6). There is a marked increase in tectonic subsidence rate during this time. The tectonic subsidence is greatest at the northern edge of the basin, accounting for $\sim$ 550 m over 20 Myr. This subsidence becomes more subdued southward as the unit thins and eventually terminates at $\sim$ 6.0°S. Given its timing, it is likely opening of the equatorial Atlantic Ocean drove this subsidence, together with the accommodation space that it created.

The concave-up exponential character of the cratonic phase of subsidence (i.e., TS-3) is suggestive of a thermal cooling mechanism, similar to that invoked for rift-type basins in extensional settings (e.g., McKenzie, 1978; Steckler and Watts, 1978; Cochran, 1983). Indeed, Crosby et al. (2010) and Armitage and Allen (2010) have argued that the tectonic subsidence history of the Congo and Williston cratonic basins can be explained by a rifting model with a stretching factor, β, in the range 1.1–1.3, if the thermal lithosphere thickness is on the order of 200 km. The thick lithosphere allows for the prolonged thermal subsidence, as the lithospheric thermal time constant is proportional to the square of the plate thickness. This mechanism is tested for Parnaíba basin in Section 5.5.

Of particular note is the consistent undisturbed nature of the Parnaíba basin tectonic subsidence curves. This contrasts with those from other cratonic basins which often show periods of accelerated subsidence (Fig. 1.5), usually attributed to secondary, short lived mechanisms, such as dynamic topography. It appears that Parnaíba basin has not been subject to such processes during its evolution and hence provides a "primary" cratonic basin style subsidence record.

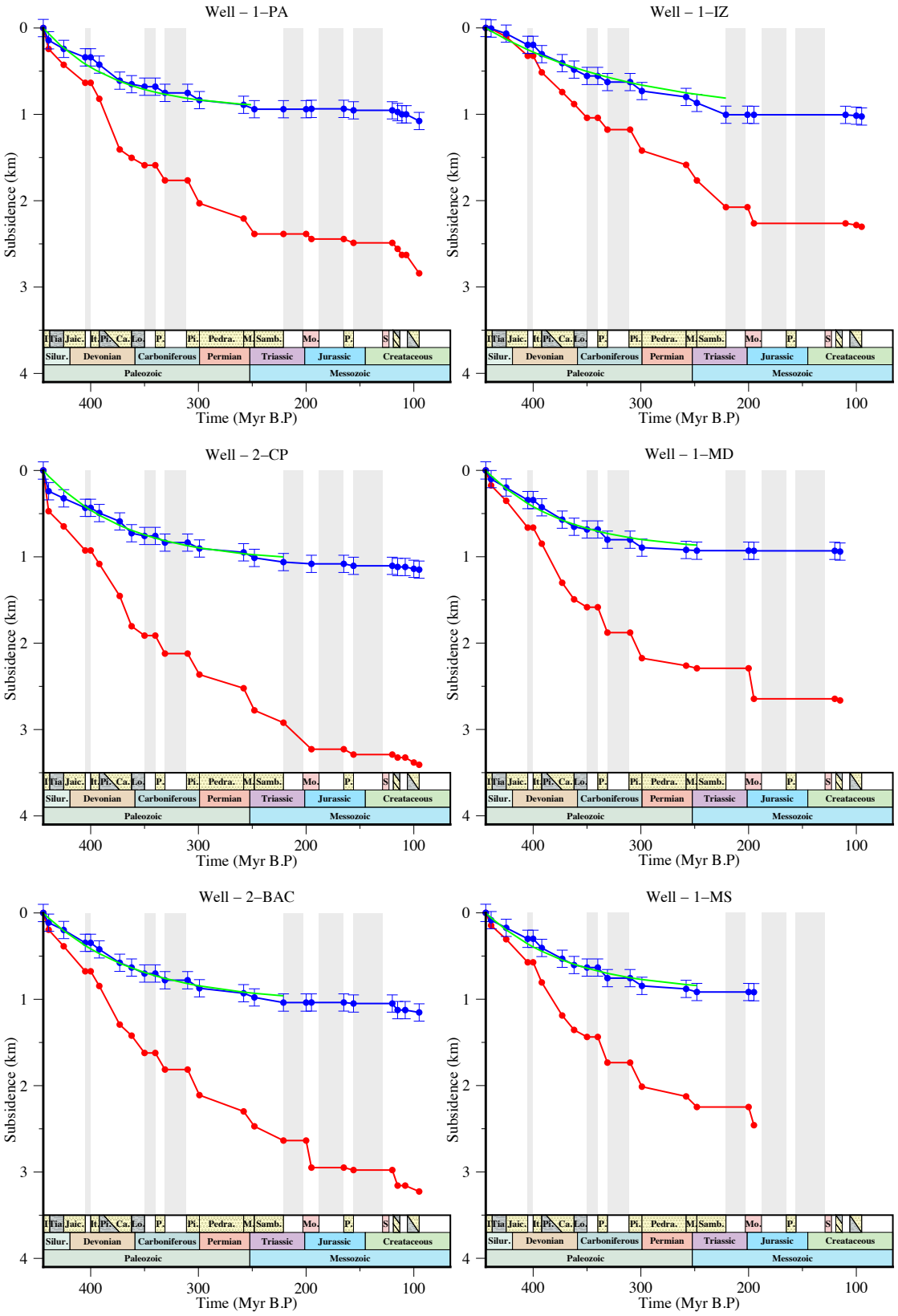


Figure 5.7: Sediment accumulation (red curves) and backstripped tectonic subsidence (blue curves) of wells which reach basement or pre-Silurian sediments within Parnaíba basin. Green curves are best fit simple exponential functions. Tectonic subsidence curves do not include eustatic sea level corrections. Error bars on tectonic subsidence curves are informal errors of $\pm$ 100 m to account for the maximum expected variations due to changes in water depth. Grey shaded regions represent gaps in the sedimentary record.

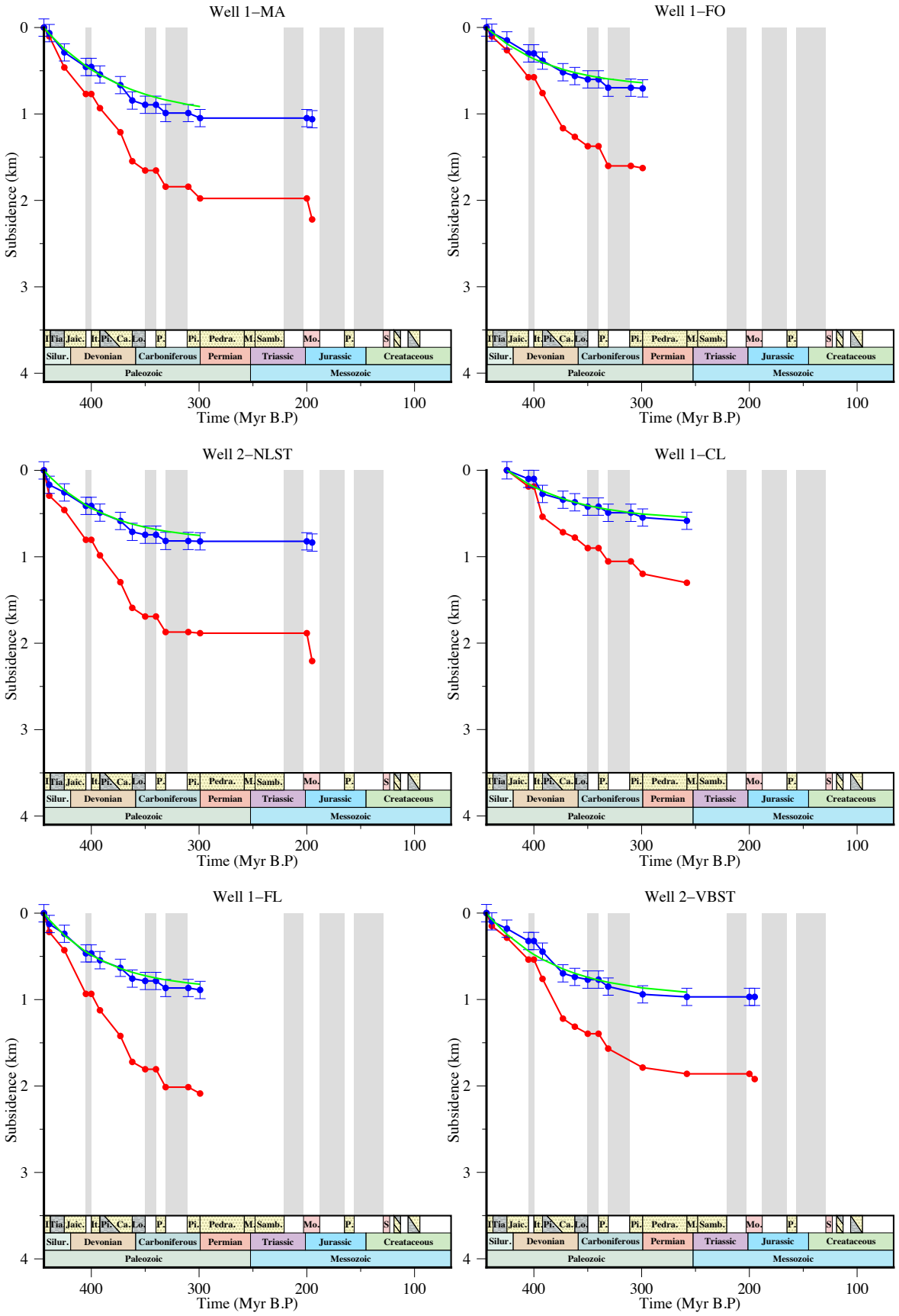


Figure 5.7 continued

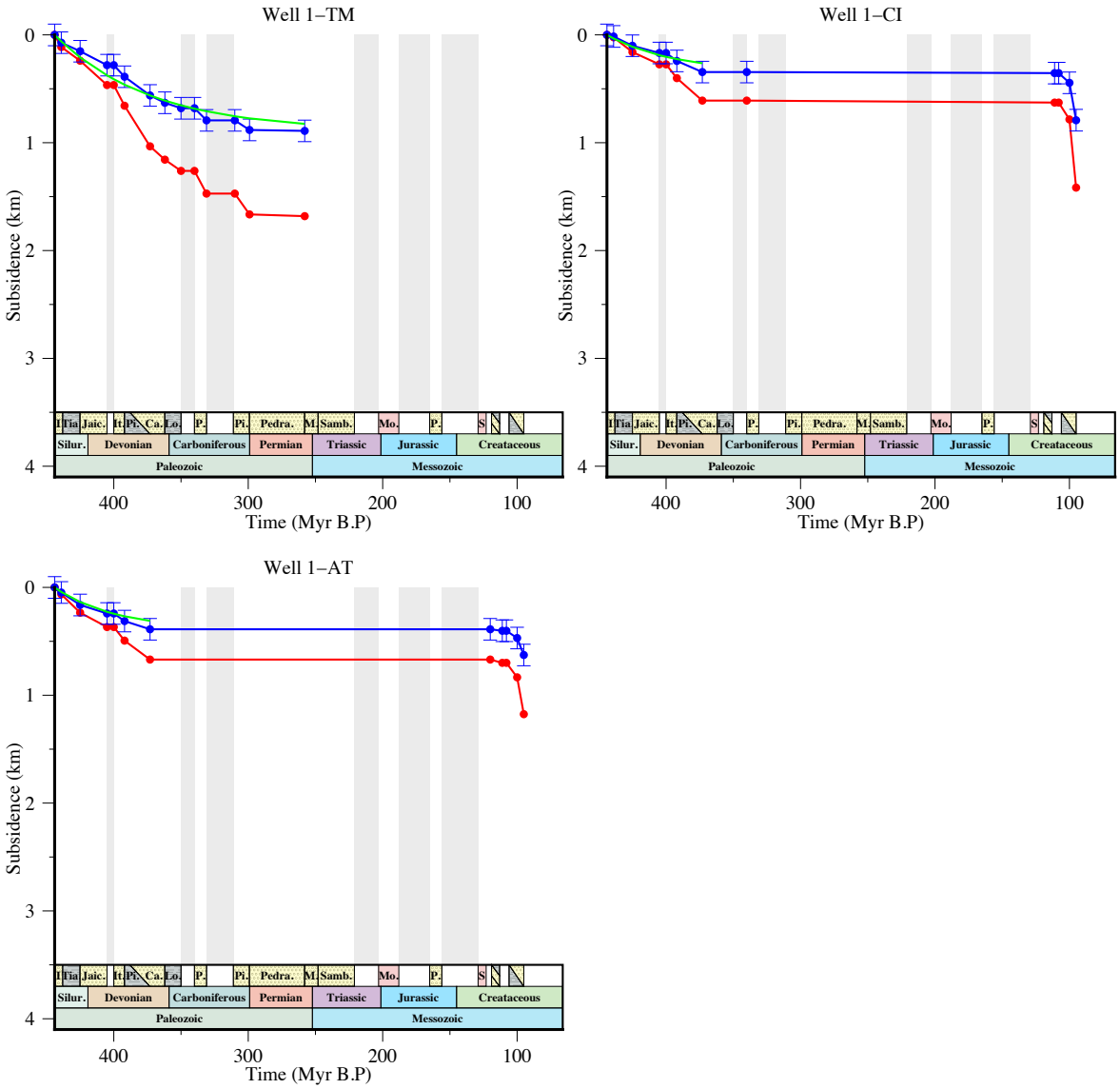


Figure 5.7 continued

5.4 Three-dimensional flexural backstripping

5.4.1 Flexural backstripping methodology

Flexural backstripping follows the same concept of Airy backstripping, however, the lithosphere retains a finite strength, such that the sediments are flexurally unloaded and regional isostasy is observed (see Section 1.1.4.1). This allows two and three-dimensional backstripping of seismic profiles and sediment isopach maps to be performed.

As described by Watts (2001), flexural backstripping is achieved by calculating the flexure caused by a sediment load $y(x)$ and then subtracting this from the observed unit thickness $S^*(x)$ to reveal the tectonic flexure $h(x)$ (Eq. 5.14):

$$h(x) = S^*(x) - y(x) \tag{5.14}$$

For this purpose, and in the absence of independent constraints, a constant flexural rigidity of the lithosphere, D is assumed. If the lithosphere is modelled as a purely elastic sheet overlying an inviscid fluid, the flexural rigidity is related to its effective elastic thickness (T_e) by Equation 5.15:

$$D = \frac{ET_e^3}{12(1-\sigma^2)} \tag{5.15}$$

Where E is Young's modulus and σ is Possion's ratio assumed from laboratory studies (e.g., Christensen, 1978). Once the flexural rigidity is determined, the frequency domain equivalent of the flexure induced by a sediment load, $Y(k)$, can be determined using Equation 5.16:

$$Y(k) = \frac{(\rho_s - \rho_w)S^*(k)}{(\rho_m - \rho_w)}\Phi_e(k) \tag{5.16}$$

Where k is the wavenumber, or wave vector $\sqrt{k_x^2 + k_y^2}$ in the three-dimensional case and $\Phi_e(k)$, the wavenumber parameter which modifies the Airy response to give the flexural response, is determined using Equation 5.17:

$$\Phi_e(k) = \left[\frac{Dk^4}{(\rho_m - \rho_w)g} + 1\right]^{-1} \tag{5.17}$$

Y(k) can then be transformed back to the space domain using the inverse Fourier transform, thus, by assuming a certain value for T_e, the tectonic subsidence for a given unit can be calculated using Equation 5.14.

5.4.2 Three dimensional Flexural backstripping input data

Isopach maps for each of the Phanerozoic formations were constructed (see Section 2.3) and used to produce a three dimensional flexural backstrip of Parnaíba basin through time (Fig. 5.8). The input isopach maps were created using all available well data and outcrop locations and benchmarked against the regional depth migrated seismic section. The isopachs are gridded at a $5.0' \times 5.0'$ interval using a minimum curvature solution for interpolation between control points. Various tension factors between 0 and 1 were tested and it was found that given the sparse data coverage, the minimum curvature solution (i.e., tension equal to zero) produced the best result for contouring the regional trends. Given the coarse grid spacing (5 minute resolution) and sparse data coverage, the isopachs should be regarded as "regional trend" maps.

It should be noted that two-dimensional seismic profiles located throughout Parnaíba basin in the southwest and southeast sections of the basin (Figs. 3.1 and 3.7) are not included in the generation of the isopachs, as they only exist in the time domain. Nevertheless, these have been interpreted by other authors (e.g., de Castro et al., 2016; Porto et al., In press) and they show that the basin stratigraphy is consistent with the isopachs presented here, with the basin-wide stratigraphy exhibiting a broad circular sag geometry, with a well developed regional unconformity at the base of the cratonic basin stratigraphic sequence (pre-Silurian unconformity). It should also be noted that these isopachs include the additional volume of

intruded volcanic material of the Sardinha (Cretaceous) and Mosquito (Jurassic) formations.

The isopach maps are shown in Figure 2.7 with the well control and outcrop boundaries used in the generation of the grids overlain. Because the boundaries of the basin are erosional, a boundary condition was imposed by placing control points of the minimum measured thickness of each formation $\sim 15\ km$ from the outcrop edge of each formation. This was included to prevent (a less realistic) thinning of the formations towards a $0\ m$ boundary condition imposed when only using the outcrop extent as the gridding boundary. It is noteworthy that this inclusion does not alter the gross pattern of any of the isopach maps, as the well control points show most formations thin towards their present day outcrop extent regardless.

5.4.3 Flexural backstripping results

Figure 5.8 shows the flexural backstrip for formations from TS-3 through TS-5, calculated from regional sediment isopach maps. A range of constant elastic thickness was tested in the backstripping ($5 < T_e < 75\ km$) and it was found that the general patterns of tectonic subsidence and uplift do not change significantly with elastic thickness. The figure shows that the earliest formation, Ipu, is characterised by a broad region of subsidence that is flanked by uplifts. The maximum subsidence was located in the centre (in the region of the MCR), and this basin shape appears to persist through the Pimenteiras and into the Longa Formation. The tectonic subsidence and uplift patterns then change: the basin narrows and by the time of the Sambaiba Formation, the main depocenter along with its flanking bulges appears to have shifted to the west. The shifts are most apparent on the eastern margin of the basin, although this may also occur on the western margin of the basin, but reactivation during the Mesozoic has obscured this (Daly et al., 2014).

The persistence of a broad sag basin from the Ipu through to the Longa Formations is of particular interest because this corresponds in time to when the best fit thermal model to the backstrip data predicts that rifting is occurring (see Section 5.5). In rift basins, synrift sequences are normally deposited in localised narrow half grabens, while the overlying postrift sequences form a broad linear regional sag. Figure 5.8 suggests that the Parnaíba basin began as a broad sag and has actually decreased in areal extent rather than increased with time, this

casts further doubt on the applicability of a rifting model to the basin. A process that results in a basin-wide sag morphology is required to explain the cratonic basin phase of subsidence of Parnaíba basin.

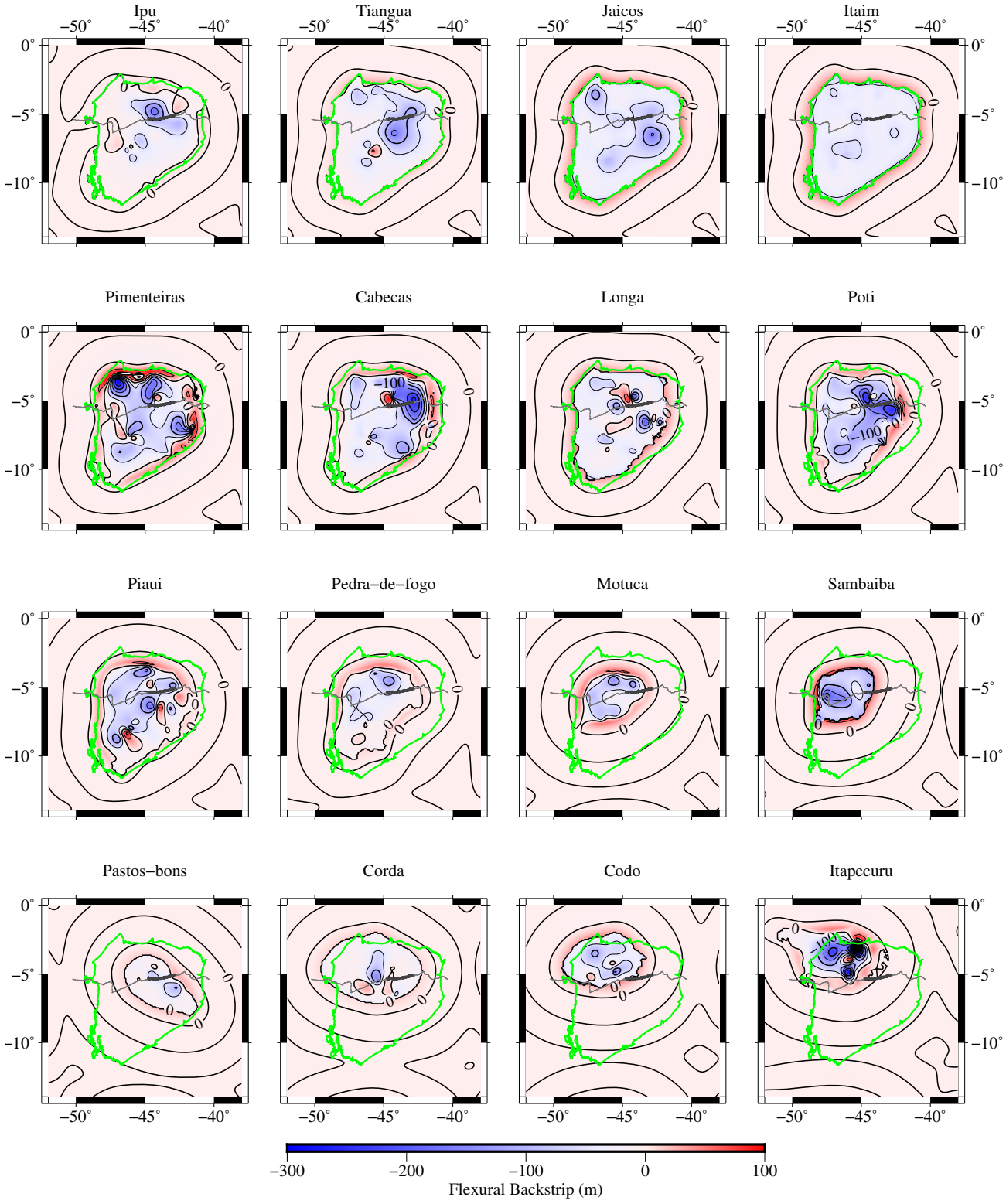


Figure 5.8: Flexural backstripping of the Ipu through Itapecuru Formations of tectonostratigraphic Units 3–5 (Fig. 2.6) showing the change in tectonic subsidence and uplift as a function of space and time assuming a constant T_e of 25 km. The backstrip shows a bowl-shaped region of subsidence that is flanked by uplifts and persists from the earliest to the latest stages of basin evolution. Green line shows the present-day extent of Parnaíba basin. Grey line shows the location of the PBAP seismic reflection profile. Thick dark grey line shows the extent of the MCR. The figure shows that the basin depocenter started to shift northwestward during the Pedra-de-Fogo Formation and during TS-5, appears constrained to the northwest and significantly smaller than during the TS-3.

5.5 Testing an extensional origin for Parnaíba basin subsidence

It is widely accepted that passive margins and "failed" continental rift basins form as a result of lithospheric extensional processes (e.g., McKenzie, 1978; Cochran, 1983; Wernicke, 1985). Two distinct phases characterise extensional subsidence, these are: an initial "syn-rift" phase that occurs due to the mechanical thinning of the lithosphere; followed by a "post-rift" thermal phase during which the heat flow anomaly produced by lithospheric thinning decays, isotherms relax back to the pre-rift steady state condition, and the lithosphere cools, contracts and subsides.

Several authors have proposed that the Parnaíba basin formed in response to lithospheric extension (e.g., Sousa, 1996; de Oliveira and Mohriak, 2003; de Castro et al., 2014; 2016), while others have postulated that extension is the primary mechanism by which all cratonic basins form (e.g., Armitage and Allen, 2010; Allen and Armitage, 2012). The backstripped subsidence curves derived in Section 5.3.4 are also suggestive of a thermal subsidence mechanism, given they are similar in form, albeit with longer time constants and rift durations, to subsidence profiles observed at passive margins. Hence, in this section, an extensional origin for Parnaíba basin is tested.

As the precise timing and style of rifting are poorly constrained, several models were run, beginning at different times during the Early Paleozoic. Within these models, the duration of the syn-rift, R_d, and amount of stretching, β, were varied. Predicted subsidence curves are compared directly with the observed backstripped curves derived in Section 5.3, in order to deduce best-fit values for both rift duration and β-factor (i.e., amount of thinning). The predicted crustal structure is then compared with Moho depths derived from seismic imaging and predicted by gravity modelling (see Chapters 3 and 4).

5.5.1 Finite rifting: Adopted modelling technique

Cochran's (1983) analytical solution for extensional subsidence is used to generate predicted subsidence curves. This modifies the original thermal model of McKenzie (1978) to simulate

a finite rift duration during the syn-rift phase and also includes two-dimensional heat flow. Only pure-shear extension (i.e., uniform extension with respect to depth) is investigated in this study. This follows the analysis of Kusznir et al. (2004), who showed using detailed stratigraphic modelling of the southern Lofoten and northern Vøring segments of the Norwegian rifted margin, that depth-dependent stretching is likely a late-stage phenomenon (occurring near or at the commencement of continental break-up) at continental margins. Hence, at the low β factors relevant to cratonic basin formation, depth dependent stretching is not anticipated.

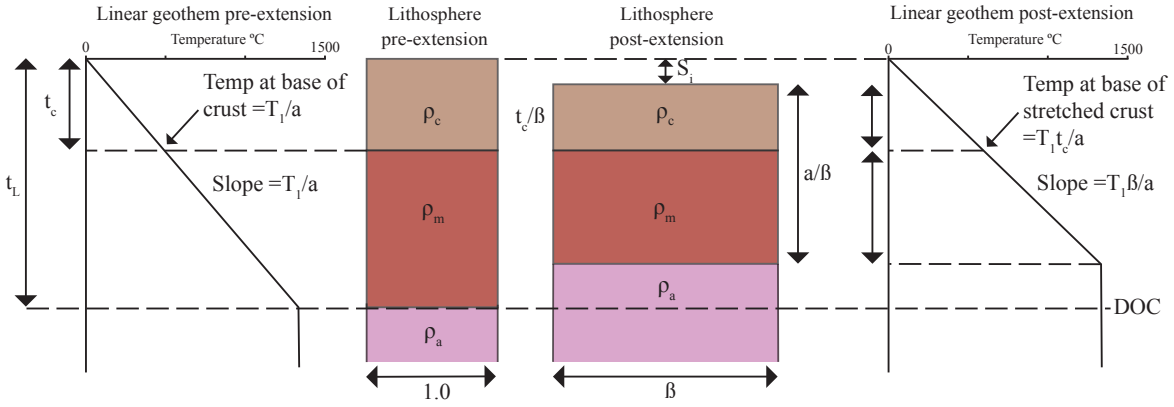


Figure 5.9: Schematic model of the principle elements of the McKenzie (1978) "syn rift" phase of an analytical lithospheric extension model (modified after, Watts, 2001). ρ_c, ρ_m and ρ_a are the densities of the crust, lithospheric-mantle and asthenosphere respectfully; t_c = Crustal thickness pre-stretching; t_L = Thickness of the lithosphere; β = = Stretching factor; T_1 = Temperature at the base of the lithosphere.

The computational solutions used in Cochran's (1983) analytical model are similar to those derived originally by McKenzie (1978), who assumed instantaneous rifting and one-dimensional heat-flow. The subsidence is calculated in two parts: first, the initial "syn-rift" subsidence S_i, is determined by balancing the pressure at the base of the pre- and post-stretched lithospheric columns following an instantaneous extension (Fig. 5.9). Assuming a linear geotherm with $T = 0°C$ at the surface of the lithosphere, and a constant thermal conductivity (i.e., no temperature dependence), α, S_i is given by (McKenzie, 1978, Equation. 1) as:

$$S_i = \frac{t_L\left[(\rho_a - \rho_c)\frac{t_c}{t_L}\left(1 - \alpha T_1 \frac{t_c}{t_L}\right) - \frac{\alpha T_1 \rho_o}{2}\right]\left(1 - \frac{1}{\beta}\right)}{\rho_a(1 - \alpha T_1) - \rho_w} \tag{5.18}$$

Where the given values are as labelled in Figure 5.9.

The "post-rift" thermal subsidence is then determined by calculating the temperature structure, and hence density structure of the lithosphere through time. This may be achieved by solving the one-dimensional (e.g., McKenzie, 1978) or two-dimensional (e.g., Cochran, 1983) heat flow equation. It was found that with the low β values and long rift durations and large spatial extent relevant to the Parnaíba basin case, that the effect of two-dimensional heat flow was $< 1\%$ of the total subsidence. The solutions for one-dimensional and two-dimensional heat flow are given by, for example, McKenzie (1978); Cochran (1983) and Madon (1995).

In order to simulate a finite rift duration, the syn-rift stage is modelled as a series of short discrete rifts (each representing one time step), during which, the temperature structure determined at the end of each time step is used as the input for the following time step. As discussed by Madon (1995) for a given rift duration R_d, the β-factor is increased exponentially from 1 at time $t = 0$ to the specified β value at $t = R_d$. Hence, the lithosphere is stretched by an amount β_{inc} at each time step:

$$\beta_{inc} = e^{ut_i} \tag{5.19}$$

where u is given by $\frac{1}{\Delta t_s} ln\beta$ and is the constant which governs the exponential increase in β and t_i is the time step.

To allow for the calculation of two-dimensional heat flow, the lithosphere is divided into discrete vertical columns. The temperature structure is then determined for each block by first solving the one-dimensional vertical heat flow in each column and then solving for one-dimensional lateral heat flow between the columns. Cochran (1983) found that a time step of 0.5 Myr was an adequate length to allow for lateral heat flow to effect the centre of adjacent

blocks while still approximating a continuous rifting scenario, provided post-rift columns are $< 10\ km$ in width.

5.5.2 Finite rifting: model parameters

Table 5.2 summarises the lithospheric parameters used during finite rift modelling. These and are the same as those used for deriving a standard continental lithospheric reference section in Section 4.6.2. It is assumed that the lithosphere has reached its present-day thickness thermal thickness of 170 km (Priestley and McKenzie, 2013) prior to basin initiation and the basin infill density is set as 1030 $kg\ m^{-3}$, i.e., a water filled basin. As discussed by Armitage and Allen (2010), the temperature at the base of the lithosphere may have been higher in the Neoproterozoic than at the present-day and will have decreased with time, given that the mantle has been cooling at a rate of 50–100°$C\ Ga^{-1}$ (Pollack et al., 1993). However, similarly to Armitage and Allen (2010), it was found that variations in the basal temperature on the order of less than a few hundred degrees had relatively minor effects on the calculated subsidence curves.

Parameter	Symbol	Value	Units
Thermal lithospheric thickness	T_L	170	km
Zero elevation crustal thickness	T_c	35	km
Crustal density at 0 °C	$\rho_* c$	2810	$kg\ m^{-3}$
Mantle density at 0 °C	$\rho_* m$	3310	$kg\ m^{-3}$
Water density	ρ_w	1030	$kg\ m^{-3}$
Coefficient of thermal expansion	α	3.28×10^{-5}	°C^{-1}
Mantle potential temperature	T_p	1333	°C
Thermal diffusivity	κ	8×10^{-6}	$m^2\ s^{-1}$
Stretching factor	β	-	-
Crustal thermal conductivity	K_c	3.138	W $m^{-1}\ K^{-1}$
Lithospheric mantle thermal conductivity	K_m	3.138	$W\ m^{-1}\ K^{-1}$
Acceleration due to gravity	g	9.81	$m\ s^{-2}$
Internal heat generation	HFC	0	HFU
Infill density	ρ_{infill}	1030	$kg\ m^{-3}$

Table 5.2: Summary of parameters used in the thermal and mechanical modelling.

5.5.3 Extensional modelling results

Figure 5.10 compares the observed backstrip curves at the 2-BAC well to the calculated subsidence assuming an initial rifting age of 444 Ma (i.e., base Silurian). The figure shows that the best fit is for a rift duration of 75 Myr and $\beta = 1.15$. This parameter pair implies a depth to Moho beneath the well of 35 $km/1.15 + 3.5$ $km = 33.7$ km which is significantly less than the minimum Moho depth of 40 km derived from wide-angle seismic data (Fig. 3.28). Models in which the initial crustal thickness is greater than 35 km were also tested

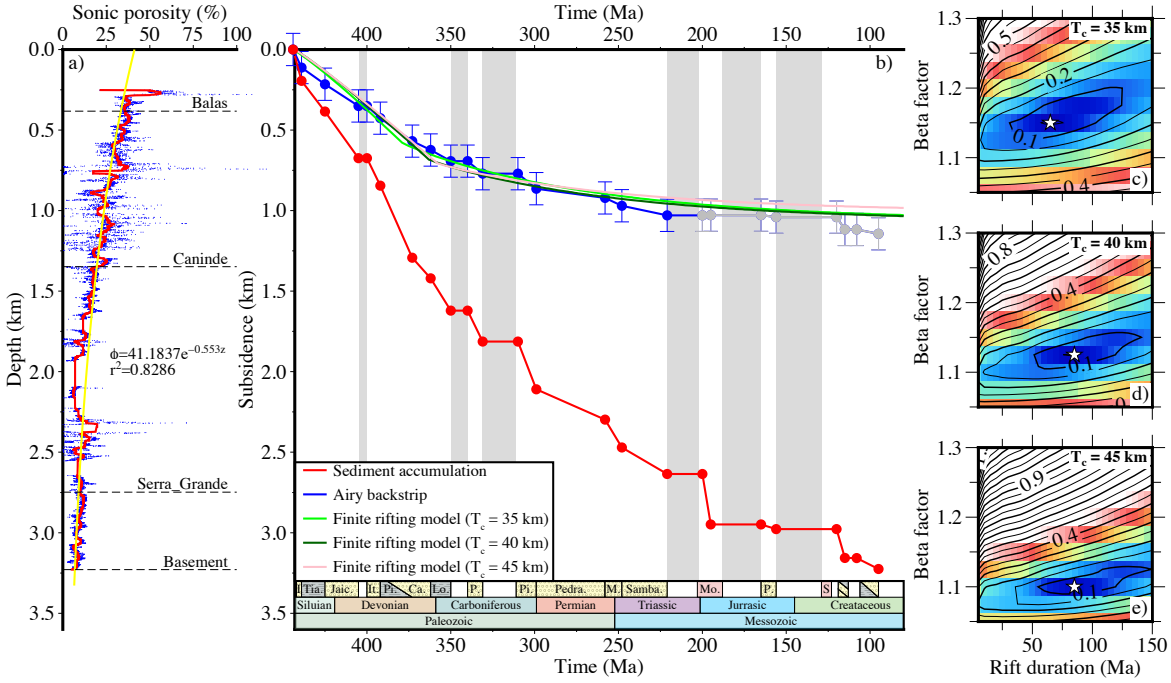


Figure 5.10: Subsidence history at well 2-BAC located in the centre of Parnaíba basin. a) Sonic porosity versus depth. Blue dots are raw data, red line is 181-point median filter, yellow curve is the best fit exponential function, and dashed black lines are megasequence boundaries. b) Tectonic subsidence and uplift history. Red curve is the total sediment accumulation through time. Blue curve is the backstripped tectonic subsidence once the sediment load is removed and shows the part of the subsidence to which the rifting has been compared. Grey curve shows what we believe to be the post-cratonic basin phase of subsidence. Light green, dark green, and pink curves are the best fit model curve based on a finite rifting extension model with a starting crustal thickness of 35, 40, and 45 km respectively. Grey vertical strips show regions of missing section. (c–e) Grid search results for the best fit stretching factor, β, and rift duration assuming a thermal thickness of 170 km for starting crustal thickness of 35, 40, and 45 km.

(e.g., Fig. 5.10d–e). It was found that an equally good fit to the observed subsidence data

can be achieved using a range of initial thicknesses, with an initial crustal thickness of $\sim$ 42 km required in order to reproduce the seismically observed Moho depth. However, as discussed in Section 4.6.2, an initial crustal thickness of > 40 km is at odds with isostatic considerations. Furthermore, irrespective of whether the depth to Moho can be reproduced, a rifting mechanism is also inconsistent with the regional reflection profile (Fig. 3.9) which lacks extensional strain features, as well as gravity modelling (Chapter 4) and the morphology of the basin depocenter through space and time, as revealed by flexural backstripping (Fig. 5.8).

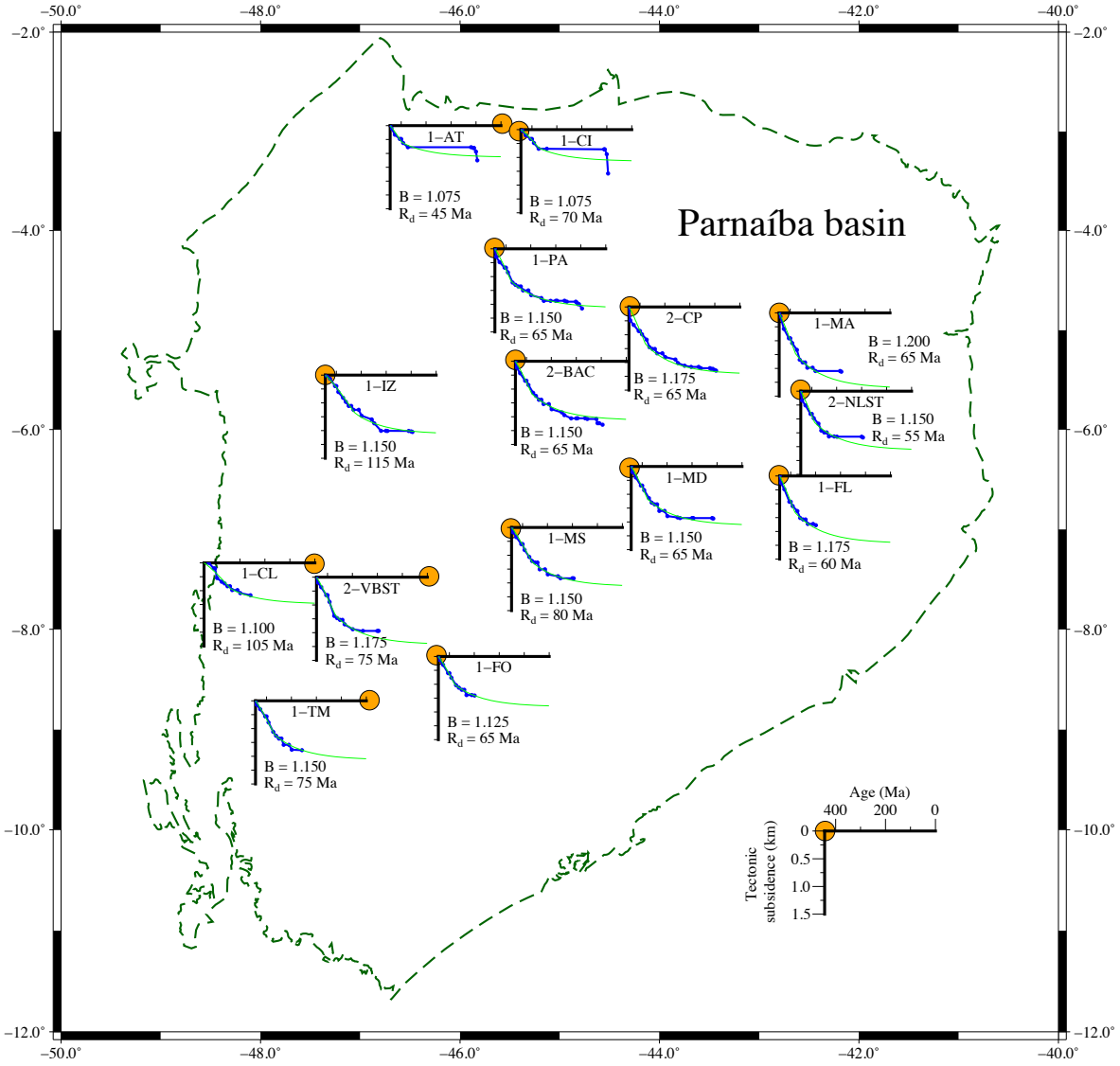


Figure 5.11: Tectonic subsidence curves for all wells that reach basement or pre-Silurian sediments (location, orange filled circle). Airy backstrip (blue) and modelled (green) subsidence curves. The best fit stretching factor, β, and rift duration (R_d) are indicated for each well. Note that best fit curves are only fit the TS-3 (cratonic basin) phase of the subsidence history.

5.6 Time dependent flexure: Buried loading and viscoelastic stress relaxation

In the previous two sections, the lithosphere was assumed to respond to loads in either an Airy ($T_e = 0$) or purely elastic manner. However, by comparing estimates of the elastic thickness derived from a variety of processes that effect the lithosphere on time scales varying from a few seconds to 10's of millions of years, for example, the passage of seismic waves (seconds);

post-seismic rebound (years); post glacial rebound ($kyr's$) and orogenic loading ($Myr's$), it has been established that continental lithosphere exhibits a greater strength (larger T_e) at the time of loading and then weakens with time (e.g., Watts, 1978; Watts, 2011; Watts et al., 2013). The mechanism responsible for such weakening is not well understood, however, Watts et al. (2013) suggest this is likely some form of stress induced relaxation that occurs by ductile and plastic flow, as such mechanisms are found in experimental rock mechanic studies and are predicted by steady-state creep laws for olivine (e.g., Mei et al., 2010). Regardless of the physical mechanism controlling the relaxation, it has been shown that such a process can be modelled using a multi-layered visoelastic plate model (e.g., Watts et al., 2013; Watts et al., 2013).

5.6.1 Viscosity structure

It is known from volcano loading (Watts and Zhong, 2000) and studies of outer rise flexure at subduction zones (Hunter and Watts, 2016) that the elastic thickness of oceanic lithosphere, T_e, is a function of both plate and load age. The strength of the lithosphere increases with plate age as it cools and increases its density, such that old seafloor is more rigid than young seafloor. But strength decreases with load age as the lithosphere relaxes from its short-term thickness to its long-term elastic thickness. There is, therefore, a "competition" between thermal cooling, which works to strengthen the plate, and a load-induced stress relaxation that weakens it.

Watts and Zhong (2000) used a multi-layered viscoelastic model in which the effective viscosity of the oceanic lithosphere is determined from its thermal structure to show that volcano loads would be supported initially by a thick, essentially elastic, structure that would then weaken with time. For example, volcano loads emplaced on 80 Ma seafloor would relax rapidly, such that $\sim$ 50 % of the final subsidence is achieved within the first $\sim$ 50,000 years following load emplacement. The rate of subsidence depends on thermal age: young seafloor subsides more rapidly than old seafloor. As the subsidence increases with age since loading, flanking flexural bulges migrate in toward the load.

For the case of continental lithosphere, thermal considerations, kimberlite and xenolith

nodules, and geochemical calculations suggest significant differences in the viscosity structure between relatively old cratonic lithosphere and that of oceanic lithosphere. Dixon et al. (2004), for example, calculated the viscosity of cratonic continental lithosphere between 75–125 km depth using a thermally activated power-law creep law and assuming a cratonic "shield intraplate" geotherm defined by Green and Falloon (1998). They derived values between 10^{23}–10^{25} $Pa\ s$ for dry cratons, assuming uniform strain rates of 10^{-15} and 10^{-16} s^{-1}. Importantly, these values are an order of magnitude greater than at equivalent depths in oceanic lithosphere (e.g., Watts et al., 2013). A consequence of such a viscosity structure is that when cratonic lithosphere is loaded, it would be expected to undergo a stress relaxation over much longer times than would oceanic lithosphere.

Unfortunately, there are no temperature/depth estimates from, for example, mantle xenoliths nodules, with which to constrain a local geotherm for the lithosphere beneath the Parnaíba basin, particularly, at the time of load emplacement relevant for modelling the subsidence. Nonetheless, Priestley and McKenzie (2006) developed a novel proxy for lithospheric temperature structure, using Rayleigh wave tomography. These authors showed that Rayleigh wave velocity is primarily a function of vertically polarised shear wave velocity, which is, in turn, a function of temperature. Hence, they were able to estimate lithospheric temperatures globally. Priestley and McKenzie (2013) provided an improved resolution of global Rayleigh wave velocity, and temperature estimates derived from these data are shown as depth slices beneath the Parnaíba basin in Figure 5.12.

Only temperature estimates from below 100 km are used as vertical resolution is $\sim$ 50 km, such that, lower crustal/upper mantle smearing occurs at shallower depths (Priestley and McKenzie, 2013). Figure 5.13a shows a geotherm for present day Parnaíba basin calculated using the parameters shown in Table 5.3 and constrained using temperature estimates from Figure 5.12 sampled at the location of well 2-BAC. The crustal portion of the geotherm is calculated using a two-layer heat conduction model (e.g., Allen and Allen, 2013), with internal heat generation rates similar to those suggested by Jaupart et al. (1998) for granulites.

The upper mantle portion of the geotherm was calculated using the method of McKenzie et al. (2005) and a temperature dependent thermal conductivity. The thermal lithospheric

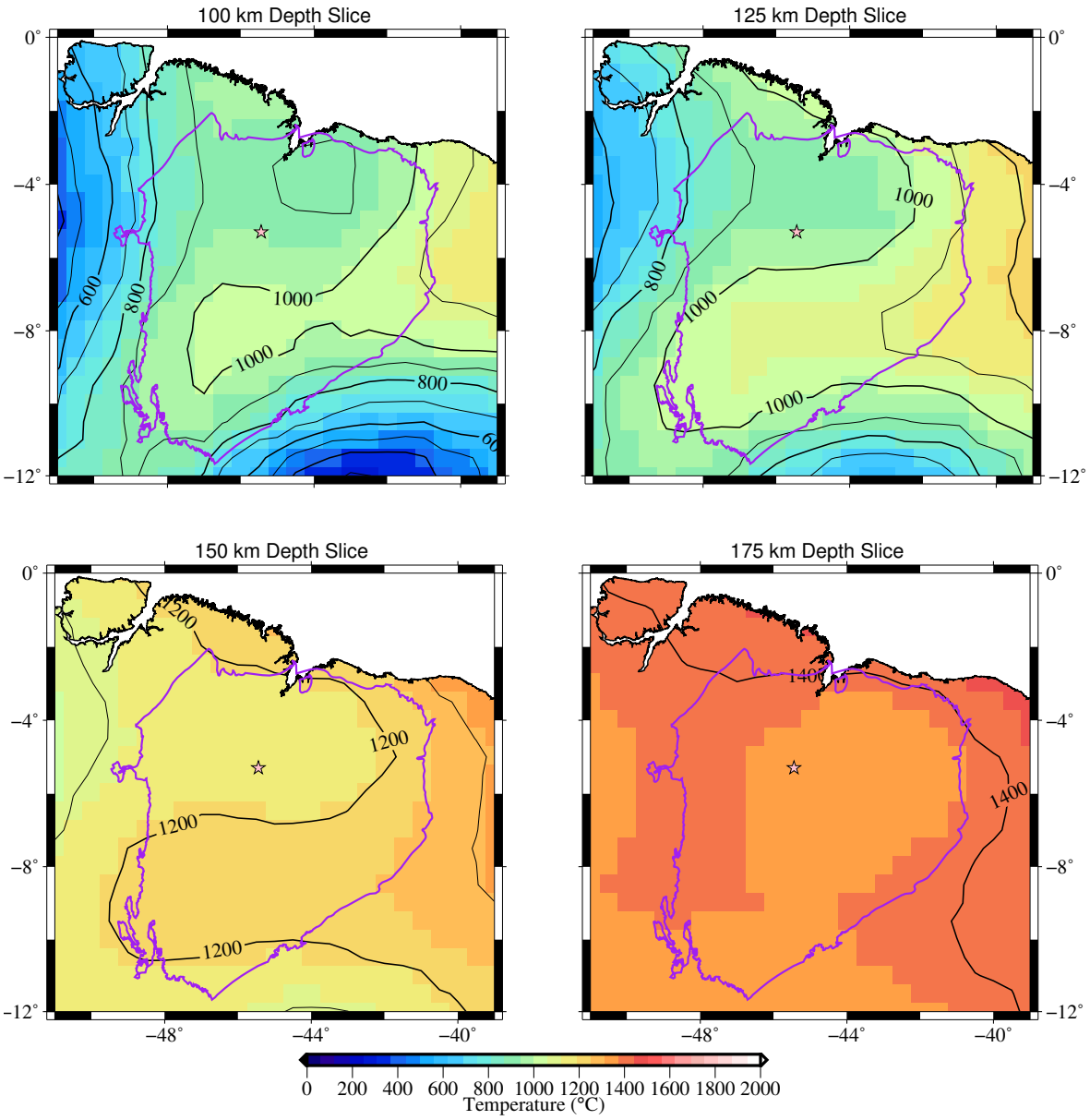


Figure 5.12: Temperature ($°C$) beneath Parnaíba basin at depths 100, 125, 150 and 175 km estimated from Rayleigh wave tomography (Priestley and McKenzie, 2013). Purple line defines Parnaíba basin outline. Pink star indicates the position of well 2-BAC where the geotherm in Figure 5.13 is calculated.

thickness is defined as the depth at which this geotherm intersects the mantle isentrope. The temperature structure of the thermal boundary layer, in which a combination of conductive and convective heat transfer occurs is not calculated, as it is has been shown that this differs by only a few percent from that of the conductive mechanical boundary layer geotherm (Priestley and McKenzie, 2013). The viscosity structure predicted from this geotherm, calculated using the same thermally-activated power law creep formulation for effective viscosity as used by

Parameter	Symbol	Value	Units
Thermal lithospheric thickness	T_L	170	km
Upper crustal thickness	Z_1	20	km
Lower crustal thickness	Z_2	20	km
Surface temperature	T_s	10	$°C$
Surface thermal conductivity	$k(T)$	3.5	$W\ m^{-1}\ K^{-1}$
Internal heat generation upper crust	A_1	$1.3e^{-6}$	$W\ m^{-3}$
Internal heat generation lower crust	A_2	$0.4e^{-6}$	$W\ m^{-3}$
Mantle heat flow	q_m	17	$mW\ m^{-2}$
Bulk crustal density	ρ_c	2810	$kg\ m^{-3}$

Table 5.3: Summary of parameters used to calculate a geothermal gradient for Parnaíba basin.

Dixon et al. (2004), and assuming a strain rate of 10^{-16}, is shown in Figure 5.13b. These values corroborate those predicted by Dixon et al. (2004) based on a global "shield intraplate" geotherm.

5.6.2 Viscoelastic modelling results

Figure 5.14 shows the calculated subsidence due to a buried load, the size of which is chosen to approximate that derived from gravity and seismic data (see Chapters 3 and 4), emplaced on a multilayered viscoelastic plate model. The model is a simple three-layered case comprising an upper 0–50 km high viscosity (10^{34} $Pa\ s$), essentially elastic layer; a middle 50–75 km layer of viscosity 10^{27} $Pa\ s$; and a lower 75–300 km layer with a viscosity of 10^{24} $Pa\ s$. The viscosity selected for the lower layer is within the range suggested by Dixon et al. (2004) for a dry rheology craton and that determined for present-day Parnaíba basin in Figure 5.13. The figure shows a rapid initial subsidence that is followed by a slow exponentially decreasing subsidence. The pattern of subsidence reflects the fact that the deeper, hotter, low viscosity layers loose their strength first through thermally activated creep while the shallower, colder, layers loose their strength much more slowly.

Figure 5.14 shows that a load induced viscoelastic stress relaxation could indeed contribute to the long tectonic subsidence history as recorded in deep wells in the Parnaíba basin. In particular, stress relaxation explains the exponential nature of the subsidence, which is recorded

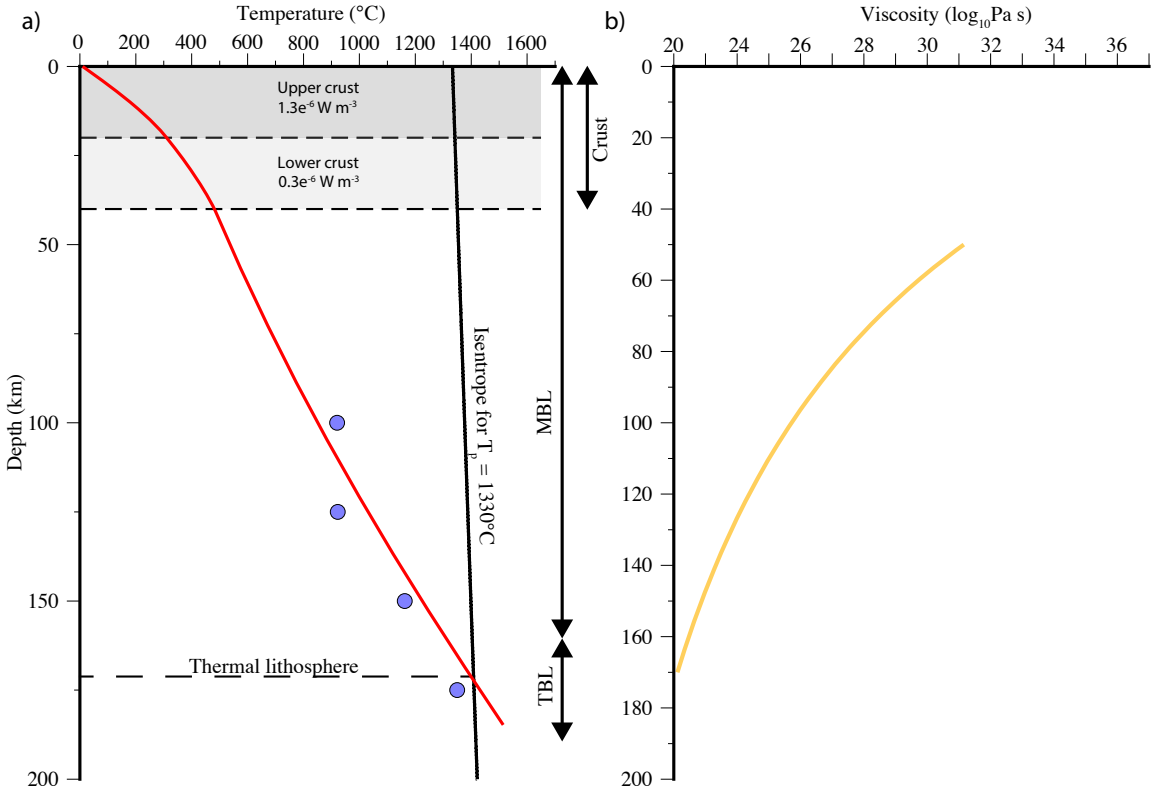


Figure 5.13: a) Geothermal gradient for present-day Parnaíba basin. The crustal component is calculated using a two layered model with radiogenic heat production in the upper and lower crust of 1.3 and 0.3 $\mu W\ m^{-3}$ respectively. The mechanical boundary layer (MBL) curve is calculated using the method of McKenzie et al. (2005) with a temperature dependent conductivity derived from Gabbro (Miao et al., 2014). The Blue circles are temperature estimates from Rayleigh wave tomography (Priestley and McKenzie, 2013). The temperature structure in the Thermal Boundary Layer (TBL) which is shown schematically, is not calculated. b) Predicted effective viscosity structure based on the method outline by Dixon et al. (2004) for a power law creep flow law for dry dislocations. Effective viscosities are only calculated below 50 km as values for the relevant flow law parameters are only available below this depth.

in the latter part of the subsidence history at each of the Parnaíba basin wells. A range of viscosity models were tested (see Section 5.6.3) and it was found that they all predict an exponentially decreasing subsidence. However, only the models in which the viscosity of the lowest viscosity layer was $\sim 10^{24}$–10^{25} $Pa\ s$ can explain the long-term basin subsidence: higher viscosities produced too slow a subsidence and lower viscosities too rapid a subsidence.

Irrespective of the actual viscosity structure, most models in which the viscosity decreases with depth also predict stratigraphic offlap at the edges of the basin. This is because as the lithosphere relaxes, the load-induced subsidence increases, and the flanking bulges migrate in toward the load. The basinward sediment younging, which is well developed in the Devonian

and Carboniferous at the eastern edge of the Parnaíba basin, will be further enhanced by regional uplift and erosion. However, it will be obscured by structural inversion subsequent to basin initiation, such as may have occurred at the western edge of the basin during the Mesozoic (Daly et al., 2014).

One problem is the initial subsidence occurs more rapidly than is observed for almost all viscosity structures. This may reflect the fact that in the model, the load is emplaced instantaneously. It is more likely that intruded material would cool over a finite time, during which, the load mass would increase as it densifies. It is expected that such a process would cause the initial elastic response to be partitioned over the cooling duration. Furthermore, there would also be a thermal subsidence component from such a process. Modelling of these effects would require a full numerical thermo-mechanical approach, which is outside the scope of this thesis. However, similarly to as applied by Stel et al. (1993), a first order estimate for the solidification time of an intrusion is given by Turcotte and Schubert (1982) as:

$$t_s = \frac{b^2}{4k\lambda_2^2} \tag{5.20}$$

Where b is the half-width of the intrusion ($10\ km$); k is thermal diffusivity ($8 \times 10^{-7}\ m^2\ s^{-1}$) and λ_2 is a constant related to the position of the solidification boundary defined by:

$$\frac{H\sqrt{\pi}}{c(T_u - T_c)} = \frac{e^{-\lambda_2^2}}{\lambda_2(1 + erf\lambda_2)} \tag{5.21}$$

Where H is the latent heat of crystallisation ($3.3 \times 10^5\ J\ kg^{-1}$); c is the heat capacity ($1.05 \times\ J\ kg^{-1}\ K^{-1}$); $T_u - T_c$ is difference in temperature between the intrusion and host rock ($250°C$).

This returns a cooling duration of $t_s = 10.5\ Myr$. Increasing the load size over this duration would be expected to provide a better fit to the observed initial subsidence trajectory by effectively shallowing the gradient of the subsidence curve during this initial phase, such

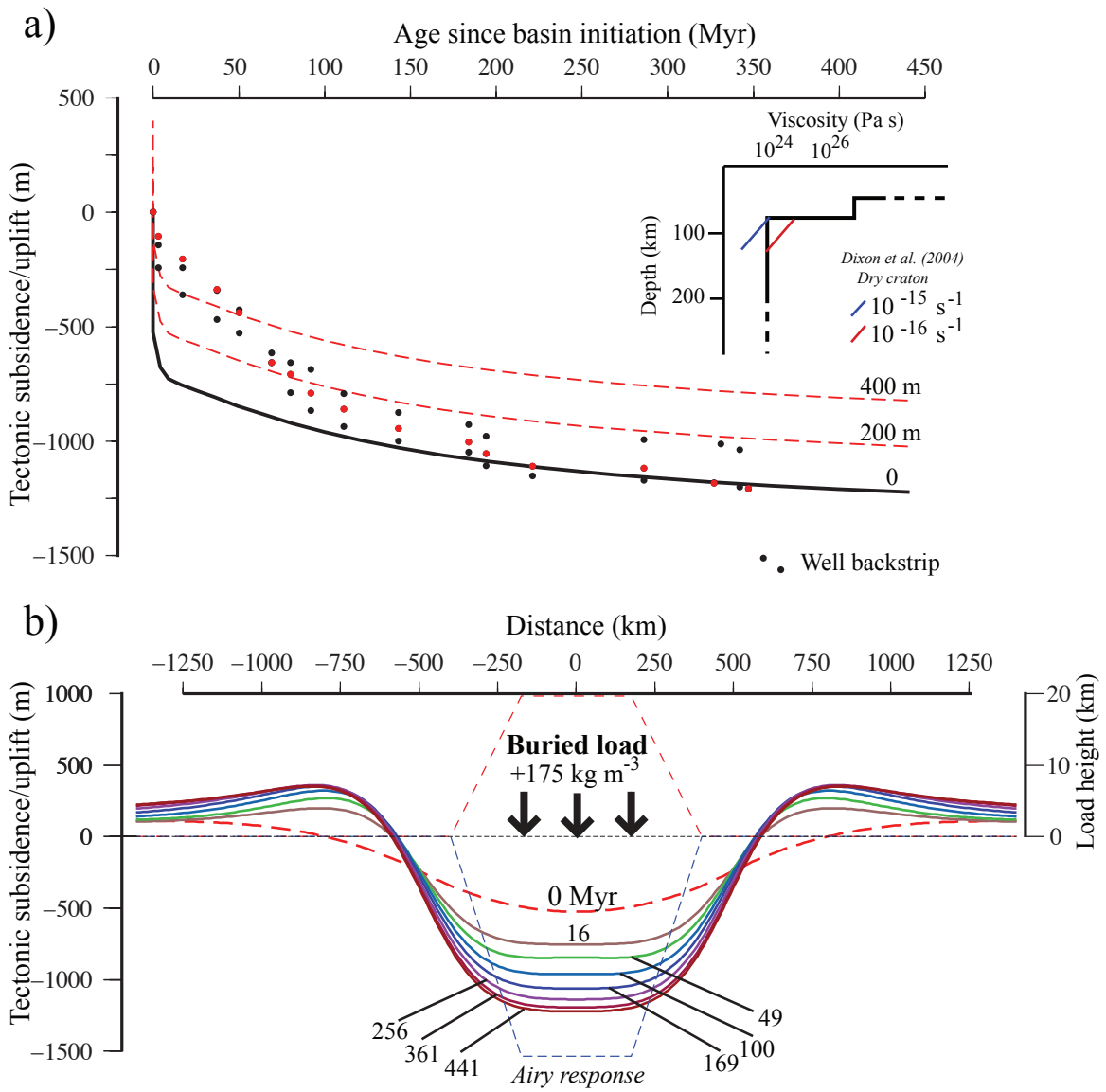


Figure 5.14: Comparison of the observed and calculated subsidence of a multilayered viscoelastic model caused by a buried load. The observed subsidence is based on the tectonic subsidence derived from backstripping wells in Figure 11. Black filled circles show wells that reached basement. Red filled circles show the backstripped tectonic subsidence at the 2-BAC well in the centre of the basin (Fig. 5.3). The calculated subsidence is based on a buried load with a geometry (i.e., top radius and bottom radius and height) constrained by the seismic and gravity data (Chapters 3 and 4) and the viscosity structure shown in the inset. Black line = calculated subsidence. Red dashed lines = subsidence shifted vertically by 200 (lower curve) and 400 m (upper curve). (a) Subsidence as a function of age since basin initiation at 443 Ma (i.e., base Silurian). (b) Subsidence as a function of distance across the (assumed) symmetric buried load.

that, the initial subsidence is not as rapid as shown in Figure 5.14.

5.6.3 Sensitivity tests

Given the number of variables involved in the viscoelastic modelling, sensitivity tests were carried out to provide estimates as to the relative control each parameter has over the subsidence history, explore the model space and test the robustness of the subsidence results. Namely, the postulated load size and weight, and the viscosity structure of the lithosphere are tested. Figure 5.15 shows the results from these sensitivity tests. Each parameter was varied while holding all other parameters fixed at the values used in the calculation of Figure 5.14 (dashed black lines in Figure 5.15). To determine the RMS misfit, the predicted subsidence curves were compared with the Airy backstrip from well 2-BAC (Fig. 5.10).

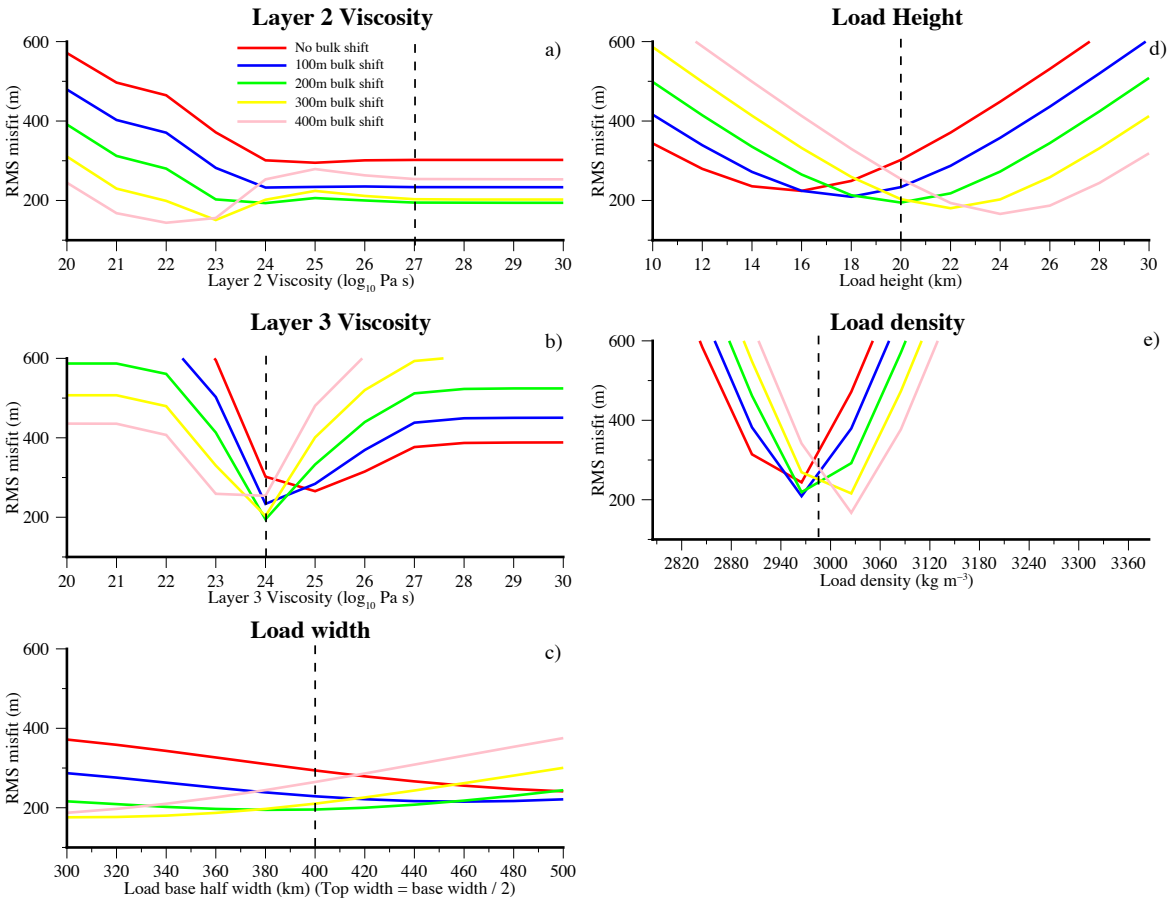


Figure 5.15: Results from single parameter sensitivity tests. Coloured curves are results from the same tests but with various bulk shift (starting topography) values as labelled in (a). Dashed black lines indicate the value used in the calculation used to create Figure 5.14. Note "V" shaped curves are suggestive of highly sensitive parameters, while horizontal curves suggest the modelling results are relatively insensitive to the given parameter.

5.6.3.1 Layer two viscosity

Figure 5.15a shows that if layer two viscosity is less than 10^{24} $Pa\ s$, this results in a worse fit to the data. This results from relaxation occurring too rapidly. Interestingly, it appears that overall RMS misfit is insensitive to layer two viscosity, provided it is greater than 10^{24}. For the case when a 400 m bulk shift is applied, RMS misfit reduces for viscosities less than 10^{24}. Inspection of the predicted subsidence curves shows, however, this results from the early part of the subsidence being fit very well, while the total tectonic subsidence is much less than is observed.

5.6.3.2 Layer three viscosity

Figure 5.15b shows that the predicted subsidence profile is very sensitive to layer three viscosity. It appears that a viscosity of 10^{23}–10^{25} is required to produce a subsidence record in the range of that observed. Both an increase and decrease in viscosity result in large increase in RMS misfit. This is because higher viscosities produced too slow a subsidence and lower viscosities too rapid a subsidence.

5.6.3.3 Load width

The load size and density are constrained independently by geophysical analysis (see Chapters three and four), however, these are subject to a degree of non-uniqueness inherent in gravity modelling. With regards to the predicted subsidence, the weight of the emplaced load (as a function of load width, height and density) is an important parameter. Figure 5.15c shows the subsidence predicted from the viscoelastic modelling is relatively insensitive to load width, within the range expected from gravity modelling.

5.6.3.4 Load Height

Figure 5.15d shows the subsidence predicted from the viscoelastic modelling is moderately sensitive to load height. For the case where no existing topography is invoked (red line),

decreasing the load height from 20 km to 16 km provides an improved fit.

5.6.3.5 Load density

Figure 5.15e shows that the predicted subsidence profile is very sensitive to the density of the load. Interestingly, this test shows that the independently derived load density contrast of $+185\ kg\ m^{-3}$ (i.e., bulk density of $2985\ kg\ m^{-3}$) is within a narrow range of density contrasts that provide a minimum in RMS misfit. Increasing or decreasing densities from this value by $\pm\ 100\ kg\ m^{-3}$ result in a poor fit to the data.

5.6.3.6 Viscosity structure: two-parameter grid search

Viscosity structure is the least well-known parameter within this model. The present-day structure is poorly constrained and the structure at the time of loading is essentially unknown. Hence, a grid search method was adopted to further test the RMS misfit produced by a range and viscosity pairs for the middle and lower layers of a three-layer case. The upper layer was held fixed as an essentially elastic layer with a viscosity of $10^{34}\ Pa\ s$.

Figure 5.16 shows the results from these tests. This shows that similarly to the single parameter tests, the layer 3 viscosity must be 10^{24}–$10^{25}\ Pa\ s$, while the model is relatively insensitive to layer 2 viscosity, provided it is above $10^{23}\ Pa\ s$.

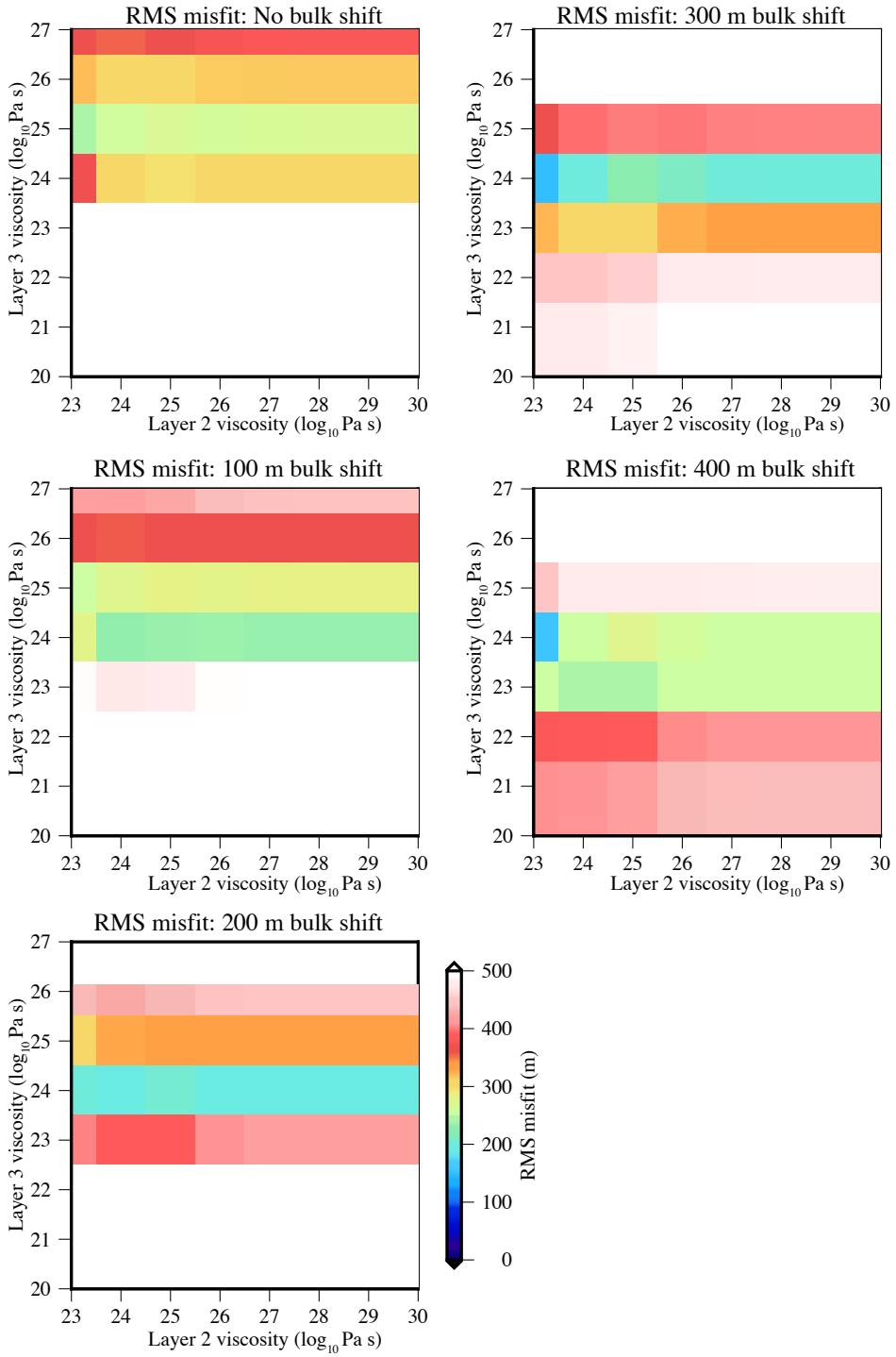


Figure 5.16: Results from viscosity structure sensitivity tests to changes in layer 2 and 3 viscosities for fitting the well 2-BAC tectonic subsidence curve. Each panel consists of the same tests but with a different bulk shift (starting elevation) applied to the calculated subsidence curve.

5.7 Summary

In this chapter, the temporal subsidence history of Parnaíba basin has been determined via Airy and flexural backstipping. These observations were used to test two geodynamic mechanisms for basin formation, namely, lithospheric extension and viscoelastic relaxation following load emplacement. The key points are as follows:

- Airy-backstripping reveals that Parnaíba basin is characterised by a simple tectonic subsidence history that is consistent in form with both a concave up, gentle negative exponential subsidence trajectory or an initial linear subsidence, followed by a subdued exponential.
- Three-dimensional flexural backstripping reveals that tectonic subsidence of Parnaíba basin initiated as a broad sub-circular region, which spatially correlates with an at least 250 km wide zone of strong Mid Crustal Reflectivity (MCR) imaged on the two-dimensional regional reflection profile (Fig. 3.9). This morphology persisted through to the Longa formation, at which time the basin appears to narrow and migrate to the Northwest.
- A finite-rifting extensional model can provide an excellent fit to the observed Airy backstripped subsidence, provided β-values are between 1.1–1.2 and the rift duration is 55–75 Myr. However, both the predicted Moho depth and gravity anomaly from an extensional model are at odds with those observed beneath the basin.
- A dense load emplaced on a viscoelastic plate that relaxes on time-scales of several tens of million years is capable of providing a long-term (100's Myr) subsidence, with a trajectory similar to that of Parnaíba basin. It is, therefore, possible that this process may play a key role in the long-term subsidence of cratonic basins.
- Other factors such as thermal cooling, sea level change, loading history and plate strengthening following magma intrusion may also contribute to Parnaíba basin subsidence and may offer explanations for the departures from the subsidence curve predicted from the simple viscoelastic loading model.

Chapter 6

A comparative study of the Parnaíba, Michigan and Congo cratonic basins

6.1 Introduction

In this chapter, analysis is extended to the Michigan and Congo cratonic basins. This analysis is conducted to facilitate a comparison of the morphology, gravity anomaly and subsidence histories of these basins and the Parnaíba basin, in order to assess whether generic conclusions regarding the formation of cratonic basins can be drawn. First, the morphology and stratigraphy of these basins are briefly outlined. Next, compilations of well and seismic data are used to create sedimentary isopach and gross thickness maps for each basin. These data are then used to produce sediment-corrected residual Bouguer gravity anomalies for each basin. Finally, well data are backstripped using an Airy approach and modelled using a viscoelastic plate loading model, similar to that applied to Parnaíba basin in the previous chapter. Comparative maps presented in this chapter are plotted using a cylindrical equal area projection, to facilitate direct spatial comparisons between the basins.

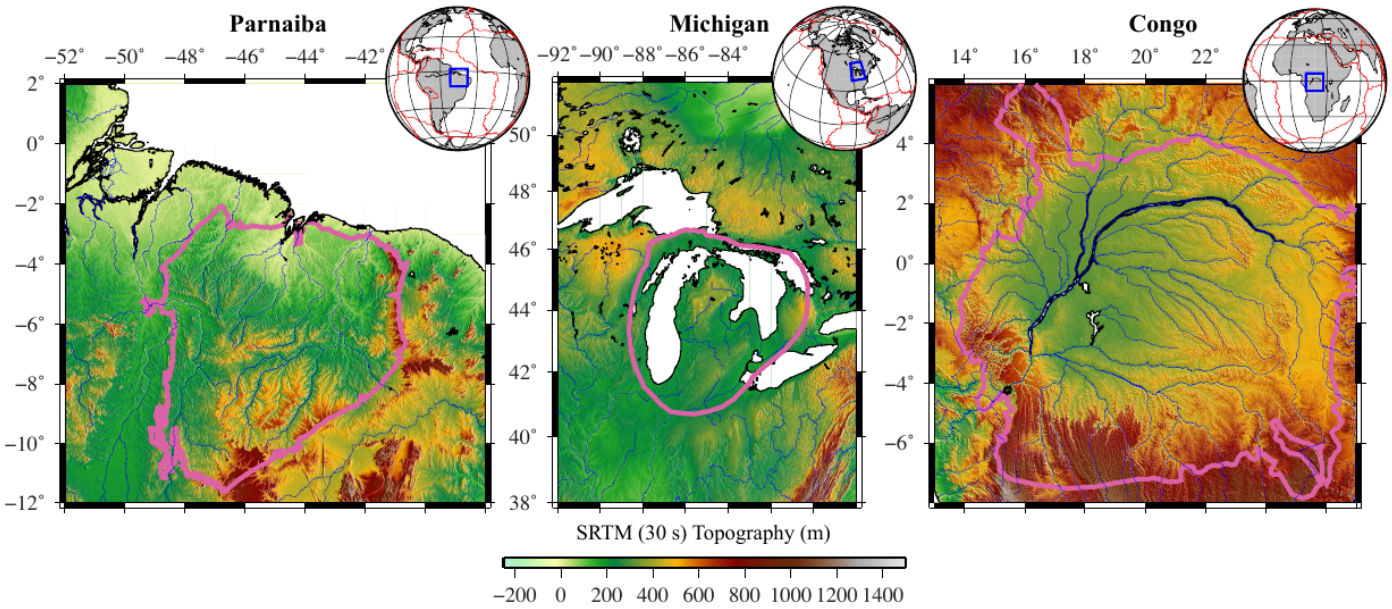


Figure 6.1: Topography of the Parnaíba, Michigan and Congo basins based on SRTM 30 × 30 s data (Farr et al., 2007). Inset globes show locations of main figures. The topography has been plotted on a Cylindrical Equal Area Projection in order to facilitate comparisons between basins. Water covered regions are masked. Thick pink lines show the present-day basin outlines. Thin blue lines show permanent rivers. Note the high topography in the south-central Parnaíba ($\sim$ 200–550 m) and north-central Michigan basins ($\sim$ 300–350 m) relative to their flanks. Congo, in contrast, is characterised by relatively low topography relative to its surroundings ($\sim$ 300–450 m).

6.2 Morphology and stratigraphy

Figure 6.1 shows the basin outlines and present-day topography within and surrounding each of the Parnaíba, Michigan and Congo basins. This shows the topographic expressions of these basins are dissimilar, with unique geomorphological patterns in each. Sedimentation within both the Parnaíba and Michigan basins terminated $>$ 100 Myr ago and the topographic variations in these basins, which is characterised by highs of $\sim$ 800 and 350 m respectively, probably reflects Quaternary geomorphological processes, such as river incision. In the case of Michigan, erosion and sedimentation associated with the Last Glacial Maximum are thought to have played a major role in shaping the current geomorphology (e.g., Kincare and Larson, 2009). Similarly, a series of incised plateau surfaces stepping down from the southern boarder of Parnaíba basin, towards the Atlantic margin in the north, are suggestive of recent crustal movements. The topography in both Parnaíba and Michigan basins therefore, unsurprisingly,

appears to be unrelated to cratonic basin formation. In contrast, the Congo basin forms a striking bowl-shaped topographic low with respect to the surrounding cratons. This correlates very closely with the shape of the sedimentary basin, which is consistent with the notion that the Congo basin maybe one of, if not the only, cratonic basin that is actively subsiding in the present day (e.g., Downey and Gurnis, 2009).

6.2.1 Michigan basin

The Michigan Basin is located in the interior of the North American plate (Fig. 6.2). Its present-day extent spans $\sim$ 336,000 km^2, and it is in-filled by $\sim$ 5 km of sediment ranging in age from Proterozoic–Jurassic, although the cratonic basin phase of subsidence began in the Cambrian and is truncated in the Pennsylvanian by a regional unconformity (Fig. 6.3).

This basin exhibits a typical concentric outcrop pattern with sediments younging towards the basin centre. Silurian and younger aged sediments are confined within the primary basin depocenter, however, with the exception of the northern basin limit, where sediments terminate against Precambrian basement, the Lower Ordovician and Cambrian sediments extend beyond the localised basin, over the surrounding arches and into the adjacent Illinois and Appalachian basins. For example, Upper Cambrian-Lower Ordovician isopachs maps of North American exhibit a widespread "platform" sediment cover that spanned the Appalachian, Michigan and Illinois regions at this time (e.g., Cook and Bally, 1975). The basin then became individualised in the Middle Ordovician, though further widespread sedimentation events did occur during the uppermost Ordovician to Late Silurian (e.g., Howell and van der Pluijm, 1990).

Sloss (1963) described the stratigraphy of the North American craton, including the Michigan basin, based on the recognition of six primary sedimentary sequences, named "Sloss sequences" separated by regional unconformities. In this study, these sequences are further subdivided in order to facilitate subsidence analysis. Nevertheless, the Sloss sequences provide useful descriptions of Michigan basin stratigraphy. The Michigan basin preserves sediments from the four oldest Sloss sequences, namely the Sauk, Tippecanoe, Kaskaskia and Absaroka sequences. In the Michigan basin, the earliest Sauk sequence spans the Late Cambrian to

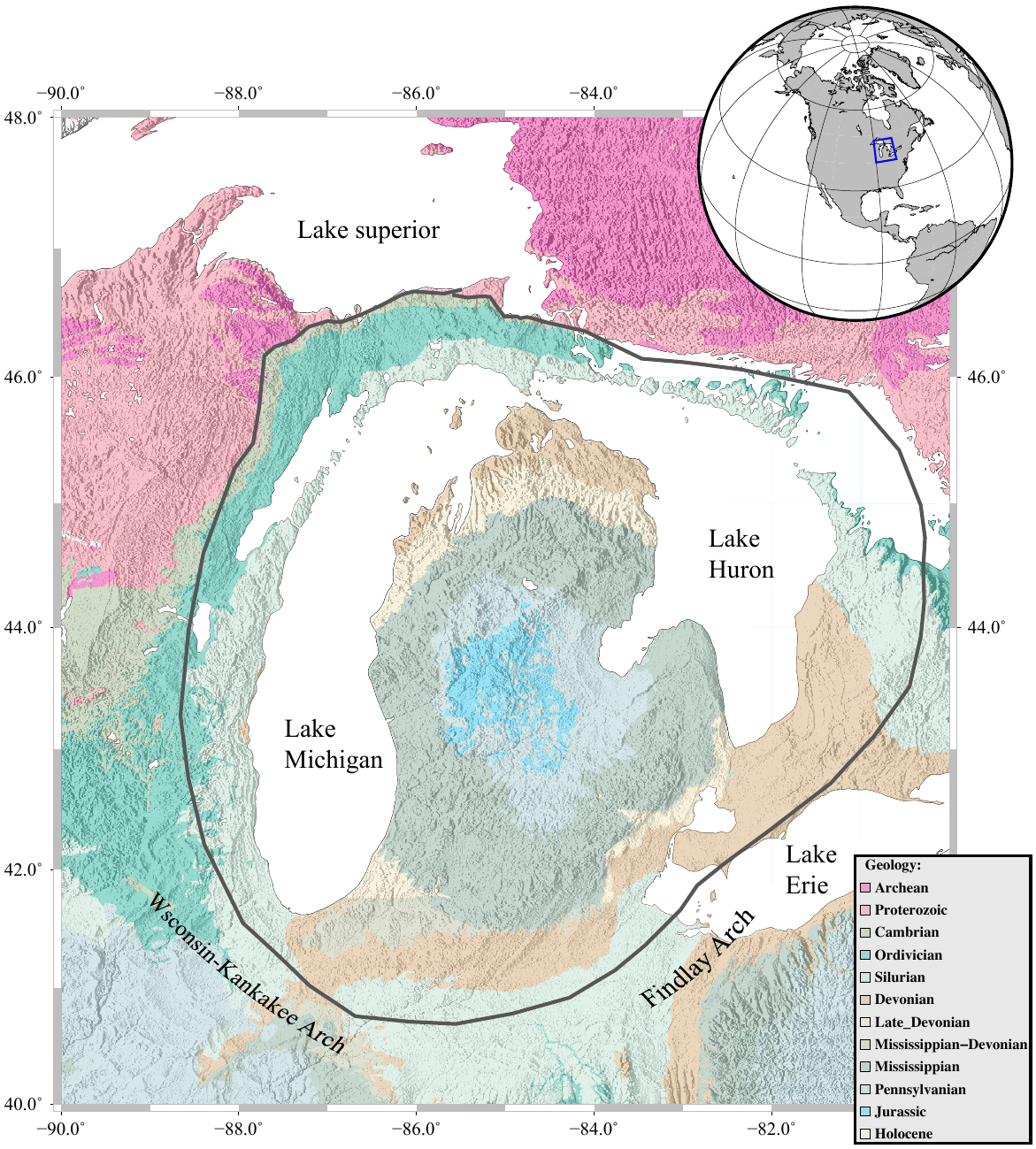


Figure 6.2: Geological map of the Michigan basin, Central USA. Solid grey line shows the areal extent of the basin. Masked regions are lakes. Inset shows global location of the main figure.

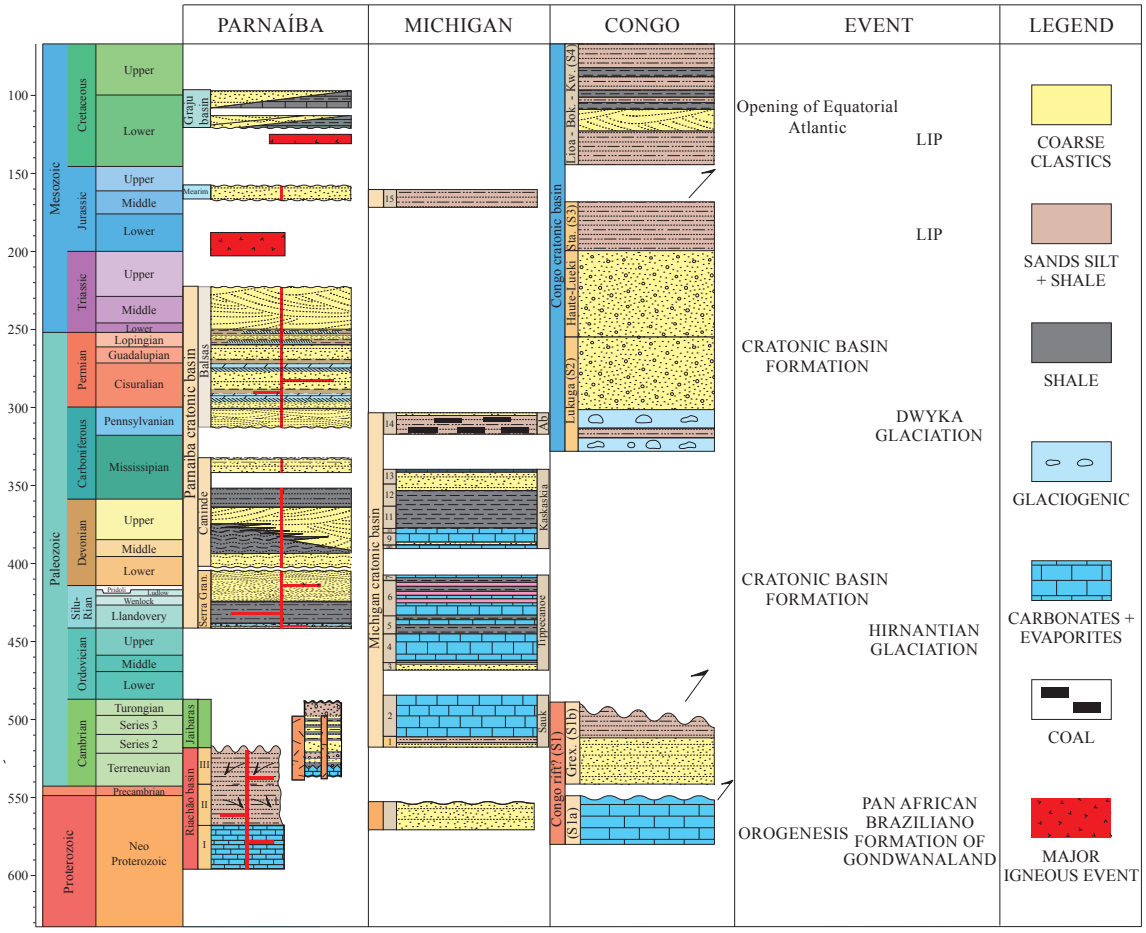
Early Ordovician (515–485 Ma) and consists primary of shallow marine sandstones with late stage carbonates. This is followed by the Tippecanoe sequence from the Middle Ordovician to Early Devonian (472–388 Ma) consisting of basal carbonates with marine shales, salt and evaporates in the Late Silurian section. The third, Kaskaskia sequence, ranges in age from Early Devonian to Mississippian (388–342 Ma) and contains basal carbonates followed by

siliciclastics dominated by shales. The final sloss sequence preserved in Michigan basin, the Absaroka, spans the Pennsylvanian to Jurassic but is terminated in the mid-Pennsylvanian at this locality (315–305 Ma). Here, this sequence is dominated by siliciclastics and marks the top of the cratonic basin section, sealed by a regional unconformity.

6.2.2 Congo Basin

The Congo Basin is located in the centre of the African plate (Fig. 6.4). This basin is much larger than the Parnaíba and Michigan basins, spanning an area of $\sim$ 1,200,000 km^2 and is in-filled by a succession of Neoproterozoic to Recent sediments that exhibit a basin wide average thickness of $\sim$ 4 km, reaching up to $\sim$ 9 km locally (e.g., Daly et al., 1992; Kadima et al., 2011). Formation ages are poorly constrained within the Congo basin owing to a paucity of biostratigraphic data and lack of exposed sections for pre-Cretaceous strata. This has led to differing interpretations regarding the age of initiation of the cratonic basin sequence (e.g., ECL, 1988; Daly et al., 1992; Kadima et al., 2011; Linol, 2013). Following the original Mbandaka-1 and Gilson-1 well interpretations of Esso Zaire SARL. (1981a) and Esso Zaire SARL. (1981b), the earliest cratonic basin sequence is considered Carboniferous in age, deposited unconformably above a tectonically deformed Neoproterozoic/Cambrian sequence. This makes the onset of Congo basin subsidence initiation atypical with respect to all other Gondwanan cratonic basins (see Fig. 1.1). It is possible, however, given the lack of age control, that the oldest cratonic basin sediments may be Early Paleozoic in age (e.g., Daly et al., 1992). The general conclusions drawn from gravity analysis in this chapter are independent of this uncertainty, however, changes in these ages have important implications for subsidence analysis, as discussed below in Section 6.5.

Regardless of their precise ages, the sediments within the Congo basin can be divided into four distinct sequences based on their seismic reflection facies and major unconformities (Figs. 6.3 and 6.5). These are the pre-cratonic basin phase, Neoproterozoic–Cambrian sequence (S1) which consists of two formations; a thinner basal formation (S1a) consisting predominantly of dolomite with some salt, sandstone and siltstone interbeds and rare anhydrite; and an overlying thicker formation (S1b) of mainly conglomerates and sandstones. The tectonic origin of


PARNAÍBA
MICHIGAN
CONGO
EVENT
LEGEND
Opening of Equatorial Atlantic
LIP
LIP
CRATONIC BASIN FORMATION
DWYKA GLACIATION
CRATONIC BASIN FORMATION
HIRNANTIAN GLACIATION
OROGENESIS
PAN AFRICAN BRAZILIANO FORMATION OF GONDWANALAND
COARSE CLASTICS
SANDS SILT + SHALE
SHALE
GLACIOGENIC
CARBONATES + EVAPORITES
COAL
MAJOR IGNEOUS EVENT
Mesozoic
Paleozoic
Proterozoic
Cretaceous
Jurassic
Triassic
Permian
Carboniferous
Devonian
Sil.-Ran
Ordovician
Cambrian
Precambrian
Neo Proterozoic
Parnaíba cratonic basin
Michigan cratonic basin
Congo cratonic basin
Grajaú basin
Marajó basin
Jaibaras
Rio Preto
Ubajara
Trombetas
Serra Grande
Cabeças
Pimenteiras
Longá
Jaicós
Poti
Piauí
Ipu
Tianguá
Gramame
Cabo
Itapecuru
Alcântara
Codó
Corda
Grajaú
Sardinha
Motuca
Sambaíba
Mosquito
Pastos Bons
Balsas
Urucuia
Ribeira basin
Rio Pardo basin
Araçuaí basin
Paraguai belt
Sergipano belt
Rio Ivaí
Rio Paraná
Rio Paraguai
Rio Pantanal
Rio Corumbá
Rio Bodoquena
Rio Apa
Rio Amambai
Rio Iguatemi
Rio Ivinhema
Rio Paranaíba
Rio Grande
Rio Tietê
Rio Paraíba do Sul
Rio Doce
Rio Jequitinhonha
Rio Pardo
Rio Mucuri
Rio Itabapoana
Rio Itapemirim
Rio Itabapoana
Rio Itapemirim
Rio Paraíba do Sul
Rio Doce
Rio Jequitinhonha
Rio Pardo
Rio Mucuri

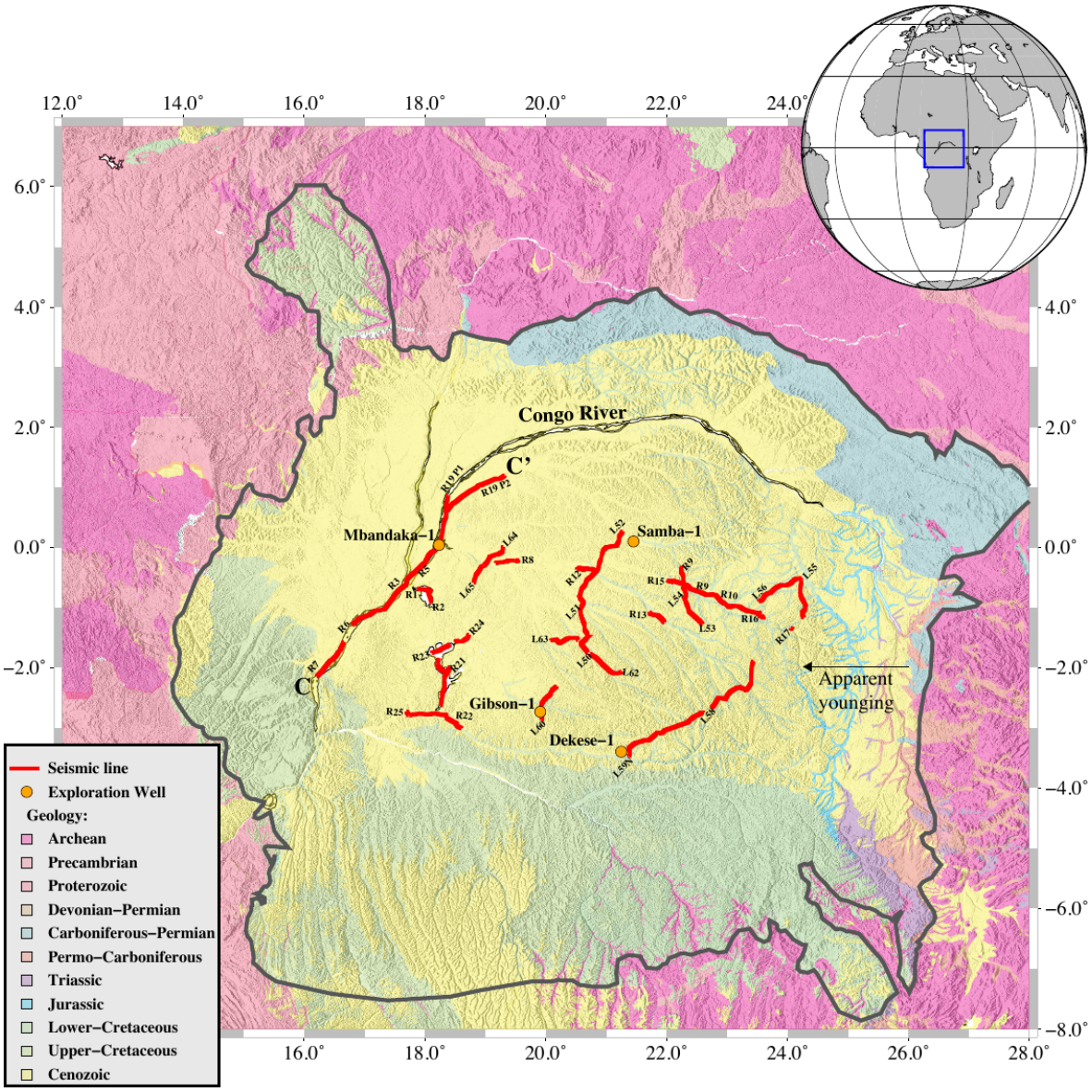


Figure 6.4: Geological map of the Congo basin, Central Africa. Solid grey line shows the areal extent of the basin. Masked regions are lakes. Inset shows global location of the main figure. Red lines show 2D reflection profiles. C–C' shows composite line shown in Figure 6.5c. Orange circles are well locations.

leyville Formation above a profound regional angular unconformity (U2), which separates S3 from the final sequence S4. However, as can clearly be seen on the sonic-porosity curve from the Mbandaka-1 well (Fig. 5.1), this unconformity occurs above the Stanleyville Formation as it is defined in this well. Hence, in this study the Stanleyville is included in sequence S3. This suggests the U2 unconformity is, therefore, Latest Jurassic/Early Cretaceous in age. The overlying upper-most sequence, S4, contains the Early–Late Cretaceous Loia/Bokungo/Kwango

sandstones and Cenozoic–Recent (65–0 Ma) fluvial to lacustrine and aeolian sediments (e.g., Esso Zaire SARL., 1981b). However, as it appears the Congo basin may be actively subsiding in the present day (potentially as a manifestation of dynamic topography (Downey and Gurnis, 2009)), these latter Cenozoic–Recent sediments may be considered as separate tectonostratigraphic unit from that of the underlying Carboniferous–Jurassic cratonic basin phase of subsidence.

It is clearly evident on seismic reflection profiles (e.g., Fig 6.5c; Daly et al., 1992), as well as in isopach maps of the major sedimentary sequences (Fig. 6.7), that the Congo basin stratigraphy is disrupted by at least two major periods of basin inversion. Compressional fold and thrust structures related to both of these events exhibit NW-SE trends and imply shortening in a NE-SE direction (Daly et al., 1992) and reactivation of structures in the latter event. Given the suspected Cambrian age of the first unconformity, it has been interpreted as resulting from late-stage Pan-African contractional deformation, related to the culmination of the West Congolian Orogeny which was active $\sim 500\ km$ west of the basin at this time (e.g., Coward, 1981). In a similar fashion, Daly et al. (1991) related the second event to Permo-Triassic compressional deformation that occurred at the southern border of Gondwana at this time. However, as mentioned above, the age of the U2 unconformity that represents this event is Latest Jurassic/Early Cretaceous in age and therefore appears difficult to relate to this Permo-Triassic event. Regardless of the origin of these inversion episodes, it is clear the Congo basin's sedimentary record has been disrupted by major inversions on at least two occasions, complicating investigation of the cratonic basin subsidence history.

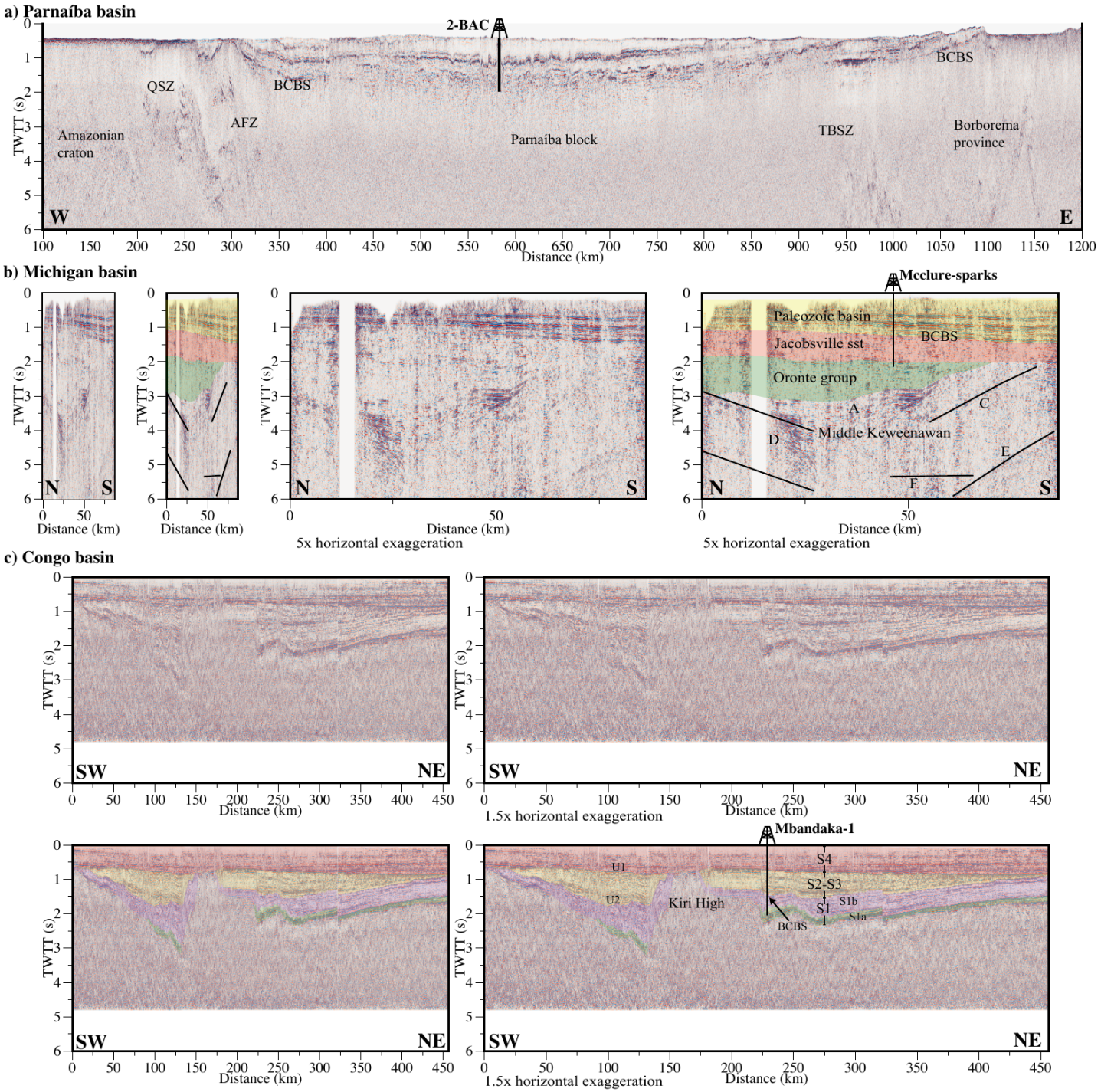
6.3 Isopachs and Sedimentary thickness maps

In order to calculate sediment corrected gravity anomalies and investigate the temporal subsidence evolution of each of these basins, isopachs and sediment thickness maps were derived from all available well and seismic data.

6.3.1 Michigan basin isopachs and flexural backstrips

Due to proven petroleum reserves, several thousand exploration wells have been drilled within Michigan basin. These data are freely available and were sourced from the Michigan Department of Environment Quality well database (DEQ, 2015) and used to construct isopach maps for fifteen "isopach-sequences", defined here primarily on the basis of stratigraphic unconformity boundaries but also on spatial distribution and number of well top records available for each horizon. Once these records were filtered to remove outlying, erroneous and duplicated horizon picks, 117,062 individual formation top records from 24,610 unique wells were retained. Thus, this dataset provides an excellent spatial coverage for all isopachs (expect the earliest – M1), with each constrained by several hundred to several thousand records. In the case of M1, only 42 records reach basement depth. Moreover, their spatial distribution is poor and biased to the basin margins, hence this isopach is the less well defined.

The well records from the DEQ database are, however, limited to the Michigan state boundaries, such that, their spatial converge does not extend to the limiting boundaries of structural arches surrounding the basin. Hence, when constructing the isopachs, data were interpolated beyond the region constrained by data. The limit of interpolation was set as the sediment outcrop limit in the north, where sediments terminate against basement and as the apex of the surrounding Kannakee and Findlay arches in the southwest and southeast respectively (Fig. 6.2). Flexurally backstripped isopachs, assuming a constant $T_e = 50\ km$, are shown in Figure 6.6. These show the general bowl-shaped morphology of the basin persisted throughout the basin's evolution, albeit with shifts in the basin depocenter through time. The origins of these depocenter shifts are difficult to reconcile. However, based on temporal correlations with predicted far-field tectonic processes, previous authors have attributed these shifts to secondary processes. For example in MS4, basin centred subsidence is replaced with tilting to the east during the Late Ordovician. Coakley and Gurnis (1995) attributed this tilting to a long wavelength, slab-induced convection draw-down, caused by subduction of a west-dipping plate beneath a rift-type margin at the eastern edge of a Laurentian plate at this time. Howell and van der Pluijm (1999) suggested that eastward tilting during MS12 could be caused by long-wavelength flexural tilting in response to Alleghanian orogenic loading.


a) Parnaíba basin
2-BAC
QSZ
BCBS
AFZ
Amazonian craton
Parnaíba block
TBSZ
BCBS
Borborema province
W
E
TWTT (s)
Distance (km)
b) Michigan basin
Mcclure-sparks
Paleozoic basin
Jacobsville sst
BCBS
Oronte group
A
C
D
Middle Keweenawan
E
F
N
S
5x horizontal exaggeration
c) Congo basin
SW
NE
1.5x horizontal exaggeration
Mbandaka-1
U1
U2
Kiri High
S4
S2-S3
S1
S1b
S1a
BCBS

6.3.2 Congo basin isopachs

In contrast to Michigan basin, the Congo basin contains just four exploration wells, none of which reach basement. However, ~ 2900 line km of 4.8–5.0 s $TWTT$ 2D seismic reflection data were acquired between 1973–1981 for oil exploration and these data were used to construct isopachs of the four sequences described above in Section 6.2.2. As these data exist only in the time domain, the isopachs were created in two-way-time and then depth converted using a time-depth relationship derived from the Mbandaka-1 well in the Northwest part of the basin (Linol, 2013). Figure 6.4 shows the spatial distribution of the seismic reflection data available within the Congo basin, which is confined to the basin centre. Figure 6.5c shows and interpreted example the Mbandaka-1 seismic reflection line (c–c'). The depth converted isopachs are shown in Figure 6.7. Flexural backstrips were not performed for the Congo basin given the sparse temporal and spatial data coverage.

6.3.3 Cratonic basin sedimentary thickness maps

Gross sedimentary thickness maps for the cratonic basin sequences of each basin, derived from the Michigan and Congo isopach data outlined above and from those presented in Chapter two for Parnaíba basin, are shown in Figure 6.8.

As discussed in Chapter three, the base of the cratonic sequence (BCBS) in the Parnaíba basin is defined as the base of the Ipu Formation and is Early Silurian in age (Grahn et al., 2005). In Michigan, the base of the cratonic sequence is chosen as the base of isopach sequence

---

Figure 6.5 ***(preceding page)*****:** Comparison of seismic reflection profile data from the Parnaíba, Michigan and Congo basins with interpretations for Congo (after, Daly et al., 1992) and Michigan (after, Zhu and Brown, 1986). Blue arrow indicates the Base of the Cratonic Basin Sequence (BCBS). Vertical lines show selected wells on or close to each profile. Profiles are located in Figure 6.8 (thick red line). a) Parnaíba basin PBAP profile. QSZ = Quatipuru Suture Zone. AFZ = Araguaina Fault Zone. TBSZ = TransBrasiliano Shear Zone. b) Michigan basin COCORP Line 1 (Zhu and Brown, 1986). UK = Upper Keweenawan clastics. MK = Mid. Keweenawan volcanics. Left is same scale as in (a); right is plotted with 5 × horizontal exaggeration. d) Congo basin Mbandaka line (Daly et al., 1992). Left is same scale as in (a); right is plotted with 1.5 × horizontal exaggeration.

M1 (which is defined here as comprising the Mount Simon Sandstone and the Munising Grit). This is Late Cambrian in age and equivalent to the base of sequence A as defined by Howell and van der Pluijm (1999). In the Congo basin, the base of the cratonic basin sequence is defined as the base of the Lukuga Formation (Fig. 6.3). However, for the purpose of this study, a prominent reflector that is evident on most of the seismic reflection profiles (Fig. 6.5) was chosen to represent this horizon. This reflector corresponds with the 'B horizon' of Kadima et al. (2011). Unfortunately, this reflection does not appear to correlate precisely with the base of the Lukuga Formation as defined in the Mbandaka-1 well (Fig. 6.5) and suggests that the base of the Congo cratonic basin sequence may be locally deeper than is shown in this figure.

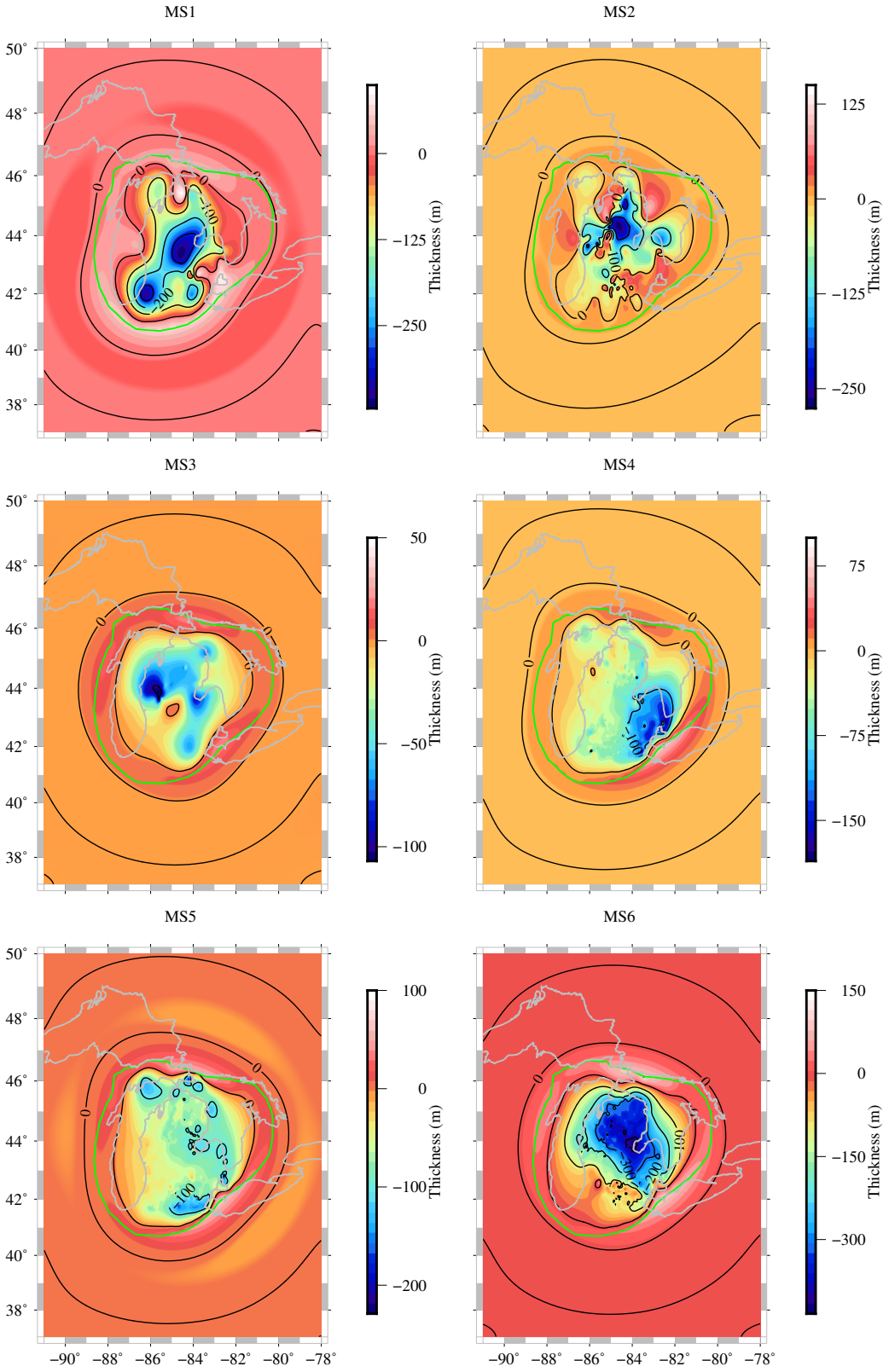


Figure 6.6: Three dimensional flexural backstripping of isopach sequences MS1-MS14 within the Michigan basin (see Fig. 6.3 for ages) performed using a constant $T_e = 50\ km$. Green line shows the present-day extent of the basin. Grey lines show shorelines of the great lakes. Note the colour scale varies for each map.

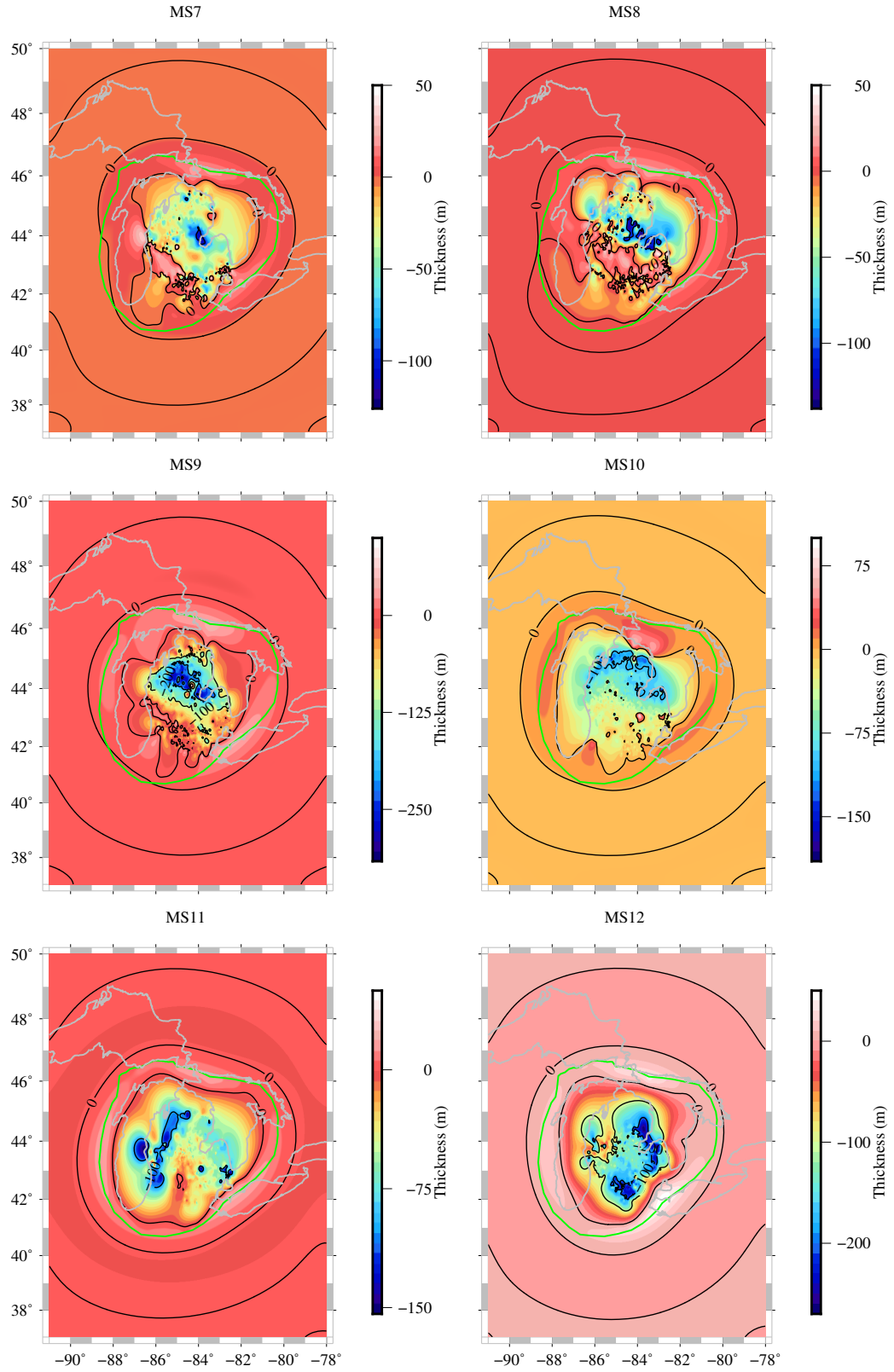


Figure 6.6 continued

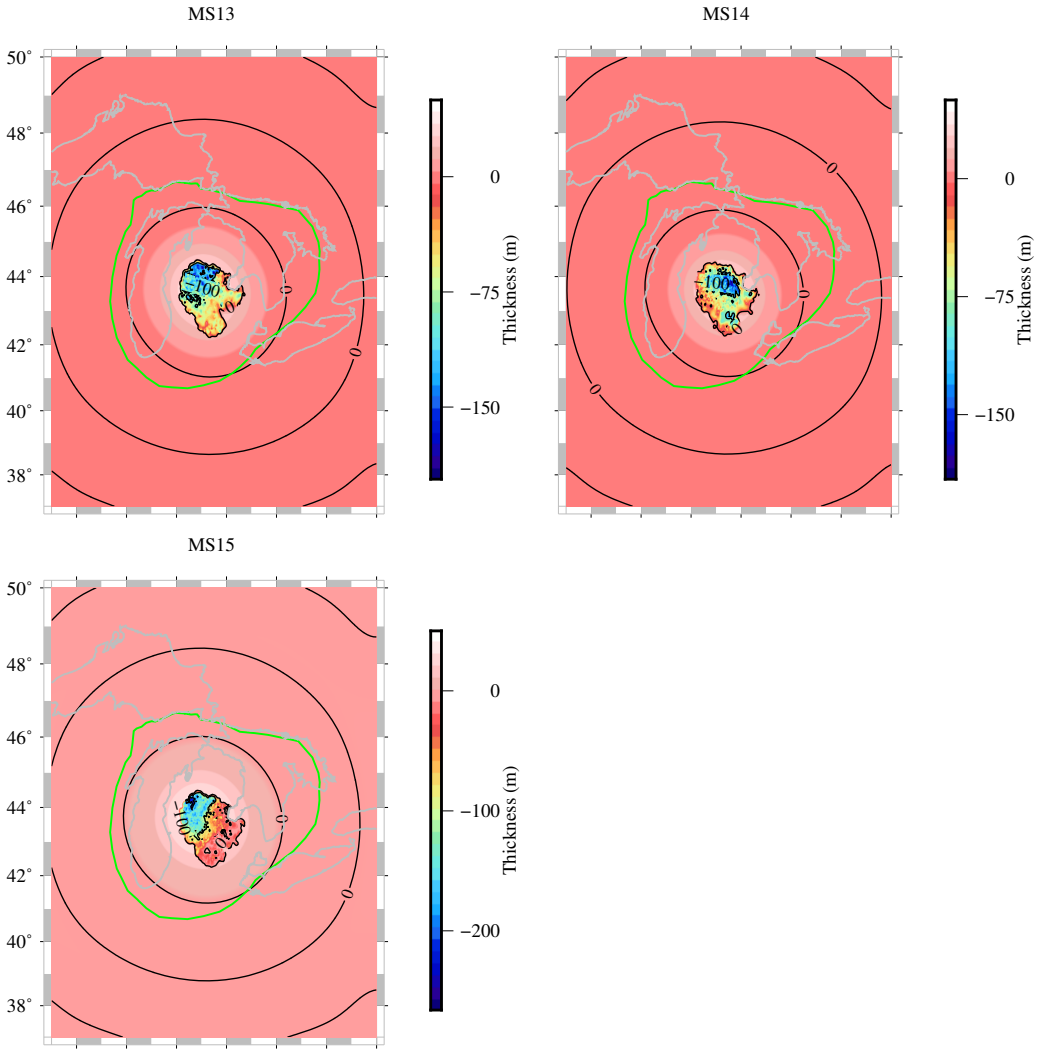


Figure 6.6 continued

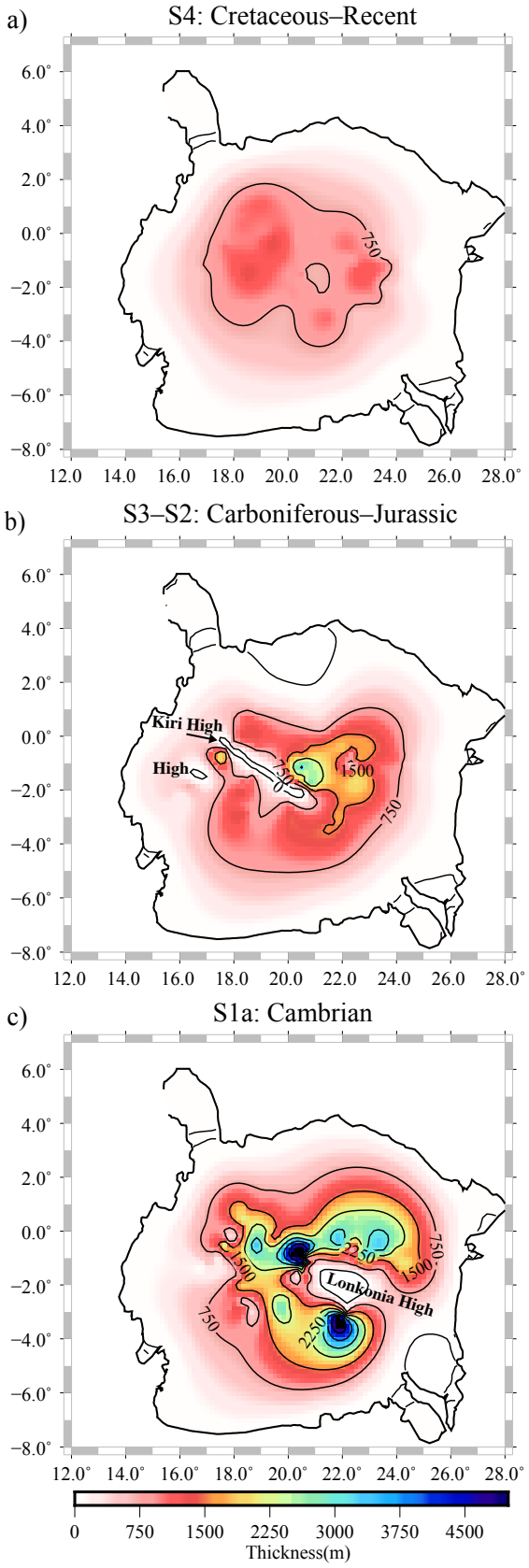


Figure 6.7: Isopach maps for Congo basin sequences S1a–S4 (Fig. 6.3). Contour interval is 750 m. Note these maps were created in the time domain and depth converted using the time–depth curve derived from well Mbandaka-1 by Linol (2013).

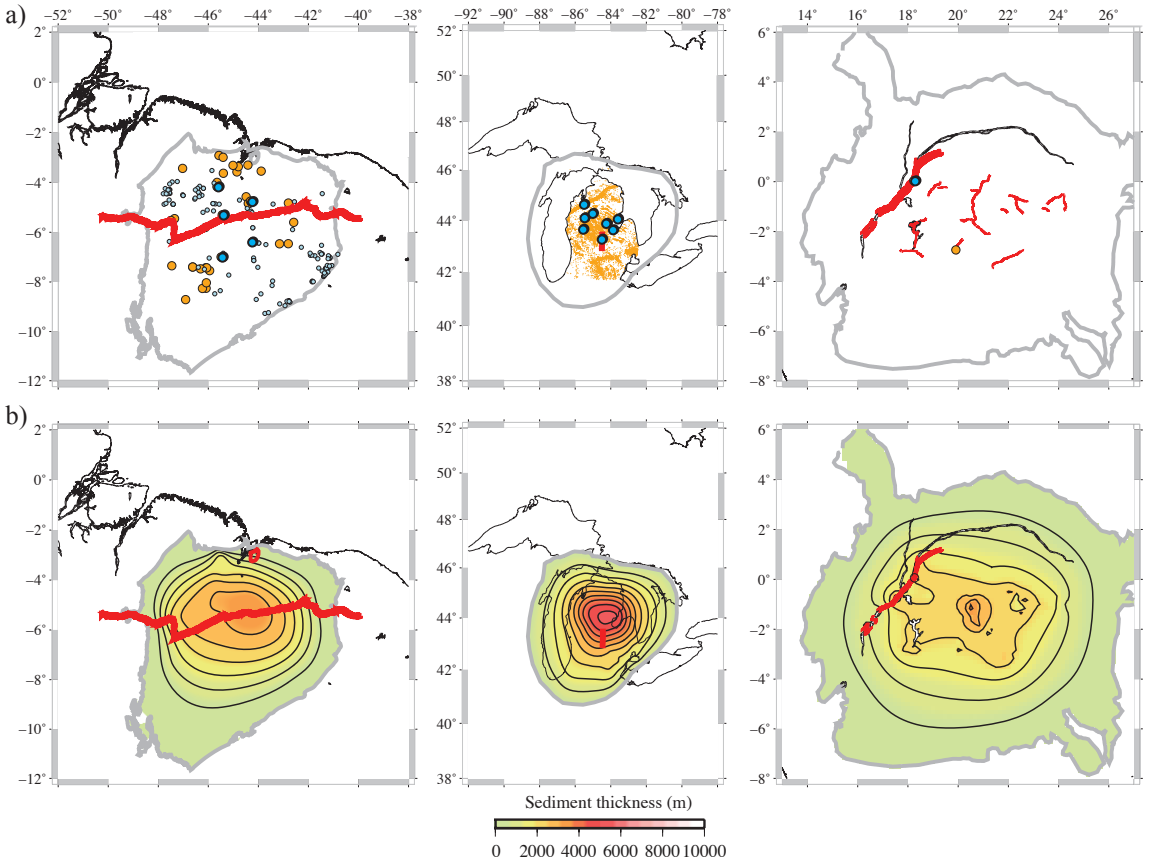


Figure 6.8: Summary of seismic, well and sediment thickness data at the Parnaíba, Michigan and Congo basins. a) Location map showing seismic reflection profiles and well data (filled orange circles) used in the construction of isopachs. Thick red lines show the location of the seismic reflection profiles presented in Figure 6.5. Blue filled circles show the backstripped wells used in Figures 6.15 and 6.16. b) Depth to the base of the cratonic basin sequence (BCBS) contoured at 500 m intervals.

6.4 Gravity anomalies

Free-air gravity anomalies for each basin derived from the EGM2008 Earth model (Pavlis et al., 2012) are shown in Figure 6.9. These data show that all three basins are characterised by free-air gravity anomaly 'lows' with respect to their surroundings. The Parnaíba and Congo basins correlate with 'lows' of -25 to -50 $mGal$ and flanking 'highs' of up to 50–60 $mGal$. In Michigan, the anomaly is more complex. The overall basin-wide anomaly is also a 'low', however, this is part of a regional 'low' that is caused by incomplete glacial rebound following the Last Glacial Maximum (e.g., James, 1992). Furthermore, the basin centre is dominated by a relatively narrow 'high' which is attributed to sub-basin Keweenawan age volcanic rocks ($\sim 1.1\ Ga$) related to the formation of the Mid-Continental rift of North America at this time (e.g., Van Der Voo and Watts, 1978). Deep borehole data suggests this sequence contains clastics and basaltic lava flows, some of which appear similar to seaward dipping reflectors observed at volcanic rifted margins (e.g., Stein et al., 2014).

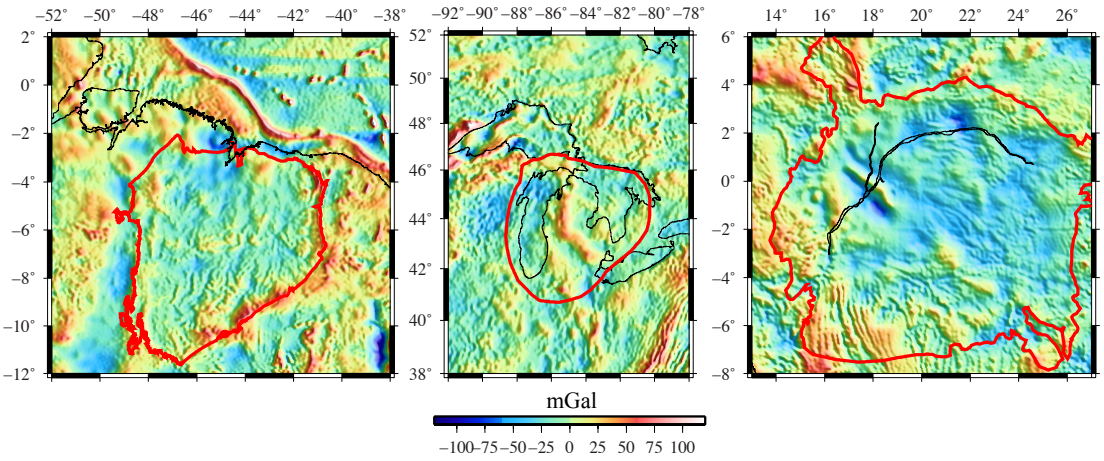


Figure 6.9: Free-air gravity anomaly based on a 2.5' × 2.5' grid of the EGM2008 Earth model (Pavlis et al., 2012) with the degree and order $n = 12$ long wavelength (equivalent wavelength $\sim 3300\ km$) field removed.

With regards to crustal structure and the tectonic history of these basins, the free-air gravity anomaly 'lows' are interesting because if the crust was thinned, and Moho elevated beneath the basins, we may expect that the long wavelength (basin-wide) gravity anomalies would reflect this in the form of more subdued, or even positive gravity anomalies — as

the negative gravity component associated with the sediments would be compensated by the positive component resulting from elevation of the mantle.

6.4.1 Sediment corrected residual gravity anomalies

Sediment-corrected residual Bouguer anomalies have been calculated for the Michigan and Congo basins, similarly to that presented in Section 4.8.1 for the Parnaíba basin. A background Bouguer reduction density of 2700 $kg\ m^{-3}$ for the unsedimented flanking upper crustal rocks was used for all three basins, similar to that used by Mooney and Kaban (2010) for continental North America. The bulk sediment densities were set as 2500 $kg\ m^{-3}$ for Michigan and 2350 $kg\ m^{-3}$ for the Congo basin sediments respectively (Kadima et al., 2011). The individual gravity anomalies/gravity effects for each basin are shown in Figures 4.18 (Parnaíba), 6.10 (Michigan) and 6.11 (Congo).

Figure 6.12 shows the sediment corrected Bouguer gravity anomalies for each of the three basins. It can be seen that they are all characterised by a sub-circular residual gravity 'highs' of $\sim$ 40–60 $mGal$ in the basin centres relative to the flanking regions, schematically outlined by the grey dashed lines. In the Michigan and Congo basins, it can be seen that the central 'highs' are broader than the narrow anomalies related to the Mid-Continent rift and fold and thrust structures (i.e., the Kiri and Lokonia highs) respectively. The black boxes show the area from which 2D profiles where sampled and used to create the ensembled averaged profiles shown in Figure 6.13a.

The ensemble averaged profiles for Congo and Michigan appear very similar to that determined for Parnaíba. The central gravity 'highs' suggest a mass excess exists locally beneath each basin, while wavelengths of these anomalies suggest they are deep sourced, most likely from the lower crust and/or upper most mantle. The Michigan basin high appears largest in amplitude, which is consistent with the additional mass excess of the upper crustal Keweenawan basaltic rocks.

As discussed for Parnaíba basin in Section 4.8, two possible sources for these anomalies are: (1) crustal thinning, which would elevate Moho and bring relatively dense mantle rocks

closer to the surface and (2) the presence of a dense body within the lower crust and/or upper most mantle.

Seismic imaging of crustal structure provides the most telling data for discriminating between these possibilities, as was utilised in the analysis of Parnaíba basin in the previous chapters. Unfortunately, no such data exists in the Congo basin. In the Michigan basin, Zhu and Brown (1986) imaged a potential Moho reflection at $\sim 43\ km$ depth using vibroseis reflection seismology, a result that has recently been corroborated by EarthScope receiver function studies (Shen et al., 2013) and USArray P_n tomography (Buehler and Shearer, 2017), which also suggests the Moho is deeper beneath the centre of Michigan basin than its flanks. Moreover, marine seismic reflection data from Lake Superior to the northwest of Michigan basin suggests Moho depths of 36–42 km (Behrendt et al., 1990).

That both the Michigan and Parnaíba crustal structure (Chapter 3) are inconsistent with crustal thinning, suggests that this process is unlikely to be responsible for the observed gravity anomaly highs. This is also corroborated by seismic reflection data, which provides no evidence for rift structures within these basins or their basement that can be easily linked to the cratonic basin phase of subsidence (e.g., Fig. 6.5). Furthermore, flexural backstripping of the Parnaíba basin and Michigan basin isopachs cases further doubt on the applicability of rifting model. These show that in the early stages of basin subsidence the basins were characterised by sub-circular depocenters (Figs. 5.8 and 6.14). This basin morphology is unlike the linear trends that usually form in rift type basins.

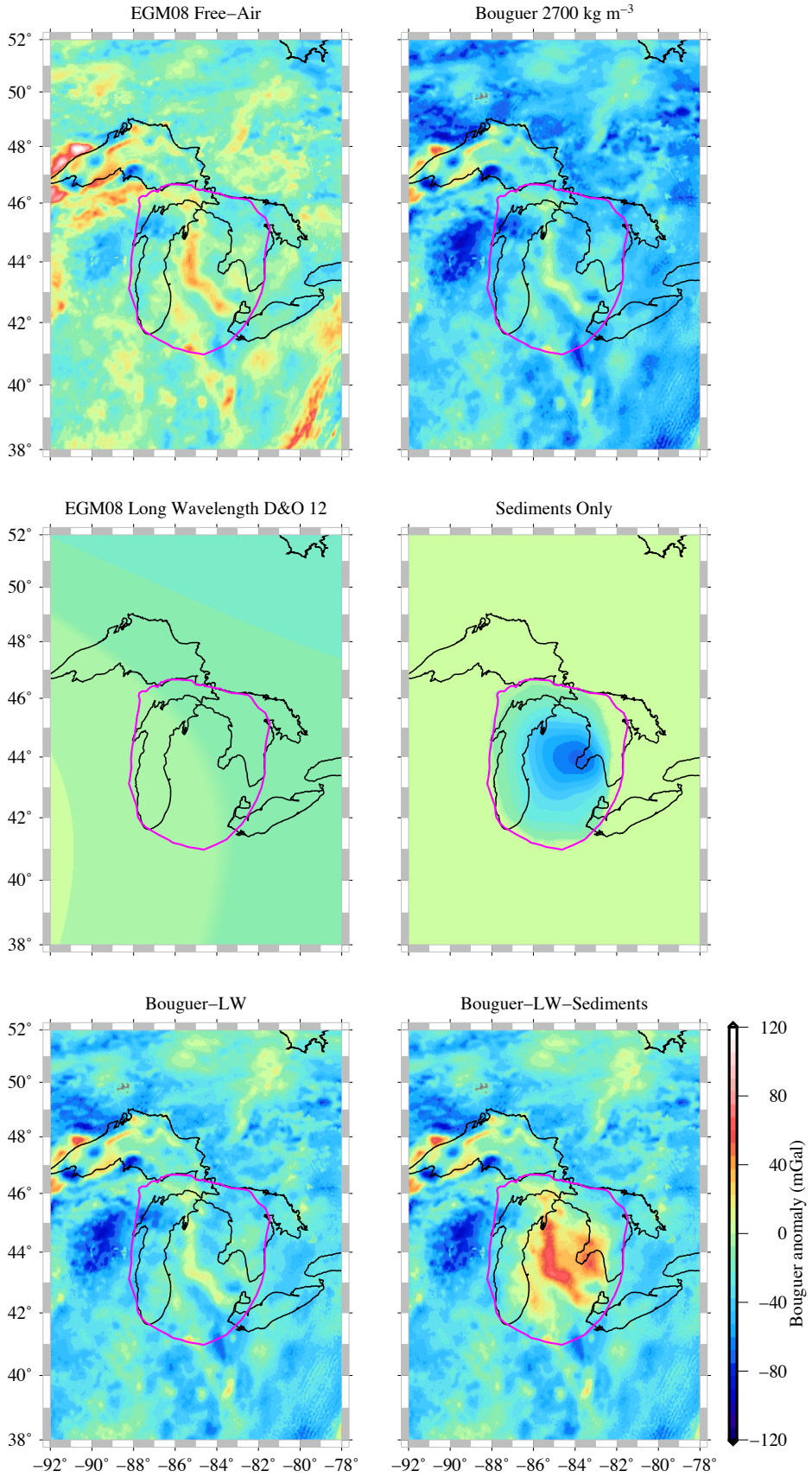


Figure 6.10: Michigan basin gravity anomalies and gravity components as labelled. LW = long wavelength. Pink line shows basin outline. Note all anomalies are plotted using the same colour scale.

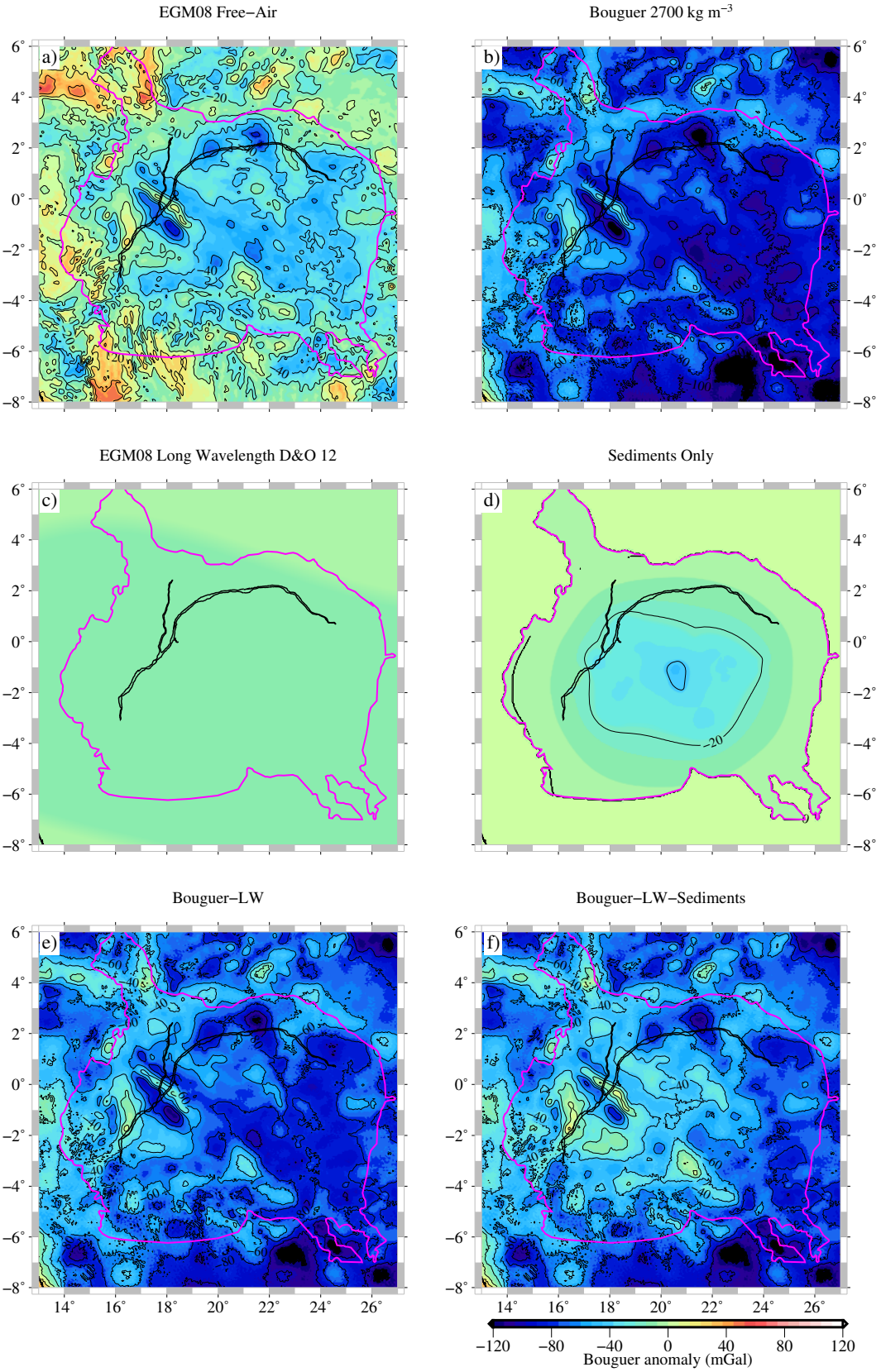


Figure 6.11: Congo basin gravity anomalies and gravity components as labelled. LW = long wavelength. Pink line shows basin outline. Note all anomalies are plotted using the same colour scale.

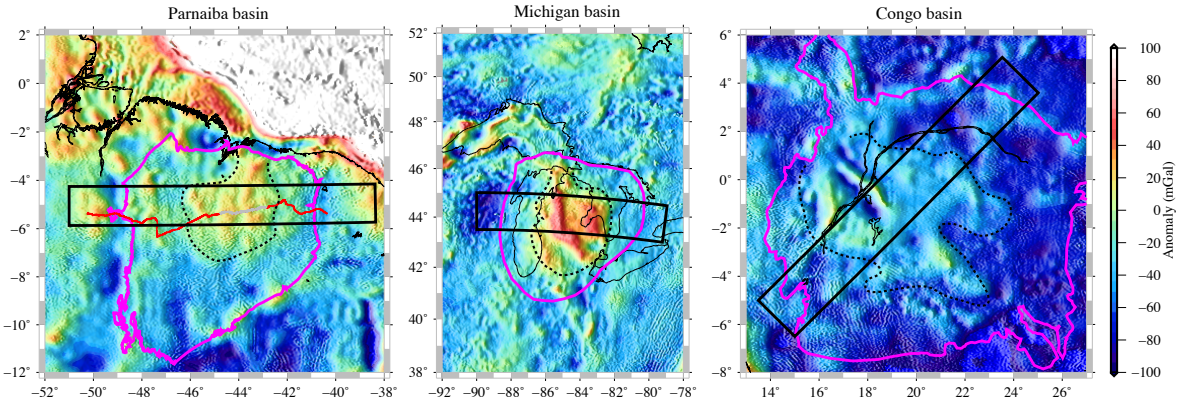


Figure 6.12: Comparison of the sediment corrected Bouguer gravity anomalies for the Parnaíba, Michigan and Congo basins. Red thick lines show basin outlines. Black box shows region used to construct ensemble averages. Dotted line outlines schematically the central high. Solid black line in the Parnaíba basin shows the extent of the Mid-Crustal Reflectivity (MCR).

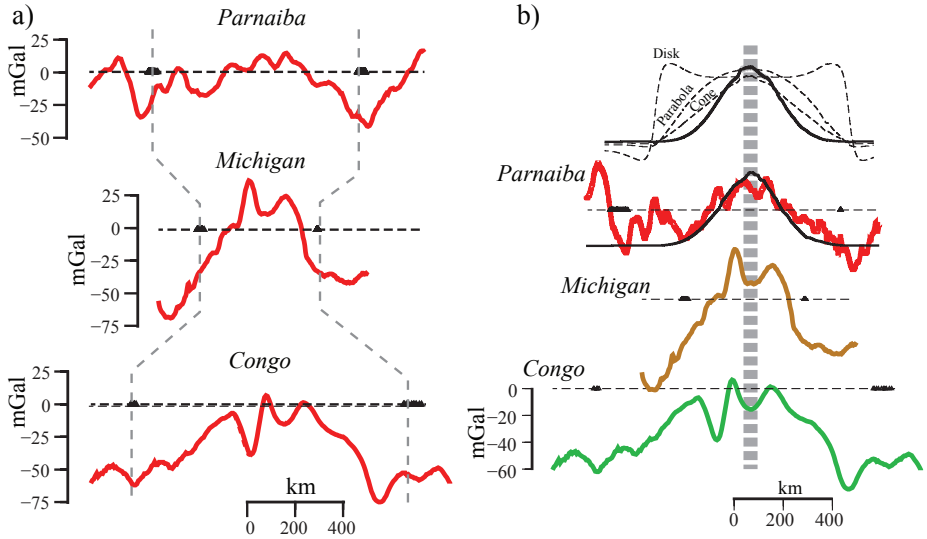


Figure 6.13: a) Comparison of the ensemble averages of the sediment corrected Bouguer gravity anomaly for the Parnaíba, Michigan and Congo basins. 'Swath' regions from which profiles were extracted to create the ensemble averaged profiles are shown in Figure 6.12. The Congo calculation is based on inclusion of S1b sequence, beneath the cratonic sequence and an average sediment density of 2350 $kg\ m^{-3}$ (e.g., Kadima et al., 2011). Note that a central 'high', which is a characteristic of each basin, rises to some 40-60 $mGal$ above the (negative) background fields at the basin edges. b) Comparison of residual gravity anomalies with those predicted for simple shaped bodies as described in Section 4.8 for Parnaíba basin.

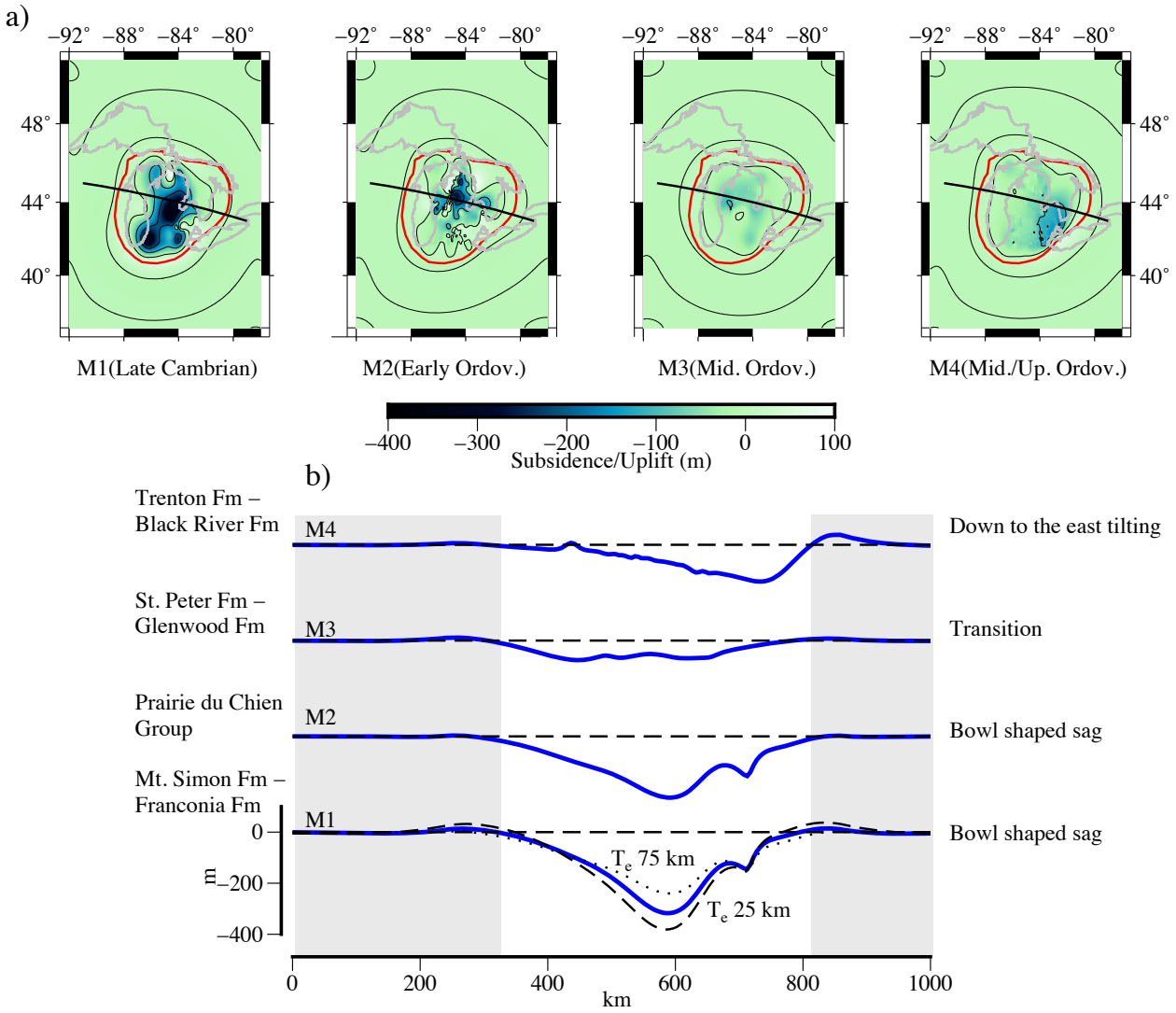


Figure 6.14: Flexural backstrip for sequences M1 to M4 in the Michigan cratonic basin. a) Flexural backstrip maps based on $T_e = 50\ km$. Contour interval = 100 m. Red solid line shows approximate extent of the basin, as defined by the arch limits. Thin black line locates the profiles in (b). b) Profiles of the flexural backstrip based on $T_e = 50\ km$. Thin dashed lines show the effect on the tectonic subsidence of using a lower (25 km) and higher (75 km) T_e. Note the change in basin depocentre from a bowl-shape at M1 to a down to the east tilt at M3 and M4.

6.5 Airy backstripping

In order to compare the temporal subsidence histories of these basins, tectonic subsidence curves were derived by Airy-backstripping stratigraphic data from wells located within each basin.

In the Michigan basin, wells within a $\sim$ 150 km radius of the basin centre that also penetrate the entire cratonic basin sequence were backstripped. As only three wells met this criteria, a further five wells which terminate within the basal Mt Simon Formation, were backstripped by extending their records to basement. This was achieved by estimating the total thickness of the Mt Simon Formation at each well location from a Mt Simon isopach map. Formation ages from the North American stratigraphic correlation chart (Swezey, 2008 and references therein) were adopted in this study. Ages are well constrained in the Michigan basin owing to the large well database and fossiliferous nature of the sediments. Porosity depth curves could not be constructed for Michigan wells due to a lack of petrophysical log data availability. In the absence of locally constrained porosity/depth relationships, average lithology values obtained from global compilations were used (Sclater and Christie, 1980; Giles, 1997; Allen and Allen, 2013). Although average bulk densities are available for the most formations, the absence of porosity data prevented the determination of grain densities. Again, typical grain density values for each lithology from global compilations were adopted (Allen and Allen, 2013).

In the Congo basin only four exploration wells have been drilled, none of which reach basement (Fig. 6.4). The Mbandaka-1 well reaches a total depth of 4350 m and a backstrip of this well, beginning from the base of the cratonic basin sequence (i.e., S2) is shown in Figure 6.15. Formation top ages were adopted from those given by Kadima et al. (2011), which are based on well reports and lithostratigraphic correlations with surrounding geology. Porosity-depth coefficients were derived from the sonic log shown in 5.1c and grain densities were taken from the compilation of Linol (2013). Several other authors who have also backstripped Congo well data include Crosby et al. (2010), Kadima et al. (2011), Linol (2013) and Lucazeau et al. (2015), each of whom used slightly different values for key backstrip parameters (such as infill

and grain densities and porosity-depth functions) resulting in slight variations on the overall shape of the subsidence curves. The largest and most important uncertainty is, however, the age of the formations, which are poorly constrained due to a lack of biostratigraphic data, especially from the continental sediments. Another important uncertainty is the amount of section that is missing across the major unconformities observed in this basin (i.e., U1 and U2 in Fig. 6.5). In the Mbandaka-1 backstrip presented in Figure 6.15, 400 m of section has been added to the Stanleyville formation, as constrained by the sonic porosity curve shown in Figure 5.1.

Figure 6.15 compares tectonic subsidence curves derived from backstripping stratigraphic data from the centre of the Parnaíba, Michigan and Congo basins from the wells shown as blue circles in Figure 6.8. Note these are water loaded subsidence curves without corrections for paleobathymetry or sea level changes applied. All backstrips show a relatively fast initial tectonic subsidence, which then slows. Rates for the initial subsidence range from 34.7 (Parnaíba) to 131.6 (Michigan) $m\ Myr^{-1}$.

In comparing the curves, they effectively highlight the different tectonic evolutions experienced by each of these basins. The simple, relatively gentle exponential nature of Parnaíba basin subsidence suggests that this basin has been relatively unaffected by secondary processes during its evolution, producing a tectonic subsidence that may be considered the "primary" cratonic basin subsidence signal. In contrast, the tectonic subsidence curves of both Michigan and Congo are interrupted by at least one increase in subsidence rate, the oldest and most prominent of which is marked by the black arrows in the Figure 6.15. In Michigan, this increase is well established and is evident in all of the wells backstripped, confirming this is not a local phenomenon. This rate increase also follows a distinct change in subsidence style, with basin centred subsidence being replaced with tilting to the east, as discussed in Section 6.3.1. In the Congo, the increase is based on only a single sample point, although Lucazeau et al. (2015) backstripped all four wells in the Congo basin and these all show a similar increase in subsidence rate in the Jurassic. The tectonic mechanism responsible for this event is unclear and improved age control is required before any tectonic interpretation can be applied with confidence to this record.

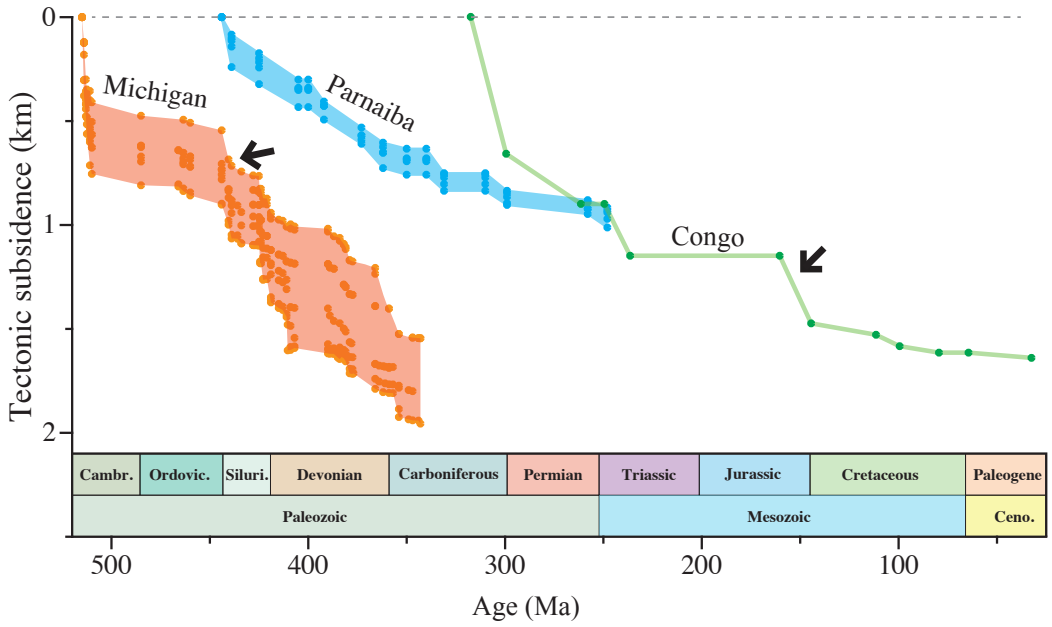


Figure 6.15: Tectonic subsidence curves derived from backstripping selected wells from the centre of the Parnaíba, Michigan and Congo basins. Thick black arrows highlight abrupt changes in the tectonic subsidence of the Michigan basin in Late Ordovician ($\sim$ 450 Ma) when Coakley and Gurnis (1995) suggest that an Iapetus sinking slab impacts and in the Congo basin in Late Jurassic.

6.6 Viscoelastic subsidence

It is clear from the comparison of the backstripped subsidence curves described in the previous section that the Michigan and Congo basins have experienced more complex subsidence histories that Parnaíba basin. Secondary processes both disrupt and obscure the cratonic basin subsidence signal. However, the residual gravity anomalies derived in Section 6.4.1 appear strikingly similar to that which was derived in Parnaíba basin in Chapter 4. It follows then, that a similar buried load induced subsidence, as proposed for Parnaíba basin, may also be chiefly responsible for the initiation and the long-term subsidence of these basins. In Figure 6.16, the initial phase of subsidence observed in the Parnaíba, Michigan and Congo basins, is compared with that predicted from a model in which a load is emplaced (representing an intrusive load within the lower crust) on a multilayered viscoelastic plate using the same mechanical parameters as were used in Figure 5.14, but with a narrower load of bottom radius 250 km and top radius of 50 km. The viscosity structure of the plate is as shown in the inset and differs slightly from that used in Figure 5.14.

This shows that, to first order, the magnitude and style of subsidence in all three basins is broadly consistent with this subsidence mechanism. Although other factors such as thermal effects, temporal changes in mechanical properties and eustatic sea level, would need to be accounted for in order to reconcile the more complex variations in the observed curves.

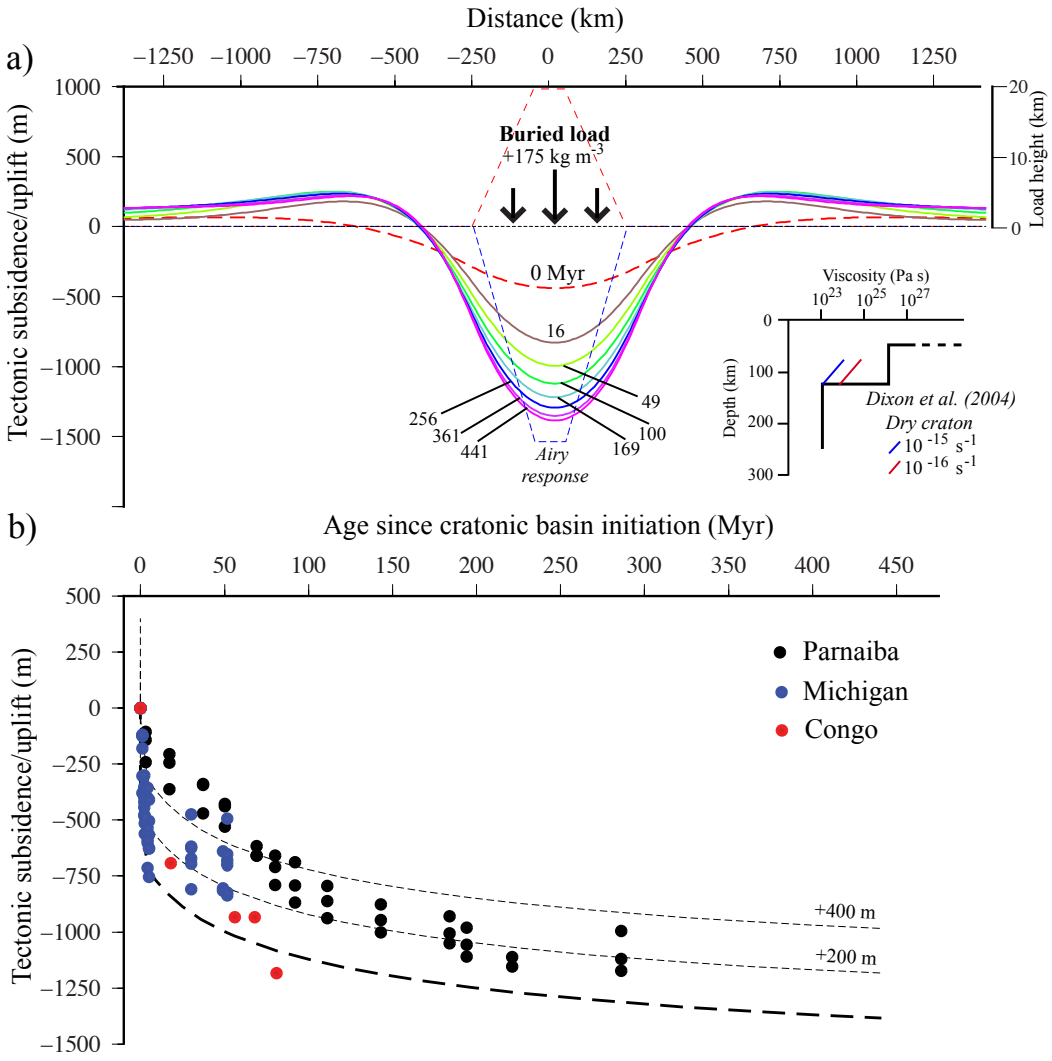


Figure 6.16: Multilayered viscoelastic model for the flexure due to a lower crustal load. a) Flexure as a function of age (in Myr) following load emplacement. Inset shows the assumed viscosity structure. Red and blue lines in the inset show the calculated viscosity of Dixon et al. (2004) for dry cratons and different strain rates. b) Comparison of the predicted subsidence based on a multilayered viscoelastic plate model to observations of the tectonic subsidence at wells in the Parnaíba (filled green circles), Michigan (filled blue circles) and Congo (filled red circles) cratonic basins. The thick dashed line is the calculated subsidence in the centre of the load in (a). The thin dashed line is the calculated subsidence shifted vertically by +200 and +400 m.

6.7 Summary

In this chapter, gravity and subsidence analysis similar to that applied to the Parnaíba basin in the previous chapters, has been extended to the Michigan and Congo cratonic basins. This has facilitated direct comparisons between these three cratonic basins and the main findings are as follows:

- Comparisons of sedimentary isopachs, flexural backstrips and tectonic subsidence from the Parnaíba, Congo and Michigan basins suggests that the cratonic basin sedimentary record of both the Michigan and Congo basins have been modified and obscured by secondary processes during their evolution. In contrast, the Parnaíba basin sedimentary record appears relatively well preserved and likely reflects the primary cratonic basin subsidence signal.

- Bouguer gravity anomalies that have been corrected for the gravitational effect of the basin sediments reveal that the Parnaíba, Michigan and Congo basins are all associated with a central gravity 'high' of wavelengths 1200–2000 km and amplitude up to + 40–60 $mGal$, suggestive of a deep crustal/upper mantle source.

- The central gravity 'high' could be due to crustal thinning at the time of basin initiation. However, available crustal structure data does not support crustal thinning, nor does seismic reflection data, which shows no evidence for extensional structures in the basement that can be related to rifting. Moreover, flexural backstripping of Michigan basin sediment isopachs show that the early (i.e., the few first few Myr) tectonic subsidence is bowl-shape similar to the morphology observed in Parnaíba basin and is inconsistent with a linear rift.

- One explanation of the central gravity 'high' is that it is caused by a relatively dense lower crustal intrusion which on solidification loads the crust and lithosphere, causing a surface flexure into which sediments can accumulate.

- Elastic and viscoelastic plate modelling of backstripped stratigraphic data from deep wells shows that a buried load can explain the first order tectonic subsidence of the

basins as well as some details of their internal stratigraphy, including the basinward younging of sediments.

Chapter 7

Discussion, conclusions and future work

7.1 Introduction

In this chapter key points and outstanding questions that have arisen from the analysis conducted in this thesis are discussed. The key conclusions are summarised, and, lastly, avenues for future research are suggested.

7.2 Discussion

7.2.1 Parnaíba basin summary

In this study, an integrated analysis of seismic reflection, refraction, gravity anomaly and subsidence history data has been carried out in order to elucidate the origin of the Parnaíba cratonic basin. As recent studies have proposed that the Parnaíba basin (and cratonic basins in general) formed as a result of lithospheric extension (e.g. de Oliveira and Mohriak, 2003; Armitage and Allen, 2010; de Castro et al., 2016), much of the analysis has focused on assessing this possibility. Although it was found that the tectonic subsidence history of the Parnaíba

basin can be well explained by a finite rifting model, it has also been shown that this process is inconsistent with the observed (seismically constrained) crustal structure and gravity data. Clearly then, other processes must be involved.

Seismic reflection imaging revealed a prominent zone of mid-crustal reflectivity extending laterally for at least 250 km beneath the centre of the basin, undulating between depths of $\sim$ 17–24 km. Moreover, wide-angle reflection and refraction and forward gravity modelling reveal that the top of this reflection package marks a large acoustic impedance contrast, with estimated increases in P-wave velocity of 0.43–0.59 $km\ s^{-1}$ and bulk density of 175 $kg\ m^{-3}$. Moreover, three-dimensional gravity analysis reveals that the basin is characterised by a residual Bouguer gravity high of $\sim$ 40–60 $mGal$ once the contribution of the sediment in-fill and very long wavelength's ($>$ 3330 km) to the gravity field are removed. In relation to Parnaíba basin subsidence, these observations suggest some form of lower crustal alteration and buried load induced subsidence may be, at least partly, responsible for the tectonic subsidence required to form the basin.

7.2.2 Assessment of proposed mechanisms for cratonic basin formation and there applicability to Parnaíba basin

As outlined in Section 1.5 many of the previous models proposed to explain the formation of cratonic basins are predicted to produce particular styles of basin morphology, crustal and lithospheric structure and subsidence histories, all of which are testable using the data analysed in this thesis. In this section, these predictions are systematically compared to observations made in this study in order subjectively assess each models applicably to Parnaíba basin.

Model & Observations	Consistent with model	Comment
Buried loading: lower crust		
Sub-circular basin shape	✓	Three dimensional flexural response
Pre-Silurian unconformity surface	✓	Following thermal uplift during load emplacement
Long-lived, quasi-exponential subsidence	✓*	Viscoelastic plate response
Strong mid-crustal reflectivity	✓	Evidenced on seismic reflection data
$\sim 40\ mGal$ residual gravity 'high'	✓	Buried load gravity contribution
Dense ($+ 175\ kg\ m^{-3}$) lower crust	✓	Buried load gravity contribution
High V_p (6.7–7.0 $km\ s^{-1}$) lower crust	✓	Buried load V_p
Basinward deepening of the Moho	✓	Flexural response to loading
Thick ($\sim 170\ km$) thermal lithosphere	♦	——
Buried loading: mantle lithosphere		
Sub-circular basin shape	✓	Three dimensional flexural response
Pre-Silurian unconformity surface	✓	Following thermal uplift during load emplacement
Long-lived, quasi-exponential subsidence	✓*	2D thermal relaxation
Strong mid-crustal reflectivity	✗	Unaltered crustal composition
$\sim 40\ mGal$ residual gravity 'high'	✓	Mantle-lithosphere buried load source
Dense ($+ 175\ kg\ m^{-3}$) lower crust	✗	Unaltered crustal composition
High V_p (6.7–7.0 $km\ s^{-1}$) lower crust	✗	Unaltered crustal composition
Basinward deepening of the Moho	✓	Flexural response to loading
Thick ($\sim 170\ km$) thermal lithosphere	✓	Required for long-lived thermal subsidence
In-plane compression		
Uninterrupted sedimentation history	♣	Sedimentary record is punctuated by several unconformities of long ($Myr's$) duration
Basinward verging thrust faulting	♣	No syn-tectonic thrust faults are observed in seismic reflection data
Sub-circular basin shape	✗	compressional tectonics is expected to produce linear features (e.g., mountain chains and foreland basins)
Pre-Silurian unconformity surface	✗	No obvious method for creating a pre-basin unconformity surface
Long-lived, quasi-exponential subsidence	✗	——
Strong mid-crustal reflectivity	✗	Unaltered crustal composition
$\sim 40\ mGal$ residual gravity 'high'	✗	Moho depression expected to produce large negative anomaly
Dense ($+ 175\ kg\ m^{-3}$) lower crust	✗	Unaltered crustal composition
High V_p (6.7–7.0 $km\ s^{-1}$) lower crust	✗	Unaltered crustal composition
Basinward deepening of the Moho	✓	——
Thick ($\sim 170\ km$) thermal lithosphere	♦	——

Dynamic topography		
Sub-circular basin shape	✓	Dynamic drawn-down circular in three dimensions
Pre-Silurian unconformity surface	♦	Dynamic drawn down will not produce an unconformity
Long-lived, quasi-exponential subsidence	✗	Subsidence rate expected to be faster than is observed
Strong mid-crustal reflectivity	✗	No crustal alteration predicted
$\sim 40\ mGal$ residual gravity 'high'	✗	——
Dense ($+ 175\ kg\ m^{-3}$) lower crust	✗	No crustal alteration predicted
High V_p (6.7–7.0 $km\ s^{-1}$) lower crust	✗	No crustal alteration predicted
Basinward deepening of the Moho	✓	Dynamic flexure of the crust
Basin preserved several 100 $Myr's$ after subsidence	♣	Dynamic topography is a transient, reversible process
Thick ($\sim 170\ km$) thermal lithosphere	♦	——
Low strain rate extension		
Central rift graben/normal faulting	♣	No such features are observed in Parnaíba basin
Sub-circular basin shape	✗	Extensional basins are distinctly linear in form
Pre-Silurian unconformity surface	♦	——
Long-lived, quasi-exponential subsidence	✓	Predicted subsidence trajectory is similar to that observed
Strong mid-crustal reflectivity	✗	Unaltered crustal composition
$\sim 40\ mGal$ residual gravity 'high'	✓	Gravitational contribution from raised Asthenosphere
Dense ($+ 175\ kg\ m^{-3}$) lower crust	✗	Unaltered crustal composition
High V_p (6.7–7.0 $km\ s^{-1}$) lower crust	✗	Unaltered crustal composition
Basinward deepening of the Moho	✗	Moho should shallow beneath the basin
Thick ($\sim 170\ km$) thermal lithosphere	✓	Required for long-lived (200 Myr) thermal subsidence
Lithospheric accretion		
Sub-circular basin shape	✗	Unclear how this process results in circular basins
Pre-Silurian unconformity surface	✓	Erosion of accretion related topography during early subsidence
Long-lived, quasi-exponential subsidence	✓	Predicted subsidence trajectory is similar to that observed
Strong mid-crustal reflectivity	✗	Unaltered crustal composition
$\sim 40\ mGal$ residual gravity 'high'	✗	No obvious source for a circular residual gravity anomaly
Dense ($+ 175\ kg\ m^{-3}$) lower crust	✗	Unaltered crustal composition
High V_p (6.7–7.0 $km\ s^{-1}$) lower crust	✗	Unaltered crustal composition
Basinward deepening of the Moho	✗	Thermal subsidence expected to be relatively uniform in spatial extent
Thick ($\sim 170\ km$) thermal lithosphere	✓	Required for long-lived (200 Myr) thermal subsidence

Lithospheric thickening–heating–erosion		
Temporal and spatial association with a Himalayan-type orogeny	✗	Potentially related to the Western Gondwana Orogeny but timing and location are arguable
Sub-circular basin shape	✓	Prediction of gravitational flow of underlying crust
Pre-Silurian unconformity surface	✓	Instantaneous erosion creates profound unconformity
Low/medium grade basement rocks (phyllites and Schists)	✗	As observed in borehole records
Long-lived, quasi-exponential subsidence	✓	Predicted subsidence trajectory is similar to that observed
Strong mid-crustal reflectivity	✗	Exhumed crust expected to be relatively homogeneous high-grade dry granulite
~ 40 *mGal* residual gravity 'high'	✗	No obvious source for a circular residual gravity anomaly
Dense ($+ 175\ kg\ m^{-3}$) lower crust	✓	——
High V_p (6.7–7.0 $km\ s^{-1}$) lower crust	✓	Dry granulite composition
"Regular" (average) V_p upper crust	✗	Dry granulite composition
Basinward deepening of the Moho	✗	Thermal subsidence expected to be relatively uniform in spatial extent
Thick ($\sim 170\ km$) thermal lithosphere	✓	Inherited from lithospheric thickening

Table 7.1: Assessment of proposed models for cratonic basin formation with respect to key interpretations and observations made in Parnaíba basin. ✓=Is explained by the given model; ✗=Is not explained by the given model; ♦=Is not explained by the given model, but is not required by the model. ♣=Model prediction that is not observed in the data analysed in this thesis. *The subsidence style predicted for this model is based on that calculated in 5.14 for the mechanical loading of a multi-layered viscoelastic plate and has an initial rapid subsidence followed by a quasi-exponential trajectory.

It is clear from Table 7.1 that a model invoking a buried load located within the lower crust is capable of explaining all of the key observations made within Parnaíba basin. For each of the other models listed in Table 7.1 there are at least two observations which are not explained by the given model. However, in some cases this does not necessarily rule the model out as the unexplained features may potentially be related to other processes which have affected the region through time. Nevertheless, some of these models are also predicted to produce specific features that are inconsistent with the observed character of Parnaíba basin, for example, the lack of extensional strain features is a strong argument against an extensional origin for the basin. It follows that the lower crustal buried loading model appears most consistent with the key observations made in this thesis. Hence, the following sections focus on discussion of the outstanding questions regarding the application of this model to the Parnaíba basin.

7.2.3 Reconciling long-lived subsidence with a mechanical loading mechanism

One problem with a mechanical loading model for cratonic basin subsidence is reconciling the relatively slow and long-lived (100's Myr) subsidence typical of cratonic basins. For example, observations of the isostatic response to loading/unloading from loads such as ice sheets, e.g., the Laurentide ice sheet of North America, show that this occurs on time-scales that are geologically instantaneous with respect to cratonic basin formation. However, this isostatic response reflects the initial elastic response to loading, as outlined in Section 1.1. When loads are maintained for sufficient durations ($Myr's$), geological observations suggest the lithosphere responds to loading in a time-dependent viscoelastic manner, most likely due to some form of load induced stress relaxation (e.g., Watts and Zhong, 2000; Watts et al., 2013). This process results in further subsidence following the initial elastic response, and the time-scale over which this occurs is largely controlled by the viscosity structure of the plate. As discussed in Chapter 5, the viscosity structure of old, cold cratonic regions, predicted from present day geotherms, is such that viscoelastic relaxation of the lithosphere occurs on a time-scale that appears consistent with cratonic basin formation. This process may therefore be capable of, at least in part, explaining the long subsidence history of Parnaíba basin and cratonic basins in general.

7.2.4 Geological origin of the proposed lower crustal buried load

Another outstanding question is the nature of the proposed buried load and its geological origin. Some previous studies that have postulated buried load models for cratonic basin formation have suggested that lower-crustal metamorphism induces a gabbro-eclogite phase change, thereby increasing density by 400–500 $kg\ m^{-3}$. Such a density contrast appears inconsistent with Parnaíba basin as this would produce a gravity anomaly far in excess of the observed Bouguer gravity anomaly over the basin. Gravity analysis conducted in Chapter 4 suggests a lower crustal density contrast of $+175\ kg\ m^{-3}$, which, interestingly, is corroborated by viscoelastic subsidence sensitivity testing (Fig. 5.15e). Furthermore, the gabbro–garnet granulite–eclogite phase transition requires the presence of interstitial water (Ahrens and Schubert, 1975), and as discussed by Armitage and Allen (2010) this is an unlikely condition in dry cratonic regions, which are isolated from processes that may produce large-scale hydration such as subduction. Alternatively, the density contrast of $+175\ kg\ m^{-3}$ may be consistent with the intrusion of mafic igneous material within the lower crust, similarly to as suggested by Stel et al. (1993) in Southern Finland. The predicted density is also similar to that of the intrusive Bushveld igneous complex of South Africa, which was emplaced $\sim$ 2.0 Ga (Roman and Jaupart, 2016). The total volume of the load, as predicted from the three-dimensional gravity and flexure calculation shown in Figure 4.18 is $2.1 \times 10^6\ km^3$, which if a melt generation rate of $0.1\ km^3\ a^{-1}$ is assumed (typical of mantle plumes (White, 1993)), would have been formed in $\sim 20\ Myr$. This is a relatively short time compared to the long time of basin evolution. Moreover, this volume estimate is a maximum as intrusion is likely to occur as discrete sills (e.g., Bryan et al., 2010), such that, the total volume of melt is less than the total volume of the load, with local metamorphism also contributing.

7.2.5 Surface magmatism?

Another outstanding question is — if the buried load is magmatic in origin, then, given its large size, why is there not more evidence for surface magmatism at the time of basin initiation?

Klein and Moura (2008) and Ganade de Araújo et al. (2014b) have described 650–620 Ma old extensive subduction-related calc-alkaline magmatism and precollisional to syncollisional metavolcano-sedimentary sequences, 620–570 Ma old collisional plutonism, 580–510 Ma old post-tectonic, and 500–460 Ma anorogenic plutonism, uplift, and extrusion tectonics from the Borborema Province which flanks Parnaíba in the east. The anorogenic granites are of particular interest as the timing and petrology of these may be consistent with lower crustal melting and the extraction of lighter, felsic melts (Huppert and Sparks, 1988; Stel et al., 1993).

However, the areal extent of the granites surrounding the basin is small and occurrences of similar age magmatism in the adjacent São Luiz and Amazon cratons, which flank Parnaíba in the north and west, respectively, appears to be limited. One possibility is that the magmatism is obscured by the Early Paleozoic sediment blanket of the Parnaíba basin. Indeed, a high conductivity "block" of magmatic material has been inferred in the basement beneath the centre of the basin using electromagnetic methods (Arora et al., 1999). Moreover, local Bouguer gravity anomaly lows have been shown to correlate with seismically opaque regions of the basement, offset from pre-Silurian grabens such as the Jaibaras (de Castro et al., 2016), leading to an interpretation of low density basement. Such low density basement could feasibly be anorogenic granitic material, emplaced adjacent to pre-Silurian Jaibaras-type grabens along bounding faults, similarly to as is observed in outcrop at the Jaibaras basin at the northeast edge of Parnaíba basin (Fig. 2.1). Interestingly, well 1-MA-3 sampled a granitic basement beneath the Parnaíba cratonic basin sequence near the centre of the basin (Fig. 2.3). However the petrology of this granite is unknown. Another possibility is that one or more regional erosional events resurfaced the Parnaíba block prior to deposition of the Silurian sediments and so removed much of the evidence for magmatism.

7.2.6 Additional and alternative subsidence mechanisms

In the analysis of buried load induced subsidence presented in Chapter 5, only the mechanical effect of loading a viscoelastic plate, which relaxes with time, was modelled. The plume-like diapiric rise of hot magmatic material in the subcrustal mantle would be expected to elevate

temperatures and cause uplift and, maybe, erosion, while its intrusion into the lower crust and subsequent cooling and contraction will cause subsidence. For example, Stel et al. (1993) have argued that a sill-like intrusion at the Moho will, depending on the amount of erosion, result in a short-term (a few million years) rapid subsidence of the crust due to crystallization and densification followed by a long-term (a few tens of million years) slow subsidence as the intrusion and lithosphere cools. As noted in Chapter 5, one consequence of this, which was not taken into account when modelling, is that the buried load volume will increase with time, as melt solidifies and metamorphism occurs. Furthermore, thermal relaxation and contraction of the lithospheric-mantle would also be expected to contribute to the long-term subsidence.

Other non-plume sources of heating have been proposed to explain the subsidence of cratonic basins. For example, Klein and Hsui (1987) have proposed that thermal insulation at the time of supercontinent assembly results in heating, melting and extension. However, it appears most cratonic basins are located on thick, not thinned crust and lithosphere (Priestley and McKenzie, 2013). McKenzie and Priestley (2016) have suggested therefore that appreciable crustal thickening during orogeny, internal radiogenic heating, and then rapid erosion of $\sim$ 40 km of crustal material might account for the long-term subsidence of cratonic basins. Although there is evidence for a Neoproterozoic orogenic belt near the region now occupied by Parnaíba basin (e.g., Ganade de Araújo et al., 2014a), such a process should result in the emplacement of granulite grade metamorphic rocks at upper crustal levels. This is at odds with basement lithologies encountered in exploration wells within Parnaíba basin, which include lower grade phyllites and schists. The upper crustal V_p values ($\sim$ 6.0–6.3 $km\ s^{-1}$) derived in the centre of the basin from forward modelling also appear lower than would be expected from high-grade rocks exhumed from $> 40\ km$ depth (e.g. Christensen and Mooney, 1995).

The basin formation analysis presented in this thesis has focused on plate processes such as flexure, and so other non-isostatic processes such as those associated with mantle dynamics have not been considered. As a number of workers have pointed out, upwelling and downwelling asthenospheric flow due, for example, to subducting slabs, may exert tractions on the base of the lithosphere which responds by vertical motions (e.g., Hager and Richards, 1989; Burgess and Moresi, 1999; Molnar et al., 2015). While the magnitude of such motions

is in dispute (Molnar et al., 2015), several workers have proposed dynamic topography as a source for the subsidence and uplift of sedimentary basins, including basins that were previously considered dominated by orogenic loading and flexure (e.g., Liu and Nummedal, 2004). Downey and Gurnis (2009) have argued on the basis of its bowl-shape and its close association with a region of high S-wave speeds in the subcrustal mantle, that the Congo cratonic basin may be a localised region of downwelling. Indeed, the ratio of the long wavelength free-air gravity anomaly to topography over the basin ($\sim 40\ mGal\ km^{-1}$) is similar to what would be expected from models of convective downwelling. However, it seems that while dynamic topography might explain some part of the subsidence of cratonic basins on short geological time scales (i.e., tens of million years), for example, the Michigan Basin during the Ordovician (Coakley and Gurnis, 1995), it is difficult to explain how such a mechanism could explain the persistence of cratonic basin subsidence on long time scales (i.e., a few hundreds of million years). It therefore seems that plate processes such as those involved in flexural isostasy are a more likely source of the stresses required to maintain subsidence over the long time scales appropriate for cratonic basin formation.

7.3 Conclusions

In this thesis, an integrated analysis of a suite of geological and geophysical data has been performed in order to constrain the crustal structure, subsidence history and tectonic evolution of the Parnaíba basin, with the aim of elucidating the tectonic mechanism responsible basin formation. Analysis was also extended to the Michigan and Congo cratonic basins, to facilitate comparison with observations and interpretations made regarding Parnaíba basin and assess whether any generic conclusions regarding cratonic basin formation can be drawn. The key findings are summarised below:

(i) Parnaíba basin structure and gravity anomalies are inconsistent with an extensional origin

Several observations made within this study appear inconsistent with a lithospheric extensional origin for Parnaíba basin. These include: (a) A lack of evidence for extensional

strain features within the sedimentary basin or underlying basement; (b) A reflection Moho that is as deep or deeper in the basin centre ($44 \pm 2\ km$) with respect to the flanking regions, suggestive of crustal warping rather than thinning; (c) A sub-circular basin morphology during basin initiation, which persisted throughout the basins evolution and (d) A $\sim -30\ mgal$ Bouguer gravity anomaly, that is inconsistent with the near 0 $mGal$ anomaly predicted for an extensional model.

(ii) Parnaíba basin resides above an anomalous lower crust

Gravity and seismic data suggest Parnaíba basin is underlain by an anomalous lower crust, with a predicted mass excess of $\sim 175\ kg\ m^{-3}$ and a V_p increase of 0.43–0.59 $km\ s^{-1}$ with respect to the upper crust. This anomalous body is interpreted as representing a highly intruded mafic lower crust. On solidification, this mass would have acted as a load to drive surface flexure within which sediments accumulated. In three dimensions, a simple Gaussian shaped body 20 km thick and with a base radius of 400 km, centred at longitude 44.1°W and latitude longitude 6.0°S emplaced on an elastic plate with $T_e = 25\ km$, is capable of reproducing the basin gravity anomaly, basement depth and first order basin shape. In this case, the zone of Mid-Crustal Reflectivity (MCR), imaged in the centre of the basin, represents the top surface of this altered lower crust.

(iii) Tectonic subsidence of Parnaíba basin is simple in form and can be reconciled with a buried loading mechanism if a load induced viscoelastic relaxation of the lithosphere is accounted for

Airy backstripping of stratigraphic well data reveals that Parnaíba basin is characterised by a simple tectonic subsidence history that is consistent in form with both a concave up, gentle negative exponential subsidence trajectory or an initial linear subsidence, followed by a subdued exponential. Ruling out an extensional origin, this subsidence profile can be reconciled with an intrusive buried load origin if the viscosity structure of cold cratonic lithosphere is considered. For a reasonable cratonic viscosity structure, viscoelastic relaxation following load emplacement is found to last for 100's Myr, and produce a subsidence trajectory similar to that observed. However, other factors such as thermal cooling, sea level change, loading history and plate strengthening following magma intrusion may also contribute, and

may account for observed departures from the predicted subsidence trajectory.

(iv) Each of the Parnaíba, Michigan and Congo basins exhibit a sub-circular, basin centred, sediment-corrected residual gravity anomaly 'highs'

These residual gravity anomalies have wavelengths up to 1200–2000 km and amplitudes $\sim$ 40–60 $mGal$, suggestive of deep sources. This implies that the intrusive buried load model postulated for Parnaíba basin formation, may also apply to these basins. Moreover, it may be that an anomalous mass excess within the lower crust is a ubiquitous feature of cratonic basins. Hence, a viscoelastic stress relaxation, following the development of a lower crustal buried load, may provide a mechanism for explaining the long-lived subsidence histories of other cratonic basins.

(v) The Parnaíba basin appears relatively well preserved with respect to the Michigan and Congo cratonic basins and therefore reflects a 'primary' cratonic basin subsidence signal

Analysis of tectonic subsidence and basin evolution of these three basins shows that unlike the Michigan and Congo basins, the Parnaíba basin has been relatively unaffected by secondary processes during its evolution, producing a tectonic subsidence that may be considered the "primary" cratonic basin subsidence signal. In contrast, the tectonic subsidence curves of both Michigan and Congo are interrupted by at least one increase in subsidence rate and these basins have been clearly modified by external tectonic processes during their evolutions. Hence, Parnaíba basin offers an excellent record with which to analyse cratonic basin formation.

7.4 Future work

The geophysical modelling conducted in this thesis has placed new constraints on the crustal structure, subsidence history and tectonic origin of Parnaíba basin, as well as the Congo and Michigan cratonic basins. However, further research, and in particular, more data is required, in order to validate the conclusions drawn from this study and to improve our understanding

of cratonic basins in general. Outlined below are suggested avenues for future work that would complement and improve on the research presented in this thesis and may help distinguish between the various proposed modes of cratonic basin formation.

7.4.1 Reconciling lower crustal composition

A crucial component of the lower crustal intrusive loading model postulated in this thesis is the existence of a highly altered lower crust beneath cratonic basins. In this study, this was predicted beneath Parnaíba basin based on geophysical evidence, namely, density modelling, wide-angle reflection V_p modelling and the presence of a zone of high amplitude Mid-Crustal Reflectivity beneath the basin. The existence of an anomalous lower crust beneath the Parnaíba basin would be best validated using explosive-source wide-angle reflection/refraction surveying, which will provide much higher resolution constraints on crustal structure due to the long offsets and P-wave velocity control offered by deep refraction phases (e.g., P_g and P_n arrivals). Such data has now been acquired in Parnaíba basin as part of PBAP and is being analysed by colleagues at the University of Brasilia. These data will place tighter constraints on P-wave velocities, interface depths and potentially include S-wave velocities, allowing the V_p/V_s ratio to be determined. In this way, the nature, physical properties and terrain boundaries of the crust beneath the Parnaíba basin will be better constrained. Furthermore, P_n refractions, which turn within the uppermost mantle, may delineate whether the anomalous body predicted in this thesis is constrained within the lower crust, or whether the upper-most mantle is also anomalous.

The presence of kimberlite pipes within and surrounding the Parnaíba basin (e.g., the Fazenda Largo kimberlite cluster adjacent to the Transbrasilano Shear Zone (Kaminsky et al., 2009)), may provide the best avenue for understanding the nature of the lower crust and mantle-lithosphere beneath the basin. If upper-mantle/lower crustal xenoliths have been rapidly brought to the surface by these pipes, then detailed geobarometry, compositional and geochemical analysis of these would provide direct observations for the presence of mafic intrusions or otherwise. Similarly, geochemical analysis and dating of the granites, particularly the $\sim 460\ Ma$ A-type granites exposed at the northeast edge of the basin, as well as any that

have been drilled within the basin, may provide corroborative evidence, if their chemistries are consistent with an origin involving lower crustal melting, prior to basin initiation.

7.4.2 Numerical modelling of basin evolution

The geological model proposed for Parnaíba basin formation in this study is based on geophysical observations and viscoelastic subsidence modelling, in which, a simple three-layer viscosity structure was prescribed prior to an instantaneous emplacement of the load mass. In order to further evaluate the plausibility of this model, as well as the proposed igneous intrusive origin of the load, a full thermo-mechanical numerical model would be beneficial. In this way, the thermal effects and time-dependent increase in load size could be included in the subsidence analysis. One criticism of numerical models is that they include many parameters, making it difficult to understand which of these are important in modulating basin evolution. However, if such modelling could explain the observed backstripped subsidence data, as well as reproduce the observed crustal structure and gravity anomaly, this would provide compelling evidence in favour of a buried load formation mechanism.

A recent study of the East Barents Sea basin used such an approach, in which thermo-mechanical, rheological and compositional feedbacks were modelled for the case of lithospheric shortening and eclogitisation of the lower crust (Gac et al., 2013). Moreover, Roman and Jaupart (2016) have used numerical calculations to model the evolution of large intrusions within continental crust, such as the Bushveld igneous complex of South Africa. They focused on the long term stability of such intrusions, noting that, once intrusions penetrate the crust, variations in flow laws and ambient temperatures can either promote or prevent foundering of the mafic cumulates. Application of such modelling to the Parnaíba basin may also provide an interesting avenue for assessing the validity of a buried load model.

7.4.3 Metamorphic petrology

In regards to alternative models for cratonic basin formation, McKenzie and Priestley (2016) suggested that if samples of metamorphic basement rocks from exploration wells and surround-

ing basement exposures can be obtained, analysis of the pressure-temperature-time (P-T-t) paths recorded by these would provide the best means for testing their model (which invokes lithospheric thickening, heating and rapid erosion). Such analysis may also be beneficial for assessing the process by which the pre-Silurian regional unconformity formed in Parnaíba basin, a feature which is also characteristic of may other cratonic basins. As noted by McKenzie and Priestley (2016), such analysis has been neglected during investigations of cratonic basin formation, but may offer key evidence regarding basin formation processes.

7.4.4 Wide-angle reflection and refraction surveying

Constraining the structure and physical properties of the crustal and upper-mantle beneath cratonic basins will provide the most pertinent data for assessing whether cratonic basins form through a single common mechanism. Wide-angle reflection/refraction surveying offers the best data for this purpose. Three basins which also have favourable physiographies for active-source refraction experiments and are also accessible for such surveying are the Paraná, Michigan and Hudson Bay basins. At least one refraction profile has already been acquired across the northern part of the Paraná basin (José Soares pers. comms. 2017).

In the case of Michigan basin, the great lakes surrounding the Michigan peninsula create an ideal physiography for onshore/offshore wide angle reflection/refraction imaging (e.g., Okaya et al., 2003). The GLIMPCE crustal-scale marine seismic reflection profiles (Behren et al., 1988), acquired within the great lakes, as well as the onshore COCORP vibroseis profiles (Brown et al., 1982), have demonstrated that good P-wave transmission is achievable within Michigan basin and it is possible to image crustal structure, despite the large volume of Keweenawan volcanic material. Furthermore, the relatively flat topography and extensive road infrastructure is favourable for onshore seismometer installation. A transect spanning the basin from the southwest to the northeast, would provide the best data coverage and sampling of the basin centre and residual gravity anomaly high. This would span from north of Chicago, across Lake Michigan, through Saginaw Bay, across Lake Huron to the South Bruce Peninsula. Ideally, this transect would consist of offshore multi-channel-seismic shooting from both sides of the peninsula recorded by both ocean bottom and onshore seismometers as

receiver gathers, as well as onshore explosive source shot gathers (e.g., Okaya et al., 2003).

Hudson Bay basin is another cratonic basin where marine seismic imaging techniques could be employed. Indeed, the sedimentary basin structure has previously been surveyed using standard multi-channel-seismic reflection profiling (e.g., Hanne et al., 2004). Repeating this analysis using a large volume, low-frequency airgun array source, and an ocean-bottom-seismometer deployment would be expected to yield crustal scale reflection/refraction arrivals. Onshore seismometers could also be deployed to record arrivals as receiver gathers, which would sample the basin edges and directly test for crustal thinning. This study would be of particular interest in light of recent studies that have interpreted Hudson Bay basin as a failed rift basin, on the basis of rift structures in the basin and basement (Hanne et al., 2004) and apparent crustal thinning beneath the basin, imaged using ambient-noise tomography (Pawlak et al., 2011).

Appendix A

Software development: geophysical modelling GUI (gmg)

A.1 Introduction

This appendix provides details regarding the development and usage of Graphical User Interface (GUI) software package designed for the integrated interpretation and analysis of two-dimensional potential field and seismic reflection data. The software is named *Geophysical Modelling GUI* (gmg) and is planned for public release as an open source software package. The source code is stored in a GitHub repository and can be obtained from (https://github.com/btozer/gmg). The current release is version Beta0.1 and installation instructions are included. Previous software packages are available (both free and commercial) that are intended for performing similar tasks to those of gmg. However, as an open source software, gmg has the advantage that the underlying source code is fully visible and editable. This is intended to allow users to contribute to development, such that, over time, users will add new functionality that is beneficial to the wider community and the software will become as "user friendly" and "user beneficial" as possible. A user guide is incorporated within the software documentation.

A.2 Software summary

gmg is primarily intended for interactive forward modelling of two dimensional gravity and magnetic anomaly profiles. Other features allow the incorporation of complementary datasets, such as well logs and seismic data. Key software features include the following:

- Import and display observed topography, gravity and magnetic data.
- Apply filters to observed data.
- Import and display seismic reflection data.
- Add and manipulate model layers/bodies using a simple interactive interface.
- "Pinch out/snap" layers against adjacent layers.
- Calculate the predicted gravity anomaly produced by any combination of model layers.
- Calculate the predicted magnetic anomaly produced by any combination of model layers.
- Model magnetic anomalies using induced and/or remanent magnetism.
- Display well horizon tops.
- Display XY data (e.g., earthquake hypocenters; geological surface contacts).
- Export model data (e.g., predicted anomalies and layer geometries) as ASCII text files.
- Save model figures as vector graphics in Portable Document Format (PDF) file.

A.3 Coding language, adopted GUI development toolkit and software dependencies

gmg is written using the Python programming language. The software makes extensive use of functions from the Scientific Computing in Python (SciPy) package (Oliphant, 2007). In particular, NumPy (Van Der Walt et al., 2011) data structures are used for data handling and

computational efficiency. Matplotlib (Hunter, 2007) plotting tools are employed for displaying and interacting with graphics. The GUI is implemented using the wxWidgets GUI toolkit, wxPython (Rappin and Dunn, 2006). Further, software dependencies include Fatiando a Terra (Uieda et al., 2013), from which, the function fatiando.polygon is used for handling model layers and ObsPy (Beyreuther et al., 2010), from which, the seismic plotting function obspy.read is used for loading seismic data.

A.4 Software architecture

The source code for gmg is mostly contained within, and run from, a top-level parent script – *gmg.py*. Figure A.1 provides a simplified software map, depicting the relationships between the top-level *gmg.py* script and its most important child classes and functions, as well as subsidiary scripts that contain auxiliary algorithms and functions.

Approximately 80 % of the software code is contained within the *gmg* ___*main*___ Class. Upon execution of the *gmg.py* python script (from the command line or desktop launcher icon) a wxPython application frame is initialised and then passed to an instance of the *gmg* ___*main*___ Class, thereby creating an active session of the software.

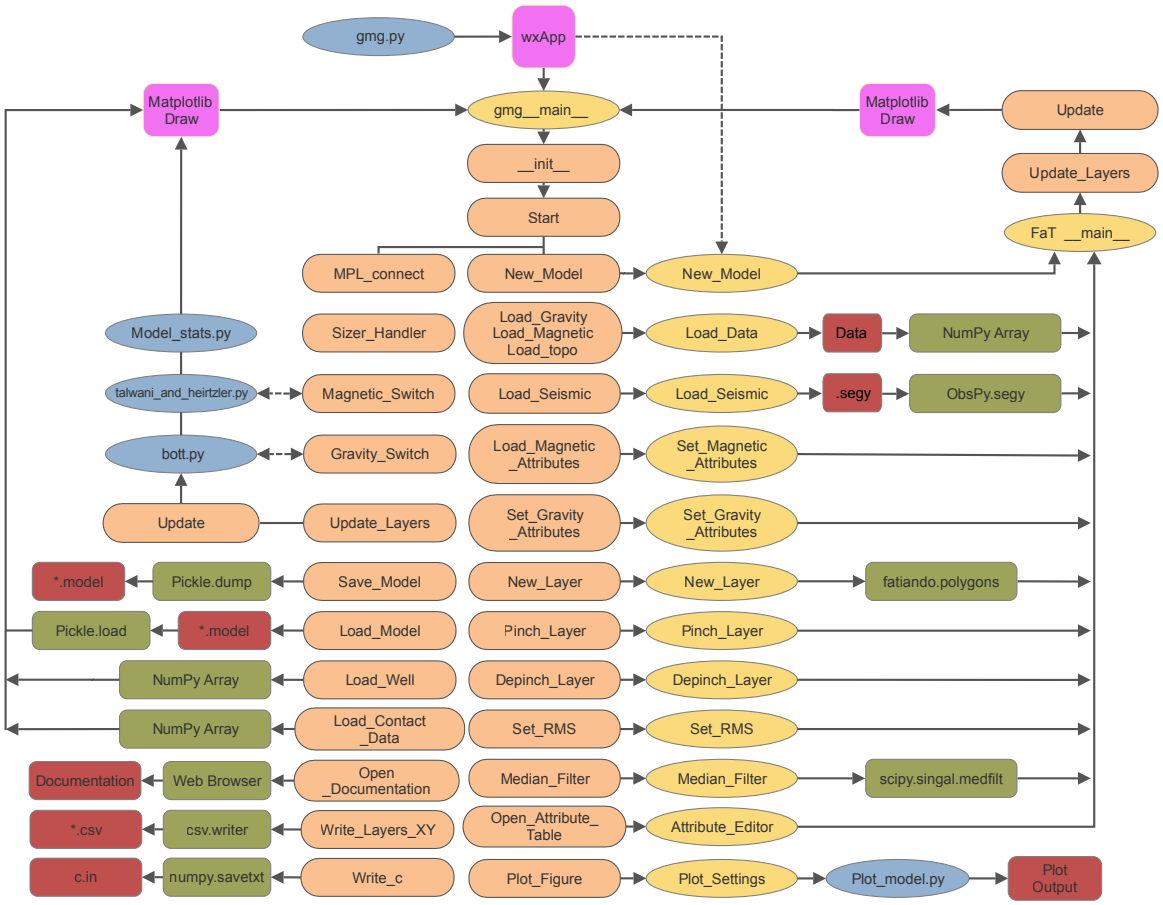


Figure A.1: Simplified software architecture map for gmg showing the principle operational relationships and inputs/outputs. Blue ellipse = Script; Pink box = auxiliary graphics function; Yellow ellipse = Python class; Clay ellipse = Python function; Green box = auxiliary algorithm/function; Red box = external disc file.

A.5 Potential field algorithms

A.5.1 Two-dimensional gravity anomalies: Bott (1965) algorithm

Two dimensional gravity anomalies are calculated using a python implementation of Bott's (1969) algorithm. This is similar to that derived by Talwani et al. (1959) and operates by setting the observation point as the origin of a Cartesian coordinate system and treating the periphery of a given body as an n-sided polygon, defined by of discrete set of nodal points. The total gravity anomaly is then calculated by evaluating the solution for a semi infinite horizontal slab with one sloping interface for each set of nodal pairs and then summing the

results. The analytic solution for this is given by Heiland (1940) page. 153 as:

$$\Delta g = 2G\Delta\rho\left[-\{x_1\sin\theta + z_1\cos\theta\}\times\left\{\sin\theta\log_e\frac{r_2}{r_1} + \cos\theta(\phi_2-\phi_1)\right\} + z_2\phi_2 - z_1\phi_1\right] \tag{A.1}$$

Where G is the Universal Gravitational Constant; $\Delta\rho$ is the density contrast between the polygon and the surrounding material; x_i, z_i and r_i are the horizontal, vertical and absolute distance between each node and the observation point, P, respectively; θ is the angle between the sloping edge and the horizontal; and ϕ_i is the angle between the x-axis and r_i respectively. The geometry of this parametrisation is shown in Figure A.2a.

The total gravity anomaly produced by a given polygon is then determined by moving progressively counter-clockwise around the polygon and summing the contribution of each side (Equation A.2).

$$\Delta g = \sum_{i=1}^{N}\Delta g_i \tag{A.2}$$

When $z_2 > z_1$ the contribution is positive and when $z_2 < z_1$ the contribution is negative, such that, in the summation, the contributions outside of the polygon cancel, leaving only the gravity anomaly produced by the polygon itself (Fig. A.2b).

The Bott (1969) algorithm is preferred to the Talwani et al. (1959) because a) it runs slightly faster and b) it does not explicitly require closed polygons.

A.5.1.1 Bott (1965) algorithm testing

To assess the accuracy of the Bott (1969) method, the gravity anomaly determined using the algorithm is compared to that of an exact analytic solution for a simple body. In this case, the solution for a buried horizontal cylinder of constant density contrast, that extends infinitely into and out of the model plane is used. The solution for this case is given by, for example,

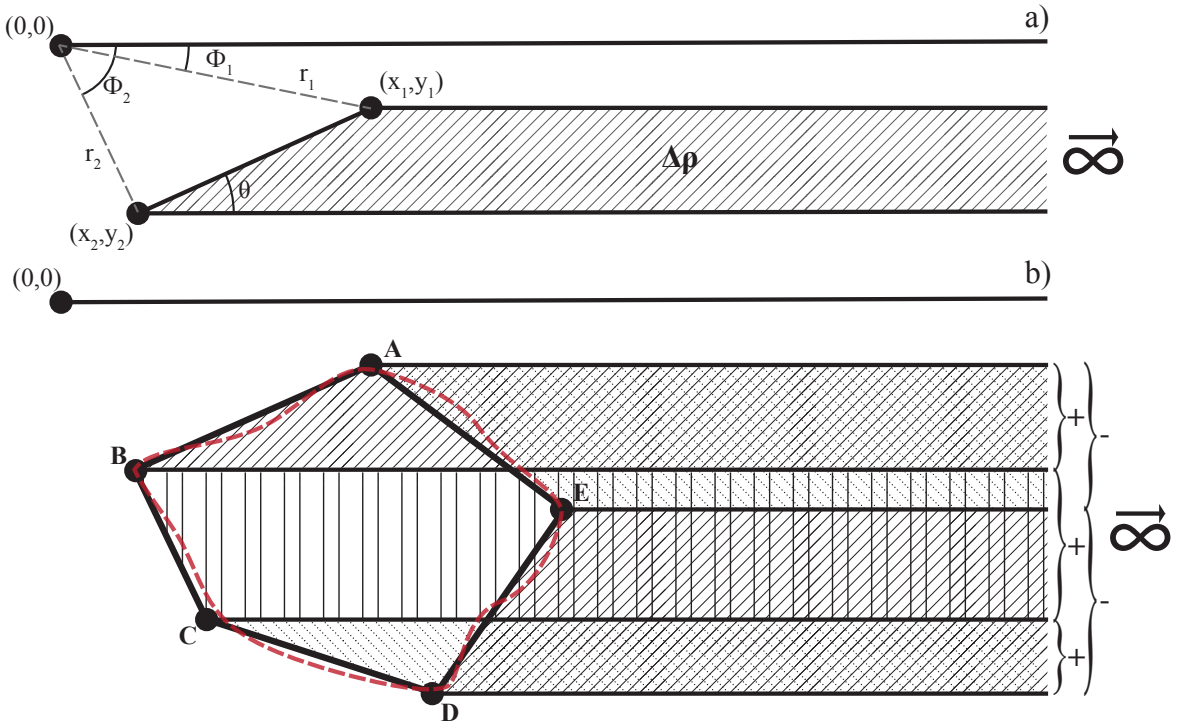


Figure A.2: a) An example of a infinite slab with one sloping horizontal side, showing the geometric values relative to the observation point (0,0) using in solving Equation A.1. b) Example of calculating the gravity anomaly due to a two dimensional body (red dashed line) estimated using five nodes (A-E) by summing the effects of the five infinite slabs with sloping sides (modified after, Kearey et al. (2013)).

Garland (1965) Pg. 70 as:

$$g_z = 2\pi G r^2 \Delta\rho \frac{z}{x^2 + z^2} \tag{A.3}$$

Where G is the Universal Gravitational Constant; r is the radius of the cylinder; $\Delta\rho$ is the density contrast between the cylinder and the surrounding material; and x and z are the horizontal and vertical distances from the observation point, P, to the centre axis of the cylinder respectively. The geometry of this parametrisation is shown in Figure A.3.

Using the Bott (1969) algorithm, the cylinder must be estimated using a series of discrete nodal points, N. A range of values for N were tested, starting from $N = 360$ (i.e., one node every 1 degree) and then halving the number of nodes for each new test until $N = 22$ (i.e., one node every ~ 16 degrees). For the $N = 360$ case, the predicted anomaly is also calculated

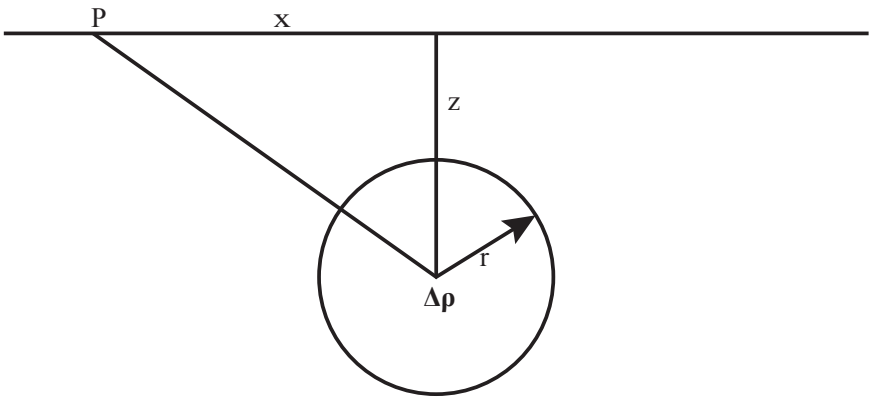


Figure A.3: Two-dimensional geometric parameters required for calculating the gravity anomaly produced by a buried cylinder.

using the Talwani et al. (1959) method for comparison. This method uses a slightly different trigonometric parametrisation.

As can be seen in Figure A.4, both the Bott (1969) and Talwani et al. (1959) methods produce almost identical anomalies, with the slight (2.9×10^{-6}) mismatch resulting from the difference between the sum of precision error, due to the different trigonometric functions that are solved by each algorithm. When $N = 360$, both methods reproduce the analytic anomaly to within an RMS misfit 9.0×10^{-4} mGal. For the $N = 22$ case the Bott (1969) method predicts the analytic solution to within 0.25 mGal. This level of accuracy is adequate for modelling large scale features, for example, sedimentary basins and lithospheric gravity anomalies and demonstrates that bodies constructed using simplified geometries with relatively few nodes, are sufficient for modelling of such features. However, for some applications, such as microgravity surveys, much higher accuracy is required and detailed polygons with many nodes may be necessary.

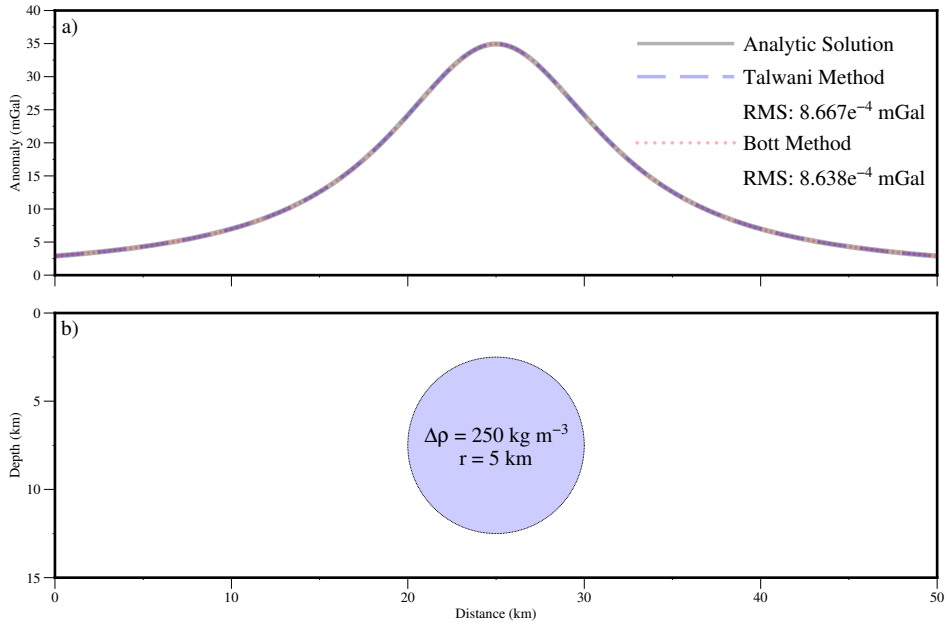


Figure A.4: a) Gravity anomaly calculated for the cylinder shown in (b) using an exact analytical solution and by the line-integral methods of Talwani et al. (1959) and Bott (1969). b) Model cylinder defined using 360, 180, 90, 45 and 22 nodes, a radius of 5 km and a density contrast of 250 $kg\ m^{-3}$.

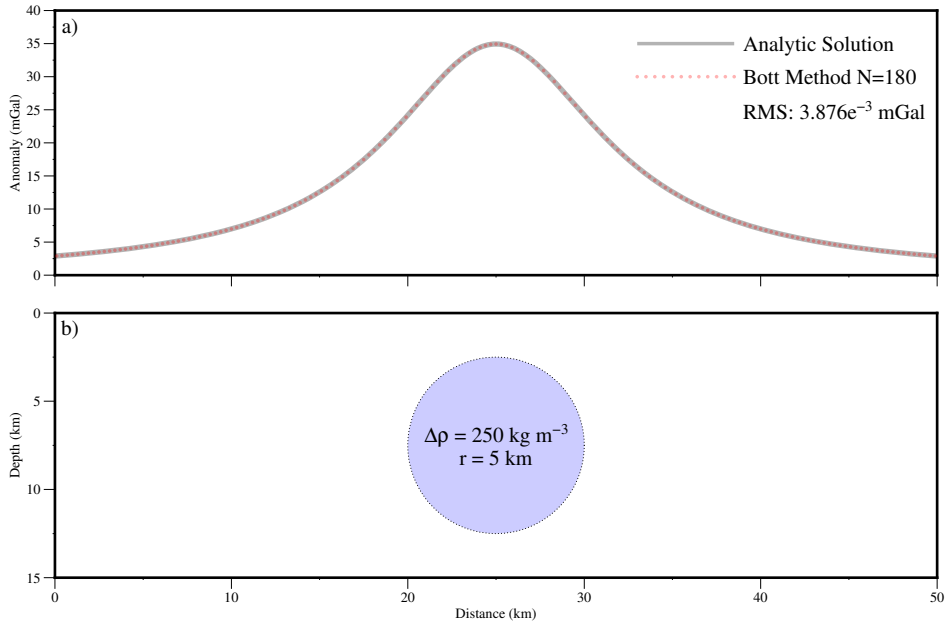


Figure A.4 continued

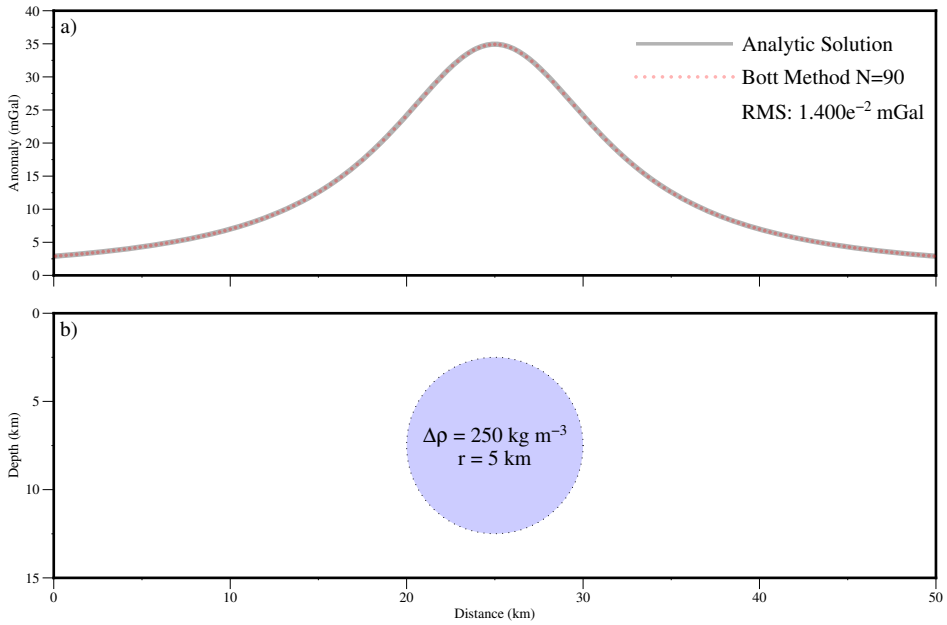


Figure A.4 continued

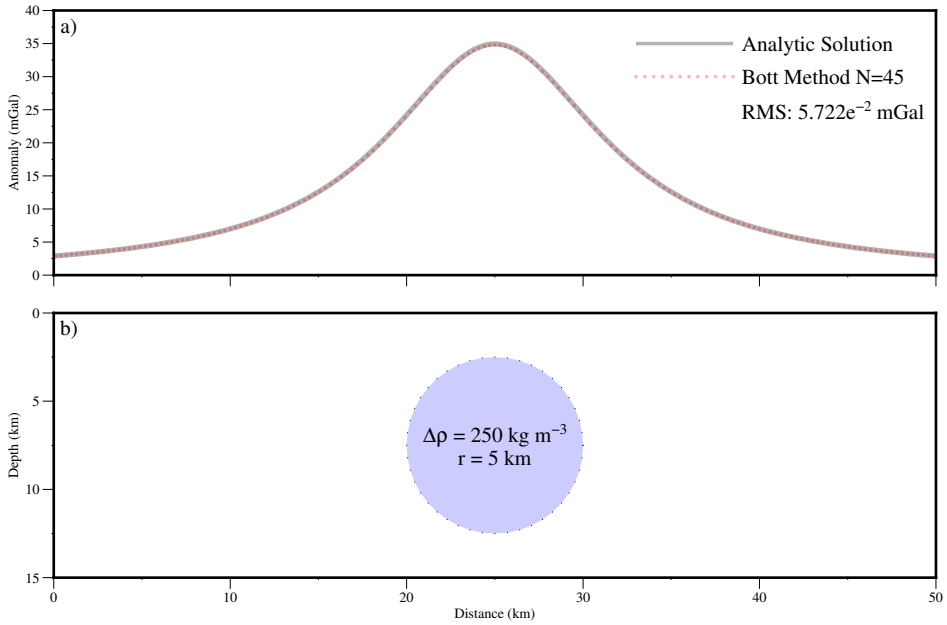


Figure A.4 continued

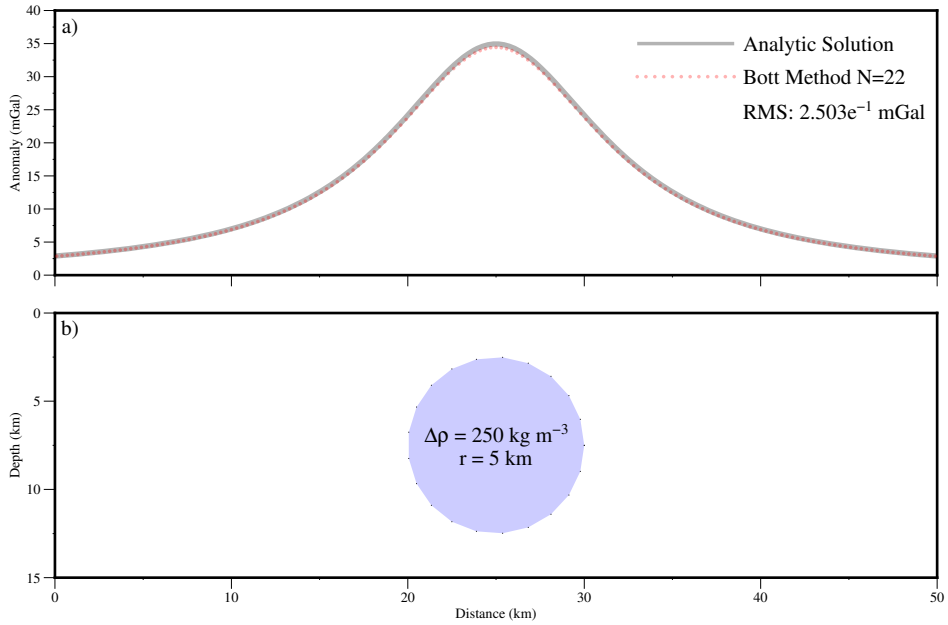


Figure A.4 continued

A.5.2 Two-dimensional magnetic anomalies: Talwani and Heirtzler (1964) algorithm

Magnetic anomalies are calculated using a python implementation of Talwani and Heirtzler's (1964) algorithm for two-dimensional uniformly magnetised bodies. This employs a similar procedure to that described in section A.5.1 for calculating two-dimensional gravity anomalies by treating a body as an n-sided polygon, solving the anomaly for each side and summing the result. However, in the case of magnetic anomalies, there is added complexity owing to the fact that a given bodies magnetisation vector is, for the case of induced magnetisation, dependent on the inclination, delineation and magnitude of the inducing magnetic field (i.e., Earth's magnetic field). Moreover, if the body has retained a remanent magnetisation, then the magnetisation vector may vary from that of the local Earth field. Furthermore, for two-dimensional modelling, the relationship between the azimuth of model profile and the magnetisation vector must also be considered.

These complexities are handled by considering the vertical and horizontal components of the total magnetisation vector separately and then summing these components at the final

calculation step. Following the trigonometric parametrisation for a two-dimensional body shown in Figure A.5, Talwani and Heirtzler (1964) showed that the horizontal and vertical components of the total magnetic field are given by:

$$V = 2(J_x Q - J_z P) \tag{A.4}$$

$$H = 2(J_x Q + J_z P) \tag{A.5}$$

where:

$$P = \frac{z_{21}^2}{z_{21}^2 + x_{12}^2}(\theta_1 - \theta_2) + \frac{z_{21} x_{12}}{z_{21}^2 + x_{12}^2} \log \frac{r_2}{r_1} \tag{A.6}$$

$$Q = \frac{z_{21} x_{12}}{z_{21}^2 + x_{12}^2}(\theta_1 - \theta_2) - \frac{z_{21}^2}{z_{21}^2 + x_{12}^2} \log \frac{r_2}{r_1} \tag{A.7}$$

and:

$$x_{12} = x_1 - x_2 \qquad z_{21} = z_2 - z_1 \qquad z_1 = \sqrt{x_1^2 + z_1^2} \qquad z_2 = \sqrt{x_2^2 + z_2^2} \tag{A.8}$$

To account for the bodies magnetisation vector and its relationship with the model profile azimuth J_x and J_z are then given by:

$$J_x = J \cos A \cos(C - B) \tag{A.9}$$

$$J_z = J \sin A \tag{A.10}$$

where angle A is measured in the vertical plane from zero at the horizontal and positive downwards. Angles B and C are measured in the horizontal plane, in a positive clockwise direction from geographic north, as shown in figure A.6. For the case when magnetisation is induced only:

$$J = kH \tag{A.11}$$

where k is the susceptibility contrast between the body and surrounding material and H is the strength of inducing field. Also, A will be equal to the inclination (I) and B will be equal to the

declination (D) (Talwani and Heirtzler, 1964). For the case when magnetisation is remanent or a combination of remanent and induced, the angles A and B will require modification by the user to account for the difference between the inducing field vector and remanent field vector.

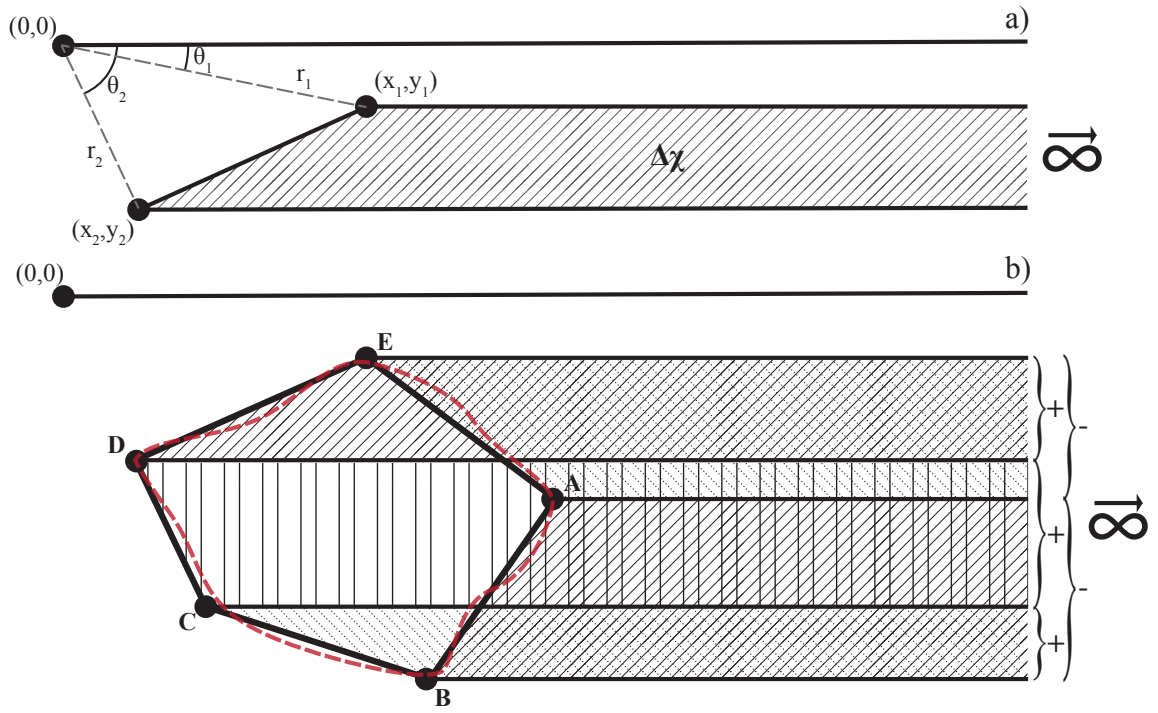


Figure A.5: a) Geometric parameters used for solving for the magnetic anomaly produced by an infinite body with one sloping interface. b) Diagram showing an example two-dimensional body (red dashed line) estimated using five nodal points (A-E) (modified after, Talwani and Heirtzler, 1964).

The total magnetic anomaly is then given as the sum of the horizontal and vertical components in the model plane:

$$T = V \sin A + H \cos A \cos(C - B) \tag{A.12}$$

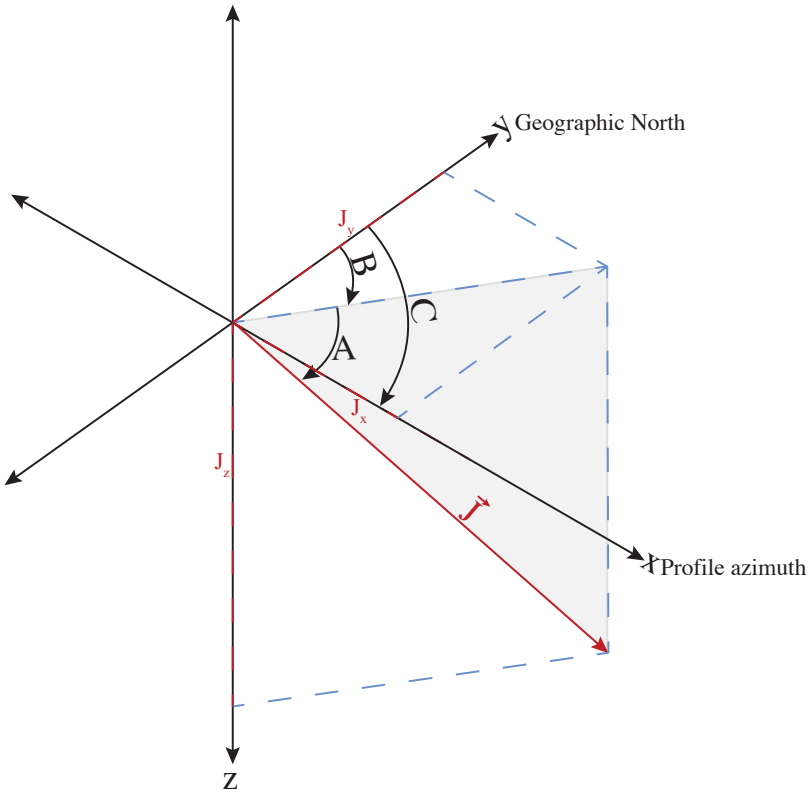


Figure A.6: Perspective three-dimensional view of the total magnetisation vector $\vec{J}$. Grey shade is a vertical plane connecting $\vec{J}$ to the horizontal x-y surface. A is the dip angle of $\vec{J}$, measured in the vertical plane and equal to the inclination for induced magnetisation. B and C are the angles between geographic north and the horizontal projection of $\vec{J}$ and model profile (positive x-axis) respectively. These are measured clockwise from geographic north and B is equal to declination for induced magnetisation (modified after, Talwani and Heirtzler (1964)).

A.5.2.1 Talwani and Heirtzler (1964) method testing

To assess the accuracy of the Talwani and Heirtzler (1964) method, the magnetic anomaly determined using the algorithm is compared to that of an exact analytic solution for a simple body. In this case, the solution for a thin (width << depth) flat topped vertical sheet with a constant dip angle and magnetisation, which extends infinitely into and out of the model plane and infinitely in depth is solved. The solution for this case is given by, for example, Reford (1964) as:

$$\Delta T = 2kTb^2w\left[\frac{h}{R^2}\sin(2I'-d) - \frac{x}{R^2}\cos(2I'-d)\right]$$
$$b^2 = 1 - \cos^2 i \sin^2 D \tag{A.13}$$

Where k is the magnetic susceptibility contrast between the sheet and its surroundings; T is the strength of the inducing field; w is the width of the flat top of the sheet; h is the depth to the top of the dyke; I' is the angle of inclination measured downwards from the horizontal and projected onto the x-z plane; C is the angle between magnetic north and the positive x axis (model profile azimuth); d is the dip of the dyke measured clockwise from the positive x axis (e.g. Fig. A.6).

This solution is used to simulate a vertical dyke of finite depth extent by calculating the anomalies produced by two bodies, one where $h = d_1$ (the top of the dyke) and a second where h = d_2 (the base of the dyke). The effect of the second dyke is subtracted from the first to leave the anomaly caused by a dyke of finite depth extent d_2.

Figure A.7 shows anomalies calculated using the analytic solution and the Talwani and Heirtzler (1964) algorithm for a thin vertical sheet beginning at a depth of 1 km and extending to 10 km with no dip and a magnetic susceptibility of 0.001. Inclination and declination are both 0°, and the model azimuth is due north, such that, the sheet strikes east-west.

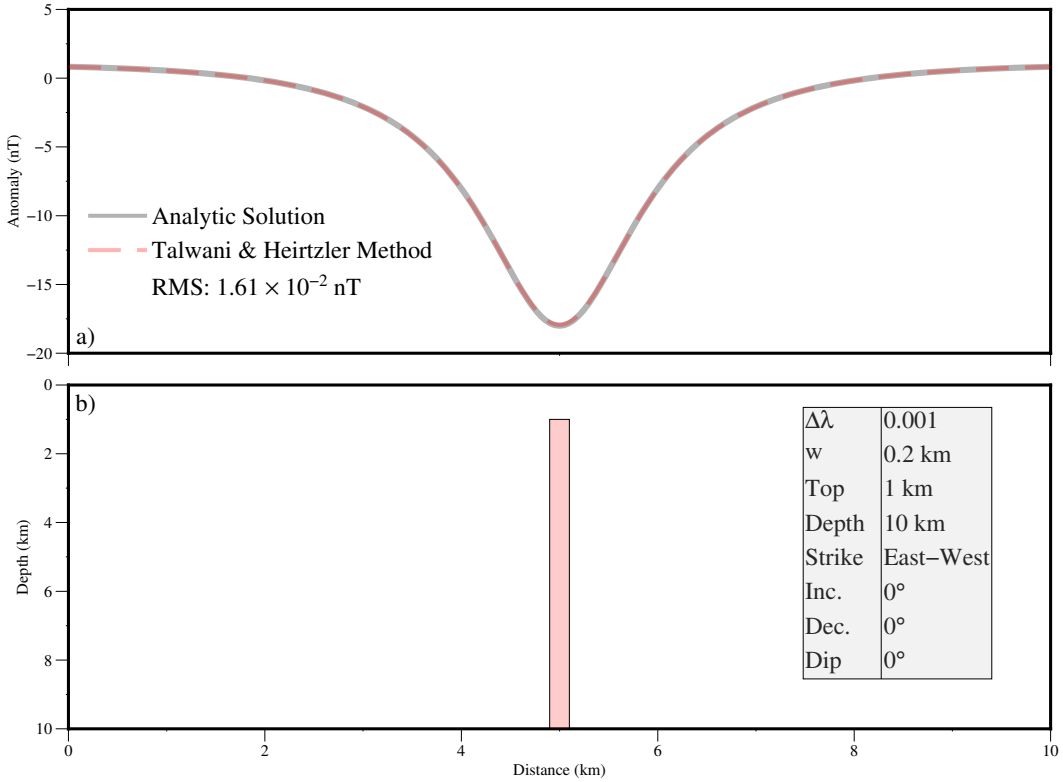


Figure A.7: a) Predicted magnetic anomalies for the model shown in (b) using the analytic solution for a thin sheet (grey line) and the Talwani and Heirtzler (1964) algorithm (red dashed line). b) Simple thin sheet model polygon used to simulate a vertical dyke. Inset table lists model parameters $\Delta\chi$ = susceptibility contrast; w = width of the flat top of the sheet; Inc. and Dec. = Inclination and Declination of inducing field.

A.6 Software layout

gmg is arranged as a simple, multi-windowed graphical user interface as shown in Figure A.8. The software consists of two primary frames, the model frame and control frame. A third frame, containing an inbuilt python console may also be displayed and used to access and edit model data via the command line. Three control bars are used to access software features. The top menu bar contains a list of drop-down menus. These are organised under various headings, such as "gravity data", each containing relevant functions. Below this menu bar is a shortcut button bar. At the base of the control frame, is a toggle bar. This contains five buttons that are used to hide/show model frame panels (topography, gravity and magnetics), the control frame and the python console frame. A "current status" bar is displayed at the

base of the model frame, providing relevant information related to the current state of the model.

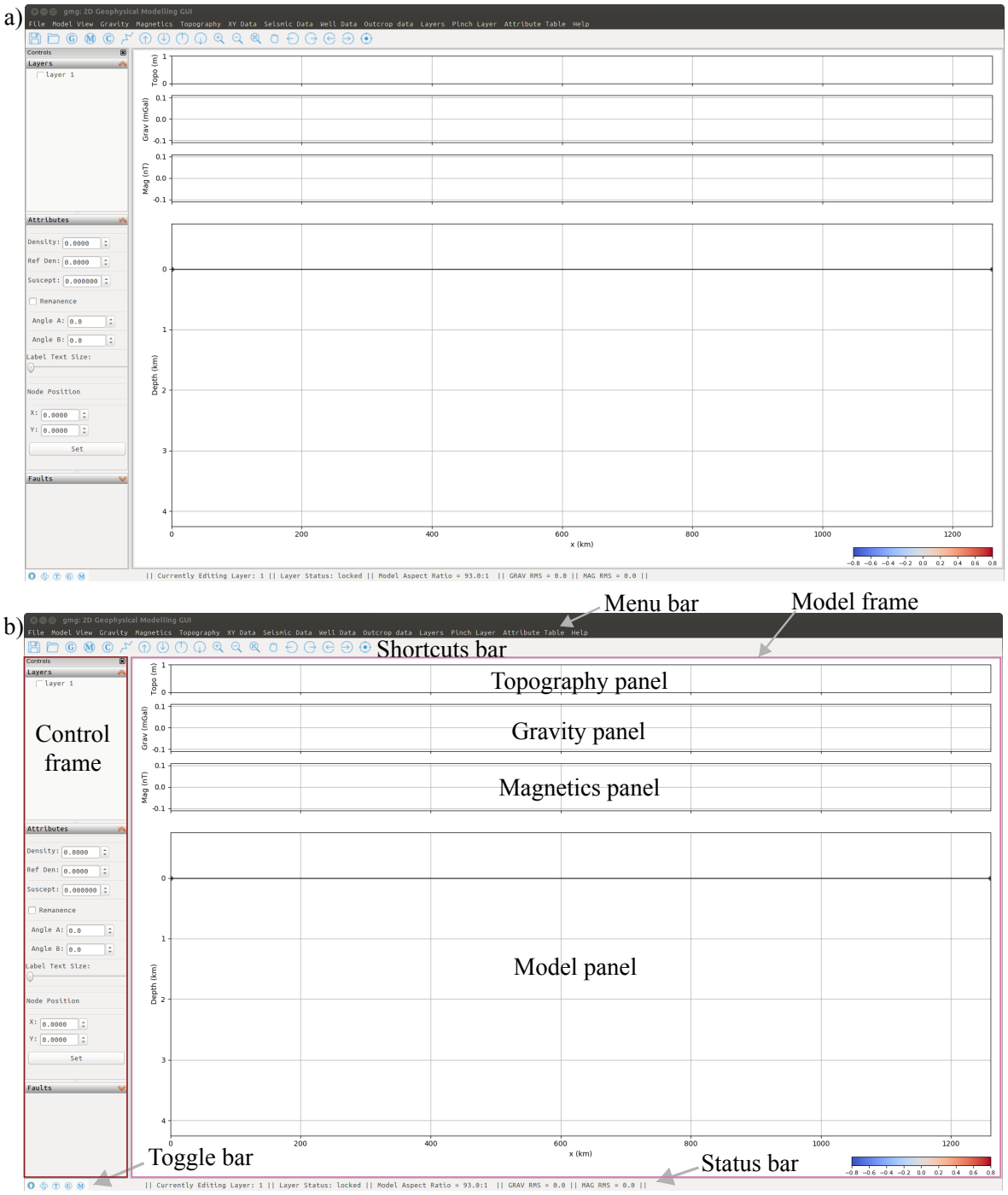


Figure A.8: a) gmg software layout. b) same as in (a) but with labels showing the key model frames (model frame = pink outline; control frame = red outline), panels and bars.

A.7 Software features

This section briefly describes the key features currently available within gmg.

A.7.1 Loading data

Observed data, such as gravity profiles are read by gmg as simple XY formatted ASCII text files and stored as *NumPy* arrays. The data are displayed using *Matplotlib* plotting tools.

A.7.2 Layer attributes

Attributes refer to the physical properties assigned to a given model layer/polygon and are used to calculate the predicted gravity and magnetic anomalies. These include:

- Layer bulk Density
- Model reference Density
- Layer susceptibility Contrast
- Magnetic Field Vector Angle A
- Magnetic Field Vector Angle B

Layer attributes are set using the *Attributes* sidebar within the modelling window or from the *Attribute Table* which can be accessed from the top menubar. gmg is designed such that attributes can be easily varied when modelling, to allow for rapid assessment of the effect of varying each attribute. A given attribute need only be set if required for the given layer, if attributes are not set, the given layer will not contribute to the modelled anomaly, be that gravity or magnetic. Angles A and B need only be set if the given layers magnetic vector differs from the inducing field, as may be the case for remanent magnetism.

A.7.3 Seismic reflection data

Two dimensional seismic reflection profiles can be loaded into the model frame, for interpretation and use as an independent constraint on model structure. The seismic data must be in the depth domain and is loaded using the *ObsPy* module *obspy.read*. Using this method, the SEGY data is stored as a *NumPy* array and displayed as *Matplotlib* image. Displaying the data in this way requires evenly spaced traces and specification of the maximum and minimum x-distance and depth range. The amplitude gain and colour palette can be varied within gmg using th relevant feature buttons.

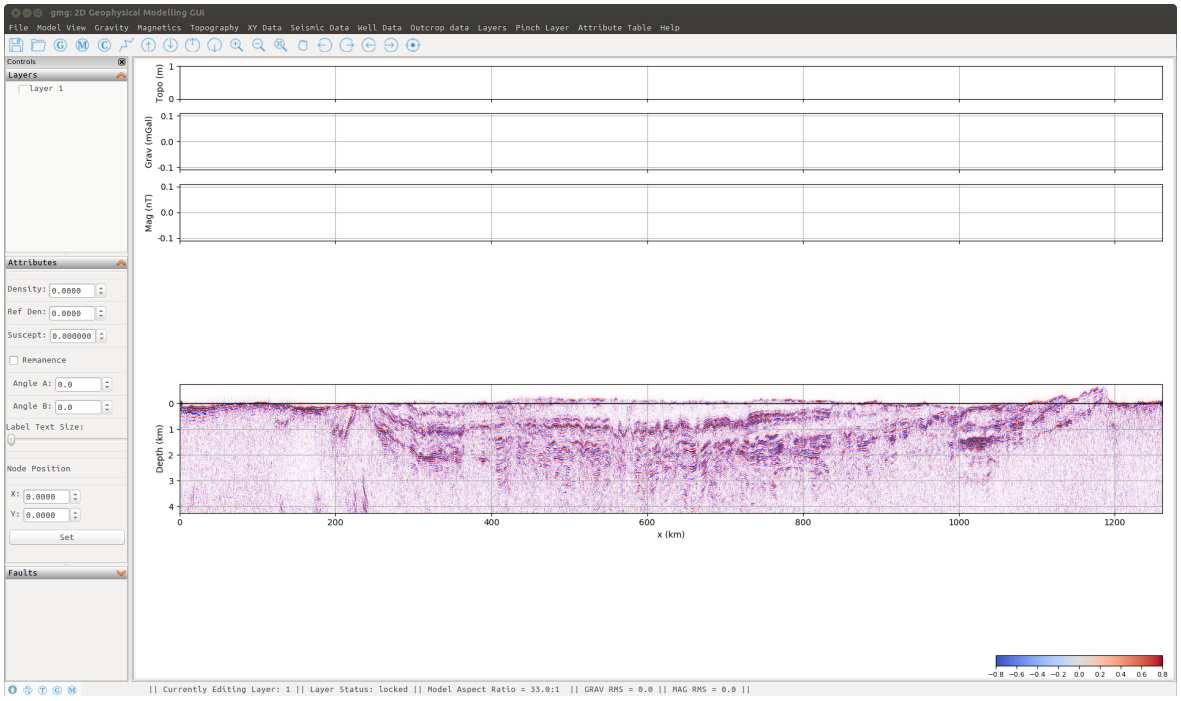


Figure A.9: Example segy image displayed within a gmg model frame.

A.7.4 Well horizon top data

Well horizon top records can be loaded into the model frame and used as an independent constraint for interface depths. These are plotted as *Matplotlib* line and text objects, and the text size for horizon top labels can be dynamically adjusted using the *Label text size* slider in the attributes frame. Once horizon tops are loaded, they can be easily hidden/shown by using

the toggle within the *Well Data* menu. Currently, wells can only be loaded as vertical profiles; in future releases well depth track plotting will be incorporated as well as petrophysical log plotting.

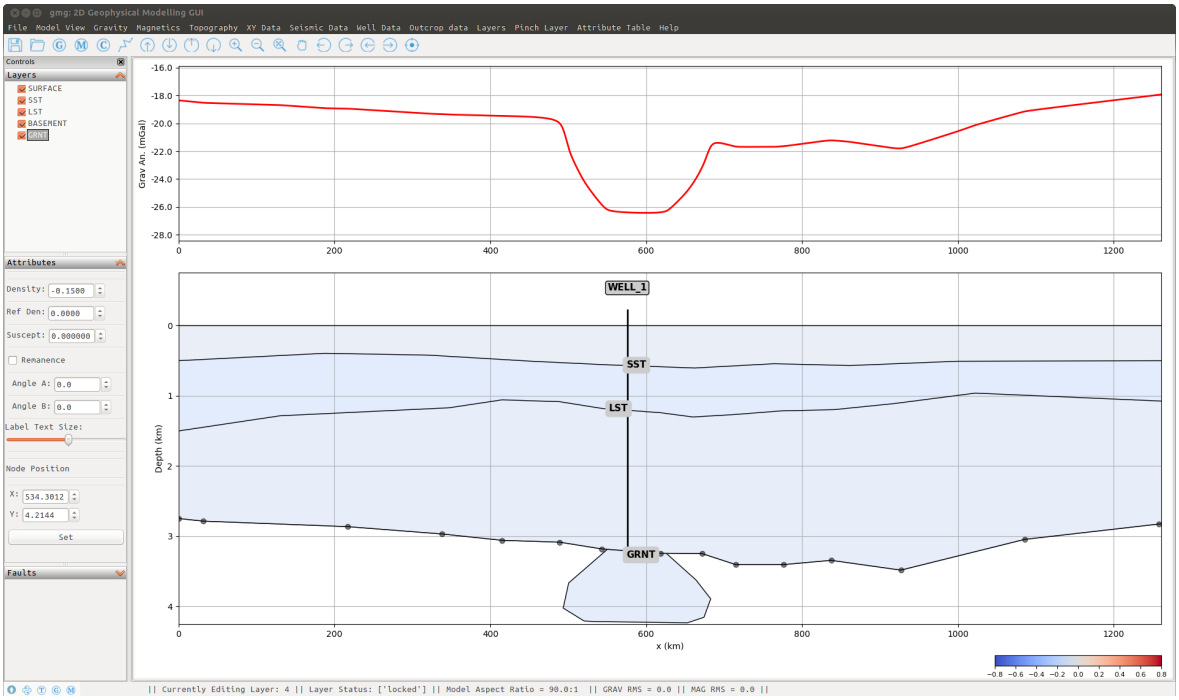


Figure A.10: Example of a well log loaded in the gmg model frame.

A.7.5 Layer pinching/snapping

Any Layer node may be pinched or "snapped" to an adjacent layer, such that, the given polygons will share a common node or series of nodes. This is useful for modelling features such as stratigraphic onlap of sedimentary basins or fault offsets. When a layer is pinched out, the gravity and magnetic effect of the pinched out section no longer contribute to the predicted anomalies.

A.7.6 Data filters

Currently, the only filter available within gmg id s median filter. However, more filter options are intended to be added. A median filter can be applied to observed anomaly profile (magnetic

or gravity) using the *Filter Anomaly* tool found within the *Gravity* and *Magnetic* menus. The filter is applied using the *SciPy* function *signal.medfilt*.

A.7.7 Exporting data

A.7.7.1 Figure export

Customised figure output is supported through the a figure construction menu, which can be accessed under the *File* menu. Figures are created using an auxiliary plot-figure.py script and are saved as vector graphics in either .svg, .ps, .eps or .pdf format. The figure export function allows the user to select which model features to include within the output figure as wee as adjust parameters such as text size.

A.7.7.2 Modelled anomalies and layers

The XY coordinates of modelled anomalies and the model layers/polygons can be exported as ASCII text files. These can then be plotted using external software such as the Generic Mapping Tools (GMT) (Wessel et al., 2013).

A.7.7.3 RayInvr c.in model export

Model layers can also be written as a formatted c.in ASCII file. This file format can then be converted to a v.in file, which is the model file format required for RayInvr (Zelt and Smith, 1992) seismic ray tracing models. This is advantageous for simultaneous potential field and seismic forward modelling.

A.7.8 Future modules

Several future improvements to gmg are currently in development or planned for development. These include:

- 2.5D modelling algorithms
- A module for creating exploration well-tie pseudo-traces
- A function for reducing magnetic data to the pole

Appendix B

Seismic processing supplementary figures

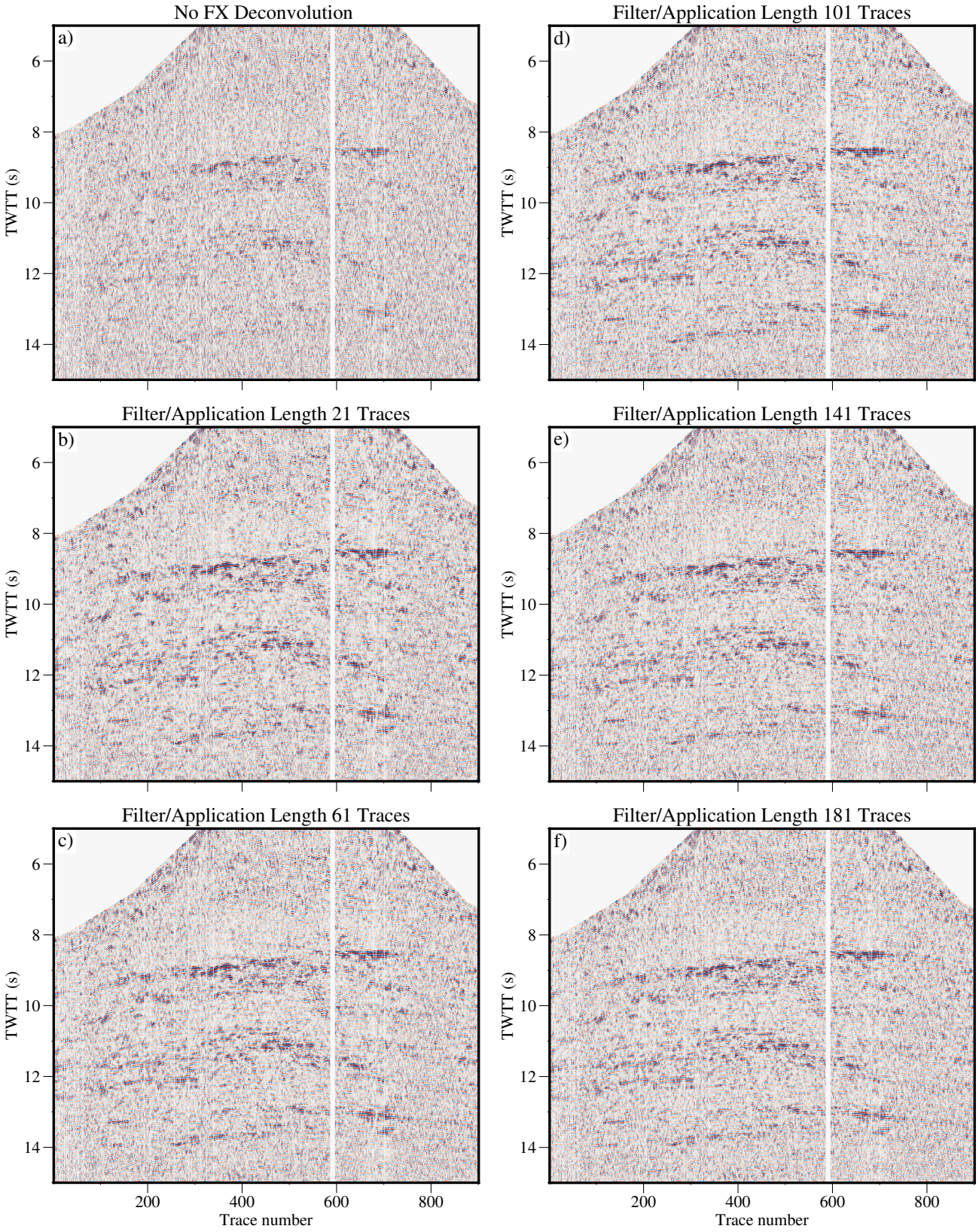


Figure B.1: Test panels for variations in number of input traces for FX deconvolution filter design. The filter design window length is held constant as 100 ms for all tests.

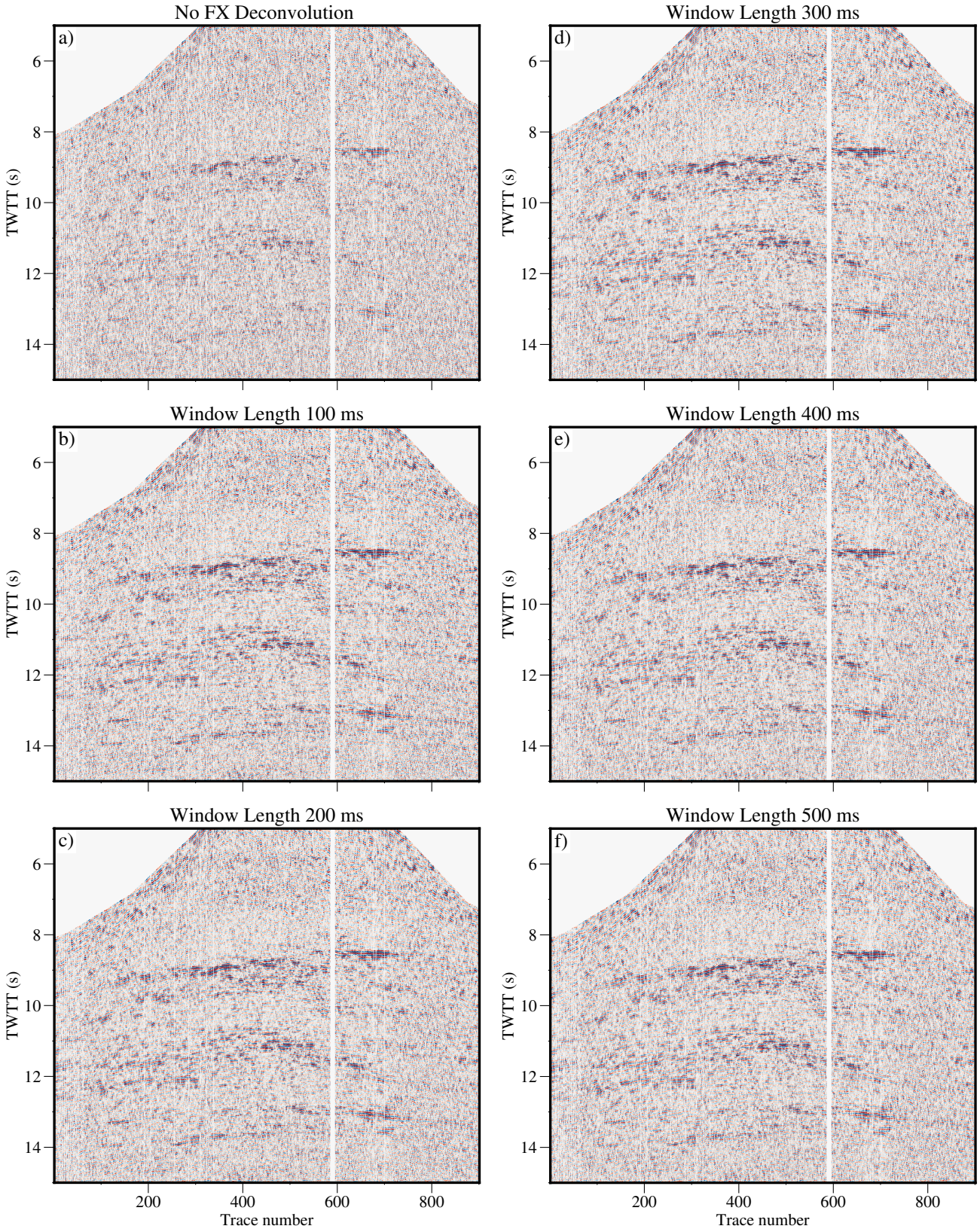


Figure B.2: Test panels for variations in time window length for FX deconvolution filter design. The number of traces used during filter design is held fixed at 101 traces for al tests. Test values are shown above panels. Test gather is Box-2.

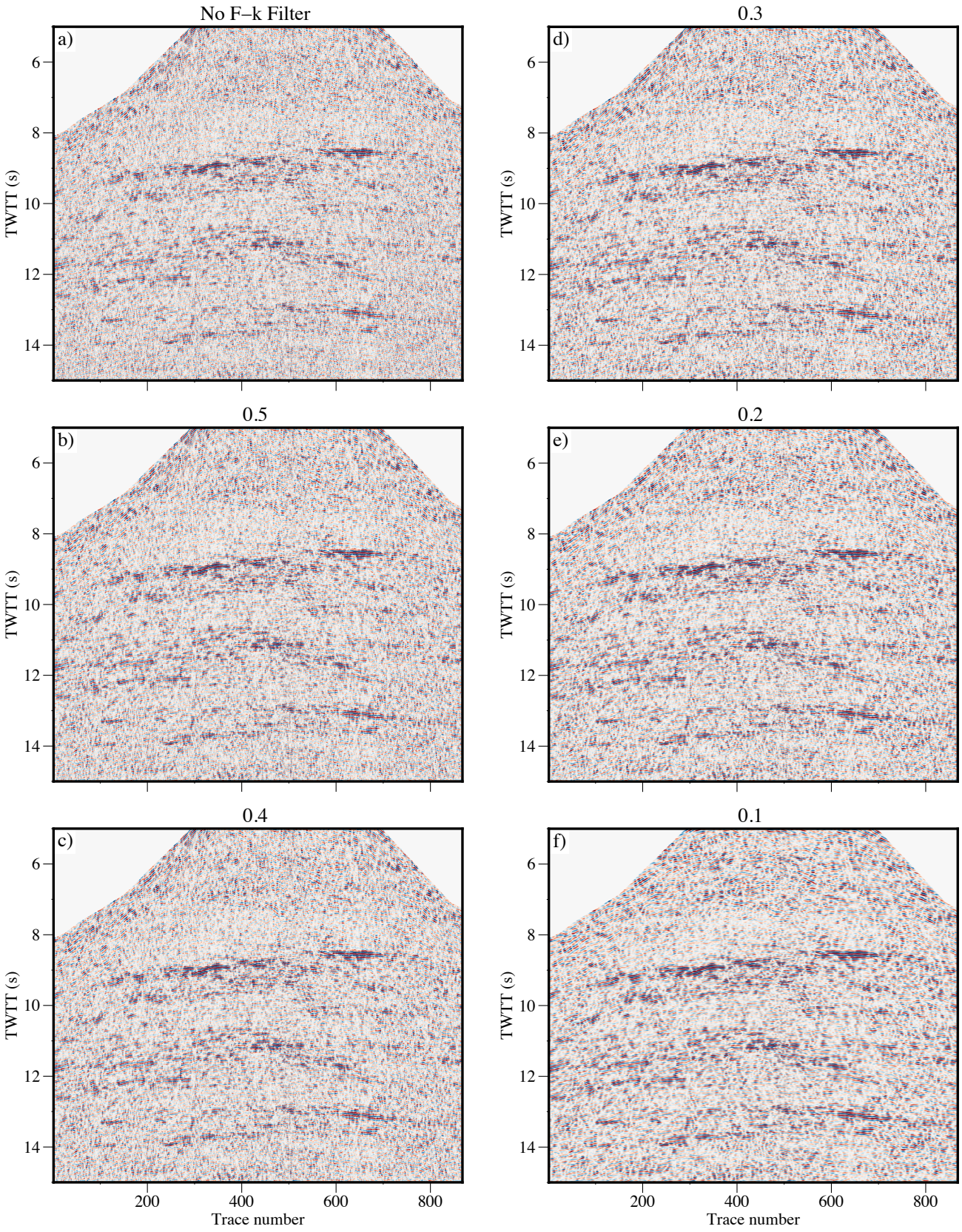


Figure B.3: Test panels for variations in the k-axis cut-off value for f—k filter design. Larger numbers are less harsh filters. Test values are shown above panels. Test gather is Box-2.

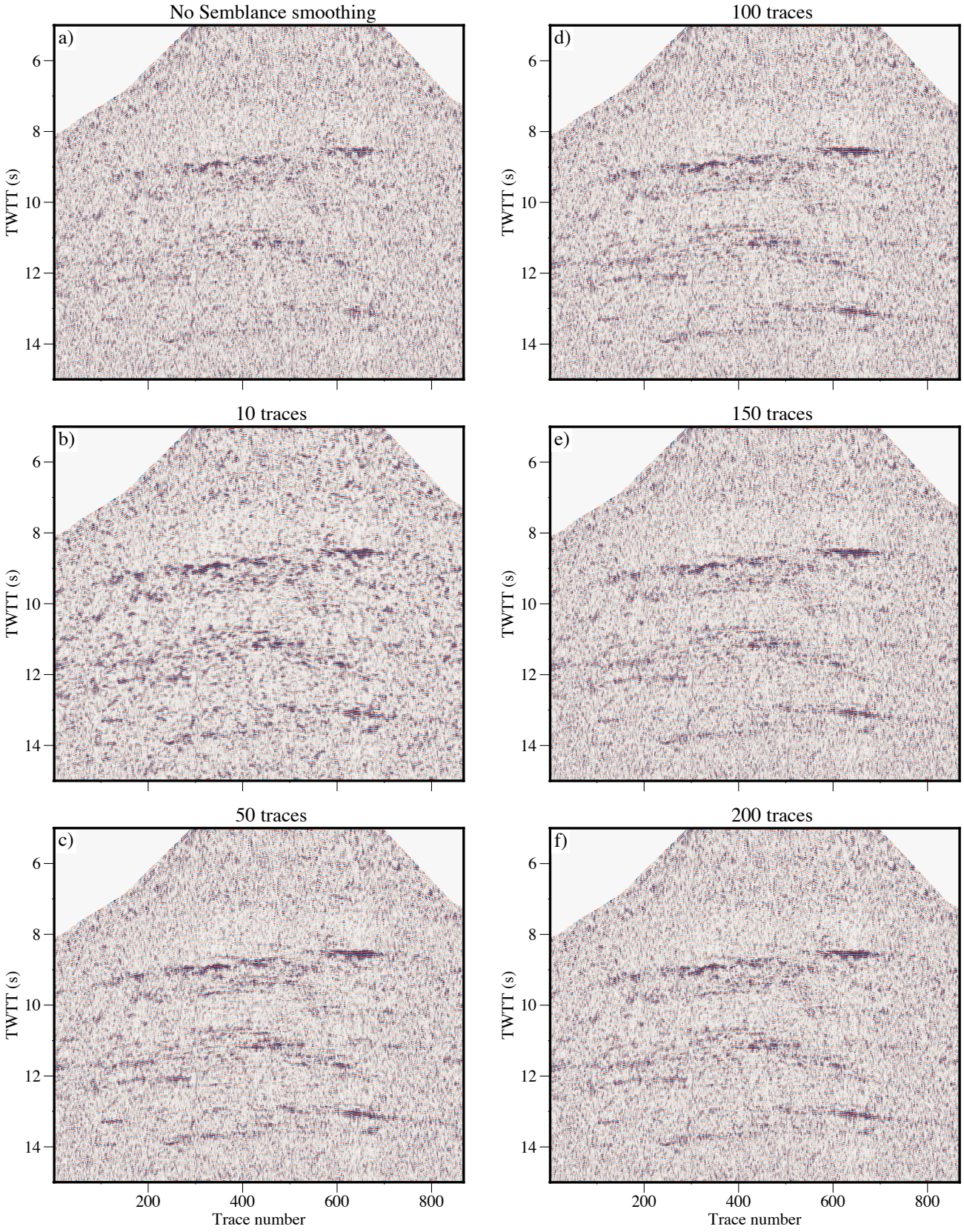


Figure B.4: Test panels for variations in number of input traces for sembsmooth filter design. Input time window is held fixed as 200 ms. Test values are shown above panels. Test gather is Box-2.

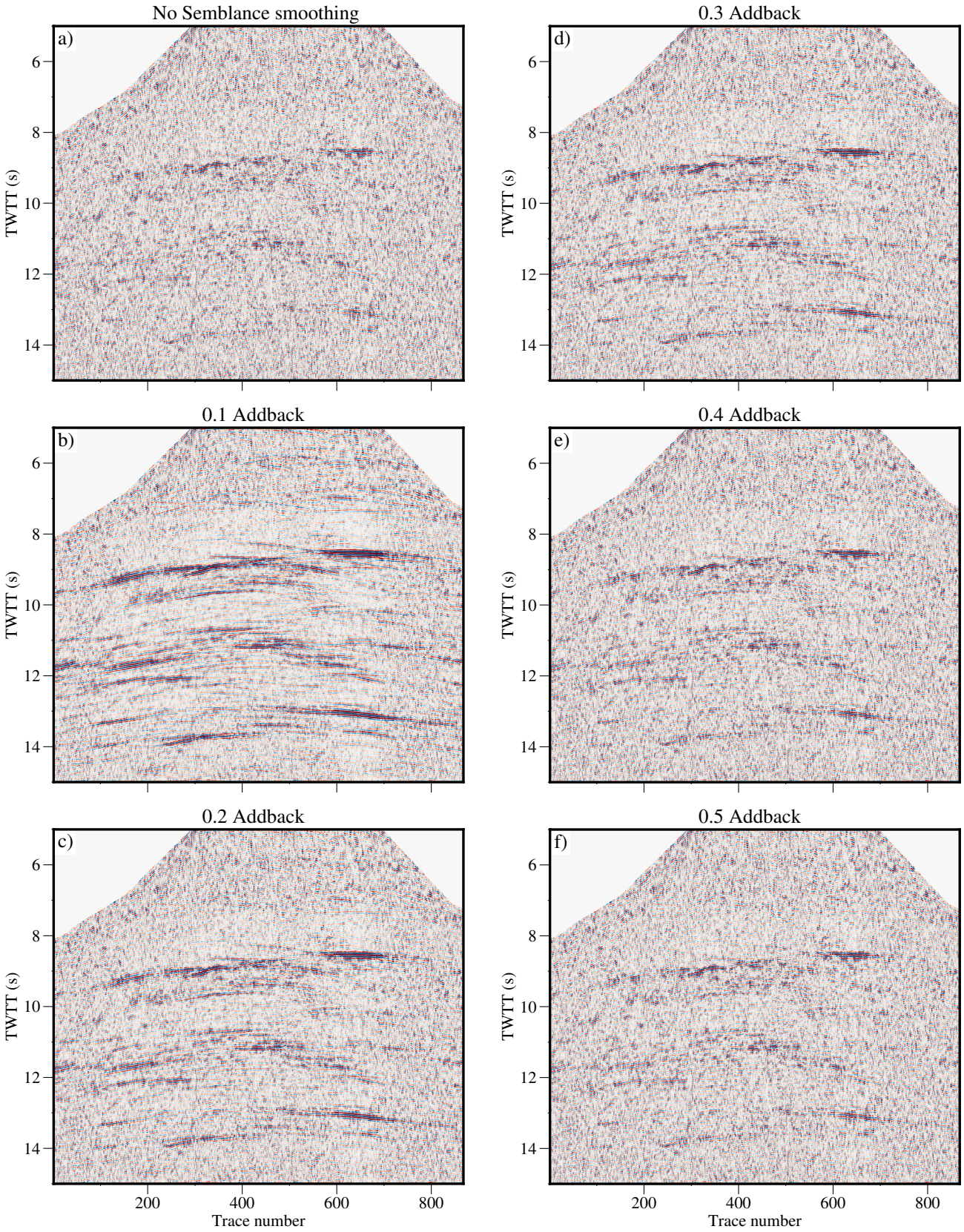


Figure B.5: Test panels for variations in the percentage add-back of the original trace for sembsmooth filter design. The number of traces used during filter design is held fixed at 101 traces for all tests and the input time window is held fixed as 200 ms. Test values are shown above panels. Test gather is Box-2.

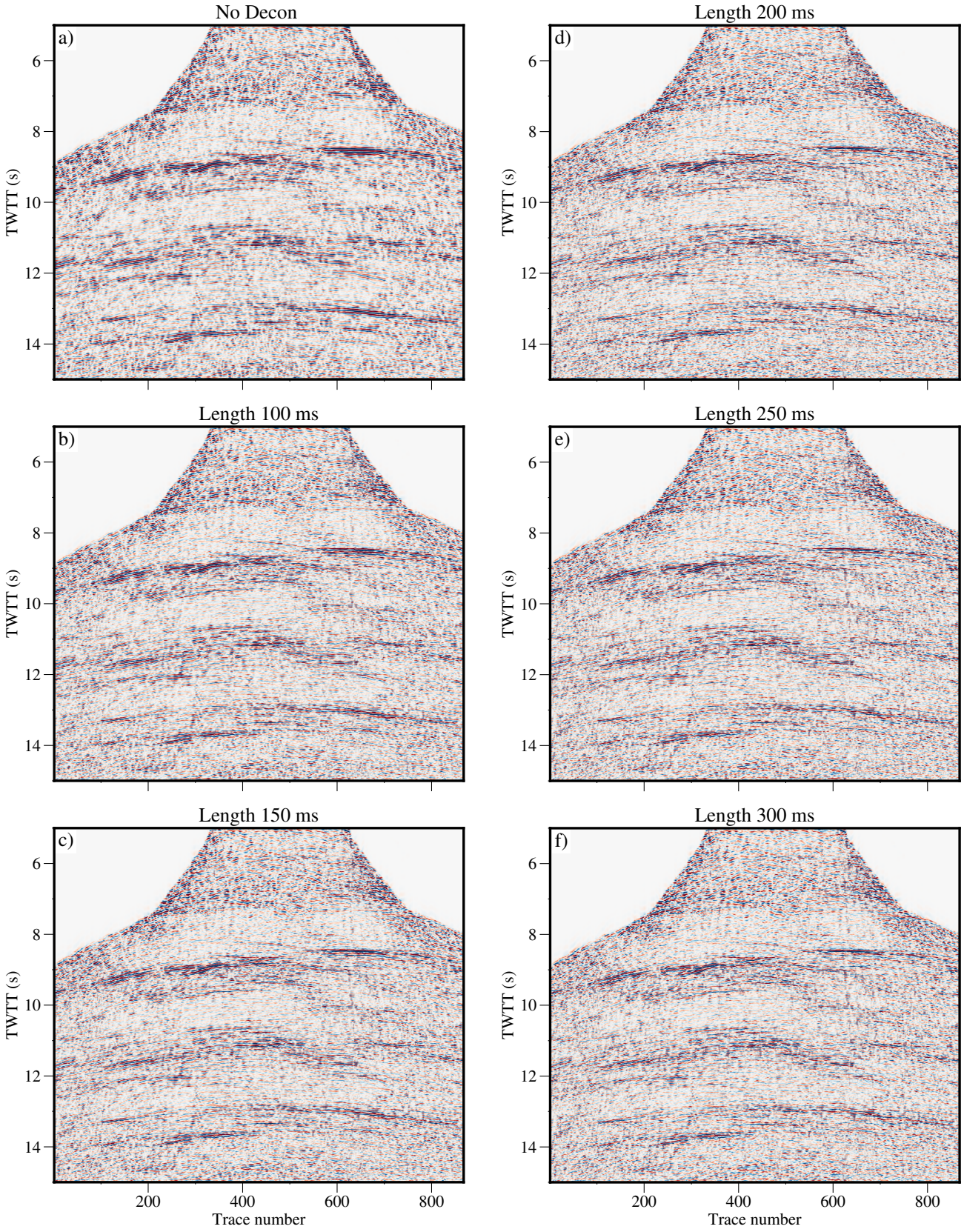


Figure B.6: Test panels for variations in filter operator length for predictive deconvolution filter design. The predictive gap is held fixed at 24 ms. Test values are shown above panels. Test gather is Box-2.

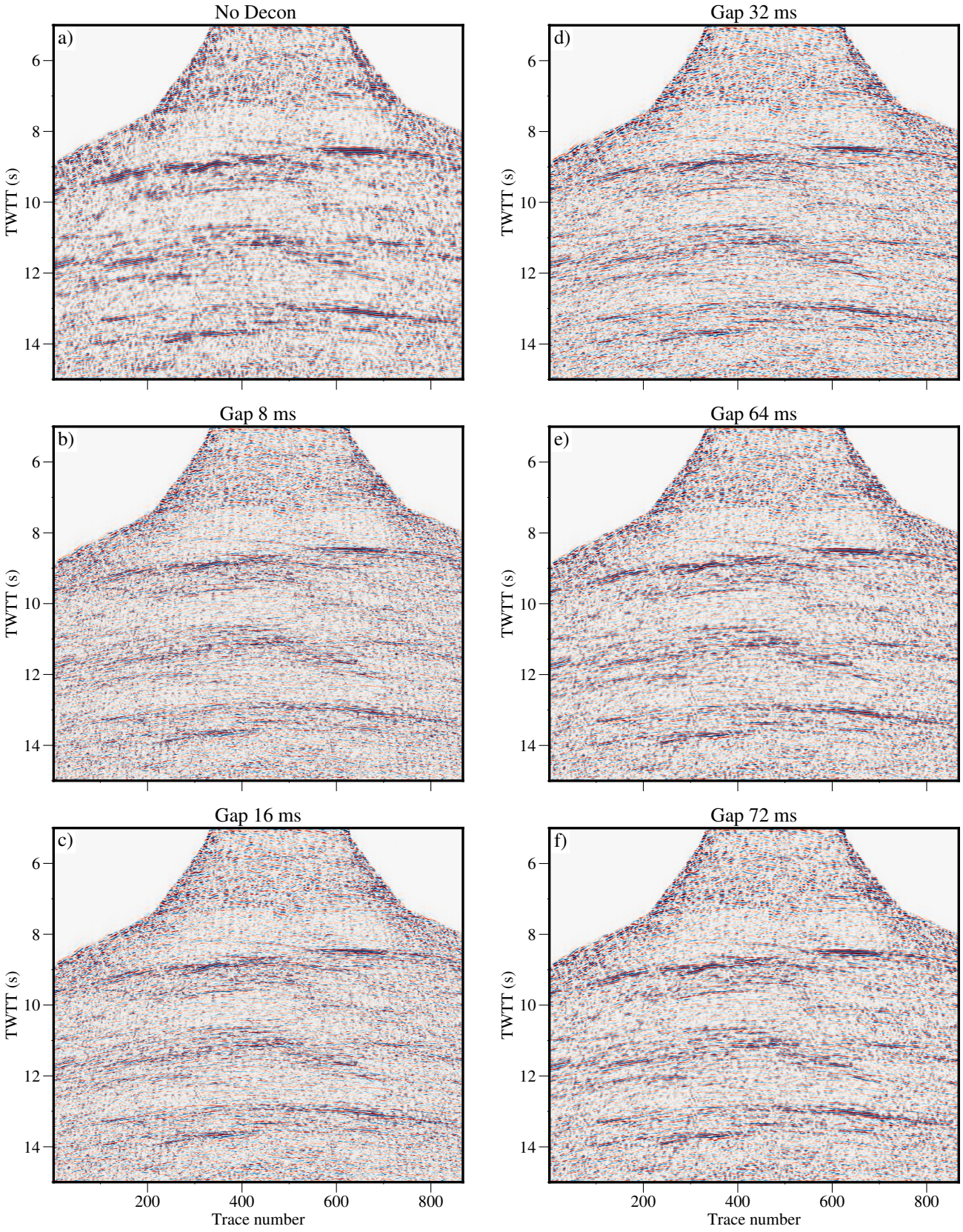


Figure B.7: Test panels for variations in gap length for predictive deconvolution filter design. The filter operator length is held fixed as 300 ms. Test values are shown above panels. Test gather is Box-2.

References

Ahern, J. L. and Mrkvicka, S. R. (1984). A mechanical and thermal model for the evolution of the Williston Basin. *Tectonics*, 3(1):79–102.

Ahrens, T. J. and Schubert, G. (1975). Gabbro-eclogite reaction rate and its geophysical significance. *Reviews of Geophysics*, 13(2):383–400.

Airy, G. B. (1855). On the Computation of the Effect of the Attraction of Mountain-Masses, as Disturbing the Apparent Astronomical Latitude of Stations in Geodetic Surveys. *Philosophical Transactions of the Royal Society of London*, 145:101–104.

Ali, M. Y. and Watts, A. B. (2009). Subsidence history, gravity anomalies and flexure of the United Arab Emirates (UAE) foreland basin. *GeoArabia*, 14(2):17–44.

Alkmim, F. F., Marshak, S., and Fonseca, M. A. (2001). Assembling West Gondwana in the Neoproterozoic: Clues from the São Francisco craton region, Brazil. *Geology*, 29(4):319–322.

Allen, P. A. and Allen, J. R. (2013). *Basin analysis: Principles and application to petroleum play assessment*. John Wiley & Sons.

Allen, P. A. and Armitage, J. J. (2012). Cratonic Basins. In Busby, C. and Azor, A., editors, *Tectonics of Sedimentary Basins: Recent Advances*, chapter 30, pages 602–620. Wiley-Blackwell, Oxford.

Almeida, F. F. M., Hasui, Y., de Brito Neves, B. B., and Fuck, R. A. (1981). Brazilian structural provinces: An introduction. *Earth-Science Reviews*, 17:1–29.

Amante, C. and Eakins, B. W. (2009). ETOPO1 1 Arc-Minute Global Relief Model: Procedures, Data Sources and Analysis. Technical report, National Oceanic and Atmospheric Administration, Boulder, CO.

Andrew, L. (2014). *Gravity and Magnetic Anomalies and the Deep Structure of the Parnaìba Cratonic Basin, NE Brazil*. PhD thesis, University of Oxford.

Araújo, R. N., Nogueira, A. C. R., Bandeira, J., and Angélica, R. S. (2016). Shallow lacustrine system of the Permian Pedra de Fogo Formation, Western Gondwana, Parnaìba Basin, Brazil. *Journal of South American Earth Sciences*, 67:57–70.

Archanjo, C. J., Launeau, P., Hollanda, M. H. B. M., Macedo, J. W. P., and Liu, D. (2009). Scattering of magnetic fabrics in the Cambrian alkaline granite of Meruoca (Ceará state, northeastern Brazil). *International Journal of Earth Sciences*, 98(8):1793–1807.

Archanjo, C. J., Viegas, L. G. F., Hollanda, M. H. B. M., Souza, L. C., and Liu, D. (2013). Timing of the HT/LP transpression in the Neoproterozoic Seridó Belt (Borborema Province,

Brazil): Constraints from UPb (SHRIMP) geochronology and implications for the connections between NE Brazil and West Africa. *Gondwana Research*, 23(2):701–714.

Armitage, J. J. and Allen, P. A. (2010). Cratonic basins and the long-term subsidence history of continental interiors. *Journal of the Geological Society*, 167(1):61–70.

Arora, B. R., Trivedi, N. B., Vitorello, I., Padilha, A. L., Rigoti, A., and Chamalaun, F. H. (1999). Overview of Geomagnetic Deep Soundings (GDS) as applied in the parnaíba Basin, North-Northeast Brazil. *Revista Brasileira de Geofisica*, 17(1):41–65.

Artemieva, I. M. (2011). *The lithosphere: An interdisciplinary approach*. Cambridge University Press.

Artemieva, I. M. and Mooney, W. D. (2001). Thermal thickness and evolution of Precambrian lithosphere: A global study. *Journal of Geophysical Research*, 106(B8):16387–16414.

Assumpção, M., Bianchi, M., Julià, J., Dias, F. L., França, G. S., Nascimento, R., Drouet, S., Garcia, C., Farrapo, D., and Lopes, A. E. (2013). Crustal thickness map of Brazil: Data compilation and main features. *Journal of South American Earth Sciences*, 43:74–85.

Athy, L. F. (1930). Density, Porosity, and Compaction of Sedimentary Rocks. *AAPG Bulletin*, 14(1):1–24.

Atta-Peters, D., Achaegakwo, C. A., and Garrey, P. (2015). Palynofacies, organic geochemical analyses and hydrocarbon potential of the takoradi 11-1 well, saltpond basin, Ghana. *Petroleum and Coal*, 57(5):478–499.

Baird, D. J., Knapp, J. H., and Steer, D. N. (1995). Upper-mantle reflectivity beneath the Williston basin, phase-change Moho, and the origin of intracratonic basins. *Geology*, 23(5):431–434.

Baksi, A. K. and Archibald, D. A. (1997). Mesozoic igneous activity in the Maranhão province, northern Brazil: 40Ar/ 39Ar evidence for separate episodes of basaltic magmatism. *Earth and Planetary Science Letters*, 151(3-4):139–153.

Baradello, L. and Accaino, F. (2013). Vibroseis deconvolution: A comparison of pre and post correlation vibroseis deconvolution data in real noisy data. *Journal of Applied Geophysics*, 92:50–56.

Barbosa, R. C. D. M., Nogueira, A. C. R., and Domingos, F. H. G. (2015). Famennian glaciation in the eastern side of Parnaíba Basin, Brazil: evidence of advance and retreat of glacier in Cabeças Formation. *Brazilian Journal of Geology*, 45:13–27.

Barnes, A. E. (2007). A tutorial on complex seismic trace analysis. *Geophysics*, 72(6):W33–W43.

Bassin, C. (2000). The current limits of resolution for surface wave tomography in North America. *Eos Trans. AGU*, 81(1):F897.

Beaumont, C. (1978). The evolution of sedimentary basins on a viscoelastic lithosphere: theory and examples. *Geophysical Journal of the Royal Astronomical Society*, 55(2):471–497.

Beaumont, C. (1981). Foreland basins. *Geophysical Journal of the Royal Astronomical Society*, 65(2):291–329.

Begg, G., Griffin, W., Natapov, L., O'Reilly, S. Y., Grand, S., O'Neill, C., Hronsky, J., Djomani, Y. P., Swain, C., Deen, T., and Bowden, P. (2015). The lithospheric architecture of Africa: Seismic tomography, mantle petrology, and tectonic evolution. *Geosphere*, 5(1):23–50.

Behren, J. C., Green, A. G., Cannon, W. F., Hutchinson, D. R., Lee, M. W., Milkereit, B., Agena, W. F., and Spencer, C. (1988). Crustal structure of the Midcontinent rift system: Results from GLIMPCE deep seismic reflection profiles. *Geology*, 16(1):81–85.

Behrendt, J. C., Hutchinson, D. R., Lee, M. I., Thornber, C. R., Cannon, W., and Green, A. (1990). GLIMPCE seismic reflection evidence of deep-crustal and upper-mantle intrusions and magmatic underplating associated with the Midcontinent Rift system of North America. *Tectonophysics*, 173(1-4):595–615.

Bellahsen, N., Daniel, J. M., Bollinger, L., and Burov, E. (2003). Influence of viscous layers on the growth of normal faults: Insights from experimental and numerical models. *Journal of Structural Geology*, 25(9):1471–1485.

Beyreuther, M., Barsch, R., Krischer, L., Megies, T., Behr, Y., and Wassermann, J. (2010). ObsPy: A Python Toolbox for Seismology. *Seismological Research Letters*, 81(3):530–533.

Bird, P. (2003). An updated digital model of plate boundaries. *Geochemistry, Geophysics, Geosystems*, 4(3).

Bizzi, L. A., Schobbenhaus, C., Vidotti, R. M., and Gonçalves, J. H. (2003). *Geologia, Tectônica e Recursos Minerais do Brazil*. CPRM.

Blakely, R. J. (1996). *Potential theory in gravity and magnetic applications*. Cambridge University Press.

Boscovich, R. G. (1755). *De litteraria expeditione per Pontificiam ditionem: Typographio Palladis*. Rome.

Bott, M. H. P. (1969). GRAVN. *Durham geophysical computer specification*, 1(7).

Bouguer, P. (1749). La Figure De La Terre.

Bowie, W. (1927). Isostacy—The Science of the Equilibrium of the Earth's Crust. *New York: EP Button and Company*.

Brocher, T. M. (2005). Empirical relations between elastic wavespeeds and density in the Earth's crust. *Bulletin of the Seismological Society of America*, 95(6):2081–2092.

Brothers, D. S., Driscoll, N. W., Kent, G. M., Harding, A. J., Babcock, J. M., and Baskin, R. L. (2009). Tectonic evolution of the Salton Sea inferred from seismic reflection data. *Nature Geoscience*, 2(8):581–584.

Brown, L., Jensen, L., Oliver, J., Kaufman, S., and Steiner, D. (1982). Rift structure beneath the Michigan Basin from COCORP profiling (USA). *Geology*, 10(12):645–649.

Brueckner, H. K., Cunningham, D., Alkmin, F. F., and Marshak, S. (2000). Tectonic implications of Precambrian Sm–Nd dates from the southern São Francisco craton and adjacent Araçuaí and Ribeira belts , Brazil. *Precambrian Research*, 99:255–269.

Bryan, S. E., Peate, I. U., Peate, D. W., Self, S., Jerram, D. A., Mawby, M. R., Marsh, J. G., and Miller, J. A. (2010). The largest volcanic eruptions on Earth. *Earth-Science Reviews*, 102(3-4):207–229.

Buehler, J. S. and Shearer, P. M. (2017). Uppermost mantle seismic velocity structure beneath USArray. *Journal of Geophysical Research: Solid Earth*, 122(1):436–448.

Bueno, J. F., Oliveira, E. P., McNaughton, N. J., and Laux, J. H. (2009). U-Pb dating of granites in the Neoproterozoic Sergipano Belt, NE-Brazil: Implications for the timing and duration of continental collision and extrusion tectonics in the Borborema Province. *Gondwana Research*, 15(1):86–97.

Bullard, E. (1936). Gravity Measurements in East Africa. *Philosophical Transaction of the Royal Society of London. Series A, Mathematical and Physical Sciences*, 235(757):445–531.

Bullard, E., Everett, J. E., and Smith, A. G. (1965). The fit of the continents around the Atlantic. *Philosophical Transactions of the Royal Society of London. Series A, Mathematical and Physical Sciences*, 258(1088):41–51.

Burgess, P. M. and Moresi, L. N. (1999). Modelling rates and distribution of subsidence due to dynamic topography over subducting slabs: Is it possible to identify dynamic topography from ancient strata? *Basin Research*, 11(4):305–314.

Caby, R. (2003). Terrane assembly and geodynamic evolution of central-western Hoggar: A synthesis. *Journal of African Earth Sciences*, 37(3):133–159.

Cacace, M. and Scheck-Wenderoth, M. (2016). Why intracontinental basins subside longer: 3-D feedback effects of lithospheric cooling and sedimentation on the flexural strength of the lithosphere. *Journal of Geophysical Research: Solid Earth*, 121(5):3742–3761.

Campos Neto, M. D. C. and Caby, R. (1999). Neoproterozoic high-pressure metamorphism and tectonic constraint from the nappe system south of the Sao Francisco Craton, southeast Brazil. *Precambrian Research*, 97(1-2):3–26.

Caputo, M. V. (1984). *Stratigraphy, tectonics, paleoclimatology and paleogeography of northern basins of Brazil*. PhD thesis, University of California: Santa Bárbara.

Carmichael, R. S. (1982). *Handbook of Physical Properties of Rocks*. CRC Press Inc., Boca Raton, Florida.

Carton, H. (2007). Seismic imaging. *Journal of Geophysical Research: Solid Earth*, 112(6).

Cella, F. (2015). GTeC-A versatile MATLAB® tool for a detailed computation of the terrain correction and Bouguer gravity anomalies. *Computers and Geosciences*, 84:72–85.

Červený, V., Molotkov, I. A., and Pšenčík, I. (1977). *Ray method in seismology*. Univerzita Karlova, Praha.

Chopra, S. and Marfurt, K. J. (2005). Seismic attributes - A historical perspective. *Geophysics*, 70(5):3SO–28SO.

Christensen, N. I. (1978). Ophiolites, seismic velocities and oceanic crustal structure. *Tectonophysics*, 47:131–157.

Christensen, N. I. (1996). Poisson's ratio and crustal seismology. *Journal of Geophysical Research*, 101(B2):3139.

Christensen, N. I. and Mooney, W. D. (1995). Seismic velocity structure and composition of the continental crust: A global view. *Journal of Geophysical Research*, 100(B7):9761–9788.

Clairaut, A. C. (1743). *Théorie de la figure de la terre, tirée des principes de l'hydrostatique.* chez David fils, libraire, ruë Saint-Jacques à la plume d'or.

Cloetingh, S. (1988). Intraplate Stresses: A New Element in Basin Analysis. In *New Perspectives in Basin Analysis*, chapter 10, pages 205–230. Springer New York.

Close, D. I., Watts, A. B., and Stagg, H. M. J. (2009). A marine geophysical study of the Wilkes Land rifted continental margin, Antarctica. *Geophysical Journal International*, 177(2):430–450.

Coakley, B. and Gurnis, M. (1995). Far-field tilting of Laurentia during the Ordovician and constraints on the evolution of a slab under an ancient continent. *Journal of Geophysical Research*, 100(B4):6313–6327.

Cochran, J. R. (1981). Simple models of diffuse extension and the pre-seafloor spreading development of the continental margin of the northwestern Gulf of Alden. *Oceanologica Acta, Special issue Open Access version.*

Cochran, J. R. (1982). The magnetic quiet zone in the eastern Gulf of Aden: Implications for the early development of the continental margin. *Geophysical Journal International*, 68(1):171–201.

Cochran, J. R. (1983). Effects of finite rifting times on the development of sedimentary basins. *Earth and Planetary Science Letters*, 66:289–302.

Coelho, M. B., Trouw, R. A. J., Ganade de Araújo, C. E., Vinagre, R., Mendes, J. C., and Sato, K. (2017). Constraining timing and P-T conditions of continental collision and late overprinting in the Southern Brasília Orogen (SE-Brazil): U-Pb zircon ages and geothermobarometry of the Andrelândia Nappe System. *Precambrian Research*, 292:194–215.

Cook, F. A. (2002). Fine structure of the continental reflection Moho. *Bulletin of the Geological Society of America*, 114(1):64–79.

Cook, T. D. and Bally, A. W. (1975). *Stratigraphic Atlas of North and Central America [cartographic Material].* Princeton, NJ: Princeton University Press.

Cooper, H. W. and Cook, R. E. (1984). Seismic data gathering. *Proceedings of the IEEE*, 72(10):1266–1275.

Corcoran, D. V. and Doré, A. G. (2005). A review of techniques for the estimation of magnitude and timing of exhumation in offshore basins. *Earth-Science Reviews*, 72:129–168.

Cordani, U. G. (1984). *Estudo preliminar de integração do pré-cambriano com os eventos tectônicos das bacias sedimentares brasileiras*, volume 15. Petrobrás, Centro de Pesquisas e Desenvolvimento Leopoldo A. Miguez de Mello, Setor de Informação Técnica e Propriedade Industrial.

Cordani, U. G., Milani, E. J., Thomaz Filho, A., and Campos, D. A. (2000). *Tectonic Evolution of South America.* Geological Society.

Cordani, U. G., Pimentel, M. M., de Araujo, C. E., Basei, M. A. S., Fuck, R. A., and Girardi, V. A. V. (2013a). Was there an ediacaran clymene ocean in central south America? *American Journal of Science*, 313:517–539.

Cordani, U. G., Pimentel, M. M., de Araujo, C. E. G., and Fuck, R. A. (2013b). The significance of the Transbrasiliano-Kandi tectonic corridor for the amalgamation of West Gondwana. *Brazilian Journal of Geology*, 43(3):583–597.

Cordani, U. G., Ramos, V. A., Fraga, L. M., Cegarra, M., Delgado, I., Souza, K. G. D., Gomes, F. E. M., Schobbenhaus, C., Chain, J. C., and Plate, S. (2016). Tectonic map of South America. Technical report, CGMW-CPRM-SEGEMAR.

Cordani, U. G., Teixeira, W., D'Agrella-Filho, M. S., and Trindade, R. I. (2009). The position of the Amazonian Craton in supercontinents. *Gondwana Research*, 15:396–407.

Coward, M. P. (1981). The Moabi syncline: The West Congolian of Gabon and its tectonic significance. *Annales de la Société géologique de Belgique*, 104(2):255–259.

Crosby, A. G., Fishwick, S., and White, N. (2010). Structure and evolution of the intracratonic Congo Basin. *Geochemistry, Geophysics, Geosystems*, 11(6):Q06010.

Curto, J. B., Vidotti, R. M., Fuck, R. A., Blakely, R. J., Alvarenga, C. J., and Dantas, E. L. (2014). The tectonic evolution of the Transbrasiliano Lineament in northern Paraná Basin, Brazil, as inferred from aeromagnetic data. *Journal of Geophysical Research: Solid Earth*, 119(3):1544–1562.

Czarnota, K. and White, N. (2016). Rifting Thick Lithosphere - Canning Basin, Western Australia. In *EGU General Assembly Conference Abstracts*, volume 18 of *EGU General Assembly Conference Abstracts*, pages EPSC2016–11002.

Daly, M. C., Andrade, V., Barousse, C. A., Costa, R., McDowell, K., Piggott, N., and Poole, A. J. (2014). Brasiliano crustal structure and the tectonic setting of the Parnaíba basin of NE Brazil: Results of a deep seismic reflection profile. *Tectonics*, 33(11):2102–2120.

Daly, M. C., Lawrence, S. R., Diemu-Tshiband, K., and Matouana, B. (1992). Tectonic evolution of the Cuvette Centrale, Zaire. *Journal of the Geological Society*, 149(4):539–546.

Daly, M. C., Lawrence, S. R., Kimuna, D., and Binga, M. (1991). Late Palaeozoic deformation in central Africa: a result of distant collision? *Nature*, 350(18):605–607.

Daly, M. C., Tozer, B., and Watts, A. B. (In revision). Cratonic basins and the Wilson Cycle: a perspective from the Parnaíba Basin Brazil. In Wilson, W., Houseman, G., McCaffrey, K., Doré, A. G., and Royden, L., editors, *Tectonic evolution: 50 years of the Wilson Cycle concept*. Special Publication of the Geological Society.

de Almeida, F. F. M., Leonardos, O. H., and Valença, J. (1967). *Review on Granitic Rocks of Northeast South America: Prepared for the IUGS/UNESCO Symposium in Recife*. International Union of Geological Sciences, Committee for the Study of Geological Documentation.

de Brito Neves, B. B. and Cordani, U. G. (1991). Tectonic evolution of South America during the Late Proterozoic. *Precambrian Research*, 53(1-2):23–40.

de Brito Neves, B. B. and Fuck, R. A. (2014). The basement of the South American platform: Half Laurentian (N-NW)+half Gondwanan (E-SE) domains. *Precambrian Research*, 244:75–86.

de Brito Neves, B. B., Fuck, R. A., Cordani, U. G., and Thomaz, F. A. (1984). Influence of basement structures on the evolution of the major sedimentary basins of Brazil: a case of tectonic heritage. *Journal of Geodynamics*, 1:495–510.

de Castro, D. L., Bezerra, F. H., Fuck, R. A., and Vidotti, R. M. (2016). Geophysical evidence of pre-sag rifting and post-rifting fault reactivation in the Parnaìba basin, Brazil. *Solid Earth*, 7(2):529–548.

de Castro, D. L., Fuck, R. A., Phillips, J. D., Vidotti, R. M., Bezerra, F. H., and Dantas, E. L. (2014). Crustal structure beneath the Paleozoic Parnaíba Basin revealed by airborne gravity and magnetic data, Brazil. *Tectonophysics*, 614:128–145.

de Miranda, F. S. (2014). Pimenteiras Shale: Characterization of an Atypical Unconventional Petroleum System, Parnaìba Basin, Brazil. In *International Conference and Exhibition*, Istanbul.

de Moraes Palheta, E. S., de Abreu, F. D. A. M., and Moura, C. A. V. (2009). Granitóides proterozóicos como marcadores da evolução geotectônica da região nordeste do Pará, Brasil. *Revista Brasileira de Geociências*, 39(4):647–657.

de Oliveira, D. C. and Mohriak, W. U. (2003). Jaibaras trough: An important element in the early tectonic evolution of the Parnaíba interior sag basin, Northern Brazil. *Marine and Petroleum Geology*, 20(3-4):351–383.

de Oliveira, R. G. and de Medeiros, W. E. (2012). Evidences of buried loads in the base of the crust of Borborema Plateau (NE Brazil) from Bouguer admittance estimates. *Journal of South American Earth Sciences*, 37:60–76.

DEQ (2015). GeoWebFace A Web Based Application to Access Michigan Maps and Geologic Information. Technical report, Michigan Department of Environmental Quality, Michigan.

di Pasquo, M. and Iannuzzi, R. (2015). New palynological information from the Poti Formation (Upper visean) at the Roncador creek, Parnaíba Basin, Northeastern Brazil. *Boletin Geologico y Minero*, 125(4):405–435.

Dietz, R. S. (1961). Continent and Ocean Basin Evolution by Spreading of the Sea Floor. *Nature*, 190(4779):854–857.

Dino, R. and Playford, G. (2002). Stratigraphic and palaeoenvironmental significance of a Pennsylvanian (Upper Carboniferous) palynoflora from the Piaui Formation, Parnaiba basin, northeastern Brazil. *Paleontological Research*, 6(1):23–40.

Dixon, J. E., Dixon, T. H., Bell, D. R., and Malservisi, R. (2004). Lateral variation in upper mantle viscosity: Role of water. *Earth and Planetary Science Letters*, 222(2):451–467.

Dong, L., Margrave, G. F., and Mewhort, L. E. (2004). Examining the phase property of nonstationary Vibroseis wavelet. In *SEG Technical Program Expanded Abstracts 2004*, pages 1961–1964. Society of Exploration Geophysicists.

Doré, A. G., Cartwright, J. A., Stoker, M. S., Turner, J. E., and White, N. J. (2002). Exhumation of the North Atlantic margin: Introduction and background. *Geological Society, London, Special Publications*, 196(1):1–12.

dos Santos, E. J., Schmus, W. R. V., Kozuch, M., and de Brito Neves, B. B. (2010). The Cariris Velhos tectonic event in Northeast Brazil. *Journal of South American Earth Sciences*, 29(1):61–76.

Downey, N. J. and Gurnis, M. (2009). Instantaneous dynamics of the cratonic Congo basin. *Journal of Geophysical Research*, 114(B6):B06401.

Duclaux, G., Ménot, R. P., Guillot, S., Agbossoumondé, Y., and Hilairet, N. (2006). The mafic layered complex of the Kabyé massif (north Togo and north Benin): Evidence of a Pan-African granulitic continental arc root. *Precambrian Research*, 151(1-2):101–118.

Dutton, C. E. (1889). On some of the greater problems of physical geology. *Journal of the Washington Academy of Sciences*, 15(15):359–369.

Eaton, D. W. and Darbyshire, F. (2010). Lithospheric architecture and tectonic evolution of the Hudson Bay region. *Tectonophysics*, 480(1):1–22.

Ebert, H. D., Chemale, F., Babinski, M., and Schmus, W. R. V. (1996). Tectonic setting and U/Pb zircon dating of the plutonic Socorro Complex in the Transpressive Rio Paraíba do Sul Shear Belt, SE Brazil. *Tectonics*, 15(2):688–699.

ECL (1988). Hydrocarbon Potential of Cuvette Centrale (Republic of Zaire). Technical report, Exploration Consultants Limited, Cellule Technique Petroliere, Petrozaire.

Esso Zaire SARL. (1981a). Geological Completion Report. Gilson-1. Technical report, Unpublished internal report.

Esso Zaire SARL. (1981b). Geological Completion Report Mbandaka-1. Technical report, Unpublished internal report.

Farr, T. G., Rosen, P. A., Caro, E., Crippen, R., Duren, R., Hensley, S., Kobrick, M., Paller, M., Rodriguez, E., Roth, L., Seal, D., Shaffer, S., Shimada, J., Umland, J., Werner, M., Oskin, M., Burbank, D., and Alsdorf, D. (2007). The Shuttle Radar Topography Mission. *Reviews of Geophysics*, 45(2).

Fetter, A. H., Van Schmus, W. R., Santos, T. J. S., Nogueira Neto, J. A., and Arthaud, M. H. (2000). U-Pb and Sm-Nd geochronological constraints on the crustal evolution and basement architecture of Ceará State, NW Borborema Province, NE Brazil: Implications for the existence of the Paleoproterozoic Supercontinent "Atlantica". *Revista Brasileira de Geociências*, 30(1):102–106.

Fonseca, M. A., de Oliveira, C. G., and Evangelista, H. J. (2004). The Araguaia Belt, Brazil: Part of a Neoproterozoic continental-scale strike-slip fault system. *Journal of the Virtual Explorer*, 17.

Fowler, C. M. R. and Nisbet, E. G. (1985). The subsidence of the Williston Basin. *Canadian Journal of Earth Sciences*, 22(3):408–415.

Fuck, R. A., de Brito Neves, B. B., and Schobbenhaus, C. (2008). Rodinia descendants in South America. *Precambrian Research*, 160(1):108–126.

Gac, S., Huismans, R. S., Simon, N. S. C., Podladchikov, Y. Y., and Faleide, J. I. (2013). Formation of intracratonic basins by lithospheric shortening and phase changes: A case study from the ultra-deep East Barents Sea basin. *Terra Nova*, 25(6):459–464.

Ganade de Araújo, C. E., Cordani, U. G., Agbossoumounde, Y., Caby, R., Basei, M. A., Weinberg, R. F., and Sato, K. (2016). Tightening-up NE Brazil and NW Africa connections: New U-Pb/Lu-Hf zircon data of a complete plate tectonic cycle in the Dahomey belt of the West Gondwana Orogen in Togo and Benin. *Precambrian Research*, 276:24–42.

Ganade de Araújo, C. E. G., Cordani, U. G., Basei, M. A., Castro, N. A., Sato, K., and Sproesser, W. M. (2012). U–Pb detrital zircon provenance of metasedimentary rocks from the Ceará Central and Médio Coreaú Domains, Borborema Province, NE-Brazil: Tectonic implications for a long-lived Neoproterozoic active continental margin. *Precambrian Research*, 206:36–51.

Ganade de Araújo, C. E. G., Rubatto, D., Hermann, J., Cordani, U. G., Caby, R., and Basei, M. A. (2014a). Ediacaran 2,500-km-long synchronous deep continental subduction in the West Gondwana Orogen. *Nature communications*, 5:5198.

Ganade de Araújo, C. E. G., Weinberg, R. F., and Cordani, U. G. (2014b). Extruding the Borborema Province (NE-Brazil): A two-stage Neoproterozoic collision process. *Terra Nova*, 26(2):157–168.

Garland, G. D. (1965). *The Earth's Shape and Gravity*. Elsevier.

GEBCO (2003). Intergovernmental Oceanographic Commission (IOC), GEBCO 1-minute grid [CD-ROM], UNESCO.

Gilbert, G. K. (1890). *Lake Bonneville*. US Government Printing Office.

Giles, M. (1997). *Diagenesis: A Quantitative Perspective; Implications for Basin Modelling and Rock Property Prediction*. Springer Netherlands.

Glangeaud, F., Mari, J. L., and Coppens, F. (1999). *Signal Processing for Geologists and Geophysicists*. Technip Ed.

Global Geophysical Services (2012). Parnaiba basin - 2D. Technical report, Global Geophysical Services, Rio de janeiro.

Góes, A. M. O. and Feijó, F. J. (1994). Bacia do Paranaíba. *Boletim de Geociencias da Petrobras*, 8(1):57–67.

Góes, A. M. O., Souza, J. M. P., and Teixeira, L. B. (1990). Estágio exploratório e perspectivas petrolíferas da bacia do Parnaíba. *Boletim Geociências da Petrobras*, 4(1):55–64.

Góes, A. M. O., Travassos, W. A. S., and Nunes, K. C. (1993). Projeto Parnaíba: Reavaliacao e perspectivas exploratorias: Relatorio Petrobras, DEXNOR-DINTER. Technical report.

Grahn, Y. (1992). Revision of Silurian and Devonian strata of Brazil. *Palynology*, 16(1992):35–61.

Grahn, Y., De Melo, J. H. G., and Steemans, P. (2005). Integrated Chitinozoan and Miospore Zonation of the Serra Grande Group (Silurian-Lower Devonian), Parnaíba Basin, Northeast Brazil. *Revista Española de Micropaleontología*, 37(2):183–204.

Green, D. H. and Falloon, T. J. (1998). Pyrolite: A Ringwood concept and its current expression. *The Earth's mantle: Composition, structure, and evolution*, pages 311–378.

Guimarães, I. P., Da Silva Filho, A. F., Melo, S. C., and Macambira, M. B. (2005). Petrogenesis of a-type granitoids from the Alto Moxoto and Alto Pajeu terranes of the Borborema Province, NE Brazil: Constraints from geochemistry and isotopic composition. *Gondwana Research*, 8(3):347–362.

Gunn, R. (1943). A quantitative evaluation of the influence of the lithosphere on the anomalies of gravity. *Journal of the Franklin Institute*, 236(1):47–66.

Haddoum, H., Guiraud, R., and Moussine-Pouchkine, A. (2001). Hercynian compressional deformations of the Ahnet-Mouydir Basin, Algerian Saharan Platform: Far-field stress effects of the Late Palaeozoic orogeny. *Terra Nova*, 13(3):220–226.

Hager, B. H. and Richards, M. A. (1989). Long-Wavelength Variations in Earth's Geoid: Physical Models and Dynamical Implications. *Philosophical Transactions of the Royal Society A: Mathematical, Physical and Engineering Sciences*, 328(1599):309–327.

Hallam, A. (1973). *A revolution in the Earth Sciences*. Oxford University Press, Oxford.

Hamdani, Y., Mareschal, J. C., and Arkani-Hamed, J. (1991). Phase changes and thermal subsidence in intracontinental sedimentary basins. *Geophysical Journal International*, 106(3):657–665.

Hamdani, Y., Mareschal, J. C., and Arkani-Hamed, J. (1994). Phase change and thermal subsidence of the Williston basin. *Geophysical Journal International*, 116(3):585–597.

Hammer, S. (1939). Terrain Corrections for Gravimeter Stations. *Geophysics*, 4(3):184–194.

Hanne, D., White, N., Butler, A., and Jones, S. (2004). Phanerozoic vertical motions of Hudson Bay. *Canadian Journal of Earth Sciences*, 41:1181–1200.

Haq, B. U., Hardenbol, J., and Vail, P. R. (1987). Chronology of Fluctuating Sea Levels Since the Triassic. *Science*, 235(4793):1156–1167.

Haq, B. U. and Schutter, S. R. (2008). A chronology of Paleozoic sea-level changes. *Science*, 322(5898):64–68.

Harrison, M. P. (1990). F-x linear prediction filtering of seismic images. Technical report.

Hartley, R. W. and Allen, P. A. (1994). Interior cratonic basins of Africa: Relation to continental break-up and role of mantle convection. *Basin Research*, 6:95–113.

Hatton, L. and Worthington, M. H. (1986). *Seismic Data Processing: Theory and Practice*. Blackwell Scientific, Oxford.

Hawkesworth, C. J. A., Dhuim, B., Pietranik, A. B., Cawood, P. a., Kemp, A. I. S., Dhuime, B., Pietranik, A. B., Cawood, P. a., Kemp, A. I. S., Storey, C. D., Dhuim, B., Pietranik, A. B., Cawood, P. a., and Kemp, A. I. S. (2010). The generation and evolution of the continental crust. *Journal of the Geological Society, London*, 167(2):229–248.

Haxby, W. F., Turcotte, D. L., and Bird, J. M. (1976). Thermal and mechanical evolution of the Michigan Basin. *Tectonophysics*, 36(1-3):57–75.

Heiland, C. A. (1940). *Geophysical exploration*. Prentice-Hall, Incorporated.

Henrys, S., Wech, A., Sutherland, R., Stern, T. A., Savage, M. K., Sato, H., Mochizuki, K., Iwasaki, T., Okaya, D., Seward, A., Tozer, B., Townend, J., Kurashimo, E., Iidaka, T., and Ishiyama, T. (2013). SAHKE geophysical transect reveals crustal and subduction zone structure at the southern Hikurangi margin, New Zealand. *Geochemistry, Geophysics, Geosystems*, 14(7):2063–2083.

Herz, N., Hasui, Y., Costa, J. B. S., and Matta, M. A. D. S. (1989). The Araguaia fold belt, Brazil: A reactivated Brasiliano-Pan-African cycle (550 Ma) geosuture. *Precambrian Research*, 42(3-4):371–386.

Hess, H. H. (1962). History of Ocean Basins. In Engel, A. E. J., James, H. L., and Leonard, B., editors, *Petrologic Studies: A Volume to Honor A F Buddington*, pages 599–620. The Geological Society of America.

Hinze, W. J., von Frese, R. R. B., and Saad, A. H. (2013). *Gravity and Magnetic Exploration*. Cambridge University Press.

Hirt, C. and Rexer, M. (2015). Earth2014: 1 arc min shape, topography, bedrock and ice sheet models - available as gridded data and degree 10,800 spherical harmonics. *International Journal of Applied Earth Observation and Geoinformation*, 39:103–112.

Hjelt, S. E. (2006). *Pragmatic inversion of geophysical data (Vol. 39)*. Springer.

Hobro, J. W. D., Singh, S. C., and Minshull, T. A. (2003). Three-dimensional tomographic inversion of combined reflection and refraction seismic travel-time data. *Geophysical Journal International*, 152(1):79–93.

Hoffman, P. F. (1991). Did the Breakout of Laurentia Turn Gondwanaland Inside-Out? *Advancement Of Science*, 252(5011):1409–1412.

Hole, J. A. (1992). Nonlinear high-resolution three-dimensional seismic travel time tomography. *Journal of Geophysical Research*, 97(B5):6553–6562.

Holt, P. J., Allen, M. B., and van Hunen, J. (2014). Basin formation by thermal subsidence of accretionary orogens. *Tectonophysics*, 639:132–143.

Holt, P. J., Allen, M. B., van Hunen, J., and Bjørnseth, H. M. (2010). Lithospheric cooling and thickening as a basin forming mechanism. *Tectonophysics*, 495(3):184–194.

Holzman, M. (1963). Chebyshev optimized geophone arrays. *Geophysics*, 28(02):145–155.

Howell, P. D. and van der Pluijm, B. A. (1990). Early history of the Michigan basin: Subsidence and Appalachian tectonics. *Geology*, 18(12):1195–1198.

Howell, P. D. and van der Pluijm, B. A. (1999). Structural sequences and styles of subsidence in the Michigan basin. *Geological Society of America Bulletin*, 111(7):974–991.

Hubbert, M. K. (1948). A line-integral method of computing the gravimetric effects of two-dimensional masses. *Geophysics*, 13(2):215–225.

Hunter, J. and Watts, A. B. (2016). Gravity anomalies, flexure and mantle rheology seaward of circum-Pacific trenches. *Geophysical Journal International*, 207(1):288–316.

Hunter, J. D. (2007). Matplotlib: A 2D graphics environment. *Computing in Science and Engineering*, 9(3):99–104.

Huppert, H. E. and Sparks, R. S. J. (1988). The fluid dynamics of crustal melting by injection of basaltic sills.

Issler, D. R. (1992). A new approach to shale compaction and stratigraphic restoration, Beaufort-Mackenzie Basin and Mackenzie Corridor, northern Canada. *AAPG Bulletin*, 76(8):1170–1189.

James, T. S. (1992). The hudson bay free-air gravity anomaly and glacial rebound. *Geophysical Research Letters*, 19(9):861–864.

Jaupart, C., Mareschal, J. C., and Davaille, A. (1998). Heat flow and thickness of the lithosphere in the Canadian Shield. *Journal of Geophysical Research*, 103(B7):15269–15286.

Jeffreys, H. (1926). On the nature of isostasy. *Gerlands Beitrage zur Geophysik*, 15(2):167–186.

Jordan, T. H. (1975). Lateral heterogeneity and mantle dynamics. *Nature*, 257:745–750.

Kadima, É., Delvaux, D., Sebagenzi, S. N., Tack, L., and Kabeya, S. M. (2011). Structure and geological history of the Congo Basin: An integrated interpretation of gravity, magnetic and reflection seismic data. *Basin Research*, 23(5):499–527.

Kamel, M. H., Mabrouk, W. M., and Bayoumi, A. I. (2002). Porosity estimation using a combination of Wyllie–Clemenceau equations in clean sand formation from acoustic logs. *Journal of Petroleum Science and Engineering*, 33(4):241–251.

Kaminski, E. and Jaupart, C. (2000). Lithosphere structure beneath the Phanerozoic intracratonic basins of North America. *Earth and Planetary Science Letters*, 178(1):139–149.

Kaminsky, F., Sablukov, S., Sablukova, L., and Zakharchenko, O. (2009). The Fazenda Largo off-craton kimberlites of Piauí State, Brazil. *Journal of South American Earth Sciences*, 28:288–303.

Karner, G. D. (1982). Spectral Representation of isostatic models. *Journal of Australian Geology and Geophysics*, 7(1):55–62.

Karner, G. D. and Watts, A. B. (1983). Gravity anomalies and flexure of the lithosphere at mountain ranges. *Journal of Geophysical Research: Solid Earth*, 88(B12):10449–10477.

Kauffmann, M., Jasper, A. A., Uhl, D., Meneghini, J., Osterkamp, I. C., Zvirtes, G., and Pires, E. F. (2016). Evidence for palaeo-wildfire in the Late Permian palaeotropics—Charcoal from the Motuca Formation in the Parnaíba Basin, Brazil. *Palaeogeography, Palaeoclimatology, Palaeoecology*, 450:122–128.

Kearey, P., Brooks, M., and Hill, I. (2013). *An Introduction to Geophysical Exploration*. Blackwell Publishing.

Kincare, K. and Larson, G. (2009). Evolution of the Great Lakes. In *Michigan Geography and Geology*, number March, pages 174–190.

Klein, E. L. and Moura, C. A. V. (2008). São Luís Craton and Gurupi Belt (Brazil): Possible links with the West African Craton and surrounding Pan-African belts. *Geological Society, London, Special Publications*, 294(1):137–151.

Klein, E. L., Moura, C. A. V., Krymsky, R. S., and Griffin, W. L. (2005). The Gurupi Belt, northern Brazil: Lithostratigraphy, geochronology, and geodynamic evolution. *Precambrian Research*, 141(3):83–105.

Klein, G. D. (1991). Origin and evolution of North American cratonic basins. *South African journal of geology*, 94(1):3–18.

Klein, G. D. (1995). Intracratonic basins. *Tectonics of Sedimentary Basins*, pages 459–478.

Klein, G. V. V. and Hsui, A. T. (1987). Origin of cratonic basins. *Geology*, 15(12):1094–1098.

Koptev, A. I. and Ershov, A. V. (2011). Thermal thickness of the Earth's lithosphere: A numerical model. *Moscow University Geology Bulletin*, 66(5):323–330.

Korenaga, J., Holbrook, W. S., Kent, G. M., Kelemen, P. B., Detrick, R. S., Larsen, H. C., Hopper, J. R., and Dahl-Jensen, T. (2000). Crustal structure of the southeast Greenland margin from joint refraction and reflection seismic tomography. *Journal of Geophysical Research*, 105(B9):21591–21614.

Korsch, R. J., Huazhao, M., Zhaocai, S., and Gorter, J. D. (1991). The Sichuan basin, southwest China: a late proterozoic (Sinian) petroleum province. *Precambrian Research*, 54(1):45–63.

Krishna, M. R., Chand, S., and Subrahmanyam, C. Y. (2000). Gravity anomalies, sediment loading and lithospheric flexure associated with the Krishna-Godavari basin, eastern continental margin of India. *Earth and Planetary Science Letters*, 175:223–232.

Kusznir, N. J., Hunsdale, R., and Roberts, A. M. (2004). Timing of depth-dependent lithosphere stretching on the S. Lofoten rifted margin offshore mid-Norway: Pre-breakup or post-breakup? *Basin Research*, 16(2):279–296.

Lambeck, K. (1983a). Structure and evolution of the intracratonic basins of central Australia. *Geophysical Journal International*, 74(3):843–886.

Lambeck, K. (1983b). The role of compressive forces in intracratonic basin formation and mid-plate orogenies. *Geophysical Research Letters*, 10(9):845–848.

Laux, J. H., Pimentel, M. M., Dantas, E. L., Armstrong, R., and Junges, S. L. (2005). Two neoproterozoic crustal accretion events in the Brasília belt, central Brazil. *Journal of South American Earth Sciences*, 18(2):183–198.

Linol, B. (2013). *Sedimentology and Sequence Stratigraphy of the Congo and Kalahari Basins of South- Central Africa and Their Evolution During the Formation and Break-Up of West Gondwana*. PhD thesis, Nelson Mandela Metropolitan University.

Liu, S. and Nummedal, D. (2004). Late Cretaceous subsidence in Wyoming: Quantifying the dynamic component. *Geology*, 32(5):397–400.

Loureiro, A., Afilhado, A., Matias, L., Moulin, M., and Aslanian, D. (2016). Monte Carlo approach to assess the uncertainty of wide-angle layered models: Application to the Santos Basin, Brazil. *Tectonophysics*, 683:286–307.

Lucazeau, F., Armitage, J. J., and Kabongo, É. K. (2015). *Thermal Regime and Evolution of the Congo Basin as an Intracratonic Basin*, pages 229–244. Springer Berlin Heidelberg, Berlin, Heidelberg.

Ludwig, W. J., Nafe, J. E., and Drake, C. L. (1970). Seismic refraction. In Maxwell, A. E., editor, *The Sea*, volume 4, pages 53–84. Wiley-Interscience, New York.

Luz, R. M. N., Julia, J., and do Nascimento, A. F. (2015a). Bulk crustal properties of the Borborema Province, NE Brazil, from P-wave receiver functions: Implications for models of intraplate Cenozoic uplift. *Tectonophysics*, 644-645:81–91.

Luz, R. M. N., Julià, J., and do Nascimento, A. F. (2015b). Crustal structure of the eastern Borborema Province, NE Brazil, from the joint inversion of receiver functions and surface wave dispersion: Implications for plateau uplift. *Journal of Geophysical Research: Solid Earth*, 120(5):3848–3869.

Mabesoone, J. M. (1977). Paleozoic-mesozoic deposits of the Piauí-Maranhão syneclise (Brazil): Geological history of a sedimentary basin. *Sedimentary Geology*, 19:7–38.

Madon, M. B. (1995). *Tectonic evolution of the Malay and Penyu Basins, offshore Peninsular Malaysia*. Dphil, University of Oxford.

Madon, M. B. and Watts, A. B. (1998). Gravity anomalies, subsidence history and the tectonic evolution of the Malay and Penyu Basins (offshore Peninsular Malaysia). *Basin Research*, 10(4):375–392.

Matos, R. M. D. (1992). The northeast Brazilian rift system. *Tectonics*, 11(4):766–791.

Matthews, K. J., Maloney, K. T., Zahirovic, S., Williams, S. E., Seton, M., and Müller, R. D. (2016). Global plate boundary evolution and kinematics since the late Paleozoic. *Global and Planetary Change*, 146:226–250.

Maxwell, A. E. (1971). New concepts of sea floor evolution: Regional observations concepts. In *The Sea (Vol. 4)*. Harvard University Press, New York.

Mazzarini, F., Corti, G., Manetti, P., and Innocenti, F. (2004). Strain rate and bimodal volcanism in the continental rift: Debre Zeyt volcanic field, northern MER, Ethiopia. *Journal of African Earth Sciences*, 39(3):415–420.

McKay, A. E. (1954). Review of Pattern Shooting. *Geophysics*, 19(3):420–437.

McKenzie, D. P. (1967). Some remarks on heat flow and gravity anomalies. *Journal of Geophysical Research*, 72(24):6261–6273.

McKenzie, D. P. (1978). Some remarks on the development of sedimentary basins. *Earth and Planetary Science Letters*, 40(1):25–32.

McKenzie, D. P., Jackson, J., and Priestley, K. (2005). Thermal structure of oceanic and continental lithosphere. *Earth and Planetary Science Letters*, 233(3):337–349.

McKenzie, D. P. and Parker, R. L. (1967). The North Pacific: An Example of Tectonics on a Sphere. *Nature*, 216(5122):1276–1280.

McKenzie, D. P. and Priestley, K. (2016). Speculations on the formation of cratons and cratonic basins. *Earth and Planetary Science Letters*, 435:94–104.

Meert, J. G. and Van Der Voo, R. (1997). The assembly of Gondwana 800-550 Ma. *Journal of Geodynamics*, 23(3-4):223–235.

Mei, S., Suzuki, A. M., Kohlstedt, D. L., Dixon, N. A., and Durham, W. B. (2010). Experimental constraints on the strength of the lithospheric mantle. *Journal of Geophysical Research: Solid Earth*, 115(B8).

Meinesz, F. A. V. (1941). *Gravity over the Hawaiian Archipelago and over the Madeira area, conclusions about the Earth's crust.*

Merle, R., Marzoli, A., Bertrand, H., Reisberg, L., Verati, C., Zimmermann, C., Chiaradia, M., Bellieni, G., and Ernesto, M. (2011). 40Ar/39Ar ages and Sr-Nd-Pb-Os geochemistry of CAMP tholeiites from Western Maranhão basin (NE Brazil). *Lithos*, 122(3-4):137–151.

Mesner, J. C. and Wooldridge, L. C. P. (1964). Maranhão Paleozoic basin and Cretaceous coastal basins, north Brazil. *Bulletin of the American Association of Petroleum Geologists*, 48(9):1475–1512.

Miao, S. Q., Li, H. P., and Chen, G. (2014). Temperature dependence of thermal diffusivity, specific heat capacity, and thermal conductivity for several types of rocks. *Journal of Thermal Analysis and Calorimetry*, 115(2):1057–1063.

Middleton, M. F. (1989). A model for the formation of intracratonic sag basins. *Geophysical Journal International*, 99(3):665–676.

Milani, E. J. and De Wit, M. J. (2008). Correlations between the classic Paraná and Cape–Karoo sequences of South America and southern Africa and their basin infills flanking the Gondwanides: du Toit revisited. *Geological Society, London, Special Publications*, 294(1):319–342.

Milani, E. J. and Zalan, P. V. (1999). An Outline of the Geology and Petroleum Systems of the Paleozoic Interior Basins of South America. *Episodes*, 22(3):7.

Milkereit, B. and Spencer, C. (1989). Noise suppression and coherency enhancement of seismic data. In Agterberg, F.P. and Bonham-Carter, G., editor, *Statistical application in the earth sciences*, volume 89-9, pages 243–248. Geological Survey of Canada.

Molnar, P., England, P. C., and Jones, C. H. (2015). Mantle dynamics, isostasy, and the support of high terrain. *Journal of Geophysical Research: Solid Earth*, 120(3):1932–1957.

Mooney, W. D. and Kaban, M. K. (2010). The North American upper mantle: Density, composition, and evolution. *Journal of Geophysical Research*, 115(B12):1–24.

Morais Neto, J. M., Hegarty, K. A., Karner, G. D., and Alkmim, F. F. (2009). Timing and mechanisms for the generation and modification of the anomalous topography of the Borborema Province, northeastern Brazil. *Marine and Petroleum Geology*, 26(7):1070–1086.

Morel-A-L Huissier, P., Green, A. G., and Pike, C. J. (1987). Crustal refraction surveys across the Trans-Hudson Orogen/Williston Basin of south central Canada. *Journal of Geophysical Research: Solid Earth*, 92(B7):6402–6420.

Morgan, W. J. (1968). Rises, Trenches, Great Faults and Crustal Blocks. *Journal of Geophysical Research*, 73(6):1959–1982.

Moulin, M., Aslanian, D., and Unternehr, P. (2010). A new starting point for the South and Equatorial Atlantic Ocean. *Earth-Science Reviews*, 98(1-2):1–37.

Moura, C. A. V., Pinheiro, B. L. S., Nogueira, A. C. R., Gorayeb, P. S. S., and Galarza, M. A. (2008). Sedimentary provenance and palaeoenvironment of the Baixo Araguaia Supergroup: constraints on the palaeogeographical evolution of the Araguaia Belt and assembly of West Gondwana. *Geological Society, London, Special Publications*, 294(1):173–196.

Müller, R. D., Sdrolias, M., Gaina, C., and Roest, W. R. (2008). Age, spreading rates, and spreading asymmetry of the world's ocean crust. *Geochemistry, Geophysics, Geosystems*, 9(4):1–19.

Naimark, B. M. and Ismail-Zadeh, A. T. (1995). Numerical models of a subsidence mechanism in intracratonic basins: Application to North American basins. *Geophysical Journal International*, 123(1):149–160.

Neves, S. P. (2003). Proterozoic history of the Borborema province (NE Brazil): Correlations with neighboring cratons and Pan-African belts and implications for the evolution of western Gondwana. *Tectonics*, 22(4).

Neves, S. P., Bruguier, O., Vauchez, A., Bosch, D., da Silva, J. M. R., and Mariano, G. (2006). Timing of crust formation, deposition of supracrustal sequences, and Transamazonian and Brasiliano metamorphism in the East Pernambuco belt (Borborema Province, NE Brazil): Implications for western Gondwana assembly. *Precambrian Research*, 149(3):197–216.

Neves, S. P., Lages, G. A., Brasilino, R. G., and Miranda, A. W. A. (2015). Paleoproterozoic accretionary and collisional processes and the build-up of the Borborema Province (NE Brazil): Geochronological and geochemical evidence from the Central Domain. *Journal of South American Earth Sciences*, 58:165–187.

Neves, S. P., Monie, P., Bruguier, O., and da Silva, M. J. R. (2012). Geochronological, thermochronological and thermobarometric constraints on deformation, magmatism and thermal regimes in eastern Borborema Province (NE Brazil). *Journal of South American Earth Sciences*, 38:129–146.

Nowell, D. A. G. (1999). Gravity terrain corrections — an overview. *Journal of Applied Geophysics*, 42(2):117–134.

Nunn, J. A. and Aires, J. R. (1988). Gravity Anomalies and Flexure of the Lithosphere at the Middle Amazon Basin, Brazil. *Journal of Geophysical Research*, 93(B1):415–428.

Nunn, J. A. and Sleep, N. H. (1984). Thermal contraction and flexure of intracratonal basins: a three-dimensional study of the Michigan basin. *Geophysical Journal of the Royal Astronomical Society*, 76(3):587–635.

Okaya, D., Stern, T. A., Holbrook, S., van Avendonk, H., Davey, F., and Henrys, S. (2003). Imaging a plate boundar using double-sided onshore-offshore seismic profiling. *The Leading Edge*, 22(3):256.

Oliphant, T. E. (2007). Python for Scientific Computing Python Overview. *Computing in Science and Engineering Engineering*, pages 10–20.

Oliveira, E. P., McNaughton, N. J., Windley, B. F., Carvalho, M. J., and Nascimento, R. S. (2015). Detrital zircon U-Pb geochronology and whole-rock Nd-isotope constraints on sediment provenance in the Neoproterozoic Sergipano orogen, Brazil: From early passive margins to late foreland basins. *Tectonophysics*, 662:183–194.

Oliveira, E. P., Windley, B. F., and Araújo, M. N. C. (2010). The Neoproterozoic Sergipano orogenic belt, NE Brazil : A complete plate tectonic cycle in western Gondwana. *Precambrian Research*, 181(1):64–84.

Oncken, O., Asch, G., Haberland, C., Metchie, J., Sobolev, S., Stiller, M., Yuan, X., Brasse, H., Buske, S., Giese, P., Görze, H. J., Lueth, S., Scheuber, E., Shapiro, S., Wigger, P., Yoon, M. K., Bravo, P., Vieytes, H., Chong, G., Gonzales, G., Wilke, H. G., Lüschen, E., Martinez, E., Rössling, R., Ricaldi, E., and Rietbrock, A. (2003). Seismic imaging of a convergent continental margin and plateau in the central Andes (Andean Continental Research Project 1996 (ANCORP'96). *Journal of Geophysical Research: Solid Earth*, 108(B7).

Oriolo, S., Oyhantçabal, P., Wemmer, K., and Siegesmund, S. (2017). Contemporaneous assembly of Western Gondwana and final Rodinia break-up: Implications for the supercontinent cycle. *Geoscience Frontiers*.

Padilha, A. L., Vitorello, Í., Pádua, M. B., and Bologna, M. S. (2014). Electromagnetic constraints for subduction zones beneath the northwest Borborema province : Evidence for Neoproterozoic island arc – continent collision in northeast Brazil SO. *Geology*, 42(1):91–94.

Paixao, M. A. P., Nilson, A. A., and Dantas, E. L. (2008). The Neoproterozoic Quatipuru ophiolite and the Araguaia fold belt, central-northern Brazil, compared with correlatives in NW Africa. *Geological Society, London, Special Publications*, 294(1):297–318.

Pap, A. (1983). Source and receiver arrays. Technical report, Amoco, Canada.

Parker, R. (1973). The rapid calculation of potential anomalies. *Geophysical Journal International*, 31(4):447–455.

Parr, J. O. and Mayne, W. H. (1955). A new method of pattern shooting. *Geophysics*, 20(3):539–564.

Parsons, B. and Sclater, J. G. (1977). An analysis of the variation of ocean floor bathymetry and heat flow with age. *Journal of Geophysical Research*, 82(6):803–827.

Pavlis, N. K., Holmes, S. A., Kenyon, S. C., and Factor, J. K. (2012). The development and evaluation of the Earth Gravitational Model 2008 (EGM2008). *Journal of Geophysical Research: Solid Earth*, 117(B4).

Pawlak, A., Eaton, D. W., Bastow, I. D., Kendall, J. M., Helffrich, G., Wookey, J., and Snyder, D. (2011). Crustal structure beneath Hudson Bay from ambient-noise tomography: Implications for basin formation. *Geophysical Journal International*, 184(1):65–82.

Peacock, K. L. and Treitel, S. (1969). Predictive deconvolution: Theory and practice. *Geophysics*, 34(2):155–169.

Pimentel, M. M. (2016). The tectonic evolution of the Neoproterozoic Brasília Belt, central Brazil: A geochronological and isotopic approach. *Brazilian Journal of Geology*, 46:67–82.

Pimentel, M. M. and Fuck, R. A. (1992). Neoproterozoic crustal accretion in central Brazil. *Geology*, 20(4):375–379.

Pimentel, M. M., Fuck, R. A., Jost, H., Ferreira Filho, C. F., and Araújo, S. M. (2000). Geology of the central part of the Tocantins Province: Implications for the geodynamic history of the Brasília belt. *Tectonic Evolution of South America*, pages 195–229.

Pollack, H. N., Hurter, S. J., and Johnson, R. (1993). Heat flow from the Earth's interior: Analysis of the global data set. *Reviews of Geophysics*, 31(3):267–280.

Ponciano, L. C. M. O. and Della Fávera, J. C. (2009). Flood-dominated fluvio-deltaic system: A new depositional model for the Devonian Cabeças Formation, Parnaíba Basin, Piauí, Brazil. *Anais da Academia Brasileira de Ciências*, 81(4):769–780.

Porto, A., Daly, M. C., La Terra, E., and Fontes, S. L. (Accepted). The pre-Silurian Riachão basin: A new perspective on the basement of the Parnaíba basin, NE Brazil. *Geological Society, London, Special Publications*.

Porto, A. L. and Pereira, E. (2014). Seismic Interpretation of Igneous Intrusions and Their Implications for an Unconventional Petroleum System in Southeastern Parnaìba Basin, Northeastern Brazil. *AGU Fall Meeting Abstracts*.

Pratt, J. H. (1855). On the attraction of the Himalaya Mountains, and of the elevated regions beyond them, upon the plumb-line in India. *Philosophical Transactions of the Royal Society of London*, 145:53–100.

Price, R. A. (1973). Large-scale gravitational flow of supra- crustal rocks, Southern Canadian Rockies. In DeJong K A and Scholten, R., editor, *Gravity and tectonics*, pages 491–502. Wiley-Interscience, New York.

Priestley, K. and McKenzie, D. P. (2006). The thermal structure of the lithosphere from shear wave velocities. *Earth and Planetary Science Letters*, 244(1):285–301.

Priestley, K. and McKenzie, D. P. (2013). The relationship between shear wave velocity, temperature, attenuation and viscosity in the shallow part of the mantle. *Earth and Planetary Science Letters*, 381:78–91.

Prijac, C., Doin, M. P., Gaulier, J. M., and Guillocheau, F. (2000). Subsidence of the Paris Basin and its bearing on the late Variscan lithosphere evolution: A comparison between Plate and Chablis models. *Tectonophysics*, 323(1-2):1–38.

Putnam, G. R. (1912). Condition of the Earth's Crust. *Science*, 36(938):869–872.

Quinlan, G. M. and Beaumont, C. (1984). Appalachian thrusting, lithospheric flexure, and the Paleozoic stratigraphy of the eastern interior of North America. *Canadian Journal of Earth Sciences*, 21(9):973–996.

Raiga-Clemenceau, J., Martin, J. P., and Nicoletis, S. (1986). The concept of acoustic formation factor for more accurate porosity determination from sonic transit time data. *Society of Petrophysicists and Well log analysts*.

Rapalini, A. E., Bettucci, L. S., Tohver, E., Valencio, L. D. P. D. A., and Básicas, A. (2016). Paleomagnetic evidence of a Late ediacaran ocean in South America? In *Latinmag Letters*, volume 6, pages 1–4.

Rappin, N. and Dunn, R. (2006). *wxPython in Action*. Manning Publications.

Ravens, J. (1999). Globe Claritas seismic processing dictionary. *Institute of Geological and Nuclear Sciences Limited*.

Raymer, L. L., Hunt, E. R., and Gardner, J. S. (1980). An improved sonic transit time-to-porosity transform. *Society of Petrophysicists and Well-Log Analysts*.

Reford, S. (1964). Magnetic anomalies over thin sheets. *Geophysics*, XXIX(4):532–536.

Regone, C. J. (1997). Measurement and identification of 3-D coherent noise generated from irregular surface carbonates. In *Carbonate Seismology*, chapter 11, pages 281–306. Society of Exploration Geophysicists.

Roberts, D. G. and Bally, A. W. (2012). *Regional geology and tectonics: Phanerozoic passive margins, cratonic basins and global tectonic maps*. Elsevier.

Roman, A. and Jaupart, C. (2016). The fate of mafic and ultramafic intrusions in the continental crust. *Earth and Planetary Science Letters*, 453:131–140.

Rossetti, D. F., Paz, J. D. S., and Góes, A. M. (2004). Facies analysis of the Codó Formation (Late Aptian) in the Grajaú Area, Southern São Luís-Grajaú Basin. *Anais da Academia Brasileira de Ciencias*, 76(4):791–806.

Royden, L. and Keen, C. E. (1980). Rifting process and thermal evolution of the continental margin of Eastern Canada determined from subsidence curves. *Earth and Planetary Science Letters*, 51(2):343–361.

Saunders, A. D., England, R. W., Reichow, M. K., and White, R. V. (2005). A mantle plume origin for the Siberian traps: Uplift and extension in the West Siberian Basin, Russia. *Lithos*, 79(3-4 SPEC. ISS.):407–424.

Scherwath, M. (2002). *Lithospheric structure and deformation in an oblique continental collision zone, South Island, New Zealand*. PhD thesis, Victoria University of Wellington.

Scintrex, L. (2006). Scintrex CG-5 Operation Manual. Technical report.

Sclater, J. G. and Christie, P. A. F. (1980). Continental streching: An explanation of the post-mid-cretaceous subsidence of the central North Sea Basin. *Journal of Geophysical Research: Solid Earth*, 85(B7):3711–3739.

Scotese, C. R. (2016). PALEOMAP PaleoAtlas for GPlates and the PaleoData Plotter Program. *PALEOMAP Project*, 3(10).

Shen, W., Ritzwoller, M. H., and Schulte-Pelkum, V. (2013). Crustal and uppermost mantle structure in the central U.S. encompassing the Midcontinent Rift. *Journal of Geophysical Research: Solid Earth*, 118(8):4325–4344.

Sheriff, R. E. and Geldart, L. P. (1995). *Exploration seismology*. Cambridge University Press, Cambridge.

Sleep, N. H. (1971). Thermal Effects of the Formation of Atlantic Continental Margins by Continental Break up.

Sleep, N. H. (2009). Stagnant lid convection and the thermal subsidence of sedimentary basins with reference to Michigan. *Geochemistry, Geophysics, Geosystems*, 10(12).

Sleep, N. H., Nunn, J. A., and Chou, L. (1980). Platform basins. *Annual Review of Earth and Planetary Sciences*, 8(1):17–34.

Sleep, N. H. and Snell, N. S. (1976). Thermal contraction and flexure of midcontinent and atlantic marginal basins. *Geophysical Journal International*, 45(1):125–154.

Sloss, L. L. (1963). Sequences in the cratonic interior of North America. *Geological Society of America Bulletin*, 74(2):93–114.

Sloss, L. L. (1988). Forty years of sequence stratigraphy. *Bulletin of the Geological Society of America*, 100(11):1661–1665.

Sloss, L. L. and Scherer, W. (1975). Geometry of Sedimentary Basins: Applications to Devonian of North America and Europe. *Geological Society of America Memoirs*, 142:71–88.

Soares, P. C., Barbosa Landim, P. M., and Fulfaro, V. J. (1978). Tectonic cycles and sedimentary sequences in the Brazilian intracratonic basins. *Bulletin of the Geological Society of America*, 89(2):181–191.

Solon, F. F., Fontes, S. L., and La Terra, E. F. (2016). Electromagnetic studies in the Parnaíba Basin: structural characterization by MT imaging. In *AGU Fall Meeting Abstracts*, Porto Alegre.

Soures, S., Fuck, R. A., de Lima, M. V. A. G., Araújo, V., Lima, F., Rocha, F. A. S., and Trindade, C. R. (In review). WARR structure of the lithospere of Parnaiba Basin Brazil. *Geological Society, London, Special Publications*.

Sousa, M. A. D. (1996). *Regional Gravity Modelling and Geohistory of the Parnaiba Basin (NE Brazil)*. Phd, University of Newcastle upon Tyne.

Stampfli, G. M., Hochard, C., Vérard, C., Wilhem, C., and VonRaumer, J. (2013). The formation of Pangea. *Tectonophysics*, 593:1–19.

Steckler, M. S. and Watts, A. B. (1978). Subsidence of the Atlantic-type continental margin off New York. *Earth and Planetary Science Letters*, 41(1):1–13.

Stein, C. A., Kley, J., Stein, S., Hindle, D., and Keller, G. R. (2014). North America's Midcontinent Rift: When rift met LIP. *Geosphere*, 11(5):1607–1616.

Stel, H., Cloetingh, S., Heeremans, M., and van der Beek, P. (1993). Anorogenic granites, magmatic underplating and the origin of intracratonic basins in a non-extensional setting. *Tectonophysics*, 226(1-4):285–299.

Stern, T. A., Stratford, W. R., Seward, A., Henderson, C. M., Savage, M., Smith, E. G. C., Benson, A., Greve, S., and Salmon, M. L. (2010). Crust-mantle structure of the central North Island, New Zealand, based on seismological observations. *Journal of Volcanology and Geothermal Research*, 190(1):58–74.

Sweeney, J. F. (1977). Subsidence of the Sverdrup Basin, Canadian Arctic Islands. *Bulletin of the Geological Society of America*, 88(1):41–48.

Swezey, C. S. (2008). *Regional stratigraphy and petroleum systems of the Michigan Basin, North America*. Number 2978. Geological Survey (US).

Takin, M. and Talwani, M. (1966). Rapid Attraction Computation of the Gravitation of Topography Earth. *Geophysical Prospecting*, 4(2):119–142.

Talwani, M. and Ewing, M. (1960). Rapid computation of gravitational attraction of three-dimensional bodies of arbitrary shape. *Geophysics*, 25(1):203–225.

Talwani, M. and Heirtzler, J. R. (1964). Computation of magnetic anomalies caused by two dimensional bodies of arbitrary shape. In *Computers in the mineral industries, Part 1*, volume 9, pages 464–480.

Talwani, M., Worzel, J. L., and Landisman, M. (1959). Rapid Gravity Computations for Two-Dimensional Bodies with Application to the Mendocino Submarine Fracture Zone. *Journal of Geophysical Research*, 64(1):49–59.

Taner, M. T., Koehler, F., and Sheriff, R. E. (1979). Complex seismic trace analysis. *Geophysics*, 44(6):1041–1063.

Taner, M. T. and Sheriff, R. E. (1977). Application of Amplitude, Frequency, and Other Attributes to Stratigraphic and Hydrocarbon Determination. *AAPG Memoir: Seismic Stratigraphy–Applications to Hydrocarbon Exploration*, 165:301–327.

Taylor, H. G. (1931). Method of recording seismic waves.

Teixeira, W. and Figueiredo, M. C. H. (1991). An outline of Early Proterozoic crustal evolution in the Sgo Francisco craton, Brazil: A review. *Precambrian Research*, 53(1-2):1–22.

Teixeira, W., Tassinari, C. C. G., Cordani, U. G., and Kawashita, K. (1989). A review of the geochronology of the Amazonian Craton: Tectonic implications. *Precambrian Research*, 42(3-4):213–227.

Telford, W. M., Geldart, L. P., and Sheriff, R. E. (1990). *Applied Geophysics*. Cambridge University Press, 2 edition.

Torsvik, T. H., Van der Voo, R., Preeden, U., Niocaill, C. M., Steinberger, B., Doubrovine, P. V., van Hinsbergen, D. J. J., Domeier, M., Gaina, C., Tohver, E., Meert, J. G., McCausland, P. J. A., and Cocks, L. R. M. (2012). Phanerozoic polar wander, palaeogeography and dynamics. *Earth-Science Reviews*, 114(3):325–368.

Treitel, S. (1974). The complex wiener filter. *Geophysics*, 39(2):169–173.

Trindade, V. S. F., Carvalho, M. D. A., and Borghi, L. (2015). Palynofacies patterns of the Devonian of the Parnaíba Basin, Brazil: Paleoenvironmental implications. *Journal of South American Earth Sciences*, 62:164–175.

Trompette, R. (1997). Neoproterozoic (600 Ma) aggregation of Western Gondwana: A tentative scenario. *Precambrian Research*, 82(1-2):101–112.

Trouw, R. A., Heilbron, M., Ribeiro, A., Paciullo, F. V. P., Valeriano, C. M., Almeida, J. C. H., Tupinambá, M., and Andreis, R. R. (2000). The Central Segment of the Ribeira Belt. *Tectonic Evolution of South America*, 31:287–310.

Tsuboi, C. (1983). Gravity. *Ciel et Terre*, 99:159.

Turcotte, D. L. and Schubert, G. (1982). Geodynamics: Applications of continuum physics to geological problems.

Uieda, L., Oliveira Jr, V. C., and Barbosa, V. C. (2013). Modeling the Earth with Fatiando a Terra. *Proceedings of the 12th Python in Science Conference*, (Scipy):90–96.

Ussami, N. and Molina, E. C. (1999). Flexural modeling of the neoproterozoic Araguaia belt, central Brazil. *Journal of South American Earth Sciences*, 12(1):87–98.

Vacher, P. and Souriau, A. (2001). A three-dimensional model of the Pyrenean deep structure based on gravity modelling, seismic images and petrological constraints. *Geophysical Journal International*, 145(2):460–470.

Valeriano, C. M., Machado, N., Simonetti, A., Valladares, C. S., Seer, H. J., and Simões, L. S. A. (2004). U Pb geochronology of the southern Brasília belt (SE-Brazil): Sedimentary provenance, Neoproterozoic orogeny and assembly of West Gondwana. *Precambrian Research*, 130(1):27–55.

Valeriano, C. M., Pimentel, M. M., Heilbron, M., Almeida, J. C. H., and Trouw, R. A. J. (2008). Tectonic evolution of the Brasília Belt, Central Brazil, and early assembly of Gondwana. *Geological Society, London, Special Publications*, 294(1):197–210.

Van Der Voo, R. and Watts, D. R. (1978). Paleomagnetic results from igneous and sedimentary rocks from the Michigan Basin borehole. *Journal of Geophysical Research: Solid Earth*, 83(B12):5844–5848.

Van Der Walt, S. S., Colbert, S. C., and Varoquaux, G. G. G. (2011). The NumPy array: A structure for efficient numerical computation. *Computing in Science and Engineering*, 13(2):22–30.

Vaz, P. T., Rezende, N. G. A. M., Wanderley Filho, J. R., and Silva Travassos, W. A. (2007). Bacia do Parnaíba. *Boletim de Geociencias da Petrobras*, 15(2):253–263.

Vernengo, L. and Trinchero, E. (2015). Application of amplitude volume technique attributes, their variations, and impact. *The Leading Edge*, 34(10):1246–1253.

Vine, F. J. and Matthews, D. H. (1963). Magnetic Anomalies over ocean ridges. *Nature*, 199:947–949.

Walcott, R. I. (1970). Flexural rigidity, thickness, and viscosity of the lithosphere. *Journal of Geophysical Research*, 75(20):3941–3954.

Watts, A. B. (1978). An analysis of isostasy in the world's oceans 1. Hawaiian-Emperor Seamount Chain. *Journal of Geophysical Research: Solid Earth*, 83(B12):5989–6004.

Watts, A. B. (1982). Tectonic subsidence, flexure and global changes of sea level. *Nature*, 297(5866):469–474.

Watts, A. B. (1988). Gravity anomalies, crustal structure and flexure of the lithosphere at the Baltimore Canyon Trough. *Earth and Planetary Science Letters*, 89(2):221–238.

Watts, A. B. (2001). *Isostasy and Flexure of the Lithosphere*. Cambridge University Press, Cambridge.

Watts, A. B. (2011). Isostasy. In Gupta, H. K., editor, *Encyclopedia of Solid Earth Geophysics*, pages 647–662. Springer Netherlands.

Watts, A. B. and Fairhead, J. D. (1999). A process-oriented approach to modeling the gravity signature of continental margins. *The Leading Edge*, 18(2):258–263.

Watts, A. B. and Fairhead, J. D. (2013). Gravity anomalies and magmatism along the western continental margin of the British Isles. *Journal of the Geological Society*, 154(3):523–529.

Watts, A. B. and Moore, J. D. P. (2017). Flexural isostasy: Constraints from gravity and topography power spectra. *Journal of Geophysical Research: Solid Earth*.

Watts, A. B. and Ryan, W. B. F. (1976). Flexure of the lithosphere and continental margin basins. *Tectonophysics*, 36(1-3):25–44.

Watts, A. B., Weissel, J. K., Duncan, R. A., and Larson, R. L. (1988). Origin of the Louisville Ridge and its relationship to the Eltanin fracture zone system. *Journal of Geophysical Research: Solid Earth*, 93(B4):3051–3077.

Watts, A. B. and Zhong, S. J. (2000). Observations of flexure and the rheology of oceanic lithosphere. *Geophysical Journal International*, 142(3):855–875.

Watts, A. B., Zhong, S. J., and Hunter, J. (2013). The Behavior of the Lithosphere on Seismic to Geologic Timescales. *Annual Review of Earth and Planetary Sciences*, 41:443–468.

Wernicke, B. (1985). Uniform-sense normal simple shear of the continental lithosphere. *Canadian Journal of Earth Sciences*, 22(1):108–125.

Wessel, P., Smith, W. H. F., Scharroo, R., Luis, J., and Wobbe, F. (2013). Generic mapping tools: improved version released. *Eos, Transactions American Geophysical Union*, 94(45):409–410.

White, N. and McKenzie, D. P. (1988). Formation of the "steer's head" geometry of sedimentary basins by differential stretching of the crust and mantle. *Geology*, 16(3):250–253.

White, R. S. (1993). Melt Production Rates in Mantle Plumes. *Philosophical Transactions of the Royal Society A: Mathematical, Physical and Engineering Sciences*, 342(1663):137–153.

Wilson, J. T. (1965). A New Class of Faults and their Bearing on Continental Drift. *Nature*, 207(4995):343–347.

Worzel, J. L. and Shurbet, G. L. (1955). Gravity anomalies at continental margins. *Proceedings of the National Academy of Sciences*, 41(7):458–469.

Wyllie, M. R. J., Gregory, A. R., and Gardner, L. W. (1956). Elastic wave velocities in heterogeneous and porus media. *Geophysics*, 21(1):41–70.

Xie, X. and Heller, P. L. (2009). Plate tectonics and basin subsidence history. *Geological Society of America Bulletin*, 121(1-2):55–64.

Yilmaz, Ö. (2001). *Seismic Data Analysis*, volume 1. Society of Exploration Geophysicists, Tulsa, Okla., 2nd edition.

Zelt, C. A. (1999). Modelling strategies and model assessment for wide-angle seismic traveltime data. *Geophysical Journal International*, 139(1):183–204.

Zelt, C. A. and Smith, R. B. (1992). Seismic traveltime inversion for 2-D crustal velocity structure. *Geophysical journal international*, 108(1):16–34.

Zhang, N., Zhong, S. J., and Flowers, R. M. (2012). Predicting and testing continental vertical motion histories since the Paleozoic. *Earth and Planetary Science Letters*, 317:426–435.

Zhong, S. J. and Watts, A. B. (2013). Lithospheric deformation induced by loading of the Hawaiian Islands and its implications for mantle rheology. *Journal of Geophysical Research: Solid Earth*, 118(11):6025–6048.

Zhu, T. and Brown, L. D. (1986). Consortium for continental reflection profiling Michigan surveys: Reprocessing and results. *Journal of Geophysical Research*, 91(B11):11477–11495.